UPSETTING OF HOLLOW FLANGED COMPONENTS

By

Seyed Abbas Shahmoradi

October 1981

A thesis submitted for the degree of
Doctor of Philosophy of the University
of London and for the Diploma of
Imperial College.

Mechanical Engineering Department
Imperial College
London, S.W.7.

To

Imam Khomeini

"Whoso desires the tillage of the world to
come, We shall give him increase in his
tillage; and whoso desires the tillage
of this world, We shall give him of
it, but in the world to come he
will have no share."

(Sura Counsel, 19)

SYNOPSIS

Production of hollow flanged components by upsetting tubular billets often results in a product with one or more of the following defects: i) Bulging of the bore surface which may result in formation of a fold in the region. ii) Necking and fracture at the outer surface of the flange. iii) Non-uniform shape of the flange which necessitates an additional forming operation to obtain the desired final shape.

Studying the shape and quality of the flange and behaviour of the metal under various geometrical and frictional conditions can provide the required working conditions for the production of hollow flanged components with fewer defects.

In the present work, the mode of deformation and the required upsetting loads are studied in conventional and injection upsetting. A visual examination of the upset products is made and the effect of billet geometries and end conditions on metal behaviour is investigated by etching the split flanged products.

The finite element technique is employed and a computer program is developed for predicting the deformation during heading and open upsetting processes. The load/displacement curve, geometrical changes of the billet, particle velocities and stress and strain distributions are computed. The results indicate good agreement between predictions and experiments, which proves the usefulness of the finite element method for detailed studies of deformation characteristics. Particular attention is given to the behaviour of material in the bore region, and from this the limiting values of free height and wall thickness of the original billet for the production of a hollow flanged component with straight bore surface (free of bulge) are obtained.

The effect of restraining hydrostatic pressure applied to the flange on changes in geometries and metal flow is studied by including this pressure in the computations. The minimum required hydrostatic pressures for the production of sound hollow flanged components are obtained for various geometries.

Also using the finite element program, the conventional upsetting of hollow billets into restricted cavities is studied as an alternative way of eliminating the bulging at the bore region.

A kinematically admissible velocity field is developed for injection upsetting to obtain forming loads by using an upper-bound technique.

ACKNOWLEDGEMENTS

I sincerely express my deepest gratitude to Dr. B. Lengyel for suggesting the topic and for his guidance and invaluable advice without which this project would have not been completed.

Thanks are due also to Mr. H. Ramsey for his kind permission to use the work-shop facilities and Mr. S.G. Bedley for his kind assistance in the production of the photographs.

Special thanks are also due to Mr. G. Yantian for reading the text and to Miss Caroline Roberts who patiently typed the manuscript.

The financial support and encouragement of my brother Mr. Hossein Shahmoradi is gratefully acknowledged and highly appreciated.

Last but not least the constant encouragement of my father, my mother and also my sister is acknowledged and highly appreciated.

Seyed Abbas Shahmoradi

October 1981.

CONTENTS

	Page
Synopsis	1
Acknowledgements	3
Contents	4
List of illustrations	9
Notations	
1. Introduction	23
1.1 Preface	23
1.2 Literature survey of upsetting	24
1.2.1 Simple upsetting	24
1.2.1.1 Solid cylinders	24
1.2.1.2 Hollow cylinders	29
1.2.2 Conventional upsetting	34
1.2.3 Injection upsetting	42
1.2.4 A comparison of conventional upsetting with injection upsetting	51
1.3 Finite element method	54
1.3.1 Introduction	54
1.3.2 Previous works	56
1.3.3 Present work	67
1.4 Upper-bound analysis	69
1.4.1 Introduction	69
1.4.2 Previous works	70
1.5 Aim and scope of the present work	73
2. Experimental materials and apparatus	74

2.1 Introduction 74
2.2 Materials 74
2.3 Design considerations 75
2.4 Press 75
2.5 Instrumentation 80
2.5.1 Load cell 80
2.5.2 Displacement transducer 80
2.5.3 Data logger 80
2.5.4 Surface profile measurements 83
2.6 Description of the sub-press 83
2.6.1 General layout 83
2.6.2 Injection upsetting 85
2.6.3 Conventional upsetting 87
2.7 Experimental procedure 88

3. Experimental results and discussion 101
3.1 Conventional upsetting 101
3.1.1 Load/displacement characteristics 101
3.1.2 Mode of deformation 124
3.2 Injection upsetting 134
3.2.1 Load/displacement characteristics 137
3.2.2 Mode of deformation 150

4. Theoretical work 163
4.1 Finite element analysis 163
4.1.1 Basic finite element formulation 163
4.1.1.1 Displacement function 163

4.1.1.2 Strains 164
4.1.1.3 Stresses 164
4.1.1.4 Equivalent nodal forces 165
4.1.1.5 General formulation (equilibrium condition) 166
4.1.2 Infinitesimal elastic-plastic formulation . . 168
4.1.2.1 Plasticity relations 169
4.1.2.2 Derivation of elastic-plastic stress-strain matrix $[D]^{EP}$ 171
4.1.2.3 Derivation of elastic-plastic stiffness matrix $[K]^{EP}$ 174
4.1.3 Elastic-plastic method of solution 175
4.1.3.1 Tangential stiffness matrix . . . 175
4.1.3.2 Initial strain method 179
4.1.3.3 Initial stress method 180
4.1.4 Elements used in computer programs 182
4.1.4.1 Constant strain triangle elements . . 183
4.1.4.2 Quadrilateral elements (consisting of four constant strain triangles) 188
4.2 Upper-bound analysis 191
4.2.1 Basic equations 191
4.2.1.1 Strain rates 191
4.2.1.2 Powers 192
4.2.1.3 Continuity 194
4.2.1.4 Incompressibility 195
4.2.2 Kinematically admissible velocity field for injection upsetting of hollow billets 195
4.2.3 Upper-bound solution 200

5. Elasto-plastic finite element computer programs 211

5.1 Introduction 211

5.2 Finite element modelling of the upsetting process of hollow cylinders 211

5.2.1 Introduction 211

5.2.2 Conventional upsetting 214

5.2.2.1 Heading 214

5.2.2.2 Open upsetting 217

5.2.3 Injection upsetting 219

5.2.4 Friction 221

5.2.5 Hydrostatic pressure 222

5.3 Computational procedure 224

5.4 Applying the boundary conditions 225

5.5 Solution of the system of equations 227

5.6 Description of the programs 228

5.6.1 Using triangular elements 228

5.6.2 Using quadrilateral elements 231

6. Results and discussion 234

6.1 Introduction 234

6.2 Finite element results for conventional upsetting . . 234

6.2.1 Choice of element 234

6.2.2 True stress-strain curves 236

6.2.3 Inclusion of the surface friction in the computer program 236

6.2.4 Loads and bulge formation 238

6.2.4.1 Introduction 238

6.2.4.2 A comparison of the theoretical and

experimental results 239

6.2.4.3 Effect of the original billet geometry on deformation 247

6.2.4.4 Effect of hydrostatic pressure during conventional upsetting 258

6.2.4.5 Conventional upsetting of hollow billets into restricted cavities 280

6.3 Failure of the finite element method for injection upsetting 290

6.4 Upper-bound loads in injection upsetting 292

7. Conclusions 314

7.1 Conventional upsetting 314

7.2 Injection upsetting 316

Appendix A 318

Appendix B 334

References 357

LIST OF ILLUSTRATIONS

1-1 Simple upsetting of a solid cylinder.

1-2 Simple upsetting of hollow cylinder.

1-3 Conventional upsetting of hollow billets.

1-4 Four methods of forming the head.

1-5 Diagrammatic representation of the operation of a single-blow split-die header.

1-6 Operation of a two-blow solid-die header.

1-7 Injection upsetting of hollow billets.

1-8 Injection upsetting of tubular billets, applying hydrostatic pressure, after Fuchs *(46)*.

1-9 Combined heading and backward extrusion of solid billet.

1-10 Combined heading and indenting of solid billet.

1-11 Combined piercing and injection upsetting, after Milner *(49)*.

2-1 True stress-strain curve for lead.

2-2 True stress-strain curve for commercially pure alumunium.

2-3 True stress-strain curve for copper.

2-4 Press and data logger.

2-5 Calibration curve for load-cell.

2-6 Calibration curve for displacement transducer.

2-7 Sub-press assembly.

2-8 Layout of tooling.

2-9 Tooling for injection upsetting hollow billets.

2-10 Tooling for injection upsetting hollow billets with one end constrained.

2-11 Tooling for injection upsetting solid bars.

2-12 Tooling for injection upsetting solid bars with one end constrained.

2-13 Tooling for heading hollow billets.

2-14 Tooling for heading solid bars.

2-15 Tooling for open upsetting hollow billets.

2-16 Tooling for open upsetting solid bars.

3-1 Typical products, heading and open upsetting hollow billets.

3-2 Typical products, heading and open upsetting solid bars.

3-3 Effect of initial unsupported height on the load/displacement characteristics in heading aluminium hollow billets.

3-4 Effect of initial unsupported height on the load/displacement characteristics in heading copper hollow billets.

3-5 Effect of initial unsupported height on the load/displacement characteristics in heading lead hollow billets.

3-6 Variation of upsetting load with percentage reduction in height in heading aluminium hollow billets.

3-7 Variation of upsetting load with percentage reduction in height in heading copper hollow billets.

3-8 Variation of upsetting load with percentage reduction in height in heading lead hollow billets.

3-9 Variation of upsetting load with percentage reduction in height in the heading of hollow billets of various wall thicknesses.

3-10 Variation of upsetting load with percentage reduction in height in heading hollow billets of the three materials used.

3-11 Effect of initial unsupported height on the load/displacement characteristics in the open upsetting of aluminium hollow billets.

3-12 Effect of initial unsupported height on load/displacement characteristics in the open upsetting of copper hollow billets.

3-13 Effect of initial unsupported height on load/displacement characteristics in the open upsetting of lead hollow billets.

3-14 Variation of upsetting load with percentage reduction in height in the open upsetting of aluminium hollow billets.

3-15 Variation of upsetting load with percentage reduction in height in the open upsetting of copper hollow billets.

3-16 Variation of upsetting load with percentage reduction in height in the open upsetting of lead hollow billets.

3-17 Variation of upsetting load with percentage reduction in height in the open upsetting of hollow billets of the three materials used.

3-18 Variation of upsetting load with percentage reduction in height in the open upsetting of hollow billets of various wall thicknesses.

3-19 Comparison of load/displacement characteristics in the heading and open upsetting of aluminium hollow billets.

3-20 Effect of initial unsupported height on load/displacement characteristics in heading aluminium solid billets.

3-21 Variation of upsetting load with percentage reduction in height in heading aluminium solid billets.

3-22 Variation of upsetting load with percentage reduction in height in the heading of solid billets of the three materials used.

3-23 Variation of upsetting load with percentage reduction in height in the heading of solid billets of various diameters.

3-24 Effect of initial unsupported height on load/displacement characteristics in the open upsetting of aluminium solid billets.

3-25 Variation of upsetting load with percentage reduction in height in the open upsetting of aluminium soid billets.

3-26 Variation of upsetting load with percentage reduction in height in the open upsetting of solid billets of the three materials used.

3-27 Etched sections in the heading of aluminium hollow billets under lubricated conditions at various reductions.

3-28 Etched sections in the heading of alumimium hollow billets under dry conditions at various reductions.

3-29 Hollow billets in heading and open upsetting painted blue over their unsupported heights.

3-30 Top views of the aluminium hollow flanged products obtained in heading under different end conditions.

3-31 Etched sections in the open upsetting of aluminium hollow billets under lubricated conditions at various stages of deformation.

3-32 The etched sections from conventional upsetting of aluminium solid bars.

3-33 Typical products, injection upsetting of hollow billets.

3-34 Typical products, injection upsetting of solid bars.

3-35 Effect of gap height on the load/displacement characteristics, simple injection upsetting of aluminium hollow billets.

3-36 Effect of gap height on the load/displacement characteristics, simple injection upsetting of copper hollow billets.

3-37 Variation of upsetting load with punch displacement, simple injection upsetting.

3-38 Effect of gap height on the load/displacement characteristics. Injection upsetting of aluminium hollow billets with one end constrained.

3-39 Effect of gap height on the load/displacement characteristics. Injection upsetting of copper hollow billets with one end constrained.

3-40 Variation of upsetting load with punch displacement. Injection upsetting of hollow billets with one end constrained.

3-41 Comparison of load/displacement characteristics. Injection upsetting of hollow billets with and without end constraints.

3-42 Effect of gap height on the load/displacement characteristics. Simple injection upsetting of aluminium solid billets.

3-43 Effect of gap height on the load/displacement characteristics. Injection upsetting of solid billets.

3-44 Variation of upsetting load with punch displacement. Simple injection upsetting of solid billets.

3-45 Effect of gap height on the load/displacement characteristics. Injection upsetting of aluminium solid billets with one end constrained.

3-46 Effect of gap height on the load/displacement characteristics. Injection upsetting of copper solid billets with one end constrained.

3-47 Variation of upsetting load with punch displacement. Injection upsetting of solid billets with one end constrained.

3-48 Comparison of the load/displacement characteristics in injection upsetting of solid billets with and without end constraints.

3-49 Effect of flange thickness on thinning, simple injection upsetting of aluminium.

3-50 Irregularities in the shape of the flange due to lubrication breakdown in simple injection upsetting of aluminium.

3-51 Bottom face of an aluminium hollow flanged component in simple injection upsetting under dry conditions.

3-52 Etched sections of aluminium hollow billets in simple injection upsetting under lubricated conditions at various punch displacements.

3-53 Etched sections of aluminium hollow billets. Effect of flange thickness t_f, simple injection upsetting.

3-54 Etched sections of aluminium hollow billets in simple injection upsetting under dry conditions at various punch displacements.

3-55 Etched sections for aluminium hollow billets in injection upsetting with one end constrained at various punch displacements.

3-56 Etched sections of aluminium hollow billets in injection upsetting with one end constrained for various flange thicknesses, t_f.

3-57 Etched sections obtained in the injections upsetting of aluminium solid bars.

4-1 A two-dimensional solution domain divided into triangular elements.

4-2 Effective stress-effective strain relations.

4-3 Load versus displacement plot of typical point.

4-4 Initial strain and initial stress method.

4-5 A typical ring triangular element of an axi-symmetric solid.

4-6 Strains and stresses involved in the analysis of axi-symmetric solid.

4-7 A quadrilateral element consisting of four constant-strain triangles.

4-8 Strain rates and the associated stresses in cylindrical coordinates.

4-9 Boundary of velocity discontinuity.

4-10 Velocity field for simple injection upsetting of hollow billets.

4-11 Enlarged section of deforming regions of Fig. 6-2.

4-12 Pressure distribution at the platen surface (qualitative illustration only).

4-13 Velocity field for injection upsetting hollow billets with one end constrained.

5-1 Flow chart for the computer programs.

5-2 Metal behaviour at the specimen/mandrel interface, heading.

5-3 Nodal forces at the specimen/mandrel interface, heading.

5-4 Behaviour of metal at the die edge.

5-5 Mesh pattern for the die edge.

5-6 Mesh patterns for the die edge and punch edge, open upsetting.

5-7 Mesh pattern for the die edge, injection upsetting.

5-8 Nodal forces at the specimen/platen interface, injection upsetting.

5-9 Friction forces at the contact nodal points, heading.

5-10 Friction forces at the contact nodal points, open upsetting.

5-11 Application of hydrostatic pressure.

6-1 Meshes of 90 quadrilateral elements and 112 nodal points used in conventional upsetting.

6-2 Stress-strain curve employed in computer analysis for commercially pure aluminium.

6-3 Comparison of the theoretical and experimental load/displacement characteristics in heading hollow billets.

6-4 Grid distortions and velocity distributions obtained for hollow billets under frictionless conditions at 17 and 34 per cent reductions (h_o = 34 mm, d_i = 25 mm, d_o = 44 mm).

6-5 Grid distortions and velocity distributions obtained for hollow billets for sticking friction at 17 and 34 per cent reductions (h_o = 34 mm, d_i = 25 mm, d_o = 44 mm).

6-6 Grid distortions and velocity distributions for hollow billets at μ = 0.2, 17 and 34 per cent reductions (h_o = 34 mm, d_i = 25 mm, d_o = 44 mm).

6-7 Contours of mean effective plastic strain ($\bar{\varepsilon}_p$) for hollow billets under various end conditions at 34 per cent reduction.

6-8 Grid distortions and velocity distributions obtained for t_w/d_i = 0.38 for various initial unsupported heights at 34 per cent reduction in height.

6-9 Effect of initial unsupported height on the maximum increase in internal diameter for heading at various deformations.

6-10 Effect of initial unsupported height on the maximum increase in internal diameter for heading for various wall thicknesses at $\frac{h_o - h}{h_o} = 0.17$.

6-11 Effect of billet wall thickness on the maximum increase in internal diameter for heading.

6-12 Effect of wall thickness on the maximum increase in internal diameter for heading billets of various free heights at $\frac{h_o - h}{h_o} = 0.17$.

6-13 Grid distortions and velocity distributions obtained for heading hollow billets of h_o = 34 mm for various wall thicknesses at 34 per cent reduction in height.

6-14 Limiting values of the original size of the billet for sound products, heading.

6-15 Mean effective plastic strains ($\bar{\varepsilon}_p$) in heading hollow billets of various original geometries at 34 per cent reduction in height.

6-16 Contours of hoop stress (a, b & c) and axial stress (d) in heading

hollow billets of various original geometries at 34 per cent reduction in height.

6-17 Effect of initial unsupported height on the maximum increase in internal diameter for open upsetting.

6-18 Effect of initial unsupported height on the maximum increase in internal diameter for open upsetting for various wall thicknesses at $\frac{h_o - h}{h_o} = 0.17$.

6-19 Effect of original wall thickness on the maximum increase in internal diameter for open upsetting.

6-20 Effect of original wall thickness on the maximum increase in internal diameter for open upsetting for various original free heights at $\frac{h_o - h}{h_o} = 0.17$.

6-21 Limiting values of original geometries for sound products in open upsetting hollow billets.

6-22 Grid distortions and velocity distributions obtained for open upsetting of hollow billets of h_o = 34 mm for various wall thicknesses at 34 per cent reduction in height.

6-23 Distorted grids and velocity distributions in heading of hollow billets at 34 per cent reduction in height under various hydrostatic pressures.

6-24 Effect of hydrostatic pressure on the maximum increase in internal diameter in heading.

6-25 Effect of hydrostatic pressure on the maximum increase in internal diameter in heading at various initial unsupported heights and $\frac{h_o - h}{h_o} = 0.17$.

6-26 Effect of initial unsupported height on the maximum increase in internal diameter in heading at various hydrostatic pressures and $\frac{h_o - h}{h_o} = 0.17$.

6-27 Limiting values of hydrostatic pressure and initial unsupported height for a sound product in heading.

6-28 Effect of hydrostatic pressure on the maximum increase in internal diameter in heading at various wall thicknesses and $\frac{h_o - h}{h_o} = 0.17$.

6-29 Effect of original wall thickness on the maximum increase in internal diameter in heading at various hydrostatic pressures and $\frac{h_o - h}{h_o} = 0.17$.

6-30 Limiting values of hydrostatic pressure and original wall thickness for sound products in heading hollow billets.

6-31 Contours of radial, hoop and axial stresses in heading against hydrostatic pressure of 75 MN/m^2.

6-32 Distorted grids and velocity distributions in the open upsetting of hollow billets at 34 per cent reduction in height under various applied hydrostatic pressures.

6-33 Effect of hydrostatic pressure on the maximum increase in internal diameter in open upsetting at various deformations.

6-34 Effect of hydrostatic pressure on the maximum increase in internal diameter in open upsetting at various initial unsupported heights and $\frac{h_o - h}{h_o} = 0.17$.

6-35 Effect of original unsupported height on the maximum increase in internal diameter at various hydrostatic pressures and $\frac{h_o - h}{h_o} = 0.17$.

6-36 Effect of hydrostatic pressure on the maximum increase in internal diameter in open upsetting for various wall thicknesses at $\frac{h_o - h}{h_o} = 0.17$.

6-37 Effect of original wall thickness on the maximum increase in internal diameter in open upsetting at various values of hydrostatic pressure and $\frac{h_o - h}{h_o} = 0.17$.

6-38 Limiting values of hydrostatic pressure and initial unsupported height for a sound product in the open upsetting of hollow billets.

6-39 Limiting values of hydrostatic pressure and original wall thickness for a sound product in the open upsetting of hollow billets.

6-40 Distorted grid and velocity distribution in heading hollow billets into a restricted cavity of 52 mm diameter ($h_o = 34$ mm, $d_i = 25$ mm, $d_o = 44$ mm).

6-41 Distorted grid and velocity distribution in heading hollow billets into a restricted cavity of 50 mm diameter ($h_o = 34$ mm, $d_i = 25$ mm, $d_o = 44$ mm).

6-42 Load/displacement curve in heading hollow billets into restricted cavities of various diameters.

6-43 Contours if axial and radial stresses in heading into a restricted cavity of 52 mm diameter.

6-44 Distorted grid and velocity distribution in the open upsetting of

hollow billets into a restricted cavity of 50 mm diameter ($h_o = 34$ mm, $d_i = 25$ mm, $d_o = 44$ mm).

6-45 Load/displacement curves obtained in the open upsetting of hollow billets into restricted cavities of various diameters.

6-46 Contours of various stress components in the open upsetting of hollow billets into a restricted cavity of 50 mm diameter at 34 per cent reduction in height.

6-47 Heading of hollow billets into restricted cavities of various diameters.

6-48 Failure of finite element method for simple injection upsetting of hollow billets.

6-49 Variation of function $F(\eta)$ with η for various flange thicknesses.

6-50 Variation of punch pressure with flange diameter and thicknesses at $d_f/d_o = 1$, simple injection upsetting.

6-51 Punch pressure versus flange thickness and wall thickness at $d_f/d_o = 1$, simple injection upsetting.

6-52 Punch pressure versus flange thickness and wall thickness at $d_f/d_o = 1.5$, simple injection upsetting.

6-53 Punch pressure versus flange thickness and wall thickness at $d_f/d_o = 2$, simple injection upsetting.

6-54 Variation of punch pressure with flange diameter and thickness at $d_f/d_o = 1$, injection upsetting with one end constrained.

6-55 Punch pressure versus flange thickness and wall thickness at $d_f/d_o = 1$, injection upsetting with one end constrained.

6-56 Punch pressure versus flange thickness and wall thickness at $d_f/d_o = 1.5$, injection upsetting with one end constrained.

6-57 Punch pressure versus flange thickness and wall thickness at $d_f/d_o = 2$, injection upsetting with one end constrained.

6-58 Comparison of the upper-bound solutions for simple injection upsetting and injection upsetting with one end of the billet constrained for billets of $t_w/r_o = 0.5$ at $d_f/d_o = 1$.

6-59 Velocity field used by Milner *(49)*.

6-60 Comparison of upper-bond solutions of the present work and the results of Milner *(49)* for billets of $t_w/r_o = 0.6$ at $d_f/d_o = 1$, simple injection upsetting.

6-61 Comparison of upper-bound solutions of the present work and the results of Milner *(49)* for billets of $t_w/r_o = 0.6$ at $d_f/d_o = 1$, injection upsetting with one end constrained.

6-62 Comparison of upper-bound results with experimental findings for billets of $t_w/r_o = 0.45$ and $t_f/t_w = 1.36$, simple injection upsetting.

6-63 Comparison of upper-bound results with experimental findings for billets of $t_w/r_o = 0.45$ and $t_f/t_w = 1.36$, injection upsetting with one end of the billet constrained.

NOTATIONS

$\{\ \}$	column vector
$[\ ]$	row vector, or rectangular or square matrix
$[\ ]^T$, $\{\ \}^T$	transpose of a matrix or column vector
$[\ ]^{-1}$	inverse of a square matrix
$det[\ ]$	determinant of a square matrix
$[B]$	strain-displacement matrix
$[D]^E$	elastic stress-strain matrix
$[D]^P$	plastic stress-strain matrix
$[D]^{EP}$	elastic-plastic stress-strain matrix
$\{\delta\}_e$	element nodal displacement matrix
$\{f\}$	displacement matrix associated with an element
$\{F\}$	structural nodal point forces
$\{F\}_e$	element nodal forces matrix
$\{F\}^{\varepsilon_o}$	load matrix due to initial strain ε_o
$\{F\}^{\sigma_o}$	load matrix due to initial stress σ_o
$\{F\}^Q$	load matrix due to distributed loads
$[I]$	identity matrix
$[J]$	Jacobian matrix
$[K]$	structure stiffness matrix
$[K]^{EP}$	elastic-plastic stiffness matrix
$[K]_e$	element stiffness matrix
$[K]_e^{EP}$	elastic-plastic element stiffness matrix
$[N]$	shape function matrix
$\{Q\}$	load matrix due to distributed forces
$\{\varepsilon\}$	strain matrix
$\{\varepsilon^e\}$	elastic strain matrix

$\{\varepsilon^p\}$	plastic strain matrix
$\{\varepsilon_o\}$	initial strain matrix
$\{\sigma\}$	stress matrix
$\{\sigma_o\}$	initial stress matrix
Δ	area of a triangular element
G	shear modulus
F'	friction force
A	area
d_i	internal diameter of billet
d_o	outside diameter of billet
d_{max}	maximum internal diameter of deformed billet
d_f	flange outer diameter
E	elastic modulus of material
$\dot{E}_I$	energy dissipation rate in the deformation zone
$\dot{E}_S$	energy dissipation rate along the surfaces of discontinuity
$\dot{E}_F$	energy dissipation rate due to surface frictions
h_o	initial unsupported height of billet
h	current unsupported height of billet
k	shear yield stress of material
l_c	constrained length of billet
m	friction factor
p	punch pressure
p_h	hydrostatic pressure
r_i	internal radius of billet
r_o	outside radius of billet
r_f	flange outer radius
r_n	neutral radius in ring compression
r, z, θ	cylindrical coordinates

$\bar{r}$, $\bar{z}$	coordinates of the centroid of a triangle
t_f	flange thickness
t_w	wall thickness of billet
u_i, v_i	nodal point displacement (at nodal point i) in r and z directions
$\dot{u}_r$, U_r	flow velocities
v_p	punch velocity
$\dot{V}_S$	rate of tangential velocity discontinuity
$\dot{V}$	rate of relative velocity
$\dot{W}_D$	total power of deformation
$\dot{W}_P$	punch work rate
Y	uniaxial yield stress of material
ν	Poisson's ratio
μ	coefficient of friction
$\bar{\varepsilon}$	equivalent strain
$\bar{\varepsilon}^e$	elastic component of effective strain
$\bar{\varepsilon}^p$	plastic component of effective strain
ε_{ij}	strain component
$\bar{\varepsilon}_m$	mean effective strain
$\dot{\varepsilon}_{ij}$	strain rate component
$\dot{\bar{\varepsilon}}$	equivalent strain rate
$\bar{\sigma}$	equivalent stress
$\bar{\sigma}_o$	constant flow stress of material
σ_m	hydrostatic component of stress
$\bar{\sigma}_m$	mean effective stress
σ'	deviatoric stress component
γ	shear strain
τ	shear stress component

η parameter defining height of deformation zone in the billet

CHAPTER 1

INTRODUCTION

1.1 Preface

A large number of engineering components are similar in form to a tube with a flange at its end or a collar along the length. Different methods of production are used in the manufacture of such components. Among these casting, in spite of its simplicity may not result in products of acceptable properties. Machining generally involves additional labour costs and excessive wastage of material, particularly if the required diameter of the flange is large relative to that of the stem. In an alternative technique flanges can be blanked from plate and welded to the tubular parts. Here, if the welded flange is subjected to high stresses failure can occur due to crack propagation in the welded region. This technique also requires preparation of the surfaces, jigging for accurate positioning and additional finishing operations which all add to the cost of the components.

Upsetting is another method used in the production of hollow flanged components. The tubular initial billet is either preheated before deformation or the operation is performed at room temperature. In hot working ductility increases and the flow stress of the deforming metal is reduced resulting in better formability. The final product must be machined to size and might have to be heat treated to obtain the desired properties. Cold upsetting is often more economical: its economic advantages have been assessed by several investigators *(1,2,3)* and the results indicate that significant cost savings are possible. Good surface structure and high dimensional accuracy are some of the further advantages of cold upsetting. Furthermore, the sequence of

cold forming operations can be automated more easily than hot forming. Better mechanical properties due to work-hardening is another potential advantage. As a result of this, in some cases heat-treated alloys can be replaced by less expensive materials with properties enhanced during deformation. Furthermore, the grain flow of the material is continuous and uninterrupted resulting in further strengthening.

A comprehensive survey of simple upsetting, conventional upsetting and injection upsetting of solid and hollow billets is given in what follows.

1.2 Literature survey of upsetting

In upsetting processes the metal flow can be predicted under various working conditions and workpiece geometries are used to determine the final shape and the formation of defects in the product. Experiments have been performed by various investigators by etching sectioned specimens to show the flow of metal. The change in geometry of the free surfaces (surfaces free of external forces) was also studied since this also gives an indication of metal flow.

1.2.1 Simple upsetting

1.2.1.1 Solid cylinders

Simple upsetting (compression between parallel platens) of right cylindrical specimens are often used to determine the yield or flow stress of materials. Many papers have been written on this subject in the past 50 or so years. Some of the investigations which are related to the present study are discussed here.

A solid cylinder compressed between parallel platens is shown in Fig. 1-1. The upper platen moves towards the lower platen at a velocity $\dot{U}$ in the z direction. The radial velocity component $\dot{U}_r$ nearer

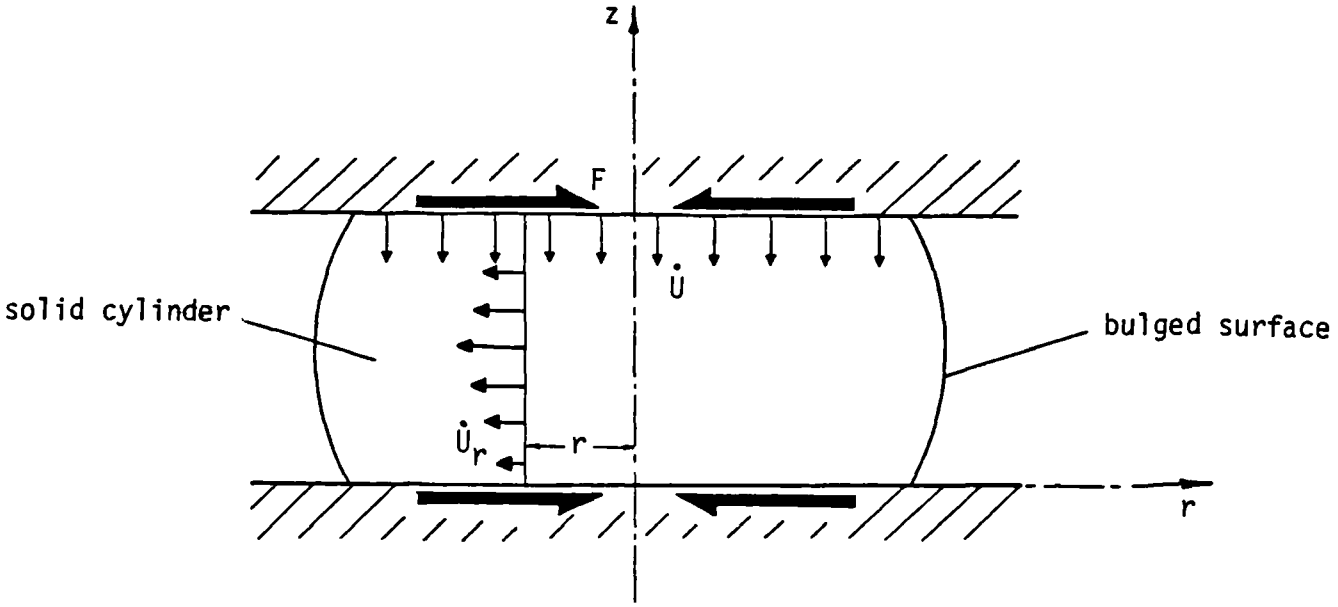


Fig. 1-1 Simple upsetting of a solid cylinder.

the surfaces in contact with the platens is smaller than that in the centre of the cylinder as a result of frictional stresses at the interface of the tool and workpiece. This nonuniform radial velocity leads to non-homogeneous deformation of the free surface which is often referred to as barrelling or bulging. The main factors affecting the form and extent of bulging are the tool-workpiece friction and the dimensions of the workpiece.

Several investigators *(4-8)* have attempted the analytical and experimental treatment of barrelling. Sachs *(4)* suggested that barrelling could be avoided by using conical platens. Some 20 years later Gartner *(5)* performed extensive work using such dies. He

compressed pure aluminium specimens of a height to diameter ratio of 2 between platens of 3° cone angle. There was no appreciable barrelling even at 50 per cent reduction in height. He also showed that, when the die angle is larger than a certain value (called by Gartner, friction angle), reverse barrelling occurs. A similar effect was found by Hsu *(6)* and Hsu and Young *(7)* who showed that, with optimum lubrication, barrelling can be avoided. Hill *(8)* proposed a general method of analysis for metal working processes with which it is possible to analyse the early stage of barrelling.

Various investigators *(9-12)* have developed theoretical methods for predicting the forming load in upsetting with bulging. Kobayashi and Thomsen *(9)*, Tarnovskii et al *(10)*, Steck and Schmid *(11)* and Avitzur *(12)* considered the bulge formation in cylindrical upsetting and suggested upper-bound solutions for calculating the forming loads. Shabaik *(13)* investigated the bulging by using the slip-line theory. These investigators assumed ideal nonstrain-hardening material and concentrated on the prediction of loads and bulge formation. Tarnovskii et al *(10)* assumed an expression for the radial displacement which contains parameters characterizing non-homogeneous deformation. A form of trigonometric relationship was assumed and, when the original diameter to height ratio was less than 0.5, they assumed the barrelled surface to be parabolic. The expressions were simplified by neglecting the effect of axial displacement distribution. In order to determine the values of the parameters used in the assumed relations, the condition of constancy of volume was used along with the principle of minimum required energy. Tarnovskii et al emphasize that for small deformations the predictions of barrelling agree well with the experimental findings and, when deformations are greater than 10 per cent, the calculations must be done

in several stages. In a similar analysis Avitzur *(12)* assumed an exponential expression for radial displacement.

Kulkarni and Kalpakjian *(14)* conducted a thorough experimental study of barrelling using aluminium cylinders. They measured the bulge profile during deformation and examined the influence of various process variables, such as friction at the tool-workpiece interface, original geometry of the specimen and the speed of deformation (strain rate).

Lee and Altan *(15)* used a technique which was basically similar to that of Avitzur. They considered the strain hardening effect by employing an incremental procedure, and at each step an average value for the material flow stress was calculated. They also performed experiments on an aluminium alloy under various end conditions and claimed good agreement between the predictions and experimental results at lower friction.

Nagamatsu et al *(16)* used the type of velocity field described by Hill *(8)* , and determined the unknown terms from the principle of virtual work. Nagamatsu et al later *(17)* outlined their analysis together with an experimental investigation. In this report, shape of bulge, deformation in the body, load, distributions of vertical pressure and of tangential stress on the cylinder-tool interface were calculated. The results showed that a double bulge appears when the height-diameter ratio is greater than 1.65.

When non-homogeneous deformation occurs in an uniaxial compression test, tensile stress components are generated on the barrelled surface which may result in surface cracking. The magnitude of these stress components are governed by friction and the initial geometry of the specimen. Several workers *(18-20,22)* have studied the formation of cracks on the barrelled surface. Histories of the stress and strain

at the point where an eventual fracture is expected are of major importance. Kudo and Aoi *(18)* in their investigation of the workability of a carbon steel, measured the strain variation at the equatorial free surface by means of indented marks. Stresses were derived by using the Levy-Mises equations and fracture was then observed under various stress and strain histories. They controlled friction by using grooved dies and conical dies, with and without lubrication. Latham and Cockroft *(19)* made various attempts to relate workability in compression to barrel shape at fracture. They finally showed that the barrel shape could not be uniquely related to the onset of cracking and that friction had an additional and important effect. Thomason *(20)* pointed out the limitations of Kudo and Aoi's method of marking grids on the specimen under examination: the grid lines usually act as stress raisers and become a source of fracture. When fracture occurs, it is no longer possible to make further meaningful measurements of surface strains. To overcome these limitations Thomason proposed the use of a ductile model material such as pure aluminium. The plastic strain increments on the equatorial surface of aluminium specimens were found to be identical to those for steel cylinders of similar height to diameter ratio. The report emphasizes that a considerable amount of anisotropy is developed by plastic flow, and the Levy-Mises equations give serious errors in the surface stress components. Thomason therefore used Hill's *(21)* anisotropic equations and the results showed that the tensile surface stresses were lower than for isotropic conditions. It was also found that reduction in friction or an increase in the height to diameter ratio lead to lower tensile surface stresses.

Kobayashi *(23)* conducted experiments on annealed SAE1040 steel, using methods almost the same as those of Kudo and Aoi *(18)* . These

included measurements of displacement distributions at the tool-workpiece interface, bulge profiles, strains at the free surface, and observations of crack formation for various friction conditions and specimen dimensions. The report concludes that under lubricated conditions the radial displacement distributions are linear, with decreasing height-diameter ratio they approach those for homogeneous deformation. The observation concerning strain and stress histories, and their effect on the mode of fracture confirm the results of Kudo and Aoi.

1.2.1.2 Hollow cylinders

When a hollow cylinder is compressed axially between flat parallel rigid platens (Fig. 1-2(a)), the free surfaces bulge because of the frictional stresses at the tool-workpiece interface. As in the case of solid cylinders the outer free surface barrels out. At the inner surface, however, two possible modes of deformation may occur: (1) The material at the inner surface flows inwards resulting in decreasing inside diameter. The boundary between the inwards and outwards flow along the thickness of the cylinder is referred to as the neutral surface (see Fig. 1-2(b)). In this surface the radial velocity vanishes, and at the neutral flow point on the tool-workpiece interface the frictional stress changes its direction. (2) The inner surface barrels out resulting in increasing inside diameter (Fig. 1-2(c)). In this case, the whole material flows outwards and the neutrtal radius r_n is smaller than the inner diameter.

Under frictionless conitions no bulging occurs and the hole size increases proportionately to the outer diameter, i.e. the cylinder compresses as would the corresponding portion of a solid cylinder. with increasing frictional constraint the rate of expansion of the hole decreases and eventually the compressive hoop stresses developed at the hole

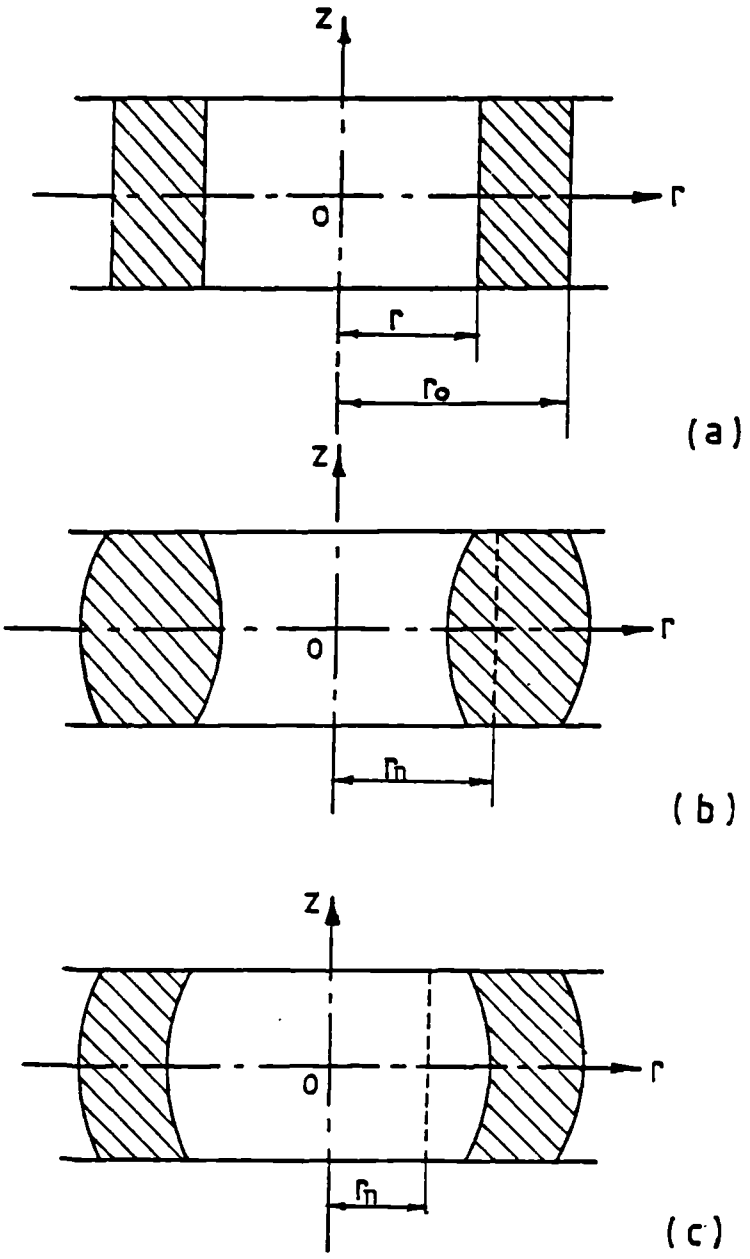


Fig. 1-2 Simple upsetting of hollow cylinder.

(a) undeformed cylinder

(b) deformed cylinder with convex outer surface and concave inner surface

(c) deformed cylinder with convex inner and outer surfaces

are sufficient to cause the hole to contract. In a process with constant friction, as the cylinder shortens the change in geometry increases the frictional constraint progressively, so that the hole may initially increase in diameter and then contract.

Several workers have investigated the changes in the geometry of the free surfaces and the position of the neutral surface. Most of the mathematical methods are based on approximate stress analysis *(22,24)* or on upper-bound solutions *(12,25-28)* using relatively simple velocity fields. Earlier analyses assumed that the strain at any radius is uniform over the whole height of the specimen. Kunogi *(24)* obtained explicit expressions of the neutral radius and corresponding geometrical changes for rigid-perfectly plastic materials. A frictional shear stress based on a friction coefficient μ and proportional to normal pressure σ_n was considered, with the limiting condition that $\mu\ \sigma_n \leqslant k$, where k is the shear yield stress. Kunogi also carried out extensive experimental work and predicted different buckled profiles for the thin-walled tubes of various geometries. Kudo *(25)* and Avitzur *(12)* derived the position of the neutral surface from the consideration of minimum energy dissipation. Avitzur's analysis is based on the following assumptions: (1) the radial velocity is uniform along the height. (2) the cylinder material obeys the Von-Mises stress-strain rate laws, and (3) the frictional shear stress $\tau = mk$, where m is constant ($0 \leqslant m \leqslant 1$) and k is the shear yield stress of the material. Male and Depierre *(26)* and Sawl et al *(27)* developed theoretical analyses based on the mathematical results of Avitzur, but considered strain hardening.

Kobayashi *(23)* compressed annealed SAE1040 steel under various geometrical and frictional conditions. The displacement distribution at the tool-workpiece interface and the development of barrelling were

measured and it was found, that i) The radial displacements depart greatly from those for homogeneous deformation even under lubricated conditions. ii) When the height-diameter ratio becomes small, the originally free surface contacts the platens even under lubricated conditions iii) The inner diameter decreases under high friction, and it increases first and then decreases when a lubricant is used; this is more pronounced for specimens with a smaller height-diameter ratio. iv) The dimensional change of the inner diameter is sensitive to the friction condition when a lubricant is used, but becomes less sensitive as the friction increases. v) For specimens of the same height, the radius of the neutral surface is larger for larger diameters and for increased friction.

Several workers *(28-30,15)* considered the bulge formation in their analytical treatment. Avitzur *(28)* extended his earlier work, assuming an exponential cusp-shaped bulge. Liu *(29)* extended the mathematical approach of Male and Depierre *(26)* by introducing the bulging effect. He later *(30)* produced a theoretical prediction for the experimental results of Kobayashi *(23)* . The radii of curvature of the bulge at the inner and outer equators were derived by assuming a parabolic curve for the bulge profile. Liu claims good agreement of his theoretical results with the experimental findings of Kobayashi. Lee and Altan *(15)* utilized a finite mesh system for computing the flow stress distribution and minimized the total energy rate of dissipation for the assumed admissible velocity field.

Travis *(31)* carried out experiments on mild steel under various end conditions such as progressive lubrication (where the operation was stopped frequently to effect relubrication), initial lubrication and dry conditions and showed the effect of friction on the rolling of

material from the walls of the specimens onto the platens, and on the interpenetration of the "dead metal zones" or " pressure cones". In the case of progressive lubrication "rolling up" was greatly reduced. Travis concluded that more effective lubrication would not necessarily reduce the non-homogeneous deformation of the workpiece; the reduction of friction induced transverse instability, such that there was lateral movement of one end of the specimen relative to the other, resulting in serious axially non-homogeneous deformation. A similar experimental work was later conducted by Biswas and Travis *(32)* on specimens of various geometries. The buckled profiles were observed to be as predicted by Kunogi *(24)* , irrespective of lubrication, for height to outside diameter ratio of 2 and less, and for wall thickness to outside diameter ratio of 1/6. They also found that specimens of height to outside diameter ratio of 3 (for all wall thickness to outside diameter ratios) tested under dry conditions, buckled asymmetrically, and not as predicted by Kunogi for thin-walled tubes.

Ring compression has been extensively used for determining the friction factor or the coefficient of friction at the billet-tool interface. This technique involves only the measurement of the change in the bore diameter (which is sensitive to friction at the die-workpiece interface) and not the mechanical properties of the metal. The method was first proposed by Kunogi *(24)* and was further developed by Male and Cockcroft *(33)* . Later Male and Depierre *(26)* described the mathematical calibration of the ring test and compared their calibration with experimental results.

In an investigation performed at the National Engineering Laboratory *(34)* on En2E steel a central mandrel was used to prevent reduction in the inner diameter. Specimens with various lengths and

different outside diameter to bore diameter ratios were upset up to 80 per cent reduction in height. Except for the shortest billet (length/wall thickness =1), in all cases a void was produced between the bore of the billet and the mandrel, the former collapsed to form a fold at the end of the process. Single folds were observed when length-wall thickness ratio was 8:1 or less, and a double fold developed for larger length-wall thickness ratios. In the case of the shortest billet the bore and the outside surface remained reasonably straight and parallel. It was also found that the deformation mode was not greatly influenced by different lubricants but was affected by the absence of lubrication, i.e. under dry conditions the movement of material away from the mandrel was restricted to a narrower zone.

1.2.2 Conventional upsetting

Simple conventional upsetting of cylindrical billets is known as heading. The term heading refers to a process when a head substantially larger than the shank or main body is formed on a workpiece. In the heading of hollow components (which is the concern of the present work) a tubular cylindrical billet is constrained in a die and then the unsupported height of the billet is deformed into a head of larger diameter. A schematic diagram of the process is shown in Fig. 1-3(a). The pressure is applied by a punch having a diameter larger than the required flange diameter. The flange forms between the punch face and the top surface of the die. A mandrel of a diameter equal to the internal diameter of the billet is used to prevent the inward flow of the material during deformation.

In order to form a flange along the length of a tubular billet the billet is constrained within dies at both ends and its unsupported region is deformed into a larger cross-sectional area over part of its

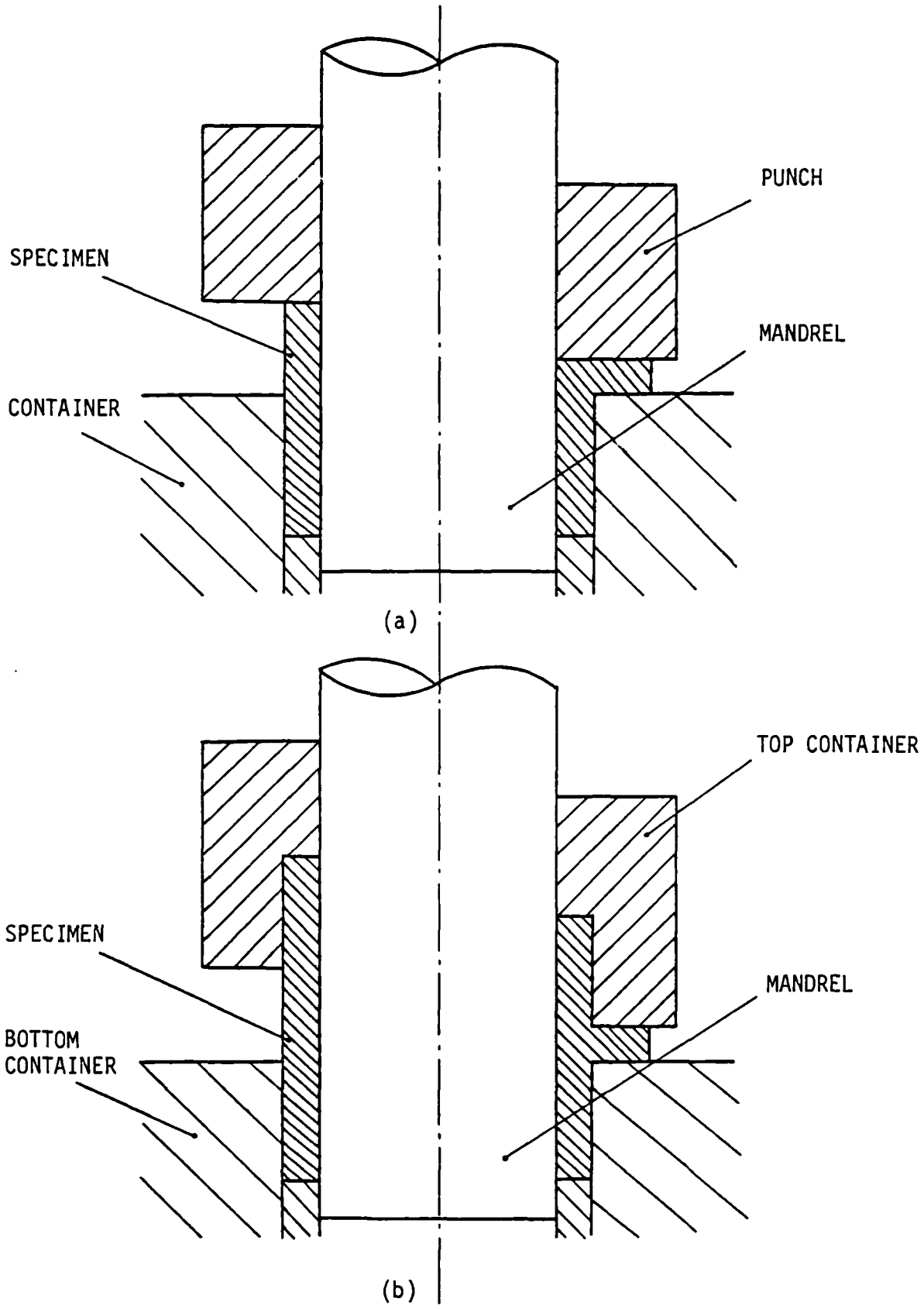


Fig. 1-3 Conventional upsetting of hollow billets.
(a) with one end constrained (heading)
(b) with both ends constrained (open upsetting)

length. This type of conventional upsetting is shown diagrammatically in Fig. 1-3(b). The method is usually known as flange forming part way along the billet or open upsetting. The latter term is used throughout the present work.

Only a few investigations have been carried out on the production of hollow flanged components by conventional upsetting. Dieterle *(35)* conducted experimental and theoretical analyses of the heading process. He examined the formation of fold at the bore surface of the specimens and studied the effect of various process variables on the occurrence of folding and concluded that the severity of the fold varies with material, increases slightly with the billet-wall thickness ratio and is significantly affected by lubrication. The theoretical part of this investigation consists of a finite element method and is discussed in section 1.3.2.

At the National Engineering Laboratory *(34)* experiments were performed using En2E steel under both dry and lubricated conditions. Products free of folding were obtained when heading tubular billets with initial free height less than approximately 1½ times the original wall thickness. When the initial free height exceeded this limit the flange developed a fold which increased with the initial free height to wall thickness ratio (h_o/t_w) and with the reduction in height. The limiting value of h_o/t_w was found to be unaffected by constraining one or both ends or by changes in the ratio of the billet diameter to wall thickness. In some heading tests an asymmetry of flow was observed which led to the tilting of the fold and to the appearance of a circular crack in the top face of the flange. This asymmetrical deformation is thought to be due to non-uniformity of surface friction and anisotropy of the material. The separation of tooling in the case of open upsetting

after about 70 per cent height reduction usually resulted in the fracture of the specimen (into two separate flanged products each with a flange of half the original thickness) across the horizontal plane on which the inner fold was formed.

Although heading is a very common metal working operation, only a few theoretical studies *(35,36)* have been undertaken to reveal the details of this process. Shah and Kobayashi *(36)* analysed the process by employing a matrix method which was first introduced by Lee and Kobayashi *(37)* . The method basically considers a variational formulation *(21)* for a rigid-plastic material, under the condition that the entire body is deforming plastically. They analysed the heading of a solid bar up to 60 per cent reduction in free height. The results are presented in terms of load-displacement relationship, strain and stress distributions and grid pattern distributions. When the results were compared with those of a corresponding simple upsetting, load-displacement relations and the changes in the upper contact area were found to be almost the same. It was therefore concluded that the deformation near the top die is independent of the condition at the bottom die. To examine the validity of their results Shah and Kobayashi carried out tests on SAE1040 steel and claimed an excellent agreement between the theoretical and experimental results.

The process of heading is most widely used in the manufacture of fasteners. Significant material saving and the possibility of high production rates are the main reasons for employing this process. Small bolts for example are made at rates of up to 400 per minute. Various methods of forming the head or collar are shown in Fig. 1-4. The head can be formed: (1) in a cavity in the punch, (2) in a cavity in the die (3) in cavities of both die and punch, or (4) between punch

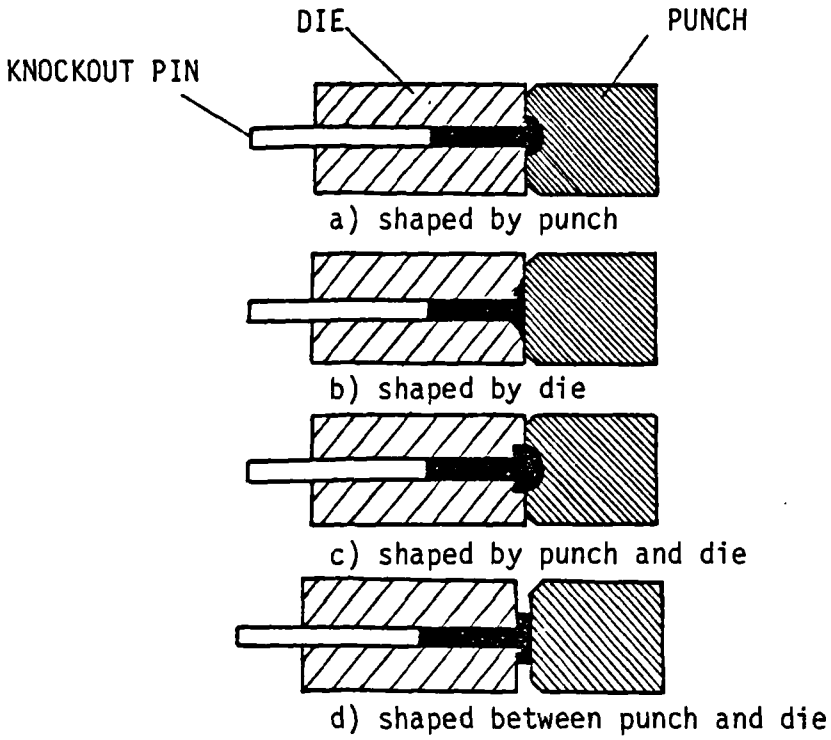


Fig. 1-4 Four methods of forming the head.

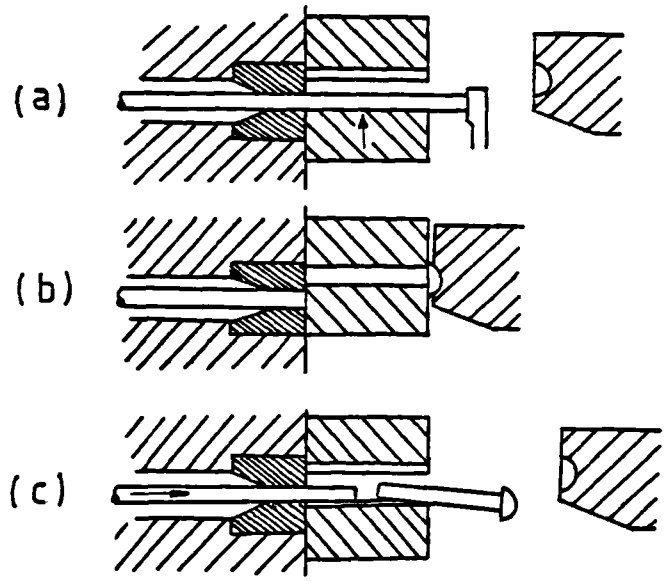


Fig. 1-5 Diagrammatic representation of the operation of a single-blow split-die header.

and die.

Smith *(38)* and Townend and Wilson *(39)* in their reports describe high speed automatic methods for forming heads and collars on wire and rod stock. Among these, the simplest is a split-die single-operation header which is diagrammatically shown in Fig. 1-5. A cylindrical rod is fed to a stop (Fig. 1-5(a)). The split-die then closes, cutting off the rod. The punch advances and forms the head (Fig. 1-5(b)). The punch withdraws, the split die opens and rod feed commences, ejecting the finished blank (Fig. 1-5(c)). The ratio of the initial unsupported length to the original diameter of the solid rod is termed the "upset ratio". As the upset ratio is increased there is an increasing tendency for the rod to buckle and so to produce unsatisfactory heads. The maximum permissible upset ratio recommended by Smith is *2.3* . This value is suggested to be *2½* by Townend and Wilson. If heads containing a greater volume of material are required, more than one operation is used. The principle of a double-operation is to support part of the rod in the punch during the first operation, thereby avoiding buckling. A second punch then shapes the material to the final form while it is still held in the same die. A schematic diagram of the double-operation heading is shown in Fig. 1-6. The reports suggest that by the use of a double-operation technique the permissible upset ratio can be increased to 4½. While it would be possible to increase further the number of upsetting operations and the upset ratio, the ductility of the material would decrease due to heavy work hardening in regions which are subjected to severe plastic deformation. In practice intermediate annealing may be necessary to restore ductility.

The effect of high strain-rates on the processes of simple upsetting, heading and open upsetting was investigated by Jones et al

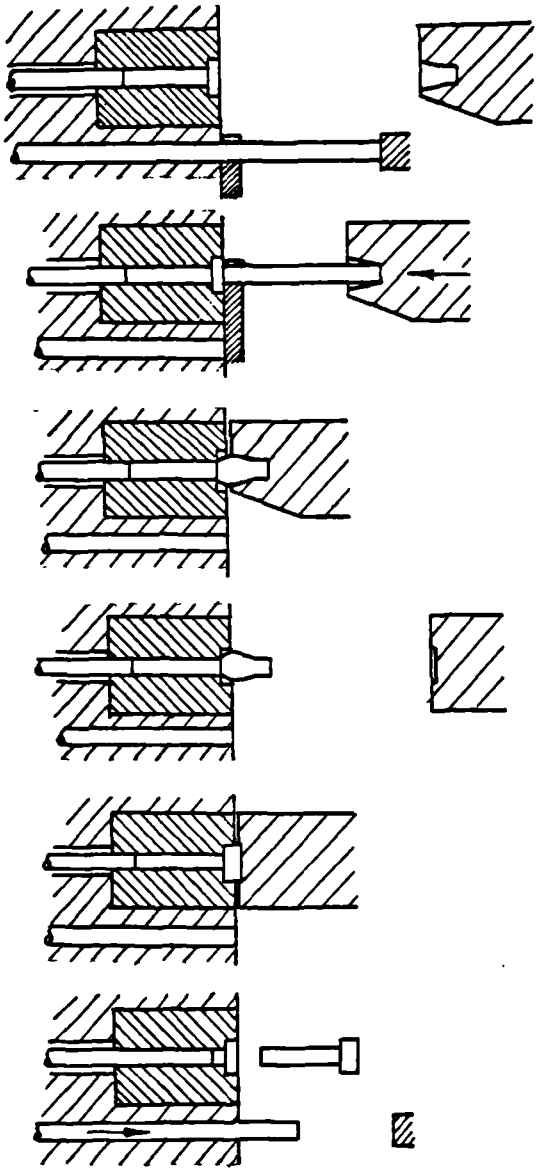


Fig. 1-6 Operation of a two-blow solid-die header.

(42) . Experiments were carried out under both high speed (impact speed of 17 m/sec) and quasistatic conditions using solid billets of an aluminium alloy and a low carbon steel. During upsetting tests on aluminium at slow speed peripheral cracking occurred above a reduction in height of about 75 per cent. This type of cracking did not occur in high-speed tests even at reductions of up to 85 per cent. For the steel, the maximum reduction that could be achieved was insufficient to cause peripheral cracking at either slow or high speed. The flow of material in heading and open upsetting was affected only to a small degree by impact speed. The effect was found to be more pronounced in simple upsetting where the deformation across the section was more uniform in the case of high-speed, indicating a greater amount of local deformation. The explanation given for this is that, since the time available for heat conduction under high-speed conditions is very small, the deformation remains more localized, and reduced frictional forces at high speeds result in more uniform deformation. Reduction of frictional forces due to high speed was proved in an experimental investigation performed by Male *(41)*. He suggests that an increase in speed promotes thick-film conditions and increases the amount of deformation before these conditions b eak down. Jones et al also found that the energy requirements at slow and high speeds were similar for simple upsetting and heading operations, but in open upsetting greater energies were required for the high-speed operation. The effect of speed on the forming pressures may be explained as follows. The main influence of high strain rates is to increase the resistance to deformation of the material. For example, for mild steel the yield stress of the material can be expected to increase up to 2.5 times in high-speed forming operations *(40)*. The increased resistance to deformation is however counteracted to some extent by

thermal softening, since less of the heat generated from the energy of deformation is conducted into the dies and to the undeformed material at high speeds because of the very short time available. Further, reduction of friction also tends to offset the increase in resistance to deformation. Jones et al explain that in open upsetting greater energies are needed for the high-speed operation because the benefit to be gained from any decrease of frictional forces are least for this process since only two small annular areas are in sliding contact. For the aluminium alloy, the required energy was less affected by increasing impact speed since increasing strain rate has only a relatively small effect on its resistance to deformation when compared with mild steel.

1.2.3 Injection upsetting

Injection upsetting in its simplest form is the production of a local increase in diameter on part of a cylindrical bar of plastically deformable material by forcing the material to flow into an annular space of fixed dimensions, the only moving part of the tooling during the process being the punch. The process is used industrially for hot forming of certain multi-flanged components. A more complicated form of this process is used extensively in the plastics industry, and very complex dies can be filled successfully by the simple application of pressure by a punch only. This is usually known as injection moulding, although it is in principle similar to injection upsetting.

For most metals injection upsetting is usually confined to the forming of simple shapes, because of the relatively high punch pressures involved. Filling of complicated dies by cold injection upsetting is extremely difficult due to the high degree of strain hardening produced locally in the material approaching a re-entrant corner of the die.

Simple injection upsetting of a hollow cylindrical billet is shown diagrammatically in Fig. 1.7(a). The tubular billet is constrained within a central mandrel and the bore of a container. At the end of this container an annular gap is provided, the height of which is adjusted according to the required flange thickness. The material is forced, by a close-fitting punch, out of the bore of the container into the annular gap.

In order to form a flange along the length of the billet by this technique another lower container is used to constrain the bottom end of the billet. The flange is therefore formed in the gap provided between the upper and lower containers. Fig. 1.7(b) shows a schematic view of the injection upsetting of a hollow billet with one end constrained.

Necking and fracture of the flange outer surface have been studied which often occur due to tensile hoop stresses. Most investigations are concerned with the upsetting of solid billets. A considerable amount of work has been carried out on the effect of superimposed radial pressure on the flange rim, in order to delay the onset of necking. The earliest work using back pressure was described by Cogan *(43)* and by Cogan and Campbell *(44)*. Aluminium specimens were upset against back pressures of up to 206 MN/m^2 (30,000 PSI) and flanges of a diameter at least four times that of the billet were made without necking. To produce the required back pressure a low melting point, low yield strength alloy (cerrobend) was allowed to flow through restricted orifices in the circumference of the die cavity. The use of the solid matrix material instead of a liquid pressure-transmitting medium which is usually used in high pressure extrusion processes eliminated the need for elaborate sealing methods.

Alexander and Lengyel *(45)* conducted experiments on aluminium,

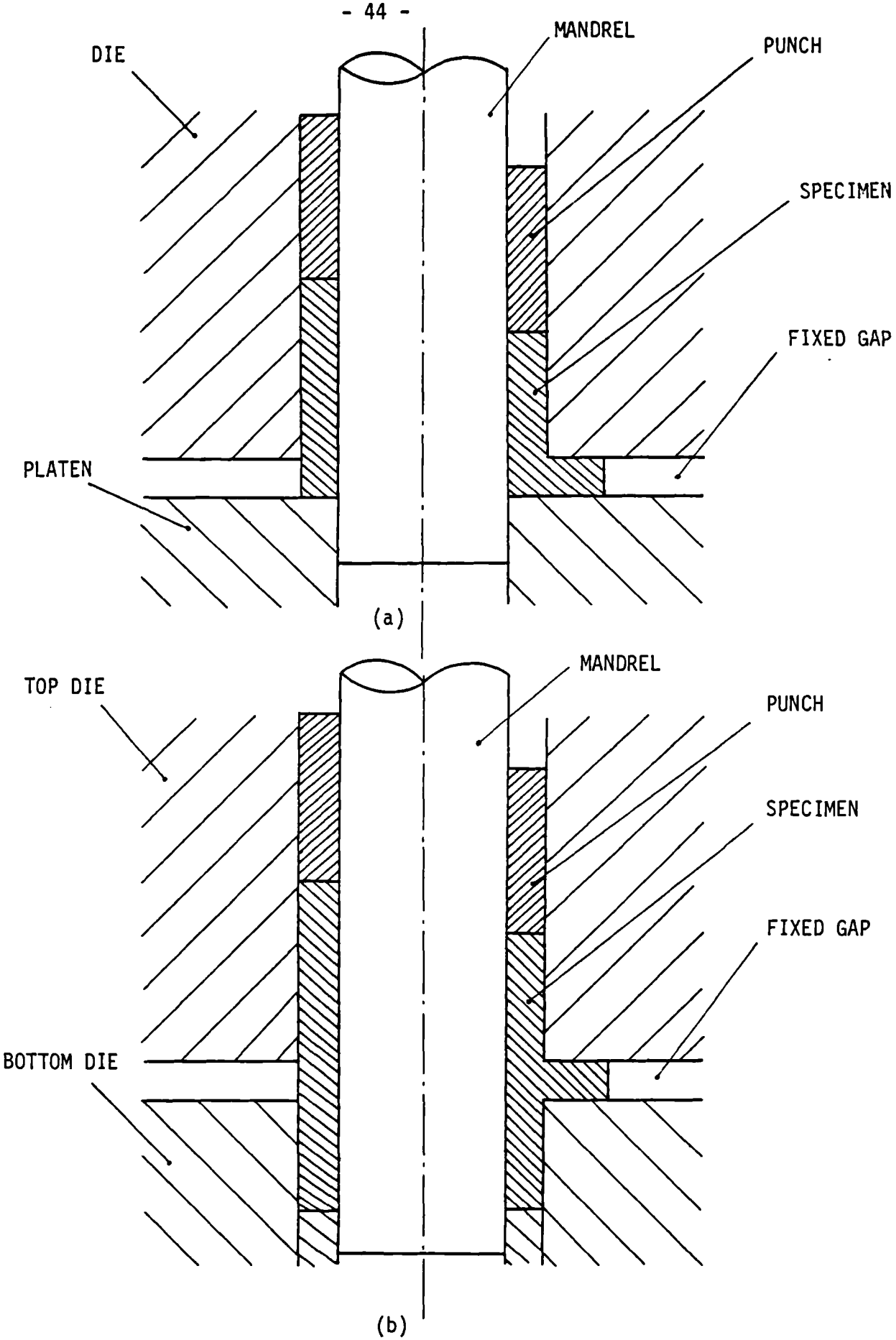


Fig. 1-7 Injection upsetting of hollow billets.
(a) simple injection upsetting
(b) injection upsetting with one end constrained

copper and 10 per cent silicon-aluminium alloy specimens, which were upset against back pressures of up to 380 MN/m^2 (25 $tons/in^2$). At this pressure the behaviour of aluminium was markedly different from that of copper; aluminium was found to form a flange of constant thickness, except near the free edge where some thinning occurred but copper flanges showed marked thinning and still necked at this back pressure. The aluminium alloy showed an appreciable ductility at 380 MN/m^2 back pressure, whereas at atmospheric pressure upsetting without early fracture was impossible. In this work a castor oil-methyl alchohol mixture was used as the pressure transmitting medium and the pressure was generated by hydraulic rams. The paper also contains an upper-bound solution and a method of estimating the mean effective strain. The analytical procedure employed in this work is discussed in section 1.4.2.

In an experimental work performed by Fuchs *(46)* hydrostatic pressure was employed in the upsetting of tubes. The tooling for this operation is shown in Fig. 1-8. The tubular billet is placed in a high-pressure chamber with a close-fitting extrusion orifice at its end. A shouldered combination high-pressure piston and mandrel is thrust into the tube and chamber from the top. At the bottom of the assembly is a hydraulically closed facing die which restrains the tubing from moving downwards. In operation, the tube is placed on the mandrel and a hydraulic ram forces the tube and mandrel down into the chamber, which has been filled with fluid. As the tube enters the orifice, the fluid can not escape, and the shoulder on the mandrel entering into the chamber acts as a piston to raise the pressure to a high level. This pressure acts radially inward on the tube to prevent buckling, while at the same time it pushes the tube down through the orifice. The tube

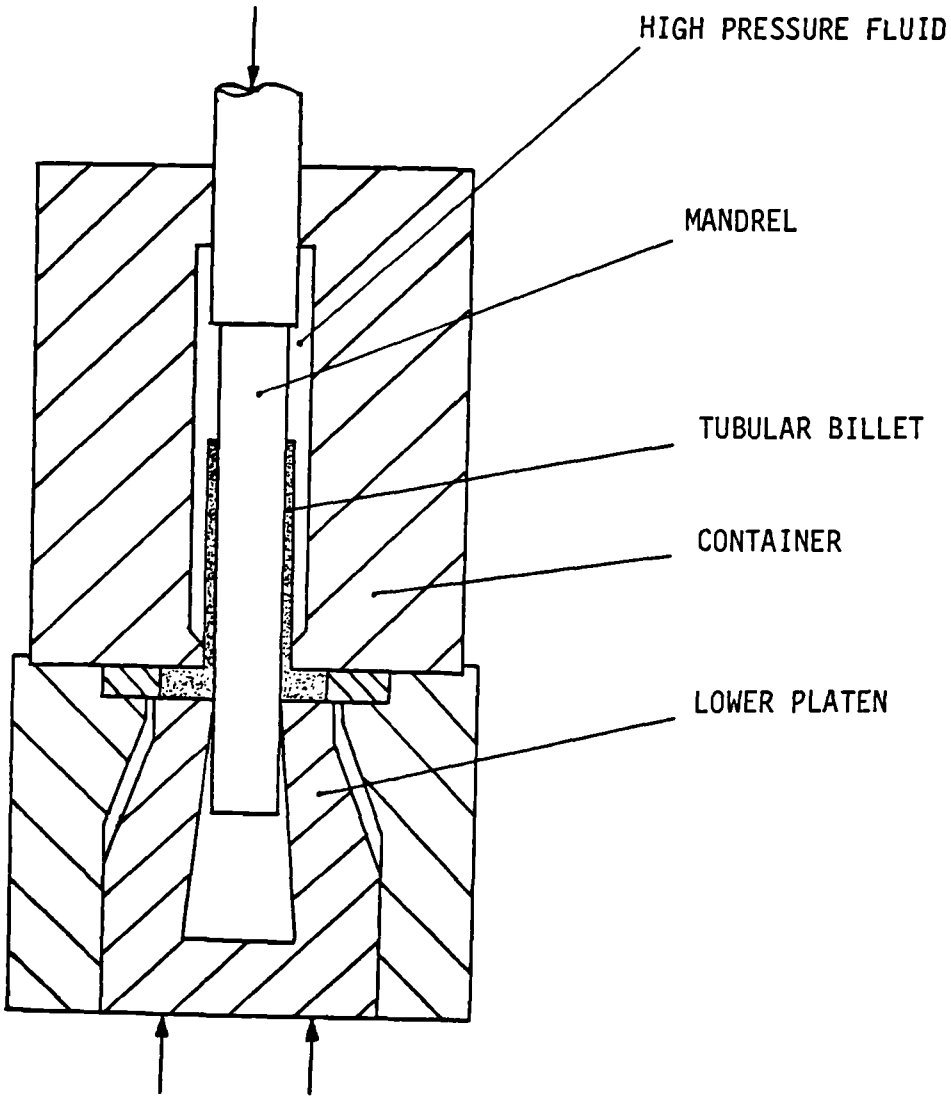


Fig. 1-8 Injection upsetting of tubular billets, applying hydrostatic pressure, after Fuchs *(46)*.

encounters the facing die and proceeds outwardly until it contacts the flange cavity wall. At this point, hydrostatic pressure begins to build up in the material. The facing die is held in place with sufficiently high force to cause this hydrostatic pressure to reach that necessary for increased ductility. For copper, this pressure was between 514 and 686 MN/m^2 (75,000 to 100,000 PSI). This technique allowed the formation of a flange with thickness over four times that of the original tube wall.

In an investigation at the National Engineering Laboratory *(47)* solid billets of En2A and En2E steel were upset in atmospheric pressure. The effect of the gap height-billet diameter ratio (t_f/d_o), and of length of the billet constrained in the bore of the die on the load/stroke characteristics and on the flow of metal were studied. For large values of t_f/d_o the products contained folds in their flange region due to instability of the unsupported height (initial buckling). For particular values of t_f/d_o there was a limiting value of billet which could be injected into the fixed gap. Exceeding this limiting value led to peripheral fracture of the flange. When one end of the billet was constrained, for t_f/d_o between 0.8 and 1.6 the maximum length of billet which could be successfully upset was found to be approximately 4.25 times its diameter. The authors remark that this was a significant improvement on the maximum length of billet, in comparison with conventional upsetting which is normally taken as a length-diameter ratio of 2.5 *(39)* .

Some years later at the National Engineering Laboratory *(48)* further experiments were performed using solid billets of six steels (En2A-En2E-En5-En8-En56A-En52). Symmetrical flanges were formed without initial buckling of the unconstrained height at values of flange thickness/billet diameter less than approximately 1.65. This limiting value was

found to be independent of material quality and billet diameter. For a fixed gap height a linear relationship existed between the length of the billet which could be upset without fracture of the flange outer surface and percentage carbon of the steel used, i.e. this length decreased with increasing percentage carbon.

Recently, in another investigation at the National Engineering Laboratory *(34)* tubular billets of steel (En2E) were upset. The experiments were performed for various wall thickness to gap height ratios (ranging from 0.5 to 1) and the products were sectioned and examined for defects in the bore region. The flanges were all found to contain folds in the inner surface. In order to produce hollow flanged components with a straight bore surface, a combination of upsetting and extrusion based on the use of solid billets was later considered, shown in Fig. 1-9. The specimen was first conventionally upset (Fig. 1-9(a)) and then it was backward extruded (Fig.1-9(b)) to form a can from the flange preform. The upset flange became distorted during the initial penetration of the extrusion punch and it was unsuitable for subsequent coining of the flange between parallel tools. In another attempt, a combination of indenting and upsetting of a solid billet was employed, shown in Fig. 1-10. The billet material was first indented by the punch and then upset as the anvils came together. This method posed further problems, namely cracking of the flange, non-conformity of the product with the tooling and, in some instances, folding at the bore of the flange. The report concludes that this process could be successfully applied if: 1) The steel was of good cold-forming quality and not susceptible to premature failure under tensile hoop stresses. 2) The initial free height of the billet and the depth of indentation

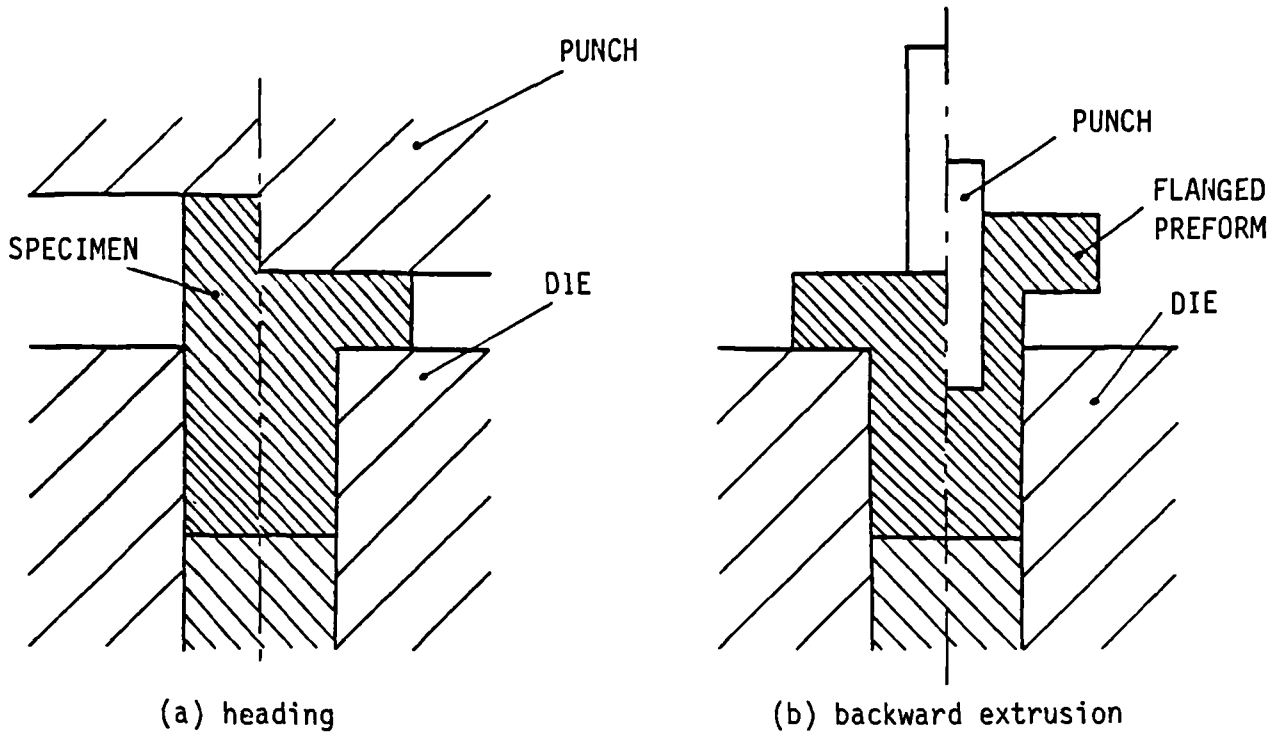


Fig. 1-9 Combined heading and backward extrusion of solid billet.

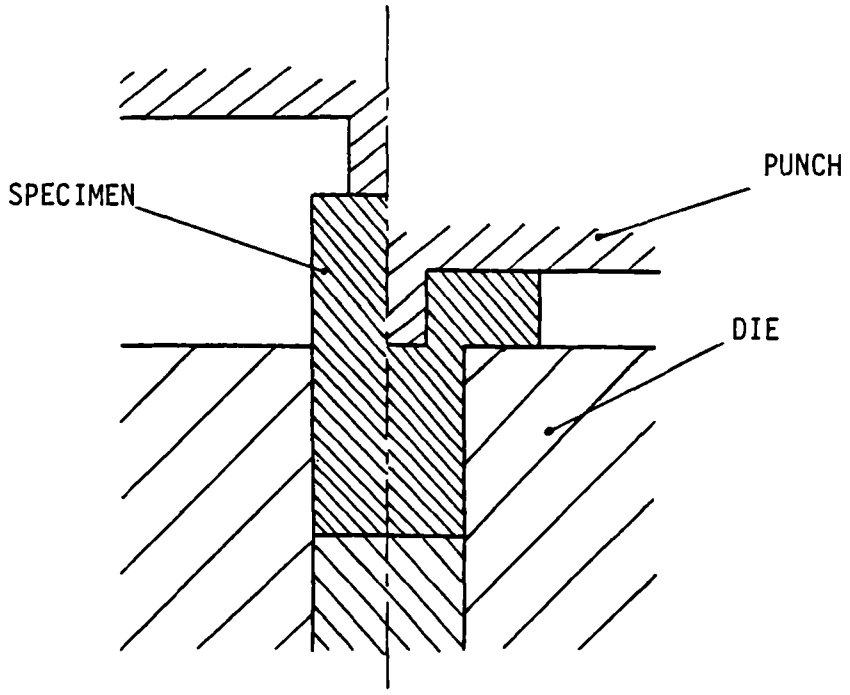


Fig. 1-10 Combined heading and indenting of solid billet.

were so chosen that no folding of the bore occurred, and 3) The flange was given a significant upset to ensure conformity of the product with the tool.

Most recently Milner *(49)* performed an experimental and theoretical analysis using solid billets of aluminium, copper and mild steel under various working conditions. In most aluminium specimens necking of the flange rim was observed when the flange radius was greater than 1.8 times the billet radius. Continuation of forming led to eventual rupture at a neck. Annealed copper was found to be considerably more ductile and flanges up to a diameter of at least 3 billet diameter were formed before visible signs of necking. Mild steel specimens usually fractured without necking at the early stage of deformation. The formability was generally found to be lower for thinner flanges and when the flange was formed part way along the billet.

Milner also examined upsetting of several brittle metals against hydrostatic pressure. The pressure which was generated by a steady flow of wax through the exhaust channels delayed the occurrence of fracture at the flange rim. When a conventional grease was used as lubricant it usually escaped into the exhaust ports and created a substantial fall in pressure, consequently a dry lubricant was used. The flanges contracted axially in much the same manner as when no hydrostatic pressure had been applied. In some cases, at some points very little axial contraction occurred, but at other points on the circumference contraction was exaggerated. This is suggested to be due to local pressure reductions caused by the escape of softened wax into the exhaust ports.

In this investigation experiments were also performed on hollow billets of an aluminium alloy (HE30) and two mazak alloys. For the

aluminium alloy flanges of up to 1.9 times the billet diameter could be formed before fracture occurred. However, flaring of the bore was observed at all flange thicknesses (ranging from 0.3 to 1.1 billet radius) and it persisted even under back pressure of up to 245 MN/m^2 (35,000 PSI). The mazak alloys fractured at the flange rim very early in the process when no back pressure was applied. Under hydrostatic pressures sufficient to induce ductility, the behaviour differed from that of HE30 in that rather than flaring at the bore, a dead zone formed in the sharp corner where the mandrel meets the platen surface. Milner later considered a combination of piercing and injection upsetting to produce hollow flanged components from solid bars (shown in Fig. 1-11). During the process a plug of metal below the mandrel nose shears away from the body of the billet. This plug is expelled through the platen hole as piercing is completed, and once the mandrel nose has entered the platen bore, the process is purely injection upsetting. Tests were carried out using billets of E1C aluminium, and were devised so that piercing was only completed marginally before the end of the radial filling of the die cavity, so that there was little opportunity for flaring to occur. There was a severe limit on the length of billet which could be pierced if radial movement of the mandrel and subsequent damage to the mandrel and the bore of the platen were to be avoided. The height limitation of the billet and the material wastage are the main disadvantages of this technique.

1.2.4 A comparison of conventional upsetting with injection upsetting

The main differences in the conventional and injection upsetting processes may be discussed as follows:

(i) In conventional upsetting the initial unsupported height of the billet is always higher than the required flange thickness, while in the

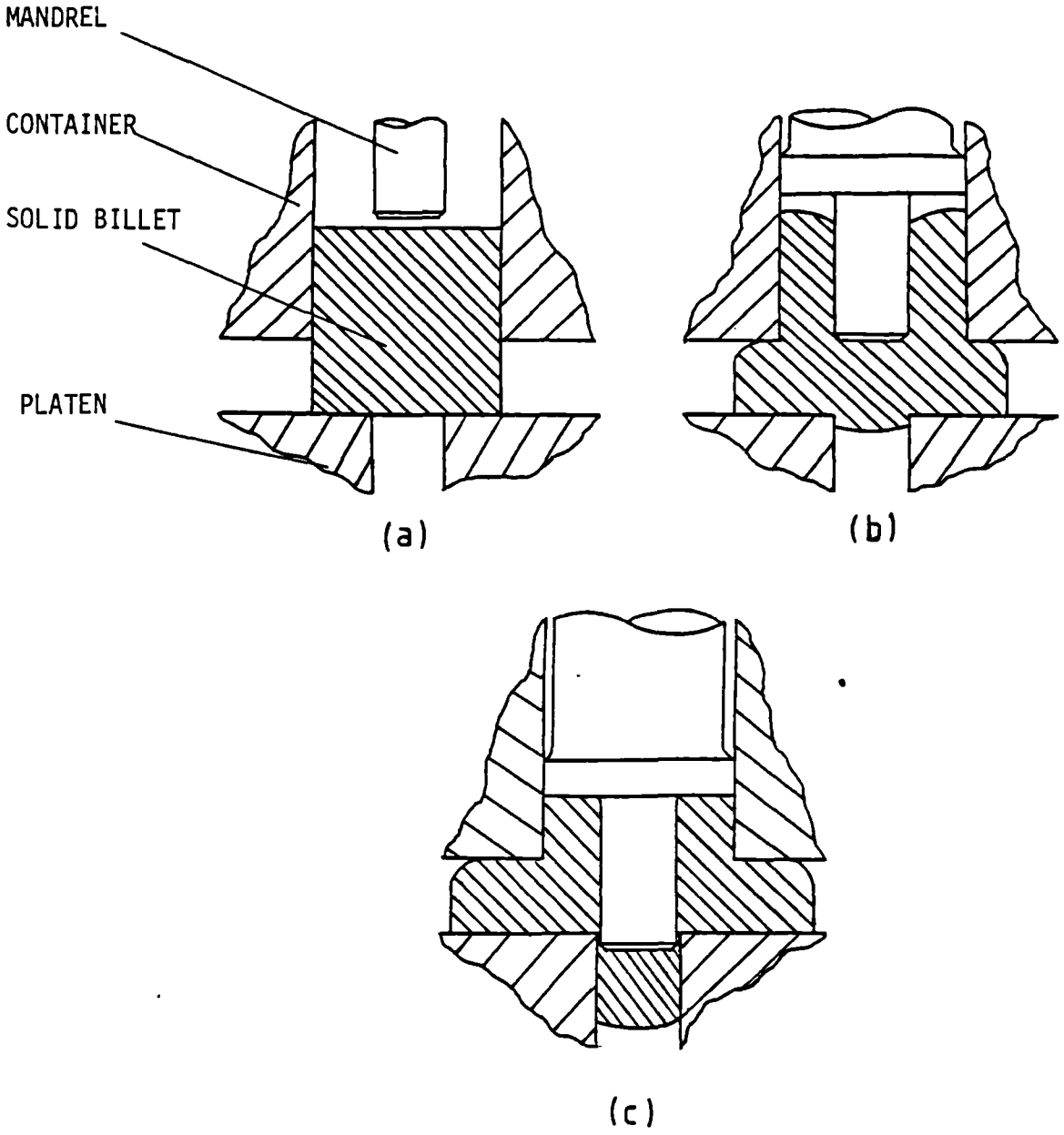


Fig. 1-11 Combined piercing and injection upsetting, after Milner *(49)*.

case of injection upsetting this height (the height of the fixed gap) is equal to the flange thickness. Therefore for similar upsetting conditions the possibility of bulging or buckling of the unconstrained part of the billet is higher in conventional upsetting. This is particularly so when flanges of large volumes are required.

(ii) When radial hydrostatic pressure is to be applied at the flange rim in order to prevent peripheral fracture injection upsetting offers the possibility of considerable practical advantages over conventional upsetting, because it can be applied easily and sealing is simple.

(iii) Injection upsetting results in flanges with non-uniform thickness and another forming operation is required if a flange with parallel surfaces is needed, while flanges of constant thickness can be formed in one operation in conventional upsetting.

(iv) In conventional upsetting the working force is applied over the whole area of the flange rather than on the billet area only. Consequently the bore stresses in the container are relatively lower in conventional upsetting, which can be higher than the limiting factor in injection upsetting.

(v) In forming a single flange the relative simplicity of conventional upsetting may be an important factor in the choice of the upsetting process.

On the other hand, when several flanges are to be formed on one cylindrical billet, conventional upsetting is impossible. Injection upsetting into split dies is then the method of forming such products.

1.3 Finite element method

1.3.1 Introduction

In the past it was a common practice to simplify the continuum problems to the point where an analytical solution could be obtained. With the advent of digital computers, the emphasis in engineering analysis has moved towards more versatile numerical methods. One class of such methods has been given the name 'finite element method'.

The finite element method was developed originally for structural analysis and it has been used for solving many complex structural problems. The method involves dividing the physical systems into small subregions or elements. Each element is an essentially simple unit, the behaviour of which can be analysed independently of the behaviour of other elements in the collection. The elements are assumed to be interconnected at a discrete number of nodal points situated on their boundaries. Variation of the required functions (such as displacement function in solid mechanics) for the element selected are approximated uniquely in terms of their values at these nodal points. The behaviour of the element is then approximated by the use of the principles of mechanics. The assemblage of elements fitted together makes a final discrete model of the continuum and its overall behaviour is then described by a system of algebric equations.

The finite element method has been applied quite successfully to a wide range of linear structural problems and recently attempts have been made to extend the method to cover non-linear problems. While the analysis of linear problems is relatively straightforward, the non-linear problem is considerably more difficult. Perhaps the most disturbing point has been that most of the computational procedures currently available are very inefficient and require excessive amounts of computer time when

applied to practical, large scale problems. The long computer-run times (ranging from minutes to several hours) severely limit the use of these non-linear approaches as design tools for the majority of users.

The nonlinearities arise from two distinct sources: material nonlinearities and geometric nonlinearities. The most commonly used nonlinear material is the elastic-plastic material. For this material the linearity of the incremental stress-strain law forms the basis of the equations, its most direct application being in the incremental type solution, where the solution is built up as series of linear increments.

Various methods have been used to solve the elastic-plastic problems utilizing the finite element approach. The formulations of these methods fall into two main catagories: initial strain (or, in a modified form, initial stress) and variable stiffness method. In the first method the plasticity effects are treated as initial stress or initial strains and the problem is solved as an elastic one, using the elastic stiffness matrix throughout. In the second method the incremental linear constitutive relation, (based on plasticity theory) in every step of load increment is introduced directly into the governing equations. This would modify the element stiffness matrices at each step, thereby changing the overall stiffness matrix.

From the computational point of view the initial strain method has one main advantage; the stiffness matrix once developed for the elastic case remains unchanged throughout the whole problem. This permits an easy implementation of the method in a general finite element program. However, when the combined (geometric and material) non-linearity is considered, the variable stiffness method becomes quite attractive. Here the non-linearity arising from the change of geometry can easily be incorporated at each incremental step together with the effects of plasticity.

1.3.2 Previous works

Since the initial paper of Turner et al *(50)* various types of elements have been developed and different kinds of non-linearities have been dealt with. Turner et al derived a direct stiffness matrix method by establishing basic conditions of continuity and equilibrium at selected points (nodes) in the structure.

The problems of material nonlinearity and geometric nonlinearity due to their applicability to practical problems have received considerable attention. The early works on elastic-plastic problems were restricted to infinitesimal strains, in general describing only the onset of plastic deformation.

Mendelson and Manson *(51)* studied various thermal stress problems in the elastic-plastic range. The method which is based on the equilibrium equations treated the plastic strain increments as thermal strains and developed a method called by them 'the thermal strain approach'. Subsequent papers eventually refer to the initial strain (or stress) method. The basic concept of this method is that the equations of equilibrium can be modified to compensate for the fact that the plastic strains do not cause any change in stress. Gallagher et al *(52)* used this approach in the stress analysis of heated plates of complex shapes.

The initial strain approach, which was favoured in the earliest application of the finite element method to plasticity, fails if ideal plasticity is considered or if the degree of work hardening is small. This is due to the fact that in ideal plasticity the strains can not be uniquely determined for prescribed stress levels. An alternative method which is referred to as 'initial stress' appears ideally suited here. This method was first developed by Zienkiewicz et al *(53)*, and it was applied to a number of problems such as perforated tension strip with and

without strain hardening, cantilever beam subjected to cyclic load and plastic yield during metal cutting. The report concludes that the initial stress method has shown to yield more rapid convergence than the alternative approach. A subsequent work by Nayak and Zienkiewicz *(54)* presents a general formulation which includes associated and non-associated plasticity. The paper emphasizes the advantage of the initial stress method for a wide range of problems. They attempted problems such as: cyclic loading of a composite bar, notched tension specimen, thick sphere and cylinder subjected to internal pressure, plane strain extrusion, and plane strain indentation (strain softening and strain hardening behaviour). The report suggests the possibility of including in one program a variety of iterative procedures ranging from initial stress to the single step tangential matrix operation, as the authors believe the best efficiency lies in a combination of various methods. However, they remark on some problems, such as strain softening or collapse investigations where the tangential matrix ceases to be positive definite whilst the initial stress procedure provides the most efficient approach.

At the same time as the initial strain method was being developed the tangential modulus method was also given considerable attention by several workers. The method which deals with non-linear problem as a series of piecewise linear problems was first used by Pope *(55)* and Marcal *(56)*and extensively used by Marcal and his associates *(57-59)*.

Marcal and King *(59)* solved several two-dimensional problems using the tangent modulus method. In this investigation, a partial stiffness concept has been suggested and it has been used to study plane stress, plane strain and axi-symmetrically loaded body of revolution. The derivation of the incremental stress-strain relationship from the Prandtl-Reuss equations and the Von-Mises yield criterion is presented. Comparisons

with known results have been made for the case of a long cylinder with internal pressure, a tensile specimen with a central hole in plane stress, and a notched specimen. Later Marcal *(60)* used this method for the elastic-plastic analysis of pressure vessel components. Yamada et al *(61)* followed Marcal and King's work, but used small and varying increments of load, sufficient just to cause yield in the successive elements. The method is based on a plastic stress-strain matrix which is derivable by inverting the Prandtl-Reuss equations in plasticity theory. The matrix is of a quite simple form and facilitates the incremental treatment of elastic-plastic problems. As an example, they employed their method to study notched tension specimens under conditions of plane-stress using triangular elements. Akyuz and Merwin *(62)* developed a general procedure for the solution of elastoplastic problems by using a piecewise linear load deflection relationship and a step-by-step computational algorithm. They demonstrated the problem solving capability of the method with reference to constant-strain triangular elements by treating plane strain indentation for cylindrical indenters.

Lee and Kobayashi *(63)* also used the tangent modulus method for an elastoplastic analysis of plane strain and axi-symmetric flat punch indentation into a specimen of finite dimensions. The computer programs for elastic analysis with a quadrilateral element composed of four constant-strain triangles and with higher-order quadrilateral finite elements were modified to include the elastoplastic analysis.. Studies were made on the development of the plastic zone, the load-displacement relationships, and the stress and strain distributions during continued loading, with variations in the punch friction and specimen dimensions. Unloading was considered also and the residual stresses were examined. The same authors, in another work *(64)*, attempted the problem of simple upsetting of solid cylinders and the

problem of plane strain side-pressing, using the same formulation. Solutions were obtained to a 33 per cent reduction in height in axi-symmetric upsetting and up to a 19 per cent reduction in height in side-pressing, under conditions of complete sticking at the tool workpiece interface. In both cases they refer to possibilities of the finite element method for such a class of problems, but remark that there are questions still to be solved, in order to improve the accuracy of the solutions, especially when large strains are present.

A paper by Argyris and Scharpf *(65)* completely describes all the present methods available for elastic-plastic analysis using the finite element method. The convergency of each method is studied in one particular application.

Several Japanese investigators presented solutions to a number of problems by using Yamada's approach. Nagamatsu et al *(66)* applied the same formulation to the analysis of compression of a block under conditions of plane-strain. They considered sticking friction at the tool-workpiece interface. Since only the onset of plastic deformation was considered, the influence of shape changes on the stiffness matrix was neglected. They also neglected the change of the elastoplastic strain-stress matrix to shorten the computing time. In order to check the error involved, some calculations were performed without this simplication, the error is claimed to be very small till the plastic region penetrates through the block. Although the plastic zone propagated over nearly the whole block, the maximum strain achieved was less than 0.13%. Nagamatsu and his co-workers also investigated the simple upsetting of solid cylinders *(67)* and hollow cylinders, considering the geometrical change of the nodal coordinates (such consideration was neglected in *(66)* by Nagamatsu et al). In both cases, the shape of the bulged surfaces, load, distribution of pressure and tangential stress at the

contact and distribution of strain and stress were computed.

Iwata et al *(69)* also used Yamada's procedure in an analysis of hydrostatic extrusion. In this work, the effect of frictional coefficient on the spread of plastic zone, the pressure displacement curve, and the stress and strain distributions are studied for the non-steady state in plane strain and axisymmetric extrusions. In the case of the plane strain extrusion pressure, shape of plastic strain zone, and stress states in the plastic zone agreed with those from the slip-line solution. The extrusion pressure for the axisymmetric condition was higher than that for the plane-strain condition, and it was significantly affected by the friction coefficient.

Most of the literature reviewed so far was concerned with material non-linearity. In the works considering geometrical non-linearity higher order terms are introduced into the strain displacement matrix, leading to a new class of stiffness matrices. The additional stiffness matrices required for analyzing the geometrically non-linear problem are variously termed the initial stress stiffness matrix, the geometric matrix, and the initial displacement matrix. Turner et al *(70)* extended the method of direct formulation of the stiffness matrix to cover the effect of non-uniform heating and large deformations. They used their analysis to derive the stiffness matrices for an axially loaded member and a plate element in plane stress conditions.

Geometric non-linearities, as considered by Turner et al *(70)*, were also treated by Argyris and Scharpf *(65)* Mallet and Marcal *(71)*, and Felippa *(72)*. Kapur and Hartz *(73)* developed a finite element approach for rectangular plate for various loading cases. Analysis without the use of initial displacement matrix resulted in over-estimates and it was concluded that the initial displacement matrix should be included in the

finite element analysis of large deformation and instability problems. A practical method of solution of the geometrically non-linear problem of plates is proposed in a paper by Kawai *(74)*.

In recent years a trend towards the use of non-linear equations of continuum mechanics has been observed in papers of finite element analysis. Oden *(75)* provides a general continuum mechanics theory for the finite element method. He showed that the idea of finite element models can be developed in higher-dimensional spaces, independent of specific co-ordinate systems, for any type of continuous abstract function defined on the space. Oden *(76)* later demonstrated his theory with reference to a number of applications, these include the generation of finite element models in the time domain and certain problems in wave propagation. Pian and Pin Tong *(77)* have shown that the finite element method can be formulated from the variational principles in solid mechanics by relaxing the continuity requirements along their inter-element boundaries. The combination of different variational principles and different boundary continuity conditions yields numerous types of approximation methods. In this work, plate bending problems were used to compare the relative merits of the various methods.

Zienkiewicz and Godbole *(78)* treated the problem of large, progressive deformation under plastic and visco-plastic conditions. A stream function formulation was used and a finite element solution was found for the non-newtonian flow problem. The theory was applied to the steady state extrusion and the results were found to be an improvement on those obtained by Nayak and Zienkiewicz *(54)*, although at the cost of using a finer mesh. The extrusion pressure was however still above that given by the slip-line solution. An application was also made to the analysis of non steady-state (considering the change of boundary

configuration) punch indentation. The indenting pressure was shown to be linearly dependent on the depth of penetration, and above the slip-line solution.

Gotoh *(79)* employed a polynomial shape function of triangular elements. A general formulation of the finite element analysis of shell structures is reported, considering material and geometrical non-linearity with or without anisotropy. The practical validity of the formulation was investigated through some numerical examples of elastic and elastoplastic deformation of circular isotropic and anisotropic sheet metals subjected to hydraulic pressure. Values of strain are not presented, but the whole area is brought into the plastic range.

Hofmeister, Greenbaum and Evensen *(80)* presented a method for the large strain, elastoplastic analysis of two dimensional structures by the finite element method. An incremental variational principle is used to develop the finite element equilibrium equations for use in a piecewise linear solution procedure. An equilibrium check was employed at any point in the incremental solution process to reduce any cumulative error caused by linearizing the development of equilibrium equations. The equilibrium check and corrective cycling procedure prevented the computer load-deflection behaviour from straying from the true equilibrium path. Several plane strain examples are presented to display various types and degrees of non-linear behaviour. These examples include: notched tensile specimen, hollow cylinder subjected to internal pressure, cylindrical bending problem, and the large strain sheet bending problem.

Marcal *(81)* developed incremental stiffness matrices for the small strain large displacement analysis of combined non-linear problems. The element stiffness matrices were obtained from the principle of virtual work. A general purpose finite element program for combined non-linearity

analysis is also described. Case studies, using the developed finite element program, the behaviour of axisymmetric shells, flat plates, and structures in plane stress were examined.

In a paper by Stricklin et al *(82)* an assessment of the solution procedures available for the analysis of inelastic and large deflection structural behaviour is presented. The solution procedures are applied to circular plates and shells of revolution in an attempt to compare and evaluate each with respect to computational accuracy, economy and efficiency.

Hibbit, Marcal and Rice *(83)* developed an incremental and piecewise linear finite element theory for the large displacement, large strain problems with particular reference to the elastic-plastic behaviour in metals. The resulting equations, though more complex, are in a similar form to those previously developed for large displacement, small strain problems. This similarity indicates that existing non-linear general purpose programs may be extended to include finite strains. They identify four stiffness terms, which are named small strain stiffness, initial load stiffness, initial strain stiffness and initial stress stiffness. The report suggests calculation of all these additional terms (for which the last three have a complicated form) for each increment of deformation in an elastoplastic analysis. Needleman *(84)* has a similar Lagrangian scheme, but he derives his equations from a variational principle due to Hill *(85)*. .A third Lagrangian formulation was presented by Felippa and Sharifi *(86)* who intended to place no limitation on the size of an increment of deformation. Higher order terms are thus introduced into their stiffness. However, these terms are not significant in a tangent modulus approach to elastoplastic analysis, since the increment of deformation must be small in any case to ensure that the constitutive

rate moduli do not change significantly from one increment to the next.

McMeeking and Rice *(87)* presented an Eulerian finite element formulation for problems of large elastic-plastic flow. This method is based on Hill's variational principle for incremental deformations, and is ideally suited to isotropically hardening Prandtl-Reuss materials. The formulation is given in a manner which allows any conventional finite element program, for small strain elastic-plastic analysis, to be simply adopted to problems involving arbitrary amounts of deformation. The authors remark that the conventional small strain formulation in stress analysis can be inadequate for small strain problems not only when increments of rotation greatly exceed those of strain but also when representative stress levels have attained a magnitude comparable to that of the plastic hardening modulus.

Gunasekera *(88)* deals with the application of combined forms of nonlinearity to elastic-plastic materials. He used the finite element displacement method to solve problems with small and large deformations. The nonlinearity due to large deformations is taken into account by a Lagrangian derivation based on Green's strain tensor, and examples are given to illustrate this. An alternative method is also discussed based on the Eulerian derivation. Prandtl-Reuss equations are used for the elastic-plastic material together with the yield criterion of Von-Mises. A computer program was developed based on a step-by-step analysis using small linearised increments. Application of the method to study the transient stages of a metal processing problem is demonstrated.

Dieterle *(35)* recently studied the simple upsetting and heading of tubular billets (this latter problem will be included amongst others considered in the present thesis) using a finite element formulation as

developed by Zienkiewicz *(53)* but introducing several simplifying features. Although strains are of order of 0.45 good agreement with experimental results are claimed to have been achieved, the use of large values of Poisson's ratio and the use of unrealistic boundary conditions to improve the results seem to represent too many simplifying assumptions to retain the reliability of the solutions.

Most recently Blass *(89)* developed a finite element formulation, considering both material and geometrical nonlinearities, for the elastic-plastic analysis of metal working problems. The restrictions imposed are those of isotropic material behaviour, isothermal deformation, absence of Baushinger effect and infinitesimal elastic deformation. The analysis is performed in a Lagrangian frame of reference and a computer program is implemented and applied to the analysis of radial upsetting. The computed and experimental results and also an upper-bound solution are presented and compared. The finite element results represent a slight improvement over the upper-bound solution. In general, the computed results were satisfactory at the early stages of deformation, but a progressive degradation of the solution algorithm eventually leads to failure of the program. In his conclusion, he refers to complexity of the three-dimensional process considered which leads to difficulties. He also mentions the difficulty encountered in prescribing the appropriate boundary conditions to the problem.

Much of the theoretical work, using the finite element method has been performed with unrealistic surface conditions, frequently the two limits of zero and sticking friction. In recent years a number of workers *(90-97)* have proposed various methods for the inclusion of surface friction in the finite element solution. Nagamatsu et al *(66,67,68)* modified the surface node displacement by a "slip-factor", but this

requires a prior experiment under appropriate conditions. Gordon and Wienstein *(90)*, Iwata et al *(69)* and Odell *(91)* introduced forces to the surface nodes, opposing the direction of motion. Shah and Kobayashi *(36)*, Price *(92)* and Matsumoto et al *(93)* allowed for friction by the introduction of a surface shear stress τ evaluated from an empirical constant m, with $\tau = mk$, where $k = Y/\sqrt{3}$, and Y is the yield stress of the adjacent surface element, again directed against motion. However, both the force method and the surface shear stress approach require prior knowledge of the flow direction. Where the direction of flow is known, these methods appear to be quite effective. But with processes such as ring compression, and in many other forging processes, direction of flow is not known and so these methods cannot be fully applied.

Several attempts were made by Hartley *(94)* to develop a formulation that did not require prior knowledge of the flow direction. These involved modification of the stiffness of either the surface elements or surface nodes on the ring, based on the frictional work involved or arbitrary functions. All the solutions obtained displayed incorrect modes of flow and were not pursued.

Sharman *(95)* and Zienkiewicz et al *(96)* in their analysis of forward extrusion, introduced a narrow layer of elements on the die face. The properties of this layer were assumed by Sharman *(95)* such that the surface shear stress was similar to that produced by glass lubrication used in his experimental work. Zienkiewicz et al *(96)* assumed a relationship $Y = -\mu\sigma_m$ for the yield stress of the elements, where σ_m is the mean stress of the adjacent surface element and μ is the coefficient of friction. Although only very small deformation is considered, conditions relating to the direction need not be imposed on the layer.

Most recently Hartley *(97)* describes a method for the inclusion

of the influence of surface friction into finite element analysis. The principal features of his method are first, the introduction of a surface layer of elements where stiffness is modified by a function, ($\beta = m/(1-m)$), where m is the ratio of the yield stress of the surface layer to that of the bulk material, and secondly, the forces are applied to the surface of the billet. To investigate the proposed approach it was applied to the friction sensitive process of ring compression and the change in the inner diameter with progressive deformation, and the applied forces were computed. Excellent agreement between the theoretical predictions and experiments has been claimed.

1.3.3 Present work

The present work deals with the application of the finite element method to large elastic-plastic deformation incurred during the upsetting operation. The solution techniques for the material non-linear problem are first presented with regard to accuracy and computation economy. The equations of equilibrium are developed and then various solutions which follow directly from the equilibrium equations are described.

Computer programs are developed, based on an approach similar to that due to Yamada *(61)* described in the previous section. An incremental tangential method is used and the formulation is valid for infinitesimal strains as the extra terms in the element stiffness matrix, which will be introduced in the case of large plastic deformation, are not considered. According to Marcal *(81)* for some large deformation problems it may be possible to omit the extra terms entirely. He claims that the results obtained for a large number of problems show that it can lead to excellent results. In the present approach, however, an instantaneous frame of reference is used to describe the incremental elastoplastic deformation

of the continuum. Nagamatsu et al *(67,68)* point out that this kind of strategy to some extent offsets the effect of omitting the non-linear terms and therefore strains of higher magnitude may be tackled within a certain degree of accuracy.

The computer programs presented can, however, be modified to perform a similar analysis on a large strain and large displacement formulation, such as derived by Hibbitt et al *(83)*. The modifications, as they believe, are minor and can be implemented easily in an available elastic-plastic computer program.

The strain hardening of the material is approximated by two straight lines although any other form could have been incorporated. The Prandtl-Reuss equations are used for the elastic-plastic material together with the yield criterion of Von-Mises. Anisotropy and the Bauchinger effects are neglected.

1.4 Upper-bound analysis

1.4.1 Introduction

In many metal-forming problems it is possible to find simple kinematically admissible velocity fields. These are velocity distributions which satisfy continuity and any imposed velocity boundary conditions. However, they do not necessarily have associated stress fields which satisfy the yield criterion, equilibrium, and any stress boundary conditions. The power dissipation due to plastic distortion calculated using a kinematically admissible velocity field is always equal to, or greater than, that occurring in the actual process. This is referred to as the upper-bound theorem.

When using an upper-bound technique, it is possible to build up kinematically admissible velocity fields using regions in which rigid-body motion occurs. These are separated by planes of velocity discontinuities at which all the power dissipation occurs. This system leads to a very rapid and simple means of estimating the power and force requirements. Since the power (and force) requirements calculated by the upper-bound method are in general greater than those found in the real process, the method is a useful conservative design tool.

In the present work, an upper-bound s lution for injection upsetting based on the Kudo *(102)* velocity field method is presented. The worked material is assumed to be non-hardening and rigid-plastic and follows the Von-Mises yield criterion as well as the Lavy-Mises stress-strain rate relations. In the present analysis the minimization of the total dissipated energy is carried out with respect to the position of the surface of velocity discontinuity that divides the deforming part of the billet from the undeformed part.

1.4.2 Previous works

In recent years, numerous applications of the upper-bound method have been made to the analysis of plane strain *(98-101)* and axi-symmetric *(102-108)* problems. Johnson *(98,99)* and Kudo *(100,101)* showed that the upper-bound approach is useful in finding average forming pressures for plane strain processes. Kudo *(102,103)* extended his concept of a "unit rectangular deforming region" for plane strain to the analysis of axi-symmetric forming problems. He introduced conical surfaces (straight lines on a meridian plane) as discontinuity surfaces in the cylindrical deforming region. The resulting velocity field, however, was found to yield better solutions over only a limited range of conditions when compared with that obtained by the simple uniform (or parallel) velocity field. Several forging and extrusion problems with the tools having flat working surfaces were analysed by dividing the material into several unit regions. These were the compression of a cylinder and an annulus, extrusion, piercing, extrusion-forging and symmetrically opposed extrusion-forging. Kudo also proposed upper-bound solutions to obtain the working pressure when Coulomb friction between the tools and the material exists. He also modified the upper-bound solution for a perfectly plastic material, for non-steady working processes of work-hardening material. The Kudo method for obtaining average pressures in some axi-symmetric forming problems is reviewed by Kobayashi *(104)*. Kobayashi replaced the conical surfaces (suggested by Kudo) by curved surfaces. The new proposed velocity fields yield improved upper-bound solutions in the two examples of compression of cylindrical billets illustrated in the paper.

Avitzur *(12)* analysed simple compression of solid and hollow cylinders using a parallel velocity field. He assumed a constant friction factor, m , in calculating the energy losses due to frictional forces. In

the analysis of solid cylinder bulging is described by an exponential relationship, involving an arbitrary factor. This factor is later determined by minimization of the total dissipated energy. In the case of hollow cylinder the neutral radius is determined by minimization.

Halling and Mitchell *(105)* used a double triangle arrangement of velocity discontinuities for the axi-symmetric extrusion through conical dies. The solutions are optimized using a computer program which incorporates terms to accommodate the position of the discontinuity surfaces and the effects of die friction. The results were obtained for a full range of die angles reductions and frictional conditions. The predictions were compared with experimental results and favourable agreement is reported. The authors concluded that a more refined pattern of velocity discontinuities would lead to a greater accuracy of prediction, particularly in relation to the formation of dead metal zones. Halling and Mitchell also extended their solution to incorporate the effects of strain hardening.

Lambert et al *(106)* proposed a method of obtaining velocity fields without introducing velocity discontinuities. This method which is based on a technique used by Shabaik et al *(107)* determines the velocity components by introducing a flow function obtained from experimentally observed flow lines. Lambert et al applied their method to some steady-state plastic deformation processes such as plane-strain extrusion, tube extrusion and axisymmetric piercing. The results are presented in terms of flow lines, velocity component distributions and average forming pressures.

Lange and Steck *(108)* obtained an upper-bound solution for tube extrusion through conical dies by expressing the axial and radial velocities as functions of r and z . Some of the constants in the functions were determined by the boundary conditions and the remainder were arbitrary.

Thus, the rate of internal energy dissipation could be optimised with respect to the arbitrary constants describing the velocity field.

Alexander and Lengyel *(45)* used an upper-bound solution to analyse the injection upsetting of solid bars. A kinematically admissible velocity field with a velocity discontinuity of paraboloidal surface was established. The predicted upsetting pressure was found to be in good agreement with the experimental results. Alexander and Lengyel also developed a lower-bound solution by introducing a statically admissible stress field for the deforming body.

Milner *(49)* and Parsons et al *(109)* in their work on injection upsetting of solid cylindrical billets used an upper-bound solution based on the Kudo *(103)* velocity field method for an ideal rigid-plastic material. They minimized the dissipated energy with respect to the position of the surface of velocity discontinuity which divides the deforming part of the billet from the undeformed part. Their results of the optimized upper-bound theory agreed well with the experimental findings at low values of flange thickness. The predictions were, however, found to drift from the experimental findings for greater values of flange thicknesses. Milner also used the upper-bound solution to analyse the injection upsetting of hollow billets and the injection upsetting of a billet with one end constrained.

1.5 Aim of the present work

Studying the shape and quality of the flange and behaviour of the metal under various geometrical and frictional conditions can provide the required working conditions for the production of hollow flanged components with fewer defects. The basic aim of the present work is to study the mode of deformation and the required upsetting loads in conventional and injection upsetting.

The finite element method is selected to tackle the problem theoretically. This selection was based on the strong capability of the finite element method in the analysis of metal working processes.

A computer program is developed based on the finite element formulation. The applicability of the program is demonstrated by examining heading and open upsetting processes. The validity of the results is also demonstrated by comparing them with the corresponding experimental findings.

A kinematically admissible velocity field is developed for injection upsetting to obtain forming loads by using an upper-bound technique.

CHAPTER 2

EXPERIMENTAL MATERIALS AND APPARATUS

2.1 Introduction

The main aim of the present experimental work is to obtain the upsetting load and the behaviour of metal during the conventional and injection upsetting processes under various conditions and compare the observations with the computed results.

A description of the general lay-out of the sub-press and tooling arrangements for various upsetting processes is first given. Experiments were carried out on lead, pure aluminium and copper specimens, and flanged components produced from hollow and solid billets.

Upsetting loads and values of punch displacements were measured during the tests and the effect of billet geometries on the load-displacement characteristics investigated. A visual examination of the shape and quality of the flange was made. The effects of billet geometry and frictional conditions on the mode of deformation were studied by etching the formed specimens.

2.2 Materials

The materials used in the experiments were high-conductivity copper, commercially pure aluminium and lead. Cylindrical billets of 25, 30 (solid), 44 and 50 (hollow) mm diameter were made in lengths ranging from 50 to 93 mm. All the specimens were subsequently annealed, by heating for 1 hour at 600°C, 400°C and 200°C for copper, aluminium and lead respectively and furnace cooled. The copper and aluminium specimens were lubricated with MoS_2 in grease prior to the experiments.

The true stress-strain curves were obtained by performing uniaxial compression tests using the incremental method. The results are presented in

Figs. 2-1 to 2-3.

2.3 Design considerations

The main design considerations for the sub-press are as follows:

1) The sub-press must accommodate various tooling for the upsetting of hollow and solid cylinders of different geometries.
2) It should be possible to adapt the sub-press for the various upsetting techniques described in section 1.2, by minimal changes in the tooling.
3) The internal diameters of hollow specimens or the initial diameters for solid bars to be in the region of 25 mm (1 inch) to demonstrate the usefulness of the analysis under production conditions.
4) The design should utilize the special features of an existing hydraulic press which will be described in section 2.4.
5) To simplify the manufacture of the tools the internal diameter of hollow billets should be kept constant with the wall thicknesses varied.
6) The sub-press to be suitable for forming flanges with large diameters.
7) It should be possible to produce flanges of various thicknesses in injection upsetting.
8) The surfaces over which the flanges are to be formed should have a reasonably uniform roughness in the various directions.
9) Instrumentation should be provided for the simultaneous recording of upsetting-load and punch-displacement.

2.4 Press

The experimental work was carried out on a hydraulic vertical upstroking press with a 1960 N (200 tonf) working capacity, Fig. 2-4. It has a stationary top platen and a bottom ram of 150 mm (6 inch) stroke. The maximum load could be limited to a value smaller than the nominal capacity by a pressure relief valve. Throughout the experiments the speed

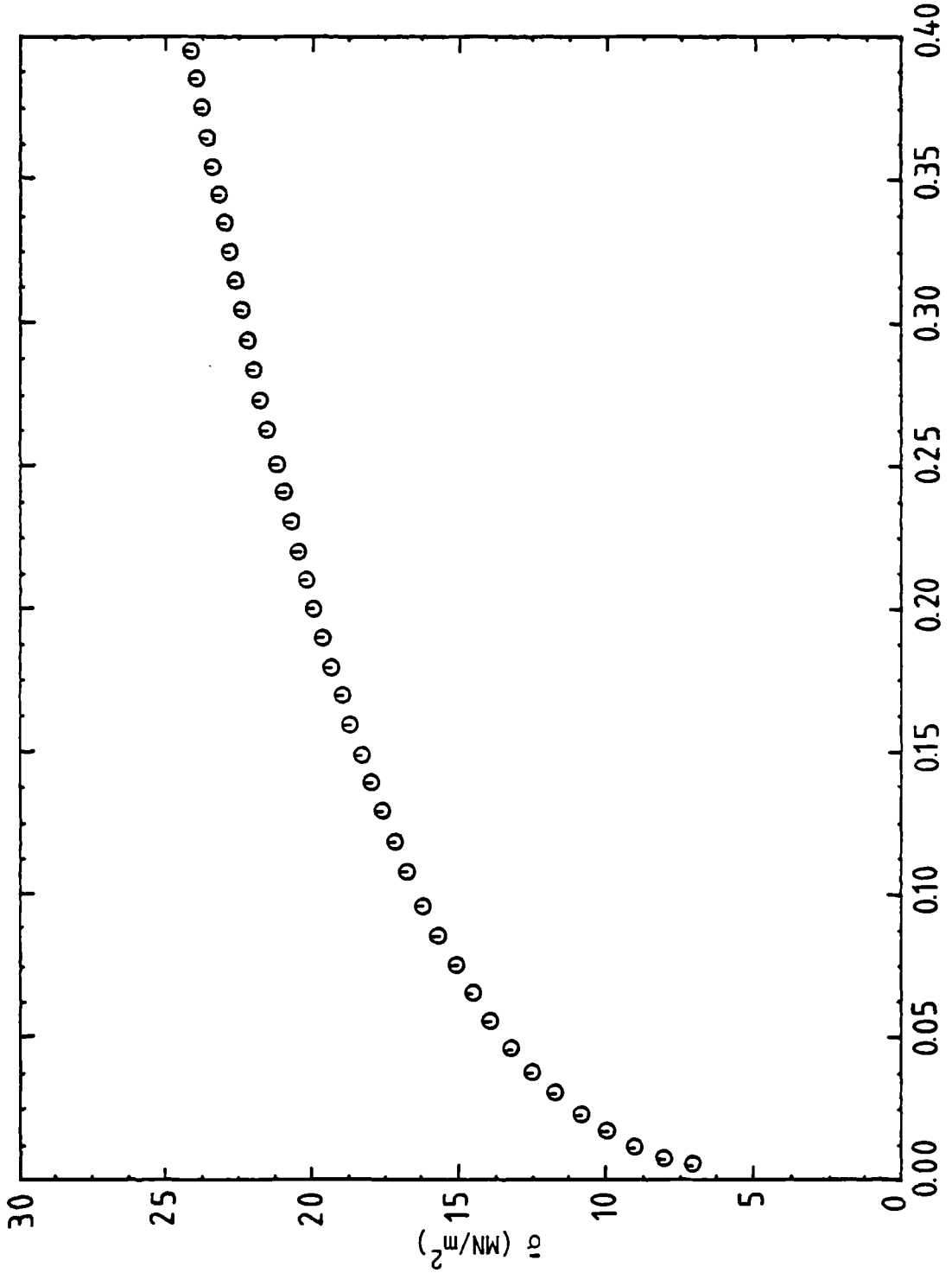


Fig. 2-1 True stress-strain curve for lead.

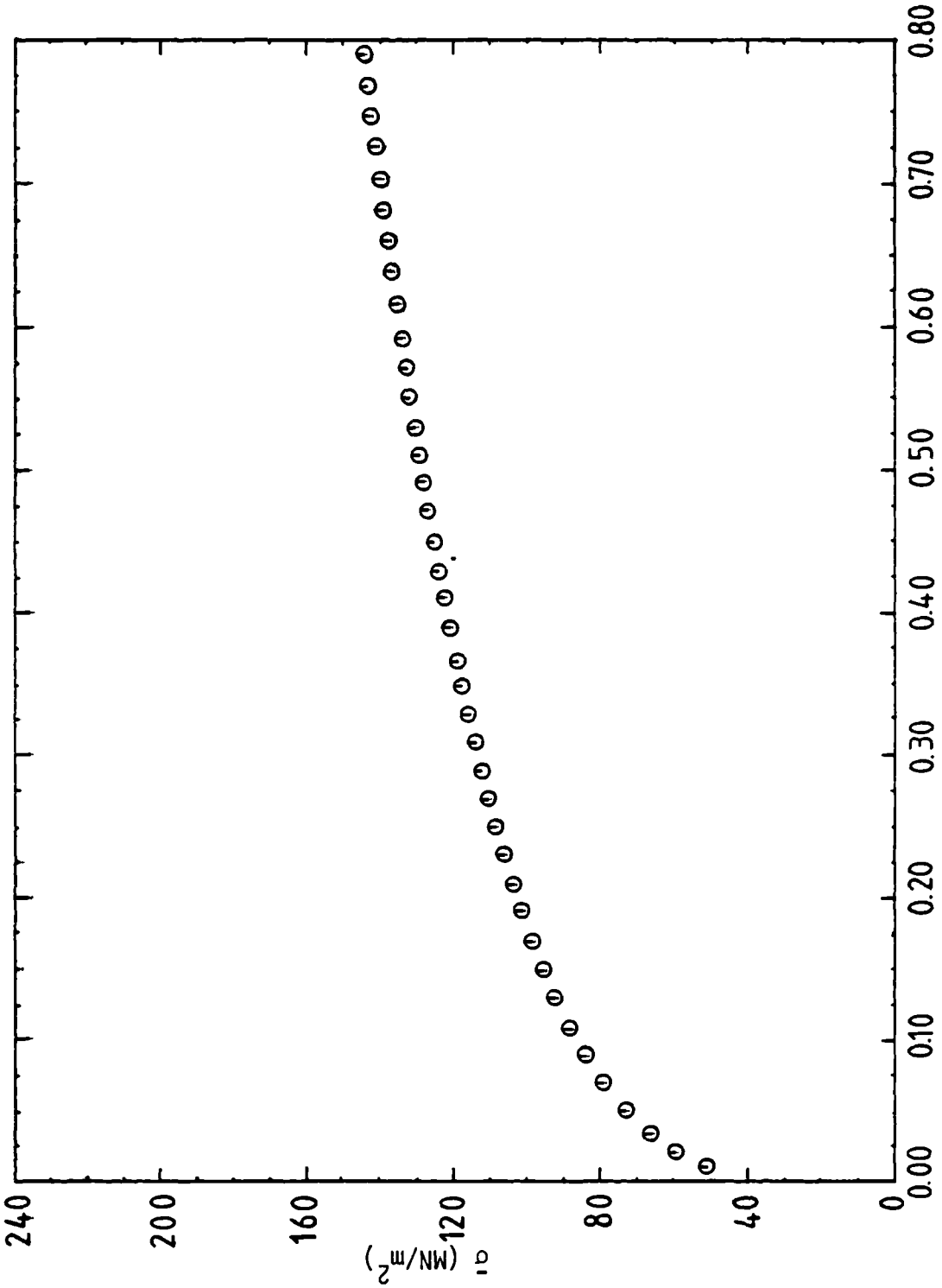


Fig. 2-2 True stress-strain curve for commercially pure aluminium.

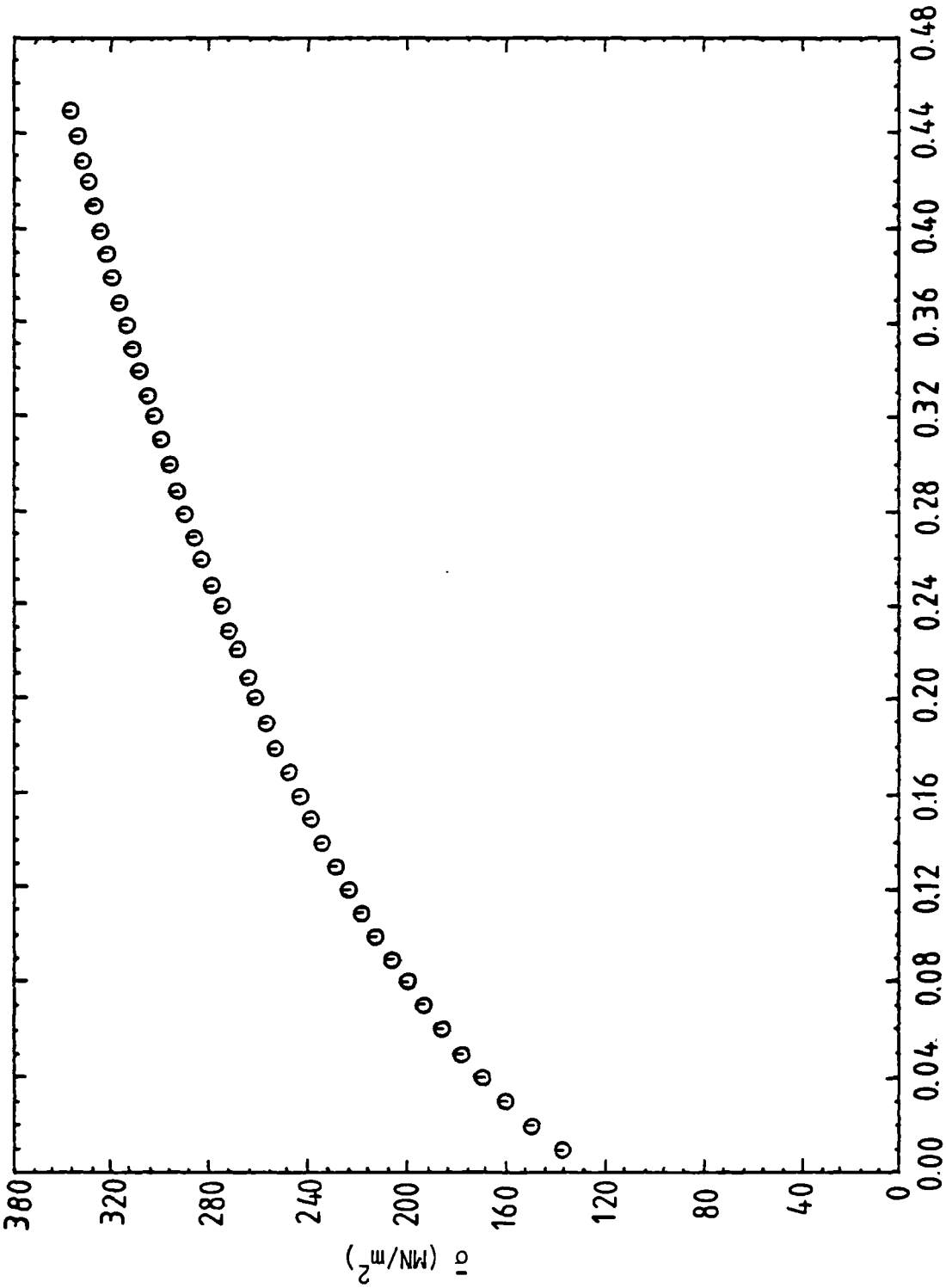


Fig. 2-3 True stress-strain curve for copper.

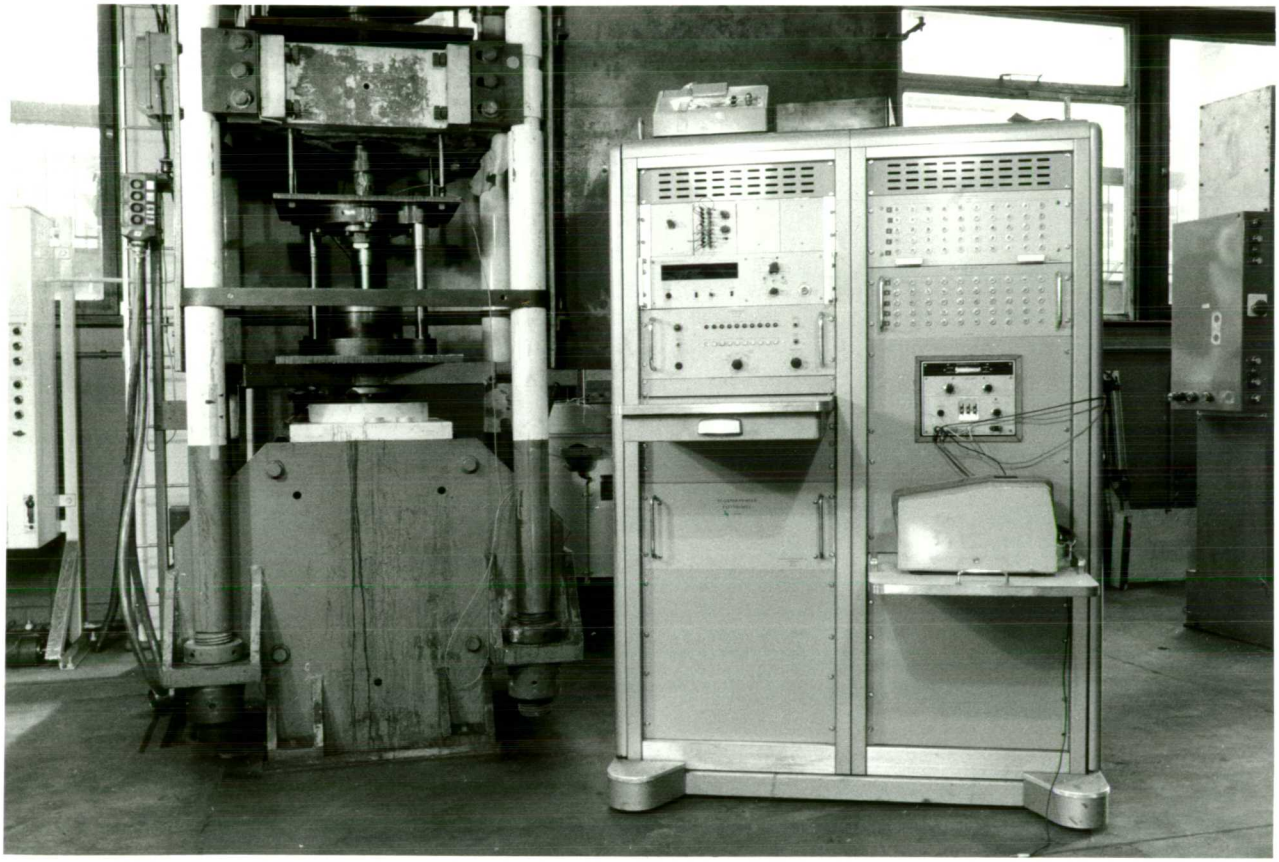


Fig. 2-4 Press and data logger.

of the press-ram was maintained at 1 mm/min (0.04 in/min).

2.5 Instrumentation

Measurement of the press-ram load and displacement was effected electrically. The various tool arrangements included a strain-gauged load cell and a linear potentiometer stroke gauge.

2.5.1 Load cell

The load cell was made of KEA180 oil hardening tool steel and designed to carry up to 70 tonf (687 kN). Eight electric resistance strain gauges were mounted on the outside diameter of the load cell and connected to an AC bridge system. The load cell was calibrated against a Tinius Olsen testing machine. The calibration curve is shown in Fig. 2-5. To minimize the hysteresis loss the load cell was repeatedly loaded prior to use. The configuration of the workpiece was shown to have a negligible effect on the calibration of the load cell.

2.5.2 Displacement transducer

The displacement of the punch was measured by a potentiometric displacement transducer which was attached to the fixed platen of the press. A probe fixed to the bottom platen moved a contact around the coil of the transducer. This resulted in the changing of resistance between the contact and one end of the coil which was then converted to voltage. To calibrate the transducer the punch displacement was measured by a high accuracy dial gauge and plotted against the corresponding voltage values printed by the data logger. The calibration curve is shown in Fig. 2-6.

2.5.3 Data logger

The outputs from the load cell and displacement transducer were both fed into a Solartron digital data recorder. The analogue signals were

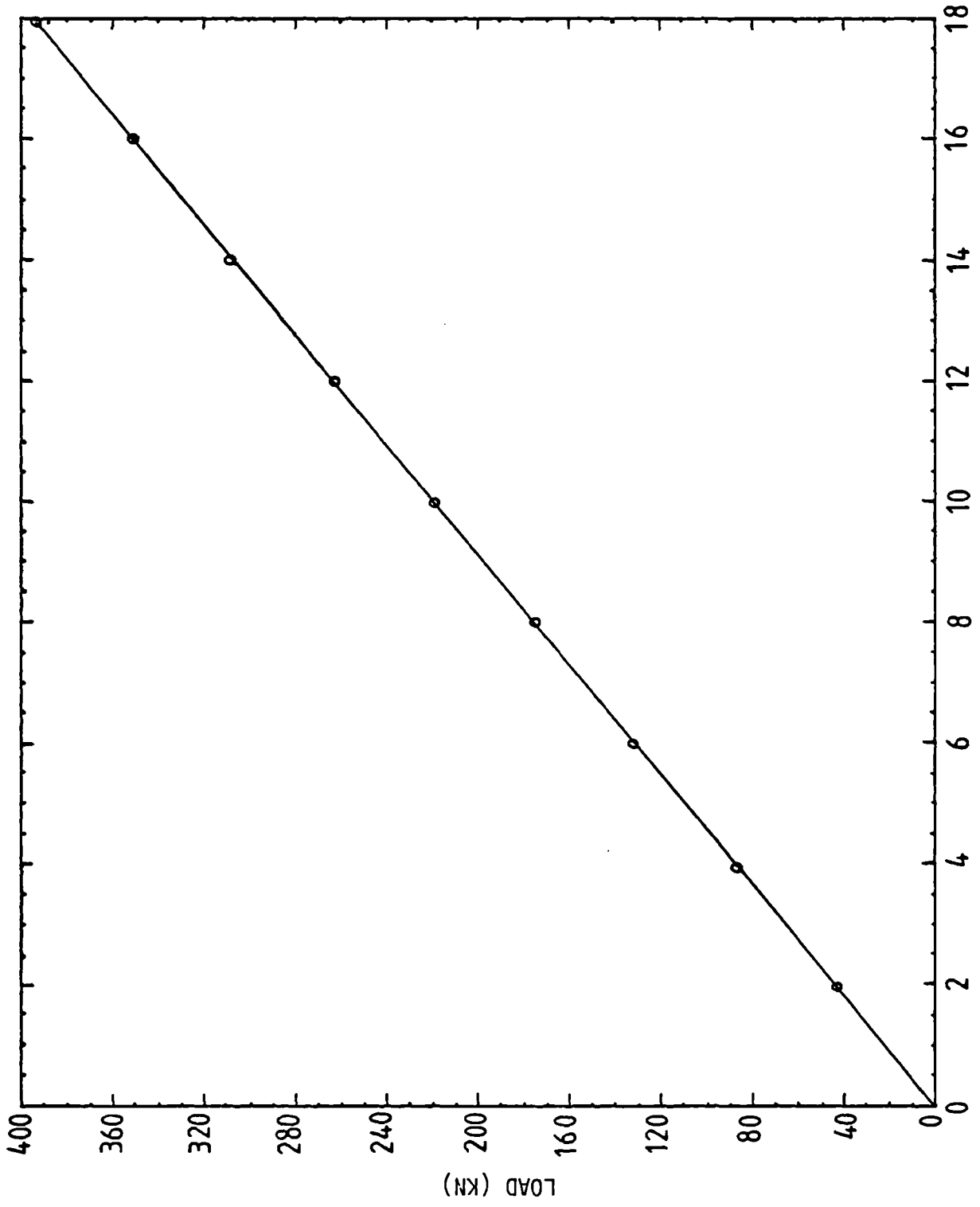


Fig. 2-5 Calibration curve for load-cell.

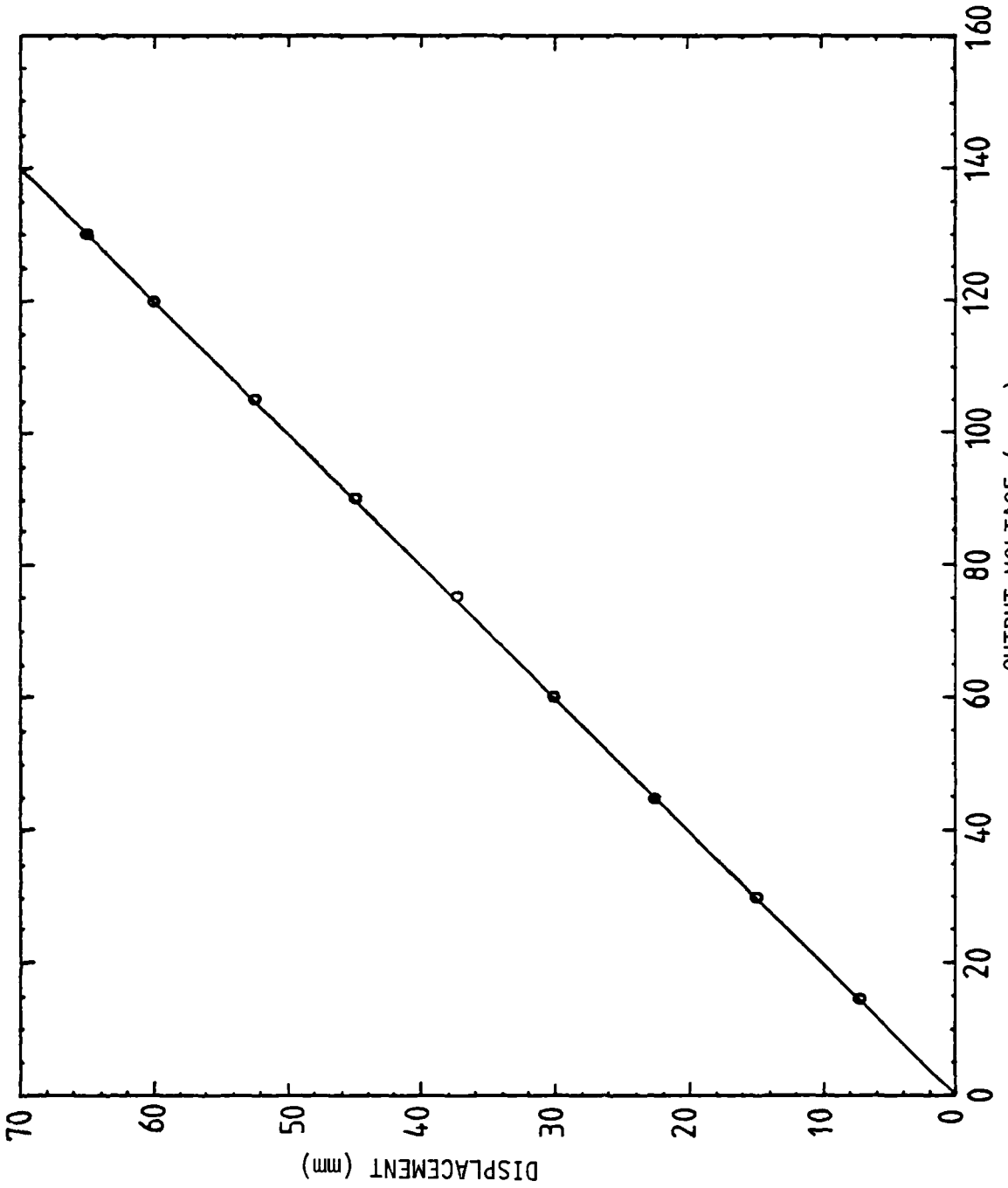


Fig. 2-6 Calibration curve for displacement transducer.

converted to digital form and their values could be observed on an in-line illuminated display unit. The values were printed out by a numeric printer connected to the data-logger; the figures included the channel identity, the polarity and the voltage values. This recorder can be given a maximum of 100 analogue input signals which could be scanned in sequence at 6 different speeds varying between 10 samples per second and one per four seconds. A constant voltage of 6 volts was provided by the data-logger to activate the load cell and displacement transducer. The data-logger is shown in Fig. 2-4.

2.5.4 Surface structure measurements

A Talysurf machine was used in measuring the surface structure of the tool. Essentially, the instrument consists of a pick-up unit having a sharply pointed stylus which is transversed across the surface by means of a motorised driving unit.

The up and down movements of the stylus are converted into corresponding changes in an electric current which are amplified, and then used to control:

1) A graph recorder which provides a profile of the surface.
2) A meter which shows the centre-line average (CLA) index of all irregularities within a standardised length of surface.

2.6 Description of the sub-press

2.6.1 General layout

The sub-press assembly is shown in Fig. 2-7 and a schematic diagram of the general layout of the sub-press (which is identical in all cases) in Fig. 2-8. A two-pillar die-set is mounted on the moving platen of the press. The top platen of the die-set is attached to a mild steel plate which is in turn bolted to the top stationary platen of the press. The lengths of these bolts were chosen to accommodate the various sub-press assemblies for

the available limiting stroke of the main ram (150 mm). The upper die-set platen and the top square plate had uniaxial bores of 45 mm and 25 mm respectively at their centres. The holes were provided to allow access to the upper face of the mandrel which is used in the experiments on hollow billets (Fig. 2-9). It had to be ensured that, prior to upsetting, the mandrel extended through the specimen and into the insert. The position of the mandrel relative to the insert could be estimated by taking measurements through the top platens.

The load cell is located above the mild steel square plate with its axis in line with that of the main ram. The load cell is backed by a pressure block to fill the gap to the upper platen of the press (Fig. 2-8).

The punch holder can accommodate punches of appropriate lengths and diameters. It is secured to a retainer which in turn is bolted to the top platen of the die-set.

A container of 80 mm height and 220 mm outside diameter is fixed on the lower platen of the die-set. This container holds a hollow block of 140 mm outside diameter which in turn contains the various inserts for the different sets of experiments. Care was taken to ensure good alignment between the punch and die assemblies.

Dies of different sizes were supported by a retainer bolted to the container by four ½" diameter socket-head cap screws. An initial gap between the adjoining surfaces of the retaining plate and the container allows the screws to be tightened when the die arrangements are in position. Since high stresses were expected to act on these screws during injection upsetting due to the lifting load acting on the lower face of the retainer it was thought necessary to make the container hard to prevent the threads deforming plastically. To comply with this requirement the container was made from EN24 quality steel and heat treated in vacuo to 50/52 RC hardness.

The tooling arrangements for the four various methods of upsetting are described in the following sections. EN24 quality steel was used for the tools. The punches, dies and mandrels were honed after being heat treated in vacuo to a hardness ranging from 42 to 45 RC and all flat surfaces were ground. The surfaces on which the flanges were to be formed were ground in alternate directions so as to obtain a uniform surface structure of 0.25 μm (10 μin) CLA to ensure the forming of symmetrical flanges.

Figs. 2-9 to 2-16 show the tooling arrangements for simple injection upsetting, injection upsetting with one end of the billet constrained, heading and open upsetting of hollow and solid cylindrical billets. Since the tooling for injection upsetting was designed first and it was then adapted to suit conventional upsetting, the tool arrangement for injection upsetting is explained first.

2.6.2 Injection upsetting

The tooling arrangements used in the injection upsetting experiments consist of the details for forming hollow billets and solid bars. In both cases the tools for simple injection upsetting (forming the flange at the end of the billet) are extended to serve the injection upsetting experiments when one end of the billet is constrained (for forming the flange along the billet).

The tooling for the simple injection upsetting of hollow billets is shown in Fig. 2-9; the left and right sides indicate the position of the tools before and after upsetting. The assembly features a die of 44 mm bore and height of 47 mm which is located on a ring of 90 mm inside diameter. The die assembly is held down by a retainer bolted to the container which in turn is mounted on the lower platen of the die-set. A clearance of 0.3 mm between the retainer recess and the base of the die allows the alignment of the punch and die bore prior to tightening the retainer screws. The gap

in which the upset flange will be formed is made by the underside of the die and the upper surface of the pressure block which are parallel to each other and perpendicular to the axis. Increasing the thickness of the ring mounted between the die and the bottom anvil results in an increase in the height of this gap which leads to the production of thicker flanges.

The punch, which is mounted on the upper platen is provided with a bore appropriate to a mandrel of 25 mm diameter and length of 165 mm. The design is such that the mandrel is held stationary when after upsetting, the main ram descends with the container, so that the specimen is separated from the mandrel. Before every upsetting operation, the mandrel was positioned so that it was not only located in the appropriate bore of the specimen but also extended beyond the bottom face of the billet into the bore of the lower anvil.

The punch is made to have a close tolerance sliding fit with both the die and the mandrel. A hollow insert is mounted in the hollow pressure block at the centre of the lower platen, with its flat upper face level with the top surface of this block when in position. The top surface of this insert acts as the upsetting platen together with the upper face of the hollow pressure block. This insert is provided with a bore appropriate to the mandrel diameter with sliding fit.

The tooling shown in Fig. 2-10 is for the injection upsetting of hollow billets with one constrained end. The die for simple injection upsetting is located on another container with an identical bore diameter of 44 mm. The alignment of the axis of the die and the bore axis of this container is ensured by positioning the specimen in the bore. This container acts as an upsetting anvil during the deformation process and together with the top die forms the upsetting gap in the space created by interposing a flat ring between them. As before, the height of this ring

determines the thickness of the flange produced.

In this set of experiments the billets were longer so that the length of the mandrel had to be increased to 215 mm to ensure its engagement in the bore of the insert before upsetting commenced.

The sub-press for the simple injection upsetting of solid bars is shown in Fig. 2-11. The punch and die are made to suit the punch holder and die retainer used for hollow billets. Here, the hollow insert at the centre of the bottom platen is replaced with a solid insert of identical diameter.

Fig. 2-12 shows the sub-press arrangements for the injection upsetting of solid billets with one end constrained. The die in simple injection upsetting is used together with a container of an identical bore diameter.

2.6.3 Conventional upsetting

The tooling for conventional upsetting consists of the tooling for heading and open upsetting experiments (Figs. 2-13 to 2-16). The features of the tool for heading hollow billets (Fig. 2-13) are similar to those used for injection upsetting. A ring of 21 mm height with a sliding fit tolerance to the die and mandrel is located in the die to provide a closed end bore in which the specimen is constrained. Another ring of 74 mm outside diameter with a close fit tolerance to the mandrel is placed on the top of the specimen prior to upsetting. During heading, the punch load is applied on this ring and the flange is formed between the bottom face of the ring and the top surface of the die.

The sub-press assembly for heading solid billets is shown in Fig. 2-14. To provide a closed end bore in this arrangement a pressure pad of 27 mm height is located within the die used for the simple injection upsetting of solid bars. A compression pad of 60 mm diameter with a flat lower face is located on the top of the specimen. A recess of 24 mm depth is provided at the upper face of this anvil to fit the punch diameter.

The tooling arrangements for open upsetting tubular billets is shown in Fig. 2-15. The two containers from the injection upsetting of

hollow billets with one end constrained are used in this set of experiments. Two rings with identical bore diameters of 25 mm are placed in the containers, the heights of which are selected to provide appropriate constrained lengths for the specimens. Since the length of the previous mandrel is insufficient for this set of experiments, another mandrel of 90 mm height with uniform diameter along its length is used. This mandrel is supported by a spring located in the bore of the hollow insert.

Load is applied on a pressure pad of 75 mm diameter located on the upper face of the top container. It is necessary for this container to be held in position before upsetting begins. It can be released immediately after the billet commences to deform as the frictional forces between the outer surface of the specimen and the bore surface of the die prevent it from descending.

Fig. 2-16 shows the sub-press assembly for the open upsetting of solid billets. The tools are arranged in a similar way to those for hollow billets and the dies from injection upsetting of solid bars with one end constrained are used.

2.7 Experimental procedure

The billets were made to a sliding fit in both the mandrel and the die. Prior to the experiments the billets were coated with a thin layer of MoS_2 in grease. Lubrication was also provided for the surfaces on which the flanges were to be formed. In order to investigate the effect of friction some experiments were carried out under dry conditions. The contact surfaces were prepared by cleaning with trichloroethylene, and leaving them to dry completely before starting the experiments. Lubrication was provided at the mandrel/billet and die/billet interfaces to facilitate removal of the specimen.

The correct alignment of the punch and the die was ensured before every experiment by employing the following procedure:

1) The punch was secured in the punch-holder and screwed into the punch-retainer.
2) The specimen was placed in the die which was loosely held by the die-retainer.
3) The bottom platen of the press was raised and the die and the punch were aligned by moving the die to the appropriate position. The clearance between the die and its retainer and also between the holes of the retainer and its screws allowed the correct alignment to be achieved.
4) The screws of the die-retainer were first made finger tight and then the opposite screws were each given quarter of a turn in sequence until all were fully tightened. This was to avoid tilting of the die arrangements.

Before upsetting hollow billets, the load cell and the pressure block located on the top square were removed and the free height from the top surface of the mandrel to the upper surface of the square plate was measured through the bores provided at the centre of the plate and the top platen of the die set (Fig. 2-9). Adding this to the length of the mandrel revealed the actual location of the lower face of the mandrel when all the arrangements were set. This was performed to ensure that the mandrel was engaged within the bore of the lower anvil before the billet began to upset.

After ensuring the alignment of the punch and the die and also the engagement of the mandrel and the bore surface along the billet's length, load was continuously applied until a desirable amount of deformation was obtained. To investigate the effect of the wall thickness on the mode of deformation and on the required upsetting load, hollow specimens with outside diameters of 44 and 50 mm and identical bore diameter of 25 mm were used. The effect of the billet diameter was investigated with solid cylindrical billets of 25 and 30 mm diameters.

To investigate the effect of flange thickness in injection upsetting, three groups of experiments were carried out with fixed gap heights of 7, 10 and 14 mm. The length of the billets were selected so as to allow a free height of 3 mm in the die bore after inserting the specimens. This was to provide the free height required in the bore to enable alignment of the punch and the bore before impact.

In conventional upsetting the effect of the unsupported height of the billets was investigated by choosing specimens of appropriate lengths.

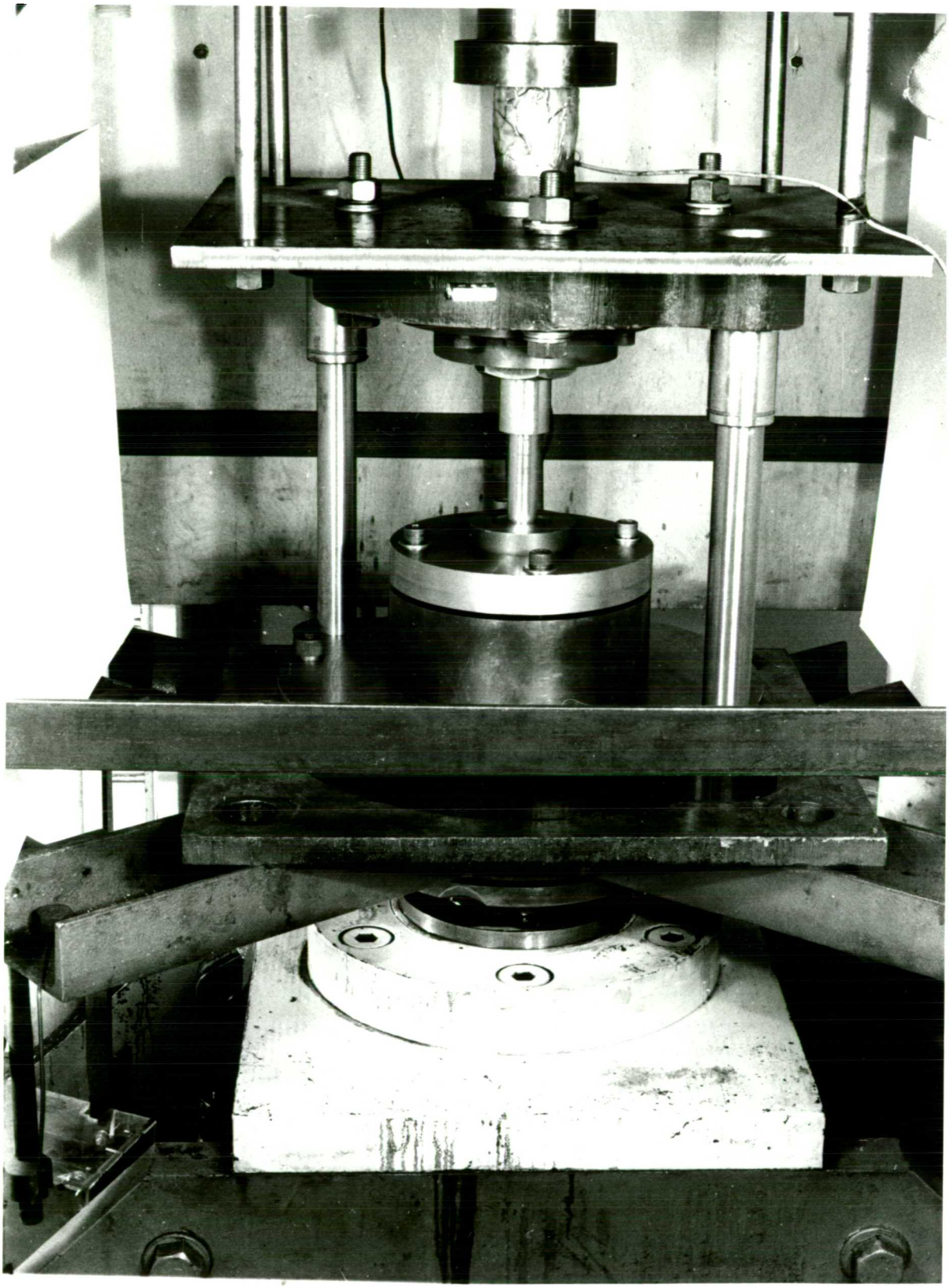


Fig. 2-7 Sub-press assembly

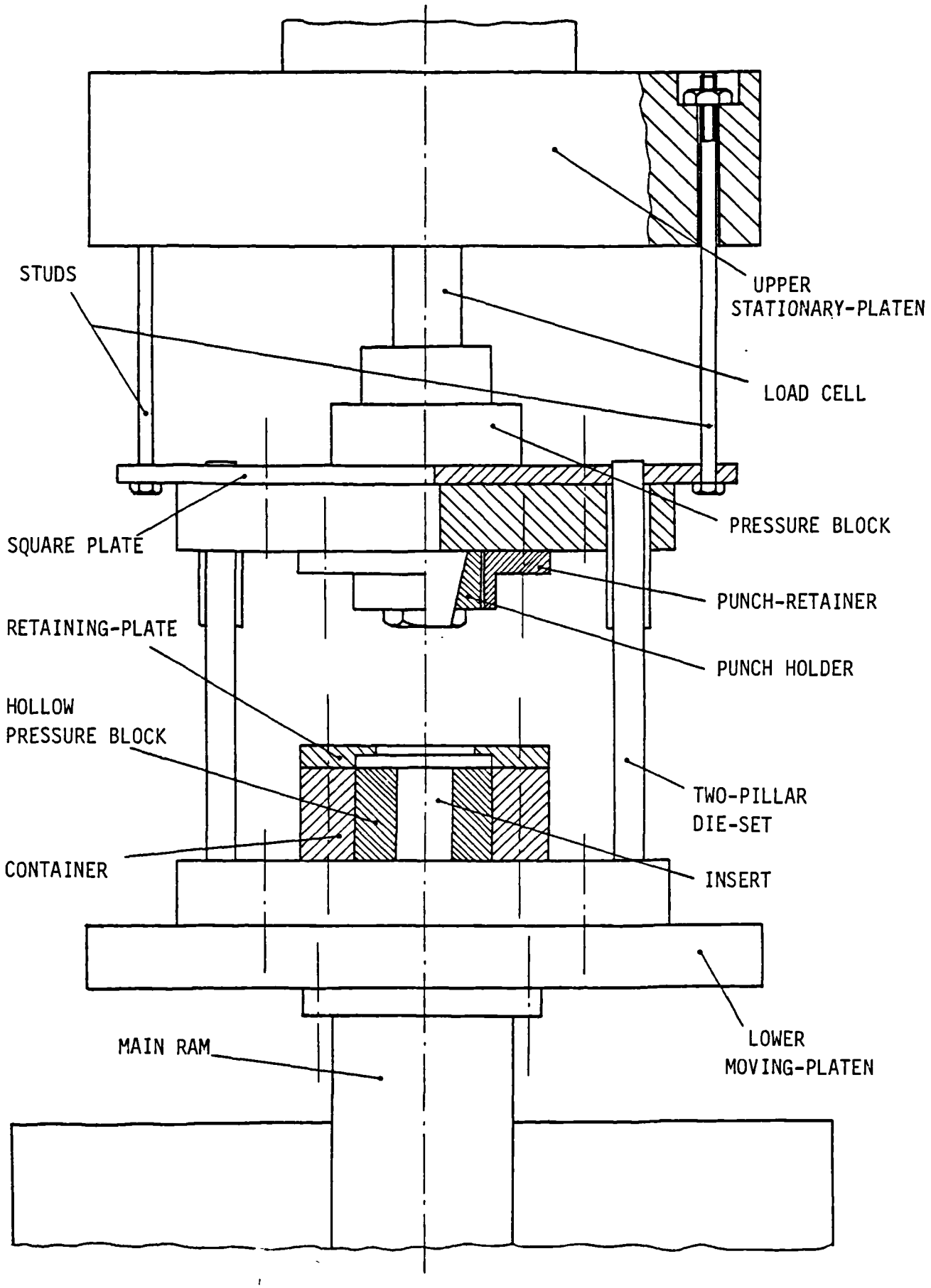


Fig. 2-8 Layout of tooling.

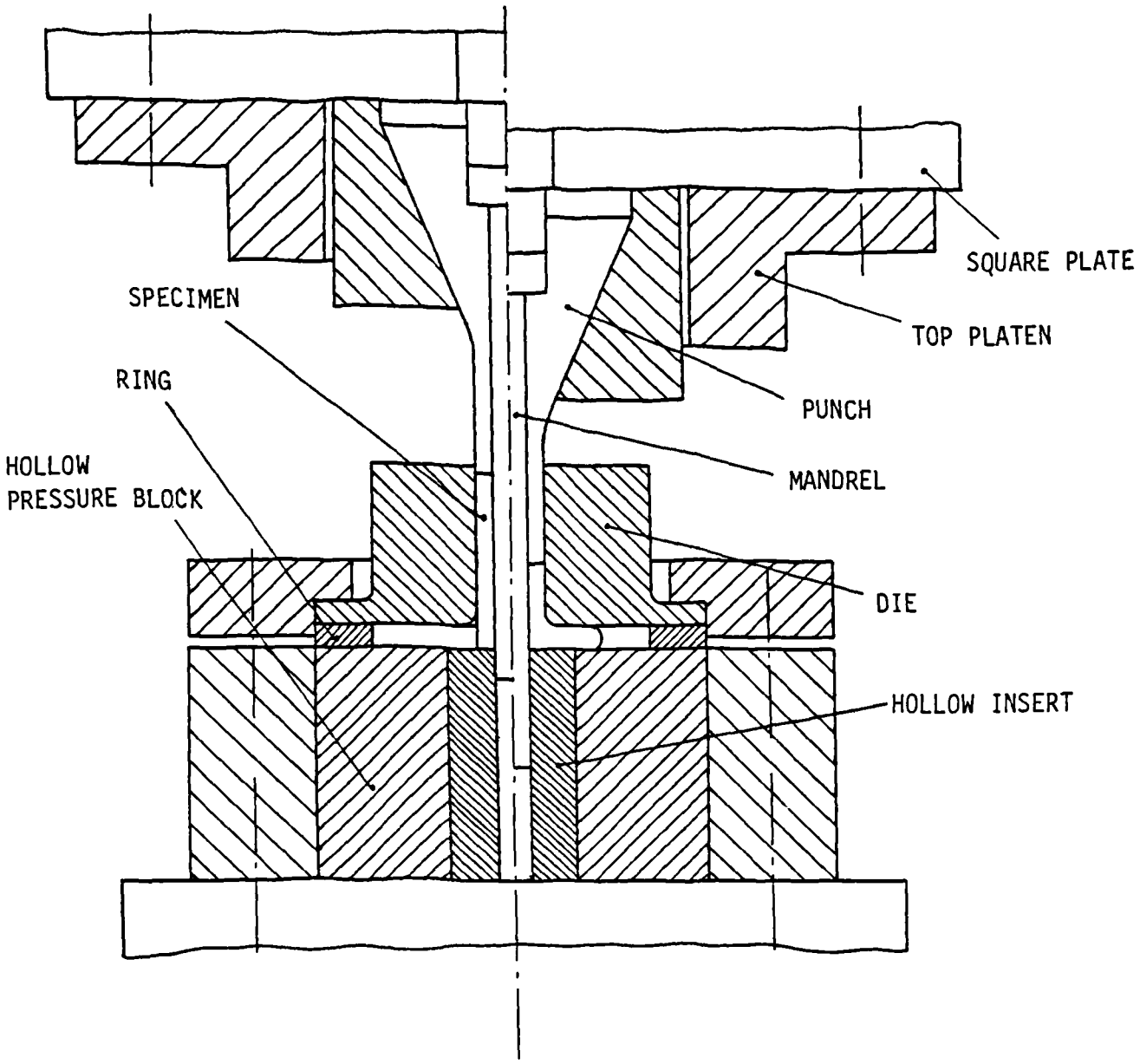


Fig. 2-9 Tooling for injection upsetting hollow billets.

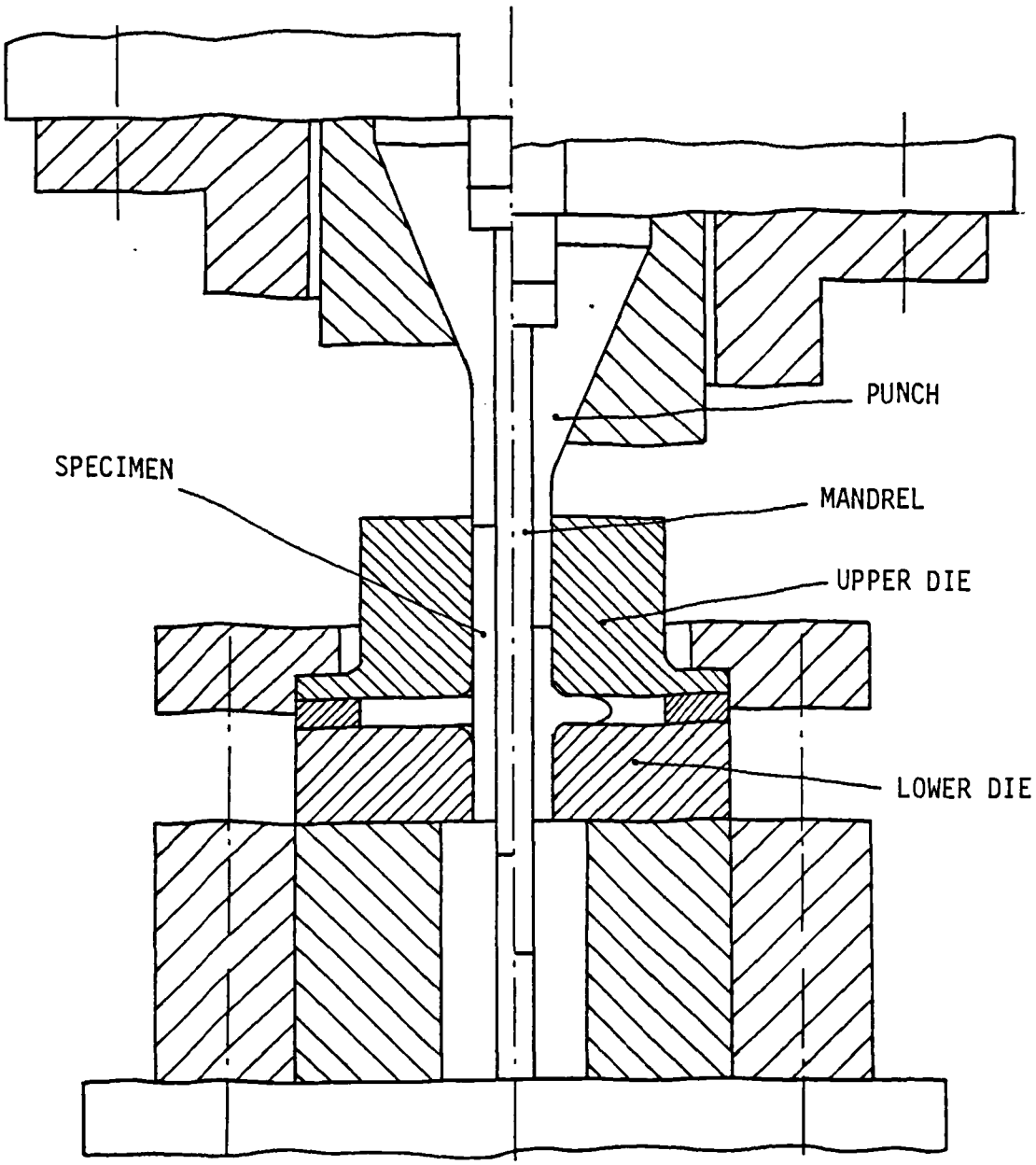


Fig. 2-10 Tooling for injection upsetting hollow billets with one end constrained.

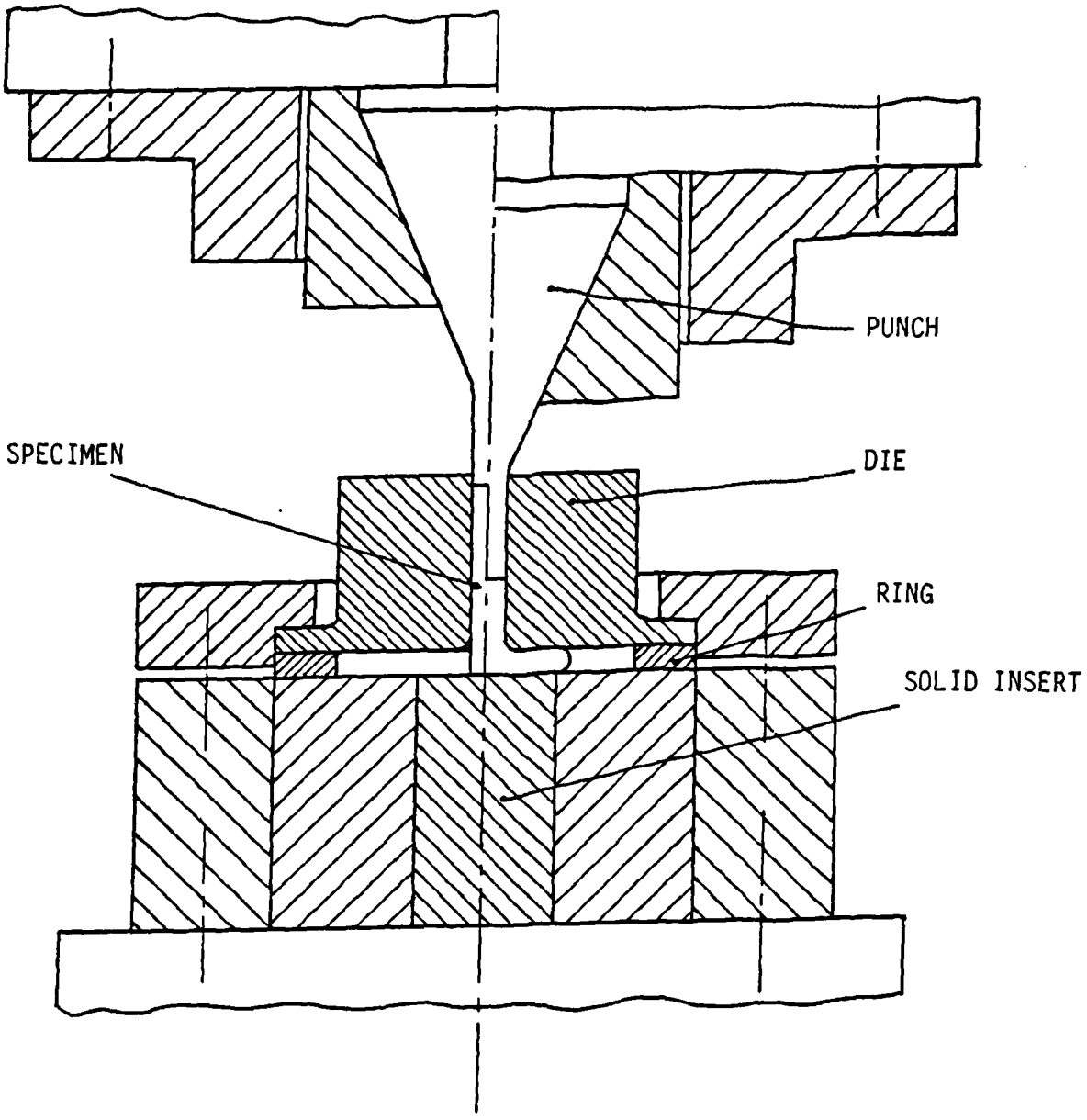


Fig. 2-11 Tooling for injection upsetting solid bars.

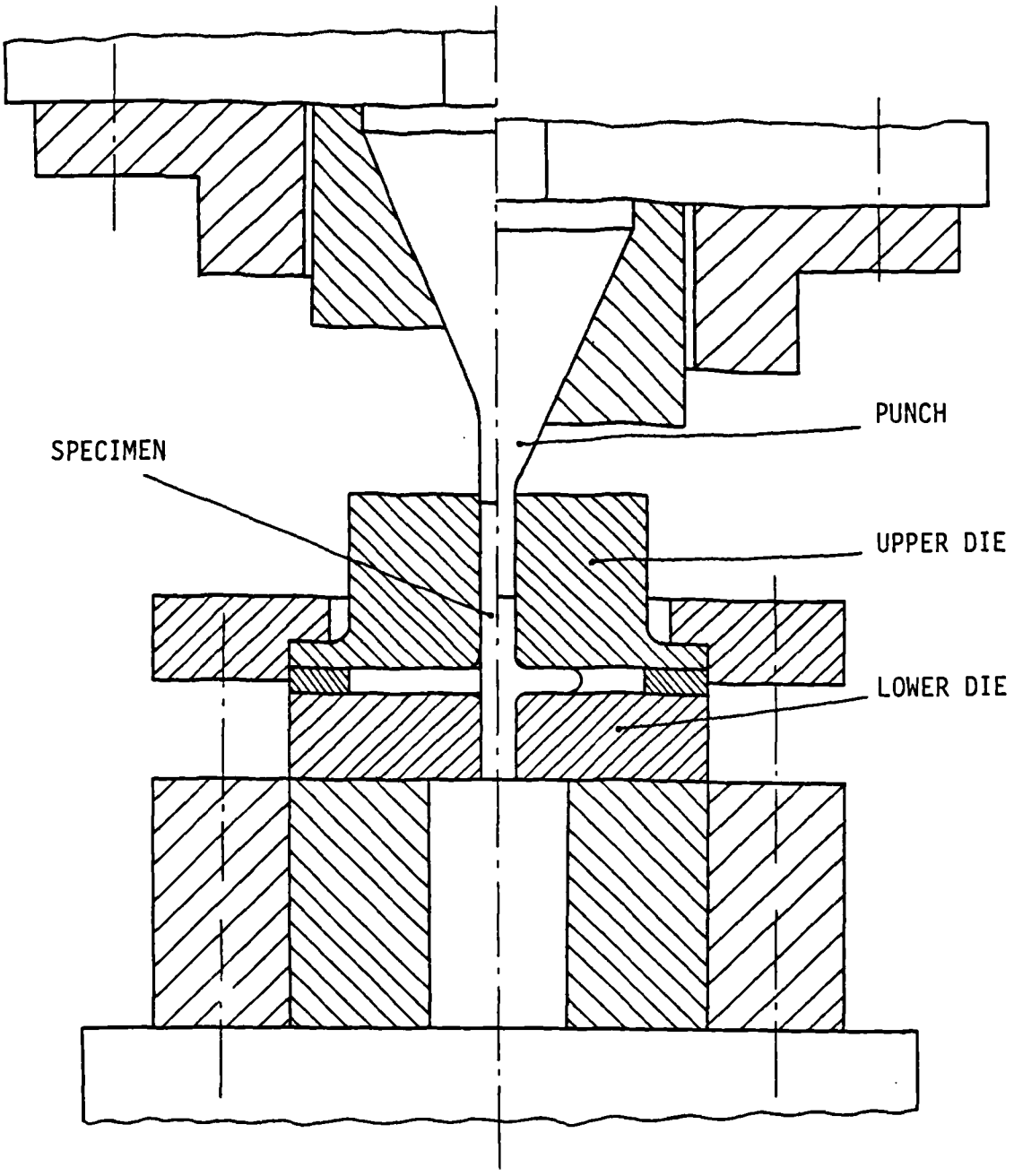


Fig. 2-12 Tooling for injection upsetting solid bars with one end constrained.

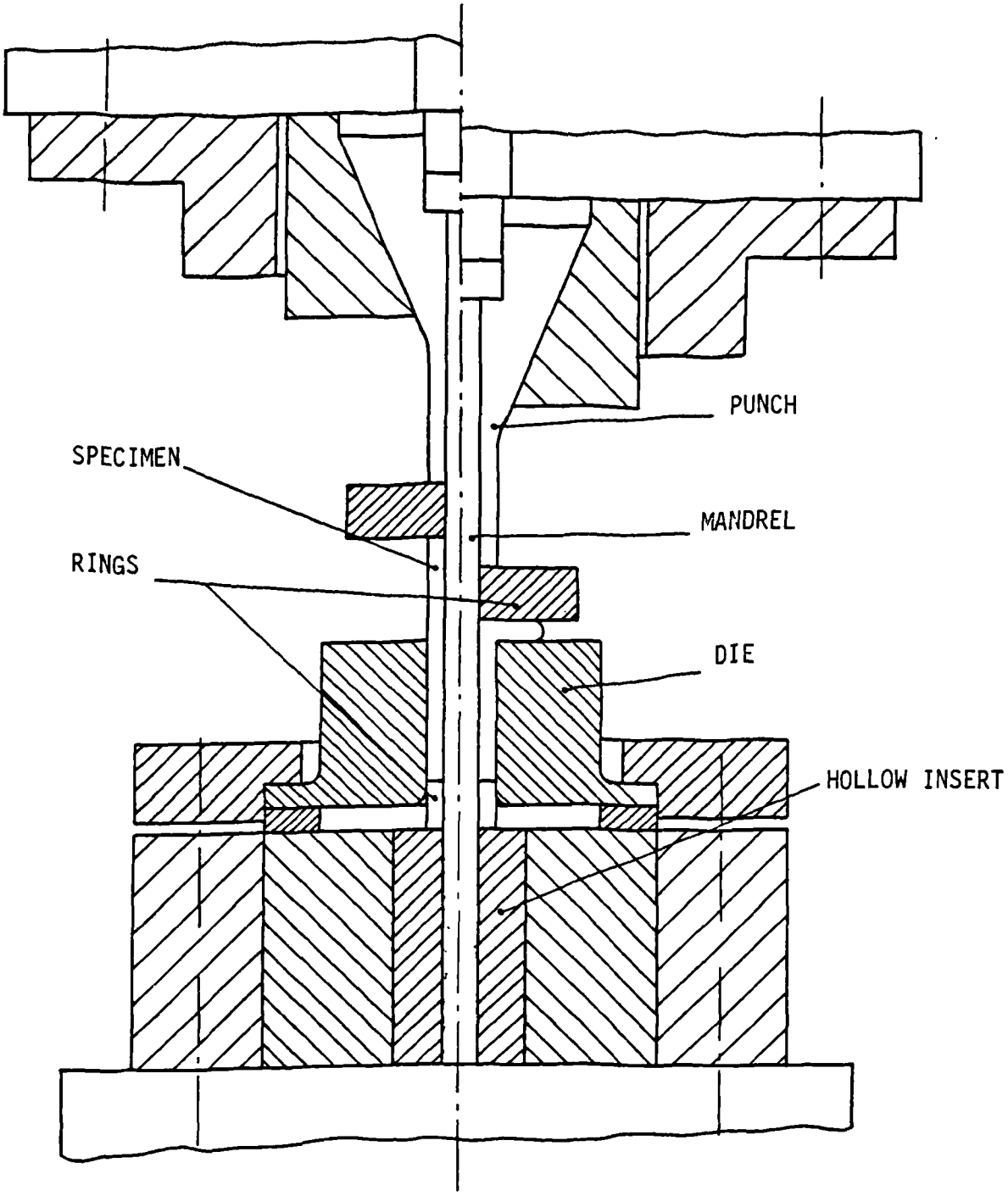


Fig. 2-13 Tooling for heading hollow billets.

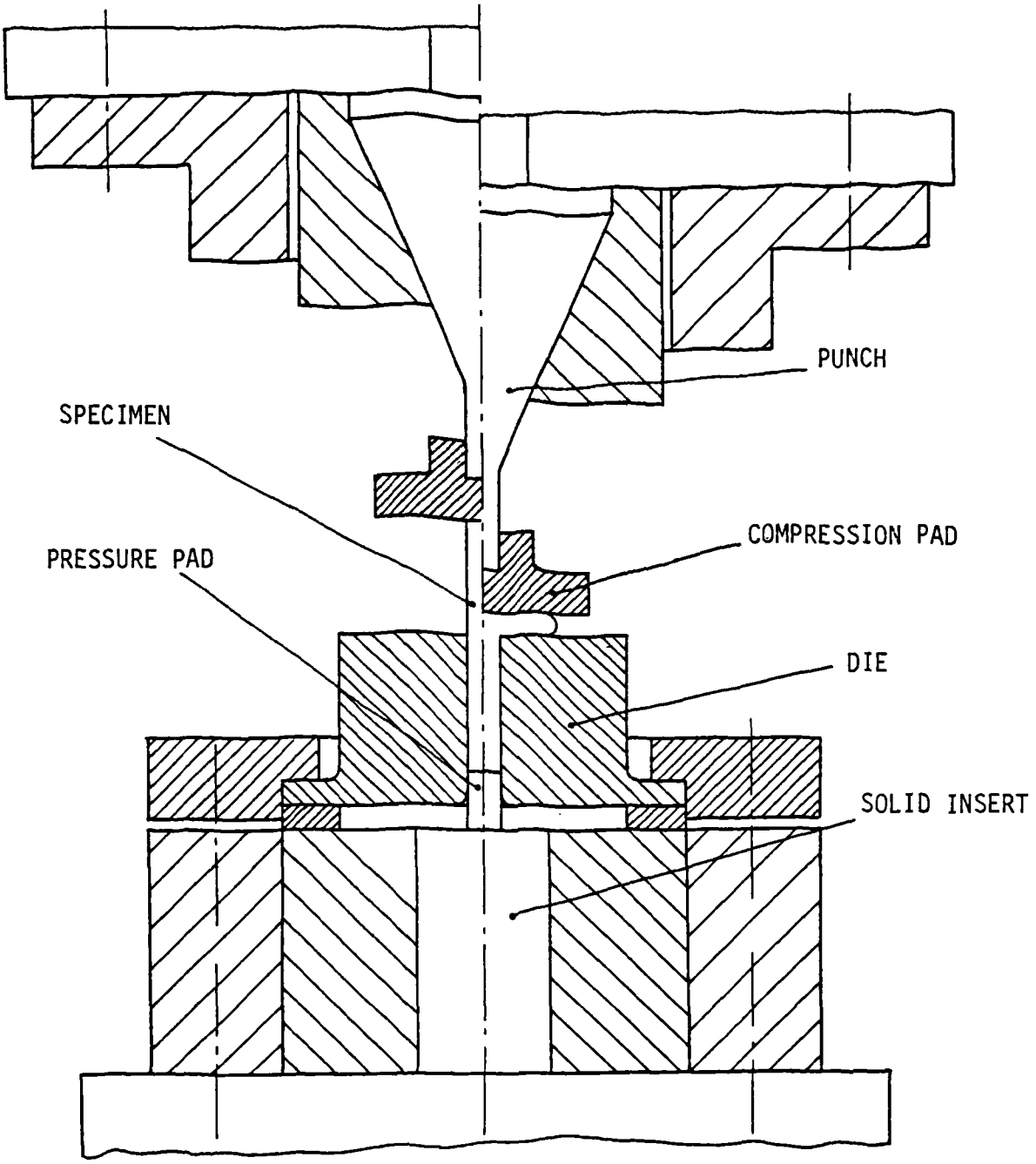


Fig. 2-14 Tooling for heading solid bars.

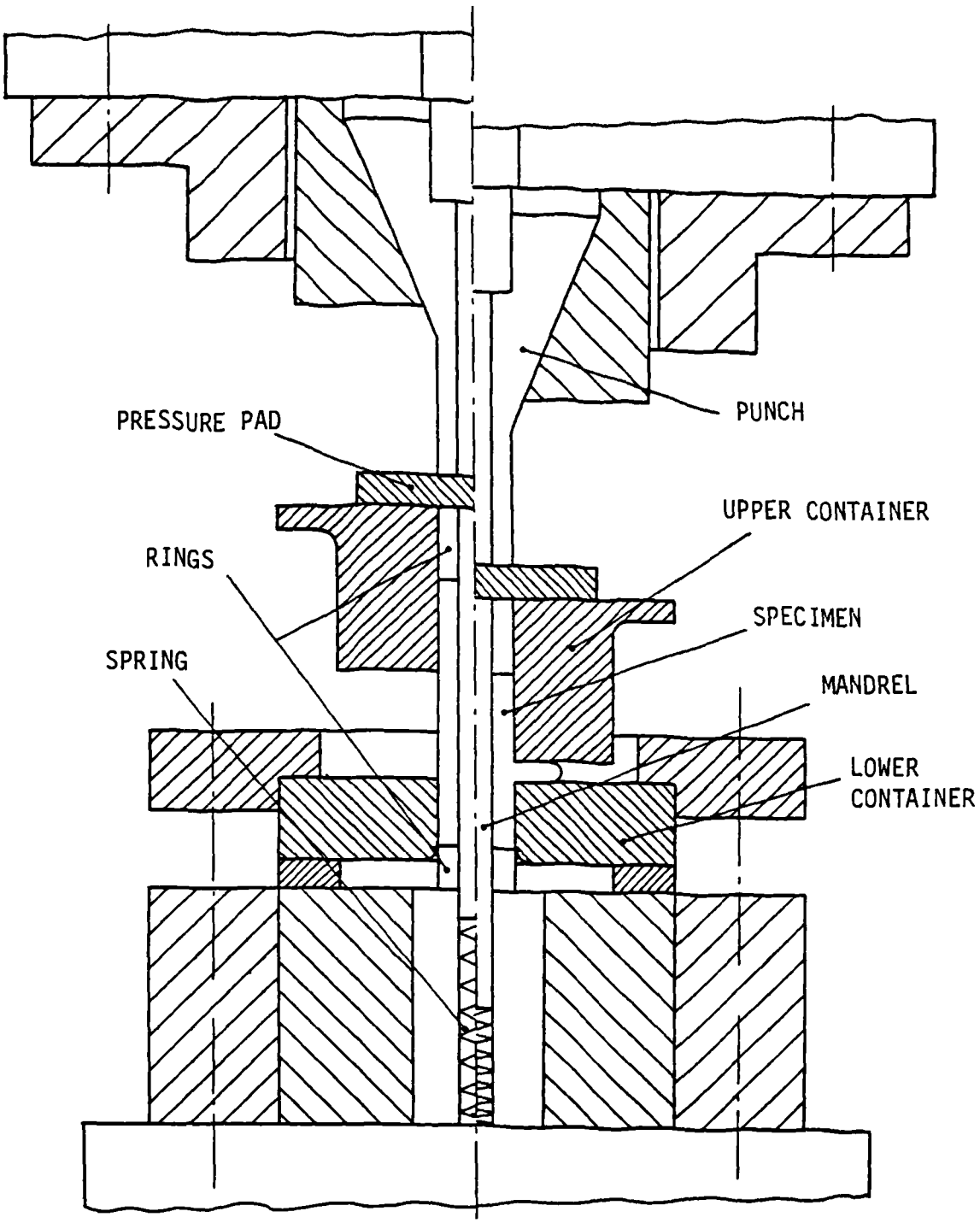


Fig. 2-15 Tooling for open upsetting hollow billets.

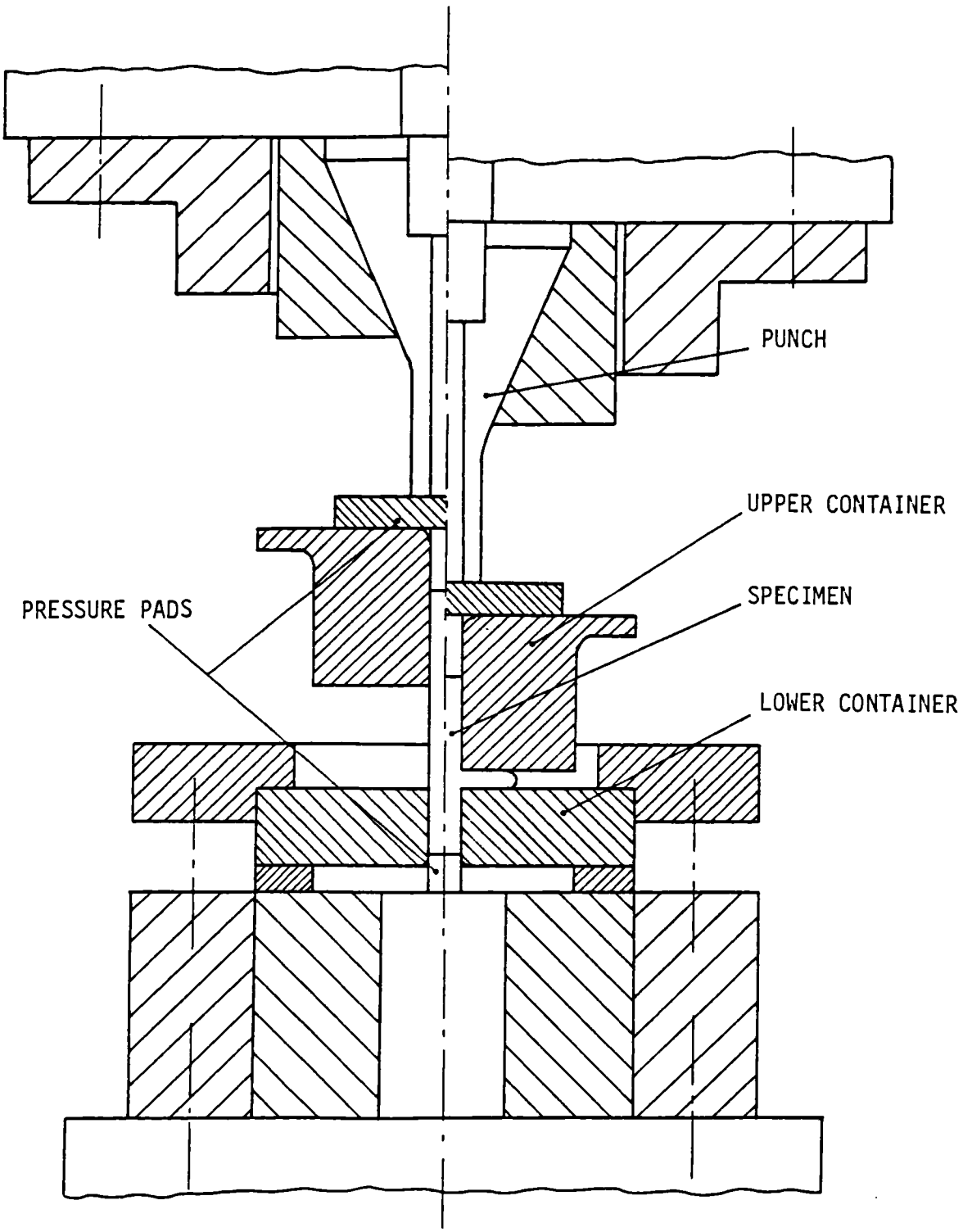


Fig. 2-16 Tooling for open upsetting solid bars.

CHAPTER 3

EXPERIMENTAL RESULTS AND DISCUSSIONS

3.1 Conventional upsetting

In the conventional upsetting of cylindrical billets constrained at one or both ends, specimens of three different original unsupported heights were deformed. Typical hollow and solid flanged components produced by conventional upsetting are shown in Fig. 3-1 and 3-2.

During the experiments load and displacement were recorded. Some experiments were stopped at various stages, the upset specimens were cut into halves, etched and the mode of deformation was studied.

3.1.1 Load/displacement characteristics

The effect of the original unsupported height and the wall thickness of the billet or billet diameter (for solid bars) on the load/displacement characteristics is studied in two sets of experiments when billets are constrained at one end (heading) or both ends (open upsetting) for lead, aluminium and copper.

Load/displacement curves for the conventional upsetting of hollow billets are shown in Figs. 3-3 to 3-19. The general trend of the curves are almost identical in all cases; the load increases sharply at the beginning of deformation then further increase is steady, which becomes greater at some value of punch displacement, followed by a very sharp increase at the final stage of the process. A similar trend is shown for the load/displacement characteristics in the upsetting of solid bars, Figs. 3-20 to 3-26.

In heading part of the billet is constrained within the die which, although highly stressed, is prevented from deforming by the walls of the container, while the unsupported part of the billet undergoes significant



Fig. 3-1 Typical products, heading and open upsetting hollow billets.



Fig. 3-2 Typical products, heading and open upsetting solid bars.

plastic deformation so that along the boundary there is a zone of intense shear. In the upper part of the deforming region, near the punch contact surface, a cone-shaped zone of relatively undeformed material is present because of the restraints on the flow of metal, caused by frictional forces acting at the tool/workpiece interface.

At some stage of the deformation the original free surface of the billet rolls on to the contact surfaces to form the current extreme edge of the flange. The continued rolling of the free surface onto the punch and die surfaces results in a progressive enlargement of the contact area and hence an increase in the surface friction. This phenomenon is thought to be responsible for the rapid increase of the upsetting load at some value of punch displacement.

At the final stages of the process the pressure cone (formed at the punch contact) meets the lower undeformed part of the billet, which results in the sharp increase of the upsetting load. This is similar to observations which have been made in simple upsetting of solid cylinders and rings *(references 15 & 31)* where the intersection of two pressure cones at the ends of the workpiece cause a rapid increase in compression load. Shah and Kobayashi *(36)* in their work on heading of solid bars concluded that the sharp increase in upsetting load is due to the onset of the rolling phenomenon. This conclusion is not supported by the present study since rolling begins much earlier than the rapid increase in load.

When the upsetting loads are plotted against percentage reduction the results become independent of the original height of the billet (Figs. 3-6 to 3-8). Fig. 3-9 compares the variation of punch load with percentage reduction in height for hollow billets of different wall thicknesses (9.5 and 12.5 mm) but the same bore diameter of 25 mm. Clearly, a specimen of greater wall thickness requires larger upsetting loads partly

because of a larger volume under deformation and due to the larger contact area which results in an increase in frictional forces.

Load/displacement curves in the heading of lead, aluminium and copper hollow billets are compared in Fig. 3-10, obtained under identical conditions. The load becomes higher with increasing yield stress and the rate of increase in load is representative of the rate of work hardening of the corresponding material.

Load/displacement curves obtained in the open upsetting of hollow billets are shown in Figs. 3-11 to 3-18. A comparison of Fig. 3-9 and 3-18 reveals that the effect of wall thickness on the upsetting load is more distinct in the case of open upsetting which could be explained in the following manner. In heading one end of the billet is in full sliding contact with the punch surface whereas in open upsetting only two small annular areas are in sliding contact and the deforming region is mostly in shearing contact with the solid constrained metal at both ends. The restraint on the flow of metal when shearing the deforming metal from the rigid zone is higher than the restraint caused by frictional forces at the contact surfaces. Consequently, the increase in upsetting load for any increase in the wall thickness is greater in open upsetting. Fig. 3-19 compares the curves of upsetting loads in open upsetting and in heading under similar conditions. The points obtained in two cases appear to be scattered around a common curve at the early stages of deformation but the curves separate later, at approximately 24 per cent reduction in height for the billet in Fig. 3-19, with the curve in open upsetting taking a greater rate of increase in punch load. Generally, greater punch load was expected in open upsetting because of more restraint to the radial flow of metal. This additional restraint imposed at the top of the deforming region results in increased non-uniform deformation of the flange and therefore

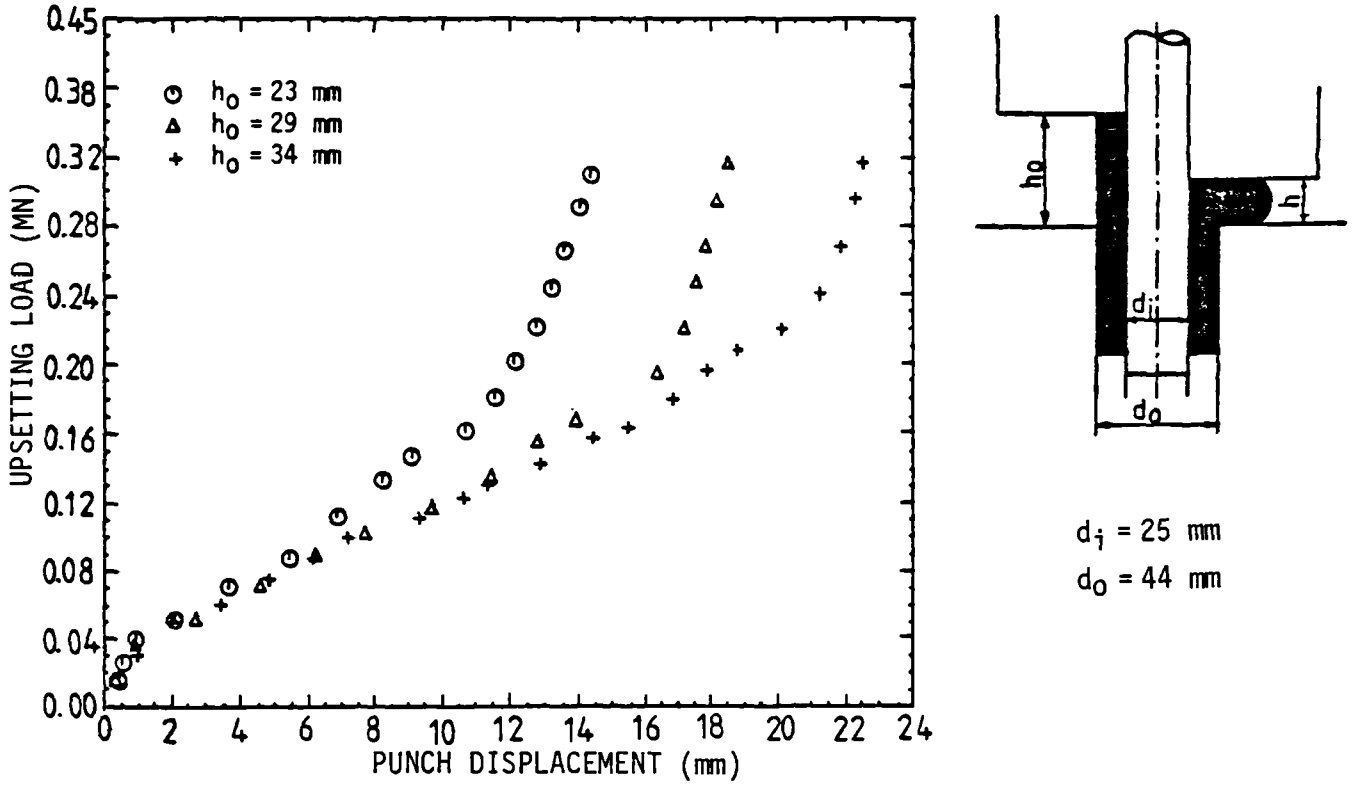


Fig. 3-3 Effect of initial unsupported height on the load/displacement characteristics in heading aluminium hollow billets.

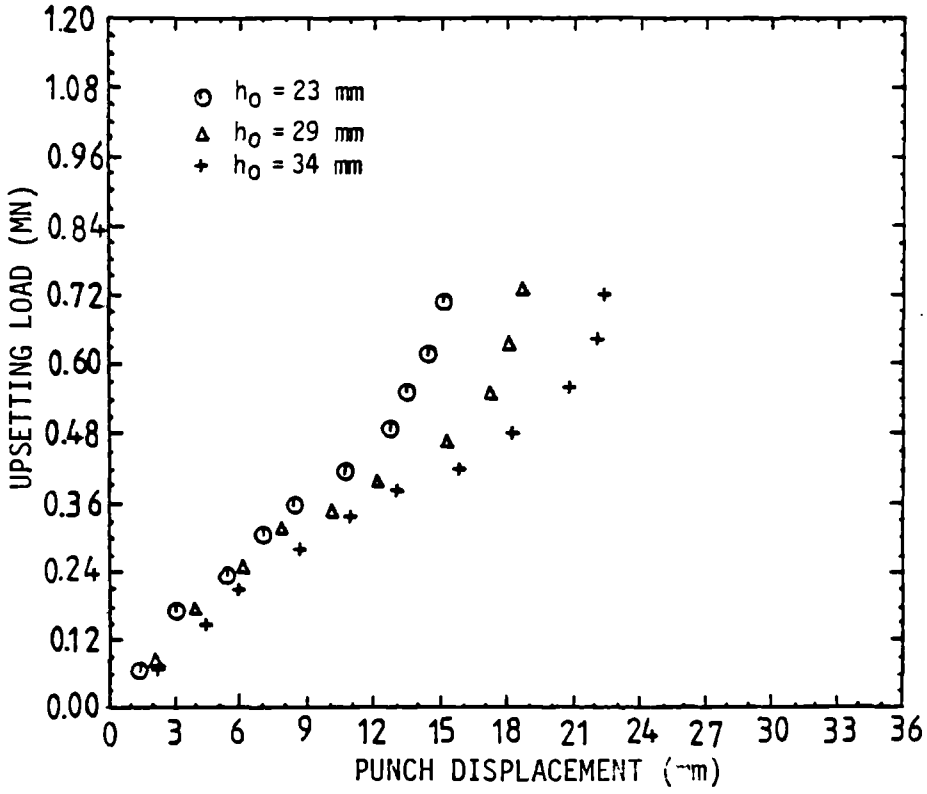


Fig. 3-4 Effect of initial unsupported height on the load/displacement characteristics in heading copper hollow billets.

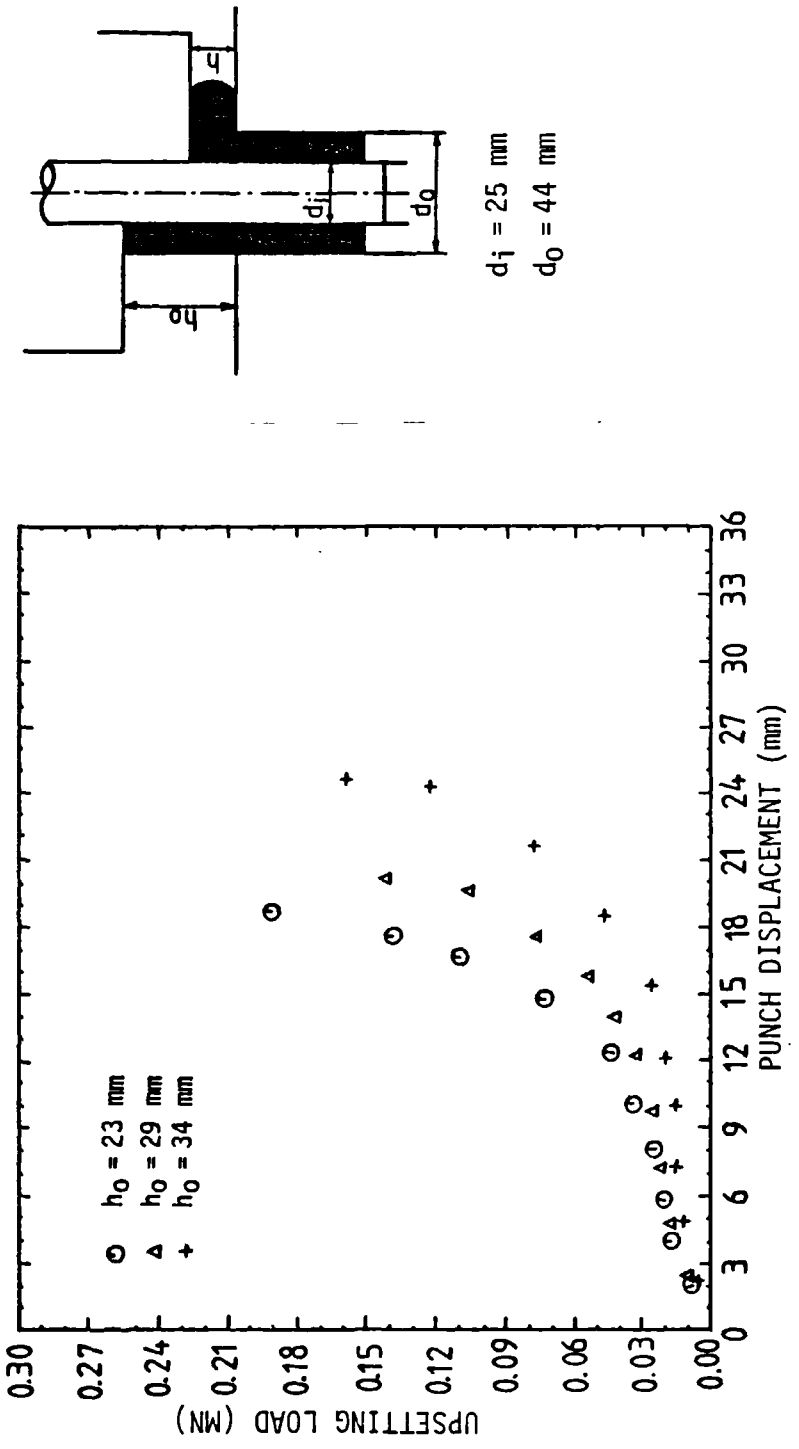


Fig. 3-5 Effect of initial unsupported height on the load/displacement characteristics in heading lead hollow billets.

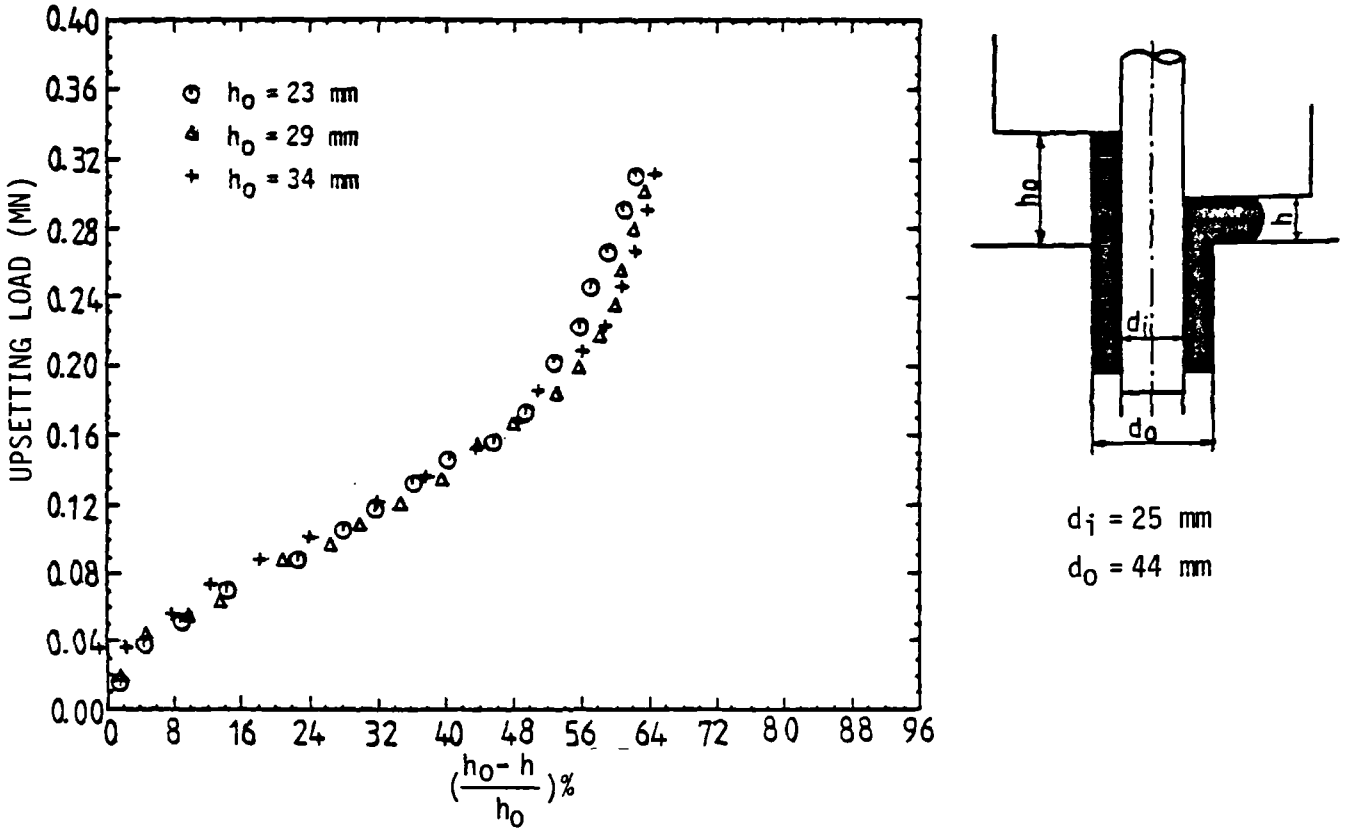


Fig. 3-6 Variation of upsetting load with percentage reduction in height in heading aluminium hollow billets.

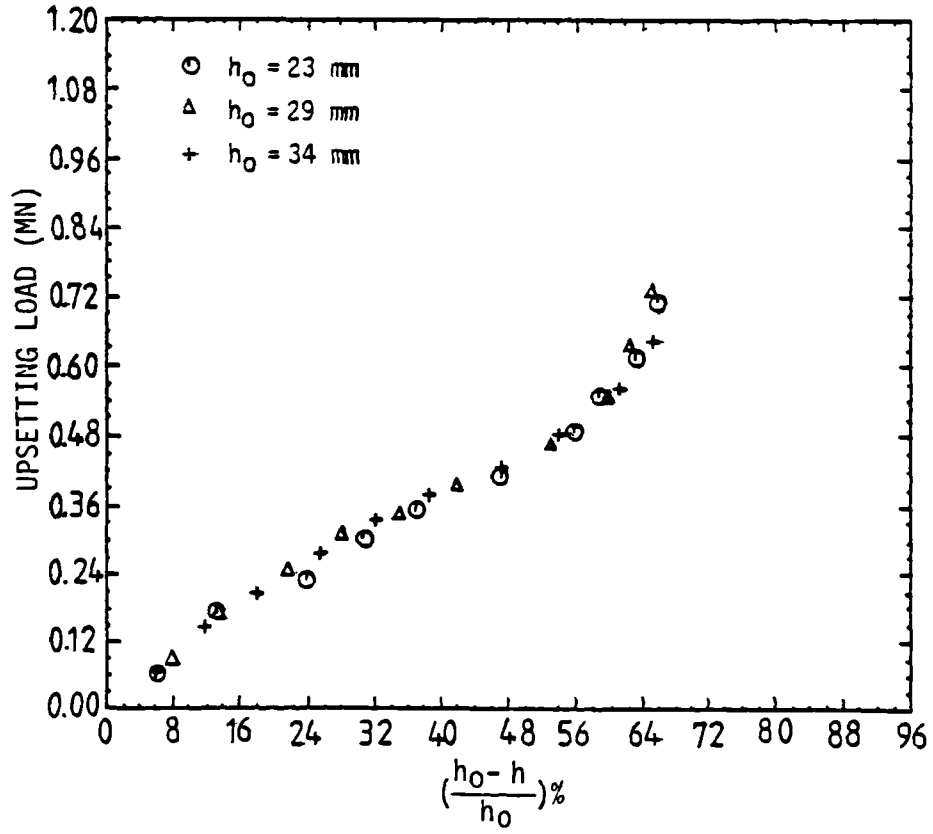


Fig. 3-7 Variation of upsetting load with percentage reduction in height in heading copper hollow billets.

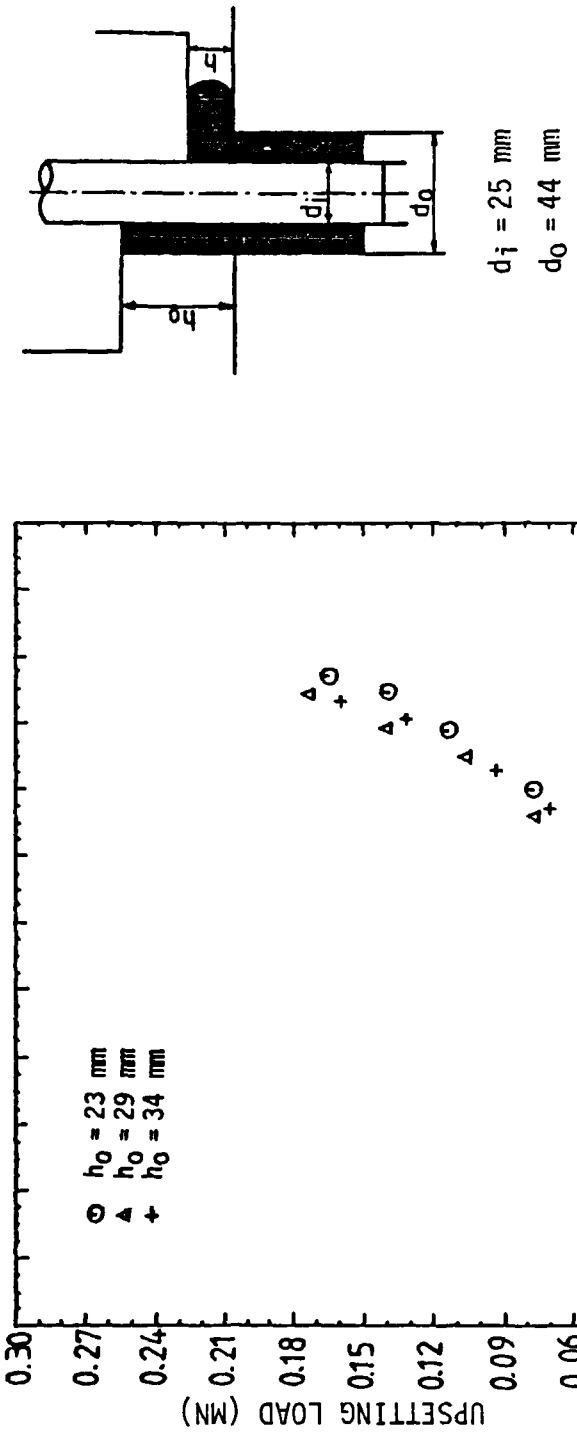


Fig. 3-8 Variation of upsetting load with percentage reduction in height in heading lead hollow billets.

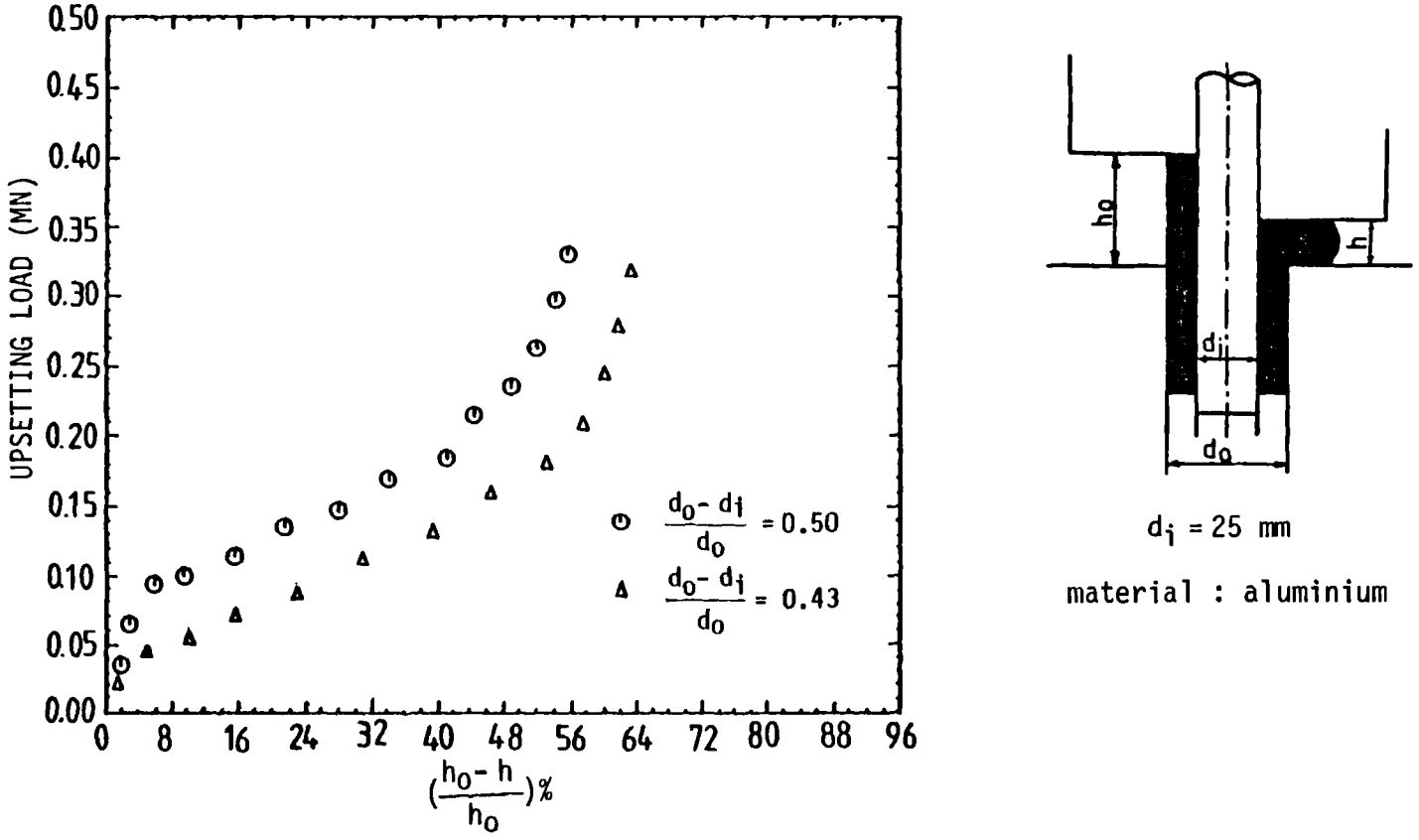
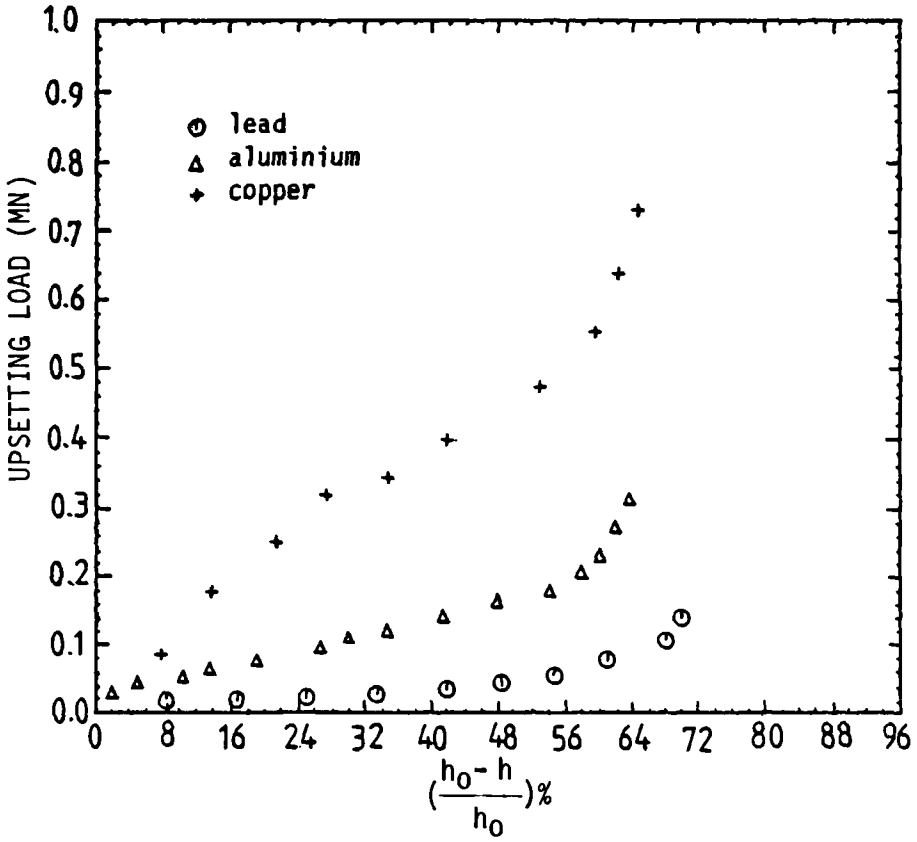
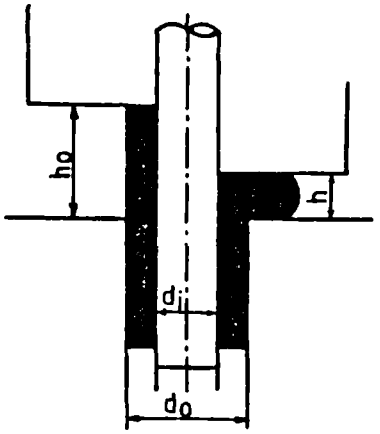


Fig. 3-9 Variation of upsetting load with percentage reduction in height in the heading of hollow billets of various wall thicknesses.





$d_i = 25$ mm

$d_0 = 44$ mm

Fig. 3-10 Variation of upsetting load with percentage reduction in height in heading hollow billets of the three materials used.

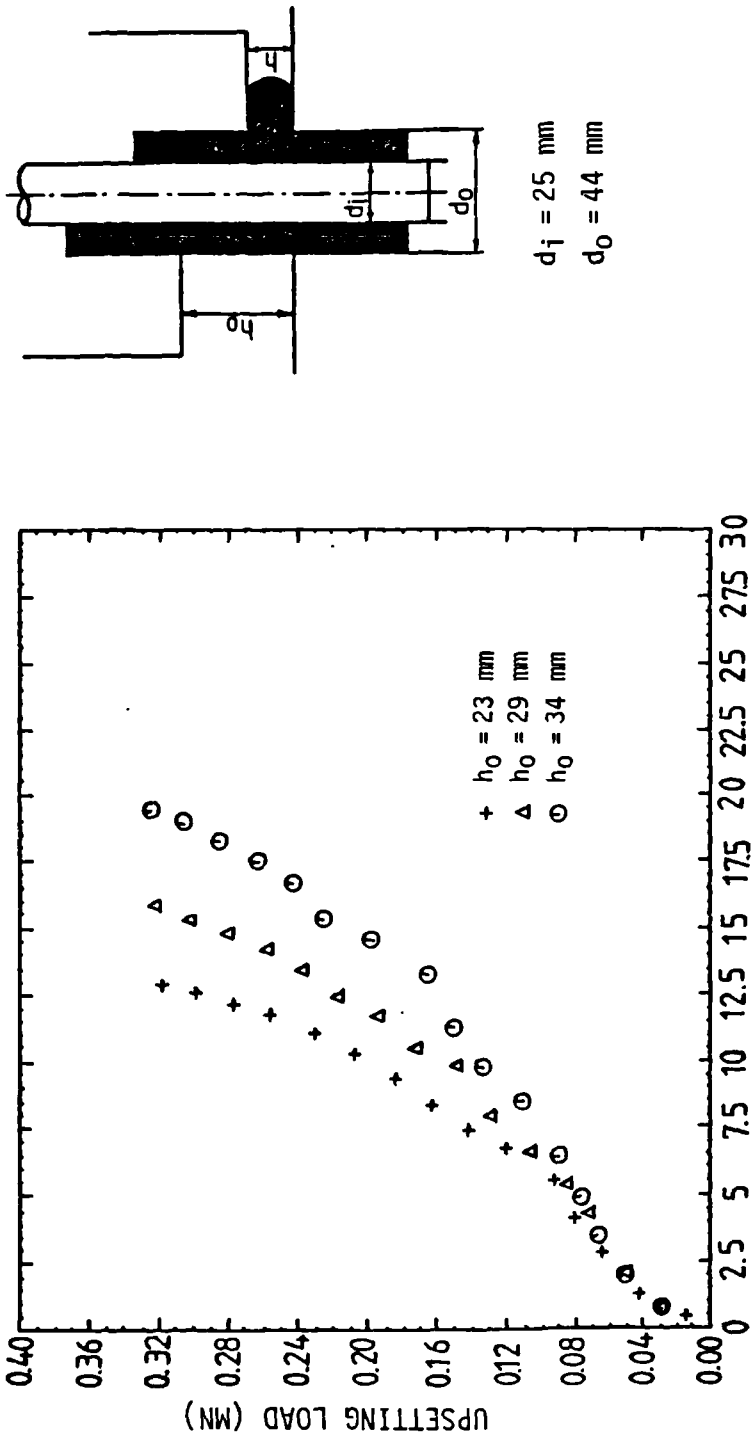


Fig. 3-11 Effect of initial unsupported height on the load/displacement characteristics in the open upsetting of aluminium hollow billets.

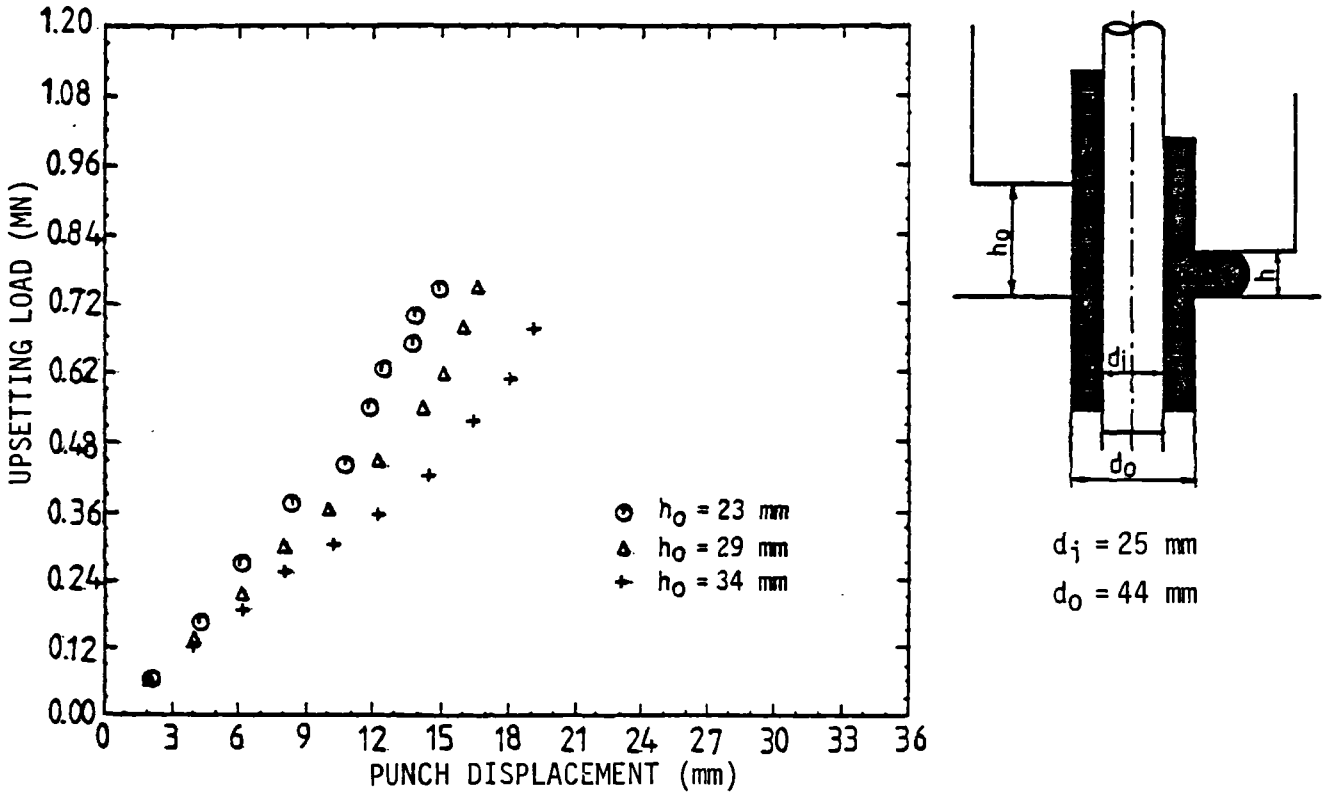


Fig. 3-12 Effect of initial unsupported height on load/displacement characteristics in the open upsetting of copper hollow billets.

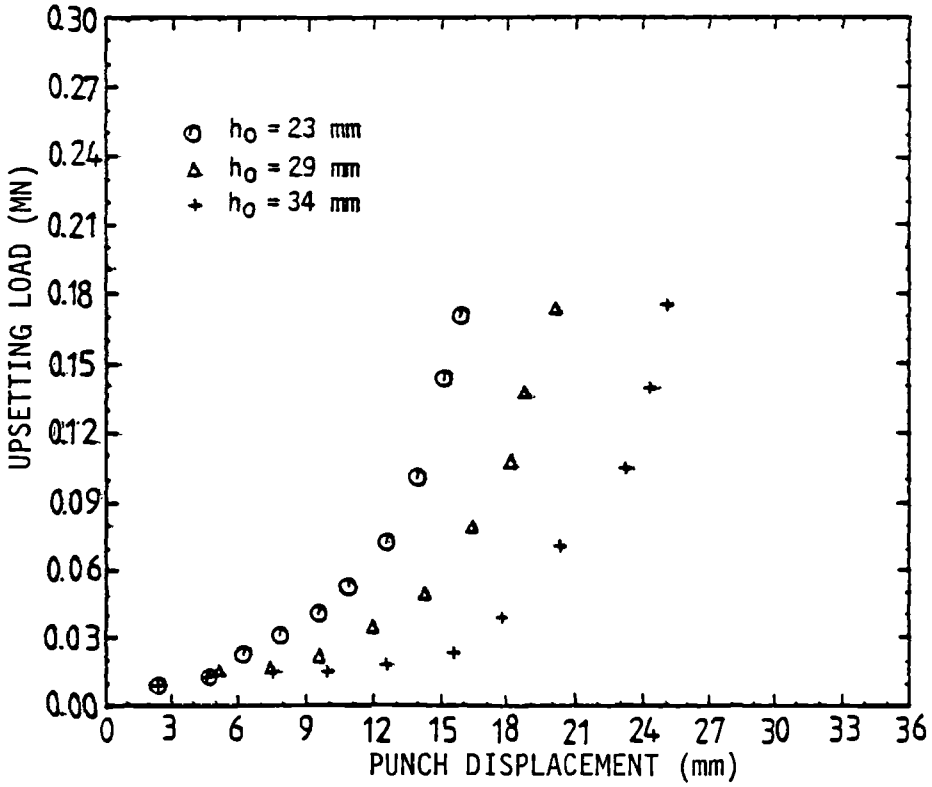


Fig. 3-13 Effect of initial unsupported height on load/displacement characteristics in the open upsetting of lead hollow billets.

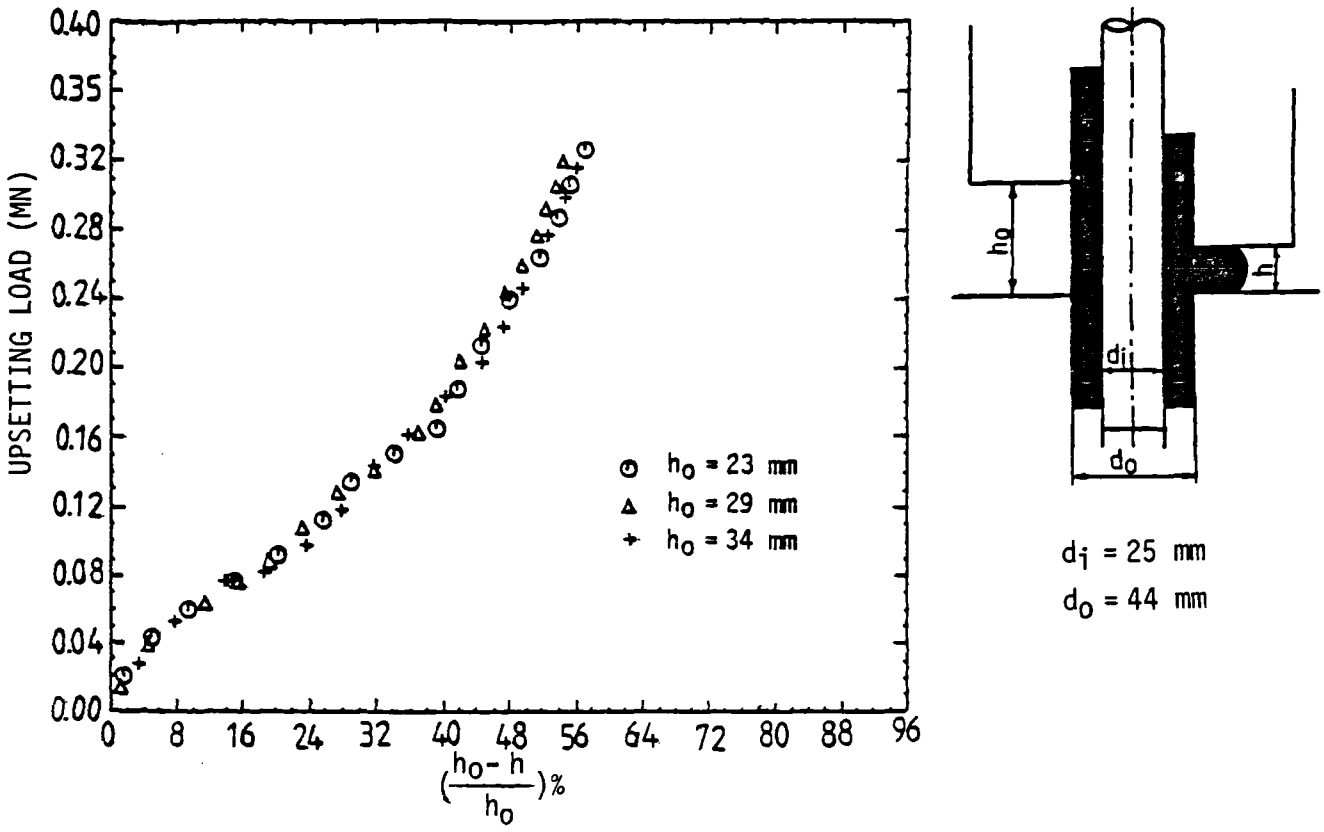


Fig. 3-14 Variation of upsetting load with percentage reduction in height in the open upsetting of aluminium hollow billets.

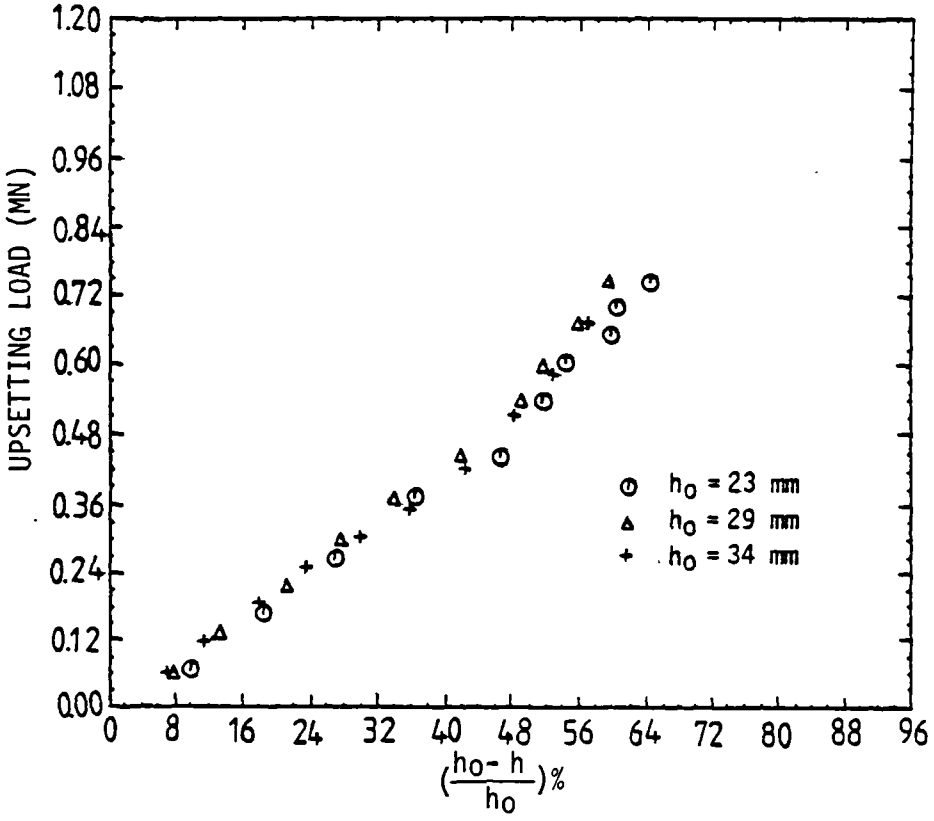


Fig. 3-15 Variation of upsetting load with percentage reduction in height in the open upsetting of copper hollow billets.

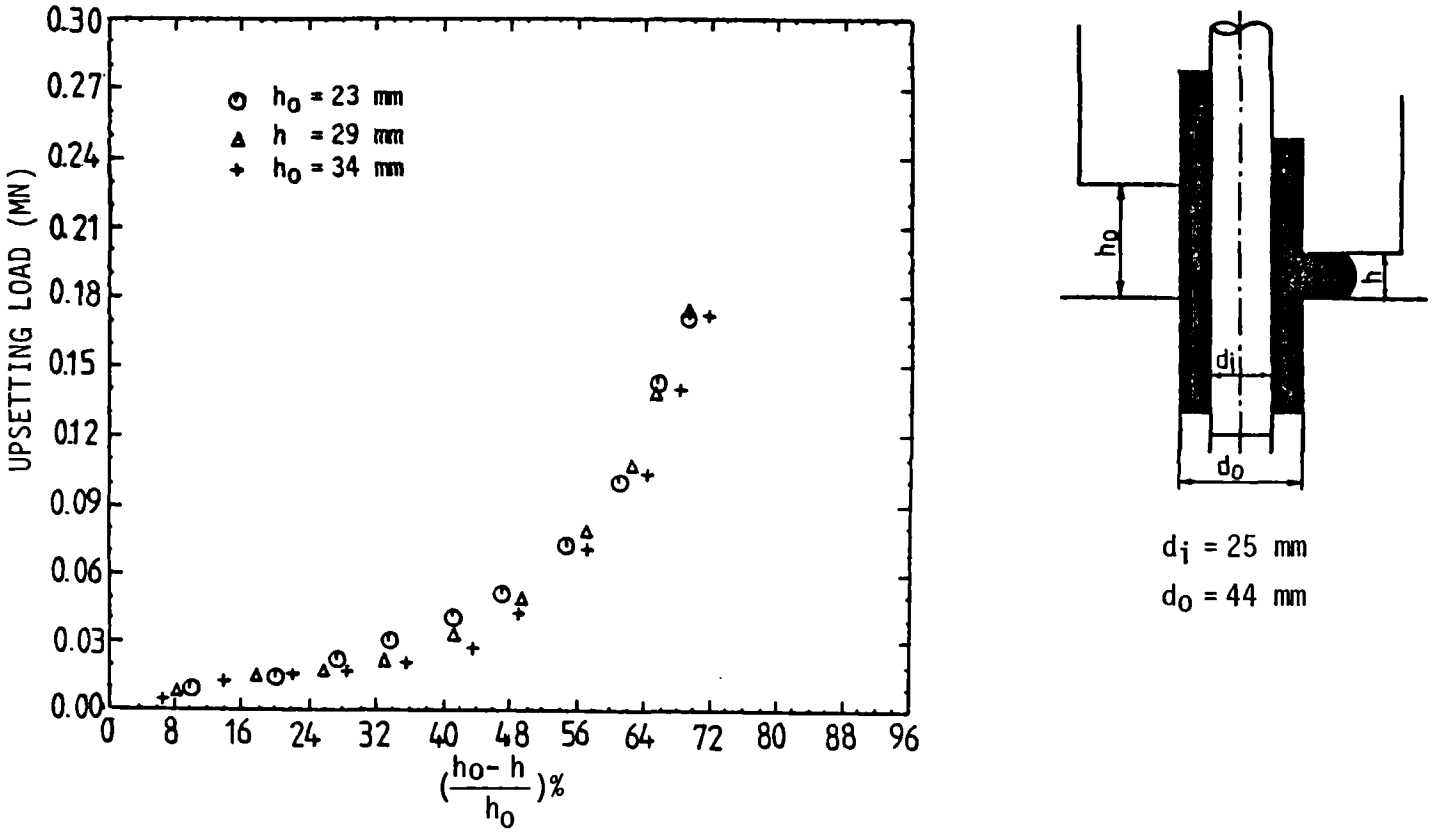
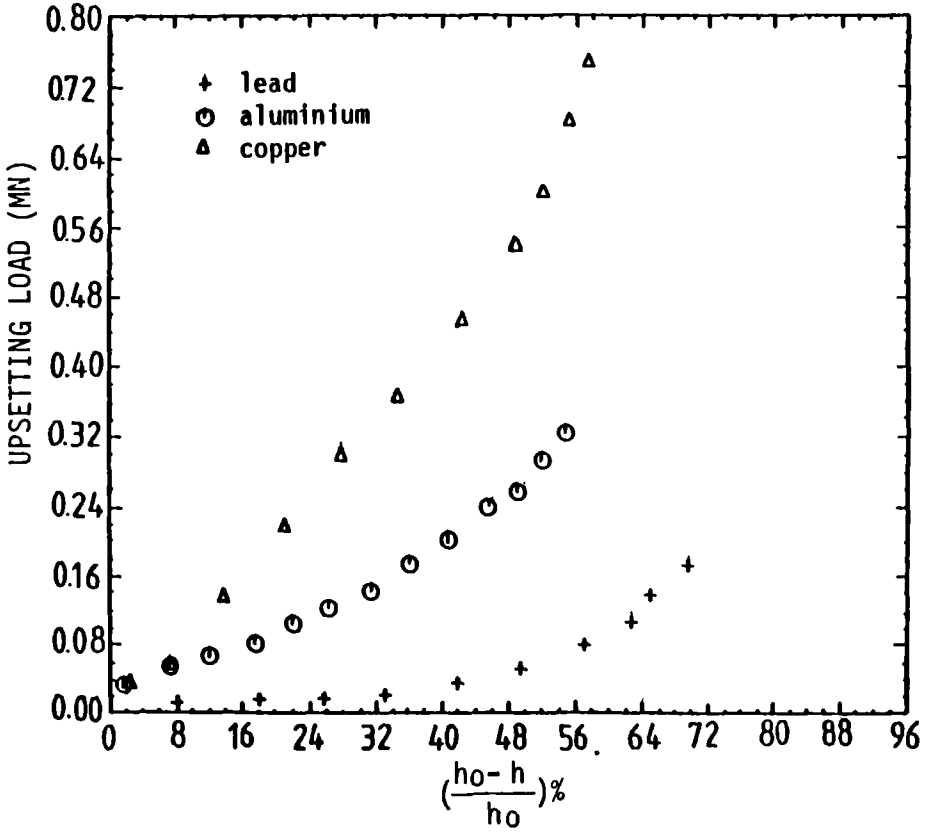


Fig. 3-16 Variation of upsetting load with percentage reduction in height in the open upsetting of lead hollow billets.



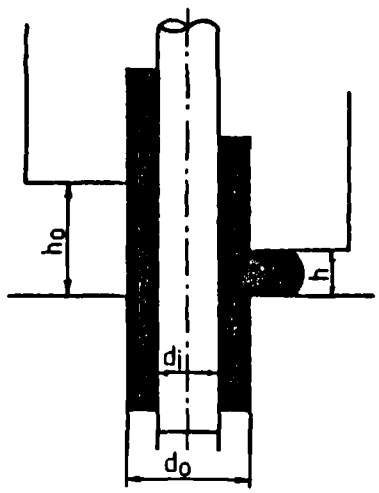


Fig. 3-17 Variation of upsetting load with percentage reduction in height in the open upsetting of hollow billets of the three materials used.

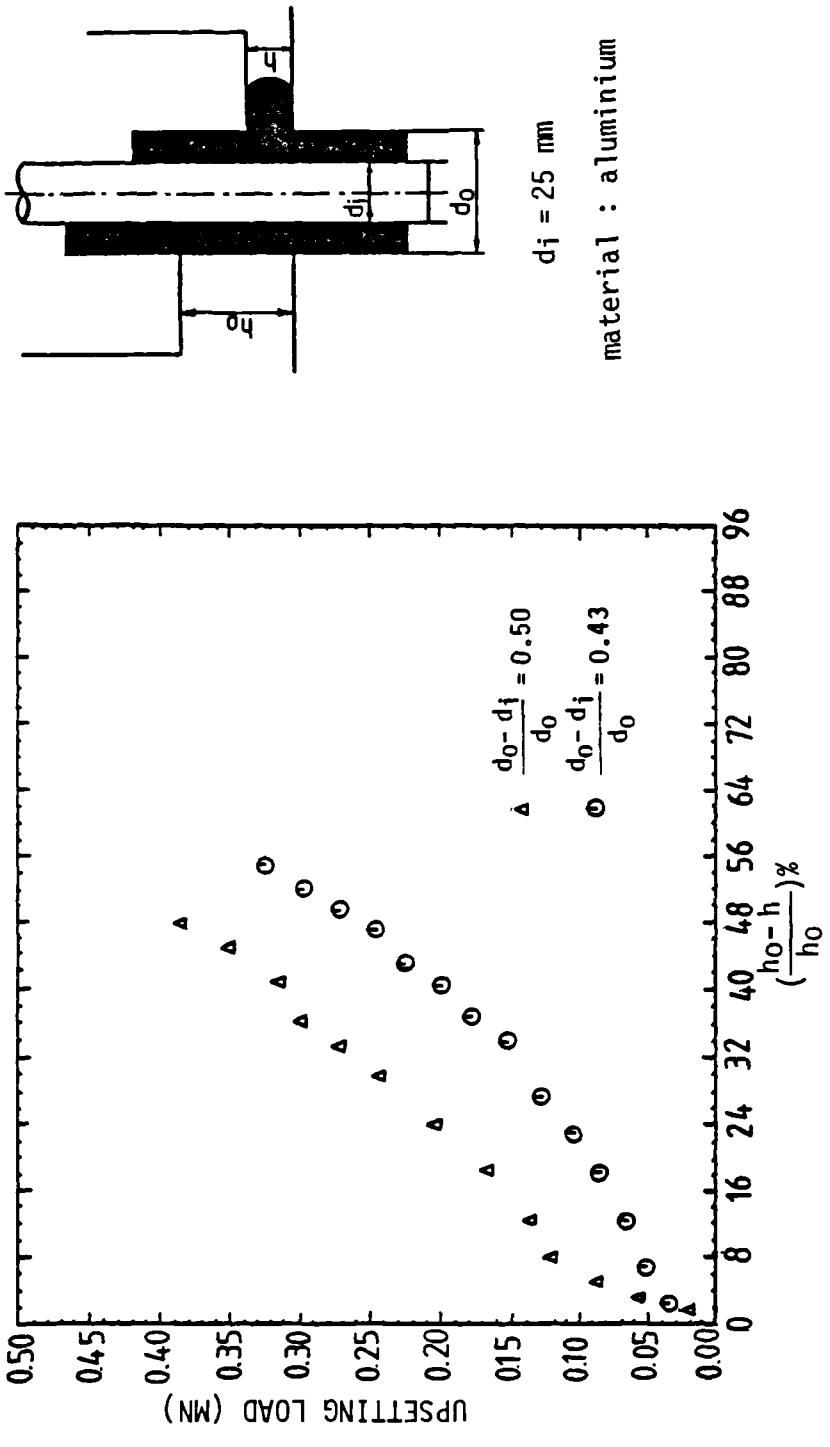


Fig. 3-18 Variation of upsetting load with percentage reduction in height in the open upsetting of hollow billets of various wall thicknesses.

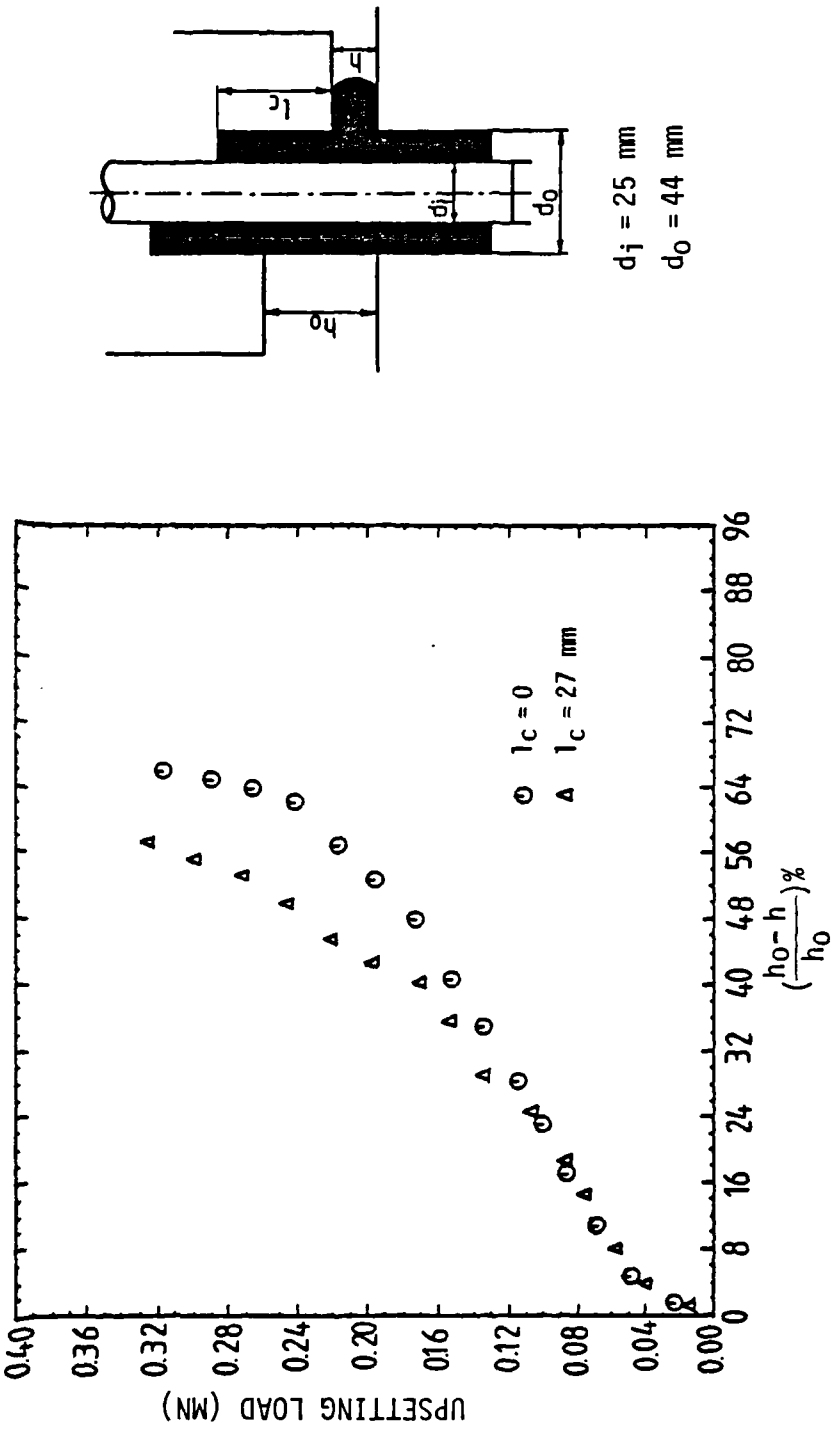


Fig. 3-19 Comparison of load/displacement characteristics in the heading and open upsetting of aluminium hollow billets.

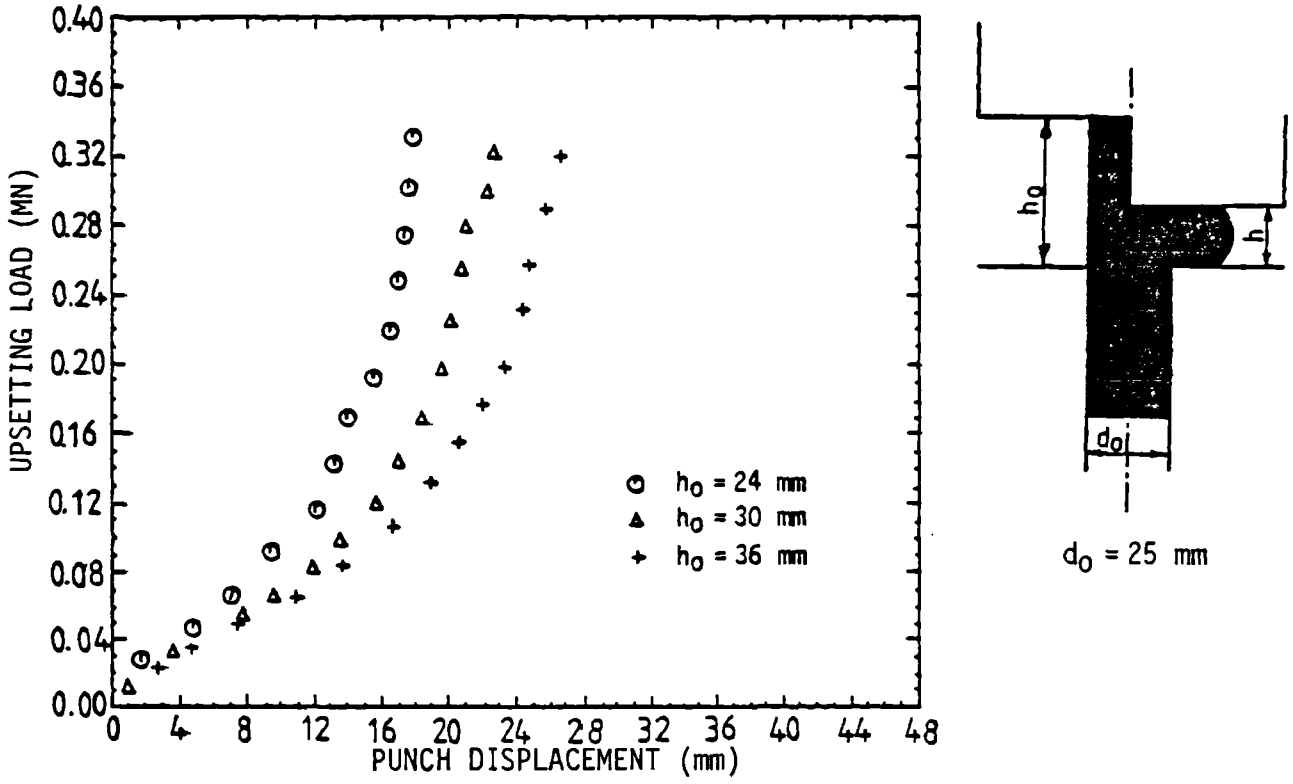


Fig. 3-20 Effect of initial unsupported height on load/displacement characteristics in heading aluminium solid billets.

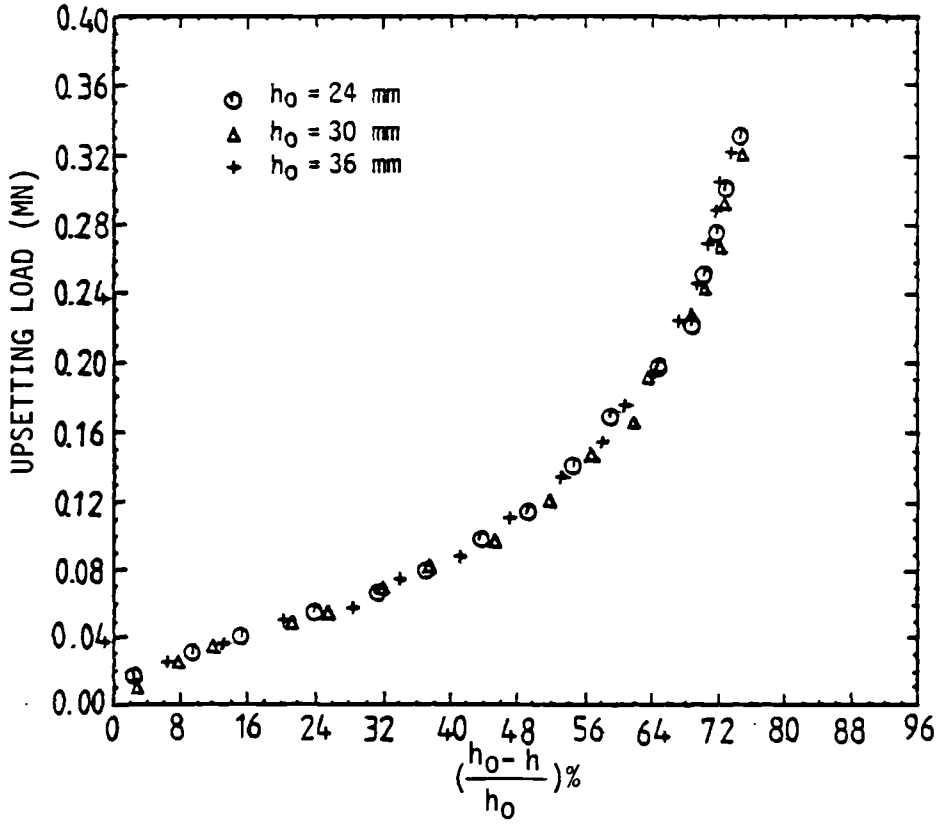


Fig. 3-21 Variation of upsetting load with percentage reduction in height in heading aluminium solid billets.

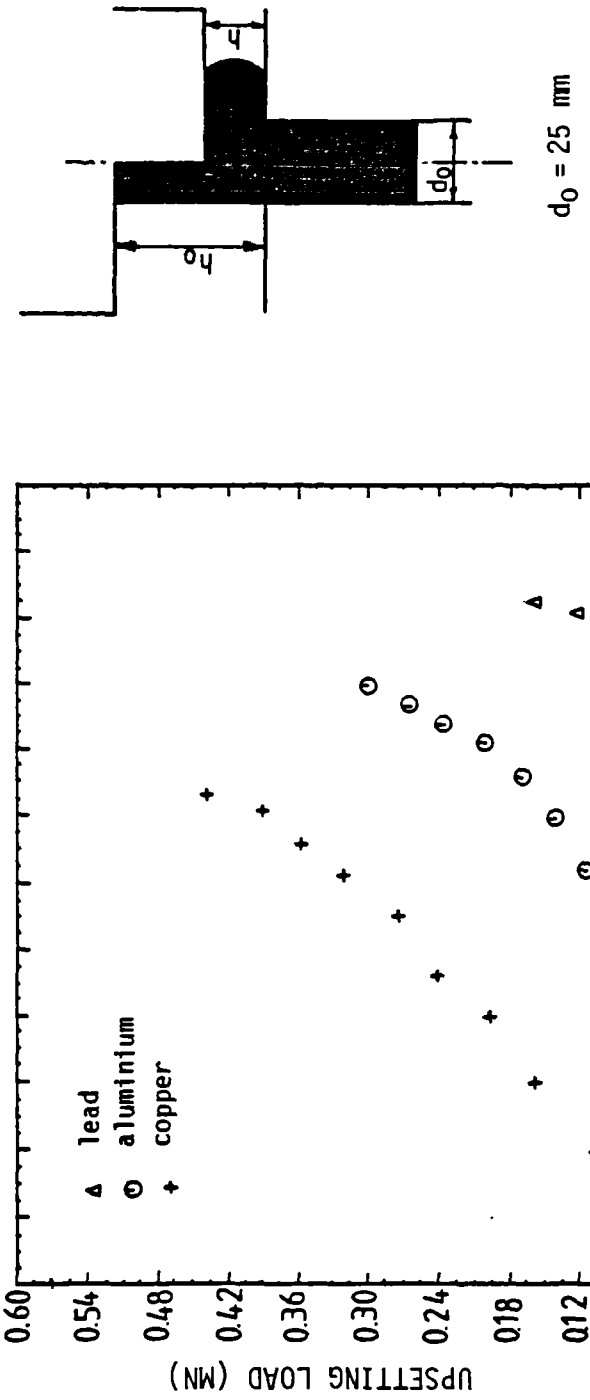


Fig. 3-22 Variation of upsetting load with percentage reduction in height in the heading of solid billets of the three materials used.

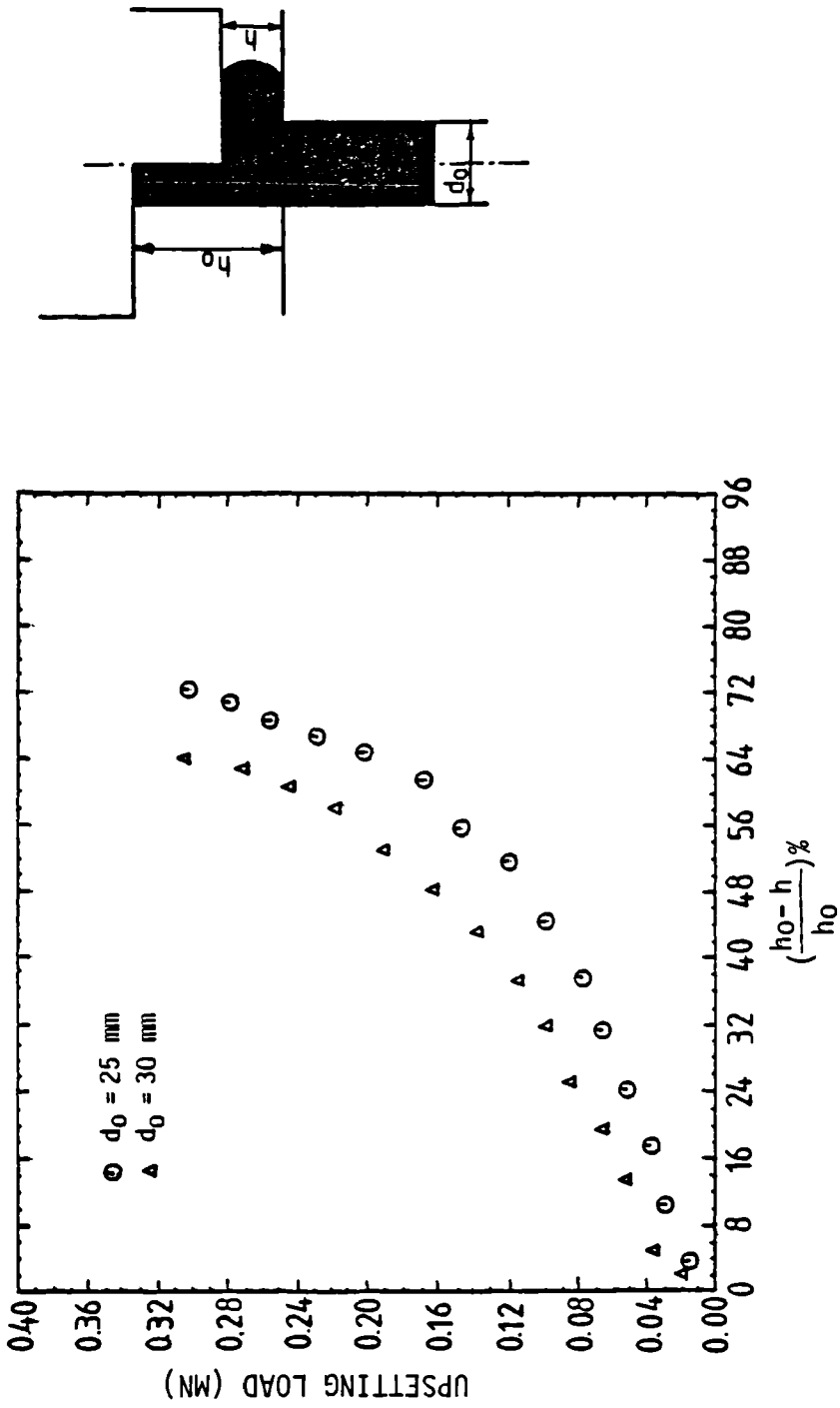


Fig. 3-23 Variation of upsetting load with percentage reduction in height in the heading of solid billets of various diameters.

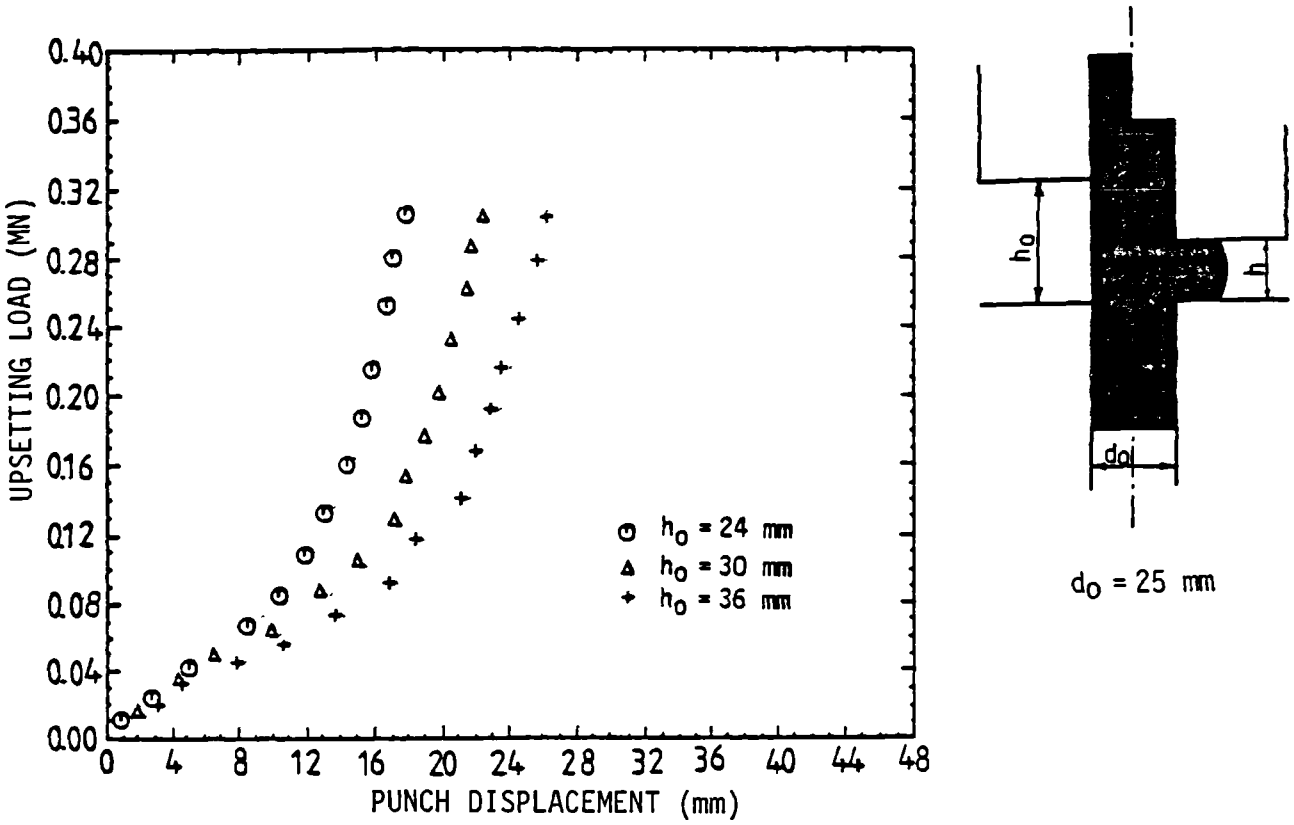


Fig. 3-24 Effect of initial unsupported height on load/displacement characteristics in the open upsetting of aluminium solid billets.

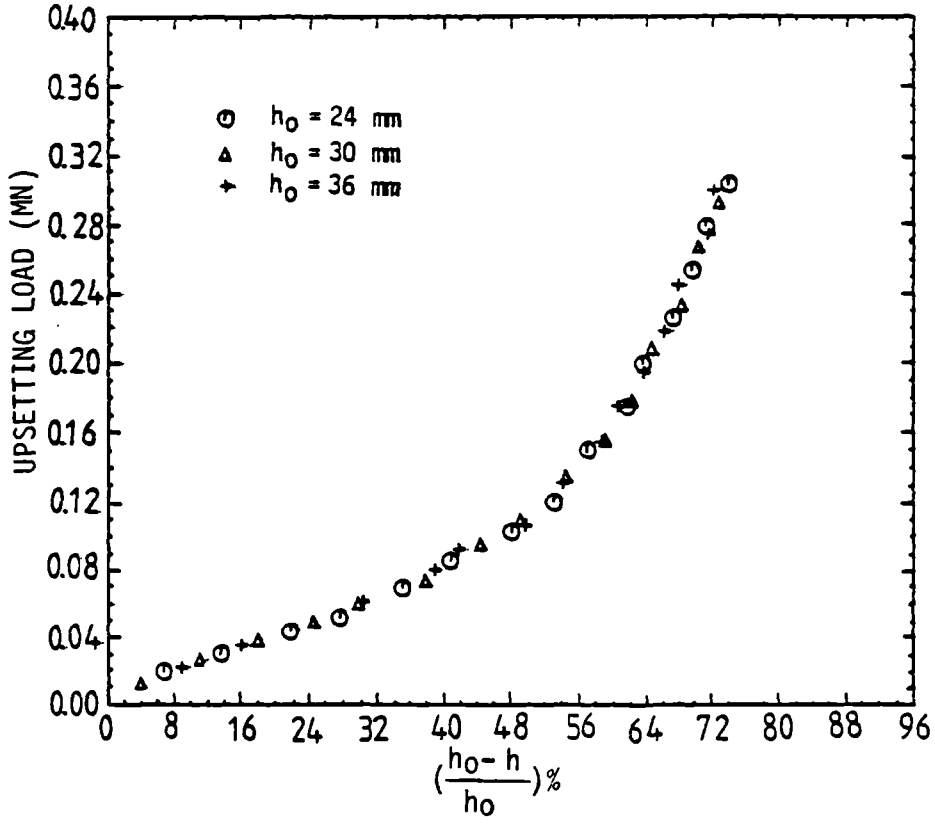


Fig. 3-25 Variation of upsetting load with percentage reduction in height in the open upsetting of aluminium solid billets.

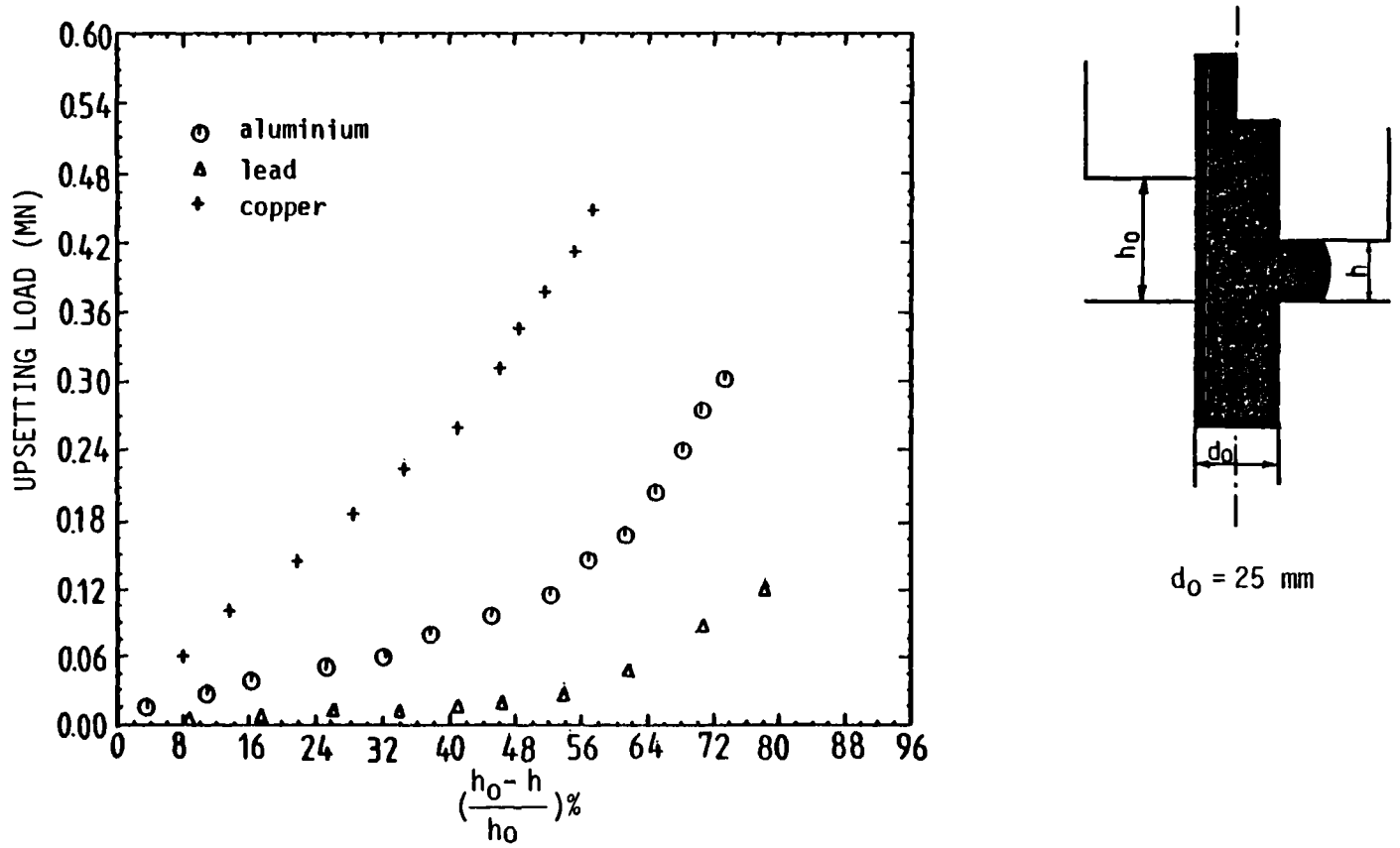


Fig. 3-26 Variation of upsetting load with percentage reduction in height in the open upsetting of solid billets of the three materials used.

earlier occurrence of rolling of the free surface onto the platen surfaces. The sharp increase of the upsetting load, which marks the final stage of deformation, also occurs at an earlier stage in open upsetting because undeformed zones meet earlier. At the early stages of deformation, however, the increase of punch load in open upsetting (which is a result of higher restraint on the flow of metal) is matched by a similar rise in heading due to more uniform deformation and consequent increase in the contact area between the punch and deforming material.

3.1.2 Mode of deformation

The mode of deformation of aluminium specimens was studied in conventional upsetting. This material was chosen because it can be polished easily and the flow patterns are clear when etched. A similar mode of deformation could be expected from other metals under similar conditions, as shown by several previous workers, who suggest that the deformation mode is not influenced by the material. Thomason *(20)* found that the metal flow of pure aluminium specimens during compression is identical to that of steel specimens with similar geometry and used pure aluminium to predict metal flow in steel specimens. Travis *(31)* used plasticene as a substitute material to demonstrate the deformation patterns in steel specimens. According to Male and Cockroft *(33)* ring specimens of aluminium with different hardness values, and copper, with similar original geometries and frictional conditions, showed identical geometrical changes.

To identify the material flow pattern and to study the development of the fold which occurs in the bore region, some experiments were stopped at various stages and the upset specimens were cut along the axis, polished and etched in a solution of 15 volumes hydrochloric acid, 10 volumes hydrofluoric acid and 90 volumes water.

The sectioned and etched specimens at various stages of the heading

operation under lubricated conditions are presented in Figs. 3-27. At the initial stage the downwards movement of the punch causes the material in the unsupported region of the billet to flow radially outwards. As a result of the restraints imposed on the radial flow of metal by frictional forces at the contact surfaces and also because the lower part of the deforming region is constrained, the radial velocity along the free height varies which in turn brings about the bulging of the inner and outer surfaces in the unconstrained region. Apart from bulging, at the early stages of deformation localized deformation is absent. Later the boundary between the deforming metal and the constrained lower part of the billet becomes distinct. The deformation is then largely concentrated along lines of heavy shear, which start from the die edge and meet the bore at approximately 45°. As the deformation continues an annular wedge of relatively undeformed material is formed at the upper end of the deforming region, at the punch/workpiece contact. The increasing movement of this annular wedge towards the shear line at the lower end of the deforming region causes the deforming metal to move radially outwards and results in a progressive increase of the internal diameter at midpoint along the deformed zone. The void so produced between the bore of the billet and the mandrel surface closes up at some stage of the deformation and forms a fold. Further displacement of the punch results in more radial flow of the deformed metal and increasing penetration of the fold into the upset flange until at the final stage of deformation, the two wedges come together. At this point, as it was discussed earlier in section 3.1.1, the load/displacement curve increases sharply and excessive load is required for a small increase in reduction.

The mode of deformation of the upset specimens in heading under dry conditions is shown in Fig. 3-28. Higher frictional forces at the contact

surfaces result in greater variation of radial velocity along the deforming zone, thus in more pronounced bulging at the beginning of deformation. There is no significant increase in the bore diameter near the punch so that the movement of material away from the mandrel is restricted to a narrower zone, the greater part of the bore remaining straight and parallel and close to the mandrel, i.e. some inward flow of material occurs. The combination of inward flow and high friction is typical of the deformation in the ring compression under dry conditions *(33)*.

A comparison of Figs. 3-27 and 3-28 reveals that shear lines at the bottom of the deforming region and the annular wedge at the punch contact surface are formed at an earlier stage when no lubricant is used. The larger volume of the relatively undeformed material at the top of the deforming region under dry conditions closes the void earlier between the billet and the mandrel.

It is of interest to note that when a lubricant is used, at some stage of the deformation the specimen ceases to be axi-symmetric and inhomogeneous deformation develops. This is due to lubrication breakdown at some areas of the contact surface, which produces a local retardation of the radial flow. In heading under dry conditions, however, the deformation is homogeneous and the flange is circular. This may be due to a reasonably uniform surface roughness of the platens between which the flange is upset, which produces uniform frictional conditions. The different deformation modes are clearly indicated at 50 per cent reduction in Fig. 3-27 and 3-28 and also in Fig. 3-30 where the top views of the upset products are given.

In order to investigate the effect of the initial unsupported height and wall thickness on metal behaviour in heading, upset products of various initial geometries obtained under lubricated conditions were sectioned and examined for the development of fold in the bore region. No folding occurred

during upsetting of the billet with the shortest original unsupported height (23 mm) although the bore exhibited typical bulging. With increased initial free height of the billet distortion at the bore became more pronounced and folding occurred, with larger penetration as the initial unsupported height increased. For the largest original free height (38 mm) deformation occurred almost entirely by bulging with no significant upsetting.

When the sectioned products of two different wall thicknesses (9.5 and 12.5 mm) with identical initial free height of 34 mm were compared, the relatively small fold produced in the thicker-wall hollow billet contrasted sharply with the severe folding observed in the thinner-wall billet for the same amount of reduction in height.

The sectioned and etched products of the open upsetting experiments under lubricated conditions are shown in Fig. 3-31. The photographs show the material flow patterns at various stages of deformation for a billet with an original free height of 34 mm.

In heading the upper face of the specimen was in sliding contact with the punch face at the initiation of the process. In open upsetting, however, the material is constrained in the punch cavity and higher restriction is therefore imposed on the flow of metal. This causes movement of the material away from the mandrel to be restricted to a much narrower zone, the greater part of the bore remaining straight and parallel and conforming to the mandrel during upsetting. Due to similar contact conditions at the ends of the deforming region identical annular wedges are formed, with the shear lines initiated from the flange corners, and the flange is horizontally symmetric. The bulge produced at the bore surface closes up at an earlier stage when compared with the heading operation performed under similar conditions.

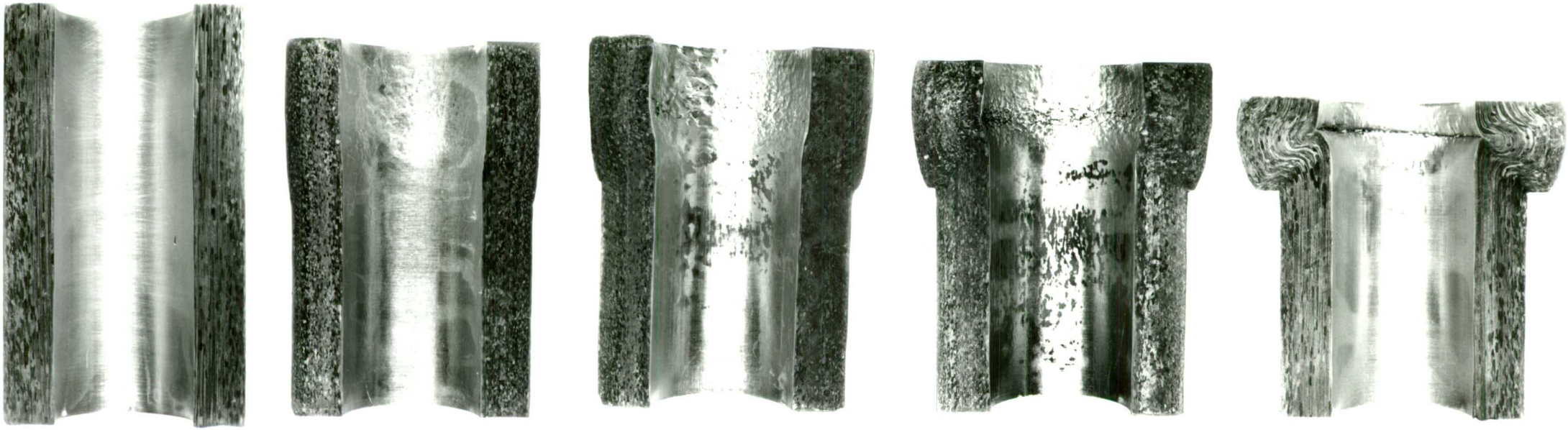
In heading the different frictional conditions on the free and

constrained ends of the billet affected the flow of metal and the fold formed in the upset flange was inclined to the horizontal plane of the flange. In open upsetting, however, the fold is formed in the horizontal plane because of the identical frictional conditions at the ends of the upset region.

In open upsetting the mode of deformation was almost identical for dry and lubricated conditions. This similarity for various end conditions must be due to the small annular contact areas between the flange and tools which reduce the effect of surface friction to a great extent. This small effect of frictional conditions on the mode of deformation can be due to the fact that the contact areas are mostly formed by rolling of the free outer surface of the billet onto the platens and no significant sliding of the deforming metal relative to the contact surfaces occurs. This will be discussed further, later in this section.

To acquire a visual assessment of the degree of inhomogeneous deformation, i.e. the "rolling up" of wall material onto the platens during upsetting, some of the billets were painted blue over the outer surface of their free height, Fig. 3-29. When the products of heading under lubricated and dry conditions were compared at the same amount of height reduction, smaller blue annular rings on the flange surfaces were noted for the lubricated products, Fig. 3-30. This reveals that the "rolling up" phenomenon occurs at an earlier stage of deformation when upsetting is performed under dry conditions. This difference is, however, less distinct in open upsetting since surface friction has less effect on the process.

It is of interest to note that when the blue annular rings on the top surfaces of the headed products at various amounts of punch displacement were compared, it was found that after "rolling up" starts, the metal particles on the initial contact surface still have an outward velocity.



a) 0% b) 16% c) 27% d) 34% e) 50%

Fig. 3-27 Etched sections in the heading of aluminium hollow billets under lubricated conditions at various reductions.



a) 0%

b) 16%

c) 27%

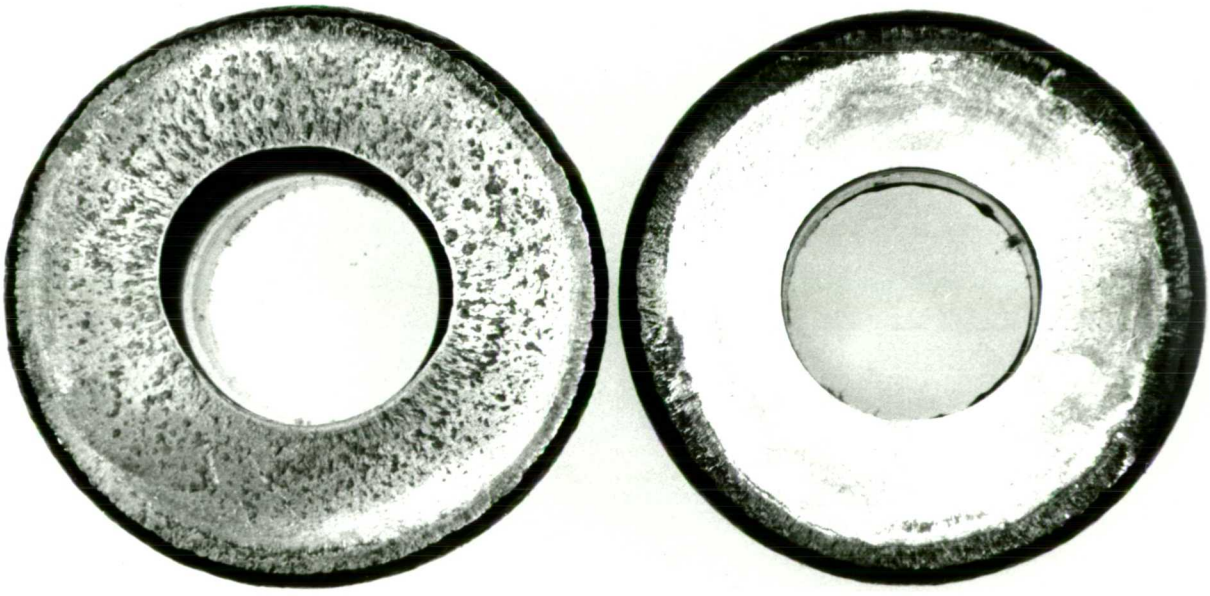
d) 34%

e) 50%

Fig. 3-28 Etched sections in the heading of aluminium hollow billets under dry conditions at various reductions.

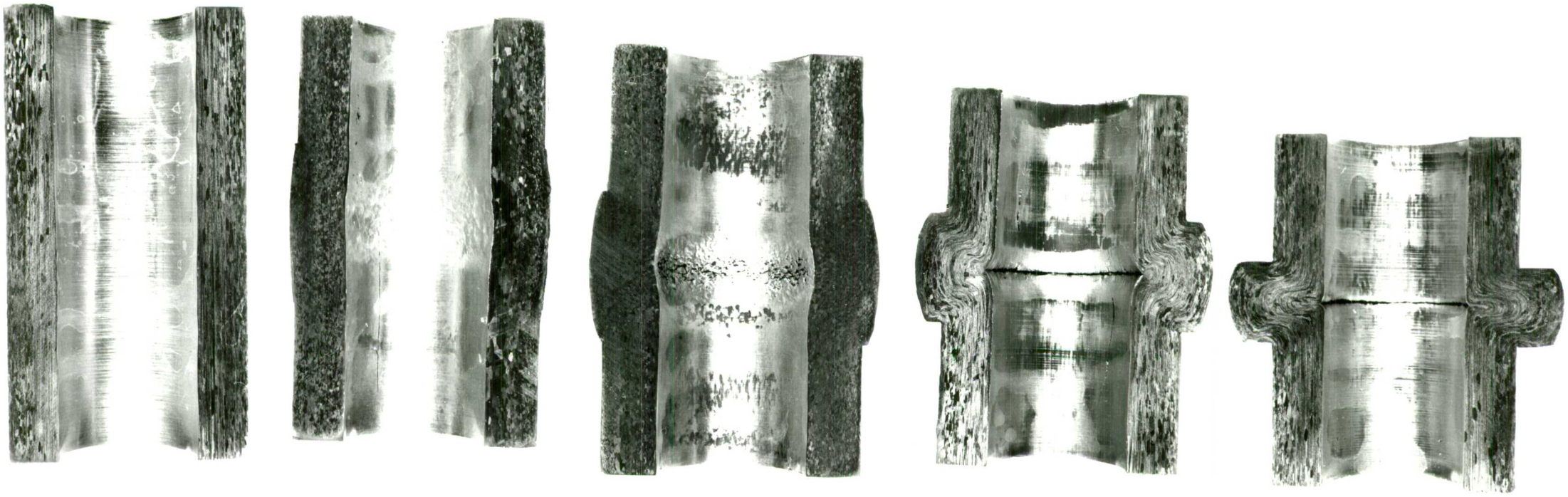


Fig. 3-29 Hollow billets in heading and open upsetting painted blue over their unsupported heights.



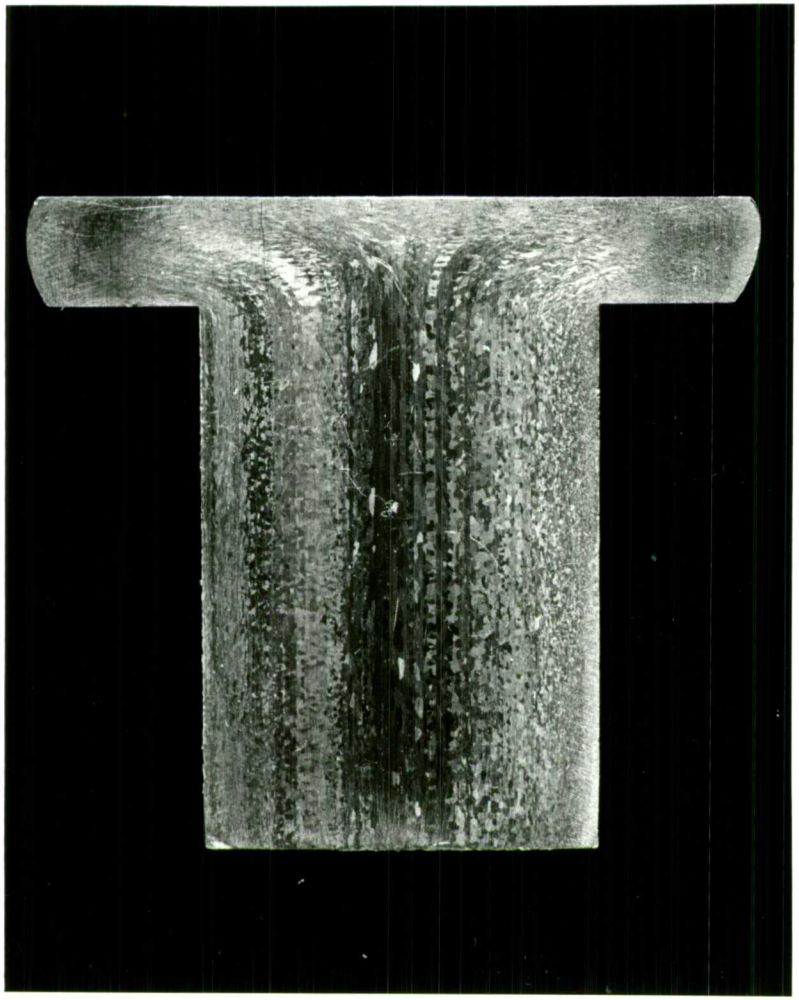
a) lubricated b) dry

Fig. 3-30 Top views of the aluminium hollow flanged products obtained in heading under different end conditions.

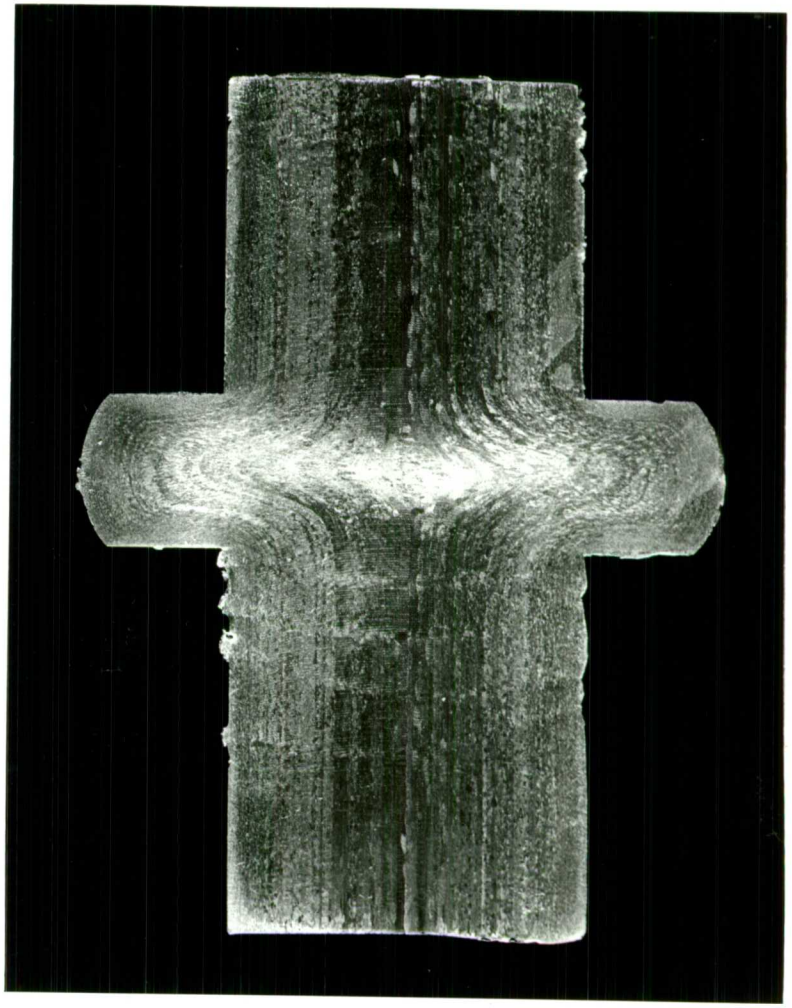


a) 0% b) 16% c) 27% d) 39% e) 56%

Fig. 3-31 Etched sections in the open upsetting of aluminium hollow billets under lubricated conditions at various stages of deformation.



a) Heading



b) Open upsetting

Fig. 3-32 The etched sections from conventional upsetting of aluminium solid bars.

This observation appeared to be more pronounced under lubricated conditions due to less restriction on the radial flow of metal.

Further study of the blue annular rings on the flange surfaces shows that there is a greater amount of rolling on the bottom surface, at the contact of the flange with the die surface. In open upsetting almost the entire contact area of the lower surface and the greater part of the upper surface were formed by the rolled material from the outer surface.

In both heading and open upsetting, for the specimens with a larger initial unsupported height, more of the originally free surface comes into contact with the die at the same reductions. This is due to more bulging of the outer free surface and less increase in the initial contact area due to upsetting.

To study the material flow patterns in the upset solid billets, two samples were sectioned and etched, Fig. 3-32. The photographs show that the flow patterns are symmetric around the axis and the heavy shear lines, which are initiated from the flange corners, meet on the axis of the billet. Contrary to what was found for hollow billets, folding in solid billets can not occur, but the formation of cavities in the central region could be envisaged.

3.1 Injection upsetting

In injection upsetting experimental results were obtained for hollow billets of two different wall thicknesses, injected into gaps with heights ranging from 7 to 15 mm. The same range of gap heights were used to injection-upset solid bars of two different diameters, 25 and 30 mm. Typical hollow and solid flanged components produced by simple injection upsetting and injection upsetting with one end of the billet constrained are shown in Figs. 3-33 and 3-34.

In this section the load/displacement characteristics of lead,



Fig. 3-33 Typical products, injection upsetting of hollow billets.



Fig. 3-34 Typical products, injection upsetting of solid bars.

aluminium and copper specimens are presented and a general discussion regarding the shape of the load/displacement curves is given. Furthermore, the behaviour of the material during deformation and also the nature and development of the fold in the bore region of hollow billets is studied by observing the sectioned etched products.

3.2.1 Load/displacement characteristics

Because both the flange thickness and the flange profile alter with the gap height, the flange diameter can not be accurately predicted in relation to punch displacement so that the load is plotted as a function of the latter.

The load/displacement curves in the injection upsetting of hollow billets are shown in Figs. 3-35 to 3-41. The general trend of the curves is almost identical in all cases, i.e. at the initial stage the load increases sharply up to some value of the punch displacement after which the rate of increase declines and the curves show a tendency to level off.

The length of the billet was originally thought to be a major factor in the load/displacement characteristics as the frictional forces at the billet/die and billet/mandrel interfaces are dependent on the size of the contact area. However, the results of some preliminary tests on lubricated aluminium and copper specimens indicated that there is little correlation between load and billet height, which has also been experimentally verified by Milner *(49)*. Milner measured the upsetting load and the load transferred to the surface of the bottom platen on which the flange is formed, and the frictional forces at the billet/container interface were assumed to be the difference between the measured loads. Several tests using lubricated billets of aluminium alloy of 20 mm diameter with various initial lengths of up to 65 mm failed to show any consistently measurable difference in loads, suggesting negligible effect of the frictional forces. However, it

can be expected that high radial stresses in the case of small gap heights or when upsetting high strength materials such as steel, could develop frictional forces high enough to affect the upsetting load significantly.

In injection upsetting with one end of the billet constrained, the load/displacement curves obtained with various constrained lengths suggest that the effect of this length on the load is negligible.

The upsetting loads in the simple injection upsetting of billets into gaps of various heights are shown in Figs. 3-35 and 3-36 for aluminium and copper respectively. The figures show that the load required for a given punch stroke is smaller for greater flange thickness. As the gap height increases the rate of decrease in the required upsetting load for a given punch stroke becomes smaller. Similar results are obtained when one end of the hollow billet is constrained, Figs. 3-38 to 3-40. The tests on copper specimens had to be stopped early since the required load became too large for the tool.

The load/displacement curves for different materials are shown in Fig. 3-37 which indicates that the load is highly dependent on the rate of work hardening of the material. For the material with a lower rate of work hardening a sharp increase in load at the early stage ends at a smaller punch displacement, followed by a gradual upward trend of the curve. This also applies to injection upsetting with one end constrained, Fig. 3-40.

In Fig. 3-41 the load/displacement curves of two aluminium specimens with and without end constraints show that initially the loads are identical but at greater values of punch displacement higher loads are required for the specimen with one end constrained, as expected due to the higher restraint imposed on the radial flow of metal at the constrained end.

The load/displacement characteristics obtained in the injection upsetting of solid bars are shown in Figs. 3-42 to 3-48. The results are similar to those for hollow billets and the discussion outlined in the

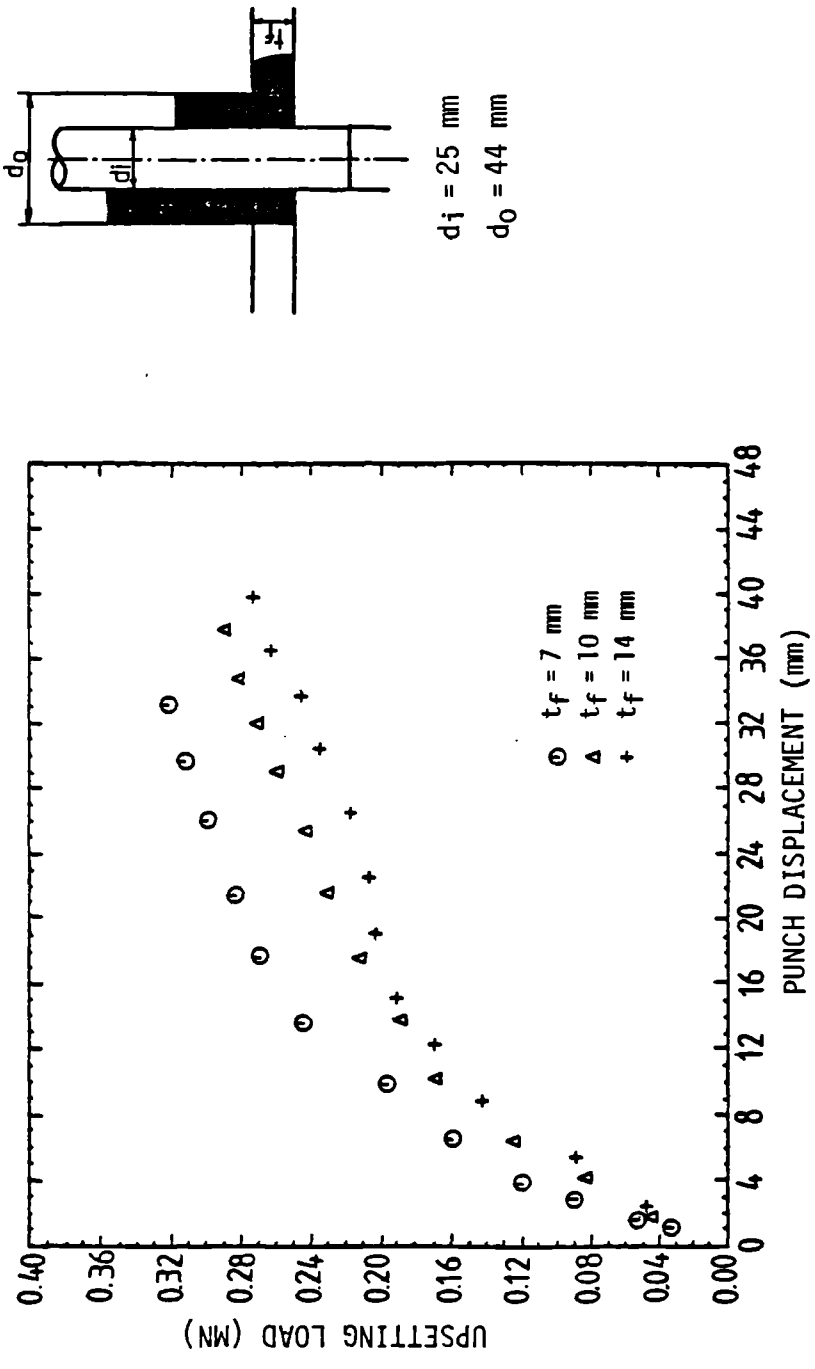


Fig. 3-35 Effect of gap height on the load/displacement characteristics, simple injection upsetting of aluminium hollow billets.

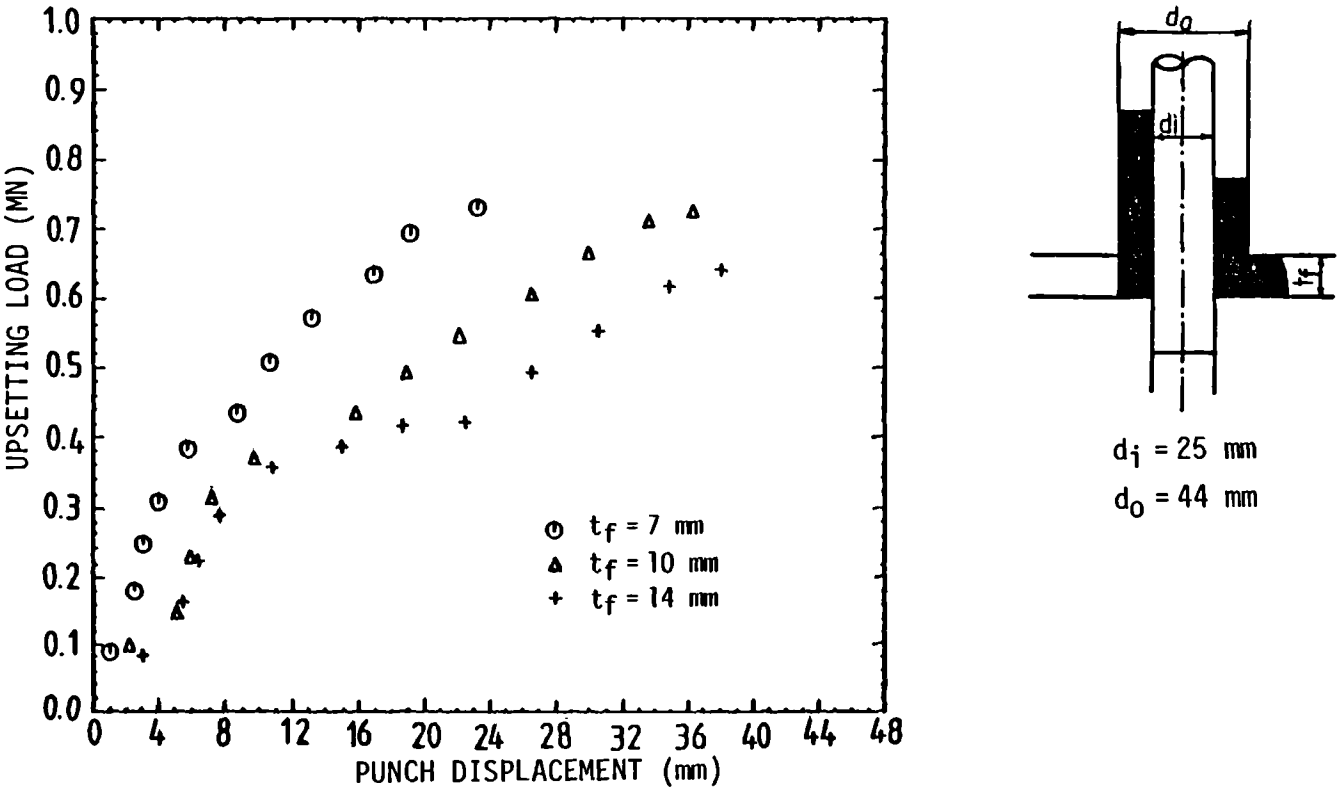


Fig. 3-36 Effect of gap height on the load/displacement characteristics, simple injection upsetting of copper hollow billets.

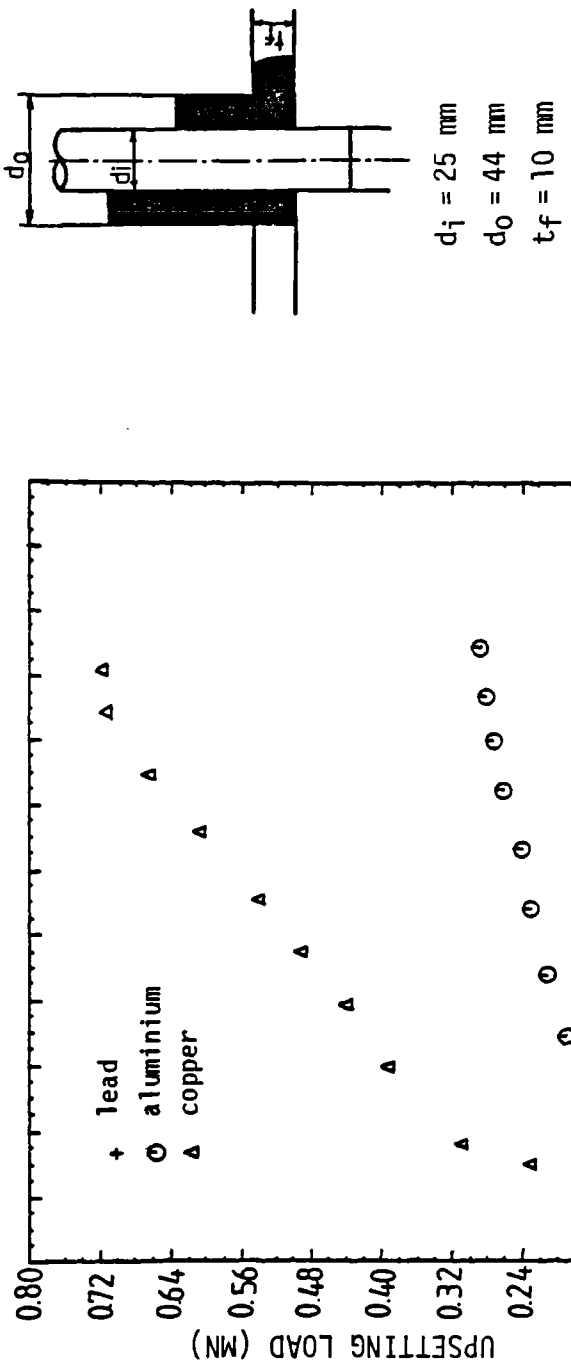


Fig. 3-37 Variation of upsetting load with punch displacement, simple injection upsetting.

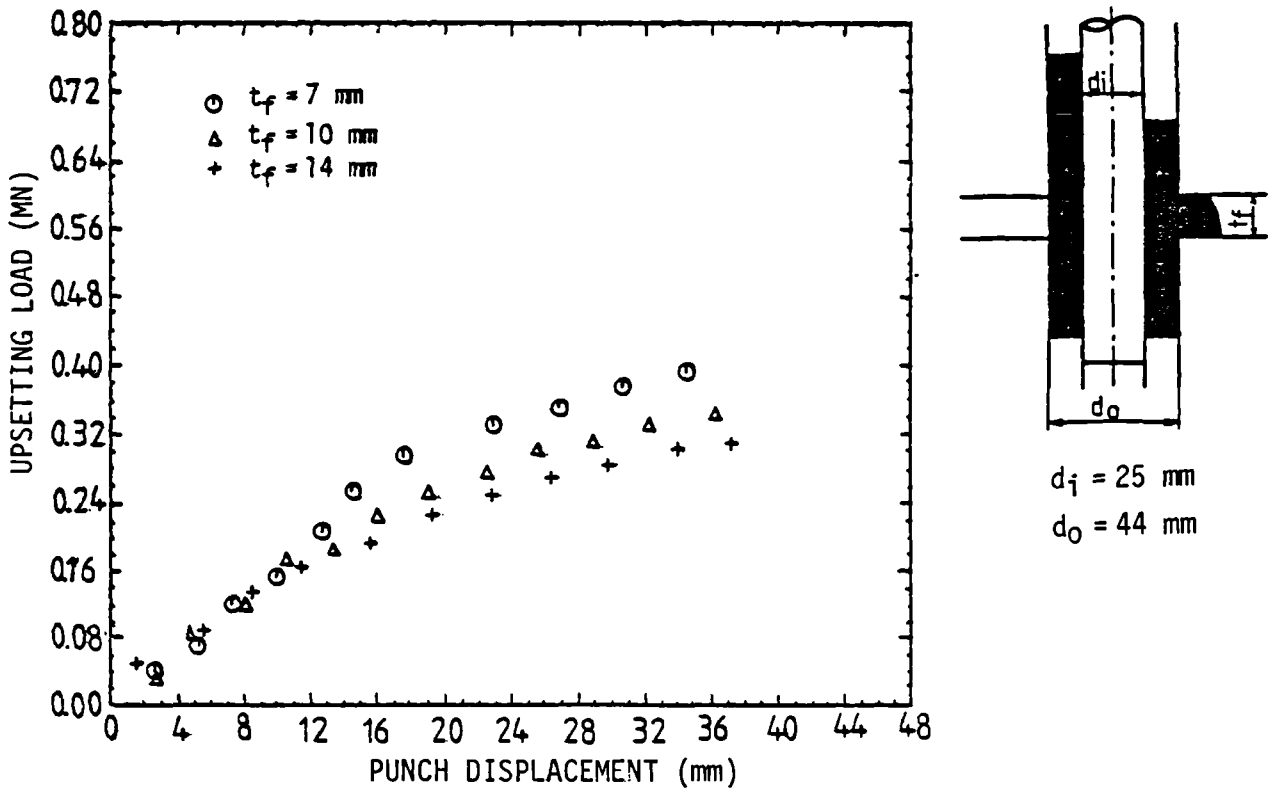


Fig. 3-38 Effect of gap height on the load/displacement characteristics. Injection upsetting of aluminium hollow billets with one end constrained.

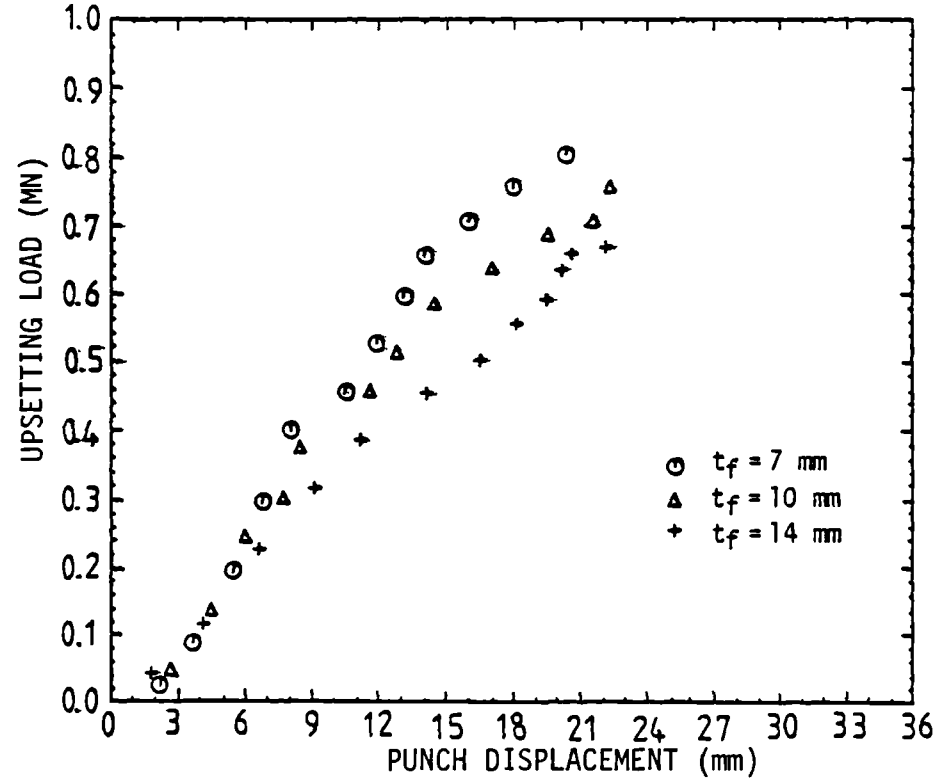


Fig. 3-39 Effect of gap height on the load/displacement characteristics. Injection upsetting of copper hollow billets with one end constrained.

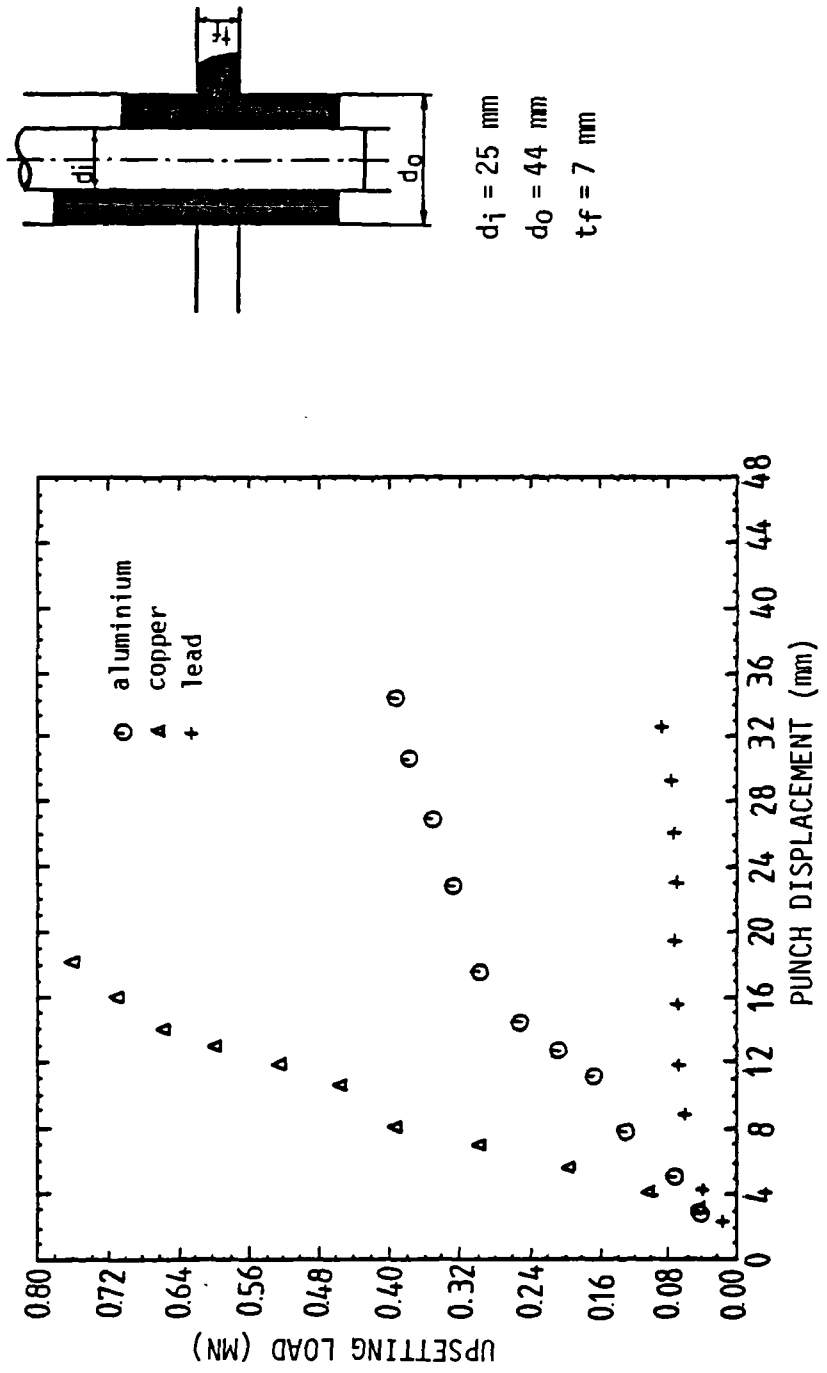
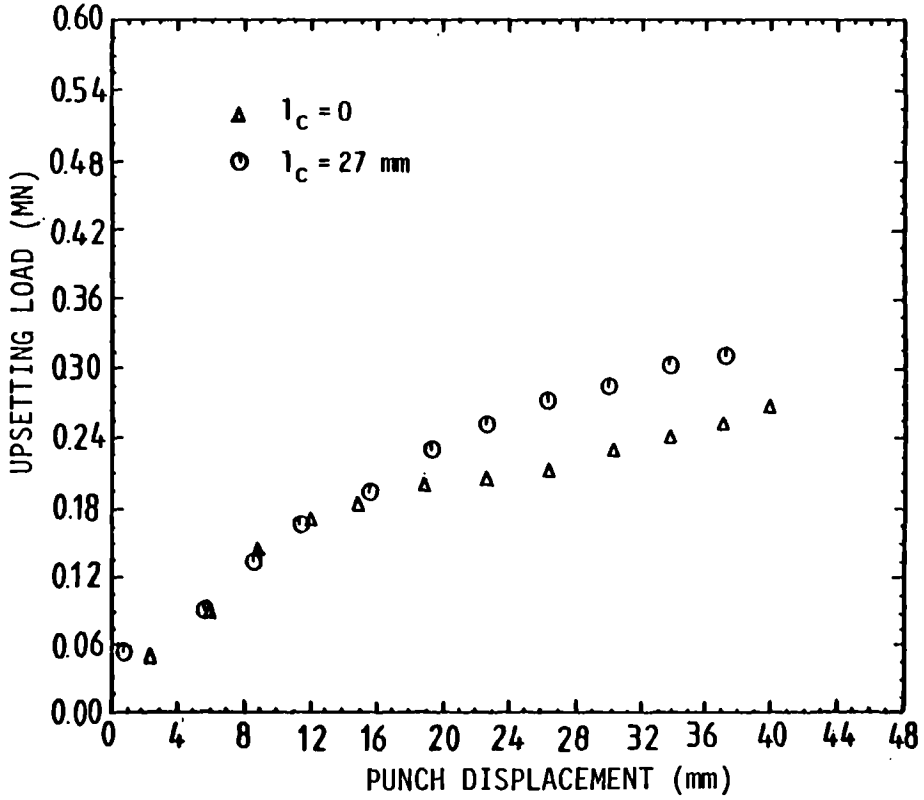
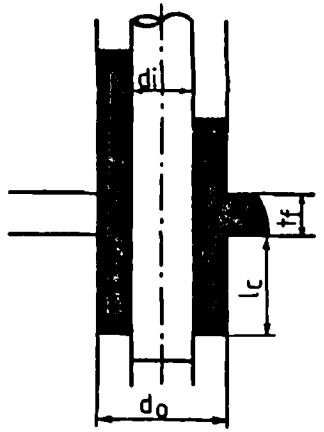


Fig. 3-40 Variation of upsetting load with punch displacement. Injection upsetting of hollow billets with one end constrained.





$d_i = 25$ mm

$d_o = 44$ mm

$t_f = 14$ mm

material : aluminium

Fig. 3-41 Comparison of load/displacement characteristics. Injection upsetting of hollow billets with and without end constraints.

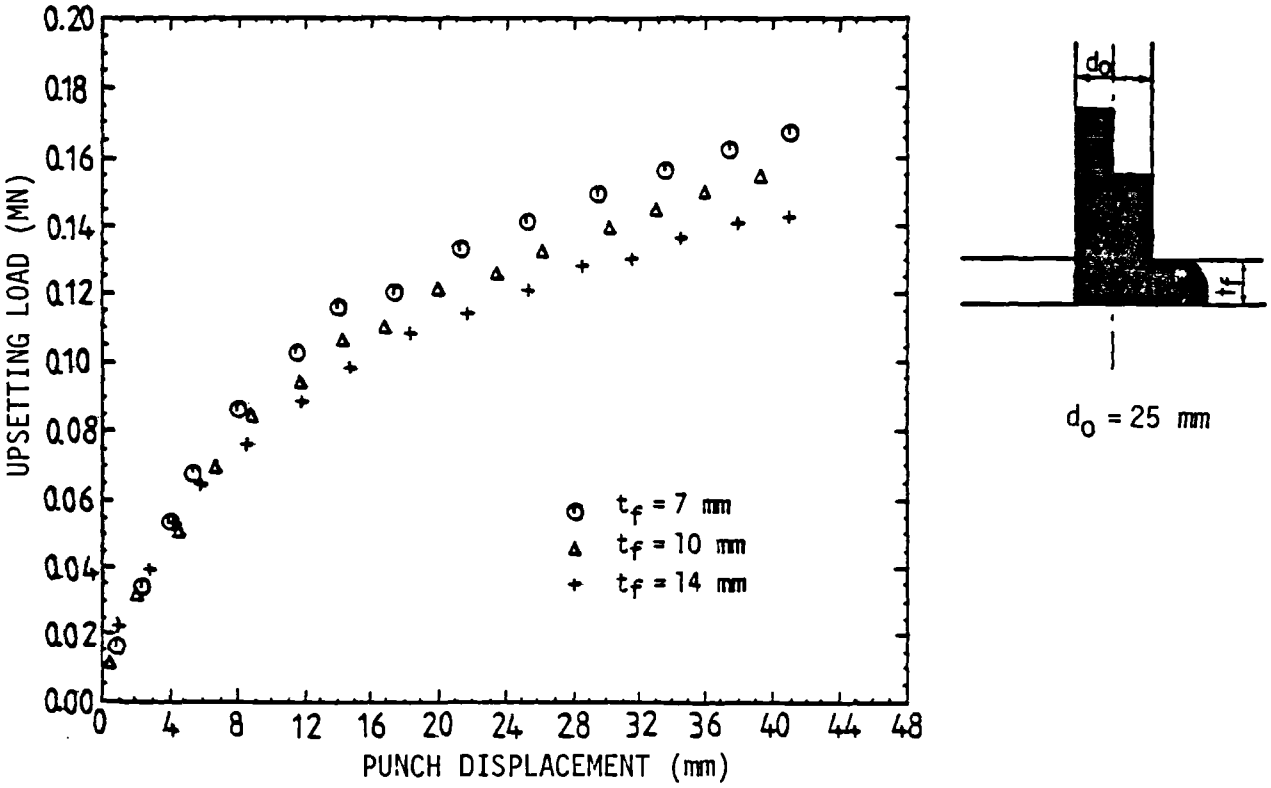


Fig. 3-42 Effect of gap height on the load/displacement characteristics. Simple injection upsetting of aluminium solid billets.

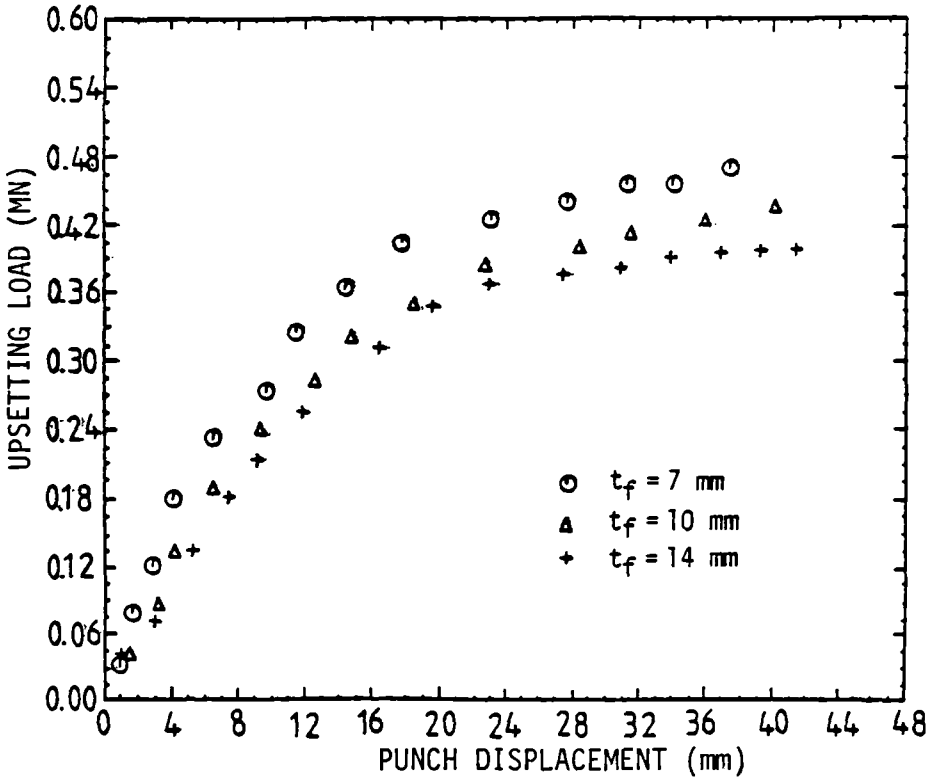


Fig. 3-43 Effect of gap height on the load/displacement characteristics. Simple injection upsetting of copper solid billets.

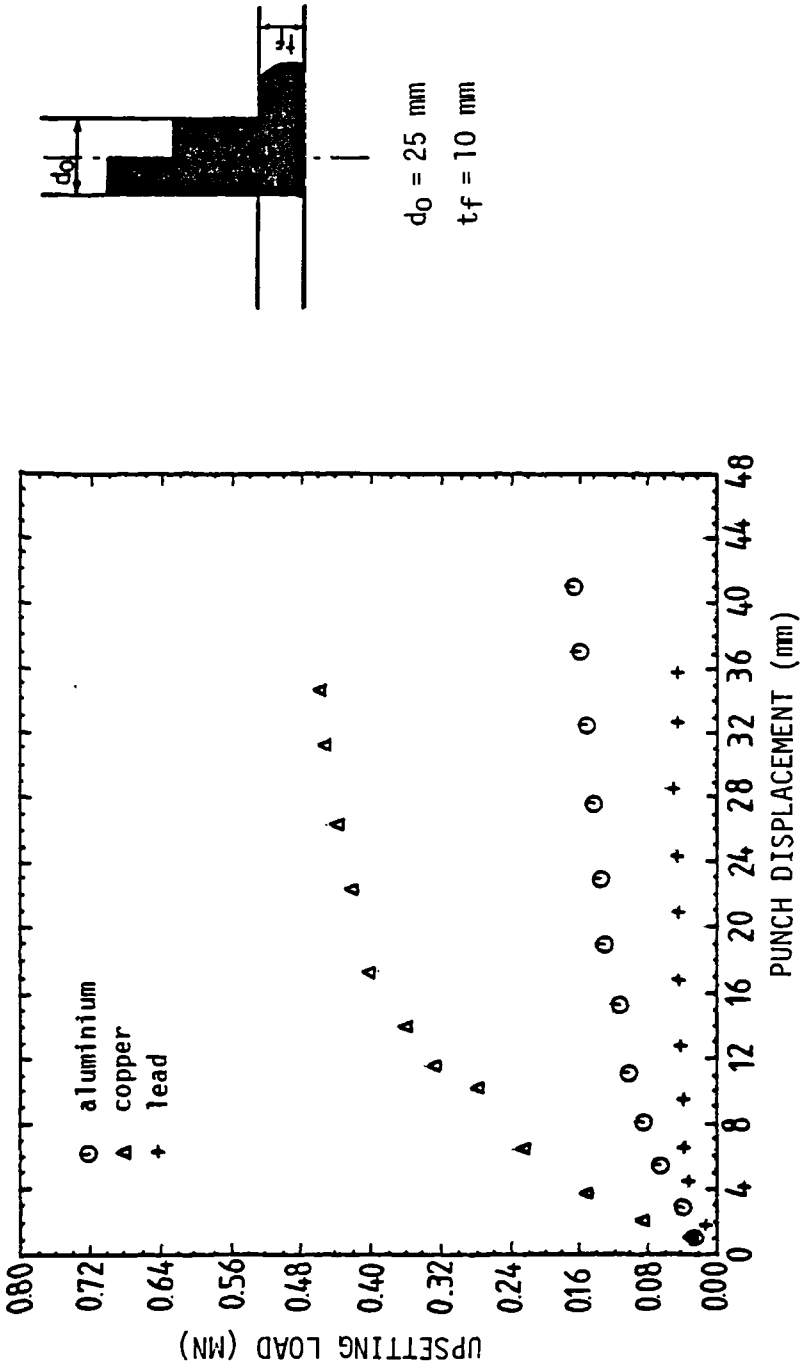


Fig. 3-44 Variation of upsetting load with punch displacement. Simple injection upsetting of solid billets.

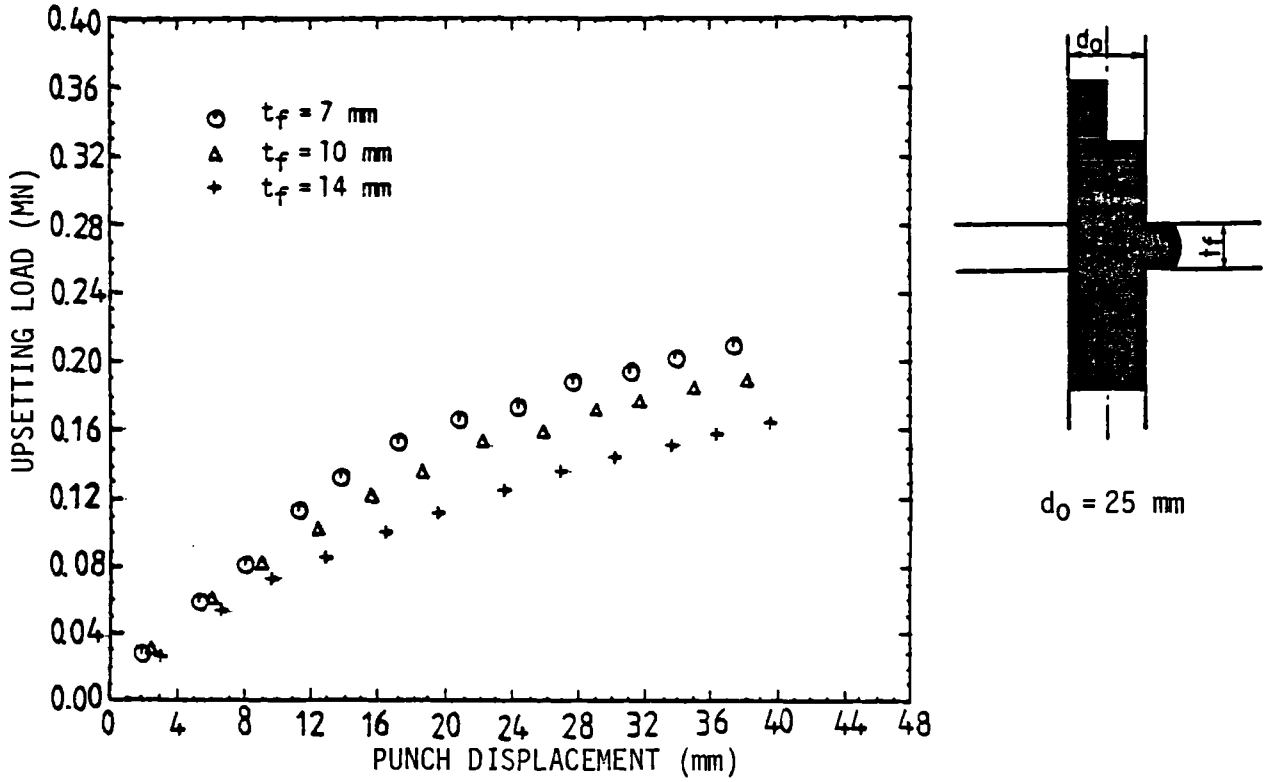


Fig. 3-45 Effect of gap height on the load/displacement characteristics. Injection upsetting on aluminium solid billets with one end constrained.

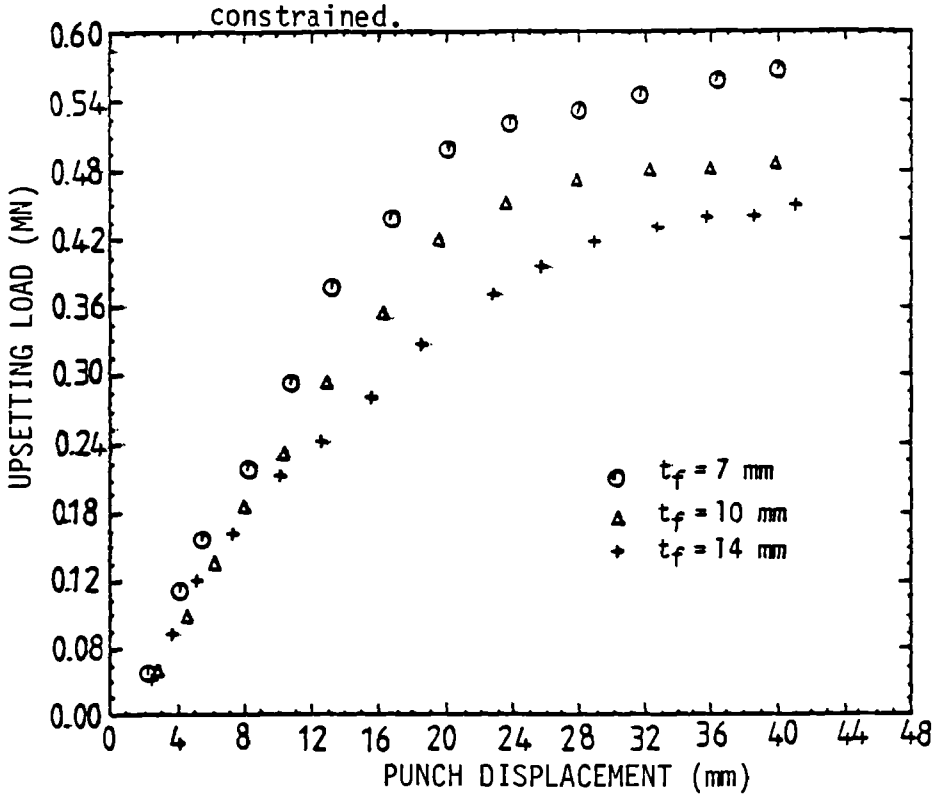


Fig. 3-46 Effect of gap height on the load/displacement characteristics. Injection upsetting of copper solid billets with one end constrained.

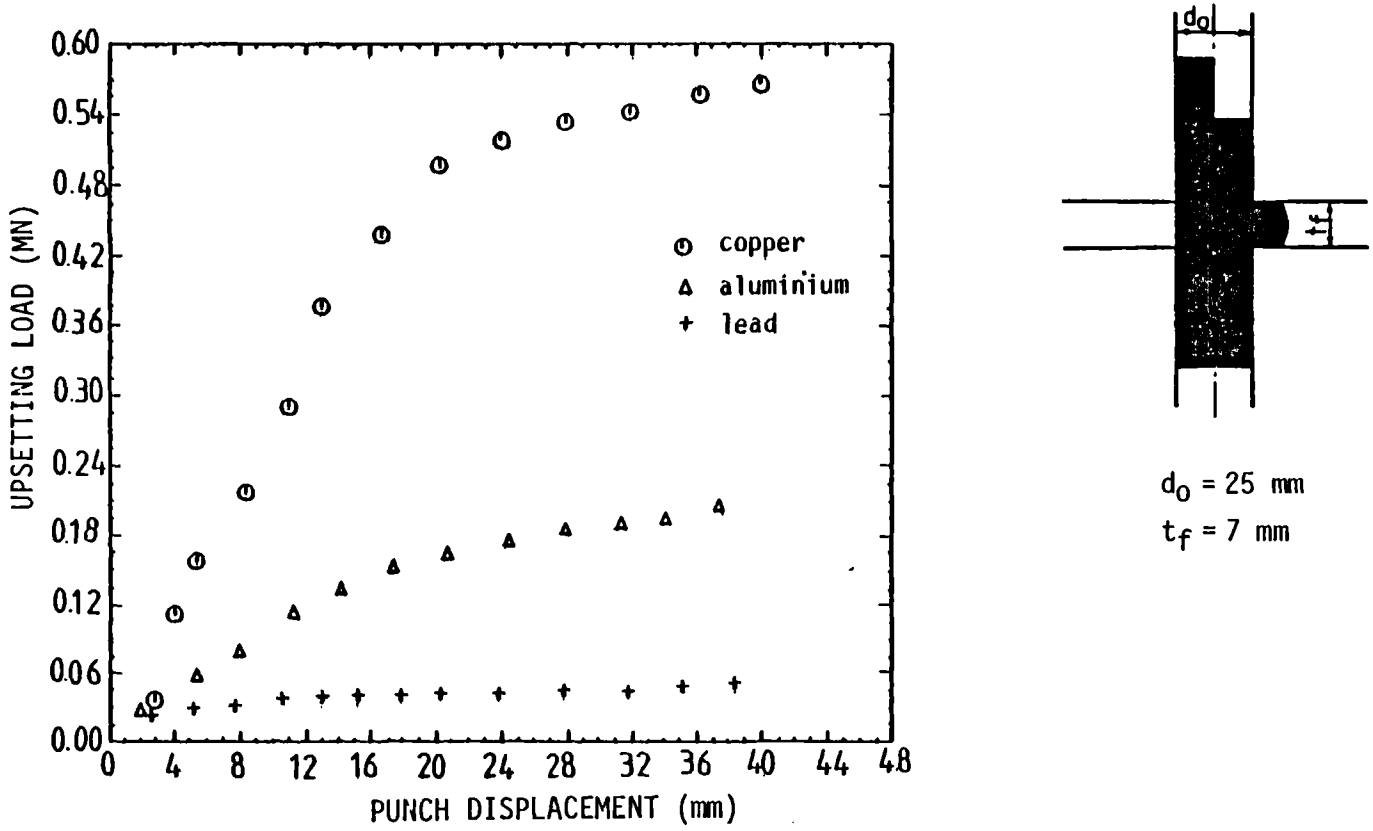
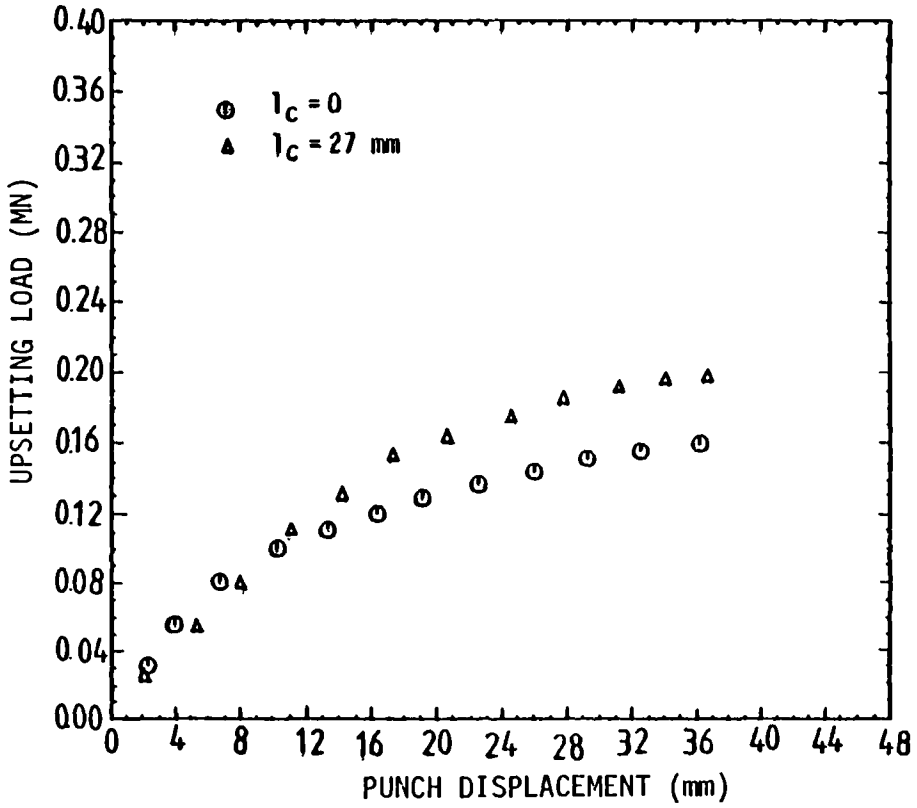
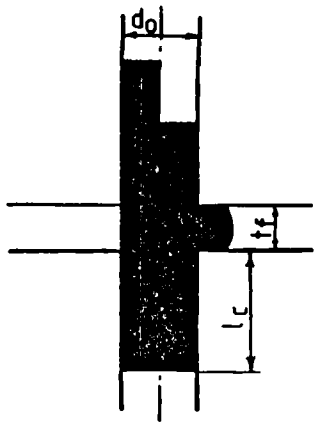


Fig. 3-47 Variation of upsetting load with punch displacement. Injection upsetting of solid billets with one end constrained.





$d_o = 25$ mm

$t_f = 7$ mm

material : aluminium

Fig. 3-48 Comparison of the load/displacement characteristics of injection upsetting of solid billets with and without end constraints.

foregoing is equally applicable to both cases.

3.2.2 Mode of deformation

A visual inspection of the specimens reveals that, whilst the shape of the bottom face of the flange is determined by the platen surface, the top face is free formed, contact is made with the top platen only at the orifice. This is in contrast to the products of conventional upsetting where the upset material conforms to the surfaces of both the top and bottom platens so that the flanges have parallel faces.

The main observation regarding the shape of the flange is its uneven thickness, usually referred to as thinning. The extent of thinning is highly dependent on the height of the gap, i.e. the effect is more pronounced in flanges injected into larger gaps. This can be clearly seen in Fig. 4-49 which compares the aluminium specimens of different flange thicknesses at the early stages of deformation.

Another characteristic which often occurred in thin flanges was bending into a dished shape, Fig. 3-53(a) and 3-57(a). The flange rim lifts from the platen surface and bends upwards at a particular flange diameter which is smaller for decreasing flange thickness. As upsetting proceeds the flange continues its upward movement until it is stopped by the container. This effect indicates the instability of a relatively thin flange under tensile hoop stresses and may be facilitated by the more localised pressure at the deforming material/bottom platen interface when the gap is small.

The formed flanges were very sensitive to irregularities of the platen surfaces. Better surface finish improved the circularity of the products except for very thick flanges, where the relatively wide area of transmission of the punch load from the flange to the platen sometimes caused isolated

areas of lubrication breakdown at the flange rim, thus producing local retardation of the radial flow of metal. This is clear from Fig. 3-50 where the bottom faces of flanges of 14 mm thickness are shown for hollow and solid flanged products. When flanges of the same thickness were formed on dry platens good circularities were observed, Fig. 3-51.

Several previous workers who performed injection upsetting on metals with less ductility than those used in the present work have reported that the amount of deformation was limited by necking and eventual fracture of the flange rim *(45, 49)*. The fracture at the flange rim due to tensile hoop stresses in this region was reported to occur at an earlier stage of deformation for thinner flanges. This is because work hardening at or near the upper edge of the flange rim increases with decreasing flange thickness, resulting in lower ductility.

All the injection upset flanged products obtained in the present work were examined for free surface fracture at the end of the tests and none of the specimens showed any sign of fracture in the flange region. In the simple injection upsetting of hollow billets of aluminium and copper into the smallest gap (7 mm height), the operations were continued until flanges with a diameter twice that of the billet were obtained.

To study the material flow patterns during the process, some of the tests on aluminium billets were stopped at various stages of deformation, the specimens were sectioned along their longitudinal axes, polished and etched. Fig. 3-52 shows a typical sequence of sections, taken from simple injection upsetting tests under lubricated conditions. Throughout the process there is no plastic deformation in the billet material constrained between the container and mandrel. The boundary between the deforming and undeformed regions appears as a shear line which initiates from the die edge and meets the bore surface at approximately 45° and remains almost unchanged

throughout the process. At the early stage of deformation the unconstrained part of the billet bulges outwards with no significant increase in the wall thickness, as shown at a punch displacement of 10.5 mm. Since the material at the top of the deforming region is restrained by the container and because of negligible frictional forces on the billet/platen interface, the largest radial velocity and therefore the maximum increase in diameter occurs at the lowest part of the billet. As punch displacement increases, introduction of new material to the deforming region results in a change of the radial velocity distribution, so that particles in contact with the platen cease to have the highest radial velocity. Retardation in the radial flow of metal in contact with the platen surface results in the formation of a fold in the inner bulged region. This can be clearly seen in the deformation patterns obtained for a punch displacement of 17 mm. As deformation proceeds the fold is forced into the flange by new material from the billet, it is eventually closed and becomes part of the flange, Fig. 3-52(d).

To investigate the effect of gap height on the mode of deformation, flanges of various thicknesses were sectioned and etched. The deformation patterns obtained for gap heights of 7, 10 and 14 mm are shown in Fig. 3-53. The results show that for smaller gaps the fold forms nearer the bore and its penetration into the upset material is less severe since the initial bulging of the unconstrained height is less pronounced.

Under dry conditions the radial flow of metal in the vicinity of the platen surface is highly restrained due to high frictional forces acting at the billet/platen interface (Fig. 3-54), which brings about a more uniform radial velocity along the length of the unconstrained region at the beginning of the deformation so that, at the early stages of deformation, a significant increase in wall thickness and more upsetting occurs in comparison with the lubricated case, but some bulging is visible at the

mid-point of the unconstrained length. Although this bulging is on a much lower scale than in the lubricated case it is sufficient for the initiation of a fold at the bore surface. Later this fold is forced into the flange and forms part of it, together with a triangular region of relatively undeformed material at the lower part of the deforming region. The boundary of this dead zone is a line just below the fold across the flange.

One further difference between the dry the lubricated conditions is that, in the former, the flange has the largest diameter near the die, while in the latter this is near the platen.

In injection upsetting with one end of the billet constrained, at the early stages of deformation (at a punch displacement of 13.5 mm, Fig. 3-55) the wall thickness of the billet increases almost uniformly in the region of the gap. The shape of the upset flange and the mode of deformation are almost identical to those obtained in the corresponding simple injection upsetting when no lubricant was used on the lower platen surface, Fig. 3-54. This was expected because shearing of the deformed metal from the constrained material presents high restraints to radial flow in the lower region of the flange. A major difference occurs in the bore region, where instead of a bulge at the bore and formation of a fold, the defects at the bore surface appear as small wrinkles. This results in the formation of several folds with different degrees of penetration into the upset region. A comparison of the bore surfaces obtained at punch displacements of 13.5 and 27 mm reveals that the voids close as more material is injected into the free gap. The boundaries between the deforming and undeformed regions can be seen more clearly in the sectioned product at a punch displacement of 27 mm (Fig.3-55(c)). The boundary at which the new material enters the deforming region is similar to that observed in simple injection upsetting and the shear line

at the bottom of the deforming region is on level with the lower surface of the flange.

Flow patterns obtained for three different gap heights of 7, 10 and 14 mm are shown in Fig. 3-56 for injection upsetting with one end constrained. The photographs show that the defects of the bore surface are less severe for thinner flanges and the deformation shifts further into the tubular part with decreasing gap height.

The deformation patterns when solid billets are injected into a gap of 7 mm are shown in Fig. 3-57 for injection upsetting with and without end constraints. The patterns obtained for simple injection upsetting with lubricant show uniform and parallel flow lines throughout the upset region. This is in contrast to the non-uniform flow patterns observed in hollow billets particularly near the lower contact surface (Fig. 3-52). This suggests that in the injection upsetting of hollow billets more uniform deformation would result for billets with smaller internal diameters. The photographs also show that the lines of heavy shear which initiate from the flange corners occur in a similar manner to those in hollow billets.

In injection upsetting with one end of the solid billet constrained there is no folding problem, but the configuration of the flow lines near the centre line indicates that conditions are favourable for the opening of cavities and central burst.



(a) (b) (c)

Fig. 3-49 Effect of flange thickness on thinning, simple injection upsetting of aluminium.

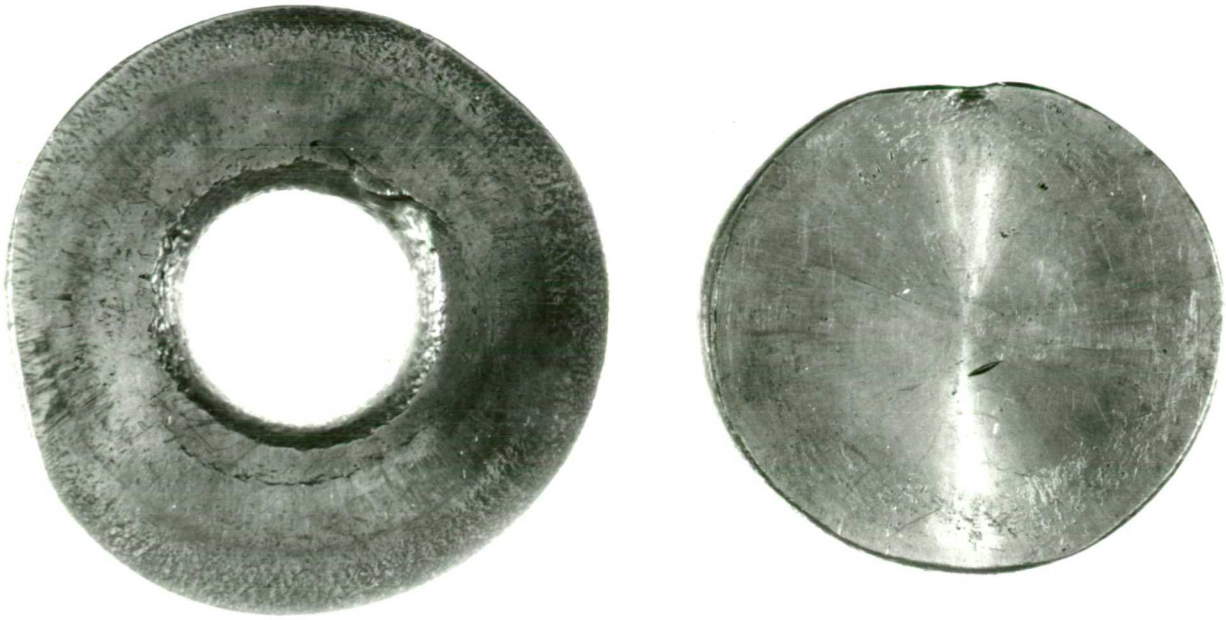
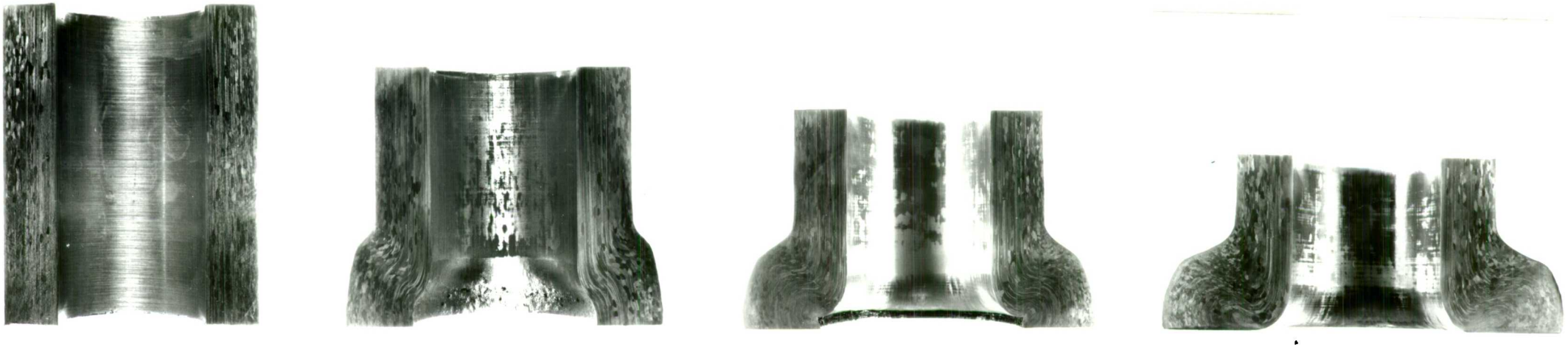


Fig. 3-50 Irregularities in the shape of the flange due to lubrication breakdown in simple injection upsetting of aluminium.



Fig. 3-51 Bottom face of an aluminium hollow flanged component in simple injection upsetting under dry conditions.



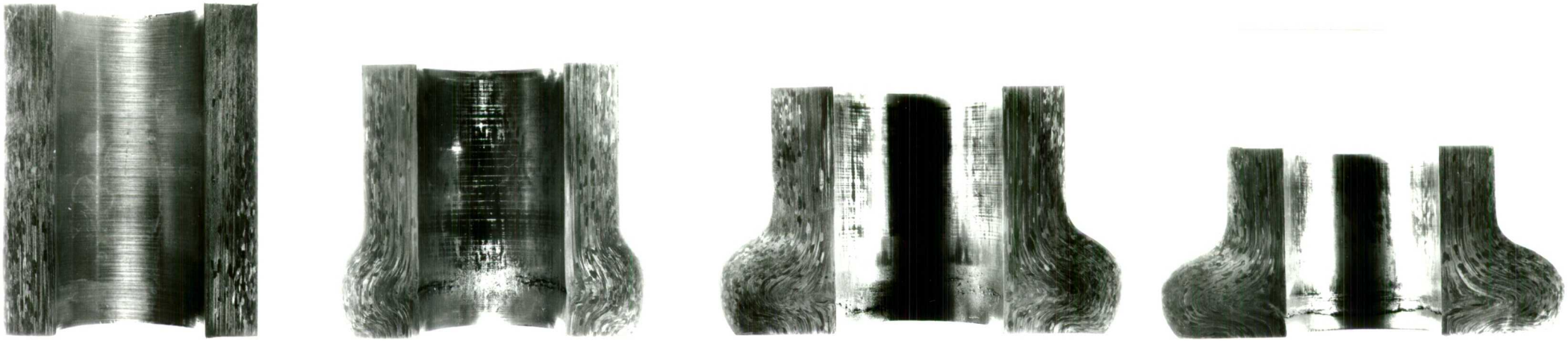
a) 0 b) 10.5 mm c) 17 mm d) 25 mm

Fig. 3-52 Etched sections of aluminium hollow billets in simple injection upsetting under lubricated conditions at various punch displacements.



a) 7 mm b) 10 mm c) 14 mm

Fig. 3-53 Etched sections of aluminium hollow billets. Effect of flange thickness t_f, simple injection upsetting.



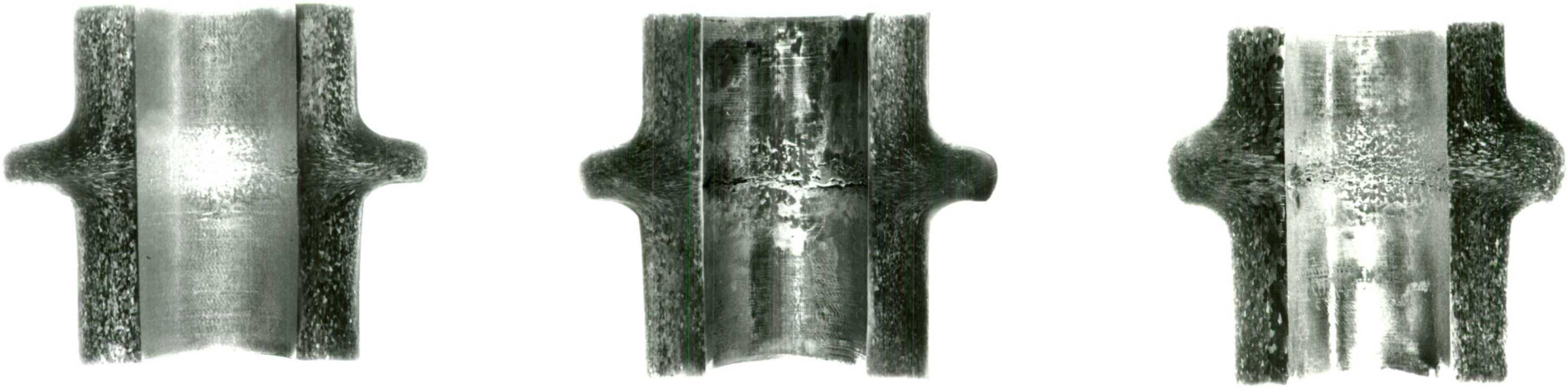
a) 0 b) 3 mm c) 19 mm d) 25 mm

Fig. 3-54 Etched sections of aluminium hollow billets in simple injection upsetting under dry conditions at various punch displacements.



a) 0 b) 13.5 mm c) 27 mm

Fig. 3-55 Etched sections for aluminium hollow billets in injection upsetting with one end constrained at various punch displacements.

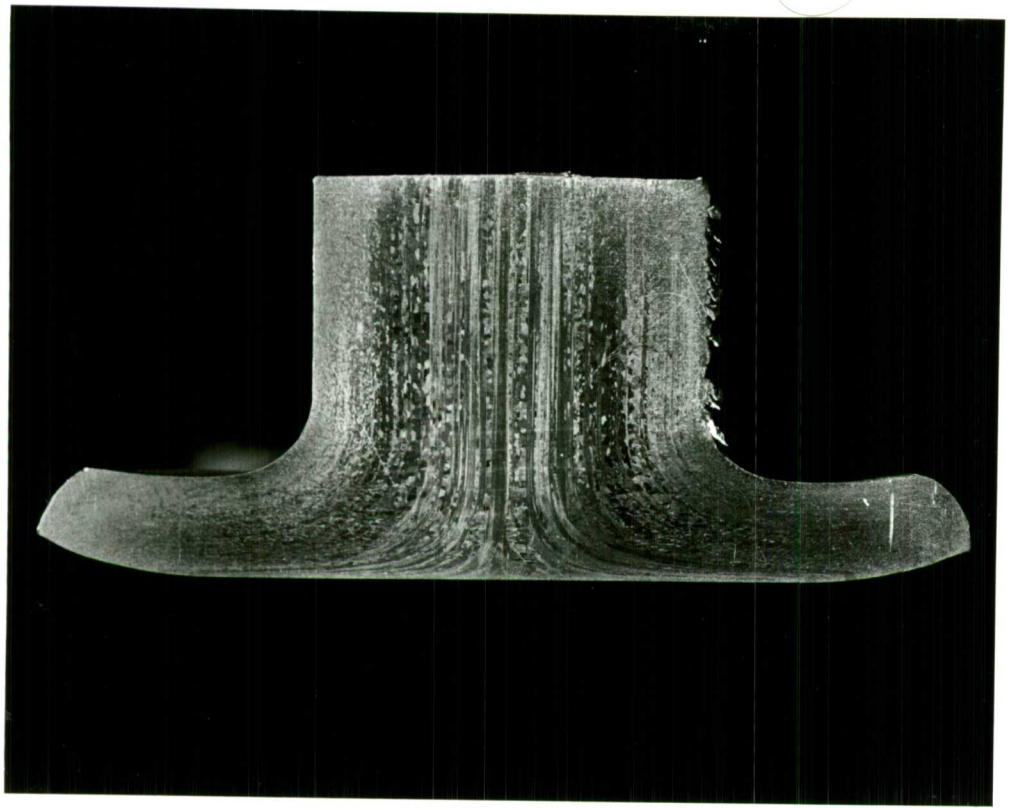


a) 7 mm

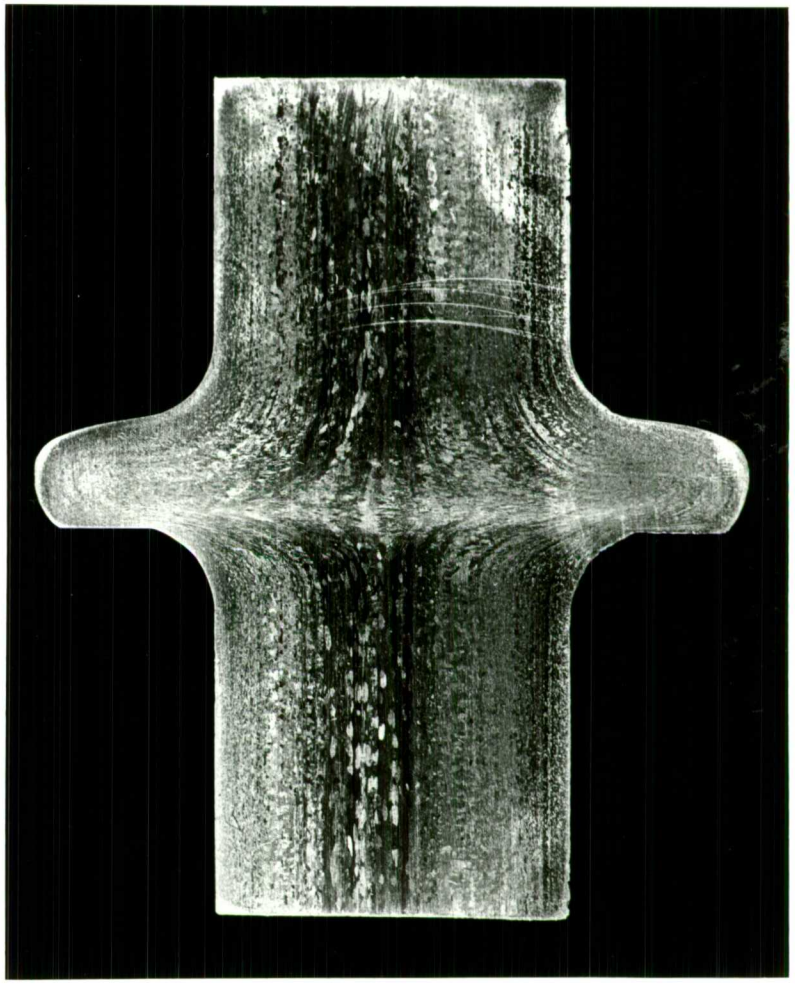
b) 10 mm

c) 14 mm

Fig. 3-56 Etched sections of aluminium hollow billets in injection upsetting with one end constrained for various flange thicknesses, t_f.



a) Simple injection upsetting



b) One end constrained

Fig. 3-57 Etched sections obtained in the injection upsetting of aluminium solid bars.

CHAPTER 4

THEORETICAL WORK

4.1 Finite element analysis

4.1.1 Basic finite element formulation

In many phases of engineering the solution of stress and strain distributions in continua is required. Special cases of such problems may range from two-dimensional plane stress or strain distributions, axi-symmetrical solids, plate bending, and shells to fully three-dimensional solids.

It is desirable to obtain the results in a general form applicable to any situation. In this section the general form of the equations are derived by applying the virtual work principle to a single element. Some basic difinitions which are used during the formulation are first given. It is also worthwhile to present some considerations regarding the notations to be used.

Incremental variables are characterised by the prefix 'd'. Vectors affected by the super-indices 'E','P' and 'EP' are referred to as elastic, plastic or elastic-plastic conditions, respectively. Finally, vectors associated with element nodal points are identified by subscript 'e'.

4.1.1.1 Displacement function

A typical finite element,e, is defined by nodes i,j,m, etc., and straight line boundaries (Fig. 4-1). The displacements at any point within the element can be expressed as a linear combination of the displacements at a finite number of nodal points in the same element, i.e. in matrix language:

$$\{f\}_e = [N]\ \{\delta\}_e = [N_i,\ N_j,\ N_m\ \ldots] \begin{Bmatrix} \delta_i \\ \delta_j \\ \delta_m \\ \vdots \\ \vdots \end{Bmatrix} \tag{4.1}$$

in which the components of $[N]$ are in general functions of position and $\{\delta\}_e$ represents nodal point displacements for a particular element. The function $[N]$ is referred to as the shape function. In a two-dimensional case, shown in Fig. 4-1, $\{f\}$ represents horizontal and vertical movements of a typical point within the element.

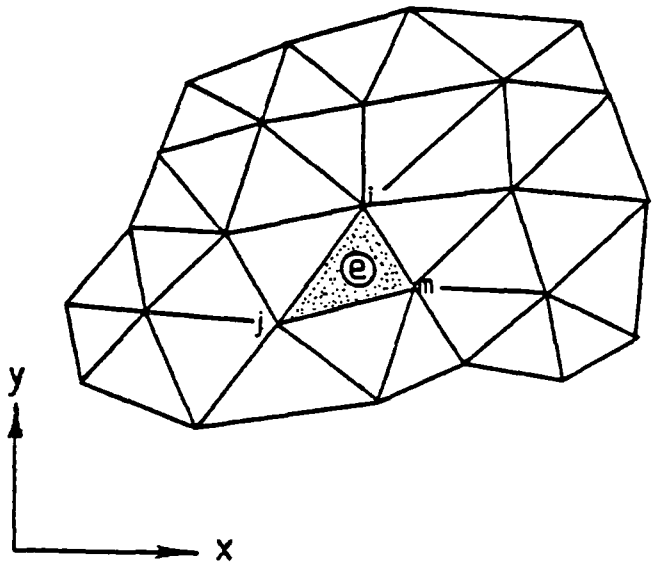


Fig.4-1 A two-dimensional solution domain divided into triangular elements.

4.1.1.2 Strains

With displacements known at all points within the element the strains at any point can be determined. These will always result in a relationship which can be written in matrix notation as

$$\{\varepsilon\} = [N]\ \{\delta\}_e \qquad (4.2)$$

The matrix $[N]$ is commonly called the strain-displacement matrix.

4.1.1.3 Stresses

In general, the material within the element boundaries may be subjected to initial strains such as may be due to temperature changes,

shrinkage, and so on. If such strains are denoted by $\{\varepsilon_0\}$ then the stresses will be caused by the difference between the actual and initial strains.

In addition it is convenient to assume that at the outset of analysis, the body is stressed by some known residual stresses $\{\sigma_0\}$. Assuming general elastic behaviour, the relationship between stresses and strains will be linear and of the form

$$\{\sigma\} = [D]^E (\{\varepsilon\}-\{\varepsilon_0\}) + \{\sigma_0\} \qquad (4.3)$$

where $[D]^E$ is an elasticity matrix containing the appropriate material properties.

4.1.1.4 Equivalent nodal forces

$$\{F\}_e = \begin{Bmatrix} F_i \\ F_j \\ F_m \\ \cdot \\ \cdot \\ \cdot \end{Bmatrix}$$

defines the nodal forces which are equivalent statically to the boundary stresses and distributed loads on the element. Each of the forces $\{F_i\}$ must contain the same number of components as the corresponding nodal displacement $\{\delta_i\}$ and be ordered in the appropriate, corresponding directions.

The distributed loads $\{Q\}$ are defined as those acting on a unit volume of material within the element with directions corresponding to those of the displacements $\{f\}$ at that point.

4.1.1.5 General formulation (equilibrium condition)

Whether the material behaviour is linear or non-linear, the equilibrium condition between internal and external forces has to be satisfied. To make the nodal forces statically equivalent to the actual boundary stresses and distributed loads, the simplest procedure is to impose an arbitrary (virtual) nodal displacement and to equate the external and internal work done by the various forces and stresses during that displacement. The virtual displacement at the nodes is denoted by $d\{\delta\}_e$. This results, by Eqs. (4.1) and (4.2) in displacement and strains within the element equal to:

$$d\{f\} = [N]\, d\{\delta\}_e \quad \text{and} \quad \{\varepsilon\} = [B]\, d\{\delta\}_e \tag{4.4}$$

respectively.

The work done by the nodal forces is equal to the sum of the products of the individual force components and corresponding displacements, i.e. in matrix language

$$(d\{\delta\}_e)^T \{F\}_e \tag{4.5}$$

Similarly, the internal work per unit volume done by the stresses and distributed forces is

$$d\{\varepsilon\}^T \{\sigma\} - d\{f\}^T \{Q\} \tag{4.6}$$

or

$$(d\{\delta\}_e)^T ([B]^T \{\sigma\} - [N]^T \{Q\}) \tag{4.7}$$

Equating the external work with the total internal work obtained by integrating over the volume of the element

$$(d\{\delta\}_e)^T\{F\}_e = (d\{\delta\}_e)^T(\int[B]^T\{\sigma\}\ d(vol) - \int[N]^T\{Q\}\ d(vol)) \tag{4.8}$$

As this relation is valid for any value of the virtual displacement, the equality for the multipliers must exist. On substitution of Eqs. (4.2) and (4.3), therefore

$$\{F\}_e = (\int[B]^T[D][B]\ d(vol))\{\delta\}_e - \int[B]^T[D]\{\varepsilon_o\}\ d(vol) + \int[B]^T\{\sigma_o\}\ d(vol) - \int[N]^T\{Q\}\ d(vol) \tag{4.9}$$

the stiffness matrix becomes

$$[K]_e = \int[B]^T[D][B]\ d(vol) \tag{4.10}$$

nodal forces due to distributed loads are

$$\{F\}_e^Q = -\int[N]^T\{Q\}\ d(vol) \tag{4.11}$$

and those due to initial strains are

$$\{F\}_e^{\varepsilon_o} = -\int[B]^T[D]\{\varepsilon_o\}\ d(vol) \tag{4.12}$$

Due to initial stress present at the outset of the analysis nodal forces contributed are

$$\{F\}_e^{\sigma_o} = \int[B]^T\{\sigma_o\}\ d(vol) \tag{4.13}$$

4.1.2 Infinitesimal elastic-plastic formulation

Returning to the equilibrium condition established in the previous section, from Eq. (4.8)

$$\{F\}_e = \int [B]^T \{\sigma\}\, d(vol) - \int [N]^T \{Q\}\, d(vol)$$

Assuming that no distributed loads exist or, if any, they have been distributed appropriately between the nodal points, the equilibrium equation then reduces to

$$\{F\}_e = \int [B]^T \{\sigma\}\, d(vol) \tag{4.14}$$

As the plastic deformation is a path dependent phenomenon it is preferable to express the equilibrium equation in an incremental form. For small increments of load Eq. (4.14) can be written as

$$\begin{aligned}\{F\}_e + d\{F\}_e = {} & \int [B]^T \{\sigma\}\, d(vol) + \int [B]^T d\{\sigma\}\, d(vol) + \\ & \int d[B]^T \{\sigma\}\, d(vol) + \int d[B]^T d\{\sigma\}\, d(vol)\end{aligned} \tag{4.15}$$

The term $\int d[B]^T d\{\sigma\}\, d(vol)$ can be ignored in comparison with the other terms. For infinitesimal strains the change in the matrix $d[B]^T$ can also be ignored. Eq. (4.15) thus reduces to

$$\{F\}_e + d\{F\}_e = \int [B]^T \{\sigma\}\, d(vol) + \int [B]^T d\{\sigma\}\, d(vol) \tag{4.16}$$

Subtracting Eq. (4.14) from Eq. (4.16), the equilibrium equation can be obtained as

$$d\{F\}_e = \int [B]^T d\{\sigma\}\, d(vol) \tag{4.17}$$

To proceed further, the value of $d\{\sigma\}$ has to be expressed in terms of corresponding strain increments. An incremental relationship between stresses and strains will be given in section 4.1.2.2.

An equation similar to Eq. (4.17) can be obtained for the entire continuum by writing Eq. (4.17) for each element and assembling them together.

$$d\{F\} = \int [B]^T \, d\{\sigma\} \, d(vol) \tag{4.18}$$

Where $d\{F\}$ denotes the increment of loads at all the nodal points of the structure and the integral has to be taken over the entire continuum.

4.1.2.1 Plasticity relations

According to the Von-Mises criterion, yielding begins under any state of stress when the effective stress $\bar{\sigma}$ exceeds a certain limit, where

$$\bar{\sigma} = 1/\sqrt{2}((\sigma_x - \sigma_y)^2 + (\sigma_y - \sigma_z)^2 + (\sigma_z - \sigma_x)^2 + 6(\tau_{xy}^2 + \tau_{yz}^2 + \tau_{zx}^2))^{\frac{1}{2}} \tag{4.19}$$

An equivalent plastic strain increment $d\bar{\varepsilon}^p$ is defined as a combination of the separate plastic strain increments

$$d\bar{\varepsilon}^p = \sqrt{2}/3((d\varepsilon_x^p - d\varepsilon_y^p)^2 + (d\varepsilon_y^p - d\varepsilon_z^p)^2 + (d\varepsilon_z^p - d\varepsilon_x^p)^2 + 3/2(d\gamma_{xy}^p)^2 + 3/2(d\gamma_{yz}^p)^2 + 3/2(d\gamma_{xz}^p)^2)^{\frac{1}{2}} \tag{4.20}$$

The relation between effective stress and effective strain may be established by a uniaxial tension test and is shown in Fig. 4-2. Notation in the figure defines the elastic component of effective strain, $\bar{\varepsilon}^e$, and the relation between slope H' and elastic modulus E and tangent modulus E_T.

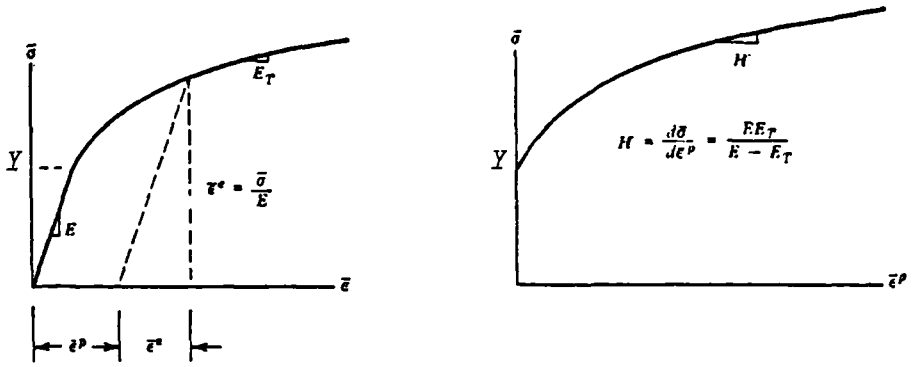


Fig. 4-2 Effective stress-effective strain relations.

Yielding first begins when $\bar{\sigma}$ exceeds Y in Fig. 4-2(a). As $\bar{\varepsilon}^p$ grows, the value of $\bar{\sigma}$ which must be exceeded to produce further yield also grows, this being due to the strain hardening characteristic of the material. If unloading occurs it is assumed that yielding resumes only when $\bar{\sigma}$ exceeds its previous maximum value. This is the assumption of isotropic hardening and ignores the Bauschinger effect.

Both sides of Eq. (4.19) are differentiated and when deviatoric stress

$$\sigma_x' = \sigma_x - \frac{\sigma_x + \sigma_y + \sigma_z}{3} = 1/3(2\sigma_x - \sigma_y - \sigma_z), \text{ etc.} \tag{4.21}$$

are substituted, Eq. (4.22) is obtained

$$d\bar{\sigma} = \{\frac{\partial\bar{\sigma}}{\partial\sigma}\}^T\{d\sigma_x\ d\sigma_y\ d\sigma_z\ d\tau_{xy}\ d\tau_{yz}\ d\tau_{zx}\} = \{\frac{\partial\bar{\sigma}}{\partial\sigma}\}^T d\{\sigma\} \tag{4.22}$$

where

$$\{\frac{\partial\bar{\sigma}}{\partial\sigma}\} = \{\frac{3\sigma_x}{2\bar{\sigma}}\ \frac{3\sigma_y}{2\bar{\sigma}}\ \frac{3\sigma_z}{2\bar{\sigma}}\ \frac{3\tau_{xy}}{\bar{\sigma}}\ \frac{3\tau_{yz}}{\bar{\sigma}}\ \frac{3\tau_{zx}}{\bar{\sigma}}\} \tag{4.23}$$

The Prandtl-Reuss relations state that

$$\{d\varepsilon^p\} = \{d\varepsilon_x^p \; d\varepsilon_y^p \; d\varepsilon_z^p \; d\gamma_{xy}^p \; d\gamma_{yz}^p \; d\gamma_{zx}^p\} = \{\frac{\partial\bar{\sigma}}{\partial\sigma}\}d\bar{\varepsilon}^p \tag{4.24}$$

The latter equation defines the six plastic strain increments that result when the effective plastic strain increment $d\bar{\varepsilon}^p$ occurs under a known state of stress.

A strain increment $\{d\varepsilon\}$ is the sum of its elastic component $d\{\varepsilon^e\}$ and its plastic component $d\{\varepsilon^p\}$. Hence, from Hook's law,

$$d\{\sigma\} = [D]^E \, d\{\varepsilon^e\} = [D]^E(d\{\varepsilon\} - d\{\varepsilon^p\}) \tag{4.25}$$

where $[D]^E$ is the conventional matrix of elastic constants. A relationship that yields $d\bar{\varepsilon}^p$ from the total strain increment $\{d\varepsilon\}$ is obtained as follows. Substitute Eq. (4.24) into Eq. (4.25) then premultiply both sides by $\{\partial\bar{\sigma}/\partial\sigma\}^T$. Using figure 4-2 and Eq. (4.22) yields $\{\partial\bar{\sigma}/\partial\sigma\}^T \, d\{\sigma\} = H' \, d\varepsilon^p$, which upon substitution into the results obtained in the previous step, Eq. (4.26) is obtained.

$$d\bar{\varepsilon}^p = \frac{\{\partial\bar{\sigma}/\partial\sigma\}^T \, [D]^E}{H' + \{\partial\bar{\sigma}/\partial\sigma\}^T \, [D]^E\{\partial\bar{\sigma}/\partial\sigma\}} \, d\{\varepsilon\} = [W] \, d\{\varepsilon\} \tag{4.26}$$

4.1.2.2 Derivation of elastic-plastic stress-strain matrix

An incremental stress-strain relationship analogous to Hook's law but valid beyond the proportional limit, can be obtained by substitution of Eq. (4.26) into Eq. (4.24) and the result into Eq. (4.25)

$$\begin{aligned} d\{\sigma\} &= ([D]^E - [D]^E\{\partial\bar{\sigma}/\partial\sigma\}[W]) \, d\{\varepsilon\} = ([D]^E - [D]^P)d\{\varepsilon\} \\ &= [D]^{EP} \, d\{\varepsilon\} \end{aligned} \tag{4.27}$$

Examination of the matrices involved shows that the plastic stress matrix $[D]^P$ and hence the elastic-plastic matrix $[D]^{EP}$ are both symmetric. Explicitly $[D]^P$ is given by:

$$[D]^P = \frac{E}{1+\nu}\begin{bmatrix}
\frac{\sigma'^2_x}{s} & & & & & \\
\frac{\sigma'_x\sigma'_y}{s} & \frac{\sigma'^2_y}{s} & & & & \\
\frac{\sigma'_x\sigma'_z}{s} & \frac{\sigma'_y\sigma'_z}{s} & \frac{\sigma'^2_z}{s} & & & \\
\frac{\sigma'_x\tau_{xy}}{s} & \frac{\sigma'_y\tau_{xy}}{s} & \frac{\sigma'_z\tau_{xy}}{s} & \frac{\tau^2_{xy}}{s} & & \\
\frac{\sigma'_x\tau_{yz}}{s} & \frac{\sigma'_y\tau_{yz}}{s} & \frac{\sigma'_z\tau_{yz}}{s} & \frac{\tau_{xy}\tau_{yz}}{s} & \frac{\tau^2_{yz}}{s} & \\
\frac{\sigma'_x\tau_{zx}}{s} & \frac{\sigma'_y\tau_{zx}}{s} & \frac{\sigma'_z\tau_{zx}}{s} & \frac{\tau_{xy}\tau_{zx}}{s} & \frac{\tau_{xy}\tau_{zx}}{s} & \frac{\tau^2_{zx}}{s}
\end{bmatrix} \quad \text{symmetric} \qquad (4.28)$$

in which $s = \frac{2}{3}\bar{\sigma}^2(1 + \frac{H}{3G})$.

Clearly, matrix $[D]^{EP}$ is given by

$$[D]^{EP} = \frac{E}{1+\nu}\begin{bmatrix} \frac{1-\nu}{1-2\nu} - \frac{\sigma'^2_x}{s} & & & & & \\ \frac{\nu}{1-2\nu} - \frac{\sigma'_x\sigma'_y}{s} & \cdot & \frac{1-\nu}{1-2\nu} - \frac{\sigma'^2_y}{s} & & & \\ \frac{\nu}{1-2\nu} - \frac{\sigma'_x\sigma'_z}{s} & \cdot & \frac{\nu}{1-2\nu} - \frac{\sigma'_y\sigma'_z}{s} & \cdot & \frac{1-\nu}{1-2\nu} - \frac{\sigma'^2_z}{s} & \\ -\frac{\sigma'_x\tau_{xy}}{s} & \cdot & -\frac{\sigma'_y\tau_{xy}}{s} & \cdot & -\frac{\sigma'_z\tau_{xy}}{s} & \cdot \frac{1}{2} - \frac{\tau^2_{xy}}{s} \\ -\frac{\sigma'_x\tau_{yz}}{s} & \cdot & -\frac{\sigma'_y\tau_{yz}}{s} & \cdot & -\frac{\sigma'_z\tau_{yz}}{s} & \cdot -\frac{\tau_{xy}\tau_{yz}}{s} \cdot \frac{1}{2} - \frac{\tau^2_{yz}}{s} \\ -\frac{\sigma'_x\tau_{zx}}{s} & \cdot & -\frac{\sigma'_y\tau_{zx}}{s} & \cdot & -\frac{\sigma'_z\tau_{zx}}{s} & \cdot -\frac{\tau_{xy}\tau_{zx}}{s} \cdot -\frac{\tau_{xy}\tau_{zx}}{s} \cdot \frac{1}{2} - \frac{\tau^2_{zx}}{s} \end{bmatrix} \quad \text{symmetric} \qquad (4.29)$$

Equation (4.27) corresponds to the inverse of the complete stress-strain relations of Prandtl-Reuss. The original stress-strain relations have been reduced to a single equation (4.27), and it must be emphasized that the elastic compressibility as well as the strain-hardening characteristics of the material are incorporated in the matrix $[D]^{EP}$. Comparing $[D]^{EP}$ with $[D]^{E}$, it can be seen that the diagonal elements of $[D]^{EP}$ are definitely less than the corresponding diagonal elements of $[D]^{E}$. This amounts to an apparent decrease of rigidity due to plastic yielding. Eqs. (4.26) and (4.27) are both valid for elastic-perfectly plastic materials, as nothing in the derivation becomes indefinite if $H' = 0$.

4.1.2.3 Derivation of elastic-plastic element stiffness matrix $[K]^{EP}$

On substituting the incremental stress-strain relationship, Eq. (4.27), and the incremental strain-displacement relationship, Eq. (4.4) into Eq. (4.17), Eq. (4.30) results.

$$d\{F\}_e = (\int [B]^T [D]^{EP} [B] \, d(vol)) \, d\{\delta\}_e \tag{4.30}$$

The elastic-plastic element stiffness matrix becomes

$$[K]_e^{EP} = \int [B]^T [D]^{EP} [B] \, d(vol)$$

This is similar to the elastic element stiffness matrix except for the use of $[D]^{EP}$ instead of $[D]^{E}$. The value of $[D]^{EP}$ is calculated from Eq. (4.29).

By writing Eq. (4.30) for every single element and assembling them together Eq. (4.31) applicable to the entire continuum will be obtained.

$$d\{F\} = (\int [B]^T [D]^{EP} [B] \, d(vol)) \, d\{\delta\} = [K]^{EP} \, d\{\delta\} \tag{4.31}$$

The term $[K]^{EP}$ is called the overall stiffness matrix or tangent stiffness matrix of the structure, the integral is taken over the entire continuum.

4.1.3 Elastic-plastic method of solution

In order to obtain the final solution to an elastic-plastic problem, equilibrium conditions between internal and external forces of the continuum have to be satisfied. This is given by

$$d\{F\} = \int [B]^T \, d\{\sigma\} \, d(vol) \tag{4.18}$$

The equation is in an incremental form and is valid only for infinitesimal strains. The complete solution to an elastic-plastic problem has to be carried out in a step-by-step method.

The value of $d\{\sigma\}$ may be obtained from any of the following relations:

$$d\{\sigma\} = [D]^{EP} \, d\{\varepsilon\} \tag{4.32}$$

$$d\{\sigma\} = [D]^{E}(d\{\varepsilon\} - d\{\varepsilon^P\}) \tag{4.33}$$

$$d\{\sigma\} = d\{\sigma\}^E - d\{\sigma\}^P \tag{4.34}$$

Depending on how the value of $d\{\sigma\}$ is substituted in Eq. (4.18) different approaches of solution will be obtained.

4.1.3.1 Tangential stiffness method

Substituting the stress increment $d\{\sigma\}$ from Eq. (4.32) into the equilibrium Eq. (4.18), leads to Eq. (4.31) which was derived in section 4.1.2.3.

$$d\{F\} = [K]^{EP} \, d\{\delta\} \tag{4.31}$$

Where $[K]^{EP}$ depends on the current state of stresses within the elements.

By applying load in increments and following the plastic action as it develops, one may properly account for the path-dependent nature of plasticity. In each load increment the value of $[K]^{EP}$ can be assumed constant and is built according to the state of stresses within the elements prior to load increments. By knowing the value of $[K]^{EP}$ and load increments the nodal point displacements can be determined.

A typical step of the solution is described with the aid of Fig. 4-3 which is a single degree of freedom problem.

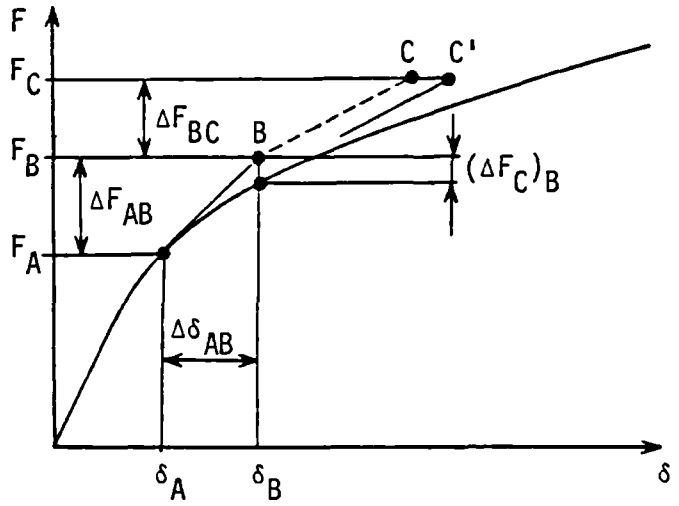


Fig. 4-3 Load versus displacement

If under loads $\{F\}_A$, the correct displacement $\{\delta\}_A$ and structure tangent stiffness matrix $[K]_A^{EP}$ are known, the displacements produced by the next load increment are computed as:

$$[K]_A^{EP}\,\Delta\{\delta\}_{AB} = \Delta\{F\}_{AB} = \{F\}_B - \{F\}_A \tag{4.35}$$

$$\{\delta\}_B = \{\delta\}_A + \Delta\{\delta\}_{AB}$$

Stresses, strains and tangent stiffness matrix must now be updated. Displacements $d\{\delta\}_e$ of an element are extracted from $\{\delta\}_{AB}$. Then for each sampling point within the element (for the centroid in the case of triangular elements), increments of strain and stress are calculated by the use of equations

$$d\{\varepsilon\} = [B]\, d\{\delta\}_e \qquad \text{from Eq. (4.2)}$$

$$d\bar{\varepsilon}^p = [W]_A\, d\{\varepsilon\} \qquad \text{from Eq. (4.26)}$$

$$d\{\varepsilon^p\} = \{\underline{\underline{\sigma}}\}\, d\bar{\varepsilon}^p \qquad \text{from Eq. (4.24)}$$

$$d\{\sigma\} = [D]^E\,(d\{\varepsilon\} - d\{\varepsilon^p\}) \qquad \text{from Eq. (4.25)}$$

For elastic elements $d\bar{\varepsilon}^p$ must be set equal to zero. Using the appropriate relationship for $[D]^{EP}$, the stiffness matrix for a yielded element is evaluated in the usual way:

$$[K]_e^{EP} = \int_{\text{Element volume}} [B]^T\, [D]^{EP}\, [B]\, d(vol)$$

For elastic elements $[D]^{EP}$ must be replaced by $[D]^E$ before the integration is carried out. Finally, elements are assembled in the usual way. Thus the current structure stiffness matrix is produced, and another load increment $d\{F\}_{BC}$ is applied.

During loading some of the elements may experience unloading, this is indicated by a negative $d\bar{\varepsilon}^p$ obtained from Eq. (4.26). For an unloaded element, $d\bar{\varepsilon}^p$ is set to zero and in the next load increment the stiffness matrix is based on elastic modulus $[D]^E$ instead of on $[D]^{EP}$. If isotropic hardening is assumed, plastic action is resumed only when the effective stress exceeds its previous magnitude.

In the procedure outlined, increments of load were denoted by

$d\{F\}$ emphasizing small increments to be employed. However, if larger increments are used a progressive drift from the actual response becomes unavoidable. Upon reaching B in Fig. 4-3, the computed displacement $\{\delta\}_B$ is smaller than the actual amount of displacement, hence the resulting stresses will be smaller than the amount required to resist the applied load F_B. If a corrective load $d\{F\}_C$ were added to the previous load increment, the computed displacement $\{\delta\}_B$ would be larger and closer to the correct value. Load ΔF_C plays the role of an unbalanced force which is the difference between applied loads and resistance produced by distorted elements. This resistance is evaluated from the term $\{\sigma_o\}$ of Eq. (4.13) with $\{\sigma_o\}$ now regarded as the total accumulated stress $\{\sigma\}$ in the element. Therefore, in general

$$\{\Delta F_C\} = \{F\} - \Sigma\int [B]^T \{\delta\}\, d(vol)$$

Correction load $d\{F\}_C$ is then applied in the subsequent step. For instance, the equation for the next step from point B is (see Fig. 4-3)

$$d\{F\}_{BC} + d\{F\}_C = [K]_B^{EP}\, d\{\delta\}_{BC'}$$

In this way the point C' will be obtained instead of point C which is closer to the real solution. If the correction load is not considered, the final answer drifts from the actual curve as the load increment increases. The drift can be minimized by making the load increments as small as possible.

4.1.3.2 Initial strain method

Substituting the stress increment $d\{\sigma\}$ from Eq. (4.33) into the equilibrium Eq. (4.17), leads to

$$d\{F\}_e = \int [B]^T [D]^E (d\{\varepsilon\} - d\{\varepsilon^p\})\, d(vol)$$

$$\therefore d\{F\}_e = \int [B]^T [D]^E\, d\{\varepsilon\}\, d(vol) - \int [B]^T [D]^E\, d\{\varepsilon^p\}\, d(vol) \qquad (4.36)$$

or in a compact form

$$d\{F\}_e = [K]_e^E\, d\{\delta\}_e - d\{M\}_e \quad \text{or} \quad [K]_e^E\, d\{\delta\}_e = d\{F\}_e + d\{M\}_e \qquad (4.37)$$

where $[K]_e^E = \int [B]^T [D]^E [B]\, d(vol)$ and $d\{M\}_e = \int [B]^T [D]^E\, d\{\varepsilon^p\}\, d(vol)$ (4.38)

To obtain the overall stiffness matrix of the whole body, stiffness matrices of the elements, based on elastic matrix $[D]^E$, are calculated and assembled. This leads to an equation similar to Eq. (4.37), thus

$$[K]^E\, d\{\delta\} = d\{F\} + d\{M\} \qquad (4.39)$$

In the solution technique using the above formulation $d\{M\}$ acts as a correction load which serves to return drifting values to the proper path. It is not essential to find the tangent stiffness matrix within a step of load, and the original elastic structure stiffness matrix may be used in all loading steps. This approach of solution is called initial strain method. The increments of plastic strains $d\{\varepsilon^p\}$ may be expressed in terms of $d\{\sigma\}$ by using Eqs. (4.22) and (4.24), thus

$$d\{\varepsilon^p\} = \{\frac{\partial \bar{\sigma}}{\partial \sigma}\}\, d\bar{\varepsilon}^p = \frac{1}{H'} \{\frac{\partial \bar{\sigma}}{\partial \sigma}\}\, \{\frac{\partial \bar{\sigma}}{\partial \sigma}\}^T\, d\{\sigma\} \qquad (4.40)$$

Clearly, solution of Eq. (4.40) is impossible if the material is assumed elastic perfectly plastic (i.e. $H' = 0$).

$d\{M\}$ in Eq. (4.39) can be evaluated in a load step by employing an iteration process. The basic steps in this method are:

1) Assume the stress increments $d\{\sigma\}$
2) Calculate $d\{\varepsilon^P\}$ from Eq. (4.40)
3) Compute $d\{M\}$ from Eq. (4.38)
4) Compute $d\{\delta\}$ from Eq. (4.39)
5) Calculate total strain increment $d\{\varepsilon\}$ from Eq. (4.4)
6) Calculate stress increment $d\{\sigma\} = [D]^{EP}\, d\{\varepsilon\}$
7) Repeat steps (2) to (6) until required accuracy is obtained.

This method of solution is not likely to be as costly as the tangential stiffness method since $[K]^E$ is not subsequently updated. However, as the yielding of the material increases the number of iterations required are expected to increase rapidly.

4.1.3.3 Initial stress method

Due to the initial strain method not being applicable to ideally elastic-plastic material an alternative method called "initial stress method" was introduced by Zienkiewicz, Valliapan and King *(53)*. Here $d\{\sigma\}$ is obtained from Eq. (4.34) and then substituted into the equilibrium Eq. (4.17), thus

$$d\{F\}_e = \int [B]^T \left(d\{\sigma\}^E - d\{\sigma\}^P\right) d(vol)$$

where $d\{\sigma\}^E = [D]^E\, d\{\varepsilon\}$ and $d\{\sigma\}^P = [D]^P\, d\{\varepsilon\}$ (4.41)

therefore

$$d\{F\}_e = \left(\int [B]^T [D]^E [B]\, d(vol)\right) d\{\delta\}_e - \int [B]^T\, d\{\sigma\}^P\, d(vol)$$

or $d\{F\}_e = [K]_e^E \, d\{\delta\}_e - d\{M\}_e$

in which $d\{M\}_e = \int [B]^T \, d\{\sigma\}^P \, d(vol)$ (4.42)

and for the entire continuum:

$$d\{F\} = [K]^E \, d\{\delta\} - d\{M\} \quad \text{or} \quad [K]^E \, d\{\delta\} = d\{F\} + d\{M\} \tag{4.43}$$

thus

$$\left[[K]^E\right]^{-1} (d\{F\} + d\{M\}) = d\{\delta\} \tag{4.44}$$

To solve Eq. (4.44) an iterative method is required. The following sequence is followed:

The iteration cycle is started with the stresses known as $\{\sigma_o\}$.

1) Assume $d\{M\}_o = 0$ and from Eq. (4.44) calculate the first displacement matrix $d\{\delta\}_o$ as given by

$$d\{\delta\}_o = \left[[K]^E\right]^{-1} d\{F\}$$

2) Using Eq. (4.4) calculate $d\{\varepsilon\}_o$

3) Calculate $d\{\sigma\}_o^E = [D]^E \, d\{\varepsilon\}_o$, $d\{\sigma\}_o^P = [D]^P \, d\{\varepsilon\}_o$ and therefore $d\{\sigma\}_o = d\{\sigma\}_o^E - d\{\sigma\}_o^P$. Find the total stress

$$\{\sigma\}_1 = \{\sigma\}_o + d\{\sigma\}_o$$

4) Knowing the $d\{\sigma\}_o^P$ calculate $d\{M\}_1$ from Eq. (4.42)

5) From Eq. (4.44), using the new value of $d\{M\}_1$ calculate the new value for $d\{\delta\}$.

6) Steps (2) to (5) are repeated until the required accuracy is obtained.

The difference between the initial stress and initial strain approaches is perhaps best illustrated diagrammatically. In Fig. 4-4 the stress-strain level reached by the first solution is shown as point 1. In the initial stress process the stresses are brought down to the correct level by introducing an initial stress $d\{\sigma_0\}$ while with the initial strain process the strains are adjusted by a correction $d\{\varepsilon_0\}$.

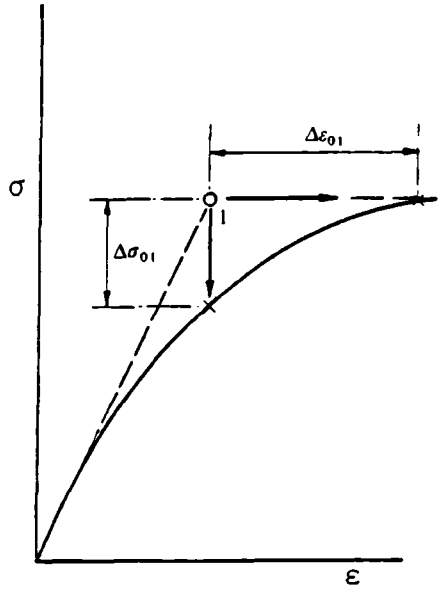


Fig. 4-4 Initial strain and initial stress methods.

The 'initial stress' method converges rapidly only when non-linearity is mild thus making a tangent modulus method preferable when large areas have yielded.

4.1.4 Elements used in computer programs

Two types of ring elements were used in discretizing a deforming continuum under axi-symmetric conditions each type being implemented in a computer program. The types of elements implemented were: constant strain triangle, and quadrilateral (built up from four triangles). In the following section the required definitions and calculations for triangular ring elements will be given.

4.1.4.1 Constant strain triangle elements

Meshes of triangular elements are widely used, owing perhaps to their simplicity and early widespread adoption. A typical ring triangular element of an axi-symmetric solid is shown in Fig. (4-5(a)). r and z denote respectively the radial and axial co-ordinates of a point, with u and v being the corresponding displacements. A diametrically cross-sectioned element is shown in Fig. (4-5(b)), with nodes i, j and m numbered in an anti-clockwise order.

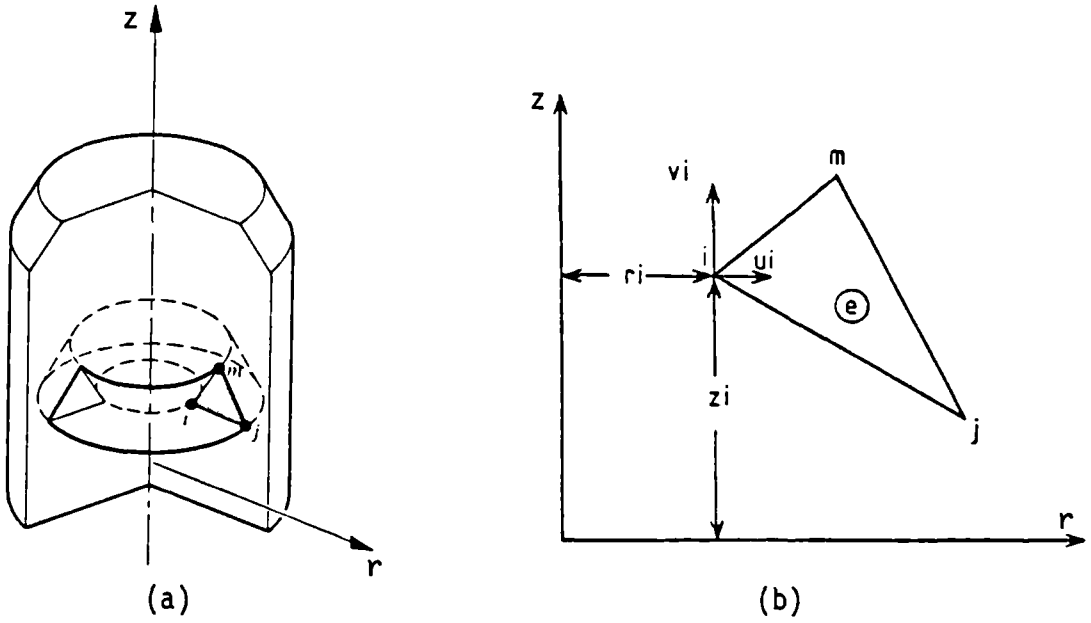


Fig. 4-5 A typical ring triangular element of an axi-symmetric solid.

The two displacement components may be written as:

$$\{\delta_i\} = \begin{Bmatrix} u_i \\ v_i \end{Bmatrix} \tag{4-45}$$

The six components of element displacement are listed as a vector

$$\{\delta\}_e = \begin{Bmatrix} \delta_i \\ \delta_j \\ \delta_m \end{Bmatrix} \tag{4.46}$$

The displacements within the element are uniquely defined by a linear shape function of the form

$$\{f\} = [N]\ \{\delta\}_e \tag{4.47}$$

where the shape function is usually expressed as

$$[N] = [IN_i\ ,\ IN_j\ ,\ IN_m]$$

in which I is a two-by-two identity matrix and

$$N_i = (a_i + b_i r + c_i z) \tag{4.48}$$

a_i, b_i and c_i are determined by inserting the nodal coordinates and the corresponding nodal displacements into Eq. (4.47).

In the case of an axi-symmetric problem four components of strain must be considered. Fig. 4-6 illustrates these strains and the associated stresses.

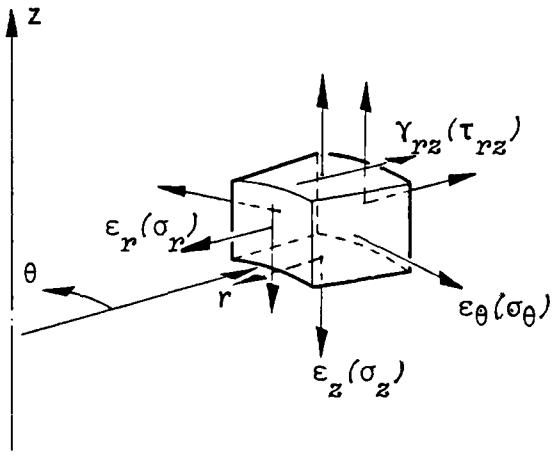


Fig. 4-6 Strains and stresses involved in the analysis of axi-symmetric solid.

The strain components are listed below in terms of the displacement of a point.

$$\{\varepsilon\} = \begin{Bmatrix} \varepsilon_r \\ \varepsilon_z \\ \varepsilon_\theta \\ \gamma_{rz} \end{Bmatrix} = \begin{Bmatrix} \dfrac{\partial u}{\partial r} \\ \dfrac{\partial v}{\partial z} \\ \dfrac{u}{v} \\ \dfrac{\partial u}{\partial z} + \dfrac{\partial v}{\partial r} \end{Bmatrix} \tag{4.49}$$

Using the displacement functions defined by Eq. (4.48)

$$\{\varepsilon\} = [B]\ \{\delta\}_e = [B_i\ ,\ B_j\ ,\ B_m]\ \{\delta\}_e$$

in which

$$[B_i] = \begin{bmatrix} \dfrac{\partial N_i}{\partial r} & 0 \\ 0 & \dfrac{\partial N_i}{\partial z} \\ \dfrac{N_i}{r} & 0 \\ \dfrac{\partial N_i}{\partial z} & \dfrac{\partial N_i}{\partial r} \end{bmatrix} = \frac{1}{2\Delta} \begin{bmatrix} 0 & a_i \\ b_i & 0 \\ \dfrac{a_i}{r} + b_i + \dfrac{c_i z}{r} & 0 \\ a_i & b_i \end{bmatrix} \text{ etc.} \tag{4.50}$$

The element stiffness matrix can be computed according to the following equation.

$$[K] = 2\pi \int [B]^T\ [D]\ [B]\ r\ dr\ dz \tag{4.51}$$

in which, $[D]$ may take either $[D]^E$ or $[D]^{EP}$, depending on the state of material. The volume integral has to be taken over the whole body of revolution indicated on Fig. 4-5(a).

As the matrix $[B]$ depends on the co-ordinates the integral has to be evaluated either by numerical integration or by an explicit multiplication and term by term integration. The simplest approximate procedure, in the case of triangular elements, is to evaluate $[B]$ for a centroidal point.

$$\bar{r} = (r_i + r_j + r_m)/3$$

$$\bar{z} = (z_i + z_j + z_m)/3$$

Then the element stiffness matrix can be approximated by

$$[K]^E = 2\pi[\bar{B}]^T[D]^E[\bar{B}]\ \bar{r}\ \Delta \qquad \text{for elastic elements}$$

$$[K]^{EP} = 2\pi[\bar{B}]^T[D]^{EP}[\bar{B}]\ \bar{r}\ \Delta \qquad \text{for plastic elements}$$

$[\bar{B}]$ indicates the value of $[B]$ at $r = \bar{r}$ and $z = \bar{z}$ with Δ being the area of a triangular element.

For axi-symmetric ring elements matrices $[D]^E$ and $[D]^{EP}$ reduce to (from Eqs. (4.28) and (4.29) respectively):

$$[D]^E = \frac{E(1-\nu)}{(1+\nu)(1-2\nu)} \begin{bmatrix} 1 & \frac{\nu}{1-\nu} & \frac{\nu}{1-\nu} & 0 \\ & 1 & \frac{\nu}{1-\nu} & 0 \\ & & 1 & 0 \\ \text{Symmetric} & & & \frac{1-2\nu}{2(1-\nu)} \end{bmatrix} \tag{4.52}$$

$$d\tau_{z\theta} = d\tau_{\theta r} = d\gamma_{z\theta} = d\gamma_{\theta r} = 0$$

in Eq. (4.29), so

$$[D^{ep}] = \frac{E}{1-\nu}\begin{bmatrix} \frac{1-\nu}{1-2\nu} - \frac{\sigma_r'^2}{s} & & & \textit{Symmetric} \\ \frac{\nu}{1-2\nu} - \frac{\sigma_r'\sigma_z'}{s} & \frac{1-\nu}{1-2\nu} - \frac{\sigma_z'^2}{s} & & \\ \frac{\nu}{1-2\nu} - \frac{\sigma_r'\sigma_\theta'}{s} & \frac{\nu}{1-2\nu} - \frac{\sigma_z'\sigma_\theta'}{s} & \frac{1-\nu}{1-2\nu} - \frac{\sigma_\theta'^2}{s} & \\ -\frac{\sigma_r'\tau_{rz}}{s} & -\frac{\sigma_z'\tau_{rz}}{s} & -\frac{\sigma_\theta'\tau_{rz}}{s} & \frac{1}{2} - \frac{\tau_{rz}^2}{s} \end{bmatrix} \tag{4.53}$$

4.1.4.2 Quadrilateral elements (consisting of four constant strain triangles)

Four constant strain triangles can be combined in such a way as to produce a quadrilateral element. In this way, accuracy and versatility can be improved since an additional degree of freedom for the combined element is introduced. This degree of freedom may be introduced to correct a specific defect of an element, or it may merely serve to improve accuracy by virtue of adding more terms to the assumed displacement field.

It is often convenient to use quadrilateral elements of arbitrary shape. Input data to the program consists of quadrilateral elements and the computer program automatically divides the elements into component triangular elements and properly assembles the stiffness of component triangles. In effect, usually the internal node is assigned co-ordinates (Fig. 4-7)

$$r_5 = \frac{r_1 + r_2 + r_3 + r_4}{4} \quad , \quad z_5 = \frac{z_1 + z_2 + z_3 + z_4}{4}$$

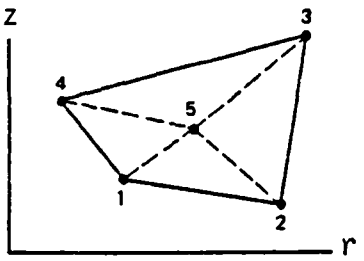


Fig. 4-7 A quadrilateral element consisting of four constant-strain triangles.

The stiffness matrix of a quadrilateral is 10 by 10. It is both convenient and efficient to eliminate the two internal degrees of freedom before assembling the elements. The element stiffness matrix is thus reduced to size 8 by 8. This process is called condensation and is performed before the solution of the complete system of equations on the elemental level prior to assembly. The condensation process is widely used,

and in some elements there may be several internal nodes to be eliminated. These nodes may appear anywhere in the nodal displacement array and may be eliminated in any order. However, the most common and easily described case is treated in the following, where all degrees of freedom to be eliminated are grouped at the end of the array.

The element stiffness equation is partitioned as follows:

$$\begin{bmatrix} K_{11} & K_{12} \\ K_{21} & K_{22} \end{bmatrix} \begin{Bmatrix} \delta_1 \\ \delta_2 \end{Bmatrix} = \begin{Bmatrix} F_1 \\ F_2 \end{Bmatrix} \tag{4.54}$$

in which $\{\delta_2\}$ represents the internal degrees of freedom to be eliminated. The right-hand side matrix represents loads applied to the element nodes. To eliminate the internal nodes, Eq. (4.54) is first solved for $\{\delta_2\}$ in terms of $\{\delta_1\}$

$$\{\delta_2\} = [K_{22}]^{-1} (\{F_2\} - [K_{21}] \{\delta_1\}) \tag{4.55}$$

Eq. (4.54) is then solved for $\{\delta_1\}$ and after substituting $\{\delta_2\}$, Eq. (4.56) results.

$$([K_{11}] - [K_{12}][K_{22}]^{-1}[K_{21}])\{\delta_1\} = \{F_1\} - [K_{21}][K_{22}]^{-1}\{F_2\} \tag{4.56}$$

The coefficient of $\{\delta_1\}$ is the element stiffness matrix of a quadrilateral. The stiffness matrices are assembled and structural equations solved in the usual way, thus determining $\{\delta_1\}$ for each element. As a final step in the solution of equations the internal degree of freedom may be found by application of Eq. (4.55) to each element.

It must be noted that condensation and solution of equations are

basically the same process. Both are processes in which unknowns are eliminated by substitution into the remaining equations. Indeed, if instead of using condensation the internal degrees of freedom were carried into the structural system of equations, exactly the same results would be obtained. However, if condensation is avoided, the array of structural equations becomes longer and has a larger bandwidth, and the numerical effort of solution can be expected to increase. The effort would be no greater if the structural equations were ordered so that all internal degrees of freedom are eliminated first, but this is exactly what is done by condensation before assembly of elements.

The value of stress of the quadrilateral element is obtained by evaluating the average value of four triangles. This way of stress calculation will result in a reasonably smooth field of stress as the triangles are of the same area.

4.2 Upper-bound analysis

4.2.1 Basic equations

4.2.1.1 Strain rates

The strain rates in cylindrical co-ordinates and the associated stresses are shown in Fig. 4.8. These strain rates as function of the velocity components ($\dot{u}_r$, $\dot{u}_\theta$ and $\dot{u}_z$) are:

$$\left.\begin{aligned}
&\dot{\varepsilon}_{rr} = \frac{\partial \dot{u}_r}{\partial r} \qquad \dot{\varepsilon}_{\theta\theta} = \frac{\dot{u}_r}{r} + \frac{1}{r}\frac{\partial \dot{u}_\theta}{\partial \theta} \qquad \dot{\varepsilon}_{zz} = \frac{\partial \dot{u}_z}{\partial z} \\
&\dot{\varepsilon}_{r\theta} = 1/2\ \left(\frac{1}{r}\frac{\partial \dot{u}_r}{\partial \theta} + \frac{\partial \dot{u}_\theta}{\partial r} - \frac{\dot{u}_\theta}{r}\right) \\
&\dot{\varepsilon}_{\theta z} = 1/2\ \left(\frac{\partial \dot{u}_\theta}{\partial z} + \frac{1}{r}\frac{\partial \dot{u}_z}{\partial \theta}\right) \\
&\dot{\varepsilon}_{zr} = 1/2\ \left(\frac{\partial \dot{u}_r}{\partial z} + \frac{\partial \dot{u}_z}{\partial r}\right)
\end{aligned}\right\} \qquad (4.57)$$

and the effective strain rate is:

$$\dot{\bar{\varepsilon}} = \sqrt{2/3}\ \left(\dot{\varepsilon}_{rr}^2 + \dot{\varepsilon}_{zz}^2 + \dot{\varepsilon}_{\theta\theta}^2 + 2\dot{\varepsilon}_{r\theta}^2 + 2\dot{\varepsilon}_{\theta z}^2 + 2\dot{\varepsilon}_{zr}^2\right)^{\frac{1}{2}} \qquad (4.58)$$

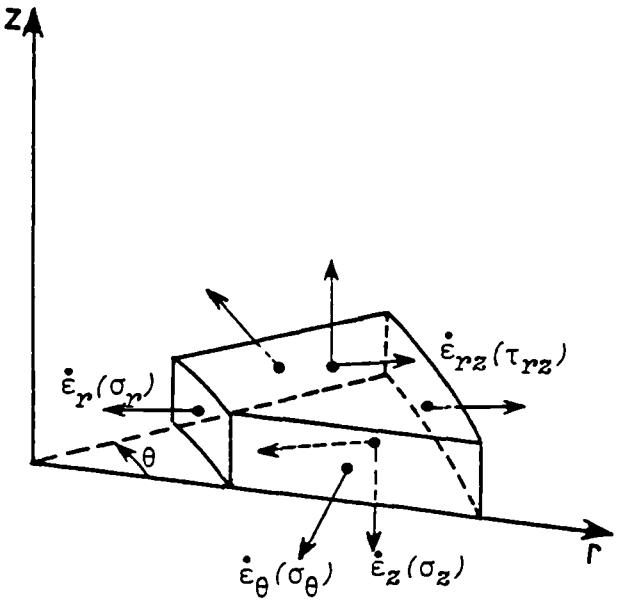


Fig. 4-8 Strain rates and the associated stresses in cylindrical coordinates.

4.2.1.2 Powers

In relation to the deformation process two different kinds of powers are identified: dissipative and active powers.

The sources of dissipation or consumption of energy for the workpiece are:

1 - Power dissipated due to continuous deformation of material in the plastic regions. The energy-dissipation rate in these regions can be calculated according to

$$\dot{E}_I = \int_{volume} \bar{\sigma}_o \, \dot{\bar{\varepsilon}} \, dV \tag{4.59}$$

where $\bar{\sigma}_o$ is the flow stress of the deforming material and $\dot{\bar{\varepsilon}}$ is the equivalent strain rate in the region. The integration must be performed over the total volume of deformation.

2 - Power dissipated on the surfaces of discontinuities. The energy-dissipation rate due to shear along these surfaces is expressed as:

$$\dot{E}_S = \int_{surface} k \, |\dot{V}_S| \, dS \tag{4.60}$$

where k is the yield shear stress and $\dot{V}_S$ denotes the rate of relative slip on a discontinuity surface, the velocity discontinuity. The integration is carried out over the whole surface of velocity discontinuity.

3 - Power dissipated due to friction at the material-tool interface. The energy-dissipation rate of this power may be expressed as:

$$\dot{E}_F = \int_{surface} \tau \, |\dot{V}| \, dS \tag{4.61}$$

where τ is the tangential stress developed at the tool-workpiece interface. τ may be defined as $\tau = mk$, where m is assumed to be a constant friction factor. $|\dot{V}|$ in equation (4.61) is the velocity discontinuity at the deforming material-tool interface.

The total power of deformation is therefore given by the sum of the three powers given by equations 4.59, 4.60 and 4.61, thus

$$\dot{W}_D = \dot{E}_I + \dot{E}_S + \dot{E}_F \tag{4.62}$$

The actual external work rate $\dot{W}_P$ is expressed by :

$$\dot{W}_P = P\ A\ |V_P| \tag{4.63}$$

where P is the punch pressure, A is the punch/billet contact area, and V_P is the punch velocity. The rate of the actual external work must equal the total value of dissipated energy given by Eq. 4.62.

$$\dot{W}_P = \dot{W}_D \tag{4.64}$$

After substituting Eq. (4.63) into Eq. (4.64) the mean punch pressure for an isotropic, non-work hardening material with flow stress of $\bar{\sigma}_o$ may be expressed non-dimensionally as follows:

$$\frac{P}{\bar{\sigma}_o} = \frac{\dot{W}_D}{A\ \bar{\sigma}_o |V_P|} \tag{4.65}$$

4.2.1.3 Continuity

Consider the section of a velocity discontinuity *AB*, Fig. 4-9, with the material moving from region 1 to region 2. $\dot{u}_{r1}$ and $\dot{u}_{z1}$ are velocity components of an element of material in the r and z direction in zone 1 just before crossing the boundary and $\dot{u}_{r2}$ and $\dot{u}_{z2}$ are corresponding the velocities in zone 2 just after crossing *AB*.

Continuity accross the boundary *AB* requires that the velocities normal to this boundary must be equal. This condition is expressed by:

$$\dot{u}_{r1} \sin\alpha + \dot{u}_{z1} \cos\alpha = \dot{u}_{r2} \sin\alpha + \dot{u}_{z2} \cos\alpha$$

$$\text{or} \quad (\dot{u}_{r1} - \dot{u}_{r2}) \tan\alpha = \dot{u}_{z2} - \dot{u}_{z1} \tag{4.66}$$

where α is the angle between the normal to the boundary and the z axis.

The components of velocity along the surface of a velocity discontinuity are usually different. The 'jump' in the tangential velocity in reality is not instantaneous across a line such as *AB* but changes occur in narrow bands.

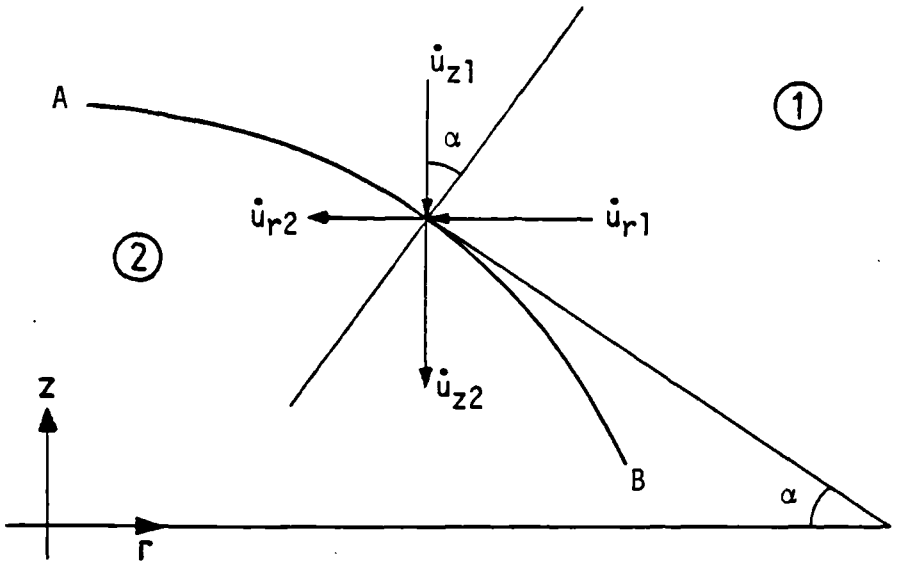


Fig. 4-9 Boundary of velocity discontinuity.

4.2.1.4 Incompressibility

A reasonable assumption in treating plastic forming processes is that the volume of the body remains constant. This will lead to the conclusion that the sum of the normal components of strain rates is zero, thus,

$$\dot{\varepsilon}_{rr} + \dot{\varepsilon}_{zz} + \dot{\varepsilon}_{\theta\theta} = 0 \tag{4.67}$$

4.2.2 Kinematically admissible velocity field for injection upsetting of hollow billets

In order to obtain an upper-bound solution for the axi-symmetric problem of injection upsetting of hollow billets, the first step is to assume a kinematically admissible pattern of deformation, that is, one satisfying the volume constancy requirement and the velocity boundary conditions. The workpiece may be partitioned into four distinct regions as shown in Fig. 4-10. Region 1 is the undeformed part of the billet, and is moving downwards as a rigid body at a punch velocity of unity, $\dot{u}_z = -1$. Region 3 is a zone of pure radial flow and region 4 is assumed to remain a dead metal zone during deformation.

To facilitate the analysis the radial velocity $\dot{u}_r$ in region 2 is considered to be independent of z, that is, in region 2 a right cylindrical surface concentric with the z axis deforms so as to remain as such. In annulus abc, Fig. 4-11, with the cylindrical surface of radius r the total metal flow passing the surface ab must be equal to that crossing the cylindrical surface bc. This results in:

$$(-1)\ (4r^2 - d_i^2)\pi/4 + \dot{u}_r\ 2\pi r\ \frac{t_f(2r - d_i)}{d_o - d_i} = 0$$

$$\text{or}\quad \dot{u}_r = (2r + d_i)(d_o - d_i)/8rt_f \tag{4.68}$$

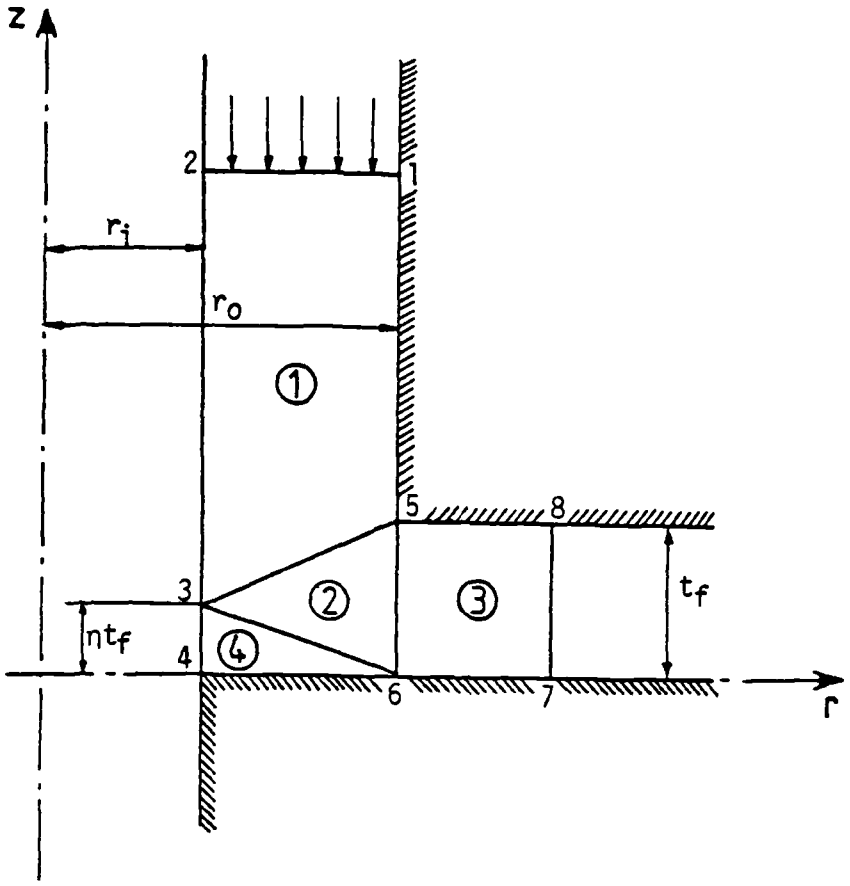


Fig. 4-10 Velocity field for simple injection upsetting of hollow billets.

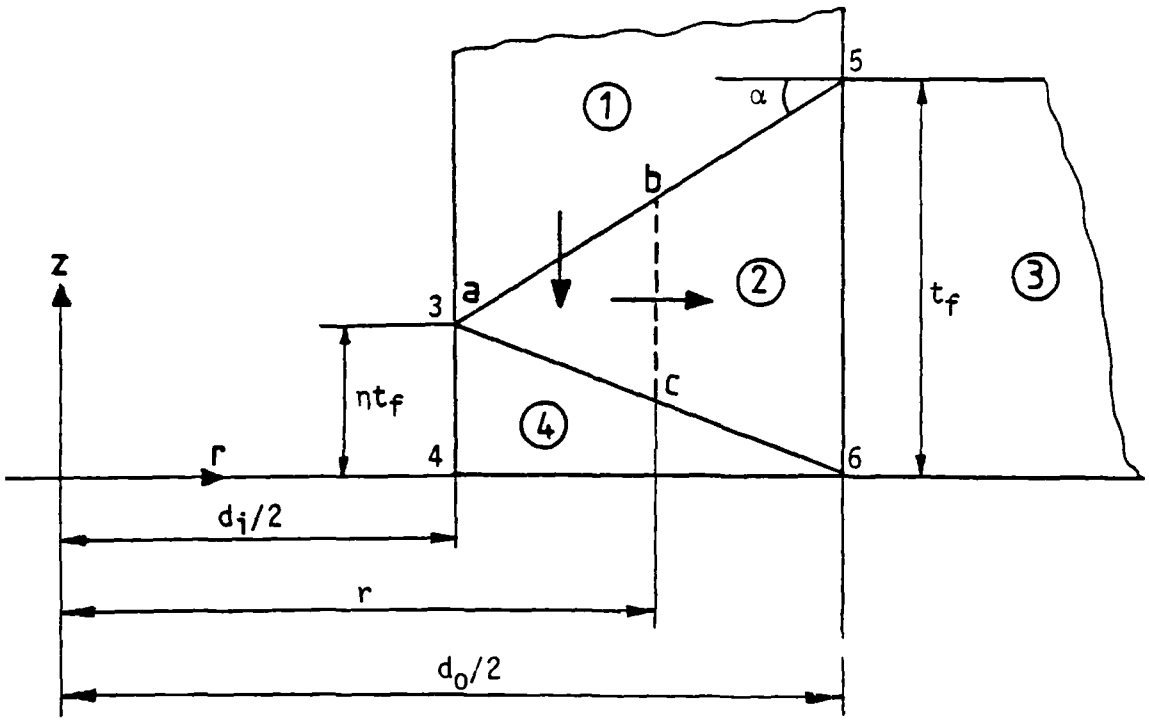


Fig. 4-11 Enlarged section of deforming regions of Fig. 6-2.

Because of axial symmetry, it is assumed that no rotation of the material occurs during deformation, so that the angular velocity component $\dot{u}_\theta$ is taken as zero. To evaluate the axial velocity component $\dot{u}_z$ in region 2 the assumption of incompressibility (Eq. 4.67) is used. Substituting Eqs. (4.57) into Eq. (4.67) results in:

$$\frac{\partial \dot{u}_r}{\partial r} + \frac{\partial \dot{u}_r}{r} + \frac{1}{r}\frac{\partial \dot{u}_\theta}{\partial \theta} + \frac{\partial \dot{u}_z}{\partial z} = 0$$

since $\dot{u}_\theta = 0$, thus

$$\frac{\partial \dot{u}_r}{\partial r} + \frac{\dot{u}_r}{r} + \frac{\partial \dot{u}_z}{\partial z} = 0 \qquad (4.69)$$

substituting $\dot{u}_r$ from Eq. (4.68) into Eq. (4.69), it follows that

$$\frac{\partial \dot{u}_z}{\partial z} = -\frac{d_o - d_i}{8t_f}\ \frac{2}{r}$$

Integrating leads to

$$\dot{u}_z = -\frac{d_o - d_i}{4t_f}\ \frac{1}{r}z + f(r) \qquad (4.70)$$

where $f(r)$ is a function of r only, which may be found from the condition of continuity at the 3-5 boundary. Substituting the components of velocity in region 1 ($\dot{u}_{r1} = 0$ and $\dot{u}_{z1} = 0$) and the radial velocity component in region 2, $\dot{u}_{r2}$, (from Eq. 4.68) into Eq. 4.66 (condition of continuity), it follows that

$$\dot{u}_{z2}\Big|_{at\ 3\text{-}5} = -1 + \frac{d_o - d_i}{8t_f}\ \frac{2r + d_i}{r}\ \tan\alpha$$

From Fig. 4-11, the following relations may be derived for the 3-5 boundary:

$$z_{35} = \frac{2(1-\eta)t_f\, r}{d_o - d_i} + \frac{(d_o\eta - d_i)t_f}{d_o - d_i} \quad , \quad \tan\alpha = \frac{2(1-\eta)t_f}{d_o - d_i} \tag{4.72}$$

where η is a non-dimensional arbitrary term which determines the position of the discontinuity surfaces, and its optimum value will be determined by minimizing the total energy. The axial component of velocity $\dot{u}_z$ at boundary 3-5 can be obtained by substituting $\tan\alpha$ from Eq.(4.72) into Eq. (4.73):

$$\dot{u}_{z2}\Big|_{at\ 3-5} = -1 + \frac{(2r + d_i)(1 - \eta)}{4r} \tag{4.73}$$

$f(r)$ in Eq. (4.70) may now be found by substituting the boundary conditions at discontinuity surface 3-5 (z_{35} from Eq. 4.72 and $\dot{u}_{z2}$ from Eq. 4.73) into Eq. 4.70. $f(r)$ is found to be:

$$f(r) = -\eta + \frac{d_o - d_i}{4r}\,\eta$$

substituting $f(r)$ into Eq. 4.70, it follows that

$$\dot{u}_z = -\frac{d_o - d_i}{4rt_f}\,(z - \eta t_f) - \eta \tag{4.74}$$

In region 3 the axial velocity component is zero since a purely radial flow is assumed to occur in this region. Flow continuity from region 1 to a cylindrical surface of radius r in region 3 requires that:

$$(-1)\ \pi/4\ (d_o^2 - d_i^2) = u_r\ 2\pi r t_f$$

i.e. in region 3 $$\dot{u}_r = \frac{d_o^2 - d_i^2}{8rt_f} \tag{4.75}$$

continuity across the 5-6 boundary is satisfied by the assumption of the flow continuity from region 1 to 3.

Thus a kinematically admissible velocity field has been obtained for the problem. The obtained velocity field may be summarized by the following table.

region	$\dot{u}_r$	$\dot{u}_z$	$\dot{u}_\theta$
1	0	-1	0
2	$\frac{(2r + d_i)(d_o - d_i)}{8rt_f}$	$-\frac{(d_o - d_i)(z - \eta t_f)}{4rt_f} - \eta$	0
3	$\frac{d_o^2 - d_i^2}{8rt_f}$	0	0
4	0	0	0

Table 4.1

4.2.3 Upper-bound solution

The velocity field obtained in the previous section is used to calculate the upper-bound to the upsetting pressure in the injection upsetting process.

The strain rates may now be found using equations 4.57. In region 1 all the strain rates are identically zero. For region 2 the strain rates are:

$$\left.\begin{aligned}
\dot{\varepsilon}_{rr} &= -\frac{d_o - d_i}{8t_f}\ \frac{d_i}{r^2} \\
\dot{\varepsilon}_{zz} &= -\frac{d_o - d_i}{4t_f}\ \frac{1}{r} \\
\dot{\varepsilon}_{\theta\theta} &= \frac{d_o - d_i}{8t_f}\ \frac{2r + d_i}{r^2} \\
\dot{\varepsilon}_{rz} &= \dot{\varepsilon}_{zr} = \frac{d_o - d_i}{8t_f}\ \frac{z - \eta t_f}{r^2}
\end{aligned}\right\} \qquad (4.76)$$

and for region 3:

$$\dot{\varepsilon}_{rr} = -\frac{(d_o^2 - d_i^2)}{8t_f}\ \frac{1}{r^2}\ ,\quad \dot{\varepsilon}_{\theta\theta} = \frac{d_o^2 - d_i^2}{8t_f}\ \frac{1}{r^2}\ ,\quad \dot{\varepsilon}_{zz} = \dot{\varepsilon}_{rz} = \dot{\varepsilon}_{zr} = 0 \qquad (4.77)$$

In computing the total power of deformation, the power due to shearing at the 3-5, 3-6 and 5-6 boundaries (Fig. 4-10) must be taken into account. On the 5-6 boundary, the tangential velocity discontinuity ($\dot{V}_{56}$) is simply the difference between the $\dot{u}_z$ values at $r = d_o/2$ for the two regions 2 and 3, hence

$$|\dot{V}_{56}| = \frac{d_o - d_i}{2d_o t_f}(z - \eta t_f) + \eta \qquad (4.78)$$

On the 3-5 boundary the tangential velocity discontinuity ($\dot{V}_{35}$) is the difference between components of velocity in regions 1 and 2 along the surface 3-5. For a point adjacent to the boundary in region 1 the

component of velocity in direction of line 3-5 may be expressed as:

$$(\dot{V}_{35})_1 = -1 \cdot \sin\alpha$$

and the corresponding velocity in region 2 is:

$$(\dot{V}_{35})_2 = \dot{u}_z \sin\alpha + \dot{u}_r \cos\alpha$$

since $|\dot{V}_{35}| = |(\dot{V}_{35})_1 - (\dot{V}_{35})_2|$

thus,

$$|\dot{V}_{35}| = |\dot{u}_z \sin\alpha + \dot{u}_r \cos\alpha + \sin\alpha|$$

where $\dot{u}_r$ and $\dot{u}_z$ are the velocity components at 3-5 boundary in region 2 and can be substituted from Eqs. 4.68 and 4.73 respectively. This results in Eq. 4.79:

$$|\dot{V}_{35}| = \frac{(d_o - d_i)(2r + d_i)}{8rt_f} \sec\alpha \qquad (4.79)$$

where $\alpha = \arctan\left|\frac{2(1-\eta)\, t_f}{d_o - d_i}\right|$

On the 3-6 boundary the slip velocity $\dot{V}_{36}$ is the difference between components of velocity along the surface $z = -\frac{2\eta t f}{d_o - d_i} r + \frac{\eta t f\, d_o}{d_o - d_i}$ in regions 2 and 4. These components are

$(\dot{V}_{36})_4 = 0$

$(\dot{V}_{36})_2 = \dot{u}_z \sin\beta + \dot{u}_r \cos\beta$

and since $|\dot{V}_{36}| = |(\dot{V}_{36})_4 - (\dot{V}_{36})_2|$

thus,

$$|\dot{V}_{36}| = |\dot{u}_z \sin\beta + \dot{u}_r \cos\beta|$$

$\dot{u}_z$ and $\dot{u}_r$ can be substituted from Eqs. 4.68 and 4.74 respectively. After substitution Eq. 4.80 would result.

$$|\dot{V}_{36}| = \frac{(d_o - d_i)(2r + d_i)}{8rt_f} \sec\beta \qquad (4.80)$$

where $\beta = \arctan\left(\frac{2\eta t_f}{d_o - d_i}\right)$

In order to evaluate the total dissipated power of the deforming body the three powers described in section 4.2.1.2 must be calculated. These include the internal power of deformation in the plastic zones, the dissipated power due to slip at the zone boundaries and power losses due to surface frictions.

According to Eq. 4.59 the internal power of deformation in a volume v of a non-work hardening plastic solid of flow strength $\bar{\sigma}_o$ is given by:

$$\dot{E}_I = \int_{volume} \bar{\sigma}_o \dot{\bar{\varepsilon}}\, dv \qquad (4.81)$$

The value of effective strain rate for region 2 can be calculated by substituting Eqs. 4.76 into Eq. 4.58, hence,

$$\dot{\bar{\varepsilon}}_2 = \sqrt{2/3}\left(\frac{d_o - d_i}{8rt_f}\right)\left[\frac{d_i^2}{r^2} + 4 + \left(\frac{2r + d_i}{r}\right)^2 + \left(\frac{z - \eta t_f}{r}\right)^2\right]^{\frac{1}{2}} \qquad (4.82)$$

Similarly, the effective strain rate for region 3 is calculated by substituting Eqs. 4.77 into Eq. 4.58, thus

$$\dot{\bar{\varepsilon}}_3 = 2/\sqrt{3}\left(\frac{d_o^2 - d_i^2}{8r^2 t_f}\right) \qquad (4.83)$$

The internal power of deformation in region 2 may now be obtained by substituting Eq. 4.82 into Eq. 4.81:

$$\dot{E}_{I2} = \int_{d_i/2}^{d_o/2} \int_{z_1}^{z_2} \sqrt{2/3}\,\bar{\sigma}_o \left(\frac{d_o - d_i}{8rt_f}\right)\left[\frac{d_i^2}{r^2} + 4 + \left(\frac{2r + d_i}{2}\right)^2 + \left(\frac{z - \eta t_f}{r}\right)\right]^{\frac{1}{2}} 2\pi r\, dr\, dz \tag{4.84}$$

where $z_1 = -\frac{2\eta t_f}{d_o - d_i}\, r + \frac{\eta t_f d_o}{d_o - d_i}$

and $z_2 = \frac{2t_f(1-\eta)}{d_o - d_i}\, r + \frac{(d_o\eta - d_i)t_f}{d_o - d_i}$

the integration in Eq. 4.84 is carried out numerically, using the NAG library subroutine E01CFF *(110)*.

The internal power of deformation in region 3 can be obtained by substituting Eq. 4.83 into Eq. 4.81. The result is as follows:

$$\dot{E}_{I3} = \int_{d_i/2}^{d_o/2} \int_{0}^{t_f} \frac{2\bar{\sigma}_o}{\sqrt{3}} \left(\frac{d_o^2 - d_i^2}{8r^2 t_f}\right) 2\pi r\, dr\, dz$$

after integrating: $$\dot{E}_{I3} = \frac{\pi\bar{\sigma}_o(d_o^2 - d_i^2)}{2\sqrt{3}}\, ln\, d_f/d_o \tag{4.85}$$

where d_f is the flange diameter.

From Eq. 4.60 the energy dissipation rate due to shear along the surfaces of velocity discontinuity is given by:

$$\dot{E}_S = \int_{surface} k\,|\dot{V}_S|\, dS \tag{4.60}$$

where k is shear yield stress from the Von-Mises yield criterion $k = \frac{\bar{\sigma}_o}{\sqrt{3}}$ and is assumed constant.

The dissipated energy due to shearing the material across 3-5 boundary is evaluated by substituting the slip velocity at the boundary $\dot{V}_{35}$ (from Eq. 4.79) into Eq. 4.61:

$$\dot{E}_{S35} = \int_{d_i/2}^{d_o/2} \frac{\pi\bar{\sigma}_o\ (d_o - d_i)}{4\sqrt{3}\ t_f\ \cos^2\alpha}\ (2r + d_i)\ dr$$

where $\alpha = \arctan\ \left[\frac{2(1-\eta)t_f}{d_o - d_i}\right]$

after integration:

$$\dot{E}_{S35} = \frac{\pi\bar{\sigma}_o\ (d_o + 3d_i)}{16\sqrt{3}\ t_f}\ \left[4t_f^2\ (1-\eta)^2 + (d_o - d_i)^2\right] \qquad (4.86)$$

Similarly, the energy-dissipation rates along the 3-6 and 5-6 boundaries can be obtained by substituting Eqs. 4.80 and 4.78 into Eq. 4.61 respectively. The results may be expressed as follows:

$$\dot{E}_{S36} = \int_{d_i/2}^{d_o/2} \frac{\pi\bar{\sigma}_o\ (d_o - d_i)}{4\sqrt{3}\ t_f\ \cos^2\beta}\ (2r + d_i)\ dr \qquad (4.87)$$

where $\beta = \arctan\ \left(\frac{2\eta t_f}{d_o - d_i}\right)$

and,

$$\dot{E}_{S56} = \int_0^{t_f} \frac{\bar{\sigma}_o}{\sqrt{3}}\ \left[\frac{d_o - d_i}{2d_o\ t_f}\ (z - \eta t_f) + \eta\right]\ \pi d_o\ dz \qquad (4.88)$$

Integration of the Eqs. 4.87 and 4.88 results in:

$$\dot{E}_{S36} = \frac{\pi\bar{\sigma}_o\ (d_o + 3d_i)}{16\sqrt{3}\ t_f}\left[4\eta^2\ t_f^2 + (d_o - d_i)^2\right] \tag{4.89}$$

$$\dot{E}_{s56} = \frac{\pi\bar{\sigma}_o\ t_f}{4\sqrt{3}}\left[(d_o - d_i) + 2\eta(d_o + d_i)\right] \tag{4.90}$$

From Eq. 4.61 the energy-dissipation rate due to frictional losses at the tool-workpiece interface is given by:

$$\dot{E}_F = \int_{surface} \tau\ |\dot{V}|\ dS \tag{4.61}$$

where τ is the tangential stress developed at the tool-workpiece interface, and is defined as $\tau = m\frac{\bar{\sigma}_o}{\sqrt{3}}$ where m is a constant friction factor. In the absence of friction $m = 0$, and for $m = 1$ the tangential stress at the interface is $\tau = \frac{\bar{\sigma}_o}{\sqrt{3}} = k$, the shear yield stress of the material so that $0 \leq m \leq 1$.

The energy losses due to friction between the inner bore and mandrel surface are neglected since in the present experiments the relative velocity of metal particles to the mandrel is negligible, because a floating mandrel is used. The energy dissipation rate due to the frictional forces acting on the billet-container interface may be obtained as follows:

from Eq. 4.61 $$\dot{E}_{F16} = \int_0^{l} \frac{m\bar{\sigma}_o}{\sqrt{3}}\ |\dot{V}|\ \pi d_o\ dz$$

where l is the length of undeformed billet in contact with the container. Substituting $|\dot{V}| = -1$ and integrating results in

$$\dot{E}_{F16} = \frac{m\,\bar{\sigma}_o\,\pi\,d_o\,l}{\sqrt{3}} \tag{4.91}$$

The experimental results, presented in chapter 3, revealed that due to the axial thinning of the flange, no contact is made between the upper face of the flange and the lower face of the die so that no frictional losses are considered there.

The extent to which contact between the flange and the platen surface is maintained is dependent on the flange thickness. Since no axial force is directly applied to the upper face of the flange, any significant frictional traction acting at the lower face must be the result of radial spreading of the punch load in the flange region. This effect is illustrated qualitatively in Fig.4-12. The larger the flange thickness, the greater will be the radial spreading of the area of face transmission to the platen.

For the case where the flange is in full contact with the tool surface, the power of deformation ($\dot{E}_{F67}$) due to slip with friction factor m is found by using Eq. 4.61:

$$\dot{E}_{F67} = \int_{d_o/2}^{d_f/2} \frac{m\bar{\sigma}_o}{\sqrt{3}} |\dot{V}|\, 2\pi r\, dr$$

Since $|\dot{V}| = \dot{u}_r$ the radial velocity in region 3, subsequently from Eq. 4.75

$$\dot{E}_{F67} = \int_{d_o/2}^{d_f/2} \frac{m\bar{\sigma}_o}{\sqrt{3}} \left(\frac{d_o^2 - d_i^2}{8rt_f}\right) 2\pi r\, dr$$

Integrating

$$\dot{E}_{F67} = \frac{m\,\bar{\sigma}_o\,\pi\,(d_o^2 - d_i^2)}{8\sqrt{3}\,t_f}\,(d_f - d_o) \tag{4.92}$$

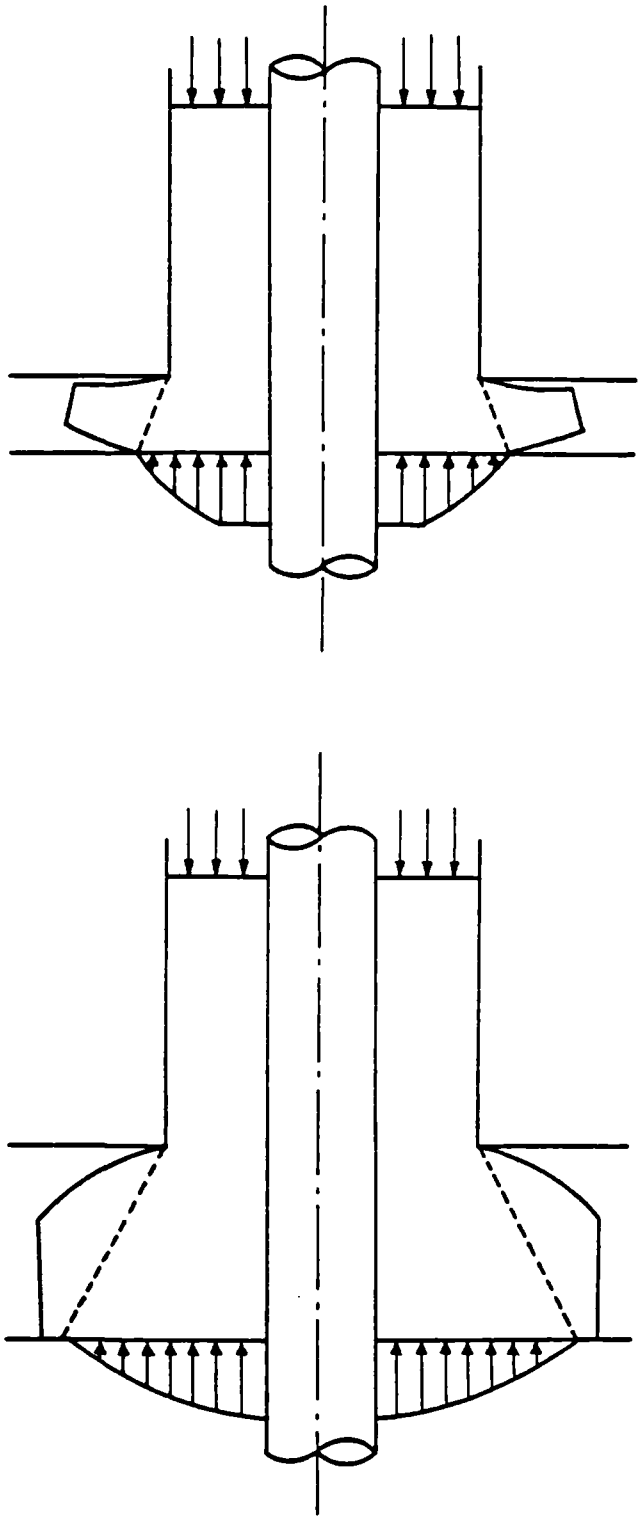


Fig. 4-12 Pressure distribution at the platen surface (qualitative illustration only).

The total rate of energy-dissipation in the deforming region is obtained by adding equations 4.84, 4.85, 4.86, 4.89, 4.90, 4.91 and 4.92

$$\dot{W}_D = \underbrace{\dot{E}_{I2} + \dot{E}_{I3}}_{\dot{E}_I} + \underbrace{\dot{E}_{S35} + \dot{E}_{S36} + \dot{E}_{S56}}_{\dot{E}_S} + \underbrace{\dot{E}_{F16} + \dot{E}_{F67}}_{\dot{E}_F} \qquad (4.93)$$

Substituting punch velocity $V_P = -1$ the area on which pressure is applied $A = \pi/4\ (d_o^2 - d_i^2)$ and $\dot{W}_D$ into Eq. 4.93, the mean punch pressure is obtained as

$$\frac{P}{\bar{\sigma}_o} = \frac{4}{\pi\bar{\sigma}_o\ (d_o^2 - d_i^2)} (\dot{E}_{I2} + \dot{E}_{I3} + \dot{E}_{S35} + \dot{E}_{S36} + \dot{E}_{S56} + \dot{E}_{F16} + \dot{E}_{F67}) \qquad (4.94)$$

where $\dot{E}_{I2}$, $\dot{E}_{S35}$, $\dot{E}_{S36}$ and $\dot{E}_{S56}$ are functions of η , a non-dimensional arbitrary parameter determining the position of the velocity discontinuity surfaces. Eq. 4.94 may therefore be rewritten as:

$$\frac{P}{\bar{\sigma}_o} = F(\eta) + \frac{4}{\pi\bar{\sigma}_o(d_o^2 - d_i^2)} (\dot{E}_{I3} + \dot{E}_{F16} + \dot{E}_{F67}) \qquad (4.95)$$

where $F(\eta) = \dfrac{4}{\pi\bar{\sigma}_o(d_o^2 - d_i^2)} (\dot{E}_{I2} + \dot{E}_{S35} + \dot{E}_{S36} + \dot{E}_{S56})$

The optimum value of the mean upsetting pressure may be obtained by minimizing $F(\eta)$ with respect to η over the required range of values $0 \leqslant \eta \leqslant 1$.

In the analysis of injection upsetting with one end constrained the deformation pattern, shown in Fig. 4-13 is used, in which the lower

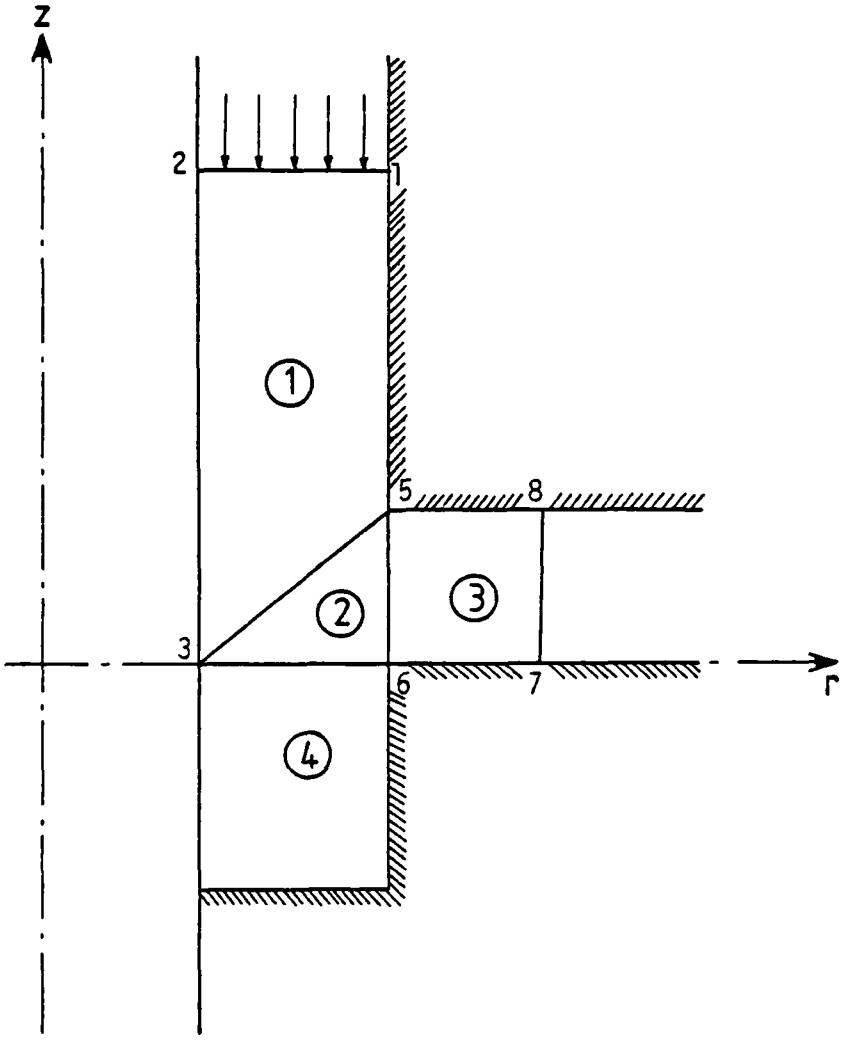


Fig. 4-13 Velocity field for injection upsetting hollow billets with one end constrained.

constrained part of the billet is considered as a dead zone. For this case the velocity field may be obtained by inserting $\eta = 0$ in the relations of Table 4.1. The energy-dissipation rates can be also found by substituting $\eta = 0$ in the corresponding relations obtained for simple injection upsetting. This would result in the following relations:

from Eq. 4.84 $$\dot{E}_{I2} = \int_{d_i/2}^{d_o/2} \int_{0}^{z} \sqrt{2/3}\, \bar{\sigma}_o \left(\frac{d_o - d_i}{8 r t_f}\right) \left[\frac{d_i^2}{r^2} + 4 + \left(\frac{2r + d_i}{r}\right)^2 + \frac{z}{r}\right] 2\pi r\, dr\, dz$$

where $$z = \frac{(2r - d_i)\, t_f}{d_o - d_i}$$

the integration is again carried out numerically, using the NAG library subroutine E01CFF *(110)*.

from Eq. 4.86 $$\dot{E}_{S35} = \frac{\pi \bar{\sigma}_o\, (d_o + 3d_i)}{16\sqrt{3}\, t_f} \left[4t_f^2 + (d_o - d_i)^2\right]$$

from Eq. 4.89 $$\dot{E}_{S36} = \frac{\pi \bar{\sigma}_o\, (d_o + 3d_i)\, (d_o - d_i)^2}{16\sqrt{3}\, t_f}$$

from Eq. 4.90 $$\dot{E}_{S56} = \frac{\pi \bar{\sigma}_o t_f\, (d_o - d_i)}{4\sqrt{3}}$$

Moreover, $\dot{E}_{I3}$, $\dot{E}_{F16}$ and $\dot{E}_{F67}$ are independent of η and therefore the same values of these energy rates (given by Eqs. 4.85, 4.91 and 4.92 respectively) are used.

CHAPTER 5

ELASTO-PLASTIC FINITE ELEMENT COMPUTER PROGRAMS

5.1 Introduction

Two computer programs developed in the present work are written in Fortran IV, using the formulation presented in the preceding chapter. A step-by-step incremental tangential method is employed. This method of solution was introduced in section 4.1.3.1.

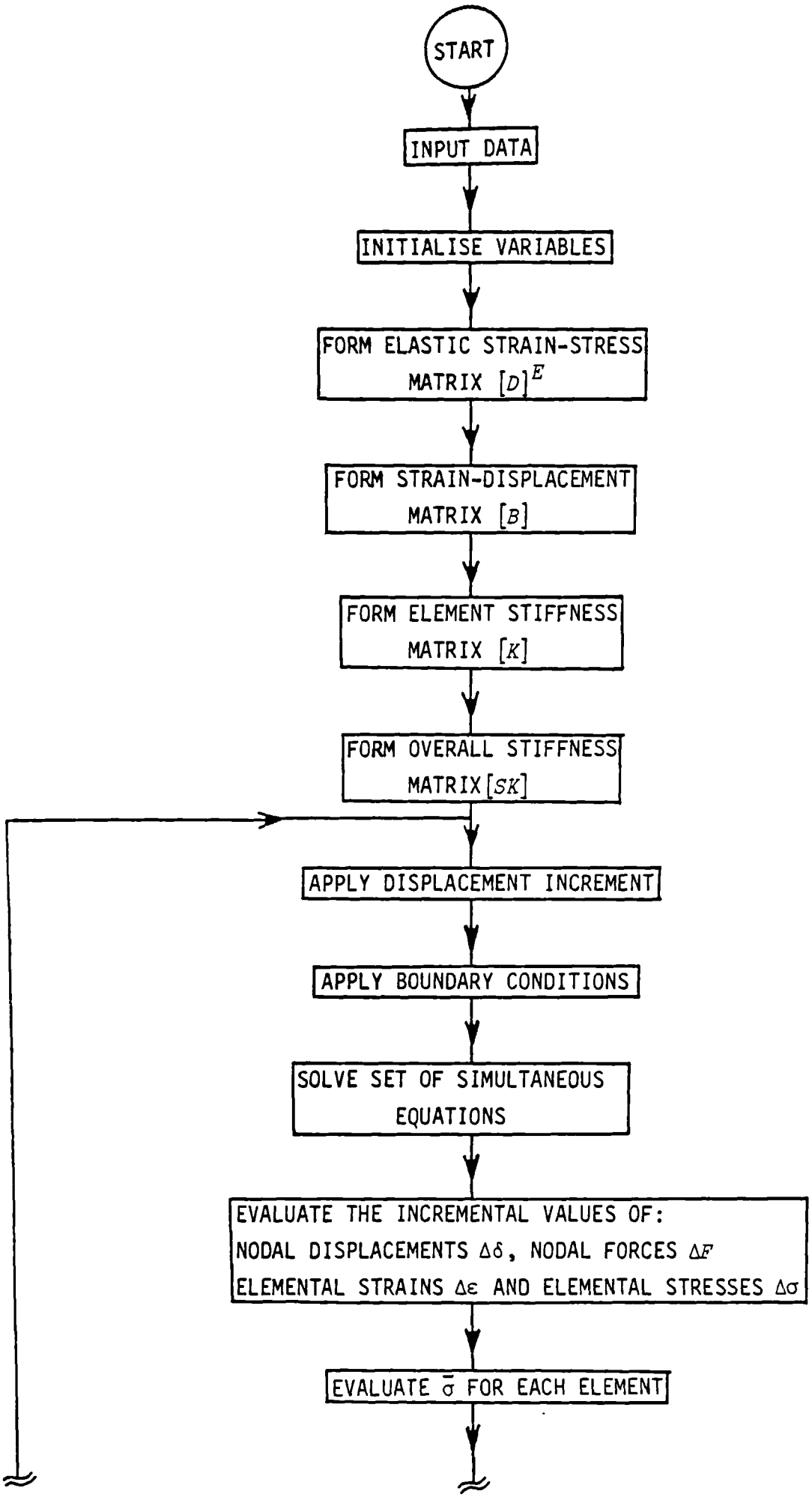
In the first program triangular ring elements, while in the second program quadrilateral elements are used. This kind of presentation not only avoids involving both types of elements in a single cumbersome program but also gives a good estimation of the effort required to introduce a new type of element into an available computer program. The programs for triangular elements and quadrilateral elements are named EPLAST1 and EPLAST2 respectively.

Although the structure of EPLAST2 differs substantially from EPLAST1 they both perform basically the same operations, since in EPLAST2 each quadrilateral element is subdivided into four constant strain triangles. A flow chart which applies to both programs is presented in Fig. 5-1. In the following the important points relating to the programs are given.

5.2 Finite element modelling of the upsetting process of hollow cylinders

5.2.1 Introduction

Various upsetting processes of hollow billets are simulated into models applicable to the finite element method. The advancement of the punch is introduced by the application of an input displacement at the nodal points positioned under the punch. The analysis is carried out step-by-step and continued until the desired punch displacement is achieved. At the end of each loading cycle certain conditions, given


START
INPUT DATA
INITIALISE VARIABLES
FORM ELASTIC STRAIN-STRESS MATRIX $[D]^E$
FORM STRAIN-DISPLACEMENT MATRIX $[B]$
FORM ELEMENT STIFFNESS MATRIX $[K]$
FORM OVERALL STIFFNESS MATRIX $[SK]$
APPLY DISPLACEMENT INCREMENT
APPLY BOUNDARY CONDITIONS
SOLVE SET OF SIMULTANEOUS EQUATIONS
EVALUATE THE INCREMENTAL VALUES OF:
NODAL DISPLACEMENTS $\Delta\delta$, NODAL FORCES ΔF
ELEMENTAL STRAINS $\Delta\epsilon$ AND ELEMENTAL STRESSES $\Delta\sigma$
EVALUATE $\bar{\sigma}$ FOR EACH ELEMENT

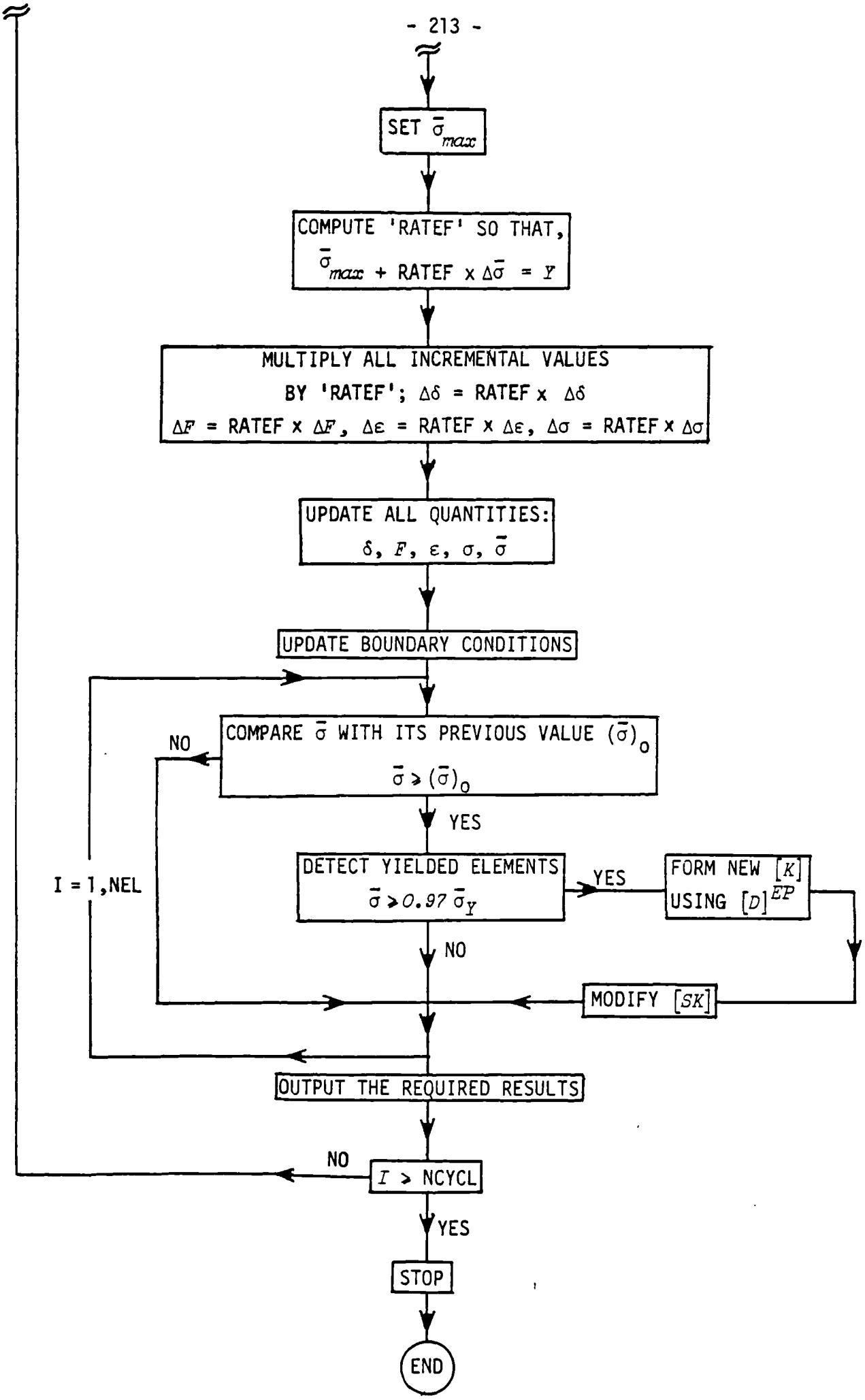


Fig. 5-1 Flow chart for the computer programs.

later in this section, are checked so that the boundary condition set at the start of the process for the cycle does not defy the physical aspect of the process. In cases where any of the conditions are contradicted a new boundary condition would be defined for the next cycle.

5.2.2 Conventional upsetting

5.2.2.1 Heading

a) Mandrel/specimen interface

The state of the nodal points on the mandrel/specimen interface can be recognized as suppressed or free surface node. To uphold the physical characteristics of the problem the radial force and displacement at these nodes must be checked continuously for the following conditions:

1) The radial forces at the suppressed nodal points must be zero or acting in the positive direction.
2) The radial displacement of the nodal points must be zero or in the positive direction.

The above conditions provide the possibility of these nodal points, according to their mode of deformation, to press against the mandrel (positive radial force) or move away from it (zero force), Fig. 5-2.

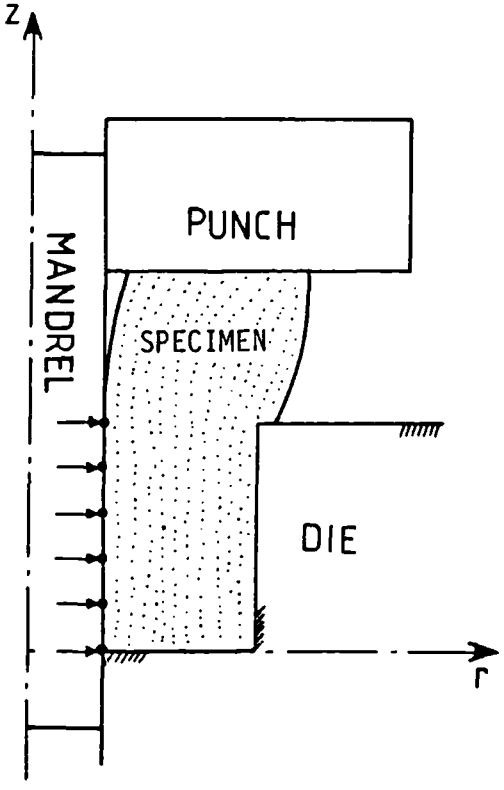


Fig. 5-2 Metal behaviour at the specimen/mandrel interface, heading.

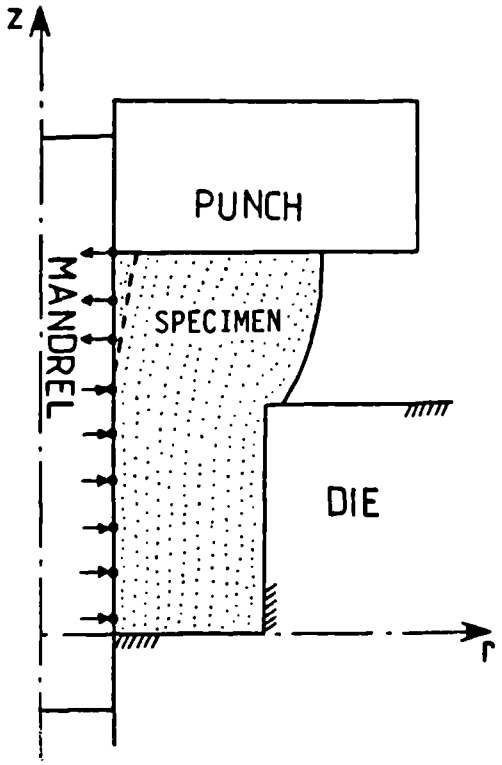


Fig. 5-3 Nodal forces at the specimen/ mandrel interface, heading.

At the start of the analysis the nodal points on the bore surface are assumed suppressed in the radial direction. At the end of each loading step the radial forces are checked for the first condition mentioned above. Nodal points with positive force remain suppressed and the ones with negative force assumed as free surface for the next loading step (Fig. 5-3). A negative force at these nodal points can develop due to wrongly assumed boundary condition of suppressed nodes, indicating that the nodes to remain in contact with the mandrel, must be held by some force. The nodal points must also be continuously checked for negative displacement and if observed the boundary condition at that node must be changed to that of suppressed.

b) Die/specimen interface

To provide the constraint introduced by the die on the workpiece during the heading process the following boundary conditions are introduced. The nodal points C and D, Fig. 5-5(a), are assumed to remain in contact with the die. Nodal points on $\overline{AC}$ are considered suppressed in the radial direction and nodes on $\overline{CD}$ are suppressed in the vertical direction.

To simulate the material flow at the die edge a mesh pattern as shown in Fig. 5-5(a) is employed. The finite element method is not capable of taking into account the behaviour of material in this region (shearing of deforming metal relative to the constrained part) which occurs

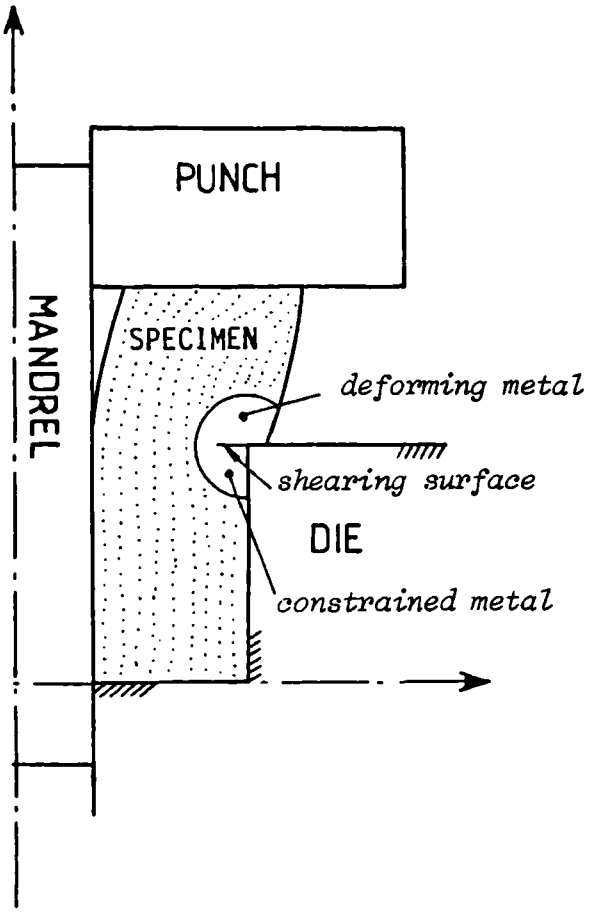


Fig. 5-4 Behaviour of metal at the die edge.

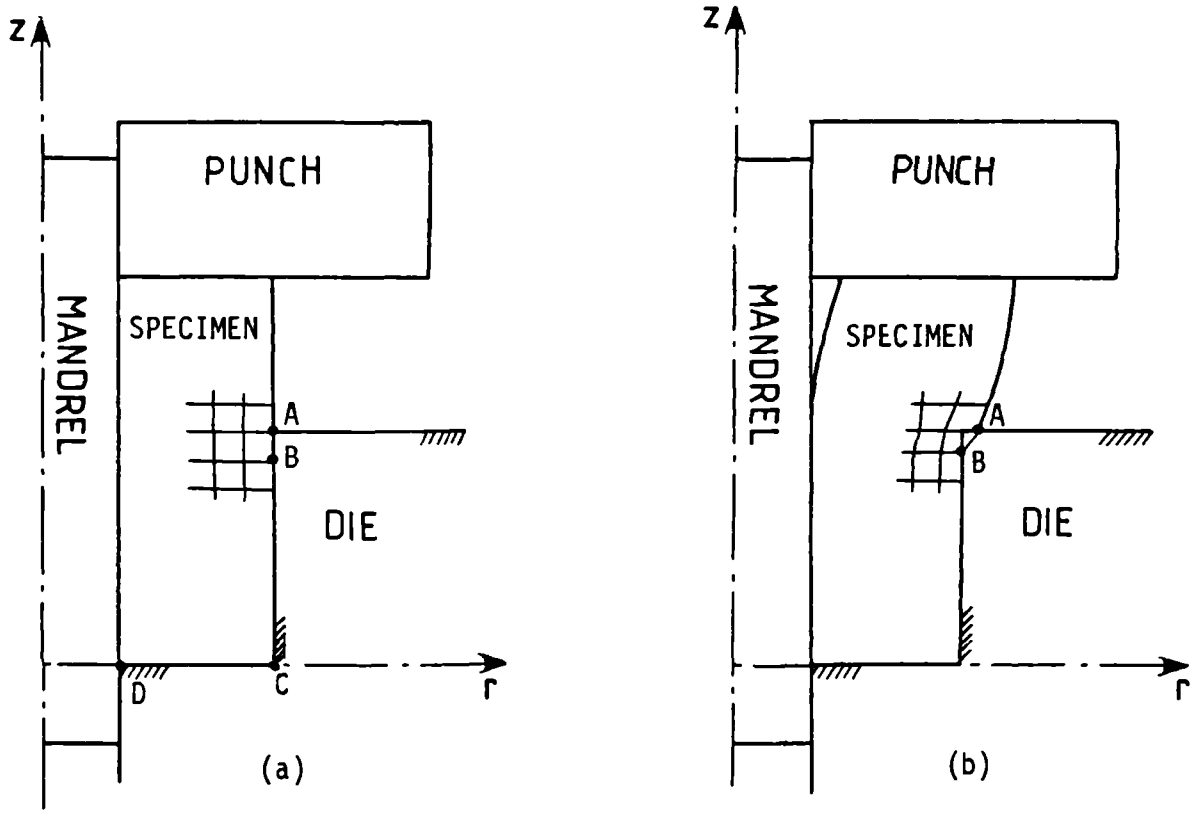


Fig. 5-5 Mesh pattern for the die edge.

in the actual heading process, Fig. 5-4. This can be rectified by allowing the nodal point A to move freely in the radial direction, Fig. 5-5(b). In order to reduce the difference between the assumed boundary conditions and the actual behaviour of material at the die edge more concentrated elements are introduced near this region.

5.2.2.2 Open upsetting

In the case of open upsetting the boundary condition at the mandrel-billet and die-billet interfaces is dealt with in a similar way to that of the heading process. The status of nodal points which are in contact with the punch are defined as follows. The nodal points on surface C'D', Fig. 5-6, and also node A' at the edge of the punch bore are given the same constant input displacement at the beginning of every loading step. The nodal points on A'C' (except node A') are suppressed in the radial direction. To simulate the material flow at the edge of the punch a mesh pattern as shown in Fig. 5-6 is employed and nodal point A' is allowed to move freely in the radial direction. Here, the same argument which was given earlier in section 5.2.2.1, for the edge of the die bore may be applied.

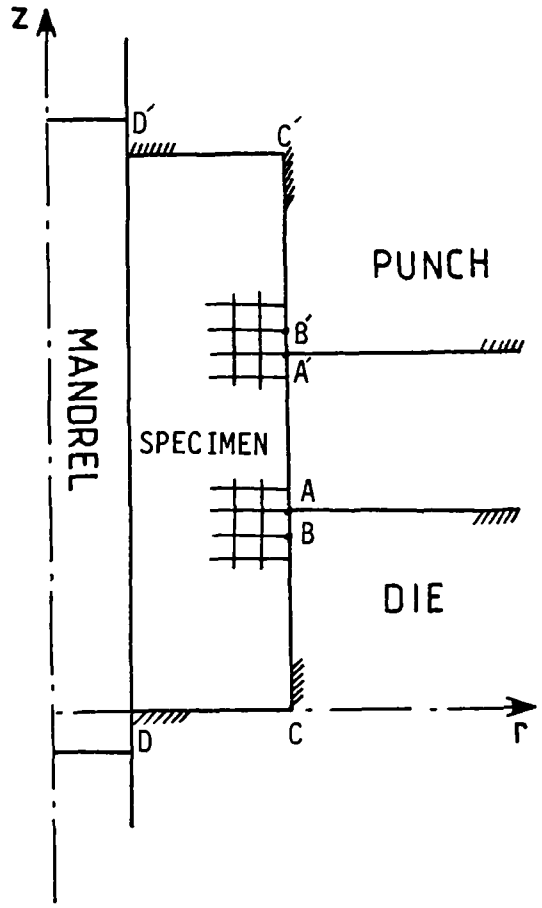


Fig. 5-6 Mesh patterns for the die edge and punch edge, open upsetting.

5.2.3 Injection upsetting

In order to introduce the boundary condition at the mandrel and punch contact surfaces in injection upsetting a similar procedure to that used in the heading process is employed. Modelling of the die-specimen and platen-specimen interface is accommodated as follows.

a) Die/billet interface

To provide the constraint introduced by the die on the specimen all the nodal points on surface $\overline{AD}$, Fig. 5-7, (except node A) are assumed to be suppressed in the radial direction and move freely vertically. To simulate the flow of material at the edge of the die bore a mesh configuration as shown in Fig. 5-7 is used. At the beginning of the analysis nodal point A is considered as a free surface point. At the end of every loading step the axial co-ordinate of node B (next node above A) is checked to find out when it leaves the die bore and enters the gap. Thereafter node B is considered as a free surface nodal point. Subsequently nodal point C, etc., are continued in the same manner and become free surface nodal points as they enter the gap.

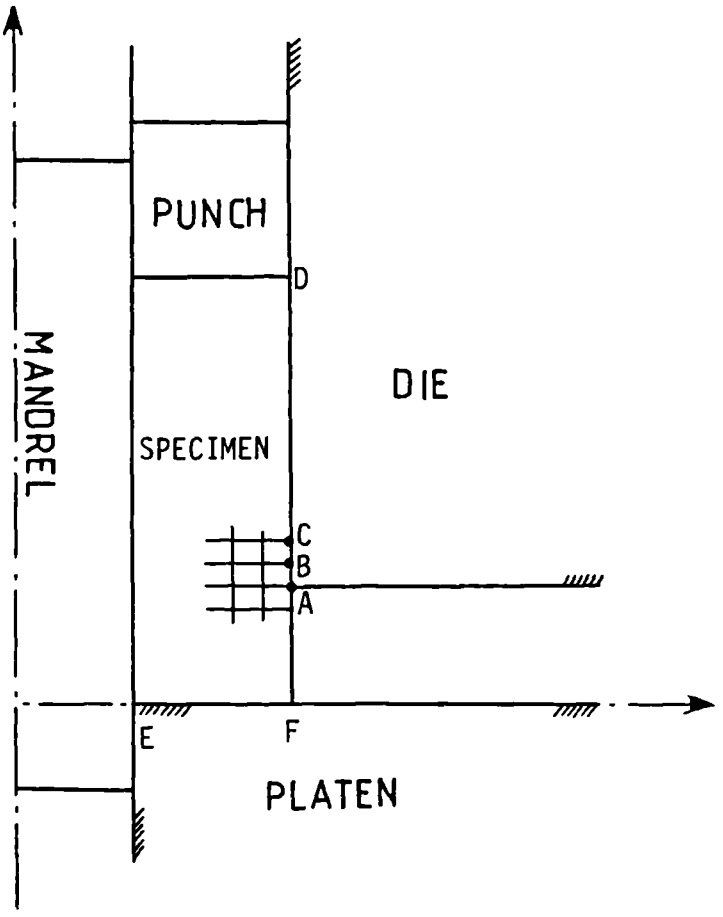


Fig. 5-7 Mesh pattern for the die edge, injection upsetting.

b) Platen/specimen interface

In the actual process of injection upsetting the deforming material usually begins to separate from the platen surface at some stage of deformation (dotted line in Fig. 5-8). To simulate this behaviour of material at the platen-specimen interface the following procedure is used. At the beginning of the analysis all the nodal points on the surface $\overline{EF}$, Fig. 5-7, are considered to be suppressed in the axial direction. At the end of each loading step the direction of the axial forces obtained at these nodal points is continually checked. The nodes remain suppressed in the axial direction only if their axial force is acting in the positive direction. A negative axial force at any of these nodes is considered to be the node's tendency to separate from the platen surface and from then onwards that node is treated as a free surface nodal point.

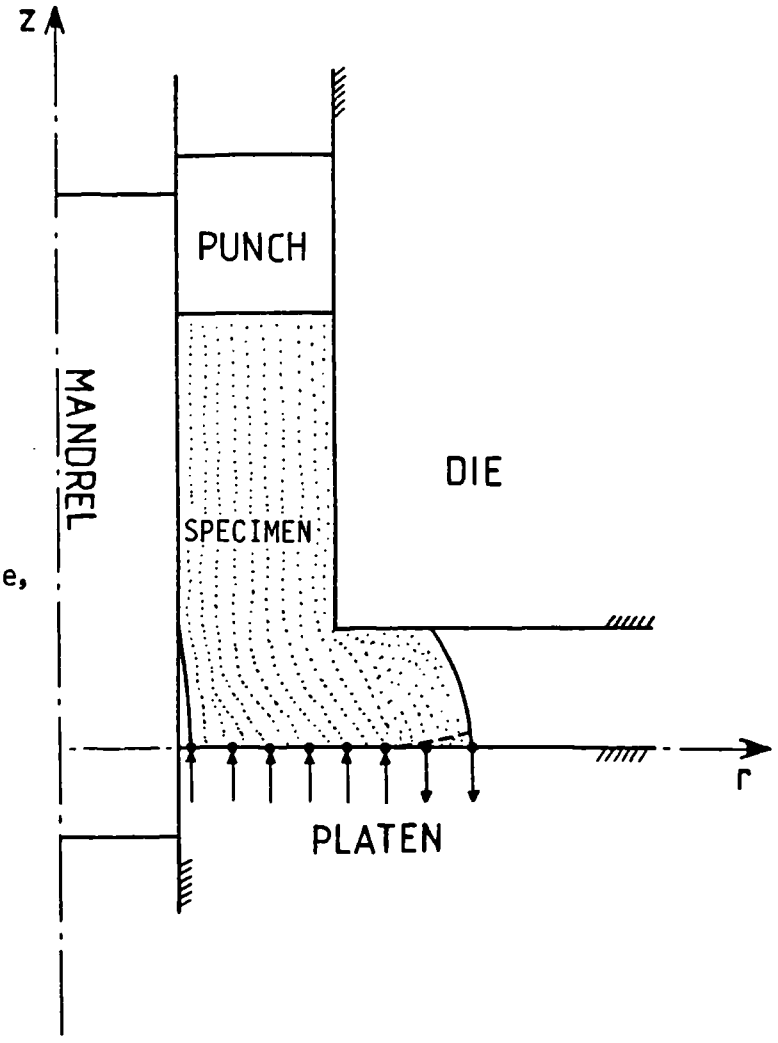


Fig. 5-8 Nodal forces at the specimen/platen interface, injection upsetting.

5.2.4 Friction

In order to include the effect of surface friction in the finite element analysis a method similar to that used by Iwata et al *(69)* is employed. This method is based on the introduction of a tangential force at any contact node, in a direction opposite to the material flow direction at that node.

In the case of heading, the frictional forces (F_r', F_z') for the nodal points situated on the contact surfaces are calculated as follows:

from Fig. 5-9 it can be written

for nodal points on $\overline{BC}$: $F_r' = \mu F_z$

for nodal points on $\overline{CD}$: $F_z' = \mu F_r$

at nodal point A: $F_r' = -\mu F_z$

where

μ is the coefficient of friction

F_r and F_z are the incremental nodal forces

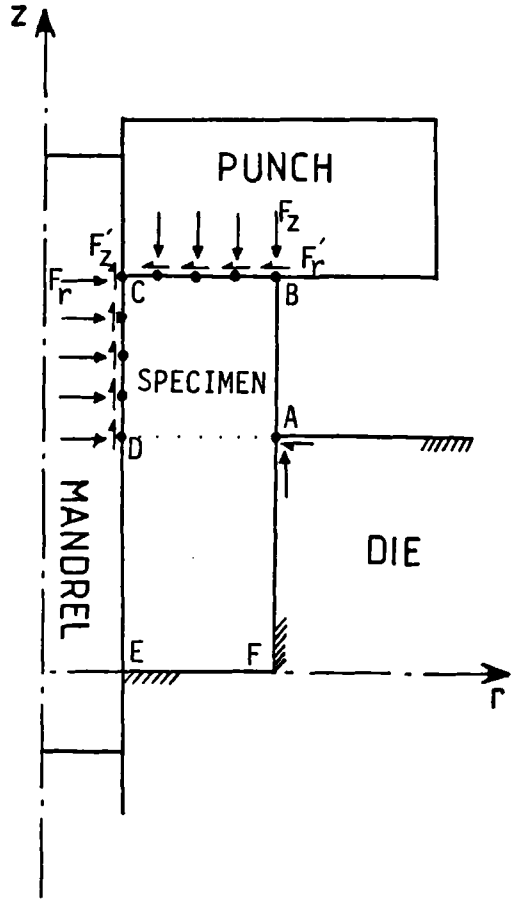


Fig. 5-9 Friction forces at the contact nodal points, heading.

F_r' , F_z' are computed at the end of every loading step and they are then considered as external loads and applied in the appropriate direction to the corresponding nodes in the next cycle.

The frictional forces at nodal points on surfaces $\overline{DE}$, $\overline{EF}$ and $\overline{FA}$ were assumed zero. This assumption was made following a primary analysis of the problem (assuming zero frictional forces) which indicated zero or minute displacement of these nodal points relative to the tools.

For the case of open upsetting the nodal points on which frictional forces are applied are shown in Fig. 5-10.

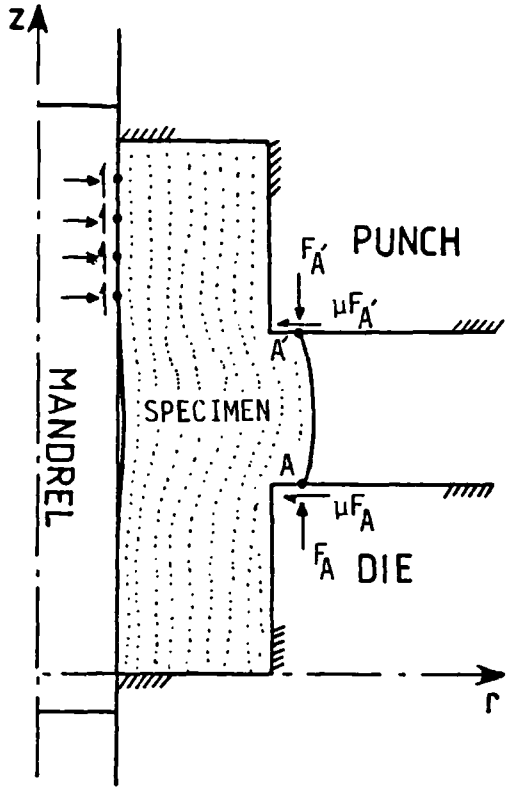


Fig. 5-10 Friction forces at the contact nodal points, open upsetting.

5.2.5 Hydrostatic pressure

As an alternative, in the theoretical analysis of conventional upsetting a constant hydrostatic pressure is applied to the outer free surface of the specimen ($\overline{AB}$ in Fig. 5-11(a)) . The pressure is introduced as external concentrated loads acting at the nodal points on surface $\overline{AB}$. The total load applied to the side of every element on the free surface is obtained and replaced by two concentrated nodal forces introduced at the two nodal points on this side, each being half the total load. For example, in the heading process shown in Fig. 5-11(b) the calculation for a typical nodal point 'i' of element 'e' may be presented as follows:

$F_h = P_h \times$ Area (ring surface of ij)

$F_r = \frac{1}{2} F_h \sin\theta$

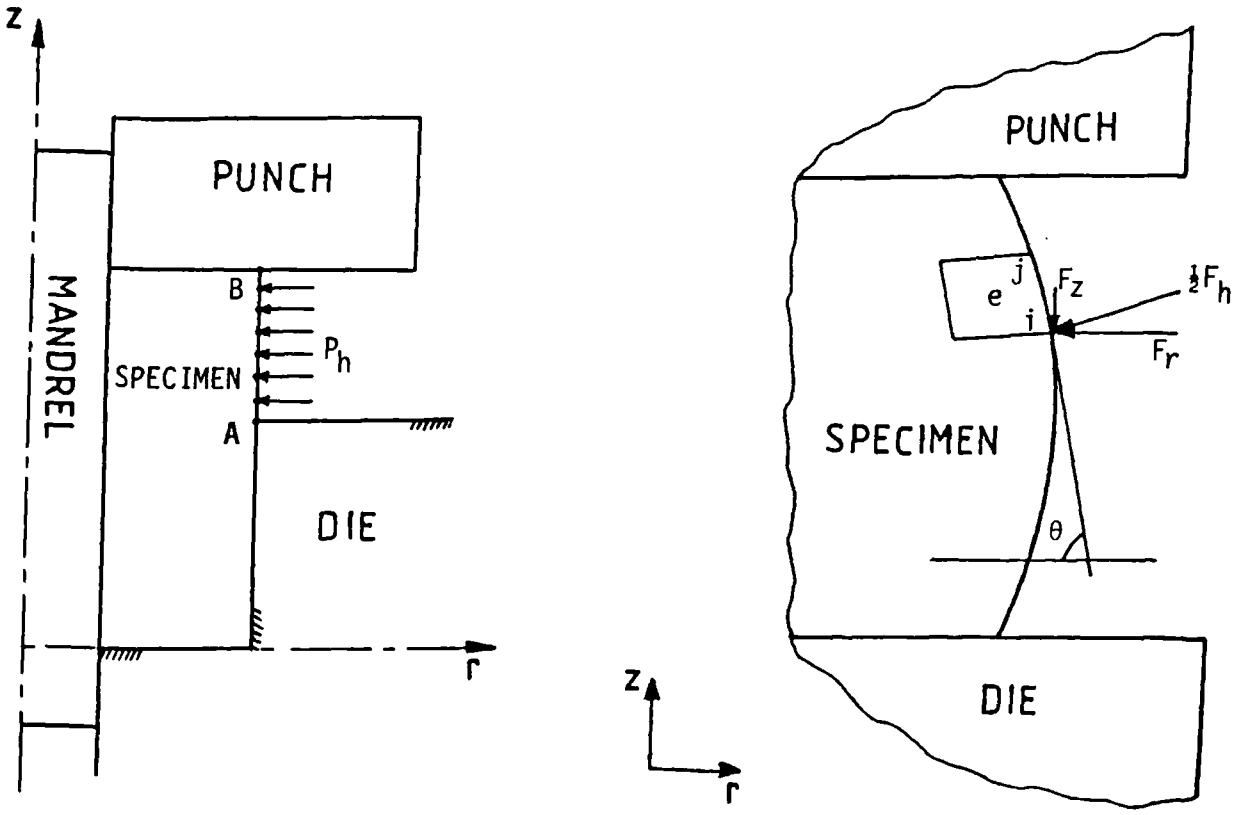
$F_z = \frac{1}{2} F_h \cos\theta$

Where: P_h = hydrostatic pressure

F_h = concentric load applied at the middle of ij and normal to it.

and $\theta = \arctan\left(\frac{z_j - z_i}{r_i - r_j}\right)$

where z_i, r_i and z_j, r_j are the axial and radial co-ordinates of points i and j respectively.



(a) (b)

Fig. 5-11 Application of hydrostatic pressure.

It should, however, be noted that to calculate the total concentrated force at a typical node 'i' the contribution of the distributed loads on the side of element 'ik' must also be considered and added to the value calculated from the side 'ij'.

5.3 Computational procedure

The programs are developed on the following sequence of computations:

1) A unit punch displacement is applied, and for the boundary condition imposed, nodal displacement and thus elastic strains, stresses and equivalent stresses ($\bar{\sigma}$) within each element are calculated.
2) The element with maximum equivalent stress ($\bar{\sigma}_{max}$) is found.
3) The rating factor is calculated according to: $r = \frac{Y}{\bar{\sigma}_{max}}$ where Y is the yield stress of the material under consideration.
4) The nodal displacements and forces and also the element strains and stresses are multiplied by the rating factor r.
5) The elements with $\bar{\sigma} > 0.97Y$ are found and are treated as yielded elements for the subsequent computations.
6) Matrices $[D]^E$ and $[K]^E$ are appropriately modified to $[D]^{EP}$ and $[K]^{EP}$ for post yielded elements.
7) The overall stiffness matrix of the whole body is modified.
8) The instantaneous boundary conditions are read-in.
9) An increment of punch displacement is applied and the corresponding values of nodal-displacement and nodal force increments and also the elemental strain and stress increments are calculated.
10) The rating factor 'r' is calculated for every element remaining in the elastic state.
11) The minimum value of r is found and if it is greater than unity, it is set equal to unity in order to avoid an unexpected increment of load.

12) Strain and stress increments for the unloaded elements are recalculated.

13) The nodal displacement and force increments and also the strain and stress increments are added to the previous displacements, forces, strains and stresses respectively.

14) Matrix $[D]$ is updated for the yielded and unloaded elements.

15) The geometrical matrices are updated using the current nodal coordinates.

16) The elemental stiffness matrices of all elements are updated.

17) The overall stiffness matrix of the whole body is modified.

18) The elements having $\bar{\sigma}$ equal to, or larger than $0.97Y$ are treated as yielded elements in the next step.

19) Sequences 8 through 18 are repeated until the required deformation is obtained.

5.4 Applying the boundary conditions

Prior to the solution of the set of N equations (equilibrium equations of the system) the boundary conditions must be introduced into these equations. To apply the force boundary condition, the known nodal forces are simply introduced into the load vector in the corresponding row. For the free surfaces, the loading terms corresponding to the nodes on the boundary are zero, and for those nodes which are subjected to surface friction or hydrostatic pressure the appropriate forces must be applied.

The displacement boundary conditions are more difficult to apply. For a specified displacement the stiffness matrix together with the load vector must be modified. In general, for ease of indexing, the size of the matrix should remain unchanged, i.e. no rows or columns of the matrix should be deleted. There are two alternative approaches in the application of boundary conditions. The two approaches are demonstrated in the following

example. In a set of N equations, the value of δ_1 is prescribed and is equal to α.

$$\begin{bmatrix} K_{11} & K_{12} & \cdots & K_{1n} \\ K_{21} & K_{22} & \cdots & K_{2n} \\ \cdot & \cdot & & \cdot \\ \cdot & \cdot & & \cdot \\ \cdot & \cdot & & \cdot \\ \dot{K}_{n1} & K_{n2} & \cdots & K_{nn} \end{bmatrix} \begin{Bmatrix} \delta_1 \\ \delta_2 \\ \cdot \\ \cdot \\ \cdot \\ \delta_n \end{Bmatrix} = \begin{Bmatrix} F_1 \\ F_2 \\ \cdot \\ \cdot \\ \cdot \\ F_n \end{Bmatrix}$$

In one method, to apply the boundary condition the load column is modified as follows.

$F_1' = \alpha$ and $F_i' = F_i - K_{i1}\,\alpha$ where $i = 2, N$

Then the corresponding row and column of the matrix is designated zero and the diagonal term is made unity. In the special but common case of $\alpha = 0$ (i.e. fixed support), it is only necessary to modify the matrix as described above, leaving the load matrix unchanged except for $F' = 0$.

In the alternative method the appropriate diagonal term is multiplied by a large number, say, 10^{12}, and in the load column only the corresponding load coefficient is suitably modified.

$K_{11}' = K_{11} \times 10^{12}$ and $F_1' = K_{11} \times 10^{12} \times \alpha$

These are the only modifications that must be carried out when the displacement in a certain direction is known. This will yield a solution in which δ_1 is very nearly equal to α. This latter method is easier to implement in computer programs than the former, and thus this method

is used in both computer programs developed in this work to introduce the required boundary conditions into the equilibrium equations of the system.

5.5 Solution of the system of equations

The system of equations are solved using the direct method of Gauss elimination. In this method the coefficient matrix is reduced to the upper triangular form by successive elimination of the variables. The procedure can be demonstrated in the following example.

Consider the set of N linear simultaneous equations.

$$\begin{bmatrix} K_{11} & K_{12} & \cdots\cdots & K_{1n} \\ \vdots & \vdots & & \vdots \\ K_{n1} & K_{n2} & \cdots\cdots & K_{nn} \end{bmatrix} \begin{Bmatrix} \delta_1 \\ \vdots \\ \delta_n \end{Bmatrix} = \begin{Bmatrix} F_1 \\ \vdots \\ F_n \end{Bmatrix}$$

The variable δ_1 is eliminated from the last $(N-1)$ equations by suitable operations with the first equation. The variable δ_2 is then eliminated from the last $(N-2)$ equations by suitable operations with the second equation, in its modified form with the coefficient of δ_1 equal to zero. The process is continued until the last equation is reached when the matrix has been reduced to the upper triangular form. The right-hand side of the equations are successively modified as the process continues and the unknowns are finally evaluated by 'back substitution'.

To solve a system of linear equations, the Gauss-Seidel method is most commonly used. This method is preferable for its ease of programming and also for its undeniable saving in computing time when using the optimum relaxation factor. However, in plasticity the relaxation factor must be successively redefined in order to take into account the decrease

of rigidity of the system of equations. There is no exact method for determining the relaxation factor and hence the convergence is neither likely to be achieved nor would the time be economical. Particularly when the system of equations becomes ill-conditioned owing to the bulk plastic yielding of the continuum.

5.6 Description of the programs

5.6.1 Using triangular elements

The program EPLAST1 is developed to analyse elasto-plastic deformation of a continuum by using constant strain triangular elements. The listing of the program and variables involved are presented in Appendix A. The program is subdivided into fourteen main sub-routines, in each of which specific operations are performed. The basic features of these sub-routines are as follows.

The input data are read in routine INPUT. The data include the number of elements, number of nodes, nodal connections of the elements, material properties and other specific information. All the variables and variable increments are initialized. The data are subsequently used in sub-routine MESH to compute additional but related data. Nodes are scanned, the nodal co-ordinates being scaled down. The boundary condition is set and a status vector NFIX is employed to specify the state of the boundary nodal points, for example:

NFIX	01	suppressed in r direction
	10	suppressed in z direction
	11	suppressed in r and z direction

The vector is used later in the program to introduce the boundary conditions into the set of N equations of the system.

Call is made to subroutine FORMD1, FORMB and FORMK to calculate the element stiffness matrices. The subroutine FORMD1 forms the elastic stress strain relationship $[D]^E$ and the FORMB routine computes the geometrical matrices related to the elements and constructs the strain displacement matrix $[B]$. Routine FORMK carries out the matrix multiplication $B^T D\ B$ which is used to calculate the element stiffness matrix. In this subroutine the element area 'AREA' and the value of $\bar{r}$ (centroid co-ordinate) are evaluated and the multiplication $2\pi r\ B^T D\ B \times$ AREA is carried out which yields the element stiffness matrix.

To form the overall stiffness matrix of the system, elements are scanned and the stiffness matrices are added in turn to the appropriate locations of the overall stiffness matrix in accordance with the nodal numbers of the element in question (the overall stiffness matrix is a banded matrix). The boundary conditions are applied to the set of N equations in subroutine BOUNDRY, using the method discussed in section 5.4. The set of N equations of the system are then solved simultaneously for unknown values of displacement and loads, using the Gauss elimination method in routine SOLVE.

Having obtained the nodal displacements from routine SOLVE, the element strains and stresses can be calculated. A call is made to routine STRAIN and STRESS in which elements are scanned and using the appropriate relations, strains and hence stresses and also equivalent stresses within the elements are computed.

In this method of solution the problem is assumed linear at each increment of displacement, so the increment of every variable at every step would be proportional to the input displacement. A rating factor 'RATEF' is defined in subroutine RFACT to specify the required amount of input displacement to cause yield in the element with maximum value of

$\bar{\sigma}$. RATEF is calculated from the following equation.

$$(\bar{\sigma} + \text{RATEF} \cdot \Delta\bar{\sigma})^2 = Y^2 = 1/2 \left[(\sigma_x + \Delta\sigma_x - \sigma_y - \Delta\sigma_y)^2 + \cdots\cdots\cdots\right]$$

RATEF is then compared with a prescribed value (i.e. unity) and if it is found greater than unity is set equal to unity. The variables such as nodal forces and displacements and also elemental strains, stresses and equivalent stresses are then multiplied by the rating factor. In the subsequent operation, a status vector ND is used to identify the state of the stresses within the elements.

ND	-1	unloaded element
	0	elastic element
	1	plastic element

In the analysis, a provision is made for some elements to be included among the yielded elements just prior to yielding. The allowance is advantageous for saving computing time. In the program, elements of $\bar{\sigma} > 0.97Y$ are considered to be plastic.

The unloaded elements are detected and the strain-, stress- and effective stress-increments are recalculated, on the basis of the elastic matrices. The yield stresses of these elements are changed to their latest attained values of effective stresses. In subroutine FORMD elements are scanned and $[D]^{EP}$ is computed for the yielded elements and the current elemental effective plastic strains (for the post-yielded elements) are calculated. If any of the post-yielded elements are unloaded, $d\bar{\varepsilon}^p$ is set equal to zero. In the following routine UPDATE1, changes in the boundary conditions are taken into account and the new boundary conditions

are set.

Having applied a number of increments, the total nodal displacements and nodal forces and elemental stresses and other required information are written on the tape in the OUTPUT routine. In the routine UPDATE, nodes are scanned and the current nodal co-ordinates are added to the corresponding nodal displacement increments. Considering the new nodal co-ordinates the strain-displacement matrix $[B]$ is updated. Depending on the recent state of the elements the elemental stiffness matrices are recalculated, so modifying the overall stiffness matrix of the whole body.

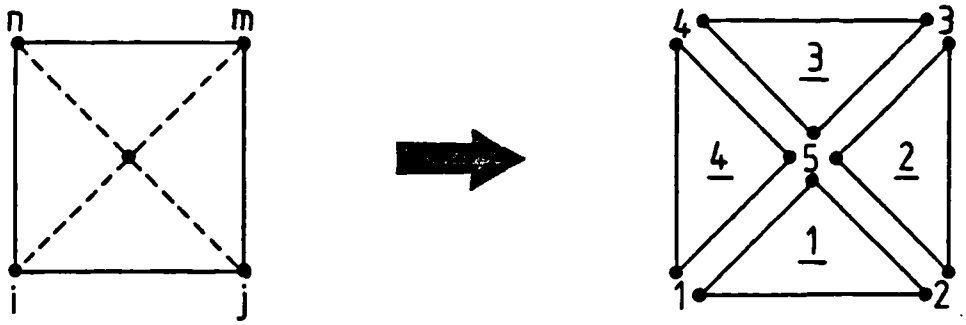
A new increment of displacement is introduced at the boundary nodal points until the desired punch penetration is obtained.

5.6.2 Using quadrilateral elements

The program EPLAST2 is developed to analyse elasto-plastic deformation of a continuum by using quadrilateral elements. Although the structure of EPLAST2 differs substantially from EPLAST1 they both perform basically the same operations, since in EPLAST2 each quadrilateral element is subdivided into four constant strain triangles. The general feature of this program is outlined below, and the listing of the program including the variables used is shown in Appendix B. It is worth mentioning that in the following, only substantial differences from EPLAST1 are presented and discussed.

In subroutine INPUT elements are scanned, average nodal co-ordinates of the element under consideration are calculated and assigned as the co-ordinates of the internal node (see the following illustration), i.e.

$$r_5 = \frac{r_1 + r_2 + r_3 + r_4}{4} \quad \text{and} \quad z_5 = \frac{z_1 + z_2 + z_3 + z_4}{4}$$



In the subsequent operation the element is subdivided anticlockwise and according to the elemental node numbering. The subdivided element is node-numbered corresponding to the node numbering of the original element. Thus the internal node is designated the last node in the substructure comprising four triangles. Having numbered the resulting four triangular elements, the stress-strain matrix and strain-displacement matrix corresponding to the triangles are calculated in subroutines FORMD1 and FORMB.

Elements are scanned in the subroutine FORMK and the stiffness matrices of the triangles, comprising the quadrilateral element under consideration, are calculated and assembled. Rows corresponding to the internal node are then eliminated obtaining the stiffness matrix of the quadrilateral element. In the usual way, the stiffness matrices of quadrilateral elements are assembled and thus the overall stiffness matrix of the whole body is built up. A substantial change in this routine is the introduction of two additional vectors to resume the displacement of the internal nodes when required.

Subroutine SOLVE solves the system of equations. Elements are scanned and using the appropriate relations the internal node displacements are

calculated and stored. As usual, for the resulting triangles the strains, stresses and effective strains are calculated. Elements are scanned and if any of the comprising triangular elements are found to have yielded, the quadrilateral stiffness matrix is recalculated and substituted in the overall stiffness matrix of the whole body.

In the program EPLAST2 provision is made to treat the unloaded quadrilateral elements. Elements are scanned and if any of the comprising triangular elements are found to be unloaded, the elemental stiffness matrix is recalculated and substituted in the overall stiffness matrix of the whole body. Two additional subroutines FRIC and HYPRES are included in this program to introduce the application of frictional forces and hydrostatic pressure respectively. The computational procedures used in FRIC and HYPRES have been previously discussed in sections 5.2.4 and 5.2.5.

When the desired magnitude of deformation is attained, the elements are scanned and average values of the effective plastic strains and also effective stresses of the comprising triangular elements are calculated and assigned as the mean values of the element under consideration.

CHAPTER 6

RESULTS AND DISCUSSION

6.1 Introduction

In the theoretical analysis of the conventional and injection upsetting of hollow cylindrical billets, initially a finite element mesh of 220 triangular elements was employed in program EPLAST1 presented in Appendix A. This program was applied to the heading and simple injection upsetting processes and the results were compared with the experimental findings. In heading, the predicted results were far from accurate, and for simple injection upsetting the program failed to produce realistic results.

Program EPLAST2 (Appendix B) was developed using 90 quadrilateral elements. This program was successfully applied to heading and open upsetting, but when applied to the injection upsetting process the results progressively drifted from those found in reality.

6.2 Finite element results for conventional upsetting

6.2.1 Choice of element

After primary computations using triangular and quadrilateral meshes, it was decided to use quadrilateral elements throughout the analysis in the conventional upsetting of hollow billets. The number of quadrilateral elements was based on a compromise of economy and accuracy. A mesh pattern of 90 quadrilateral elements and 112 nodal points, shown in Fig. 6-1a & b for heading and open upsetting respectively is employed in program EPLAST2. As the process is axi-symmetric, only half of specimen cross section is considered in the computations. In order to obtain a better approximation of the geometrical changes at the die edge and also at the punch edge (in open upsetting) the divisions are finer near these regions. The elements

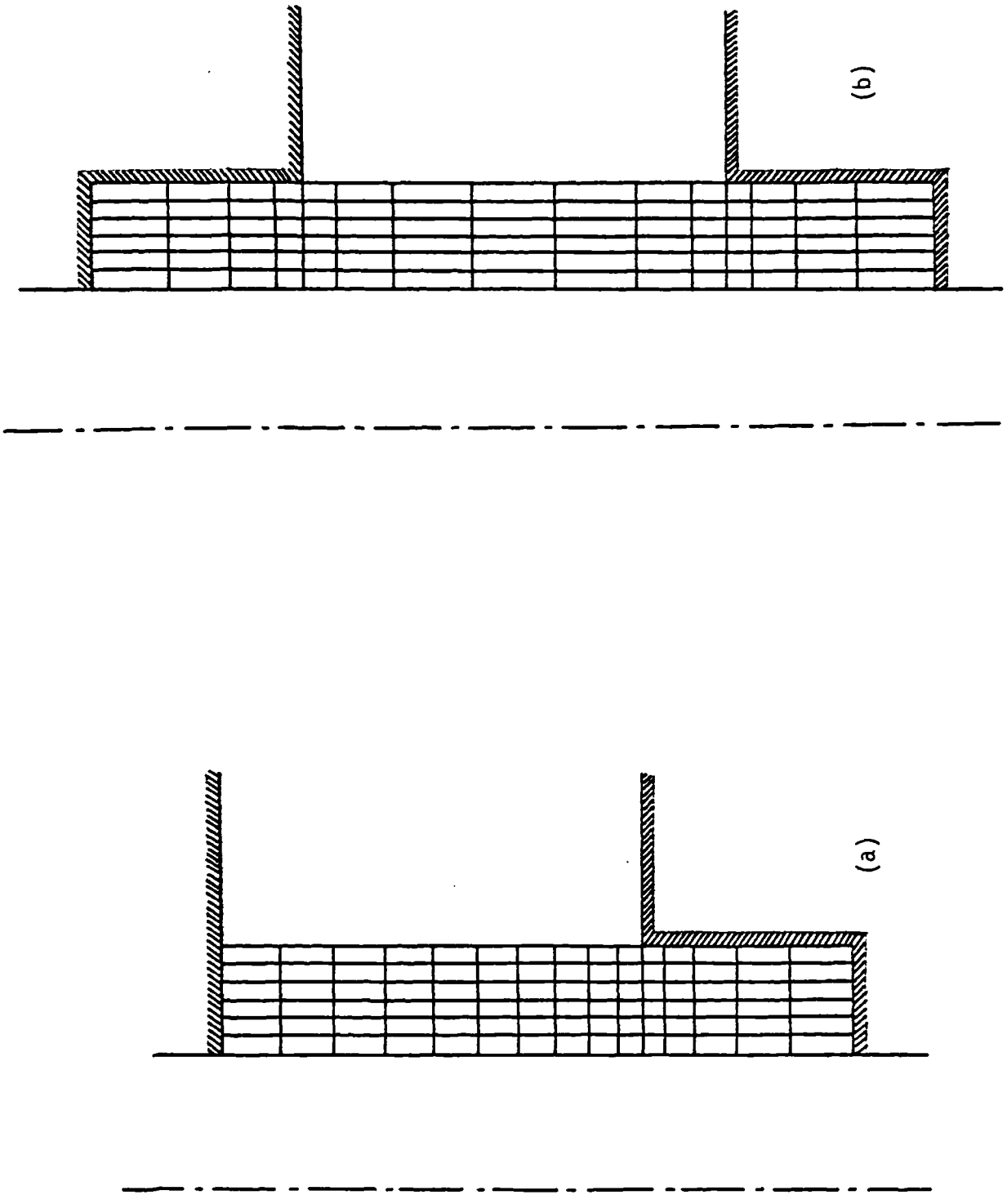


Fig. 6-1 Meshes of 90 quadrilateral elements and 112 nodal points in conventional upsetting. a) heading b) open upsetting

are numbered in an arbitrary manner, but the nodal points are numbered in such a way as to minimize the bandwidth of the overall stiffness matrix.

6.2.2 True stress-strain curve

The true stress-strain curve of commercially pure aluminium, shown in Fig. 2-2 (obtained from a uniaxial compression test) is replotted in Fig. 6-2. For use in the computer analysis, the stress-strain curve of the material was approximated by two straight lines. The material properties used in the computations were as follows:

$$E = 0.07 \times 10^6 \ MN/m^2 \qquad \nu = 0.345$$

$$\bar{\sigma} = Y_o + H_o (\bar{\varepsilon}_p) \qquad \text{for} \qquad 0.1 \geq \bar{\varepsilon}_p \geq 0$$

$$\bar{\sigma} = Y_1 + H_o (\bar{\varepsilon}_p) \qquad \text{for} \qquad \bar{\varepsilon}_p > 0.1$$

where $Y_o = 40 \ MN/m^2$ $\qquad H_o = 500 \ MN/m^2$

$Y_1 = 90 \ MN/m^2$ $\qquad H_1 = 75 \ MN/m^2$

6.2.3 Inclusion of surface friction in the computer programs

To study the effect of surface friction on the theoretical results three different conditions are employed.

1- The contact nodal points are allowed to move freely along the tool surfaces and can take no force in the direction parallel to the surfaces, i.e. these surfaces are perfectly smooth.

2- All the contact nodal points are subjected to a frictional force applied in a direction parallel to the surface. The computational procedure was explained in section 5.2.4.

In order to approximate a value for the coefficient of friction, a method suggested by Male and Cockroft *(33)*, based on the geometrical

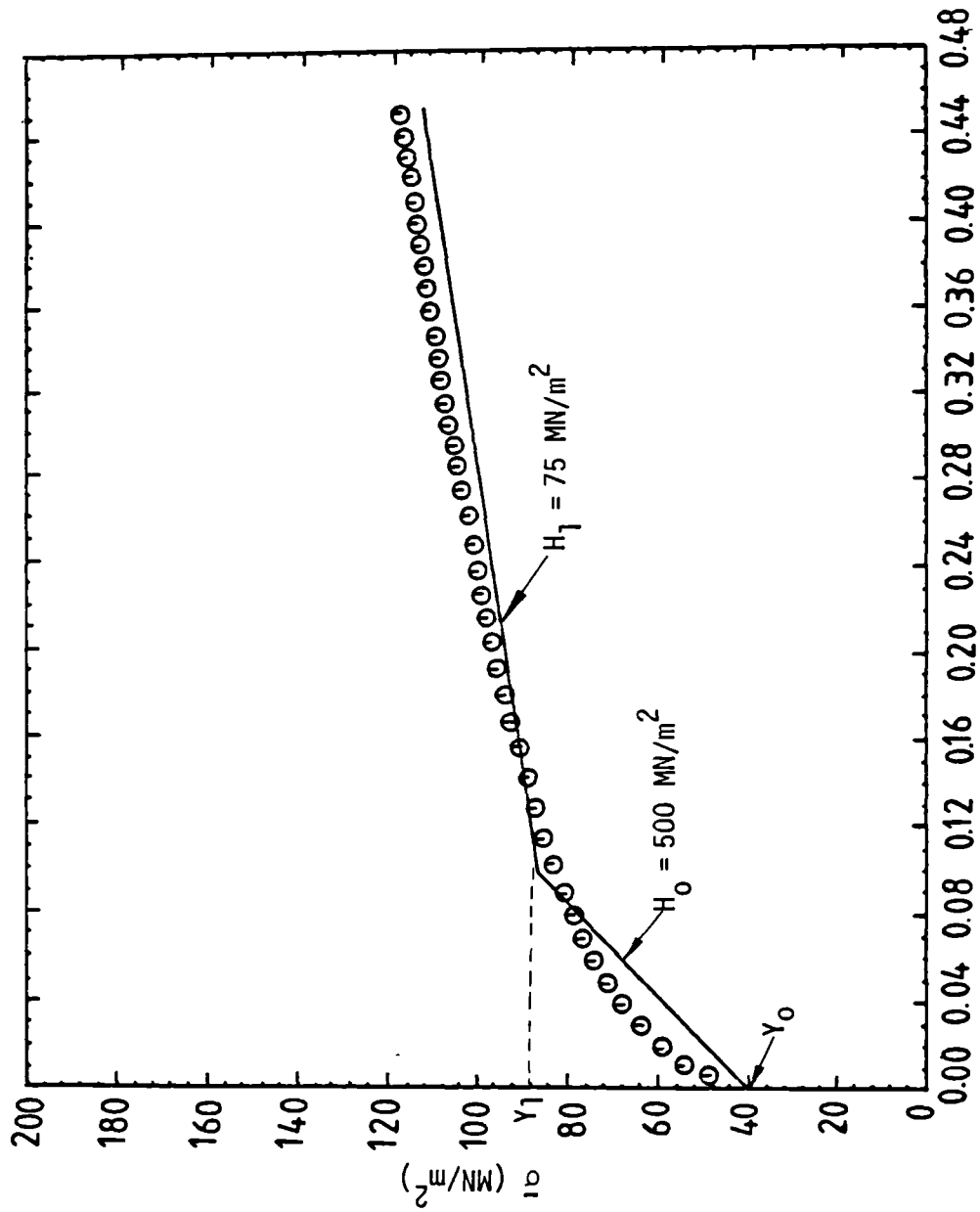


Fig. 6-2 Stress-strain curve employed in computer analysis for commercially pure aluminium.

changes of a circular ring in a uniaxial compression test was employed. The coefficient of friction for aluminium, under the experimental conditions, was found to be 0.2.

3- The contact nodal points are not allowed to move along the contact surfaces at all, i.e. these surfaces are perfectly rough, the condition of sticking friction.

6.2.4 Loads and bulge formation

6.2.4.1 Introduction

The initial computations were made on heading hollow billets for the three different frictional conditions explained in the previous section. In order to examine the validity and convergency of the computed results a comparison between theoretical and experimental results is made. The comparison which is made in terms of load/displacement curves and geometrical changes is also used to verify the amount of plastic deformation that can be introduced into the computer program without unrealistic errors developing.

For heading and open upsetting, the limiting values of free height and wall thickness of the original billet for the production of a hollow flanged component with a straight bore surface are obtained. Throughout the analysis the maximum percentage increase in the bore diameter $\frac{d_{max} - d_i}{d_i}$ is considered to represent the amount of bulging in the bore region.

The effect of restraining hydrostatic pressure on the changes in geometries and metal flow and also upsetting into restricted cavities are studied. The results are presented in terms of load/displacement characteristics, current configuration of the billet, particles' velocities, distribution of effective strain, etc.

6.2.4.2 A comparison of the theoretical and experimental results

To check the convergence and hence the validity of the computer program, a comparison of the theoretical and experimental results is made for heading a hollow billet of 25 mm inside diameter and 44 mm outside diameter which is upset to 34 per cent reduction in height. Fig. 6-3 compares the theoretical upsetting loads obtained for different friction conditions with the experimental findings.

The theoretical load/displacement curves in Fig. 6-3 consist of two distinguishable sections. In the first part, the load increases with a slope which corresponds to the elastic-plastic deformation of the material while the equivalent stresses of the post yielded elements are, in the main, less than *Y1* (see Fig. 6-2). The upsetting loads increase up to a point and then a rapid bend in the curves is observed after which the slope becomes approximately constant. This sharp bend in the load/displacement curve can be explained by considering the method of construction of the element stiffness matrices which depends on their corresponding equivalent stresses. For the post yielded elements, the stiffness matrices are first built by using the slope of the line AB in Fig. 6-2. When the equivalent stress of a post yielded element exceeds *Y1*, the element stiffness matrix is newly built using the slope of the line BC instead of AB. As the slope of the line BC is much smaller than that of the line AB (by nearly a factor of 10) this causes an abrupt drop in the element stiffness matrix and consequently a considerable drop in the element's resistance to deformation.

Comparison of the predicted load/displacement curve using a frictional condition of $\mu = 0.2$ with that obtained from the experiment reveals that at the early stages of the process the predicted loads are higher than their experimental values. The difference, however, tends to decrease after the sharp bend in the theoretical curve and the predicted loads increase at a

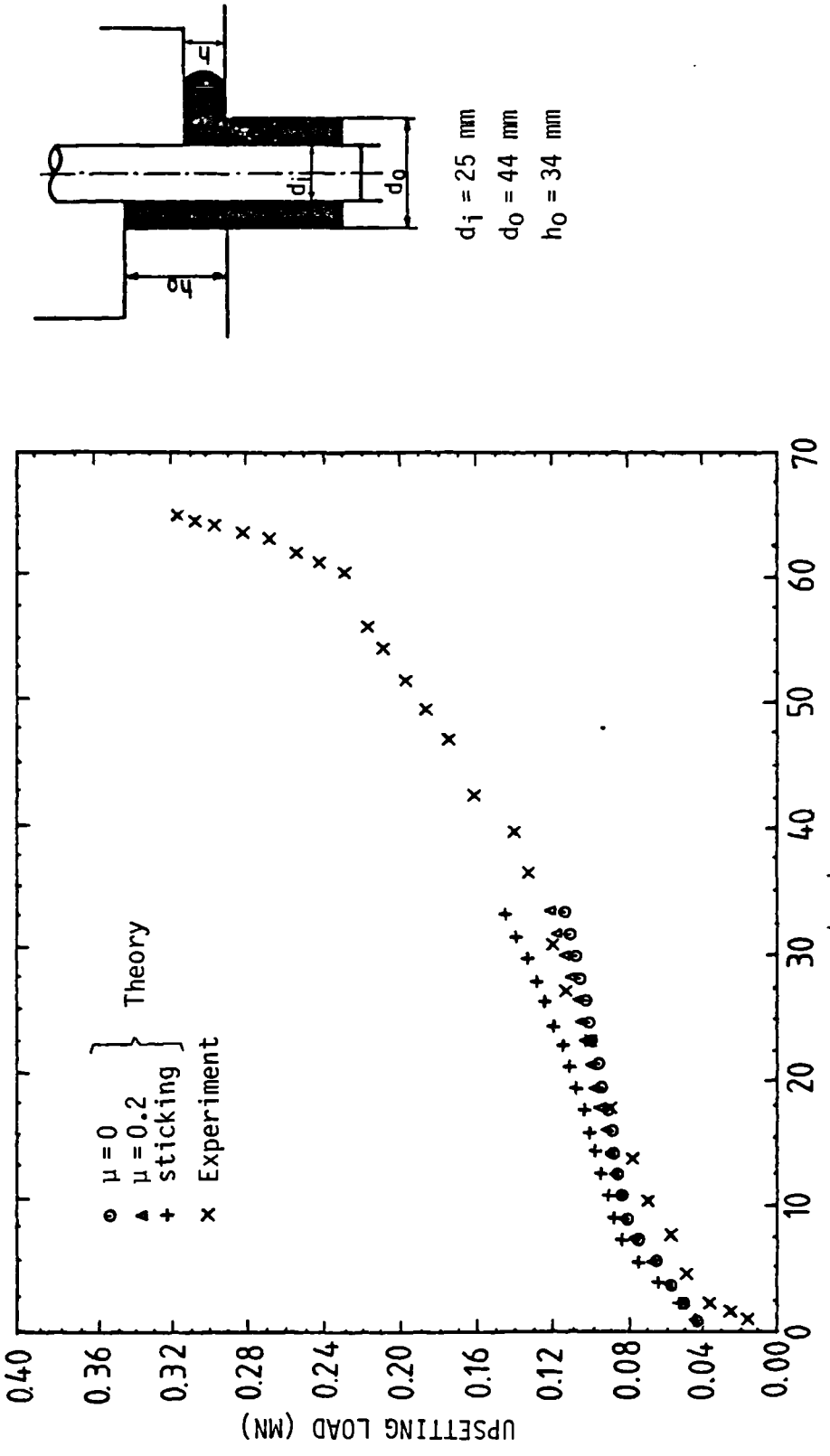


Fig. 6-3 Comparison of the theoretical and experimental load/displacement characteristics in heading hollow billets.

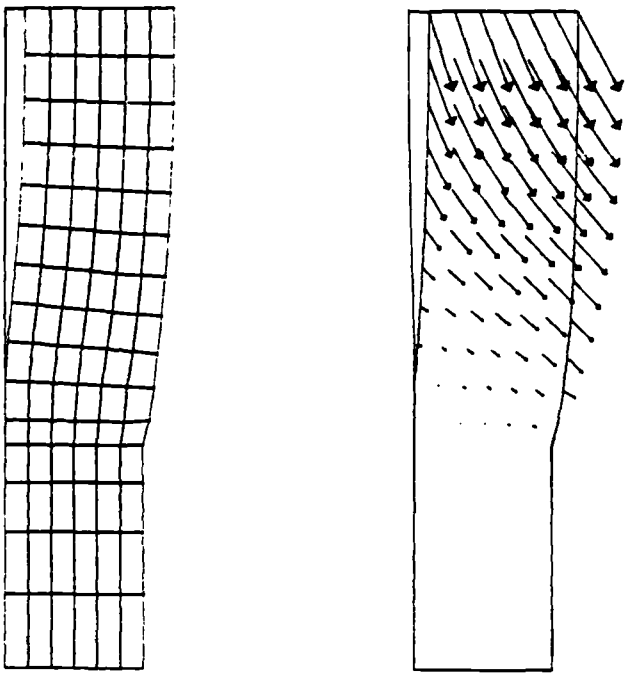
slower rate only to become lower than the experimental values at the later stages of deformation. After approximately 25 per cent reduction in height the experimental values of load begin to rise with a markedly higher rate, whereas the predicted loads continue to increase at a steady rate. This discrepancy may be explained as follows. The experimental results show that this sudden increase in load is due to rolling of the material onto the platen surfaces. As it can be seen from the distorted meshes shown in Fig. 6-6, the predictions neither produce "rolling up" nor show any tendency of this phenomenon up to a height reduction of 34 per cent. Therefore it may be concluded that the present method cannot predict the increase in upsetting load which occurs due to rolling of the metal onto the contact surfaces.

Comparison of the theoretical curves in Fig. 6-3 for the frictionless and sticking case show that the effect of the sticking friction on upsetting load is negligible at early stages of deformation and later it becomes considerable. The higher load obtained in sticking friction can be explained by additional constraints and different metal flow revealed by comparing the velocity distributions for smooth and rough platens (Figs. 6-4 and 6-5 respectively). At the early stages of the process, however, the higher load due to the deeper flow of metal in the sticking case is matched by an increase in load due to the extention of the contact surfaces the frictionless case.

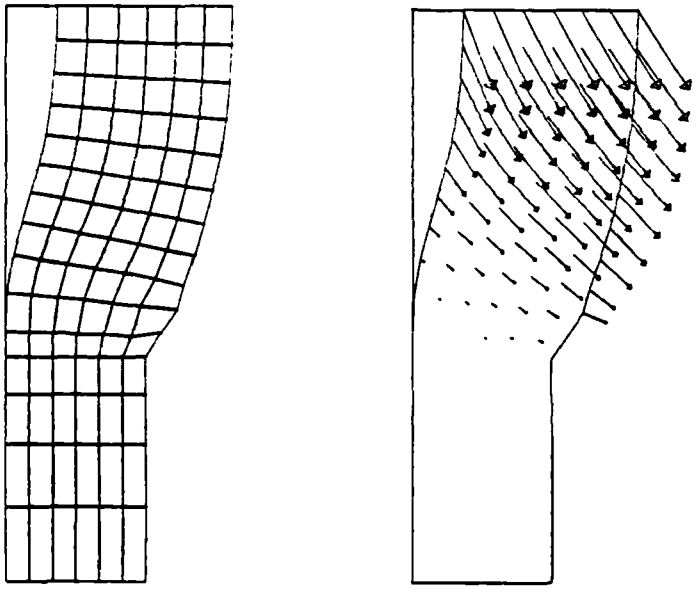
When the variation of upsetting load for Coulomb friction is compared with that of the frictionless case the curves show negligible difference. This is due to the fact that the effect of friction restraint offsets the effect of the larger contact surface obtained for smooth platens. Clearly, the friction forces result in the additional deformation of the free surface and in the prevention of extention of the contact surfaces.

In Figs. 6-6a & b, a comparison of the predicted bulge profiles is made with those observed experimentally for a hollow billet of 25 mm inside diameter, 44 mm outside diameter and the original unsupported height of 34 mm at 17 and 34 per cent height reductions (experimental free surfaces are shown in dotted lines). At 17 per cent, the theory predicts well the changes of shape but it is less accurate for 34 per cent reduction. The deviation for the outer free surface is attributed to the fact that the results of the finite element analysis do not predict rolling of the free surface material onto the platen surfaces. This discrepency is expected to increase if the computations were to proceed to deformations over 34 per cent due to the increasing amount of 'rolling up' observed in reality at larger deformations. Comparison of the bulge profiles at the inner surface is significant since the amount of initial bulge determines the extent of the fold which forms in the bore region at the final stages of the process. In spite of the discrepency observed over the shape of the bulge the predicted maximum increase in internal diameter is in reasonably good agreement with its real value even at 34 per cent reduction in height. The deviation in the shape of the inner bulge seems to be greater in the lower region, and is likely to increase since the predicted velocity distribution (Fig. 6-6b) shows that the particles in this region still have a tendency to move further away from the mandrel (in reality they continue to conform to the mandrel).

In the velocity distribution of Fig. 6-5b obtained for the sticking case, the rigid/plastic boundary at the lower part of the deforming zone and also the conical rigid zone formed at the punch/workpiece interface are shown in dotted lines. The particles in the rigid zone at the lower part have zero velocities, and those within the dead metal zone formed at the punch contact move in the z direction with the same speed as the punch.

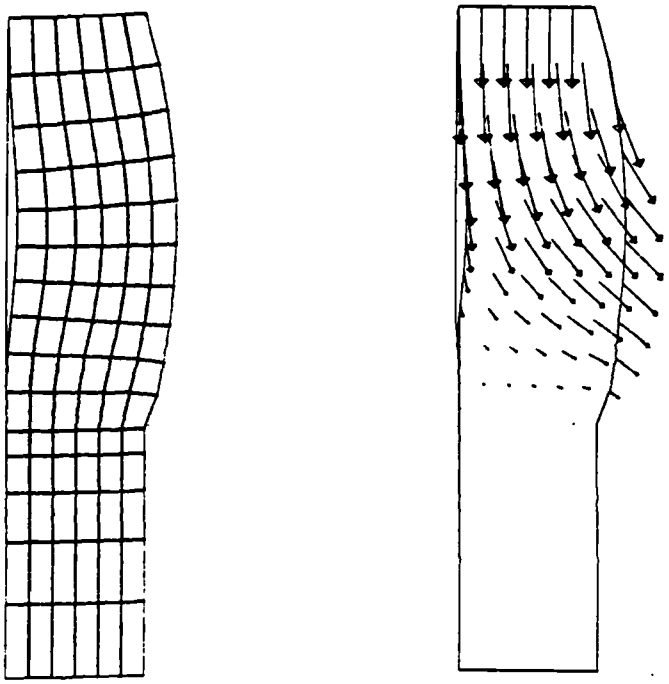


a) 17%

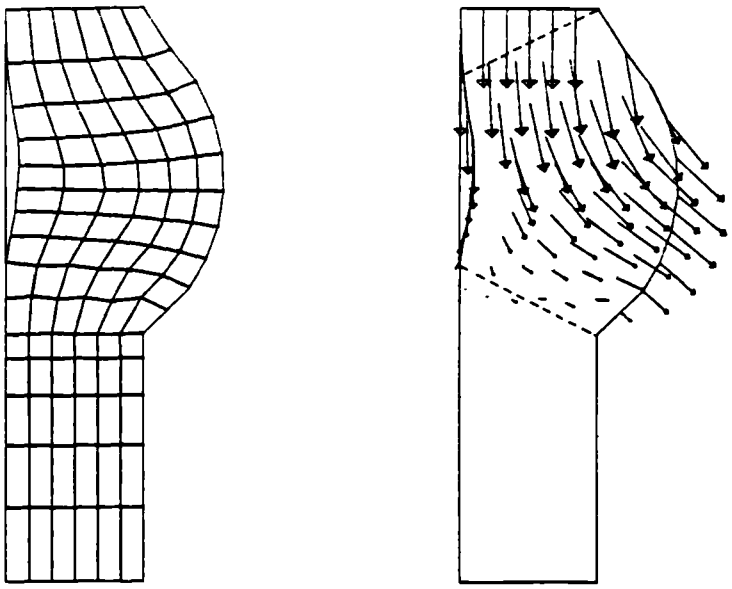


b) 34%

Fig. 6-4 Distorted grids and velocity distributions obtained for hollow billets under frictionless conditions at 17 and 34 per cent reductions (h_o = 34 mm, d_i = 25 mm, d_o = 44 mm).

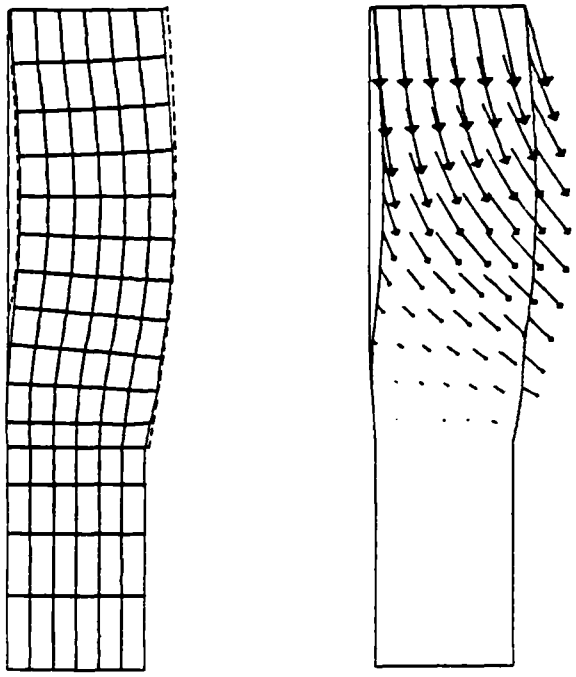


a) 17%



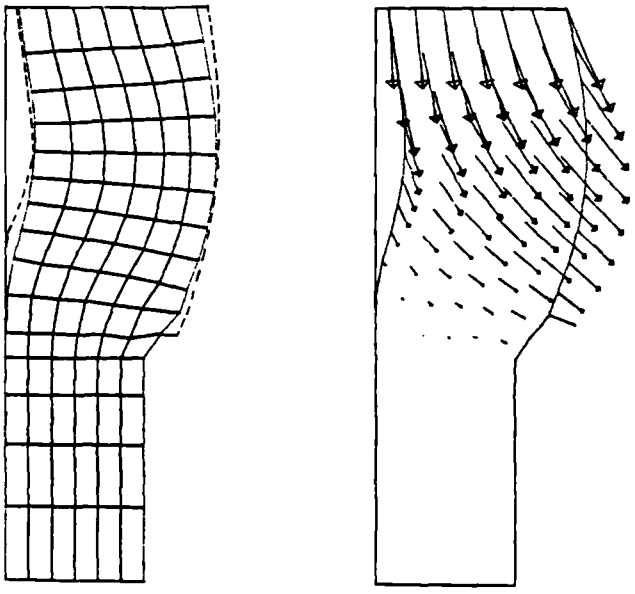
b) 34%

Fig. 6-5 Distorted grids and velocity distributions obtained for hollow billets for sticking friction at 17 and 34 per cent reductions (h_o = 34 mm, d_i = 25 mm, d_o = 44 mm).



a) 17%

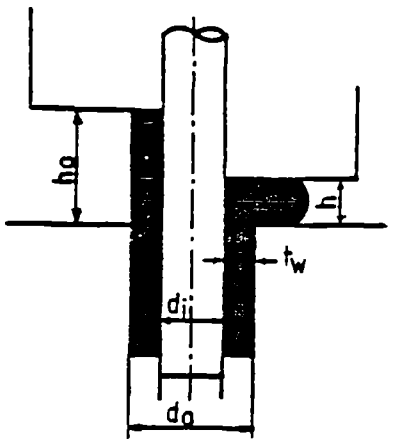
------- Experiment

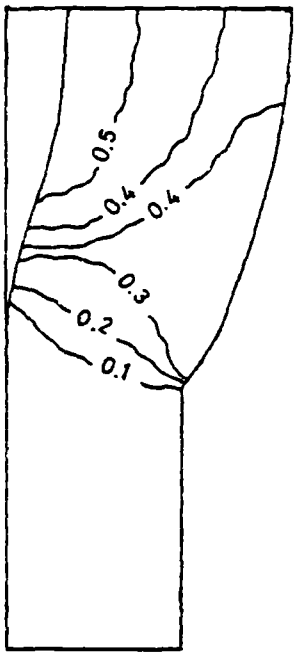


b) 34%

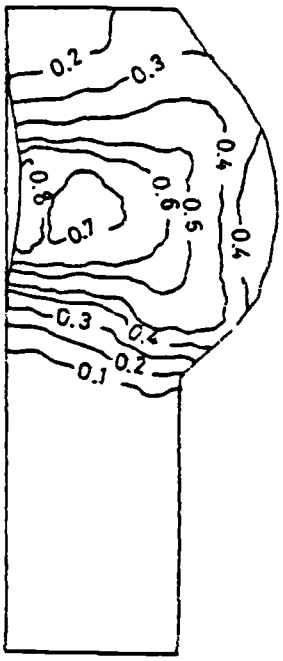
Fig. 6-6 Distorted grids and velocity distributions for hollow billets at $\mu = 0.2$, 17% and 34% reductions ($h_o = 34$ mm, $d_i = 25$ mm, $d_o = 44$ mm).

$d_i = 25$ mm
$d_o = 44$ mm
$h_o = 34$ mm





a) Frictionless



b) Sticking

Fig. 6-7 Contours of mean effective plastic strain ($\bar{\varepsilon}_p$) for hollow billets under various end conditions at 34 per cent reduction.

The boundaries approximately coincide with those observed in the etched cross section of the specimen upset under dry conditions at a corresponding amount of deformation (see Fig. 3-28d).

The distribution of the effective plastic strains for rough and smooth platens at 34 per cent reduction in height are compared in Fig. 6-7. In both cases the largest effective plastic strain occurs at the bore surface half way between the platens. The strains in the neighbourhood of the top platen are greater for smooth contact surfaces (Fig. 6-7a). This is the result of more bulging during upsetting with rough platens which leads to less deformation of the metal near the contact surfaces.

Throughout the rest of the study of the heading and open upsetting processes the frictional coefficient of $\mu = 0.2$ will be used, because of the relatively good agreement of the theoretical results with the experimental findings in that case. A maximum height reduction of 34 per cent is allowed in the computer program, since the errors of the theoretical predictions (for upsetting loads and geometrical changes) increase considerably if the computations continued.

Although there was a difference in the shape of the bulge profiles between the experimental and theoretical results, the behaviour of the material in the region of the maximum increase in internal diameter (where the final defect of the bore surface occurs) was well predicted.

6.2.4.3 Effect of the original billet geometry on deformation

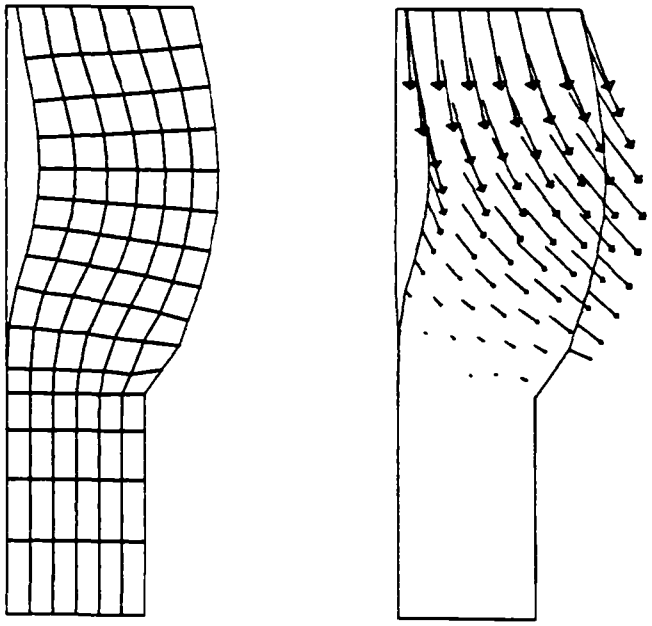
To investigate the effect of the original geometries of the billet on deformation, the program was run for billets of various wall thicknesses and different initial unsupported heights.

Fig. 6-8 compares the grid distortions and velocity distributions for identical wall thicknesses and original unsupported heights of 23 and

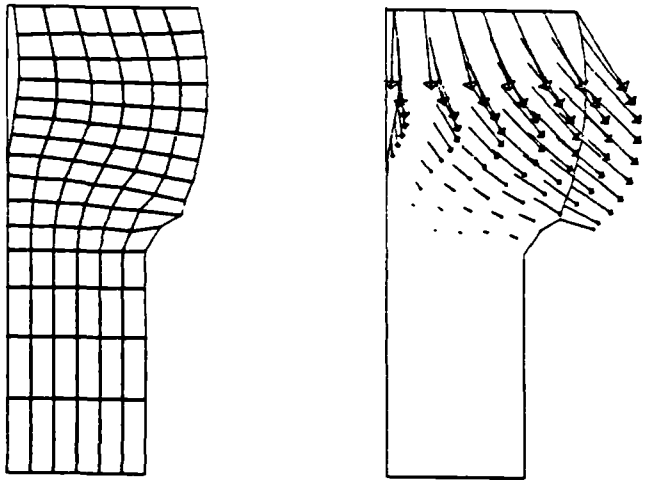
38 mm at 34 per cent reduction in height. For the greater free height the variation of the radial velocity with height and bulging of the free surfaces are more pronounced. This is because when h_o is higher the radial flow of metal particles at the middle region of the free height is less affected by the restraint of frictional forces. Larger amounts of upsetting for the billet of shorter height results in the formation of larger contact surfaces, due to less bulging of the free surfaces. The maximum increase in internal diameter for hollow billets of different original unsupported heights ranging from 23 to 38 mm is shown in Fig. 6-9 at various stages of deformation. $\frac{dmax - di}{di}$ increases with the initial unsupported height h_o, and the rate of this increase is higher for specimens greater values of h_o. The intersection of the curves with the vertical axis gives the value of h_o for which the increase in internal diameter is zero. Since all lines intersect the vertical axis at the same point, the results indicate that, if there is no bulging in the early stages of deformation, none will occur at the later stages either.

Fig. 6-10 shows the effect of the original free height on the maximum increase in internal diameter for various wall thickness/internal diameter ratios (t_w/d_i) at 17 per cent reduction in height. The maximum values of h_o for which zero increase in intenal diameter results are found for various values of t_w/d_i by extrapolating the curves to the h_o axis. The computations were repeated for these values of h_o which confirmed that zero increase in internal diameter would result.

Fig. 6-11 shows the maximum increase in internal diameter for different t_w/d_i ratios ranging from 0.14 to 0.60 and identical values of h_o at various stages of the deformation. The increase in the bore diameter increases with a decrease in wall thickness. This is because, for thinner specimens, the



a) $h_o = 38$ mm



b) $h_o = 23$ mm

Fig. 6-8 Distorted grids and velocity distributions obtained for $t_w/d_j = 0.38$ for various initial unsupported heights at 34 per cent reduction in height.

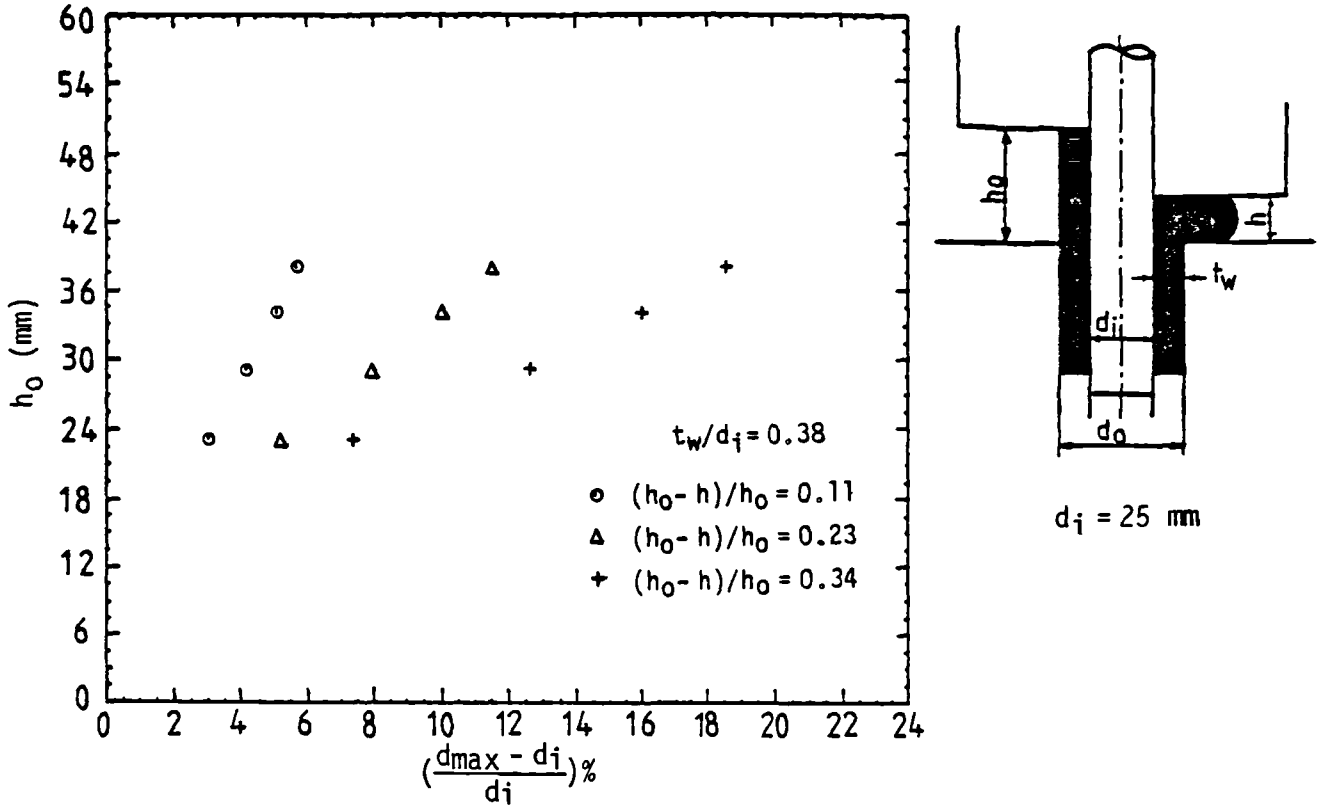


Fig. 6-9 Effect of initial unsupported height on the maximum increase in internal diameter for heading at various deformations.

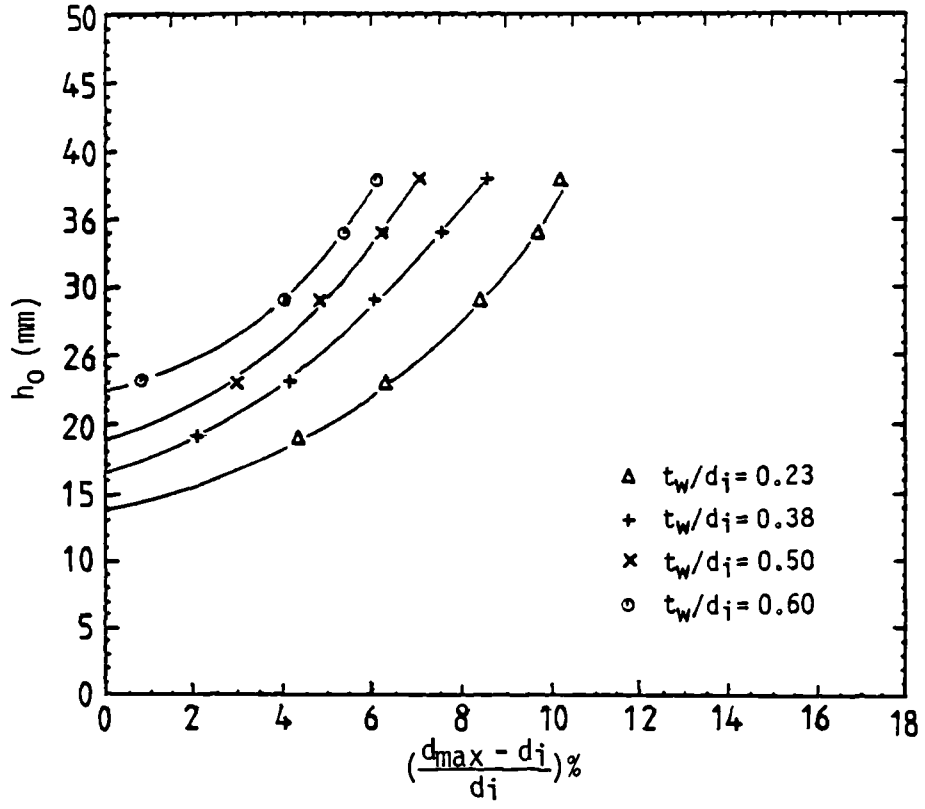


Fig. 6-10 Effect of initial unsupported height on the maximum increase in internal diameter for heading for various wall thicknesses at $\frac{h_o - h}{h_o} = 0.17$.

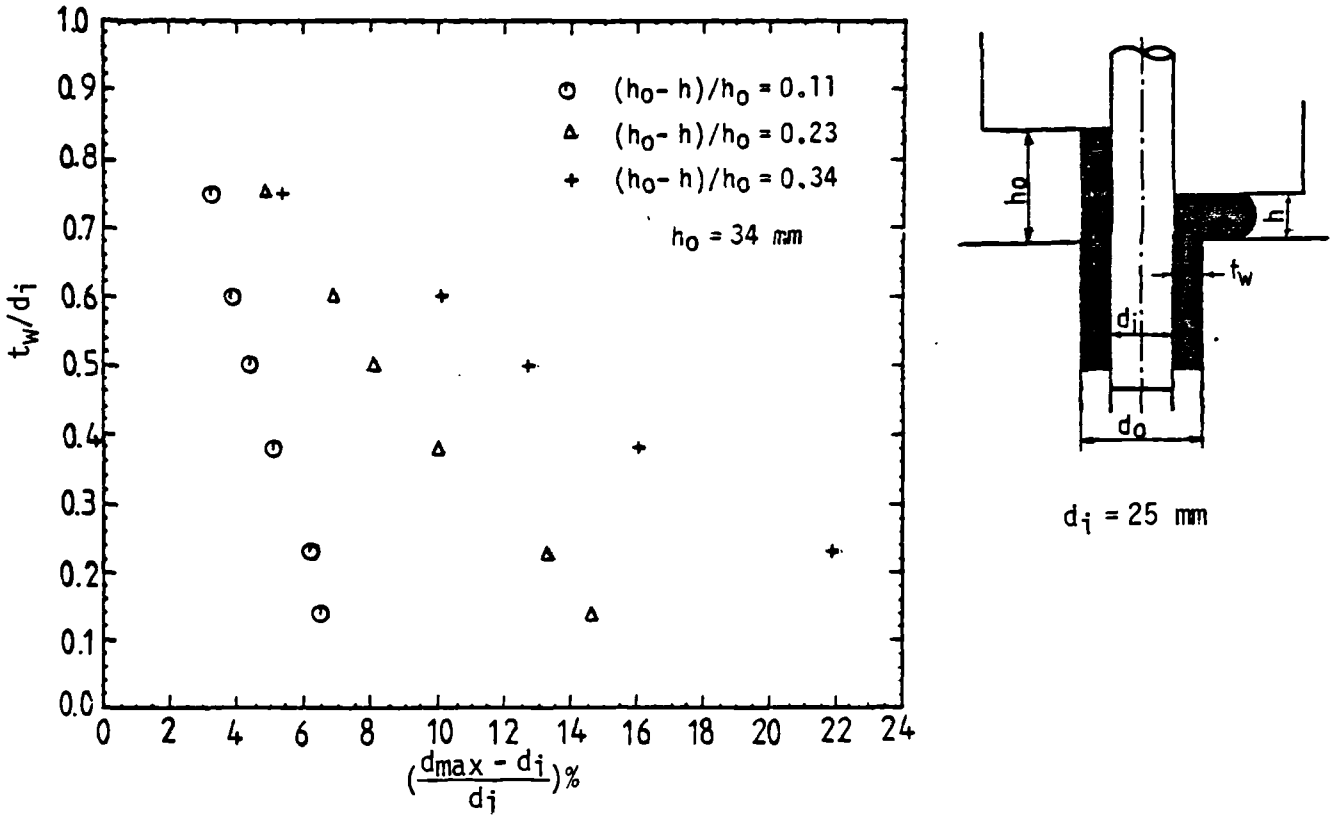


Fig. 6-11 Effect of billet wall thickness on the maximum increase in internal diameter for heading.

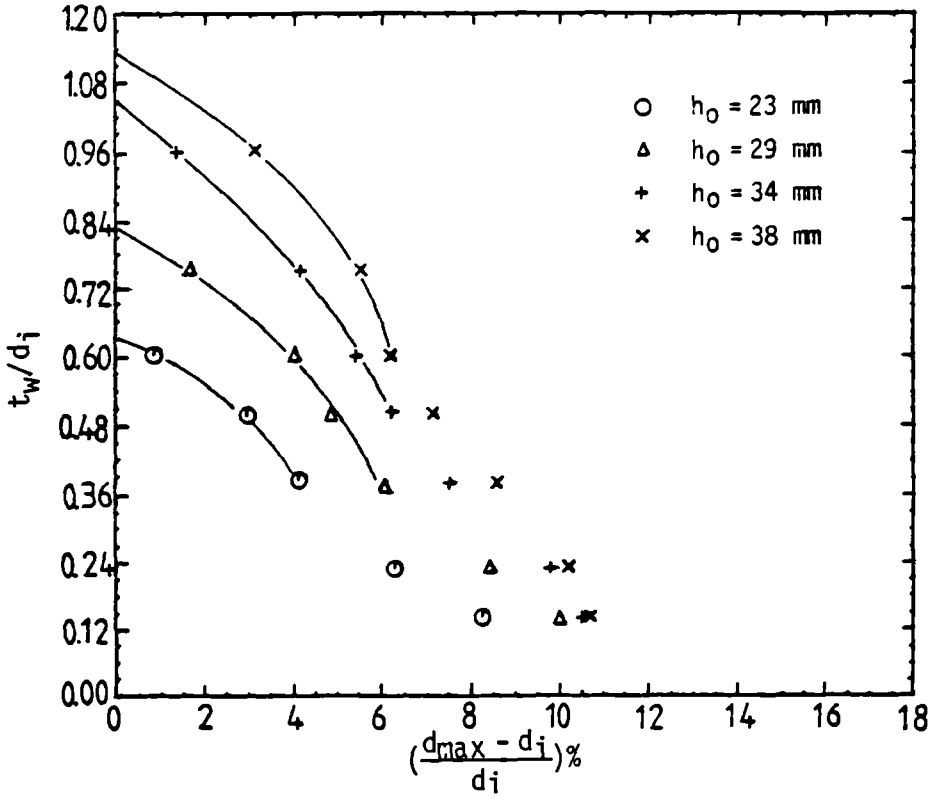
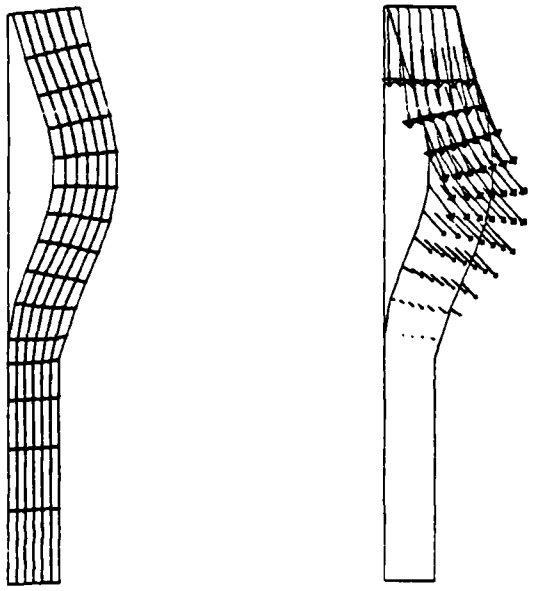
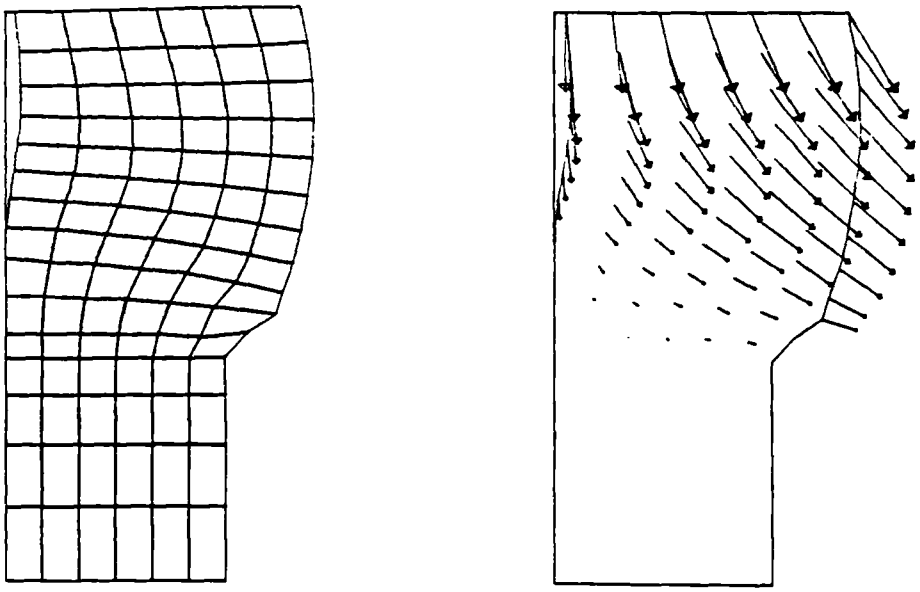


Fig. 6-12 Effect of wall thickness on the maximum increase in internal diameter for heading billets of various free heights at $\frac{h_o - h}{h_o} = 0.17$.



a) $t_w/d_i = 0.14$



b) $t_w/d_i = 0.60$

Fig. 6-13 Distorted grids and velocity distributions obtained for heading hollow billets of $h_o = 34$ mm for various wall thicknesses at 34 per cent reduction in height.

restraint imposed by the surrounding material is less at the bore region. The increased bulging for the billet of lower wall thickness can be clearly seen in Fig. 6-13, where the predicted grid distortions and velocity distributions are compared for wall thickness/internal diameter ratios of 0.14 and 0.60 at 34 per cent reduction in height. In the thinner billet the variation of the radial velocity along the free height is more pronounced and deformation occurs almost entirely by bulging with no significant increase in the wall thickness.

Again, the convergence of the curves in Fig. 6-11 indicates that $(t_w/d_i)_{at\ \frac{d_{max}-d_i}{d_i}=0}$ is independent of the amount of deformation. The effect of the wall thickness on the maximum increase in internal diameter for various original unsupported heights ranging from 23 to 38 mm is shown in Fig. 6-12, at 17 per cent reduction in height. The intersections of these curves with the vertical axis give the minimum values of t_w/d_i for which a product with parallel bore surface can be obtained, for different initial unsupported heights.

The experimental results in chapter 3 revealed that the failure in the bore region of a hollow flanged specimen which appears as a fold is a direct result of the initial bulging of the inner surface. If a hollow flanged component with a straight and parallel bore surface is termed as sound , then the limiting values of the original dimensions of the billet for a sound product (obtained from Figs. 6-10 and 6-12) are shown in Fig. 6-14.

The results obtained for the billets of various internal diameters with identical t_w/d_i and similar initial unsupported heights show that the maximum increase in internal diameter is greater for billets of the smaller bore size at the same amount of deformation. This reveals that, for two billets with identical values of t_w/d_i and h_o, the amount of bulging

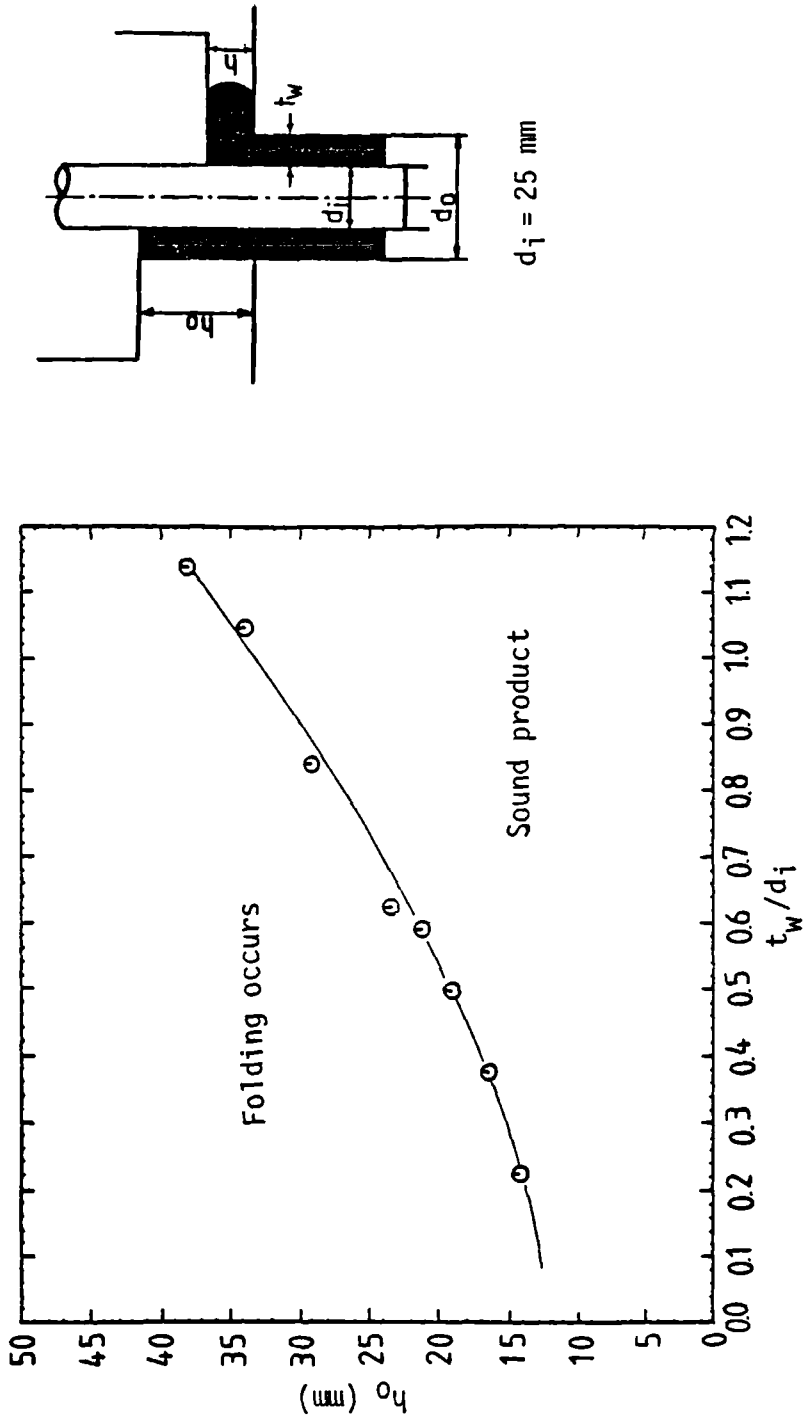


Fig. 6-14 Limiting values of the original size of the billet for sound products, heading.

and therefore the extent of folding is larger for the smaller bore diameter billet. Therefore the graph presented in Fig. 6-14 for hollow billets of $d_i = 25$ mm would be expected to shift downwards for smaller billets ($d_i < 25$ mm) and upwards for billets of larger internal diameters ($d_i > 25$ mm).

Fig. 6-15 compares the distribution of the mean effective plastic strain for specimens of various original geometries at 34 per cent reduction in height. The difference between the various cases is not significant. Generally, the maximum strain occurs in the bore region at mid-length of the head. The strain varies along the bore surface becoming more uniform along the outer free surface. There is a large gradient of strain at the lower part near the rigid zone which is indicative of the intense shear between the rigid and the deforming zones.

The hoop tensile stress is responsible for opening up the initial longitudinal defects in the outer free surface of the billet. Figs. 6-16a, b&c show the distribution of the hoop stress for different original geometries at 34 per cent reduction in height. σ_θ is compressive in most of the billet with its minimum at the bore region midway along the head, but it becomes tensile at the outer free surface. The tensile hoop stress at the free surface decreases with a decrease in the original unsupported height and increases with reduction in wall thickness.

The distribution of the axial component of stress throughout the deformed billet is shown in Fig. 6-16d for a billet of 34 mm original free height and $t_w/d_i = 0.38$ at 34 per cent reduction in height. Within the deforming region the value of σ_z appears to increase towards the bore and is almost uniform in the vicinity of the punch surface but varies greatly near the rigid zone. To check the accuracy of these predictions the

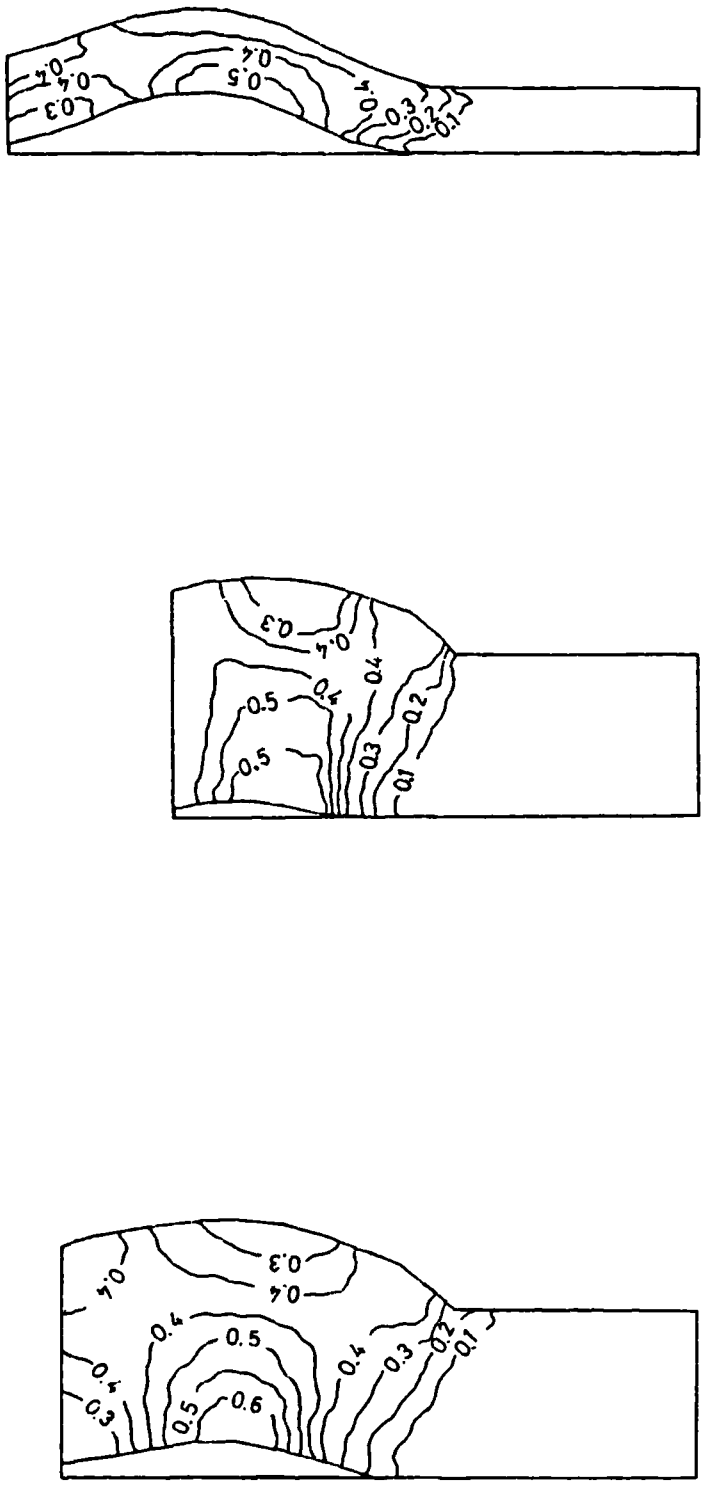


Fig. 6-15 Mean effective plastic strains ($\bar{\varepsilon}_p$) in heading hollow billets of various original geometries at 34 per cent reduction in height.

a) d_i = 25 mm, h_o = 34 mm, t_w/d_i = 0.38

b) d_i = 25 mm, h_o = 23 mm, t_w/d_i = 0.38

c) d_i = 25 mm, h_o = 34 mm, t_w/d_i = 0.14

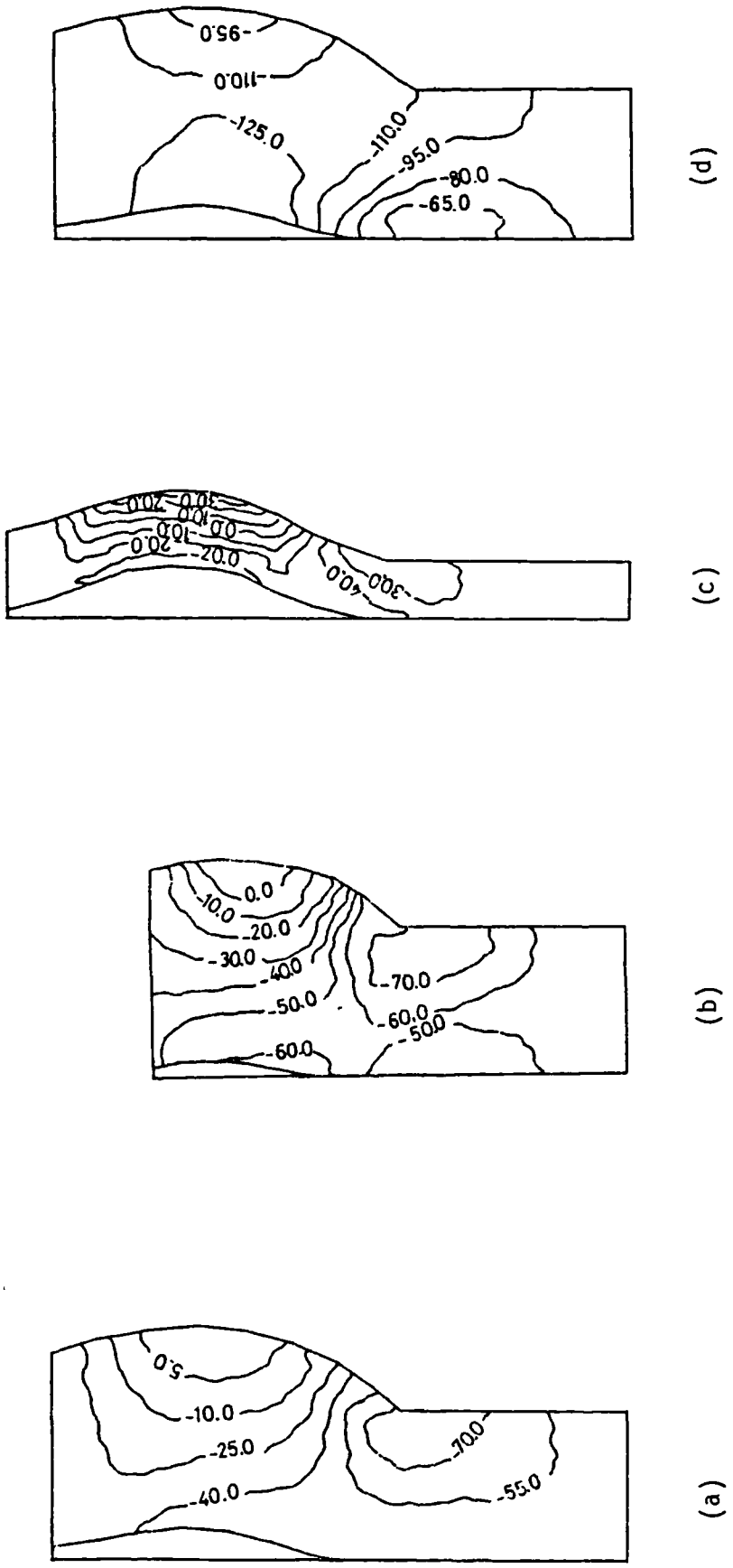


Fig. 6-16 Contours of hoop stress (a, b&c) and axial stress (d) in heading hollow billets of various original geometries at 34 per cent reduction in height.

a&d) $d_i = 25$ mm, $h_o = 34$ mm, $t_w/d_i = 0.38$

b) $d_i = 25$ mm, $h_o = 23$ mm, $t_w/d_i = 0.38$

c) $d_i = 25$ mm, $h_o = 34$ mm, $t_w/d_i = 0.14$

calculated value of axial stress at the punch contact surface was compared with the upsetting pressure obtained experimentally and good agreement was found.

Similar calculations have been performed for open upsetting and the results are presented in Figs. 6-17 to 6-21. The limiting values of the original billet geometries for the production of sound products are shown in Fig. 6-21. For comparison the corresponding curve which was obtained earlier for heading (from Fig. 6-14) is replotted here as a dotted line. Comparison of the curves show that, except for thin-walled tubes ($t_w/d_i < 0.22$), a shorter initial unsupported height is required for open upsetting to avoid bulging of the inner surface. The difference is more pronounced for billets of thicker walls because the higher restraint imposed on the radial flow of metal in open upsetting becomes more effective as the wall thickness increases. This is also clear from Figs. 6-22 and 6-13 which show the grid distortions and velocity distributions for thin ($t_w/d_i = 0.14$) and thick ($t_w/d_i = 0.60$) walled billets at 34 per cent reduction in height for open upsetting and heading.

In order to check the validity of the curves in Fig. 6-21 upsetting tests were carried out for hollow billets of $t_w/d_i = 0.38$ ($d_i = 25$ mm, $d_o = 44$ mm) with original free height of 16.5 and 19 mm for heading and open upsetting respectively. The bore surfaces of the products remained reasonably straight and parallel and close to the mandrel, thus confirming Fig. 6-21 at these particular points.

6.2.4.4 Effect of hydrostatic pressure during conventional upsetting

In recent years, the application of hydrostatic pressure in metal forming processes has become the subject of great interest. A considerable amount of work has been carried out, applying hydrostatic pressure to

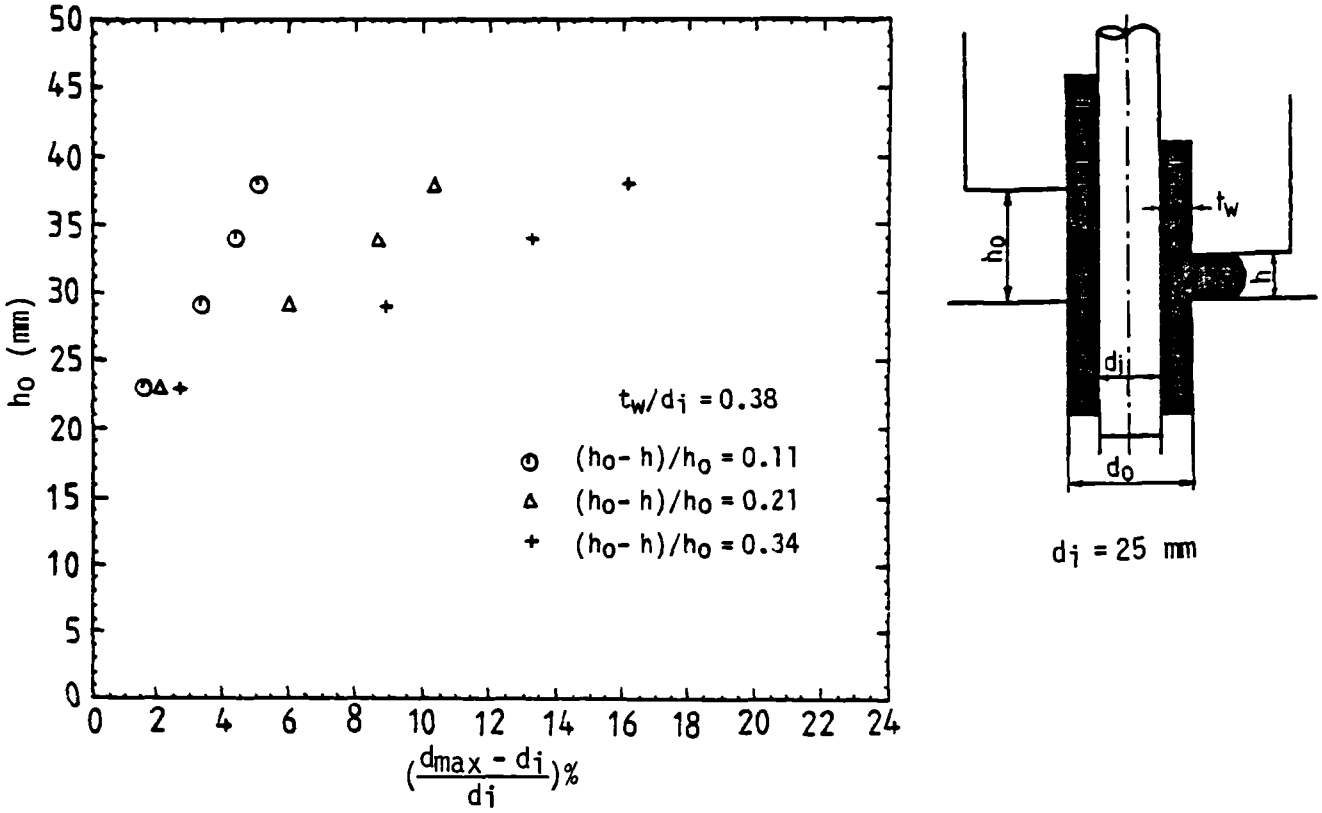


Fig. 6-17 Effect of initial unsupported height on the maximum increase in internal diameter for open upsetting.

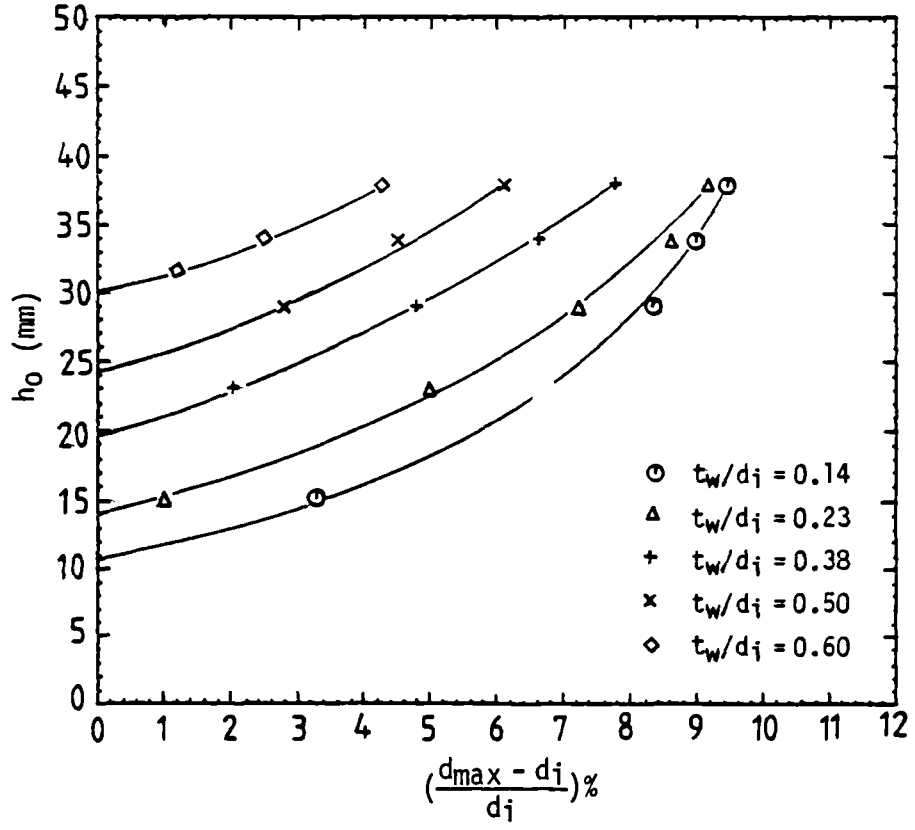


Fig. 6-18 Effect of initial unsupported height on the maximum increase in internal diameter for open upsetting for various wall thicknesses at $\frac{h_o - h}{ho} = 0.17$.

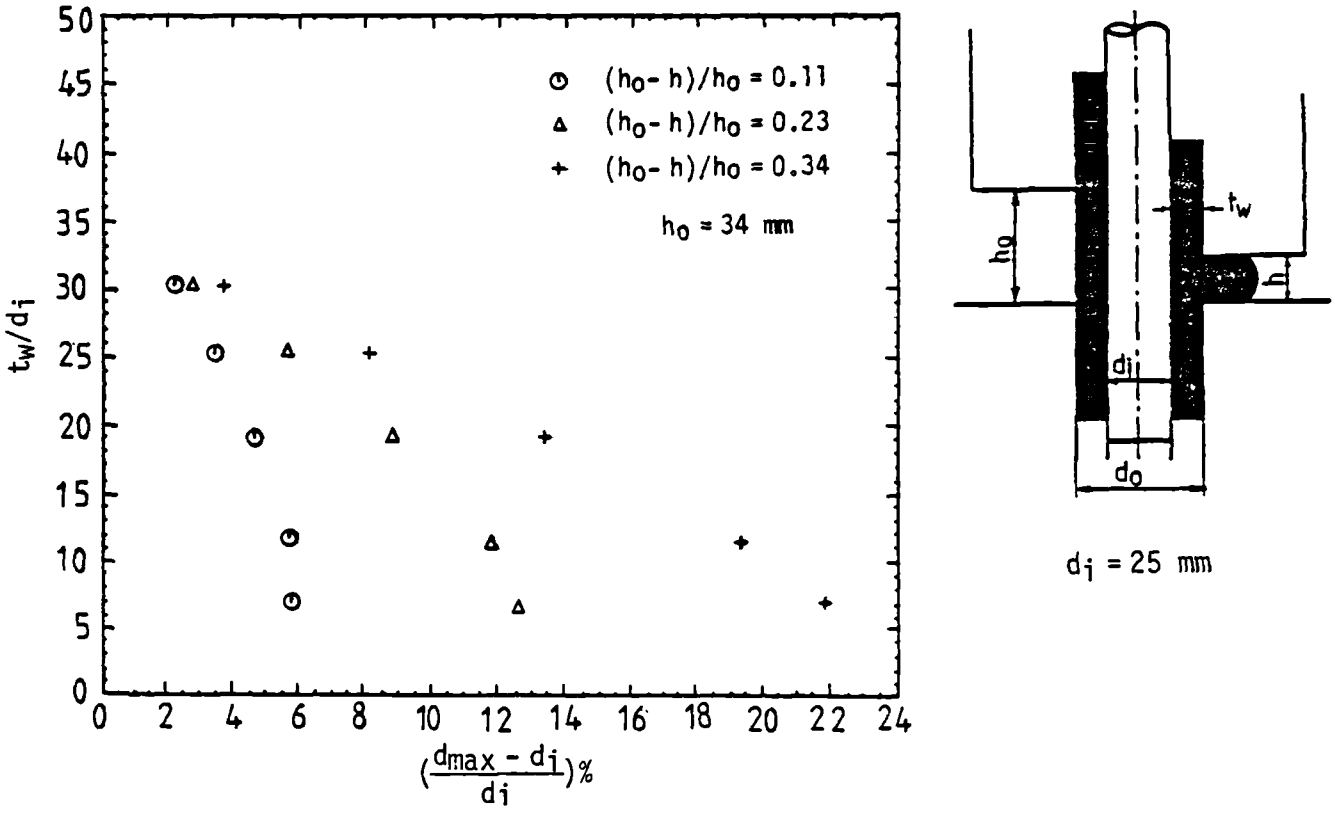


Fig. 6-19 Effect of original wall thickness on the maximum increase in internal diameter for open upsetting.

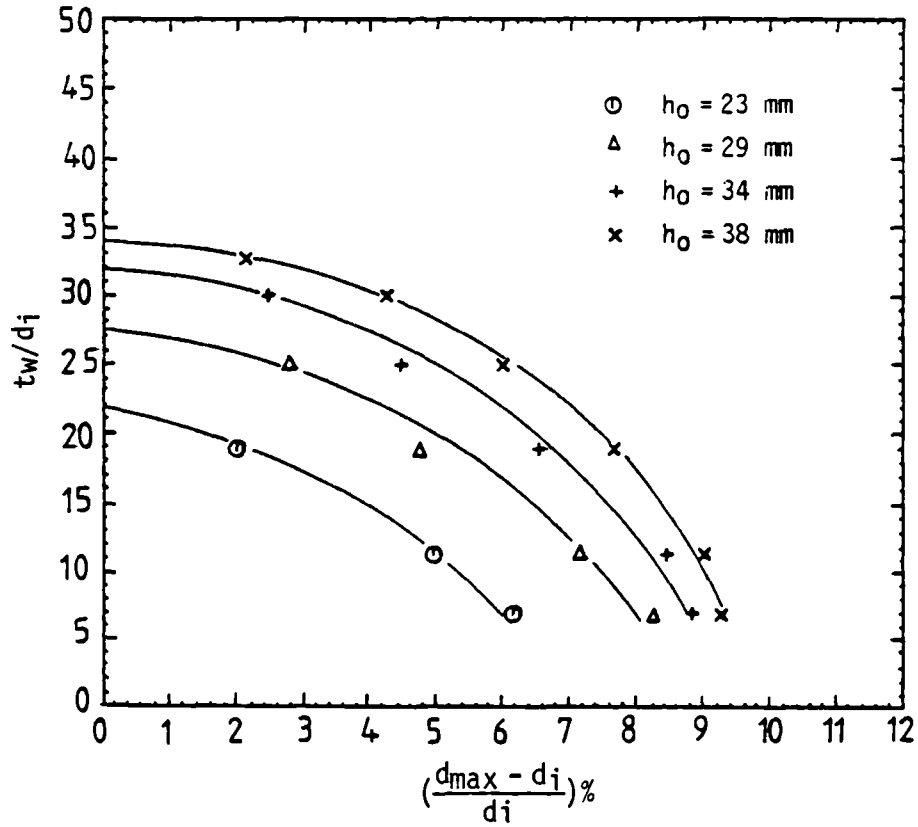


Fig. 6-20 Effect of original wall thickness on the maximum increase in internal diameter for open upsetting for various original free heights at $\frac{h_o - h}{h_o} = 0.17$.

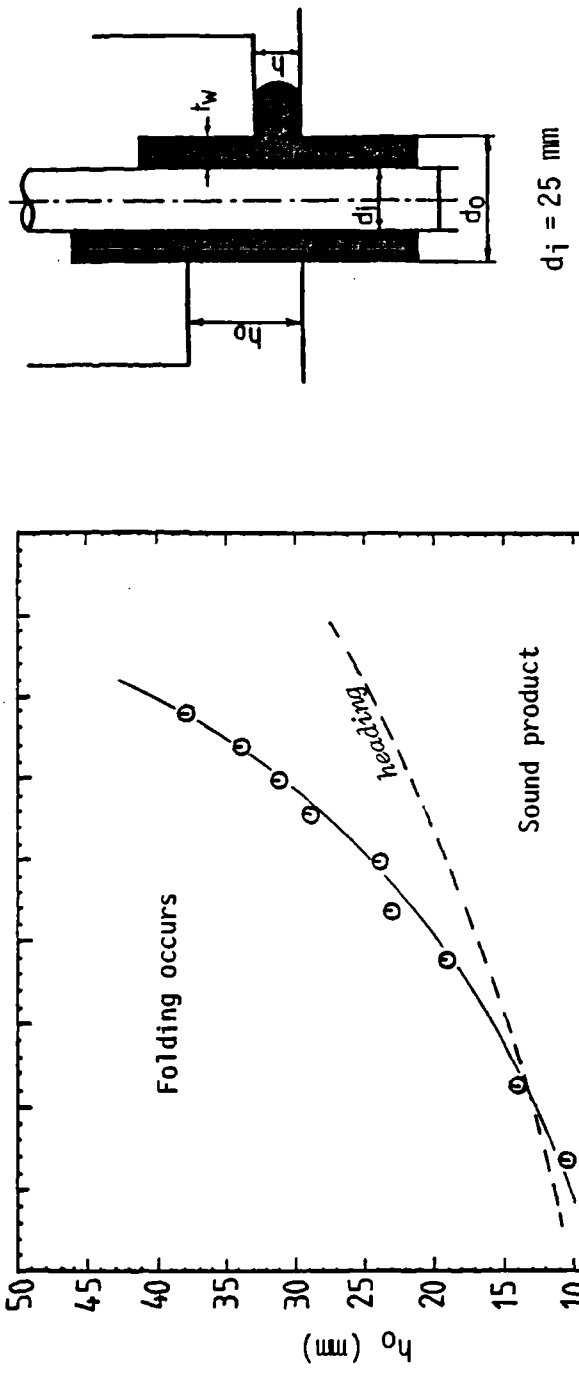
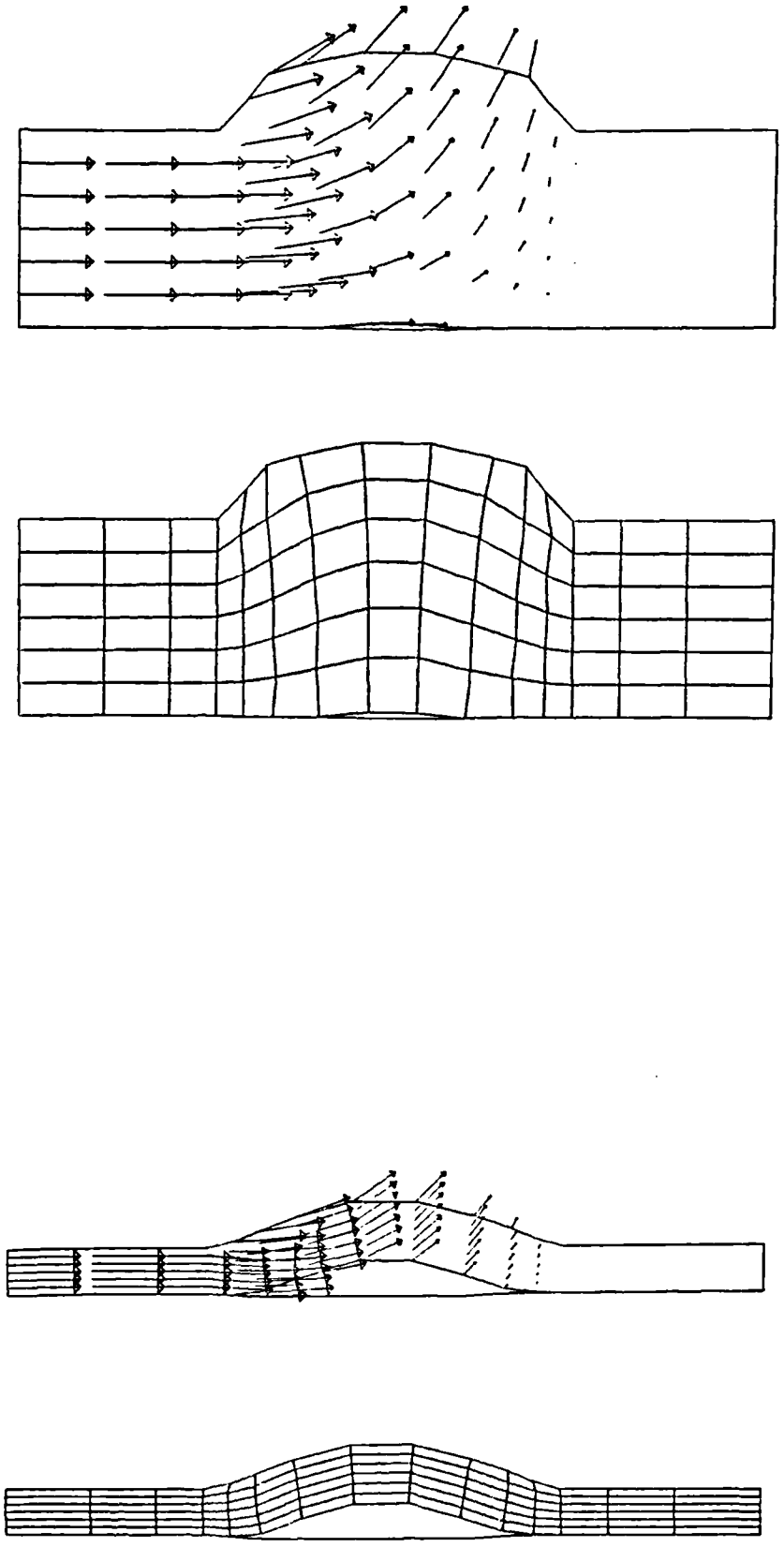


Fig. 6-21 Limiting values of original geometries for sound products in open upsetting hollow billets.



a) $t_w/d_i = 0.14$

b) $t_w/d_i = 0.60$

Fig. 6-22 Distorted grids and velocity distributions for open upsetting of hollow billets of $h_o = 34$ mm for various wall thicknesses at 34 per cent reduction in height.

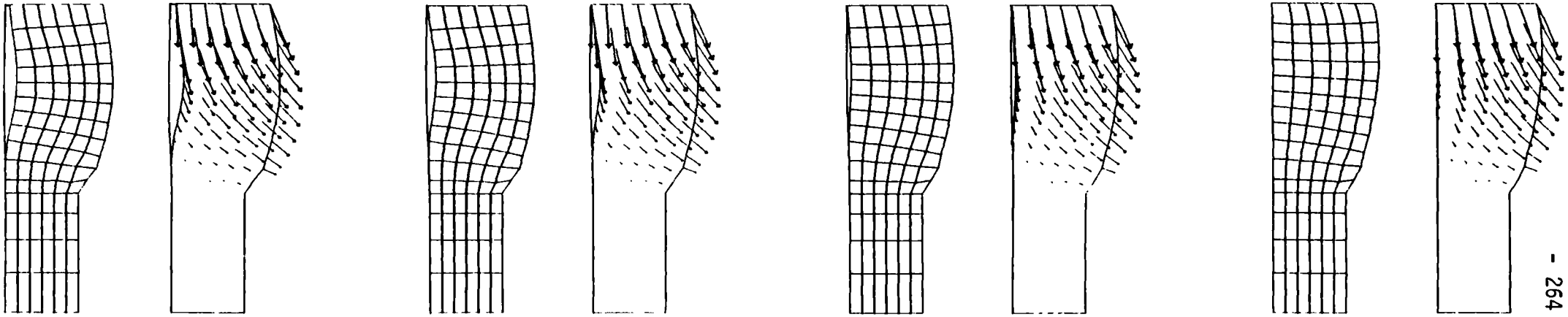
various processes such as extrusion (*98,99*), upsetting (*43-46*), drawing (*100, 101*), etc. The aim of these works has been to eliminate the defects in the products which would otherwise occur. The introduction of hydrostatic pressure, which may be implemented by a fluid or by other means, has often led to sound products.

Several investigators *(101, 102)* have studied the effect of superimposed high fluid pressure on the mechanical properties of materials. The properties, particularly ductility, of a product formed by a given deformation process were found to improve if the deformation is carried out in the presence of a high hydrostatic component of stress. This is of particular importance in the cold working of difficult materials.

Several workers *(43-46)* investigated the prevention of defects in the flange region during injection upsetting against hydrostatic pressure, such as non-uniformity of the flange thickness and the formation of cracks or necking at the flange periphery which often occur due to the generation of tensile stresses in this region. Successfully formed products are reported to have been obtained for a number of low ductility materials. The hydrostatic pressure was applied by forcing a low strength matrix material *(44)* or oil *(45)* to the flange.

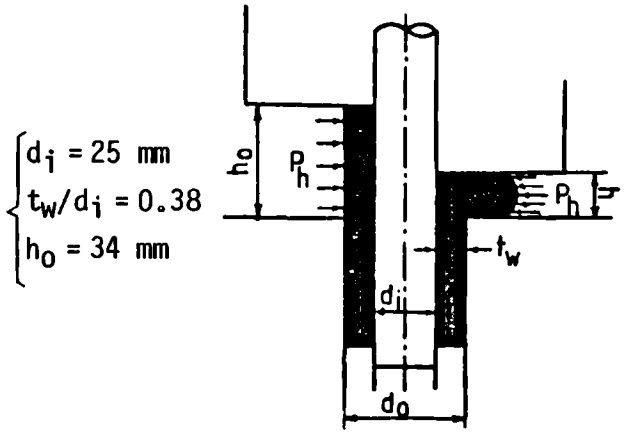
In the following the effect of hydrostatic pressure on the mode of deformation in conventional upsetting will be discussed.

The predicted grid distortions and velocity distributions obtained in heading under various amounts of hydrostatic pressure, for a specimen of 34 mm original unsupported height and t_w/d_i of *0.38* at 34 per cent reduction are shown in Fig. 6-23. The patterns of velocity distribution show that the radial velocity along the unsupported height is more uniform at larger hydrostatic pressures. When higher restraining pressure is imposed bulging of the free surface is less pronounced and the shearing of metal (which



a) $P_h = 0$ b) $P_h = 25\ MN/m^2$ c) $P_h = 50\ MN/m^2$ d) $P_h = 75\ MN/m^2$

Fig. 6-23 Distorted grids and velocity distributions in heading of hollow billets at 34 per cent reduction in height under various hydrostatic pressures.



occurs near the punch contact surface and also at the lower part of the deforming region) is less severe. The figures also show a higher increase in punch/specimen contact area for higher values of hydrostatic pressure, which is indicative of higher amounts of upsetting.

Fig. 6-24 shows the maximum increase in internal diameter for hollow billets subjected to various hydrostatic pressures, ranging from 15 to 70 MN/m^2, at various stages of deformation.

It is of interest to note that large hydrostatic pressure would be required to eliminate bulging entirely as against reducing it to a low value. For example, for a specimen at 34 per cent reduction in height a hydrostatic pressure of 50 MN/m^2 would be required to reduce $\frac{d_{max} - d_i}{d_i}$ from 16 per cent to 5 per cent but almost twice that pressure would be needed to prevent the occurrence of any bulging.

Fig. 6-25 shows the effect of hydrostatic pressure on the maximum increase in internal diameter for various original unsupported heights ranging from 23 to 38 mm, at 17 per cent reduction in height. Extrapolating the curves to intersect the vertical axis gives the minimum values of hydrostatic pressure for which billets with parallel bore surfaces can be produced for various original unsupported heights. Similarly the maximum values of original free heights, for which zero increase in internal diameter would result, are shown in Fig. 6-26. The limiting values of hydrostatic pressures and original free heights which ensure sound products for $t_w/d_i = 0.38$ are given in Fig. 6-27.

Computations have been repeated for hollow billets of various wall thicknesses, with identical original free heights of 34 mm, and the results are presented in Figs. 6-28 to 6-30. Fig. 6-29 shows that in the absence of hydrostatic pressure a reduction in wall thickness results in a greater

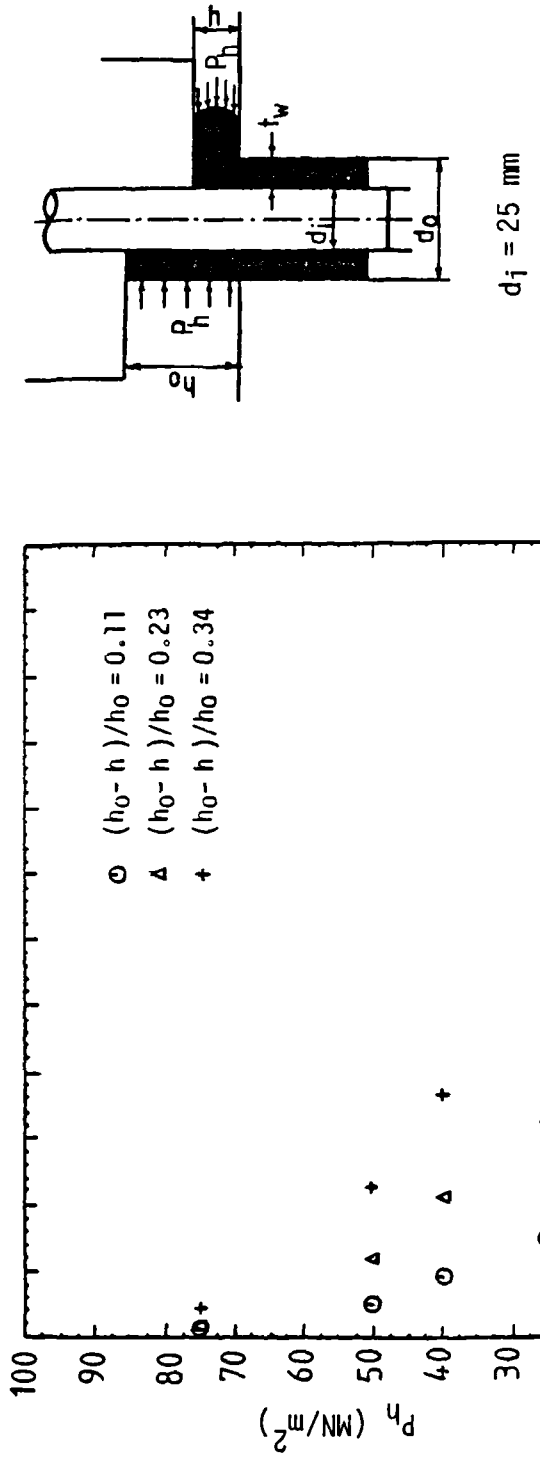


Fig. 6-24 Effect of hydrostatic pressure on the maximum increase in internal diameter in heading.

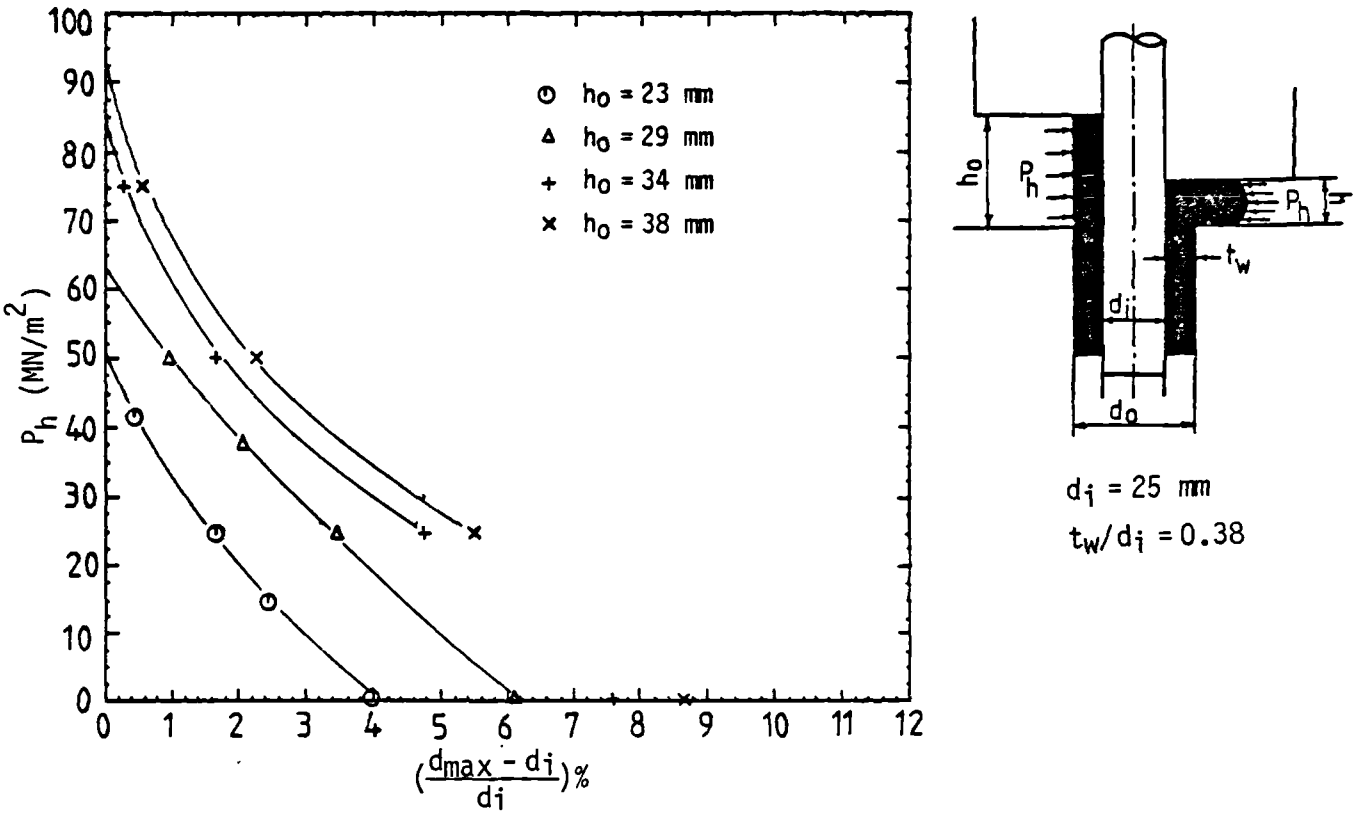


Fig. 6-25 Effect of hydrostatic pressure on the maximum increase in internal diameter in heading at various initial unsupported heights and $\frac{h_o - h}{h_o} = 0.17$.

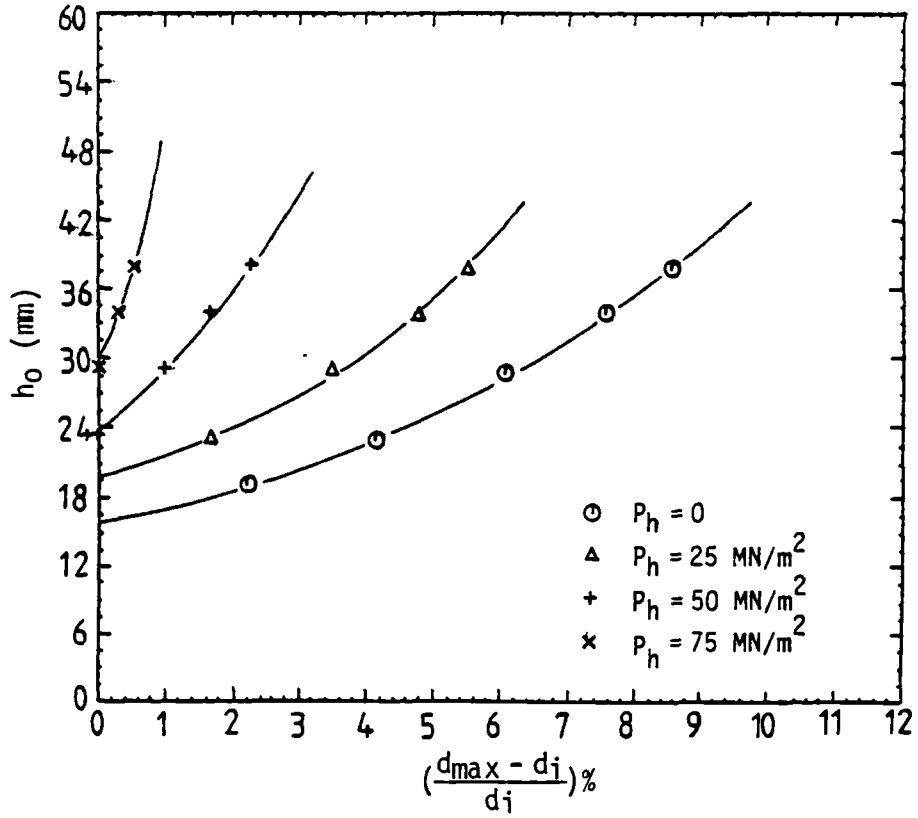
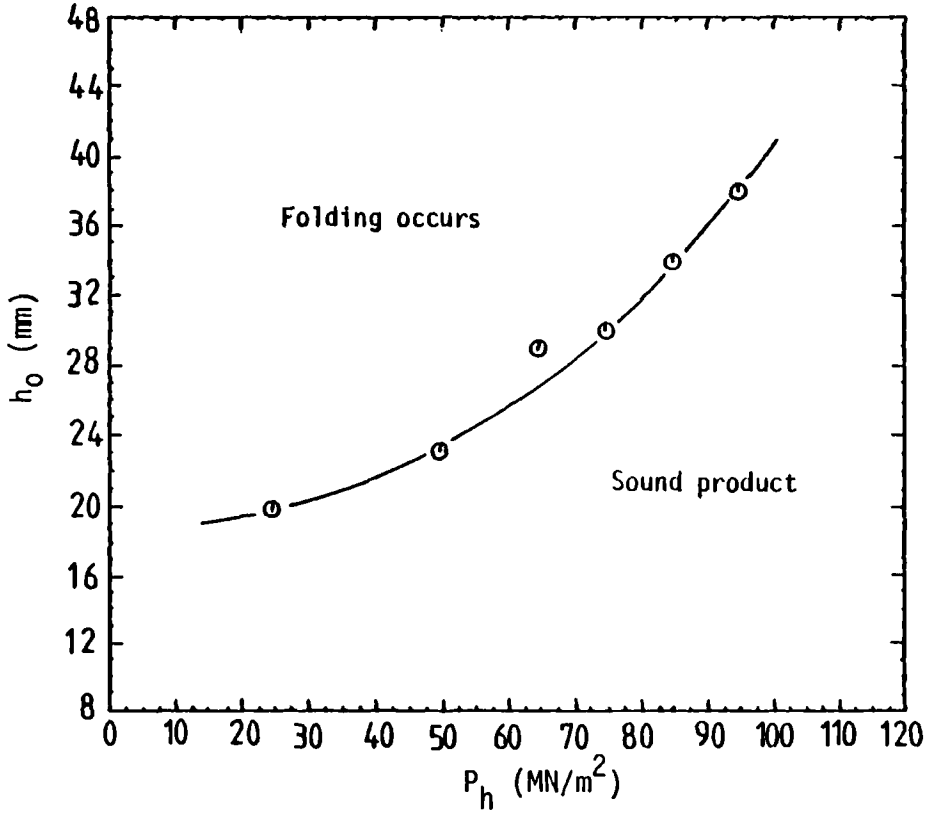
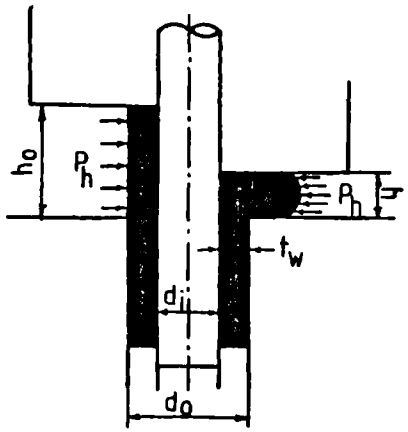


Fig. 6-26 Effect of initial unsupported height on the maximum increase in internal diameter in heading at various hydrostatic pressures and $\frac{h_o - h}{h_o} = 0.17$.





d_i = 25 mm

t_w/d_i = 0.38

Fig. 6-27 Limiting values of hydrostatic pressure and initial unsupported height for a sound product in heading.

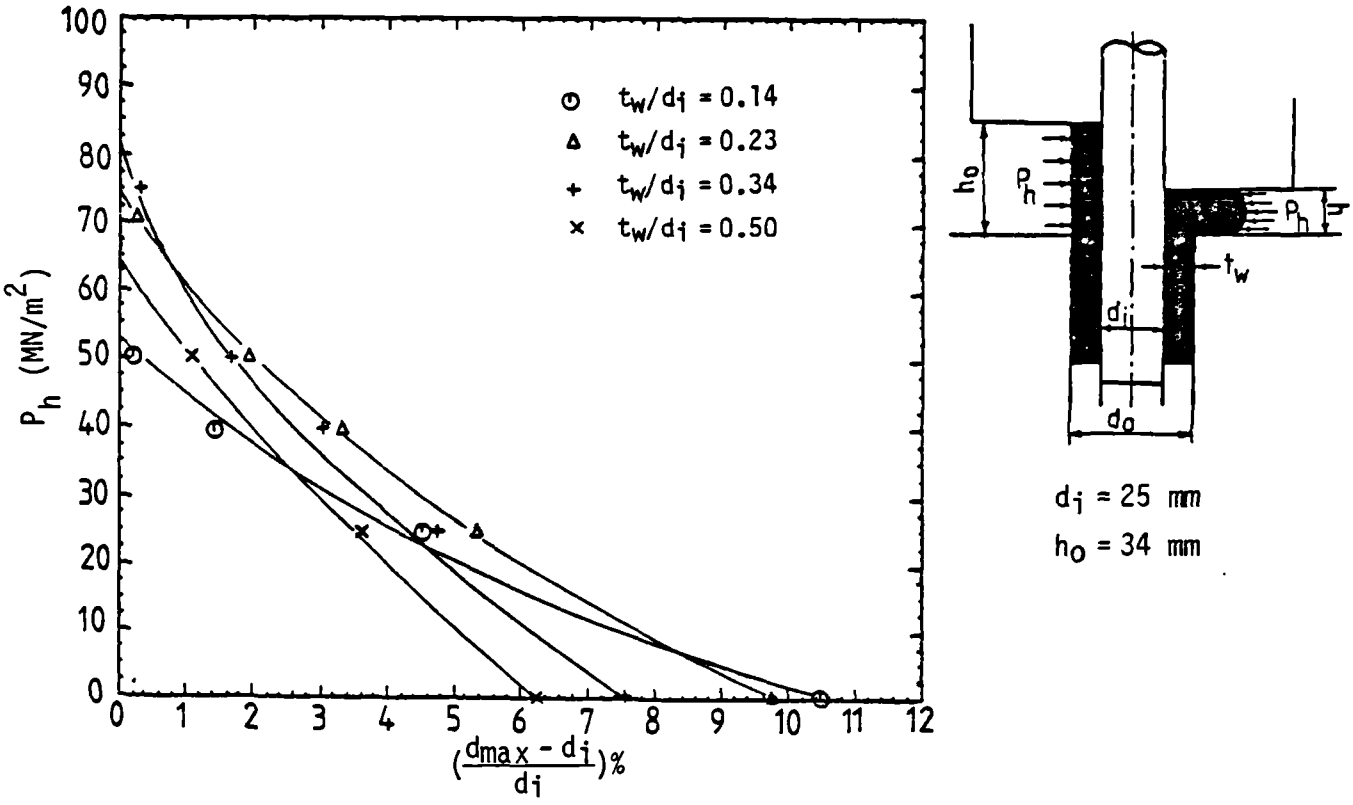


Fig. 6-28 Effect of hydrostatic pressure on the maximum increase in internal diameter in heading at various wall thicknesses and $\frac{h_o - h}{h_o} = 0.17$.

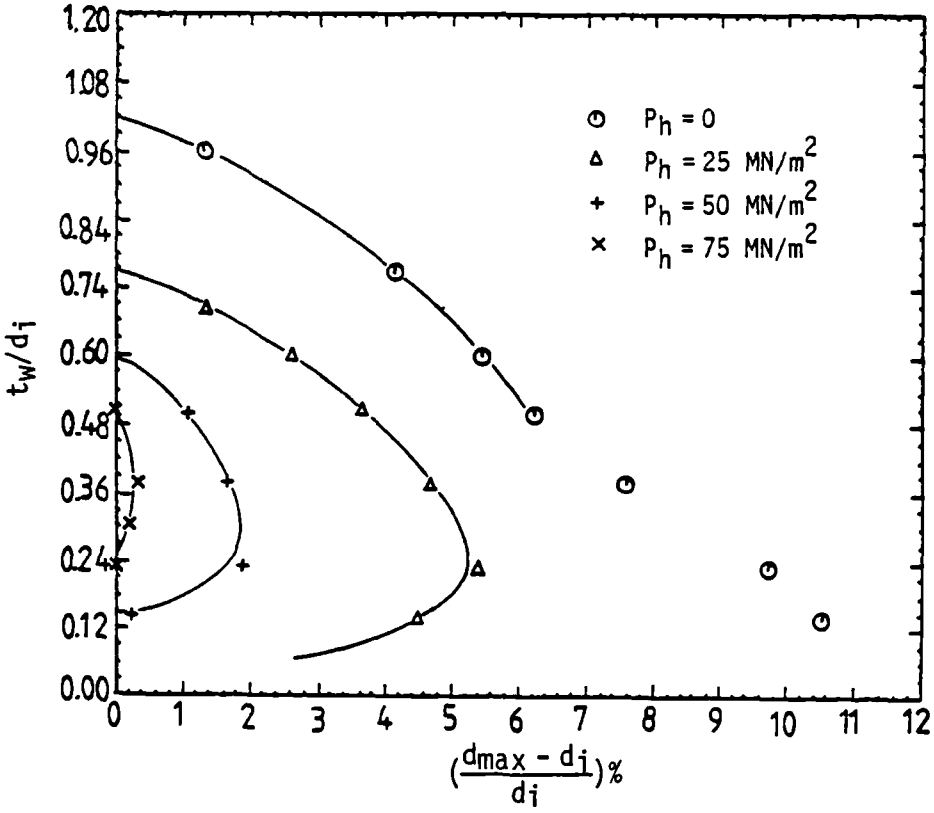
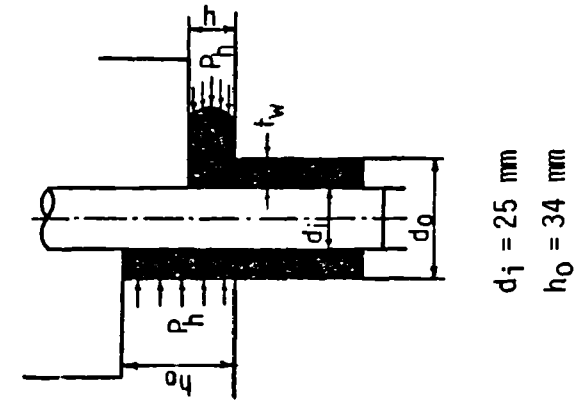


Fig. 6-29 Effect of original wall thickness on the maximum increase in internal diameter in heading at various hydrostatic pressures and $\frac{h_o - h}{h_o} = 0.17$.



d_i = 25 mm
h_o = 34 mm

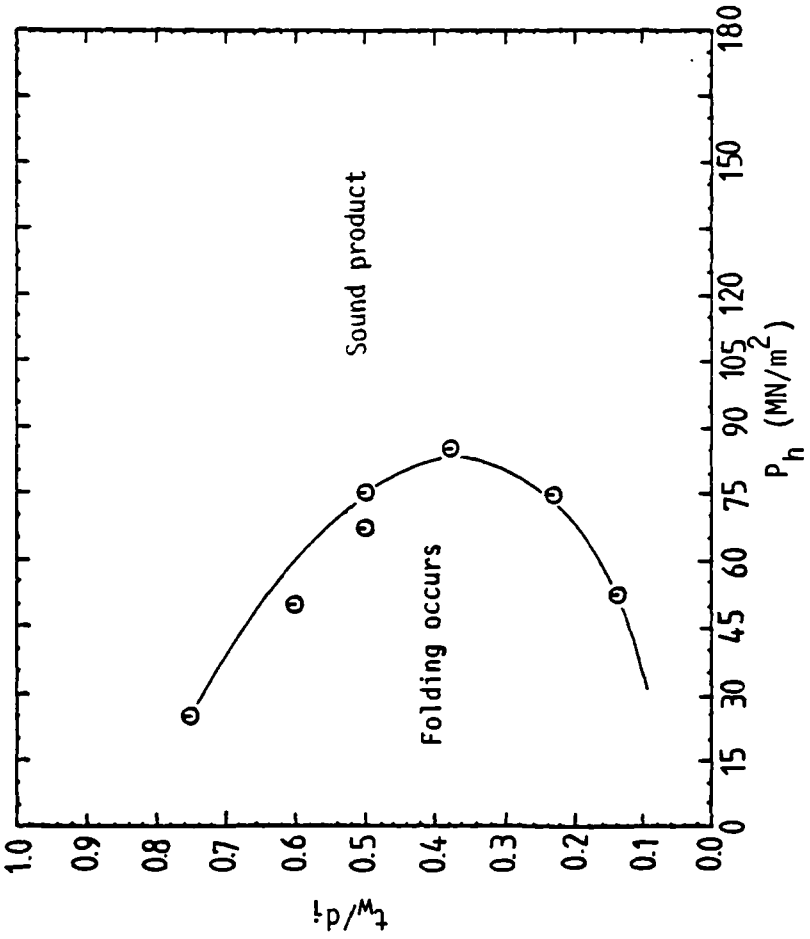


Fig.6-30 Limiting values of hydrostatic pressure and original wall thickness for sound products in heading hollow billets.

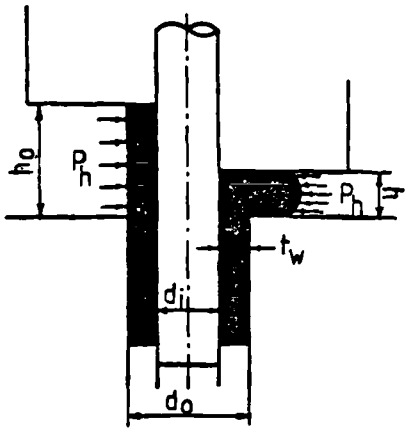
increase in bore diameter. In the presence of hydrostatic pressure, however, the values of $\frac{d_{max} - d_i}{d_i}$ first increase with t_w/d_i and then decrease at some value of t_w/d_i. The following explanation is offered for this behaviour. At the beginning of the process compressive radial stresses are generated at the bore surface of the billet due to the application of hydrostatic pressure. As the punch displacement increases these radial stresses decrease as the metal flows radially outwards. Zero radial stress at any point in the bore surface leads to the separation of that point from the mandrel. If the same hydrostatic pressure is applied to billets of various wall thicknesses, under similar conditions the radial stresses generated at the bore surface of the thinner-walled billet will be greater. Consequently, when a thinner-walled billet is upset in the presence of hydrostatic pressure, the greater tendency to bulge due to the smaller wall thickness is counteracted by greater compressive radial stresses produced in its bore.

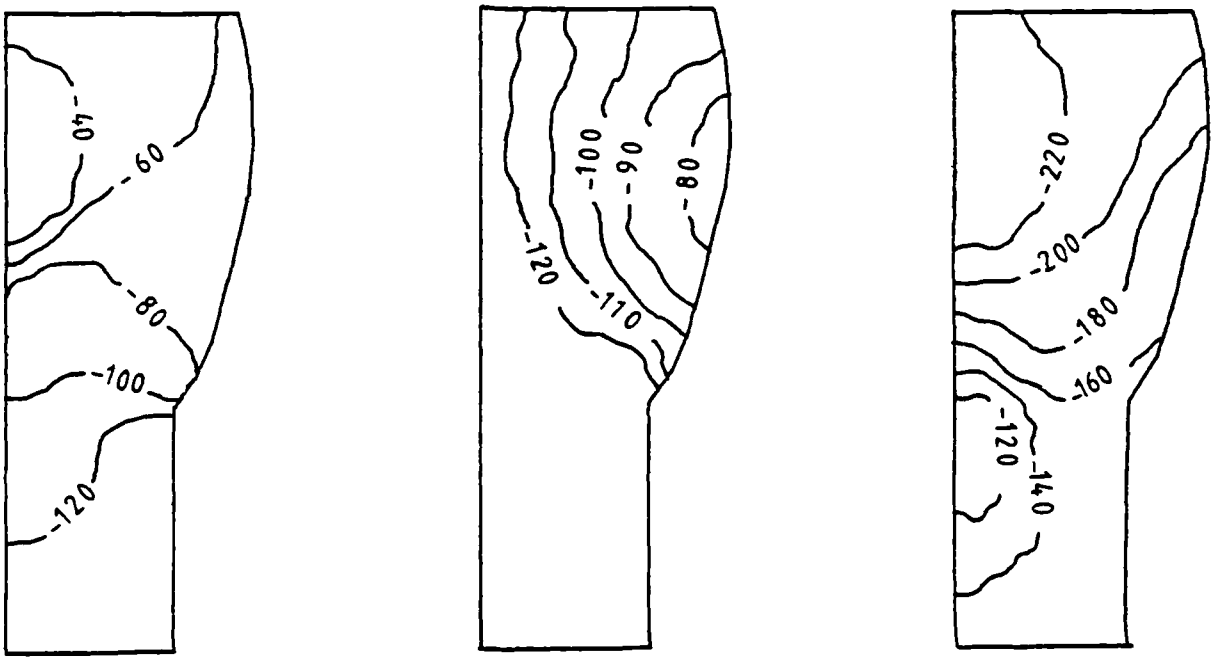
The distribution of radial stress, hoop stress and axial stress is shown in Figs. 6-31a, b&c respectively for a billet upset to 34% under a hydrostatic pressure of 75 MN/m^2. The contours of radial stress (Fig. 6-31a) show that σ_r increases towards the bore surface, becomes less compressive. Compressive radial stress at the bore surface indicates that the billet material is in contact with the mandrel.

An important observation relating the fracture, is that with an increase in hydrostatic pressure, the hoop stress near the free surface becomes compressive. This can be seen by comparing Fig. 6-31b with the corresponding contours in atmospheric pressure (see Fig. 6-16b).

The contours of the axial stress component, Fig. 6-31c, show that the variation of σ_z is high near the rigid constrained metal but more uniform within the deforming region. The upsetting pressure (σ_z at the

$d_i = 25$ mm
$t_w/d_i = 0.38$
$h_o = 34$ mm
$P_h = 75$ MN/m^2





a) Radial stress (σ_r)

b) Hoop stress (σ_θ)

c) Axial stress (σ_z)

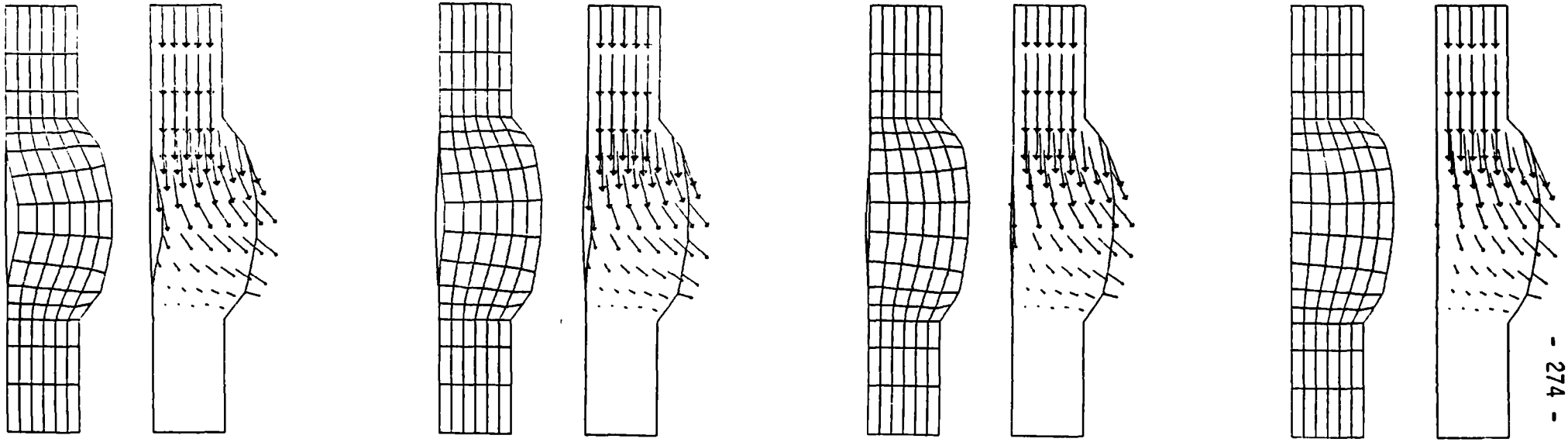
Fig. 6-31 Contours of radial, hoop and axial stresses in heading against hydrostatic pressure of 75 MN/m^2 at 34 per cent reduction in height.

punch contact surface) increases by a factor of nearly two compared to that required in heading a similar billet at atmospheric pressure (Fig. 6-16d). The corresponding upsetting load is even greater due to a considerable increase in the contact area when hydrostatic pressure is applied.

In a similar set of computations restraining hydrostatic pressure has been simulated for open upsetting and the results are presented in Figs. 6-32 to 6-39. Fig. 6-32 shows the velocity distribution and grid distortion for billets of 34 mm original free height, at 34 per cent reduction in height under various values of hydrostatic pressure. The predictions show an effect similar to that found in heading: more uniform radial velocity distribution along the free height, less pronounced shearing of the deformed metal at the plastic/rigid boundary and less bulging of the free surfaces.

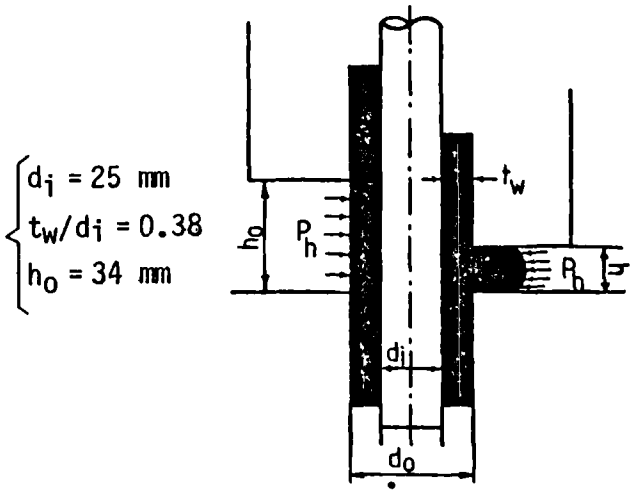
In addition to its effect on deformation, the application of hydrostatic pressure results in reduced damage to the upset flange. This damage, such as the opening up of microcracks and voids is the result of tensile stresses exceeding some critical value on the free surface. The presence of hydrostatic pressure reduces the tensile stresses below the critical value, so that the billet can be deformed to a much greater extent (producing flanges of higher diameter) without any internal or surface fracture. Furthermore, the residual ductility of the upset flange is higher when forming under pressure, which is of particular significance if the product is to be subjected to further work.

In conventional upsetting at atmospheric pressure the maximum amount of deformation was restricted when the intersection of cones of the relatively undeformed material (at the ends of the deforming region), caused a sudden increase in the upsetting load. If the operation is carried out in the presence of hydrostatic pressure the pressure cones are expected



a) $P_h = 0$ b) $P_h = 25\ MN/m^2$ c) $P_h = 50\ MN/m^2$ d) $P_h = 75\ MN/m^2$

Fig. 6-32 Distorted grids and velocity distributions in the open upsetting of hollow billets at 34 per cent reduction in height under various hydrostatic pressures.



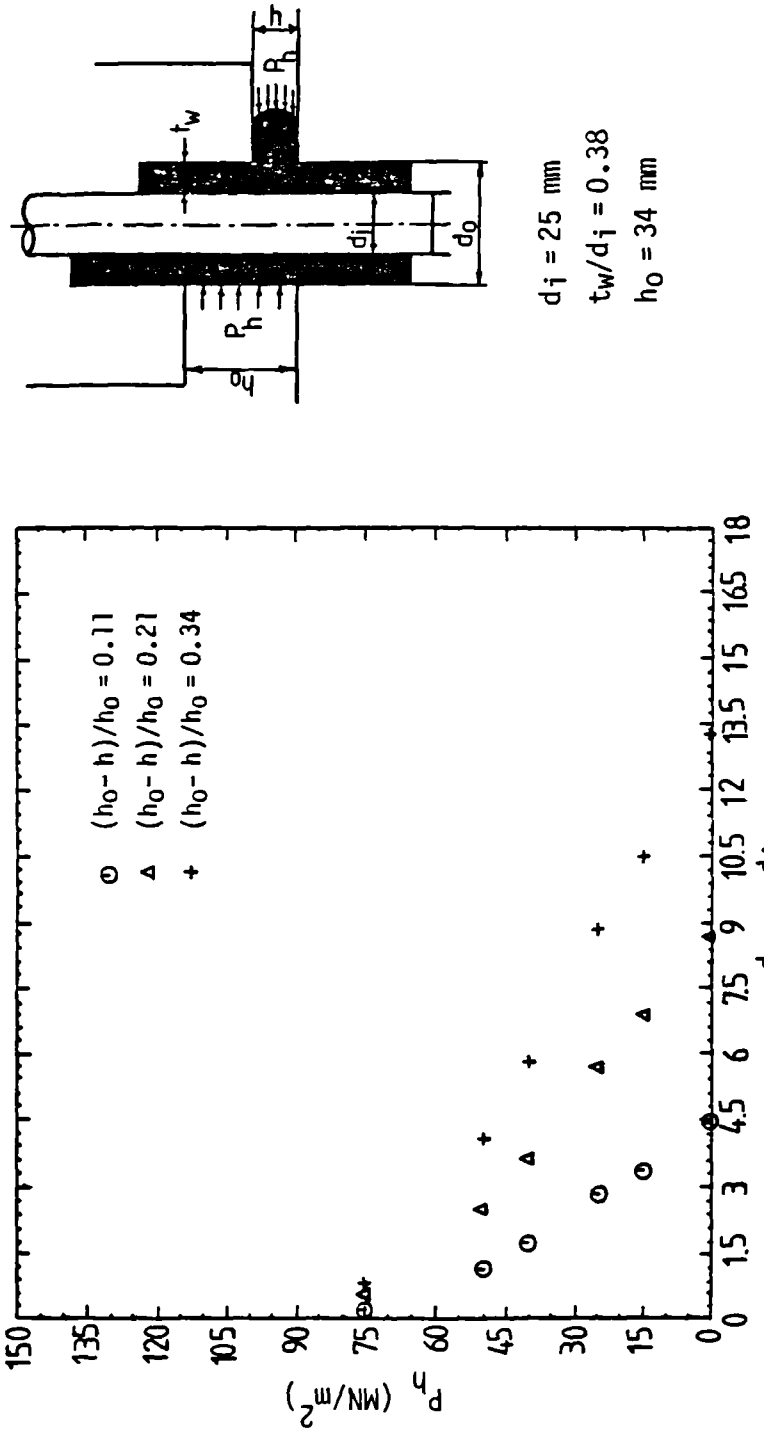


Fig. 6-33 Effect of hydrostatic pressure on the maximum increase in internal diameter in open upsetting at various deformations.

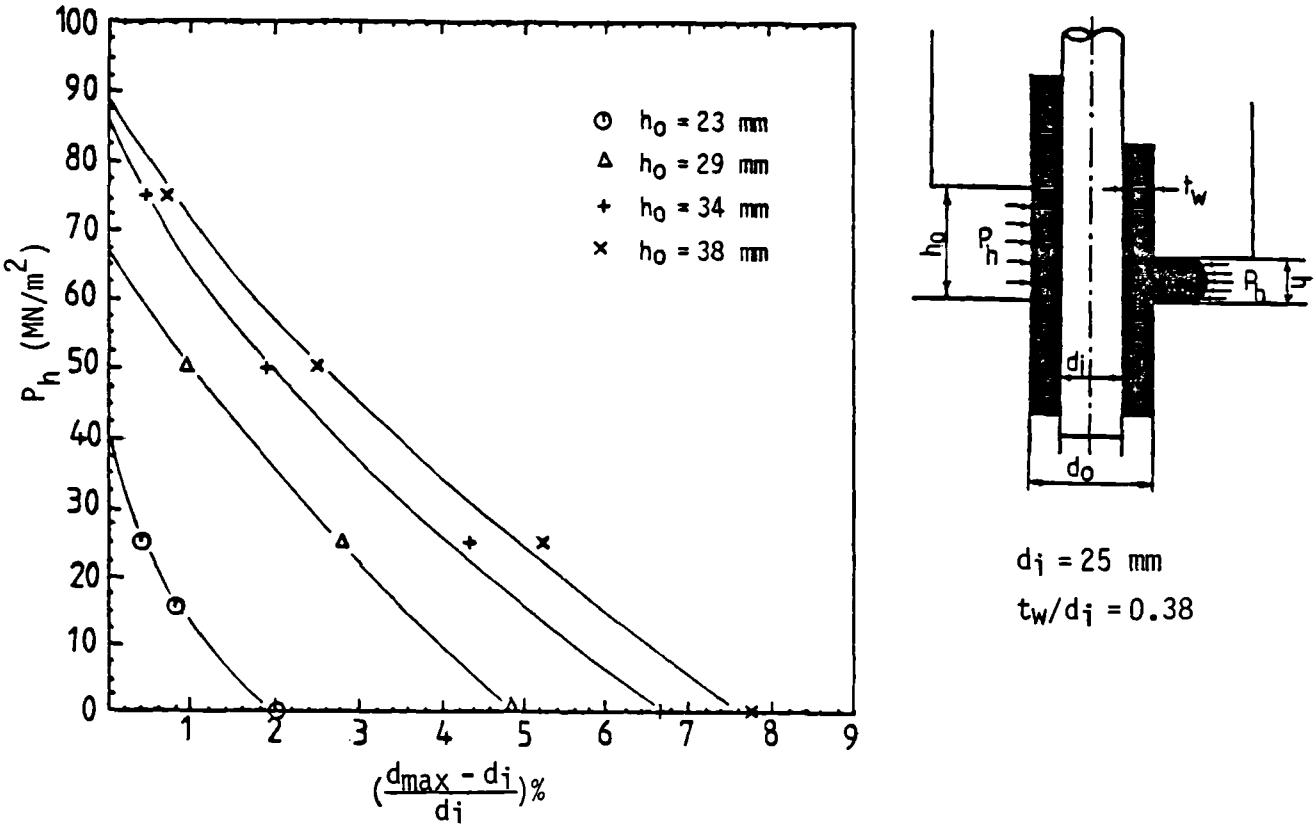


Fig. 6-34 Effect of hydrostatic pressure on the maximum increase in internal diameter in open upsetting at various initial unsupported heights and $\frac{h_o - h}{h_o} = 0.17$.

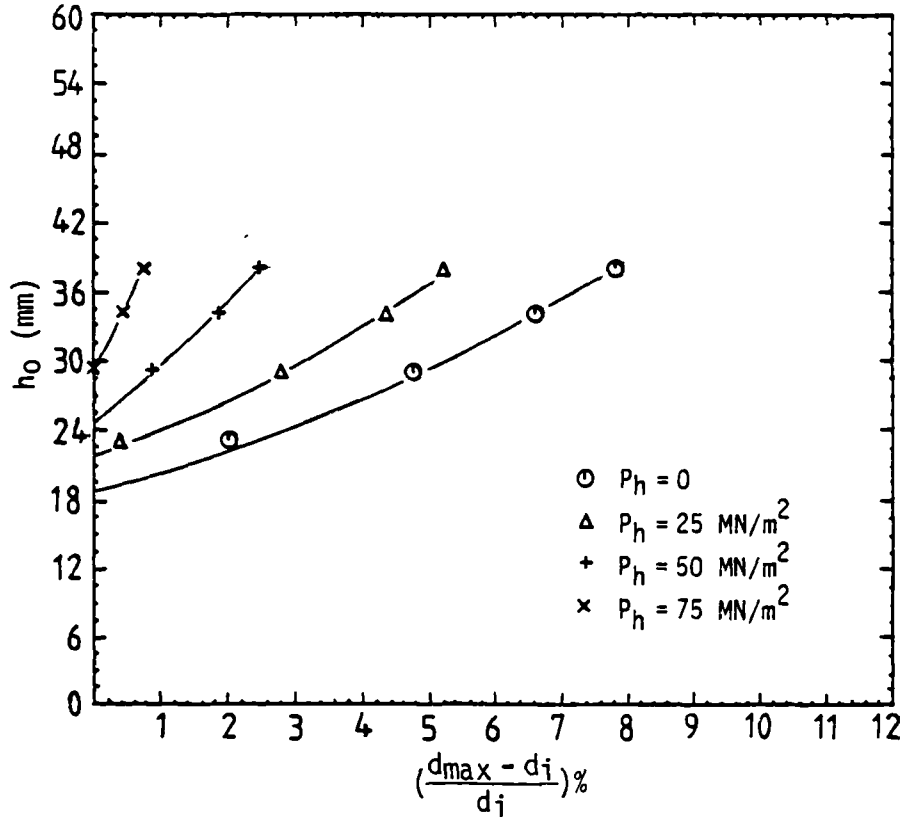


Fig. 6-35 Effect of original unsupported height on the maximum increase in internal diameter at various hydrostatic pressures and $\frac{h_o - h}{h_o} = 0.17$.

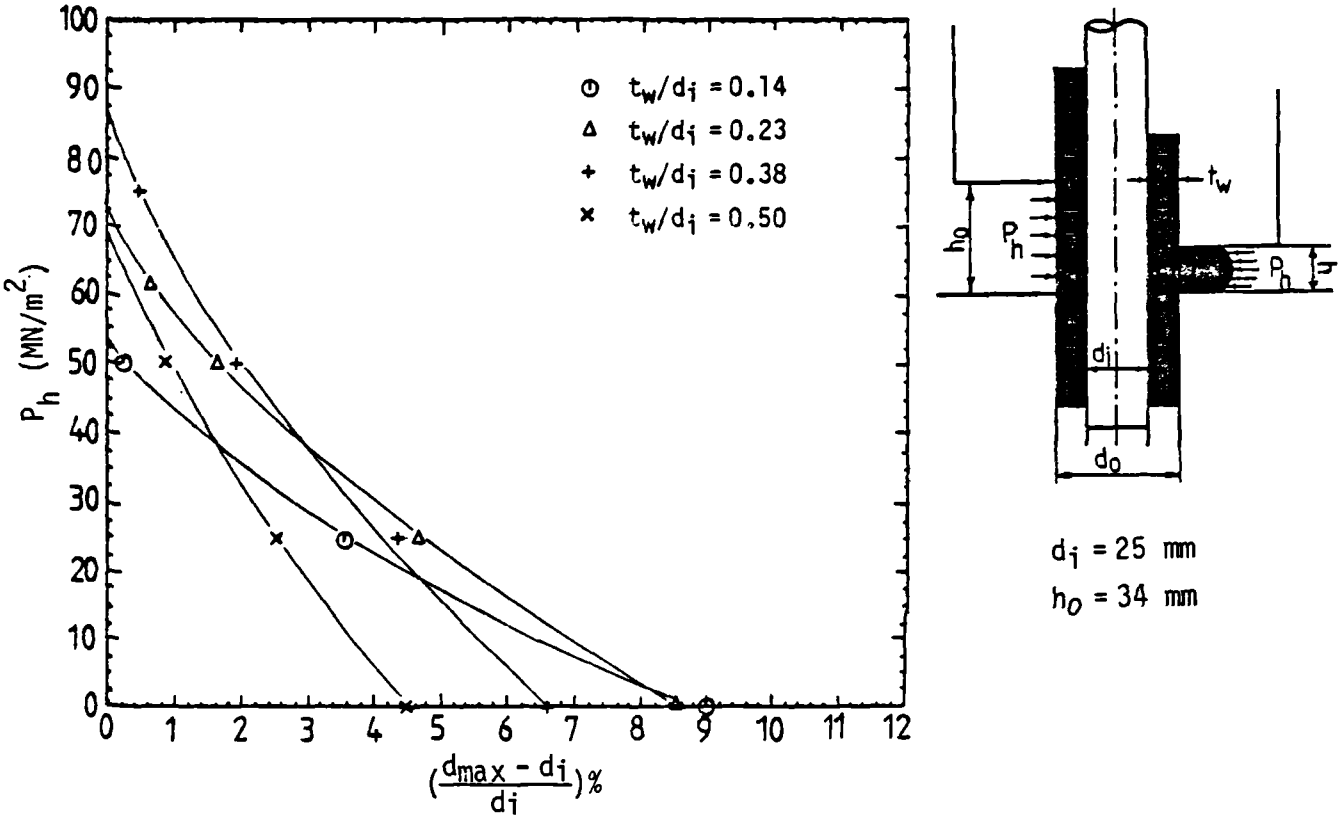


Fig. 6-36 Effect of hydrostatic pressure on the maximum increase in internal diameter in open upsetting for various wall thicknesses at $\frac{h_o - h}{h_o} = 0.17$.

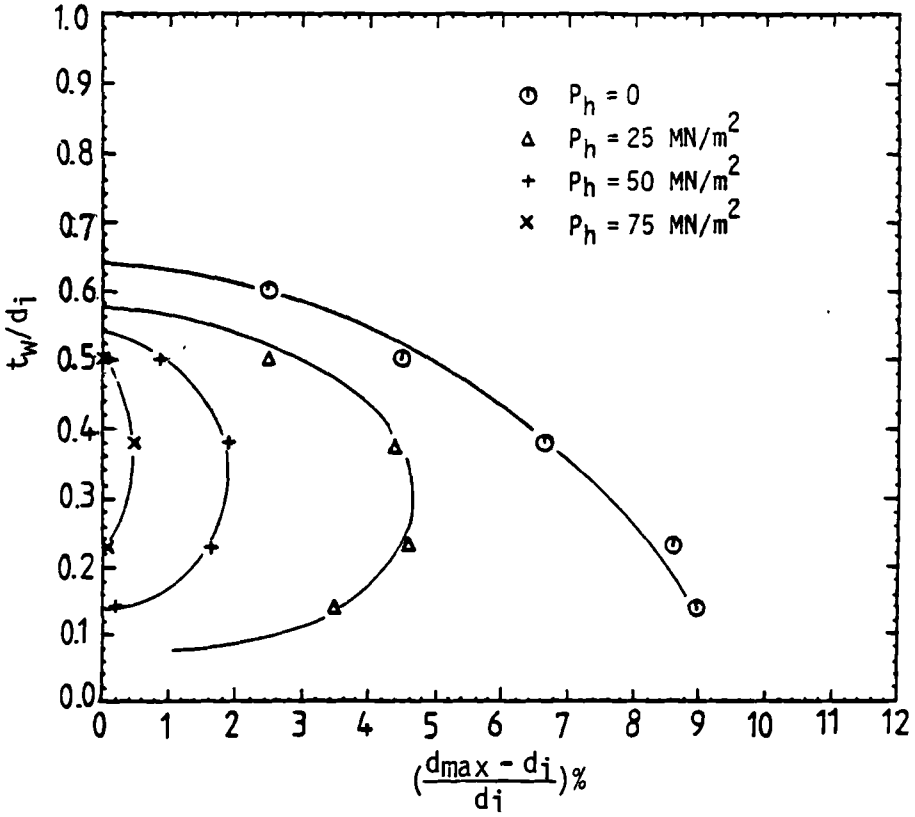
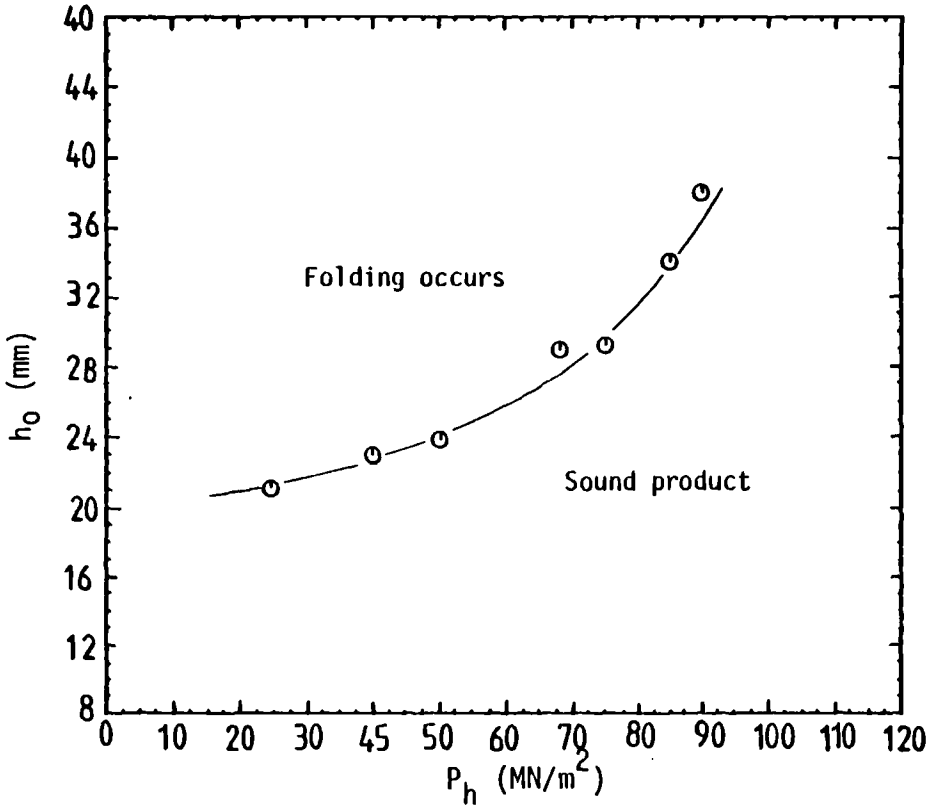
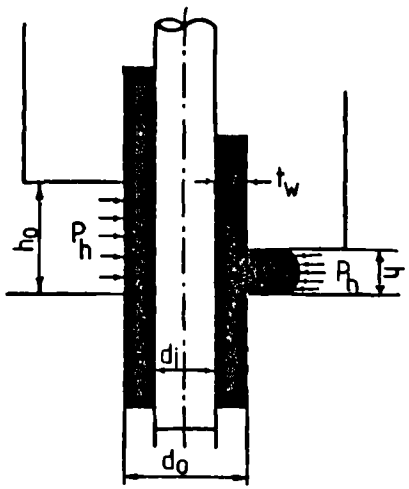


Fig. 6-37 Effect of original wall thickness on the maximum increase in internal diameter in open upsetting at various values of hydrostatic pressure and $\frac{h_o - h}{h_o} = 0.17$.





$d_i = 25$ mm

$t_w/d_i = 0.38$

Fig. 6-38 Limiting values of hydrostatic pressure and initial unsupported height for a sound product in the open upsetting of hollow billets.

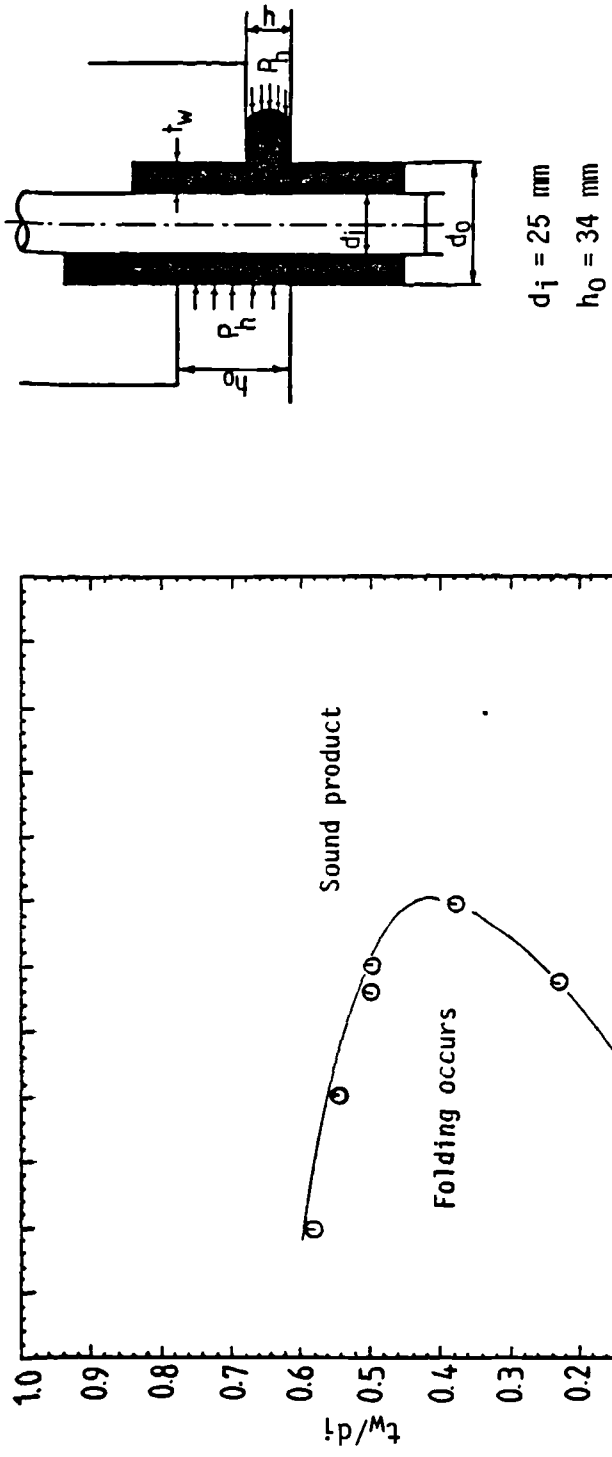


Fig. 6-39 Limiting values of hydrostatic pressure and original wall thickness for a sound product in the open upsetting of hollow billets.

to be smaller due to the larger deforming zone. Therefore the intersection of the cones would be delayed, which allows more reduction in height to be obtained.

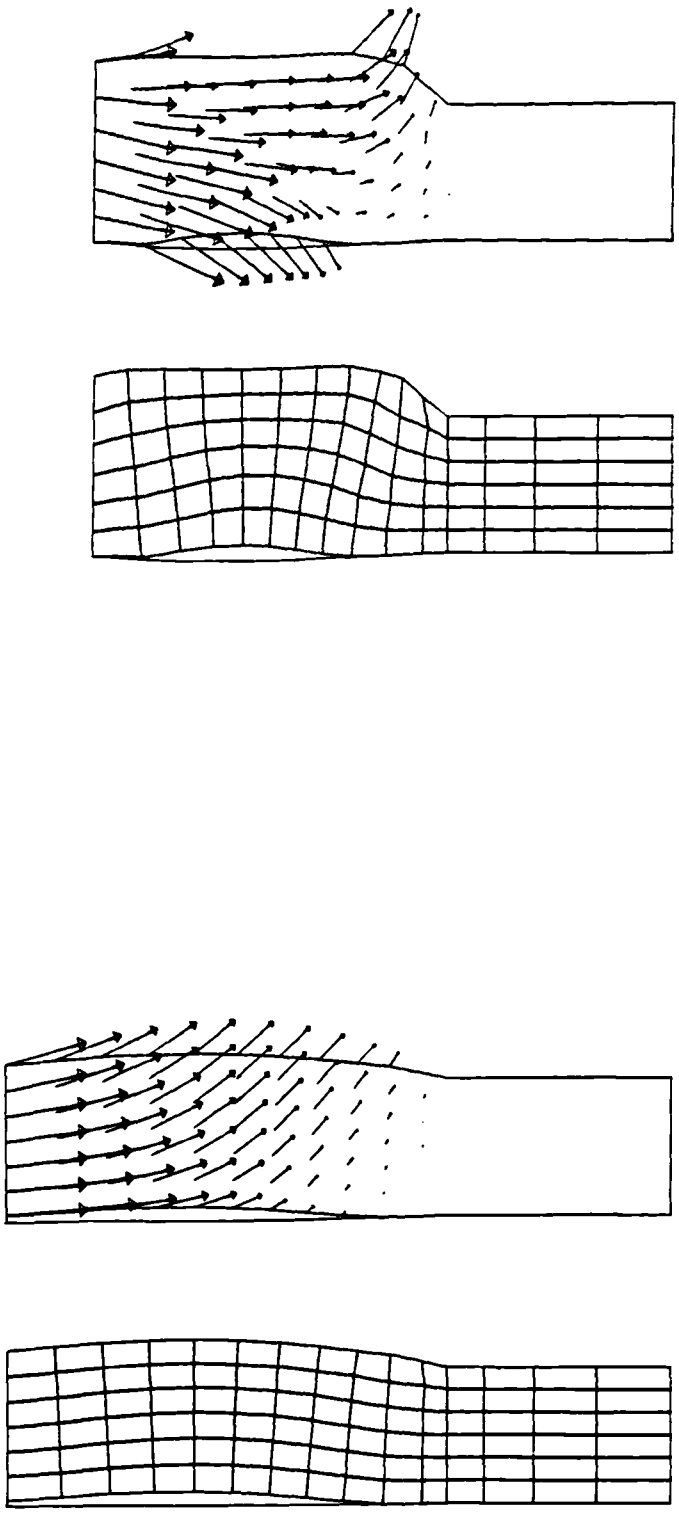
6.2.4.5 Conventional upsetting of hollow billets into restricted cavities

Heading hollow billets of original free heights of 34 mm and a wall thickness/internal diameter ratio of 0.38 has been analysed when the flange is forced into cavities of various diameters. Figs. 6-40 and 6-41 show the distorted grid and velocity distribution at 17 per cent and 34 per cent reductions with the heads forced into cavities of 52 mm and 50 mm diameter respectively.

As the flange reaches the wall of the cavity compressive stresses are generated in the deforming metal. Further punch displacement increases these stresses and eventually changes the direction of metal flow, so that it moves towards the regions of lower stress such as the top and bottom corners of the cavity, also gradually filling the gap in the bore. This is clear from the velocity distributions obtained at 34 per cent reduction in height (Figs. 6-40b and 6-41b). The results also reveal that the deforming region penetrates the rigid zone as the deforming flange reaches the outer diameter of the die.

The load/displacement characteristics in heading billets into restricted cavities of various diameters are shown in Fig. 6-42. The rate of increase in the upsetting load increases after the flange comes into contact with the wall of the cavity. This is followed by a sharp increase in load at the final stages of deformation.

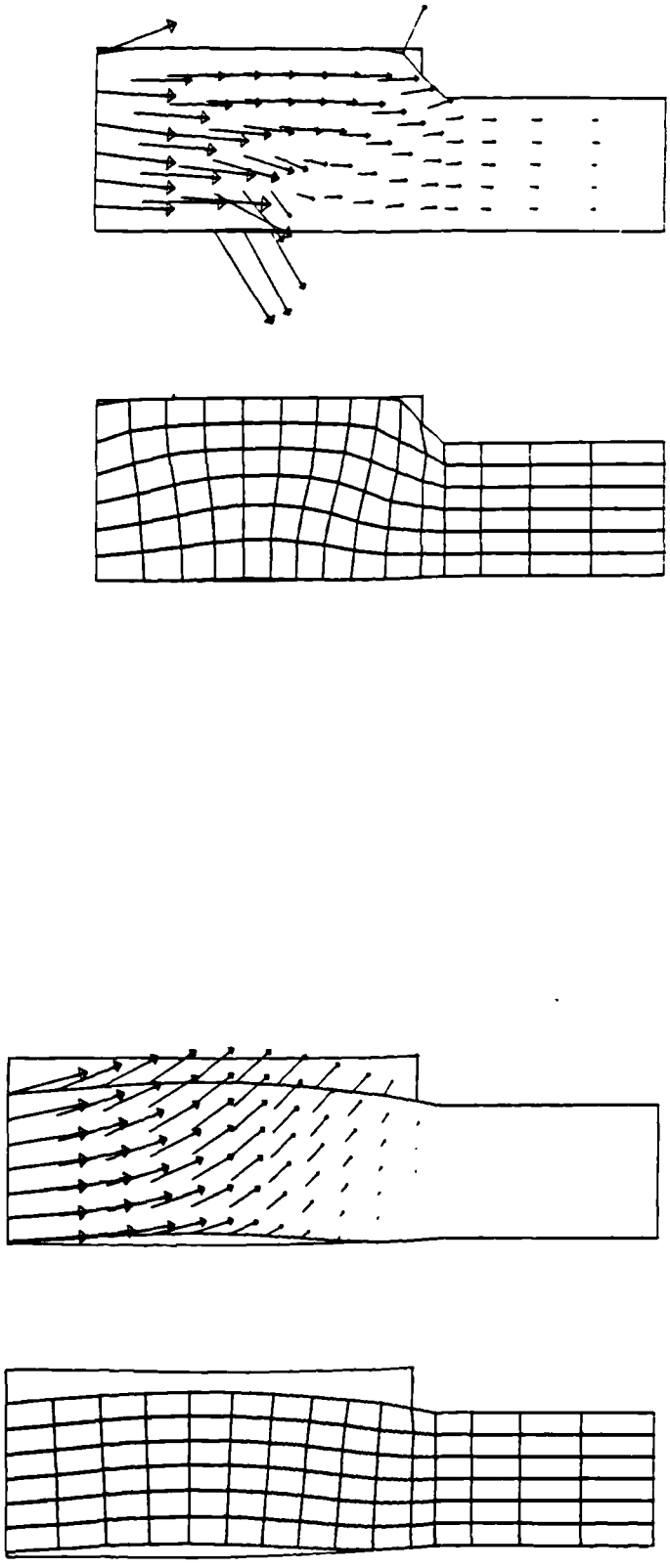
The distribution of the axial and radial components of stress at 34 per cent reduction in height are shown in Figs. 6-43a & b respectively. There is more variation in σ_z near the plastic/rigid deformation boundary



a) $\frac{h_o - h}{h_o} = 0.17$

b) $\frac{h_o - h}{h_o} = 0.34$

Fig. 6-40 Distorted grid and velocity distribution in heading hollow billets into a restricted cavity of 52 mm diameter ($h_o = 34$ mm, $d_i = 25$ mm, $d_o = 44$ mm).



a) $\frac{h_o - h}{h_o} = 0.17$

b) $\frac{h_o - h}{h_o} = 0.34$

Fig. 6-41 Distorted grid and velocity distribution in heading hollow billets into a restricted cavity of 50 mm diameter ($h_o = 34$ mm, $d_i = 25$ mm, $d_o = 44$ mm).

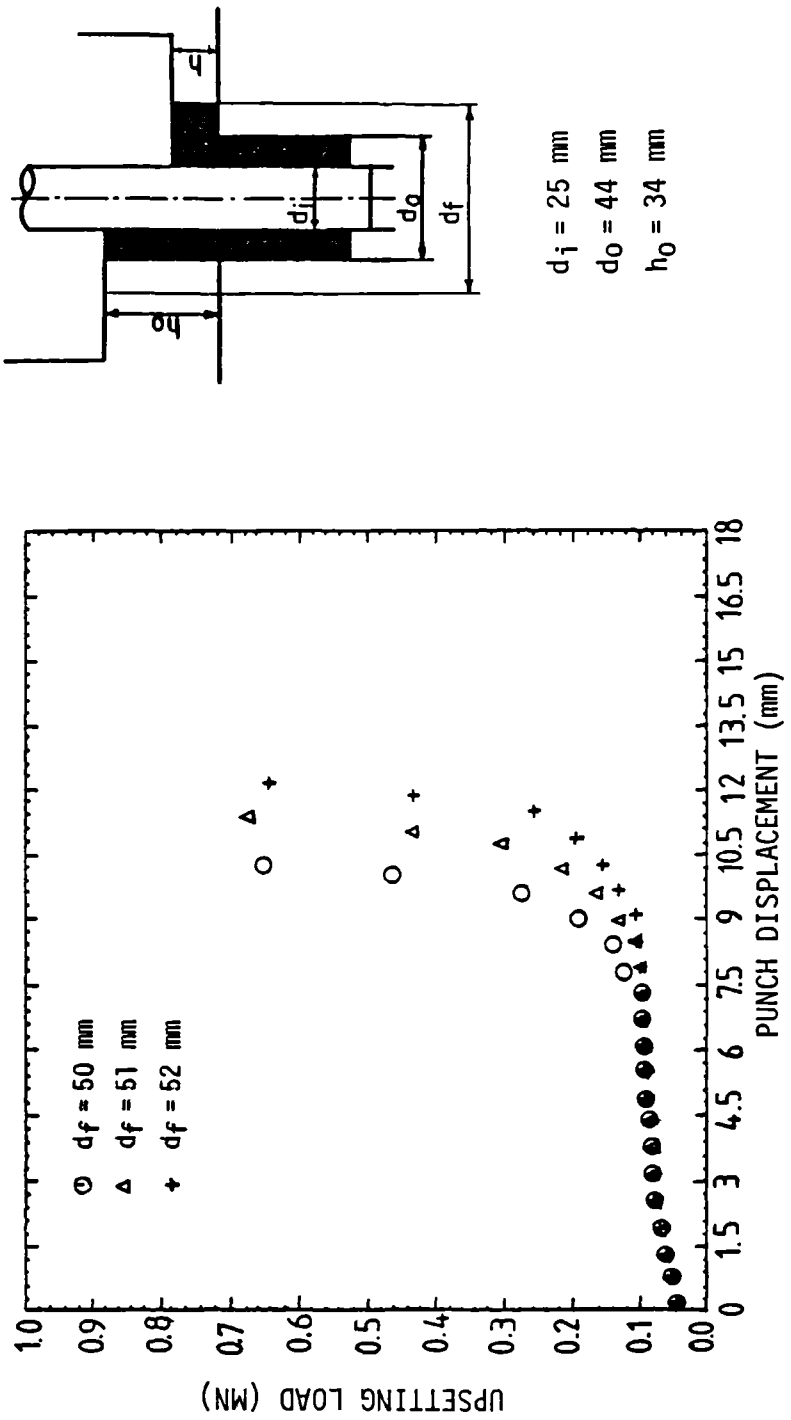
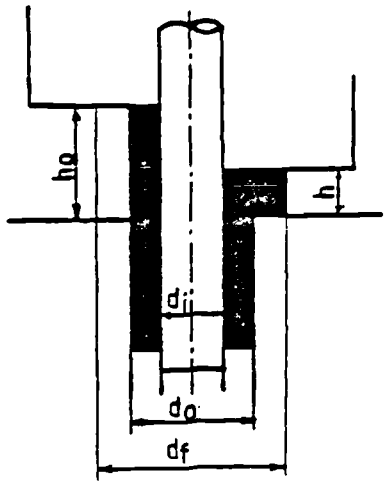
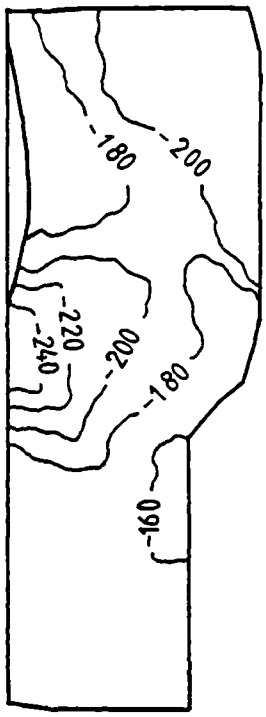


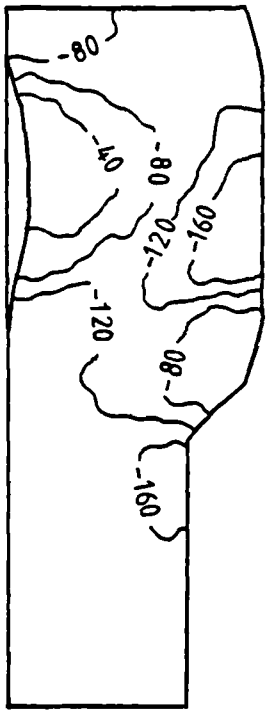
Fig. 6-42 Load/displacement curves in heading hollow billets into restricted cavities of various diameters.

d_i = 25 mm
d_o = 44 mm
h_o = 34 mm
d_f = 52 mm





a) Axial stress
(σ_z)



b) Radisl stress
(σ_r)

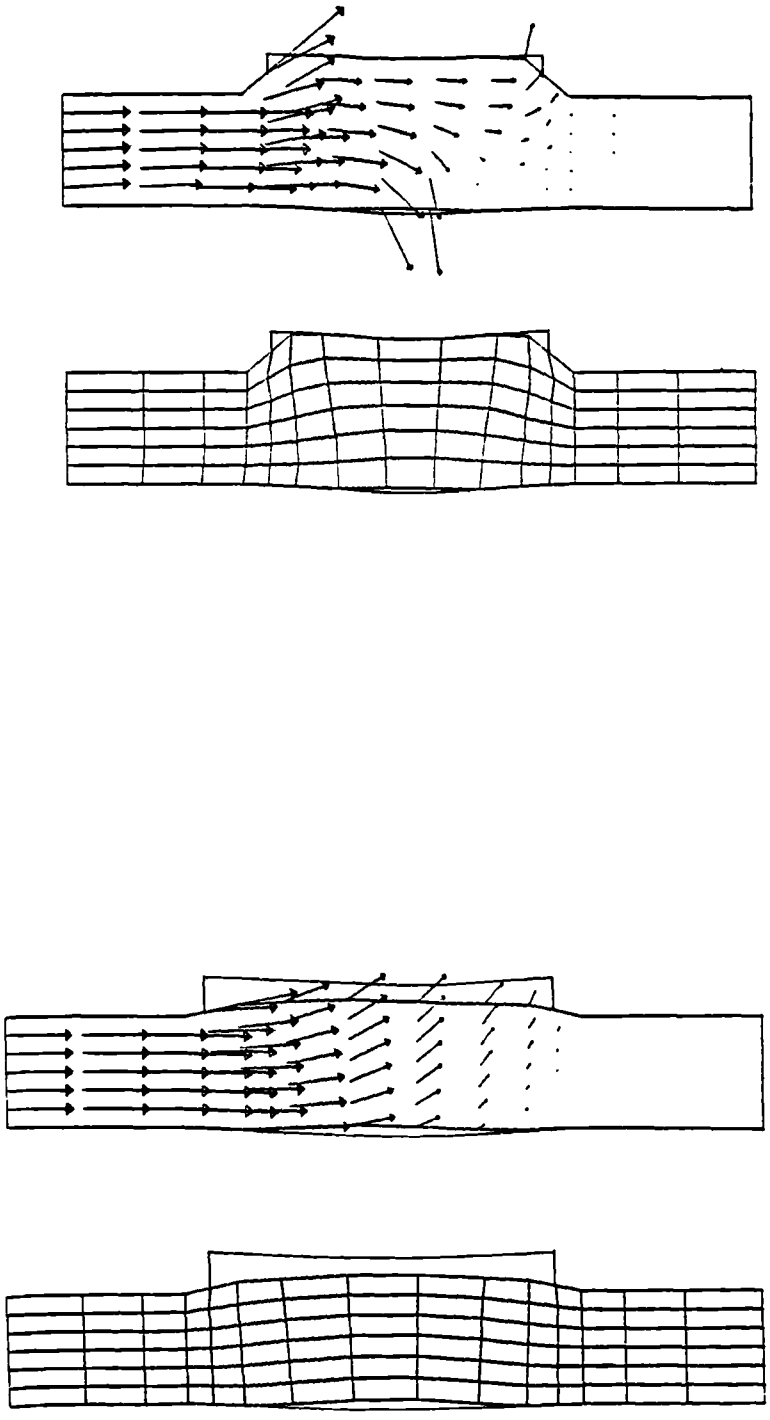
Fig. 6-43 Contours of axial and radial stresses in heading into a restricted cavity of 52 mm diameter, 34 per cent reduction in height.

than elsewhere. Contours of the radial stress show a large gradient across the flange because it reaches a high value when the material contacts the outer die diameter. The distribution of σ_r is more uniform near the punch contact surface and at the lower part of the deforming region.

The computations have been repeated for the open upsetting of a billet of similar geometries and the results are presented in Figs. 6-44 to 6-46. Fig. 6-44 shows the distorted grid and velocity distribution at 17 and 34 per cent reduction in height for a flange formed in a cavity of 50 mm diameter. The deformation pattern at 34 per cent indicates that the cavity is being filled almost fully with the deforming material.

The distribution of σ_r, σ_z and σ_θ is given in Fig. 6-46 at 34 per cent reduction. The contours of the radial stress show that the largest absolute value of σ_r occurs within the upper constrained part of the billet. A larger variation of σ_r is observed near the boundary between the upper rigid zone and the deforming region and also across the flange. The three stress components show almost the same range throughout the deformation zone except near the inner diameter where σ_r is small in comparison with σ_z and σ_θ.

Although the results of conventional upsetting into a closed space show the possibility of reduction or eventual elimination of the inner bulge for certain geometries, the practical efficiency of the technique is expected to be greatly dependent on the geometry of the original billet and product. The experimental results for unrestricted conventional upsetting show that, at some stage of the deformation, the bulge produced at the bore region closes up to form a fold which continues to penetrate into the upset flange with increasing amount of deformation. If the diameter of the closed space (which would be the required diameter of the flange) is such that the material reaches the outer die wall when the bulge is still in its barrelled shape (before formation of the fold) then the material would be forced



a) $\frac{h_o - h}{h_o} = 0.17$

b) $\frac{h_o - h}{h_o} = 0.34$

Fig. 6-44 Distorted grid and velocity distribution in the open upsetting of hollow billets into a restricted cavity of 50 mm diameter ($h_o = 34$ mm, $d_i = 25$ mm, $d_o = 44$ mm).

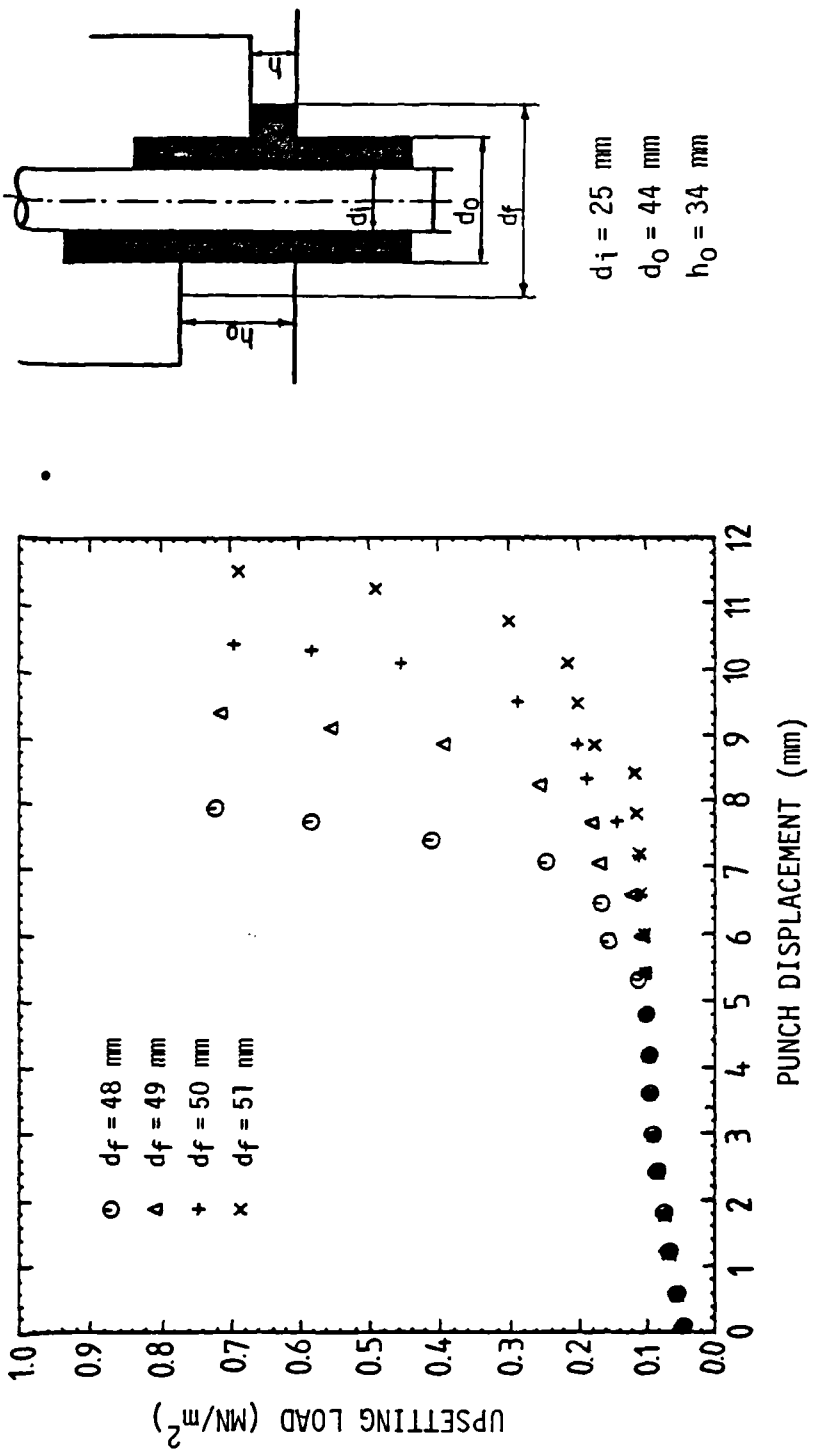
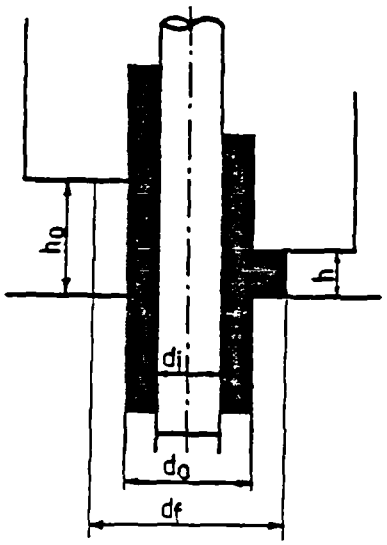
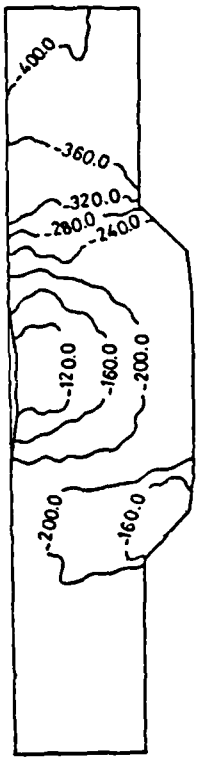


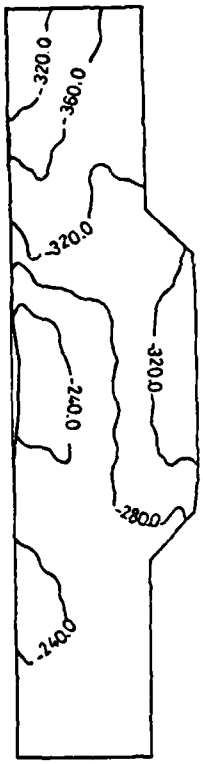
Fig. 6-45 Load/displacement curves obtained in the open upsetting of hollow billets into restricted cavities of various diameters.

$d_i = 25$ mm
$h_o = 34$ mm
$t_w/d_i = 0.38$
$d_f = 50$ mm

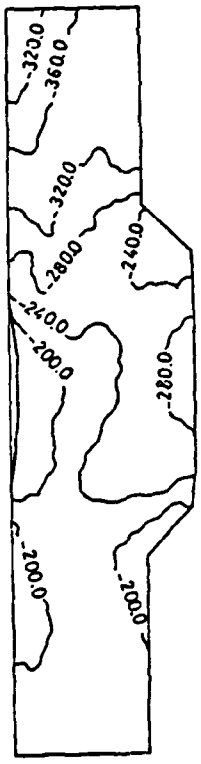




a) Radial stress
(σ_r)



b) Axial stress
(σ_z)



c) Hoop stress
(σ_θ)

Fig. 6-46 Contours of various stress components in the open upsetting of hollow billets into a restricted cavity of 50 mm diameter at 34 per cent reduction in height.

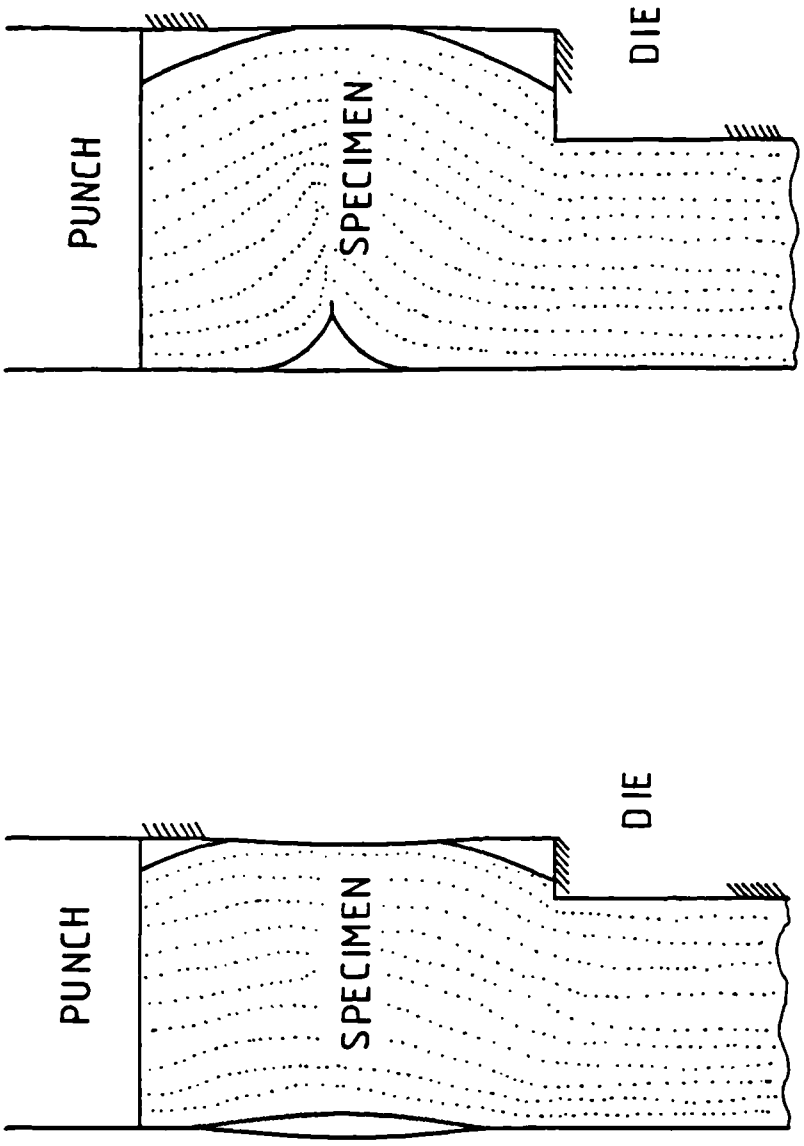


Fig. 6-47 Heading of hollow billets into restricted cavities of various diameters.

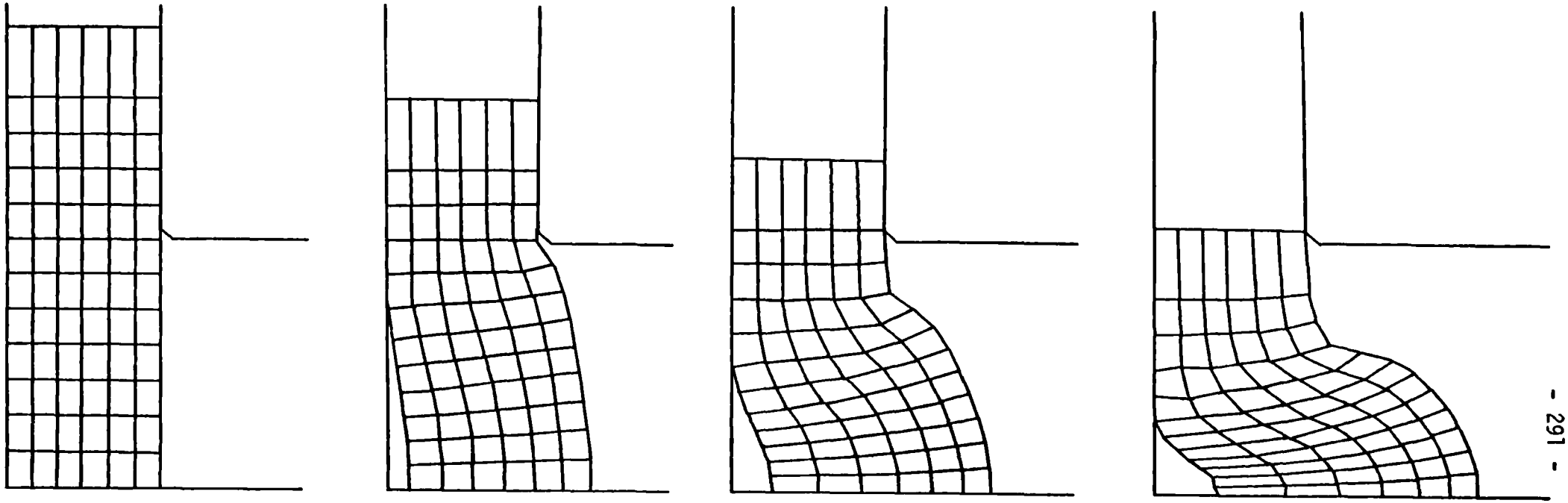
back against the mandrel (Fig. 6-47a). However, if the required flange diameter is large enough for the inner fold to be formed before the upset material meets the outer wall, further increase in punch displacement would not be able to eliminate the defect (Fig. 6-47b).

One of the main problems in the production of sound flanged-products by this method is that the load becomes high when filling of the cavity with metal is almost completed. This is realistic because it reflects increased frictional resistance, but it is also due to relatively large elements used in the computations. The use of smaller elements in the theoretical analysis would be expected to delay the sharp load increase.

6.3 Failure of the finite element method for injection upsetting

Although the finite element method was successfully used to analyse conventional upsetting, the method failed to produce realistic results when it was applied to injection upsetting. The theoretical predictions of the geometrical changes were in sharp contrast to those observed in the experiments. The distorted grid obtained for simple injection upsetting with smooth contact surfaces at various values of punch displacement are shown in Fig. 6-48. The elements in the unconstrained part of the billet deform plastically and flow into the gap, but as the deformation continues they do not show any tendency to deform and seem to remain rigid.

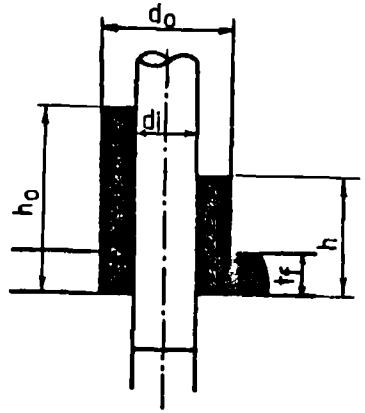
When the elements of the constrained part enter the gap the stiffness of the already deformed elements decreases, so that their low resistance causes the newly entered elements to remain rigid. In reality, the billet body may be described as a collection of very small elements with negligible difference between the stiffness of those adjacent to each other which indicates that employing a finer mesh in the finite element analyses could



a) $\frac{h_o - h}{h_o} = 0$ b) $\frac{h_o - h}{h_o} = 0.14$ c) $\frac{h_o - h}{h_o} = 0.28$ d) $\frac{h_o - h}{h_o} = 0.41$

Fig. 6-48 Failure of finite element method for simple injection upsetting of hollow billets.

$d_i = 25$ mm
$d_o = 44$ mm
$t_f = 15$ mm



reduce the difference between the predicted and experimental material behaviour.

Using rough platens in this analysis was thought to impose some restraint on the radial flow of the metal which may result in a lower reduction of the stiffness of the elements, but in fact the improvement was negligible.

6.5 Upper-bound loads in injection upsetting

The optimized upsetting pressure was obtained, using Eq. 4.94, for hollow billets injected into gaps of various heights by minimizing $F(\eta)$ in Eq. 4.95 with respect to η. Fig. 6-49 shows the variation of $F(\eta)$ with η. The changes in $F(\eta)$ (and therefore the derived punch pressure) with variation in η is seen to be almost insensitive near the optimum η. This is particularly marked in the lower values of t_f/t_w, that is the effect of the position of velocity discontinuities on predicted punch pressure is less pronounced for small flange thickness.

Calculations for various values of friction factor m $(0 \leq m \leq 1)$ show that the contribution of frictional losses is negligible compared with the frictionless upper-bound punch pressure, so in the following the former will be neglected.

The variation of $P/\bar{\sigma}_o$ with d_f/d_o is shown in Fig. 6-50 for various values of t_f/t_w ranging from 0.3 to 3. The rate of increase in $P/\bar{\sigma}_o$ is higher for thinner flanges. For a given flange diameter, the required punch pressure decreases as t_f/t_w increases, except for the largest flange thickness $(t_f/t_w = 3)$ for which the obtained line lies above those of lower t_f/t_w. The reversal in the trend of predicted forming pressure in high values of t_f/t_w is clear from Fig. 6-51, where $P/\bar{\sigma}_o$ is plotted against t_f/t_w. The figure gives

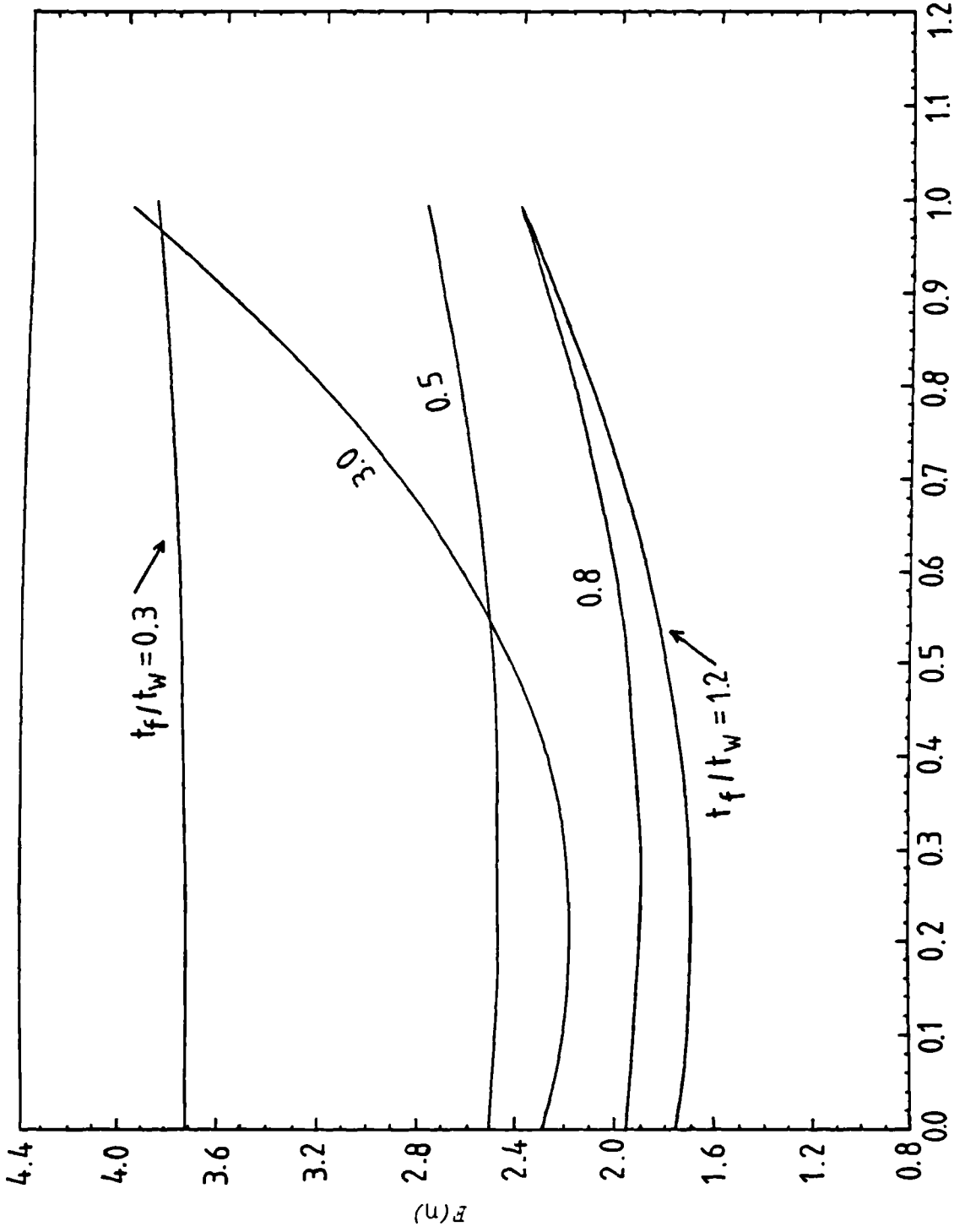


Fig. 6-49 Variation of function $F(\eta)$ with η for varius flange thicknesses.

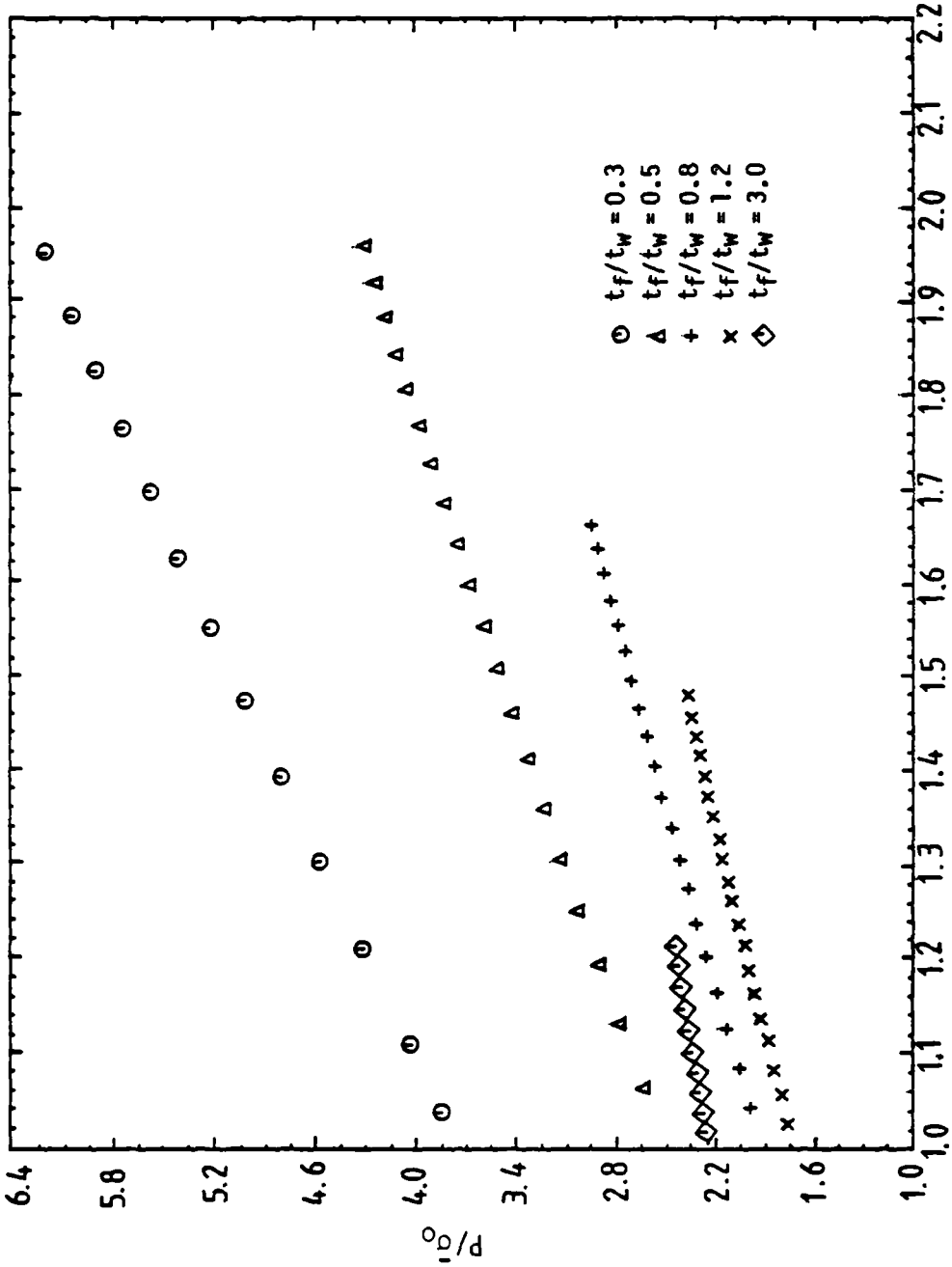


Fig. 6-50 Variation of punch pressure with flange diameter and thickness at $d_f/d_o = 1$, simple injection upsetting.

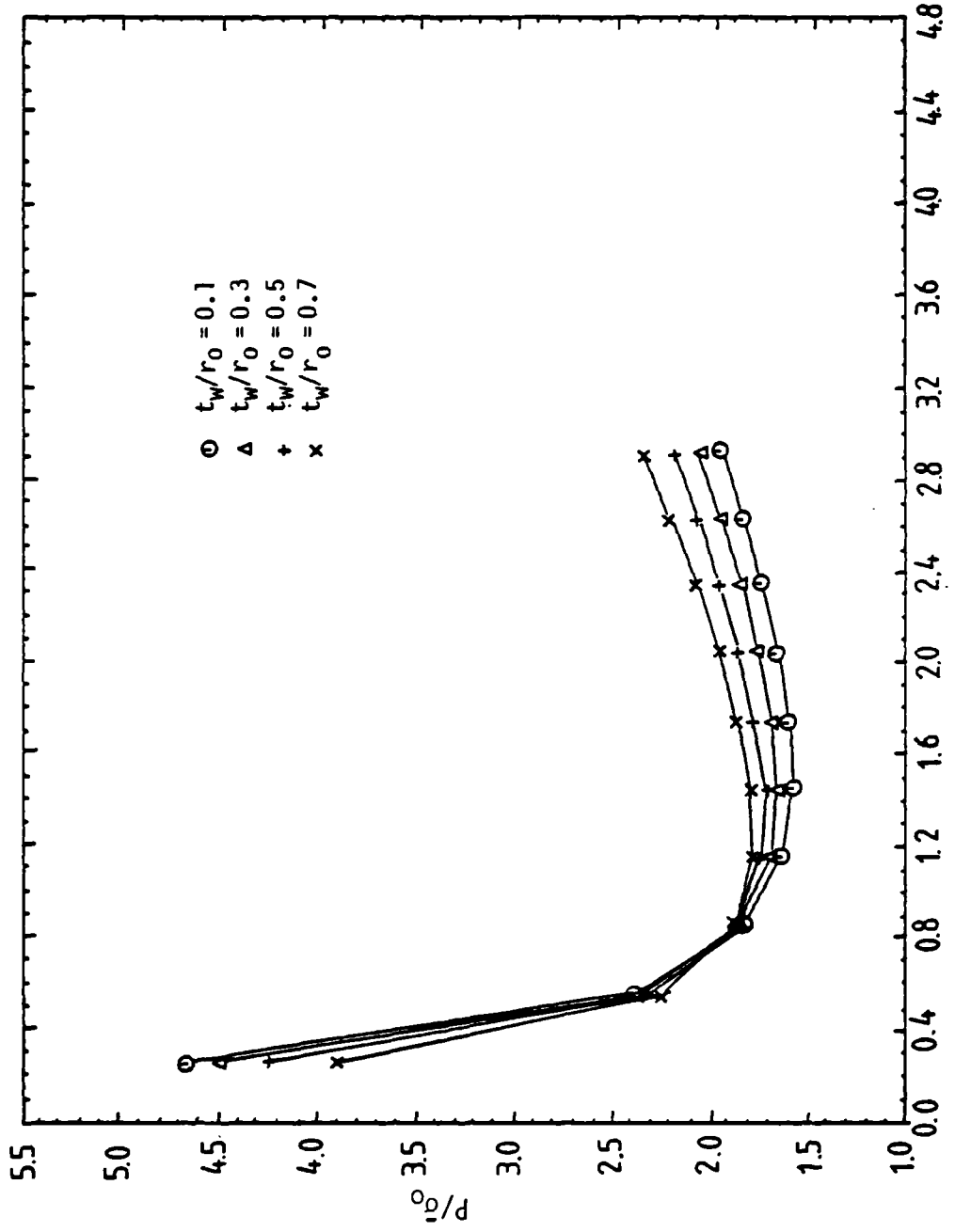


Fig. 6-51 Punch pressure versus flange thickness and wall thickness at $d_f/d_o = 1$, simple injection upsetting.

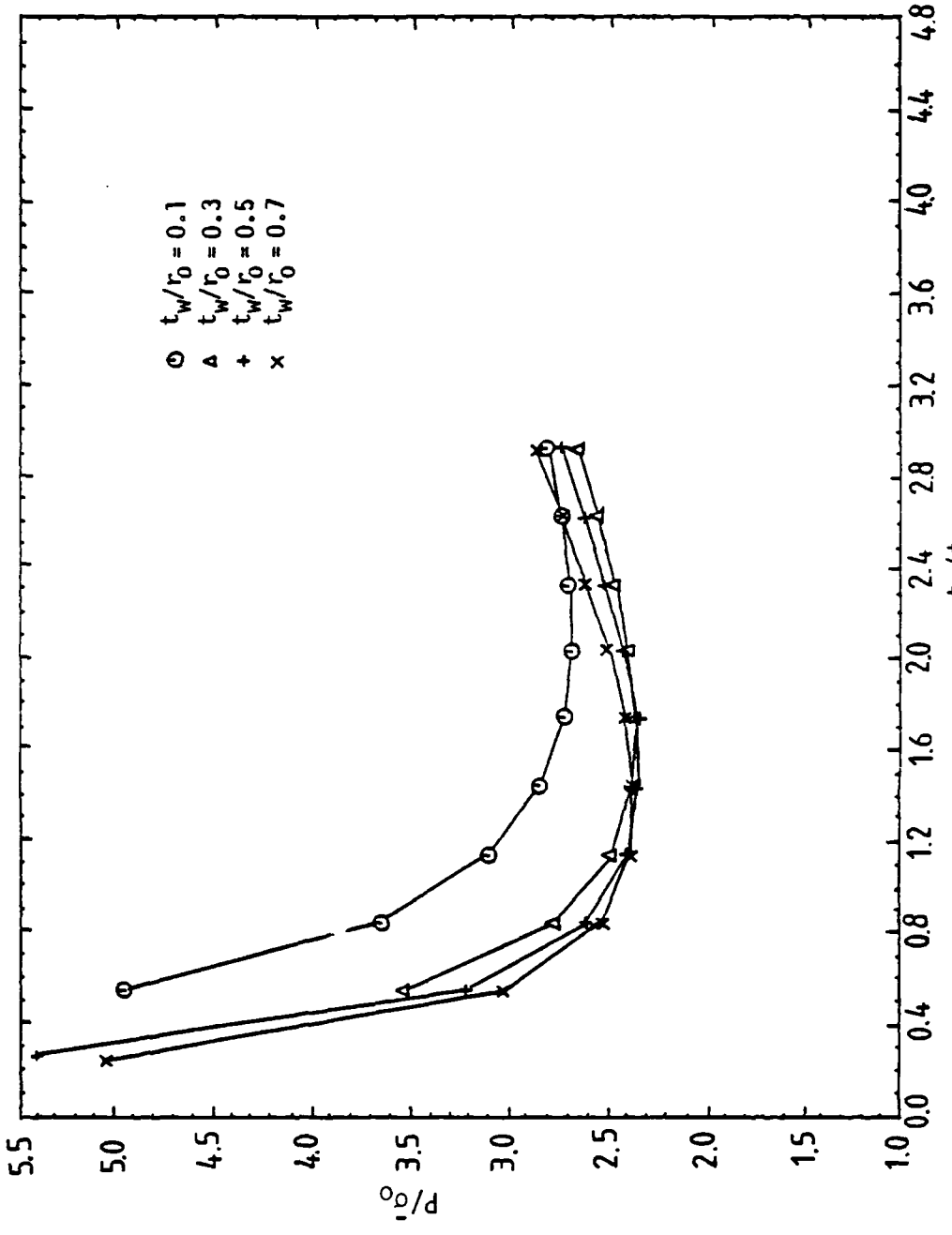


Fig. 6-52 Punch pressure versus flange thickness and wall thickness at $d_f/d_o = 1.5$, simple injection upsetting.

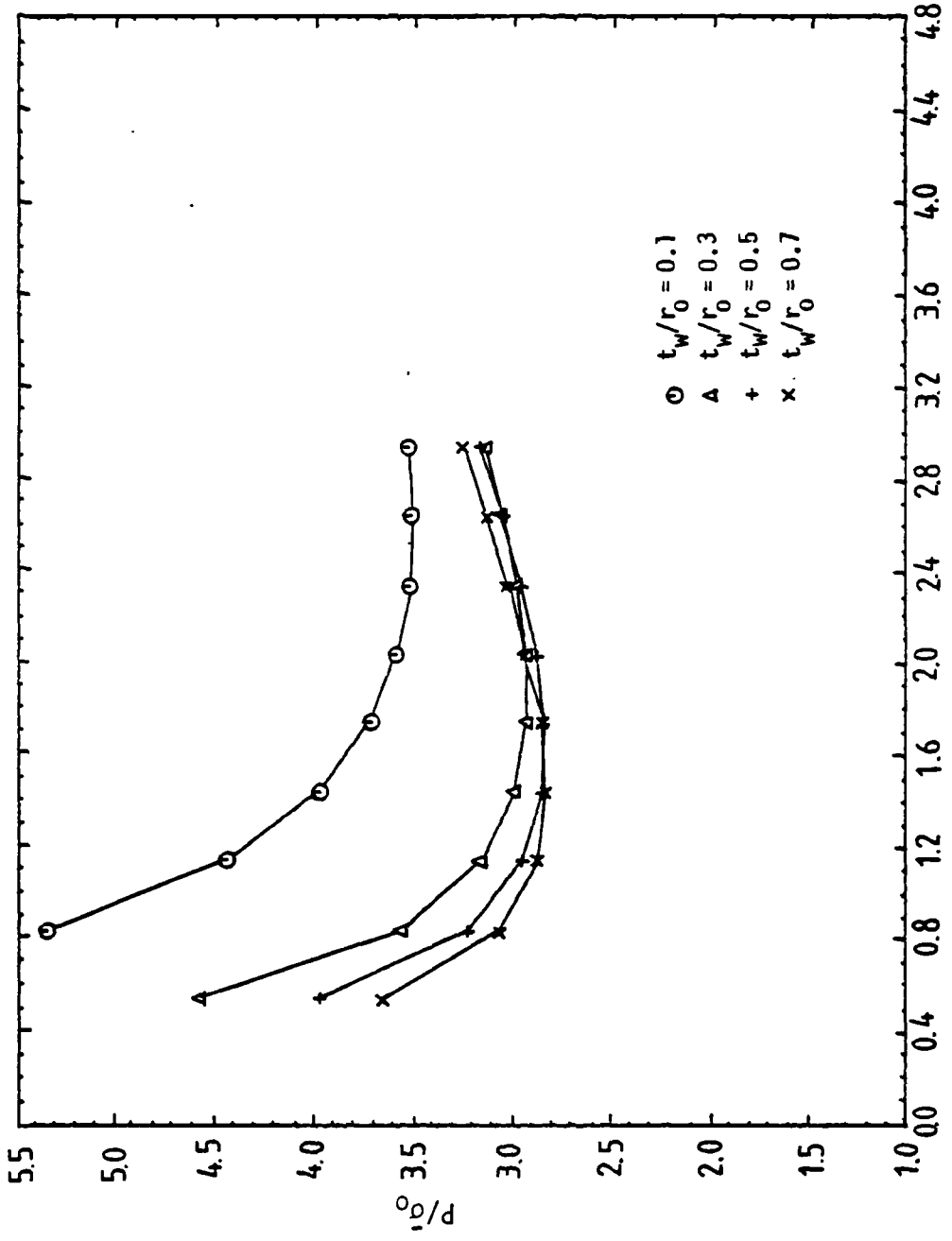


Fig. 6-53 Punch pressure versus flange thickness and wall thickness at $d_f/d_0 = 2$, simple injection upsetting.

the upsetting pressure at the beginning of deformation ($\frac{d_f}{d_o} = 1$ where d_o is the billet outside diameter and d_f is flange diameter) for billets of various sizes while t_w is kept constant. Fig. 6-51 shows that, the values of t_f/t_w in which $P/\bar{\sigma}_o$ is minimum increases with an increase in outside diameter of the billet. The variation of $P/\bar{\sigma}_o$ against t_f/t_w for billets of various sizes are also obtained at later stages of deformation shown in Figs. 6-52 and 6-53 at $\frac{d_f}{d_o} = 1.5$ and $\frac{d_f}{d_i} = 2$ respectively.

Similar results were obtained for injection upsetting with one end of the billet constrained. These are shown in Figs. 6-54 to 6-57. Fig. 6-58 compares the initial upsetting pressures (when $\frac{d_f}{d_o} = 1$) obtained for injection upsetting with and without one end of the billet constrained for various values of t_f/t_w. For small values of flange thickness ($t_f/t_w < 0.8$) the pressures are almost equal. At higher values of t_f/t_w, however, the required pressure is higher when one end of the billet is constrained and the difference increases with increasing flange thickness. This can also be seen in Fig. 6-49 where the difference between $F(0)$ and $F(\eta_{opt})$ increases when gaps of greater heights are involved.

A comparison of the upper bound upsetting pressures obtained in the present work is made with those obtained by Milner *(49)* (Figs. 6-60 and 6-61). The velocity field shown in Fig. 6-59 was used by Milner for flanges formed part way along a hollow billet. Region 1 is rigid and region 3 is a zone of pure radial flow. Region 4 is considered a dead metal zone and in region 2 $\dot{u}_r$ is taken to be independent of z. For simple injection upsetting Milner used the same deformation pattern ignoring energy losses due to shear at 2-4 boundary the dead zone 4 was replaced by a rigid platen and friction at the billet/platen interface was not considered.

Figs. 6-60 and 6-61 reveal that for small flange thickness the forming pressures predicted by Milner are lower (therefore nearer to the

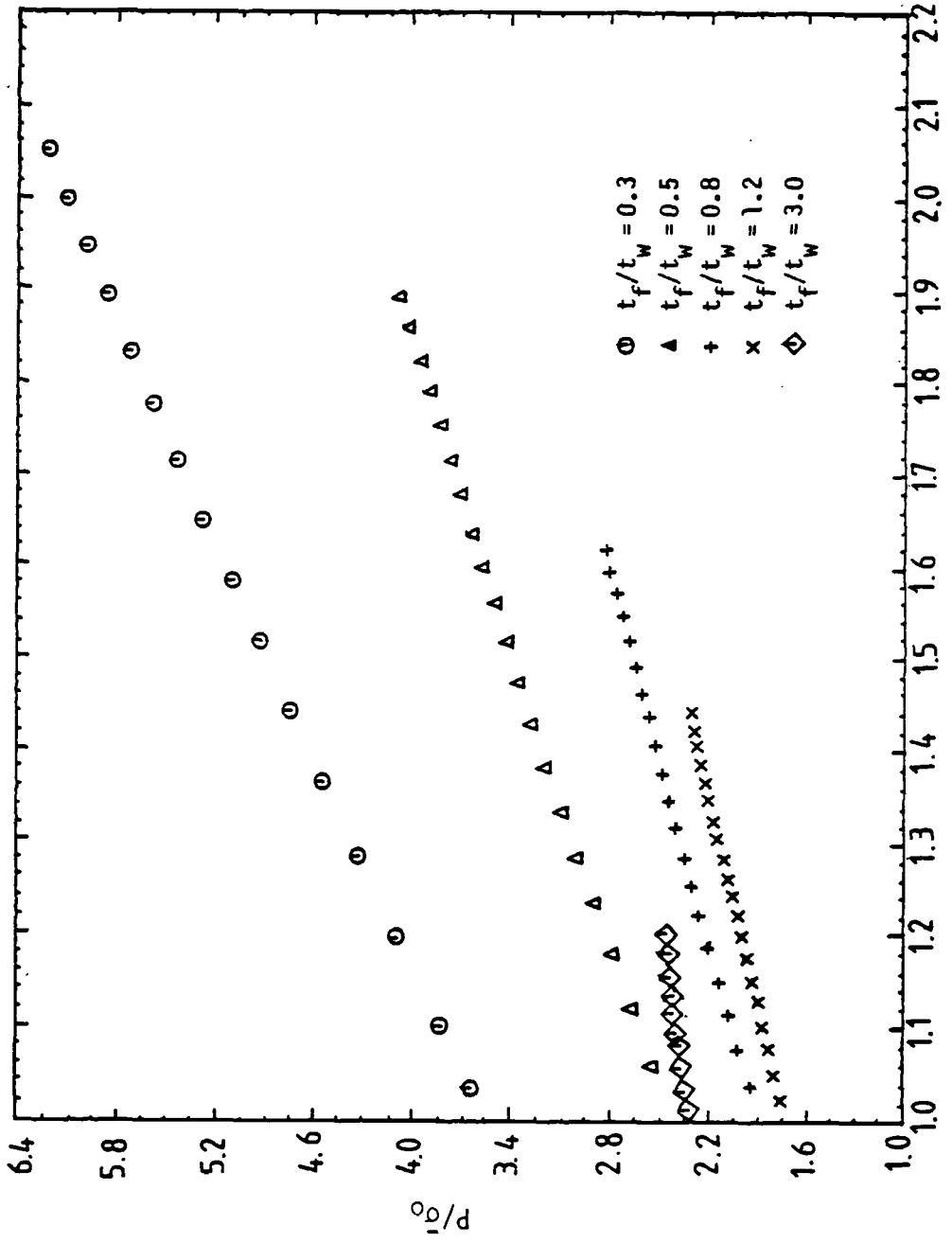


Fig. 6-54 Variation of punch pressure with flange diameter and thickness at $d_f/d_o = 1$, injection upsetting with one end constrained.

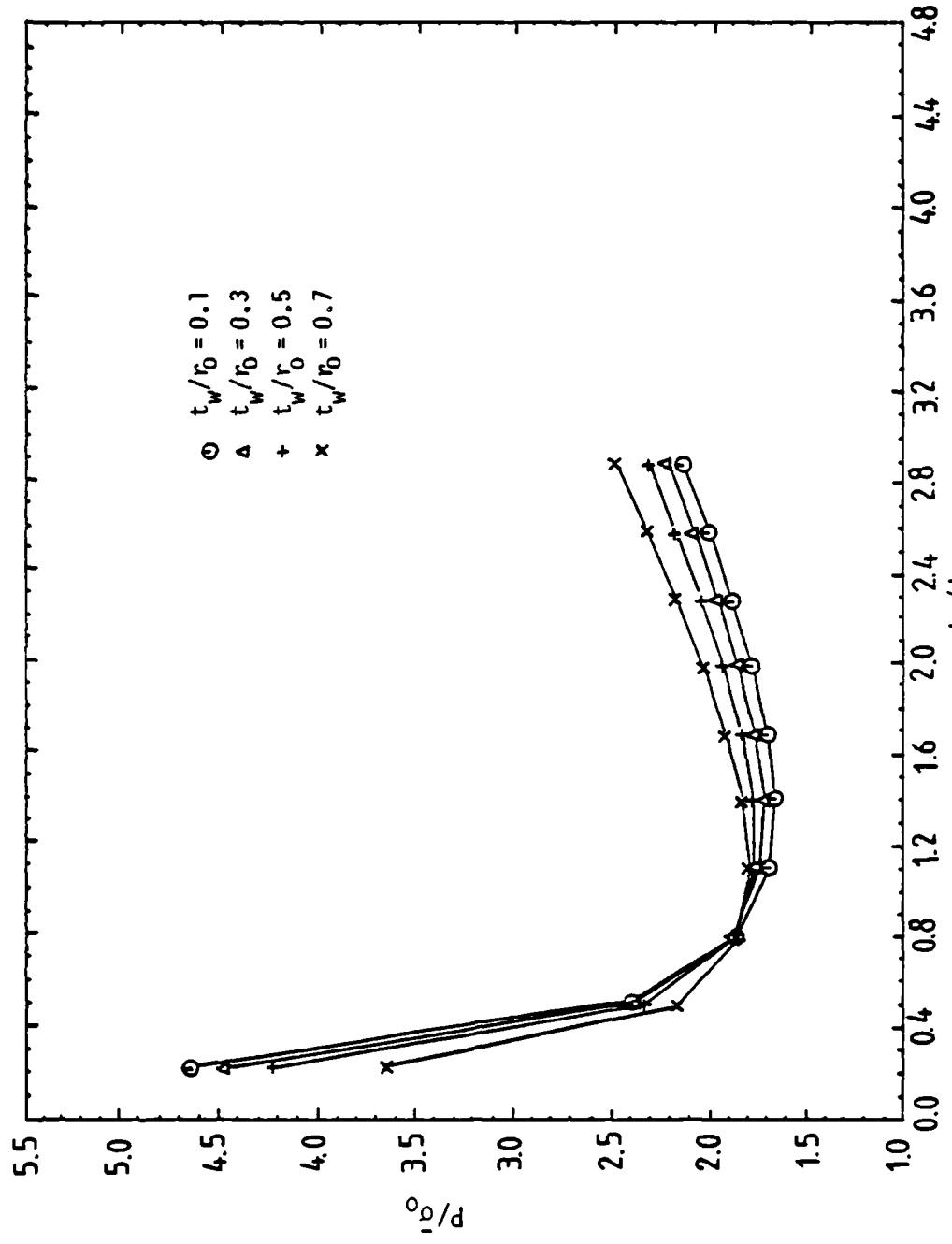


Fig. 6-55 Punch pressure versus flange thickness and wall thickness at $d_f/d_0 = 1$, injection upsetting with one end constrained.

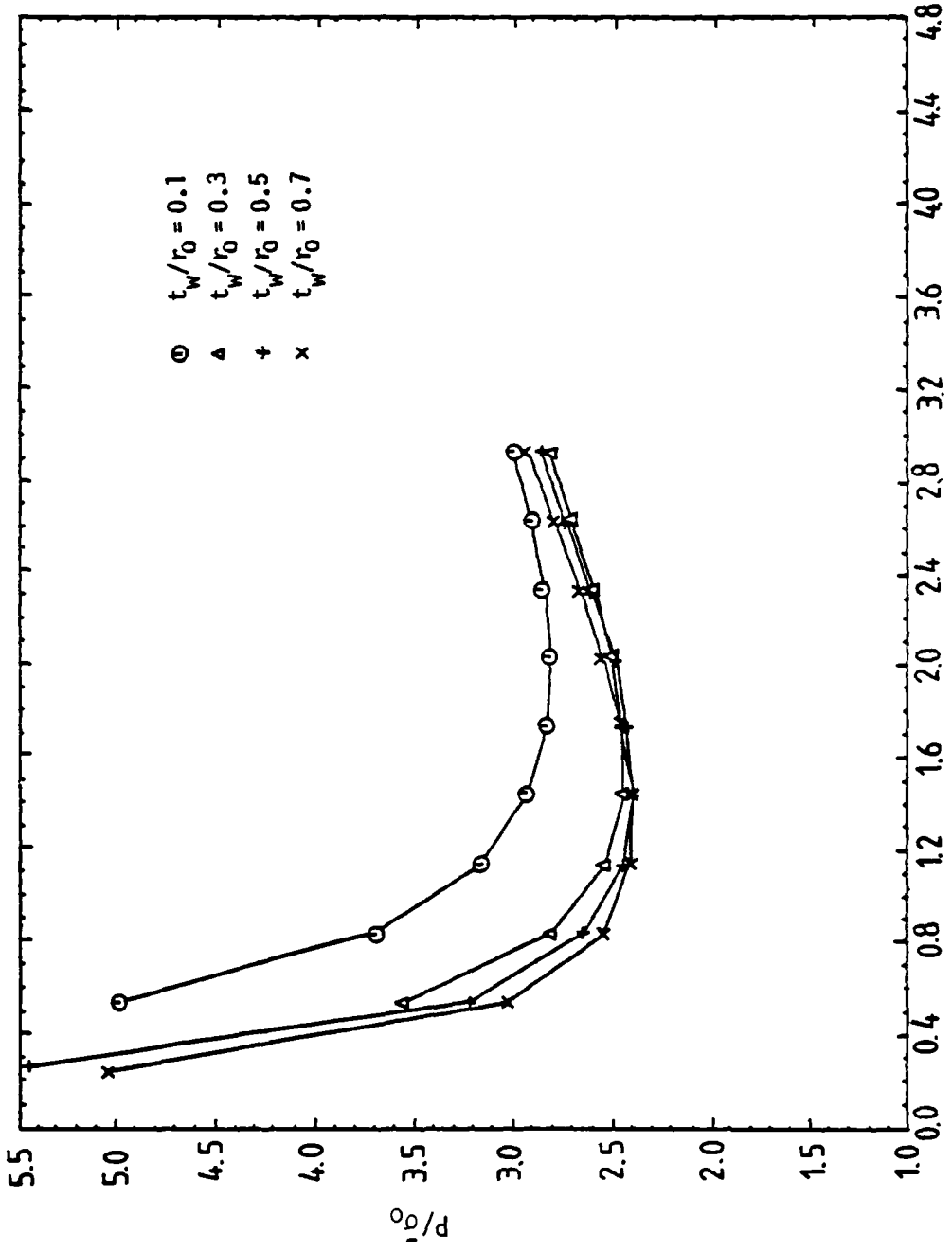


Fig. 6-56 Punch pressure versus flange thickness and wall thickness at $d_f/d_0 = 1.5$, injection upsetting with one end constrained.

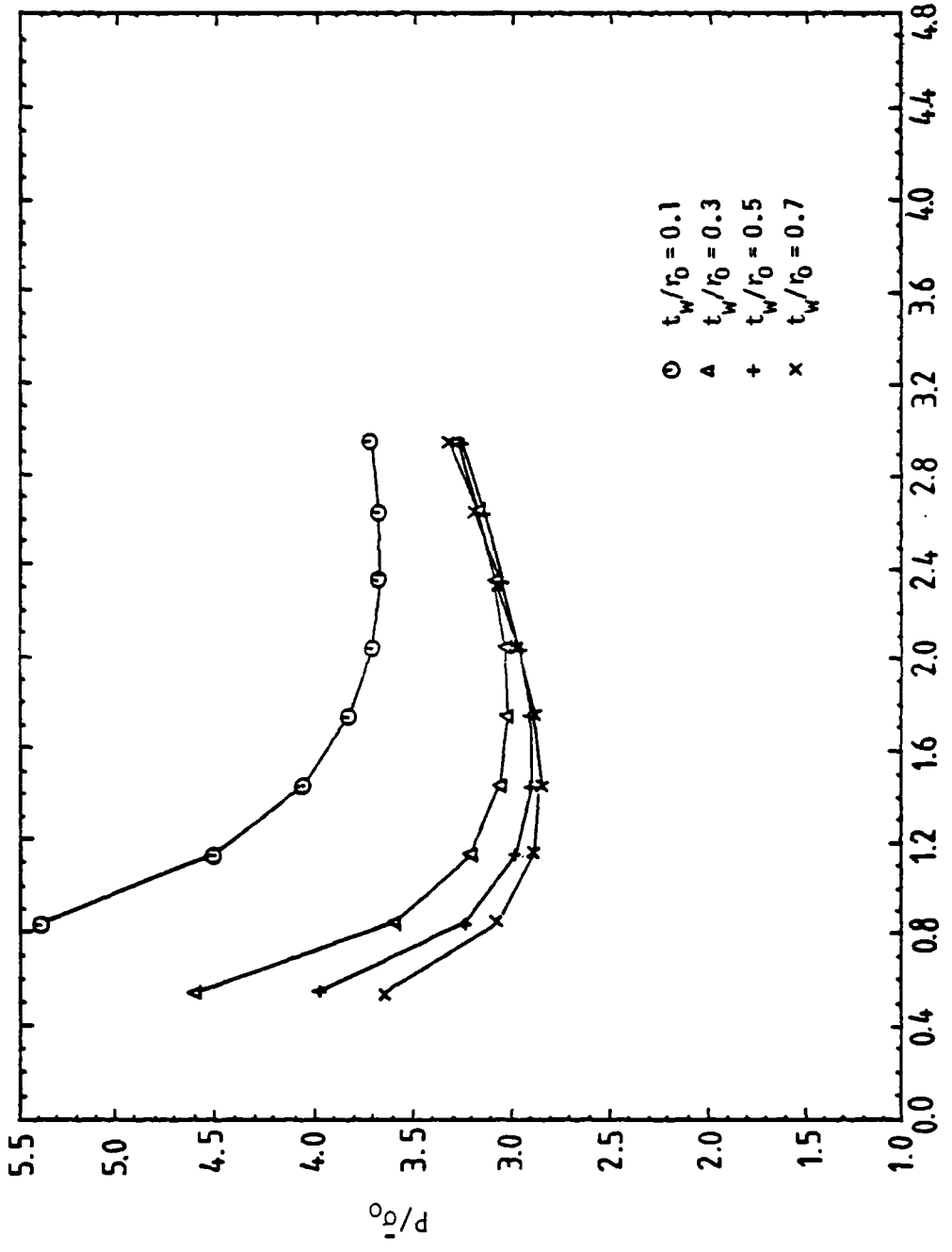


Fig. 6-57 Punch pressure versus flange thickness and wall thickness at $d_f/d_o = 2$, injection upsetting with one end constrained.

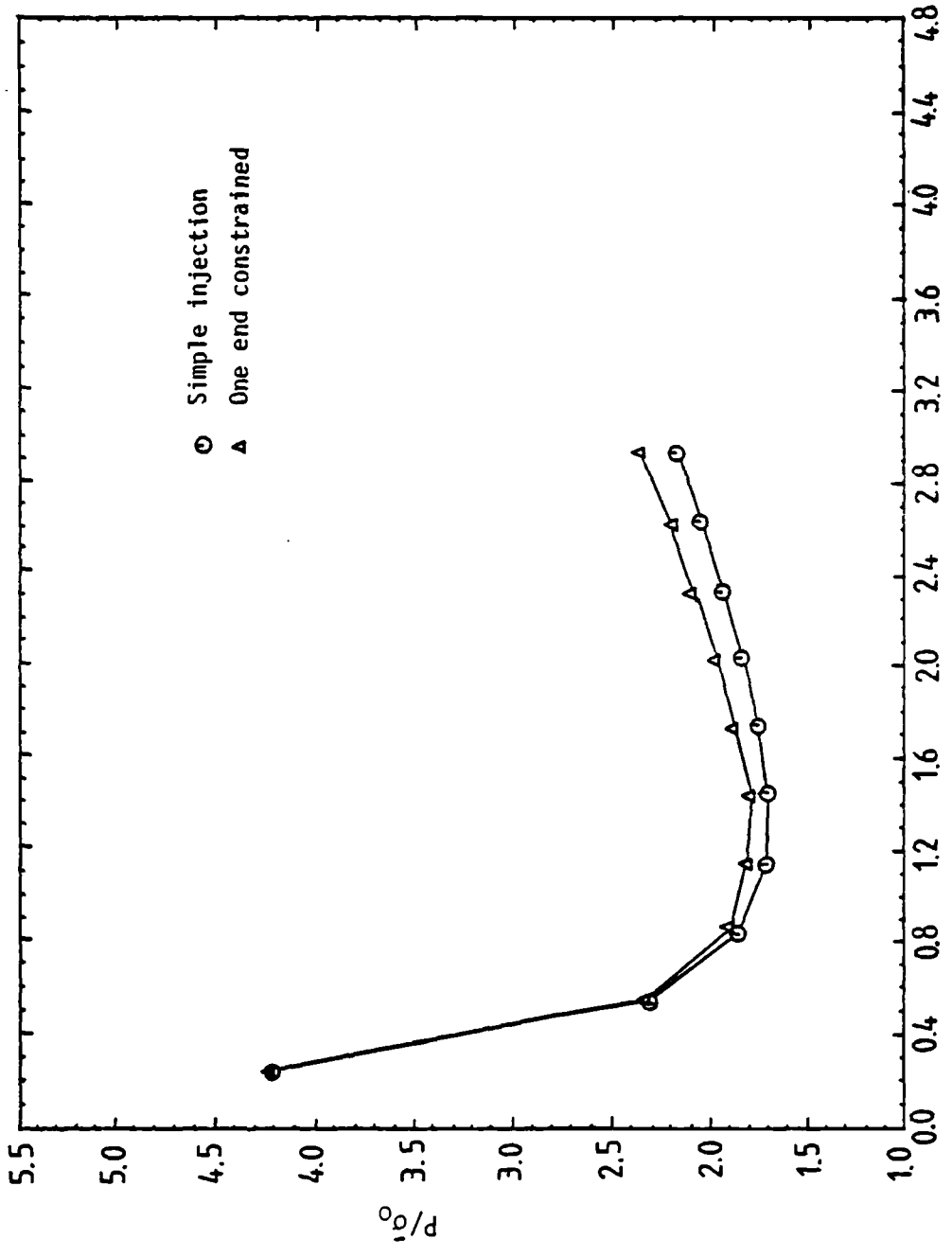


Fig. 6-58 Comparison of the upper-bound solutions for simple injection upsetting and injection upsetting with one end constrained for billets of $t_w/r_o = 0.5$ at $d_f/d_o = 1$.

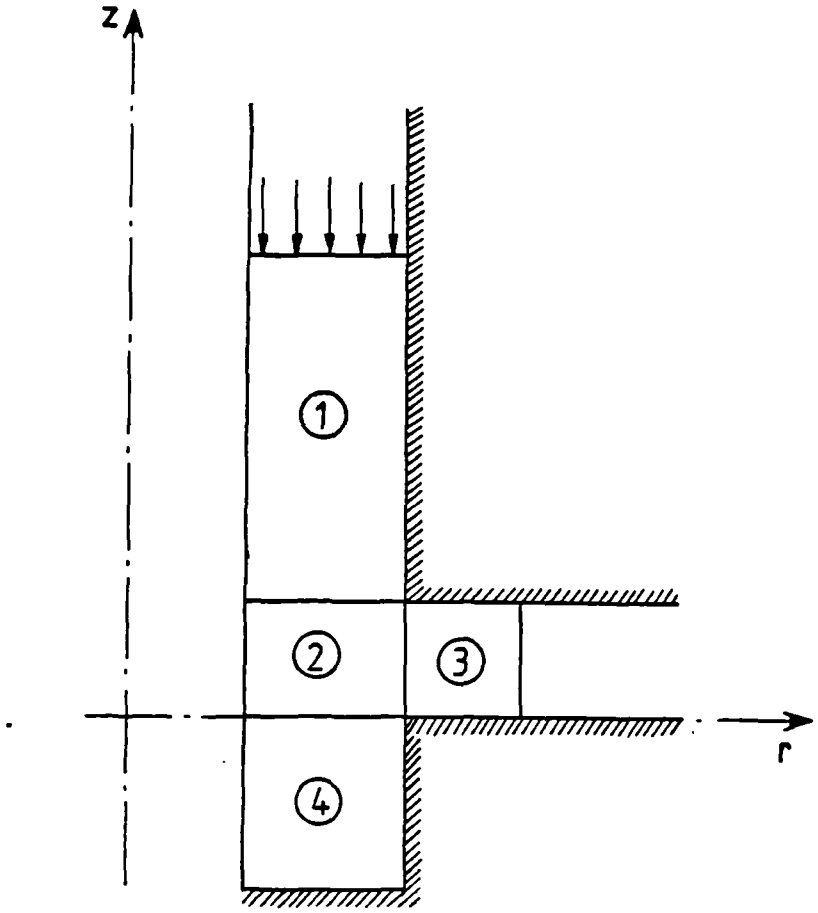


Fig. 6-59 Velocity field used by Milner *(49)*.

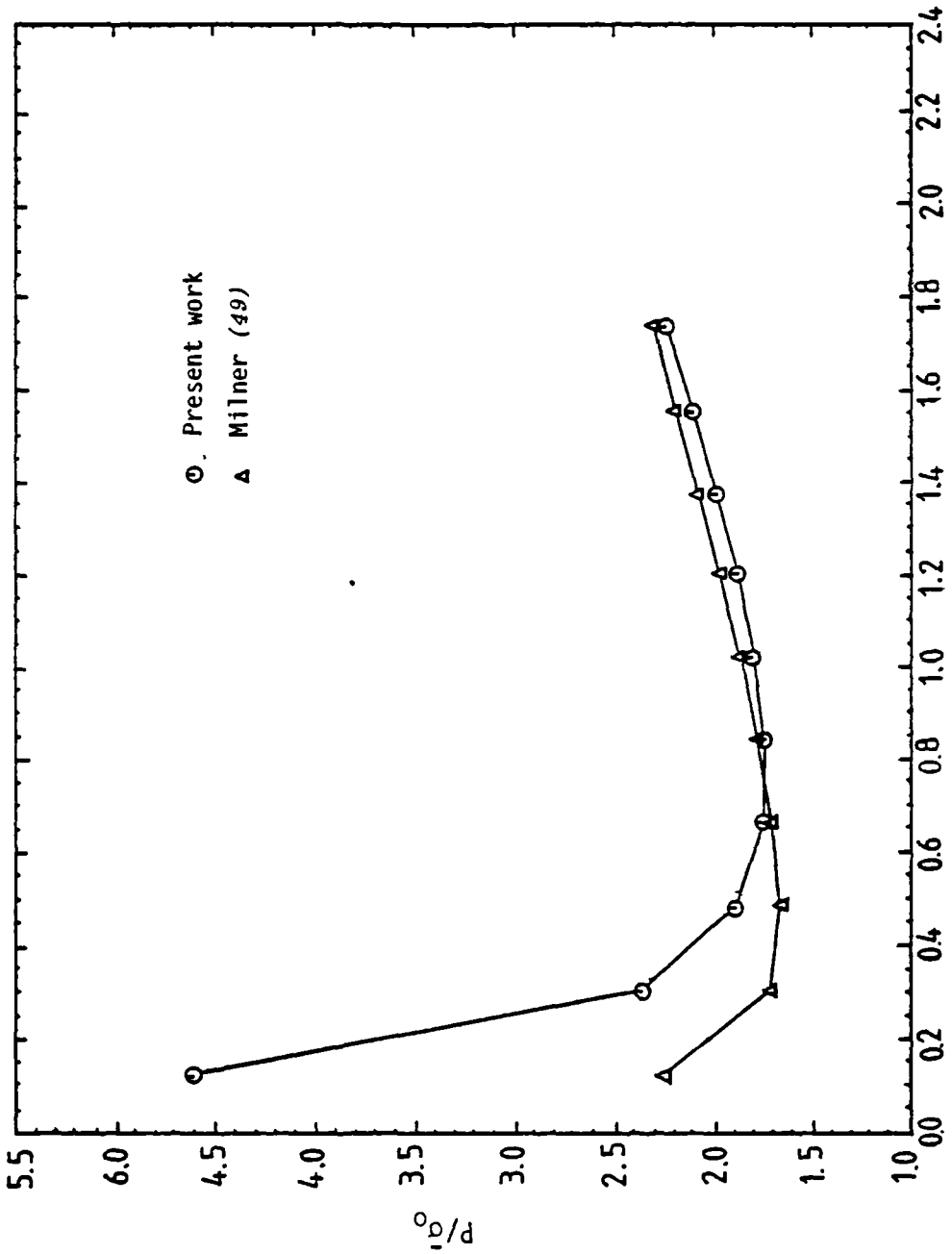


Fig. 6-60 Comparison of upper-bound solutions of the present work and the results of Milner *(49)* for billets of $t_w/r_o = 0.60$ at $d_f/d_o = 1$, simple injection upsetting.

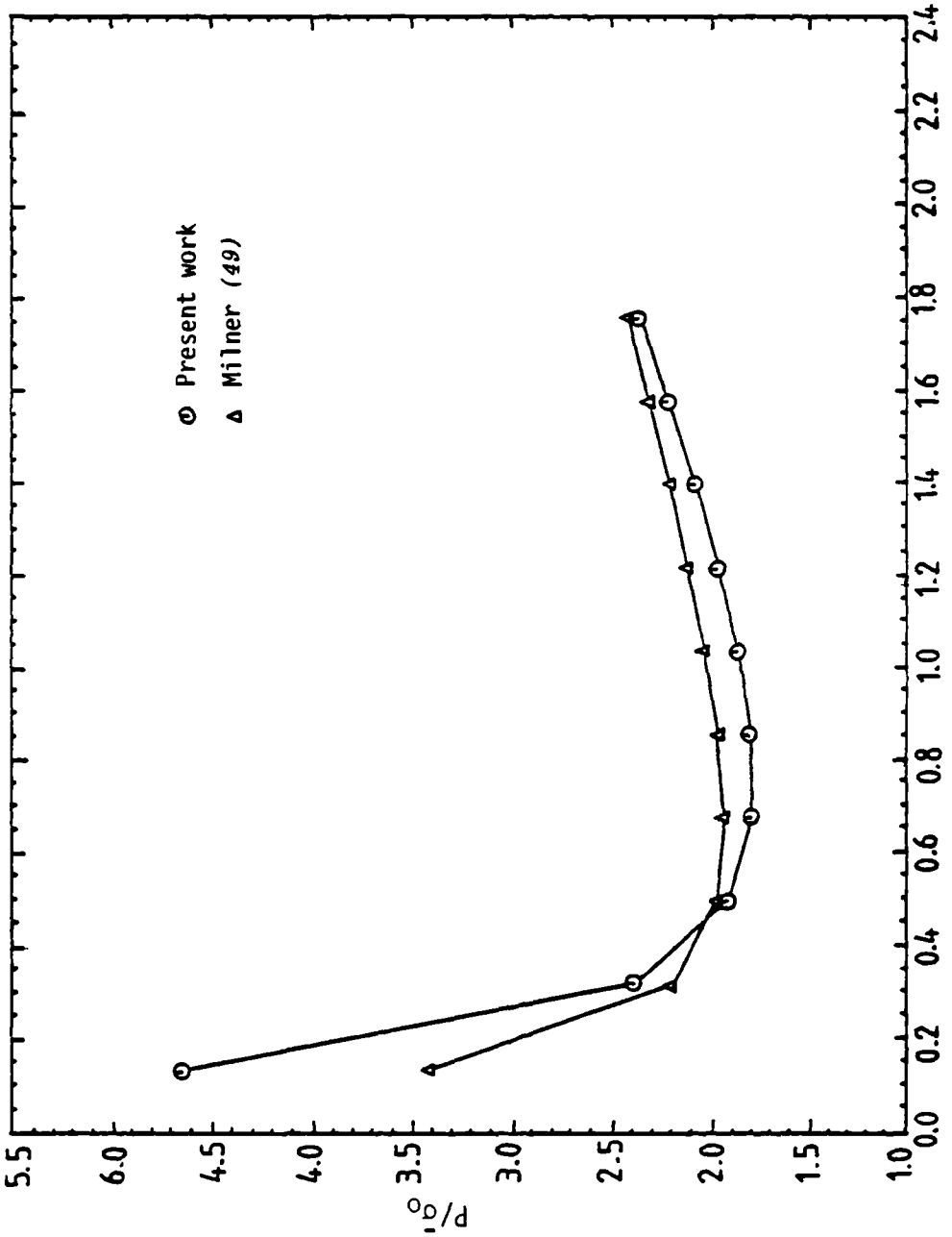


Fig. 6-61 Comparison of upper-bound solutions of the present work and the results of Milner *(49)* for billets of $t_w/r_o = 0.6$ at $d_f/d_o = 1$, injection upsetting with one end constrained.

the real value) than those obtained in the present work, while for thicker flanges the present estimates are somewhat better. This difference may be explained as follows. The experimental results show that, when forming thicker flanges, a larger portion of the radially restrained part of the billet is brought into the plastic state during deformation, i.e. at small values of gap height the central height of the deformation zone is somewhat greater than the fange thickness, whereas at larger values of gap height it is less than the flange thickness. A comparison of Figs. 4-10 and 6-59 shows that the velocity field employed by Milner provides a larger plastic zone than that of the present work, the likely reason for the better result at small values of flange thickness. The opposite is true for thicker flanges.

In order to compare the theoretical results with the experimental findings, it was necessary to assume a mean effective flow stress ($\bar{\sigma}_m$) for the work hardening materials used in the experiments. $\bar{\sigma}_m$ may be derived using the relationship

$$\bar{\sigma}_m = \frac{1}{\bar{\varepsilon}_m} \int_0^{\bar{\varepsilon}_m} \bar{\sigma}\, d\bar{\varepsilon} \qquad (6.1)$$

where $\bar{\varepsilon}_m$ is the mean effective strain for the process. The integral is the area under the stress-strain curve for the material concerned. The stress-strain curves (shown in Figs. 2-2 and 2-3 for aluminium and copper respectively) were obtained from incremental compression tests on lubricated cylindrical specimens.

To obtain $\bar{\varepsilon}_m$ in Eq. 6.1 the method used by Alexander and Lengyel *(45)* was employed. When the punch moves downwards for a time δt, it moves a distance $\dot{u}\delta t$ and each elemental ring of the undeformed billet that has previously entered regions 2 (Fig. 4-10) and 3 is distorted as it progresses

in these regions through a small distance that could be derived from the velocity field. The incremental work done by the punch is equal to that required to propel one such elemental ring from region 1 into regions 2 and 3 until it reaches the instantaneous extremity of region 3. If the mean effective strain imparted to the ring doing such a movement is $\bar{e}_m$, then the work done/unit volume of material is $\bar{\sigma}_m \bar{\varepsilon}_m$. Thus, the work done ($\delta W_P$) by the punch in time δt is

$$\delta W_P = A \ |V_P| \ \delta t \ \bar{\sigma}_m \ \bar{\varepsilon}_m$$

where A is the punch/workpiece contact area and V_P is the punch velocity. The above relation results in

$$\frac{\delta W_P}{\delta t} = \dot{W}_P = \pi \ d_o^2 \ |V_P| \ \bar{\sigma}_m \ \bar{\varepsilon}_m$$

after substituting into Eq. 4.63

$$\frac{P}{\bar{\sigma}_m} = \bar{\varepsilon}_m \qquad (6.2)$$

This expression makes no provision for frictional work since this is not responsible for plastic straining. Thus, equation 6.2 indicates that in the frictionless upper-bound solution, if $\bar{\sigma}_o$ is replaced by $\bar{\sigma}_m$, the mean effective strain ($\bar{\varepsilon}_m$) of the process becomes equal to the right-hand side of Eq. 4.94.

The above derivation of $\bar{\varepsilon}_m$ is based on the assumption that all the material in regions 2 and 3 originate from region 1. In fact the element of the billet which is initially in region 2 will not undergo the deformation associated with crossing the 1-2 boundary, and will only be subjected to

some of the deformation associated with passage through region 2, depending on its initial position within this region. Obviously, at the start of deformation $(d_f/d_o = 1)$ the actual mean effective strain is zero, since region 2 contains undeformed material. As $d_f/d_o \to \infty$, the mean effective strain approaches the value given by Eq. 6.2, since a very large portion of the material then in regions 2 and 3 will have originated from region 1. Thus, it is perhaps more correct to assume that the actual $\bar{\varepsilon}_m$ is some function of $F(d_f/d_o)$. A suitable function which satisfies the end conditions (takes the value zero when $d_f/d_o = 1$ and unity as d_f/d_o tends to infinity) has been suggested by Milner *(49)*:

$$F(d_f/d_o) = \frac{d_f/d_o - 1}{d_f/d_o - K} \quad , \quad (0 < K < 1) \tag{6.3}$$

Using this factor in Eq. 6.2 results in

$$\bar{\varepsilon}_m = \left(\frac{d_f/d_o - 1}{d_f/d_o - K} \right) \frac{P}{\bar{\sigma}_m} \tag{6.4}$$

As suggested by Milner, the value of K is selected so that, when a volume equal to that of the initially unrestrained part of the billet has been swept out by the punch, the value of F in Eq. 6.3 is 0.5.

The procedure used in obtaining the experimental values of $P/\bar{\sigma}_o$ for every step of punch displacement may be summarized as follows:

1) Evaluate d_f for a given punch displacement by using volume constancy.
2) Calculate $P/\bar{\sigma}_m$ from Eq. 4.94 inserting zero for $\dot{E}_{F16}$ and $\dot{E}_{F67}$
3) Calculate $\bar{\varepsilon}_m$ using Eq. 6.2.
4) Using the stress-strain curve, find $\bar{\sigma}_m = \frac{1}{\bar{\varepsilon}_m} \int \bar{\sigma} \, d\bar{\varepsilon}$
5) Evaluate the experimental value of $P/\bar{\sigma}_o$ for the known experimental load i.e. $P/\bar{\sigma}_o = \frac{F_P}{A} \frac{1}{\bar{\sigma}_m}$ where F_P is the punch load and $A = \pi/4(d_o^2 - d_i^2)$

is the punch/workpiece contact area.

The theoretical curves of punch pressure versus flange thickness show that the punch pressure is minimum for some value of flange thickness. Under present conditions for a wall thickness of $t_w = 0.45 r_o$ the minimum pressure is at a flange thickness of $t_f = 1.36\, t_w$. In Figs. 6-62 and 6-63 the theoretical and experimental results are compared for this flange thickness. The figures show good agreement between the theoretical and experimental punch pressures and the agreement is slightly better when one end of the billet is constrained (Fig. 6-63). This may be explained as follows. When one end of the billet is constrained the frictional forces at the billet/mandrel interface are higher and also bulging of the bore surface is less, which both cause a rise in the experimental loads.

Although the minimum of the upper-bound pressures at a particular flange thickness show good agreement with the corresponding experimental values, considerable discrepancies were observed for other values of flange thickness. This was expected for higher values of flange thickness since unlike the predictions the experimental pressures do not follow an upward trend for thicker flanges. The inaccuracy of predictions for thinner flanges is possibly due to the smaller zone of plastic deformation in the theory compared with reality.

The main sources of error which would be expected to influence the quality of agreement between theory and experiment may be mentioned as follows:

1) The major shortcoming of the upper-bound analysis is the difference between the real and predicted flow pattern.
2) The effect of an inaccurate upper bound would be accentuated by the method of calculating $\bar{\sigma}_m$, since a high upper bound would lead to an

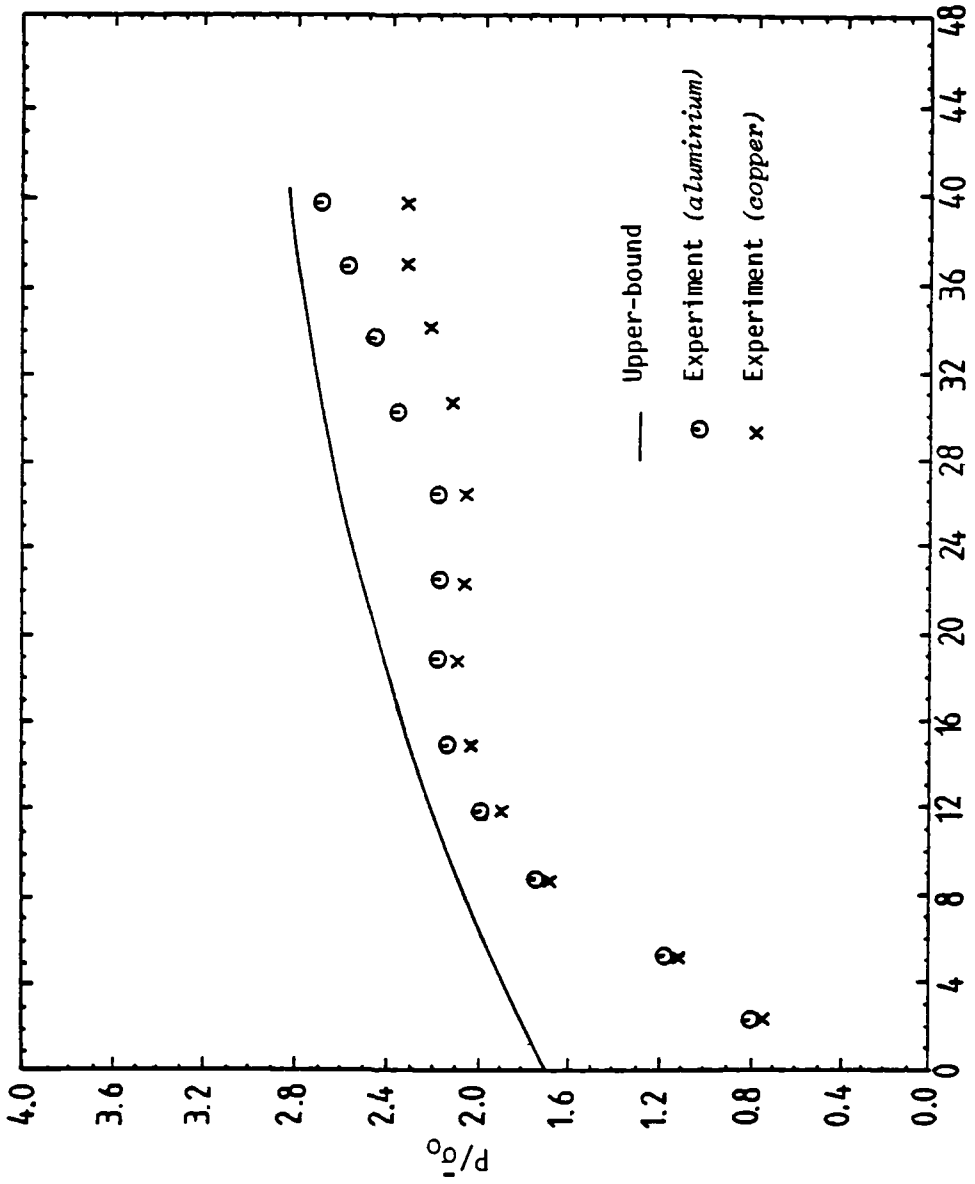


Fig. 6-62 Comparison of upper-bound results with experimental findings for billet of $t_w/r_o = 0.45$ and $t_f/t_w = 1.36$, simple injection upsetting.

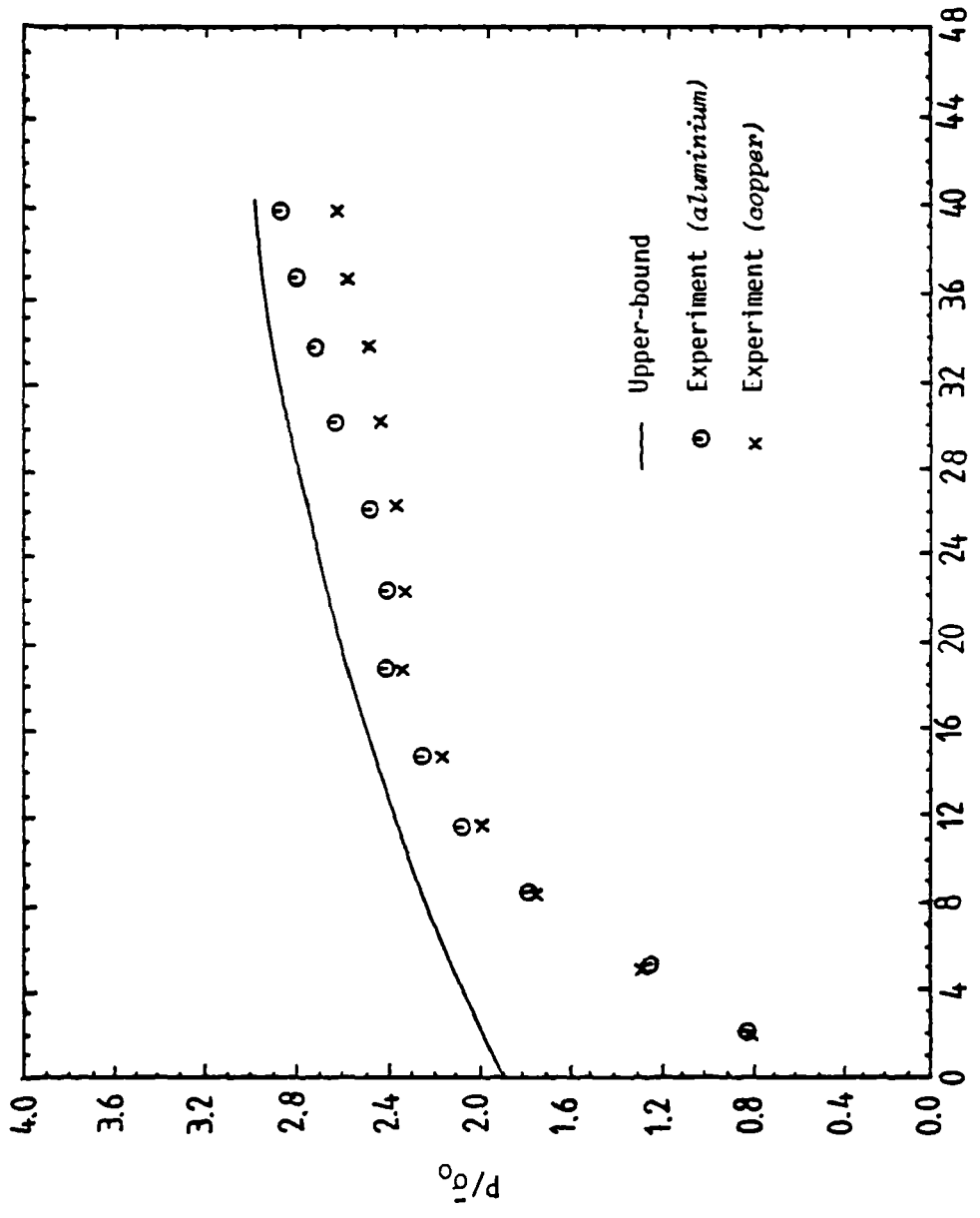


Fig. 6-63 Comparison of upper-bound results with experimental findings for billets of $t_w/r_o = 0.45$ and $t_f/t_w = 1.36$, injection upsetting with one end of the billet constrained.

overestimate of $\bar{\varepsilon}_m$, and therefore of $\bar{\sigma}_m$, in a continuously work-hardening material.

3) Friction between the tool/workpiece interface would tend to raise the experimental points relative to the upper-bound curve, since this effect was disregarded in the present theory.

4) The occurrence of bulging at the bore surface and also thinning of the upset flange are expected to lower the experimental points relative to the upper-bound curve. This is possibly the reason for the experimental pressures not reflecting the upward trend of the upper-bound curves at high values of flange thickness since these effects are more severe when flanges of larger thickness are involved.

5) Unsuitability of the function $F(d_f/d_o)$ used in Eq. 6.3 or of its parameter K. Various choices of the value of K would cause a hump or localized dip of the experimental points as the deformation proceeds, i.e. increasing the value of K moves the experimental points downwards relative to the upper-bound curve and decreasing K has the opposite effect.

CHAPTER 7

CONCLUSIONS

7.1 Conventional upsetting

1) The material on the outer free surface of the flange begins to roll up onto the contact surfaces at some stage of the deformation. This rolling up is more pronounced on the lower platen, or when dry platens are used, or for higher initial unsupported heights and in open upsetting.

2) The upsetting load increases at a higher rate after the rolling up begins with a further sharp rise when the pressure cones meet.

3) Bulging of the bore surface at a later stage causes a fold (at mid-distance of the free height) which continues to penetrate into the upset metal as deformation proceeds. The folding is more severe for higher initial unsupported height, for lower wall thickness or for dry platens. In heading, the fold is inclined to the horizontal plane of the flange while it lies in that plane in open upsetting.

4) In heading, the absence of lubricant results in more pronounced initial bulging, a greater part of the material remains in contact with the mandrel, a lower increase in punch/specimen contact area, the flange becomes more circular and rolling up is more pronounced.

   The absence of lubricant has no significant effect on the behaviour of metal in open upsetting.

5) Although the finite element formulation, presented in chapter two, was developed for small strains and displacements, the predicted

results show reasonably good agreement with the experiments even at a more advanced stage of the deformation.

6) In the axi-symmetric problem of conventional upsetting, the quadrilateral elements are more economical and more accurate than the triangular elements.

7) The inclusion of surface friction in the finite element method by the introduction of tangential forces to the surface nodes (in directions opposing the material motion) is efficient and produces realistic results.

8) The finite element method predicts the upsetting load with a very good degree of accuracy. However, the predicted loads start to deviate from their corresponding experimental values after rolling up begins.

9) The current shape of the upset billet and metal flow predicted by the finite element method are in reasonably good agreement with the experiments.

10) The application of a restraining hydrostatic pressure in the computations indicates more uniform deformation, a more even radial velocity distribution along the free height, less pronounced shearing between the plastic and rigid zones and a reduction in the amount of bulging in both the bore and outer free surfaces.

11) In the conventional upsetting of hollow billets into restricted cavities (as an alternative way of eliminating bulging in the bore region) after the upset metal reaches the outer walls the direction of metal flow changes and eventually the inner bulge is reduced.

7.2 Injection upsetting

1) The required upsetting load is smaller for flanges of greater thickness and as the gap height increases the rate of decrease in load becomes smaller.

2) Thinning occurs for all flanges produced by injection upsetting. The effect is more pronounced for flanges of greater thickness.

3) In the case of simple injection upsetting of thin flanges, the flange obtains a dish shape at some stage of deformation and it continues its upward movement until prevented by contact with the tool.

4) The formed flanges are very sensitive to irregularities on the contact surfaces. For thick flanges local retardation of the radial flow of metal occurs due to lubrication breakdown. However, for flanges formed on dry platens, circular shapes could be maintained throughout the process.

5) None of the flanged products showed any sign of free surface fracture. Even for the smallest gaps in the simple injection upsetting of annealed aluminium and copper flanges twice the billet diameter showed no sign of fracture.

6) In simple injection upsetting with lubricated platens a fold forms on the flange/platen contact surface. The extent of the fold and its penetration into the upset flange increases with flange thickness. When dry platens were used, the fold is formed in the bore region (at mid-height of the free gap) and is more severe for greater gap heights. For lubricated platens, the maximum flange diameter occurs at the lower face of the flange whereas under unlubricated conditions

the maximum diameter is near the upper face.

7) In injection upsetting of hollow billets with one end constrained, the shape of the upset flange and mode of deformation is almost identical to that obtained in the corresponding simple injection upsetting with a dry platen. Various frictional coditions have no significant effect on the deformation mode.

8) In general, the deformed zone and its penetration into the constrained region increases with decreasing flange thickness.

9) Experimental results show that the forming load decreases with increasing gap height. Results obtained by the upper-bound technique show the same tendency first, but then there is a reversal of this trend at a particular value of flange thickness, where the agreement with experimental findings is good. Elsewhere the agreement is uncertain because the upper-bound load is greatly affected by a number of parameters which makes a meaningful comparison difficult between the experimental and theoretical results.

APPENDIX 'A'

LISTING OF THE COMPUTER

PROGRAM EPLAST1

USING TRIANGULAR ELEMENTS

NOMENCLATURE

Variable	Definition
NNP	Number of nodal points
NEL	Number of elements
NEQ	Number of equations
NBAND	Number of bandwidth
NBR	Number of boundary nodal points with defined conditions
NPI, NPJ, NPM	Nodal connection of elements
R, Z	Coordinates of nodal points
BI, BJ, BM CI, CJ, CM	Local coordinates of elements
AREA	Area of elements
G	Shear modulus
NU	Poison's ratio
E	Modulus of elasticity
ET	Strain-increment of elements
SK	Overall stiffness matrix
K	Element stiffness matrix
SIGY	Yield stress of elements
B	Strain displacement matrix
D	Elastic material matrix
DP	Strain-stress matrix of elements
F	Nodal points forces
FO	Nodal points total forces
SIS	Stress-increment of elements
SIGT	Stress components

SIGD	Deviatoric stress components
SIGLM	Equivalent stress-increment of elements
SIGLMO	Equivalent stress of elements
DIS	Displacement-increments of nodal points
DIST	Total nodal points displacements
NB	Boundary nodal points that their status will be set in the program
NFIX	Status vector defining the status of nodal points as suppressed or free surfaces
ND	Pointer vector for indicating state of elements
NFRIC	Number of boundary nodal points with friction forces
NSTIC	Pointer vector for imposing friction forces
DIN	Internal diameter of the specimen
DOUT	Outer diameter of the specimen
LENGTH	Height of the specimen
IMAX	Number of load increments
RATEF	Rating factor
ZETA1, ZETA2	Tangent moduli of stress-strain curve at breaking points

```
C*********************************************************************
C*********************************************************************
C****** PROGRAM FOR ELASTIC-PLASTIC FINITE ELEMENT ANALYSIS OF THE ******
C****** AXI-SYMMETRIC TYPE, USING CONSTANT STRAIN TRIANGULAR       ******
C****** ELEMENTS.                                                 ******
C*********************************************************************
C*********************************************************************
 PROGRAM EPLAST1(OUTPUT,TAPE1,TAPE6=OUTPUT)
 COMMON NPI(224),NPM(224),NPJ(224),R(135),ET(4,224),SK(270,22),
*SKB(270,22),DIS(270),DIST(270),DISO(270),DISE(6),NB(44),Y(224),
*BJ(224),BM(224),CI(224),CJ(224),CM(224),SIGLM(224),SIS(4,224),
*SIGT(4,224),SIGO(4,224),SIGD(4,224),IN(3),W(6,6),D(4,4),
*B(4,6,224),DP(4,4,224),AREA(224),RBAR(224),SIGLMO(224), ND(224),
*NFIX(44),NMIX(44),NIX(44),F(270),FO(270),Z(135),BI(224),EEP(224),
*STY(2),NEL,NEQ,NBAND,NBR,NX,NY,NNP,MIT,STEP1,STEPO,ZETA1,ZETA2,
*NFRIC,NSTIC,L,G,RATEF,SIGY,DIN,DOUT,ECY,IOUT,IMAX,LENGTH,E,NU
C*********************************************************************
C****** INPUT OF DATA ***********************************************
 CALL INPUT
C*********************************************************************
C****** GENERATE THE MESH DATA **************************************
 CALL  MESH
C*********************************************************************
C****** FORM THE ELASTIC PROPERTY MATRIX ****************************
 CALL FORMD1
C*********************************************************************
C****** FORM THE ELEMENT DIMENSION MATRIX ***************************
 CALL FORMB
C*********************************************************************
C****** FORM THE ELEMENT STIFFNESS MATRIX AND THE OVERALL STIFFNESS *****
C****** MATRIX.                                                     *****
 CALL FORMK
C*********************************************************************
C****** APPLY THE BOUNDARY CONDITIONS *******************************
100  CALL BOUNDRY
C*********************************************************************
C****** SOLVE OF THE SYSTEM OF EQUATIONS ****************************
 CALL SOLVE
C*********************************************************************
C****** COMPUTE THE STRAIN COMPONENTS *******************************
 CALL STRAIN
C*********************************************************************
C****** COMPUTE THE STRESS COMPONENTS *******************************
 CALL STRESS
C*********************************************************************
C****** EVALUATION OF THE RATING FACTOR *****************************
 CALL RFACT
C*********************************************************************
C****** FORM THE ELASTOPLASTIC PROPERTY MATRIX **********************
 CALL FORMD2
C*********************************************************************
C****** UPDATE OF BOUNDARY CONDITIONS *******************************
 CALL UPDATE1
C*********************************************************************
C****** OUTPUT THE REQUIRED RESULTS *********************************
 CALL OUTPUT
C*********************************************************************
C****** UPDATE OF GEOMETRICAL MATRICES ******************************
```

```
      CALL UPDATE2
      GO TO 100
      END
      SUBROUTINE INPUT
      COMMON NPI(224),NPM(224),NPJ(224),R(135),ET(4,224),SK(270,22),
     *SKB(270,22),DIS(270),DIST(270),DISO(270),DISE(6),NB(44),Y(224),
     *BJ(224),BM(224),CI(224),CJ(224),CM(224),SIGLM(224),SIS(4,224),
     *SIGT(4,224),SIGO(4,224),SIGD(4,224),IN(3),W(6,6),D(4,4),
     *B(4,6,224),DP(4,4,224),AREA(224),RBAR(224),SIGLMO(224), ND(224),
     *NFIX(44),NMIX(44),NIX(44),F(270),FO(270),Z(135),BI(224),EEP(224),
     *STY(2),NEL,NEQ,NBAND,NBR,NX,NY,NNP,MIT,STEP1,STEPO,ZETA1,ZETA2,
     *NFRIC,NSTIC,L,G,RATEF,SIGY,DIN,DOUT,ECY,IOUT,IMAX,LENGTH,E,NU
      REAL NU,LENGTH
      E=700000.$NU=0.345$SIGY=400.$SIGY2=870.$ZETA1=4000.$ZETA2=700.
      STEP1=-0.003$STEPO=-0.0005
      NSTIC=1
      IOUT=20$IMAX=400
      G=E/(2*(1+NU))
      LENGTH=5.29$DIN=2.5$DOUT=4.4
      NY=14$NX=8$NBR=44$NBAND=22
      NFRIC=54
      STY(1)=SIGY$STY(2)=SIGY2
      NEL=2*NX*NY
      NNP=(NX+1)*(NY+1)
      NEQ=NNP*2
      MIT=0
      DO 280 L=1,NEL
      EEP(L)=0.
      SIGLMO(L)=0.
      Y(L)=1.
      ND(L)=0
      DO 280 I=1,4
      SIGO(I,L)=0.
      ET(I,L)=0.
280   CONTINUE
      DO 214 N=1,NEQ
      FO(N)=0.
      DIS(N)=0.
      DISO(N)=0.
214   F(N)=0.
      RETURN
      END
      SUBROUTINE MESH
      COMMON NPI(224),NPM(224),NPJ(224),R(135),ET(4,224),SK(270,22),
     *SKB(270,22),DIS(270),DIST(270),DISO(270),DISE(6),NB(44),Y(224),
     *BJ(224),BM(224),CI(224),CJ(224),CM(224),SIGLM(224),SIS(4,224),
     *SIGT(4,224),SIGO(4,224),SIGD(4,224),IN(3),W(6,6),D(4,4),
     *B(4,6,224),DP(4,4,224),AREA(224),RBAR(224),SIGLMO(224), ND(224),
     *NFIX(44),NMIX(44),NIX(44),F(270),FO(270),Z(135),BI(224),EEP(224),
     *STY(2),NEL,NEQ,NBAND,NBR,NX,NY,NNP,MIT,STEP1,STEPO,ZETA1,ZETA2,
     *NFRIC,NSTIC,L,G,RATEF,SIGY,DIN,DOUT,ECY,IOUT,IMAX,LENGTH,E,NU
      REAL LENGTH
      INTEGER P,Q
      ZN=-LENGTH/FLOAT(NY)
      I1=1$I2=(NX+1)*NY+1$II=NX+1
      DO 50 I=I1,I2,II
      R(I)=DIN/2.
      ZN=ZN+LENGTH/FLOAT(NY)
```

```
      Z(I)=ZN
      J=I+NX-1
      DO 50 P=I,J
      Q=P+1
      R(Q)=R(P)+(DOUT-DIN)/(2.*FLOAT(NX))
50    Z(Q)=Z(P)
      DO 200 K=1,NX
      DO 200 I=1,NY
      J=I/2*2-I
      M1=(NY+1)*(I-1)+I+K -1
      M2=M1+NX
      II=NX*(I-1)+I+K-1
      NPI(M1)=II
      NPJ(M1)=II+1
      NPM(M1)=II+NX+2+J
      NPI(M2)=II-J
      NPJ(M2)=II+NX+2
      NPM(M2)=II+NX+1
200   CONTINUE
      I1=1$I2=(NX+1)*NY+1$II=NX+1
      I=0
      DO 210 N=I1,I2,II
      I=I+1
      NB(I)=N
210   NFIX(I)=10
      DO 220 N=2,II
      I=I+1
      NB(I)=N
      NFIX(I)=1
      IF(NSTIC.EQ.1)NFIX(I)=11
220   CONTINUE
      I3=I2+NX
      I4=I2+1
      DO 230 N=I4,I3
      I=I+1
      NB(I)=N
      NFIX(I)=1
      IF(NSTIC.EQ.1)NFIX(I)=11
230   CONTINUE
      I5=2*(NX+1)
      DO 240 N=I5,NFRIC,II
      I=I+1
      NB(I)=N
      NFIX(I)=10
      IF(N.EQ.NFRIC)NFIX(I)=1
      IF(NSTIC.EQ.1)NFIX(I)=11
240   CONTINUE
      I6=NFRIC+II$I7=I2-1
      DO 250 N=I6,I7,II
      I=I+1
      NB(I)=N
250   NFIX(I)=-1
      DO 410 N=1,NBR
410   NMIX(N)=NFIX(N)
      I2=NY+1
      NFIX(I2)=1$NFIX(1)=11
      IF(NSTIC.EQ.1)NFIX(I2)=11
      RETURN
```

```
      END
      SUBROUTINE FORMD1
      COMMON NPI(224),NPM(224),NPJ(224),R(135),ET(4,224),SK(270,22),
     *SKB(270,22),DIS(270),DIST(270),DISO(270),DISE(6),NB(44),Y(224),
     *BJ(224),BM(224),CI(224),CJ(224),CM(224),SIGLM(224),SIS(4,224),
     *SIGT(4,224),SIGO(4,224),SIGD(4,224),IN(3),W(6,6),D(4,4),
     *B(4,6,224),DP(4,4,224),AREA(224),RBAR(224),SIGLMO(224), ND(224),
     *NFIX(44),NMIX(44),NIX(44),F(270),FO(270),Z(135),BI(224),EEP(224),
     *STY(2),NEL,NEQ,NBAND,NBR,NX,NY,NNP,MIT,STEP1,STEPO,ZETA1,ZETA2,
     *NFRIC,NSTIC,L,G,RATEF,SIGY,DIN,DOUT,ECY,IOUT,IMAX,LENGTH,E,NU
      INTEGER P,Q
      REAL NU
      DO 92 P=1,4
      DO 92 Q=1,4
92    D(P,Q)=0.
      W1= NU
      W2=1.-W1
      W3 = 1. + W1
      W4 = 1. - 2. * W1
      W5=E/(W3*W4)
      D(1,1)=W5*W2
      D(1,2)=W5*W1
      D(1,3)=W5*W1
      D(2,1)=W5*W1
      D(2,2)=W5*W2
      D(2,3)=W5*W1
      D(3,1)=W5*W1
      D(3,2)=W5*W1
      D(3,3)=W5*W2
      D(4,4)=W5*W4/2.
      DO 150 L=1,NEL
      DO 150 M=1,4
      DO 150 N=1,4
150   DP(M,N,L)=D(M,N)
      RETURN
      END
      SUBROUTINE FORMB
      COMMON NPI(224),NPM(224),NPJ(224),R(135),ET(4,224),SK(270,22),
     *SKB(270,22),DIS(270),DIST(270),DISO(270),DISE(6),NB(44),Y(224),
     *BJ(224),BM(224),CI(224),CJ(224),CM(224),SIGLM(224),SIS(4,224),
     *SIGT(4,224),SIGO(4,224),SIGD(4,224),IN(3),W(6,6),D(4,4),
     *B(4,6,224),DP(4,4,224),AREA(224),RBAR(224),SIGLMO(224), ND(224),
     *NFIX(44),NMIX(44),NIX(44),F(270),FO(270),Z(135),BI(224),EEP(224),
     *STY(2),NEL,NEQ,NBAND,NBR,NX,NY,NNP,MIT,STEP1,STEPO,ZETA1,ZETA2,
     *NFRIC,NSTIC,L,G,RATEF,SIGY,DIN,DOUT,ECY,IOUT,IMAX,LENGTH,E,NU
      INTEGER P,Q
      DO 72  L = 1, NEL
      I = NPI (L)
      J = NPJ (L)
      M = NPM (L)
      BI (L) = Z (J) - Z (M)
      BJ (L) = Z (M) - Z (I)
      BM (L) = Z (I) - Z (J)
      CI (L) = - R (J) + R (M)
      CJ (L) = - R (M) + R (I)
      CM (L) = - R (I) + R (J)
      AREA(L)= (BJ (L) * CM (L) - BM (L) * CJ (L)) / 2.
      IF(AREA(L).LE.0.)GO TO  216
```

```
      RBAR(L) = (R (I) + R (J) + R (M)) / 3.
      W1=(2.*AREA(L))/(3.*RBAR(L))
      W2=1./(2.*AREA(L))
      DO 200 P=1,4
      DO 200 Q=1,6
200   B(P,Q,L)=0.
      B(1,1,L)=BI(L)*W2
      B(1,3,L)=BJ(L)*W2
      B(1,5,L)=BM(L)*W2
      B(2,2,L)=CI(L)*W2
      B(2,4,L)=CJ(L)*W2
      B(2,6,L)=CM(L)*W2
      B(3,1,L)=W1*W2
      B(3,3,L)=W1*W2
      B(3,5,L)=W1*W2
      B(4,1,L)=CI(L)   *W2
      B(4,2,L)=BI(L)   *W2
      B(4,3,L)=CJ(L)   *W2
      B(4,4,L)=BJ(L)    *W2
      B(4,5,L)=CM(L) *W2
      B(4,6,L)=BM(L)    *W2
72    CONTINUE
      RETURN
216   WRITE(6,100)L
100   FORMAT(33H1ZERO OR NEGATIVE AREA ELEMENT NO,I5)
      STOP
      END
      SUBROUTINE FORMK
      COMMON NPI(224),NPM(224),NPJ(224),R(135),ET(4,224),SK(270,22),
     *SKB(270,22),DIS(270),DIST(270),DISO(270),DISE(6),NB(44),Y(224),
     *BJ(224),BM(224),CI(224),CJ(224),CM(224),SIGLM(224),SIS(4,224),
     *SIGT(4,224),SIGO(4,224),SIGD(4,224),IN(3),W(6,6),D(4,4),
     *B(4,6,224),DP(4,4,224),AREA(224),RBAR(224),SIGLMO(224), ND(224),
     *NFIX(44),NMIX(44),NIX(44),F(270),FO(270),Z(135),BI(224),EEP(224),
     *STY(2),NEL,NEQ,NBAND,NBR,NX,NY,NNP,MIT,STEP1,STEPO,ZETA1,ZETA2,
     *NFRIC,NSTIC,L,G,RATEF,SIGY,DIN,DOUT,ECY,IOUT,IMAX,LENGTH,E,NU
      DIMENSION K(6,6)
      INTEGER P,Q,O
      REAL K
      DO 95 N=1,NEQ
      DO 95 M=1,NBAND
      SKB(N,M)=0.
95    SK(N,M)=0.
      DO 301 L=1,NEL
      IN(1)=NPI(L)
      IN(2)=NPJ(L)
      IN(3)=NPM(L)
      DO 93  P = 1, 4
      DO 93  Q = 1, 6
      W(P,Q)=0.
      DO 93  O = 1, 4
93    W(P,Q)=W(P,Q)+DP(P,O,L)*B(O,Q,L)
      DO 94  P = 1, 6
      DO 94  Q = 1, 6
      K (P, Q) = 0.
      DO 94  O = 1, 4
94    K(P,Q)=K(P,Q)+B(O,P,L)*W(O,Q)*2.*3.14159265*RBAR(L)*AREA(L)
      DO 96 JJ=1,3
```

```
      NROW=(IN(JJ)-1)*2
      DO 96 J=1,2
      NROW=NROW+1
      I=(JJ-1)*2+J
      DO 98 KK=1,3
      NCOL=(IN(KK)-1)*2
      DO 99 KI=1,2
      LL=(KK-1)*2+KI
      NCL=NCOL+KI+1-NROW
      IF (NCL)99,99,100
100   SK(NROW,NCL)=SK(NROW,NCL)+K(I,LL)
99    CONTINUE
98    CONTINUE
96    CONTINUE
301   CONTINUE
      DO 170 N=1,NEQ
      DO 170 M=1,NBAND
170   SKB(N,M)=SK(N,M)
      RETURN
      END
      SUBROUTINE BOUNDRY
      COMMON NPI(224),NPM(224),NPJ(224),R(135),ET(4,224),SK(270,22),
     *SKB(270,22),DIS(270),DIST(270),DISO(270),DISE(6),NB(44),Y(224),
     *BJ(224),BM(224),CI(224),CJ(224),CM(224),SIGLM(224),SIS(4,224),
     *SIGT(4,224),SIGO(4,224),SIGD(4,224),IN(3),W(6,6),D(4,4),
     *B(4,6,224),DP(4,4,224),AREA(224),RBAR(224),SIGLMO(224), ND(224),
     *NFIX(44),NMIX(44),NIX(44),F(270),FO(270),Z(135),BI(224),EEP(224),
     *STY(2),NEL,NEQ,NBAND,NBR,NX,NY,NNP,MIT,STEP1,STEPO,ZETA1,ZETA2,
     *NFRIC,NSTIC,L,G,RATEF,SIGY,DIN,DOUT,ECY,IOUT,IMAX,LENGTH,E,NU
      IP=((NX+1)*NY)*2
      STEP=STEP1
      IF(MIT.EQ.0)STEP=STEPO
      DO 106 N=1,NEQ
      DO 107 I=1,NBAND
107   SK(N,I)=SKB(N,I)
      F(N)=0.
106   DIS(N)=0.
      DO 500 N=1,NBR
      NIX(N)=NFIX(N)
      MX=10
      I=NB(N)
      NR=2*(I-1)
      DO 490 M=1,2
      ALPHA=0.
      NR=NR+1
      IC=NIX(N)/MX
      IF(IC)450,450,430
430   NCP=NR-IP
      IF(NCP)420,460,460
460   IF(NCP-NCP/2*2)420,480,420
480   ALPHA=STEP
420   F(NR)=SK(NR,1)*ALPHA*(10**8)
      SK(NR,1)=SK(NR,1)*(10**8)
      NIX(N)=NIX(N)-MX*IC
450   MX=MX/10
490   CONTINUE
500   CONTINUE
      RETURN
```

```
      END
      SUBROUTINE SOLVE
      COMMON NPI(224),NPM(224),NPJ(224),R(135),ET(4,224),SK(270,22),
     *SKB(270,22),DIS(270),DIST(270),DISO(270),DISE(6),NB(44),Y(224),
     *BJ(224),BM(224),CI(224),CJ(224),CM(224),SIGLM(224),SIS(4,224),
     *SIGT(4,224),SIGO(4,224),SIGD(4,224),IN(3),W(6,6),D(4,4),
     *B(4,6,224),DP(4,4,224),AREA(224),RBAR(224),SIGLMO(224), ND(224),
     *NFIX(44),NMIX(44),NIX(44),F(270),FO(270),Z(135),BI(224),EEP(224),
     *STY(2),NEL,NEQ,NBAND,NBR,NX,NY,NNP,MIT,STEP1,STEPO,ZETA1,ZETA2,
     *NFRIC,NSTIC,L,G,RATEF,SIGY,DIN,DOUT,ECY,IOUT,IMAX,LENGTH,E,NU
      DO 300 N=1,NEQ
      I=N
      DO 290 L=2,NBAND
      I=I+1
      IF(SK(N,L))240,290,240
240   C=SK(N,L)/SK(N,1)
      J=0
      DO 270 K=L,NBAND
      J=J+1
      IF(SK(N,K))260,270,260
260   SK(I,J)=SK(I,J)-C*SK(N,K)
270   CONTINUE
      SK(N,L)=C
      F(I)=F(I)-F(N)*C
290   CONTINUE
300   F(N)=F(N)/SK(N,1)
      N=NEQ
      DIS(N)=F(N)
350   N=N-1
      IF(N)500,500,360
360   L=N
      DO 400 K=2,NBAND
      L=L+1
      IF(L.GT.NEQ)GO TO 600
      IF(SK(N,K))370,400,370
370   DIS(N)=DIS(N)+SK(N,K)*DIS(L)
400   CONTINUE
600   DIS(N)=F(N)-DIS(N)
      GO TO 350
500   DO 800 N=1,NEQ
800   F(N)=0.
      DO 905 N=1,NBR
      NIX(N)=NFIX(N)
      J=NBAND-1
      MX=10
      I=NB(N)
      NR=2*(I-1)
      DO 950 ME=1,2
      FM=0.
      IIA=2*((NX+1)*NY+1)$IIB=NEQ-1
      NR=NR+1
      IC=NIX(N)/MX
      IF(IC)955,955,960
960   IF(NR.LT.IIA.OR.NR.EQ.IIB)DIS(NR)=0.
      M=NR
      KK=1
      DO 910 K=1,J
      KK=1+KK
```

```
      MM=NR-K
      IF(MM)915,915,920
920   C=SKB(MM,KK)
      FM=FM+C*DIS(MM)
910   CONTINUE
915   DO 925 L=2,NBAND
      M=M+1
      IF(M-NEQ)930,930,935
930   C=SKB(NR,L)
      FM=FM+C*DIS(M)
925   CONTINUE
935   F(NR)=FM+DIS(NR)*SKB(NR,1)
955   NIX(N)=NIX(N)-MX*IC
      MX=MX/10
950   CONTINUE
905   CONTINUE
      RETURN
      END
      SUBROUTINE STRAIN
      COMMON NPI(224),NPM(224),NPJ(224),R(135),ET(4,224),SK(270,22),
     *SKB(270,22),DIS(270),DIST(270),DISO(270),DISE(6),NB(44),Y(224),
     *BJ(224),BM(224),CI(224),CJ(224),CM(224),SIGLM(224),SIS(4,224),
     *SIGT(4,224),SIGO(4,224),SIGD(4,224),IN(3),W(6,6),D(4,4),
     *B(4,6,224),DP(4,4,224),AREA(224),RBAR(224),SIGLMO(224), ND(224),
     *NFIX(44),NMIX(44),NIX(44),F(270),FO(270),Z(135),BI(224),EEP(224),
     *STY(2),NEL,NEQ,NBAND,NBR,NX,NY,NNP,MIT,STEP1,STEPO,ZETA1,ZETA2,
     *NFRIC,NSTIC,L,G,RATEF,SIGY,DIN,DOUT,ECY,IOUT,IMAX,LENGTH,E,NU
      DO 276 L=1,NEL
      IN(1)=NPI(L)
      IN(2)=NPJ(L)
      IN(3)=NPM(L)
      DO 316 I=1,3
      II=2*I-1
      KK=2*IN(I)-1
      DO 316 J=1,2
      II=II+J-1
      KK=KK+J-1
316   DISE(II)=DIS (KK)
      DO 315 I=1,4
      ET(I,L)=0.
      DO 315 J=1,6
315   ET(I,L)=ET(I,L)+B(I,J,L)*DISE(J)
      DO 314 I=1,4
      SIS(I,L)=0.
      DO 314 J=1,4
314   SIS(I,L)=SIS(I,L)+DP(I,J,L)*ET(J,L)
276   CONTINUE
      RETURN
      END
      SUBROUTINE STRESS
      COMMON NPI(224),NPM(224),NPJ(224),R(135),ET(4,224),SK(270,22),
     *SKB(270,22),DIS(270),DIST(270),DISO(270),DISE(6),NB(44),Y(224),
     *BJ(224),BM(224),CI(224),CJ(224),CM(224),SIGLM(224),SIS(4,224),
     *SIGT(4,224),SIGO(4,224),SIGD(4,224),IN(3),W(6,6),D(4,4),
     *B(4,6,224),DP(4,4,224),AREA(224),RBAR(224),SIGLMO(224), ND(224),
     *NFIX(44),NMIX(44),NIX(44),F(270),FO(270),Z(135),BI(224),EEP(224),
     *STY(2),NEL,NEQ,NBAND,NBR,NX,NY,NNP,MIT,STEP1,STEPO,ZETA1,ZETA2,
     *NFRIC,NSTIC,L,G,RATEF,SIGY,DIN,DOUT,ECY,IOUT,IMAX,LENGTH,E,NU
```

```
      DO 555 L=1,NEL
      DO 321 I=1,4
321   SIGT(I,L)=SIGO(I,L)+SIS(I,L)
      SIG=(SIGT(1,L)+SIGT(2,L)+SIGT(3,L))/3.
      DO 325 I=1,3
325   SIGD(I,L)=SIGT(I,L)-SIG
      SIGD(4,L)=SIGT(4,L)
      SIGM=0.
      DO 322 I=1,3
322   SIGM=3.*SIGD(I,L)*SIGD(I,L)/2.+SIGM
      SIGM=SIGM+3.*SIGD(4,L)*SIGD(4,L)
      SIGLM(L)=SQRT(SIGM)
555   CONTINUE
      RETURN
      END
      SUBROUTINE RFACT
      COMMON NPI(224),NPM(224),NPJ(224),R(135),ET(4,224),SK(270,22),
     *SKB(270,22),DIS(270),DIST(270),DISO(270),DISE(6),NB(44),Y(224),
     *BJ(224),BM(224),CI(224),CJ(224),CM(224),SIGLM(224),SIS(4,224),
     *SIGT(4,224),SIGO(4,224),SIGD(4,224),IN(3),W(6,6),D(4,4),
     *B(4,6,224),DP(4,4,224),AREA(224),RBAR(224),SIGLMO(224), ND(224),
     *NFIX(44),NMIX(44),NIX(44),F(270),FO(270),Z(135),BI(224),EEP(224),
     *STY(2),NEL,NEQ,NBAND,NBR,NX,NY,NNP,MIT,STEP1,STEPO,ZETA1,ZETA2,
     *NFRIC,NSTIC,L,G,RATEF,SIGY,DIN,DOUT,ECY,IOUT,IMAX,LENGTH,E,NU
      DIMENSION RF(360),SY(3)
      SY(1)=STY(1)$SY(2)=STY(2)
      IF(MIT.EQ.0)GO TO 305
      RFT=1.
      DO 500 L=1,NEL
      RF(L)=1.
      IF(ND(L))580,560,570
570   IF(ND(L).GT.1)GO TO 500
      I=2
      GO TO 150
560   I=1
      GO TO 150
580   I=3
      SY(3)=Y(L)
150   J=L
      DSIG=((SIS(1,J)-SIS(2,J))**2+(SIS(2,J)-SIS(3,J))**2+
     *(SIS(1,J)-SIS(3,J))**2+6.*(SIS(4,J)**2))/2.
      DSIGLM=SIGLM(J)-SIGLMO(L)
      BR=DSIG-DSIGLM**2-2*DSIGLM*SIGLMO(L)
      DELTA=BR**2+4*DSIG*(SY(I)**2-SIGLMO(L)**2)
      RF(L)=(BR+SQRT(DELTA))/(2*DSIG)
500   CONTINUE
      DO 600 I=1,NEL
      IF(RFT.LT.RF(I))GO TO 600
      RFT=RF(I)
600   CONTINUE
      IF(RFT.GT.1.)RFT=1.
      IF(RFT.LT.0.05)RFT=0.05
      STEP=STEP1*RFT
      RATEF=RFT
      WRITE(6,900)STEP,RATEF
900   FORMAT(2E16.5)
      DO 10 N=1,NEQ
      DIS(N)=DIS(N)*RATEF
```

```
10    F(N)=F(N)*RATEF
      DO 20 L=1,NEL
      DO 277 I=1,4
      ET(I,6)=ET(I,L)*RATEF
277   SIS(I,L)=SIS(I,L)*RATEF
20    CONTINUE
      CALL STRESS
305   DO 535 L=1,NEL
      IF(SIGLM(L)/Y(L)-0.99)555,565,565
555   ND(L)=-1
      GO TO 490
565   I=1
      IF(SIGLM(L)/STY(1)-0.9)480,545,545
545   IF(SIGLM(L)/STY(2).GT.0.9)I=I+1
      IF(ND(L).EQ.I)GO TO 601
      ND(L)=I
      RFF=STY(I)/SIGLM(L)
      SIGLM(L)=STY(I)
      DO 400 J=1,4
      SIGT(J,L)=SIGT(J,L)*RFF
400   SIGD(J,L)=SIGD(J,L)*RFF
601   GO TO 490
480   ND(L)=0
490   SIGLMO(L)=SIGLM(L)
      DO 160 I=1,4
160   SIGO(I,L)=SIGT(I,L)
      IF(ND(L).LT.0)GO TO 535
      Y(L)=SIGLMO(L)
535   CONTINUE
      RETURN
      END
      SUBROUTINE FORMD2
      COMMON NPI(224),NPM(224),NPJ(224),R(135),ET(4,224),SK(270,22),
     *SKB(270,22),DIS(270),DIST(270),DISO(270),DISE(6),NB(44),Y(224),
     *BJ(224),BM(224),CI(224),CJ(224),CM(224),SIGLM(224),SIS(4,224),
     *SIGT(4,224),SIGO(4,224),SIGD(4,224),IN(3),W(6,6),D(4,4),
     *B(4,6,224),DP(4,4,224),AREA(224),RBAR(224),SIGLMO(224), ND(224),
     *NFIX(44),NMIX(44),NIX(44),F(270),FO(270),Z(135),BI(224),EEP(224),
     *STY(2),NEL,NEQ,NBAND,NBR,NX,NY,NNP,MIT,STEP1,STEPO,ZETA1,ZETA2,
     *NFRIC,NSTIC,L,G,RATEF,SIGY,DIN,DOUT,ECY,IOUT,IMAX,LENGTH,E,NU
      AA=0.$ECY=0.
      DO 310 L=1,NEL
      IF(ND(L)-1)320,315,315
315   ZETA=ZETA1
      IF(ND(L).EQ.2)ZETA=ZETA2
      SC=SIGLM(L)*(1.+ZETA/(3.*G))
      C=(3.*G)/(SIGLM(L)*SC)
      DEEP=0.
      DO 201 I=1,4
      DEEP=SIGD(I,L)*ET(I,L)/SC+DEEP
      DO 201 J=1,4
201   DP(I,J,L)=D(I,J)-C*SIGD(I,L)*SIGD(J,L)
      IF(DEEP.LT.0.)DEEP=0.
      EEP(L)=EEP(L)+DEEP
      ECY=ECY+DEEP
      AA=AA+EEP(L)
      GO TO 310
320   DO 325 N=1,4
```

```
      DO 325 M=1,4
325   DP(M,N,L)=D(M,N)
310   CONTINUE
      RETURN
      END
      SUBROUTINE UPDATE1
      COMMON NPI(224),NPM(224),NPJ(224),R(135),ET(4,224),SK(270,22),
     *SKB(270,22),DIS(270),DIST(270),DISO(270),DISE(6),NB(44),Y(224),
     *BJ(224),BM(224),CI(224),CJ(224),CM(224),SIGLM(224),SIS(4,224),
     *SIGT(4,224),SIGO(4,224),SIGD(4,224),IN(3),W(6,6),D(4,4),
     *B(4,6,224),DP(4,4,224),AREA(224),RBAR(224),SIGLMO(224), ND(224),
     *NFIX(44),NMIX(44),NIX(44),F(270),FO(270),Z(135),BI(224),EEP(224),
     *STY(2),NEL,NEQ,NBAND,NBR,NX,NY,NNP,MIT,STEP1,STEPO,ZETA1,ZETA2,
     *NFRIC,NSTIC,L,G,RATEF,SIGY,DIN,DOUT,ECY,IOUT,IMAX,LENGTH,E,NU
      IIH=2*((NX+1)*NY)+1
      IJ=NY+1
      DO 281 N=1,NEQ
      FO(N)=FO(N)+F(N)
      DISO(N)=DISO(N)+DIS(N)
281   CONTINUE
      DO 229 N=1,IJ
      I=NB(N)
      NR=2*I-1
      IF(FO(NR))750,229,229
750   NFIX(N)=-1
      IF(NR.EQ.1.OR.NR.EQ.IIH)NFIX(N)=1
      FO(NR)=0.
229   CONTINUE
      DO 800 N=1,IJ
      I=NB(N)
      NR=2*I-1
      IF(DISO(NR))700,800,800
700   NFIX(N)=NMIX(N)
      DISO(NR)=0.
800   CONTINUE
      RETURN
      END
      SUBROUTINE OUTPUT
      COMMON NPI(224),NPM(224),NPJ(224),R(135),ET(4,224),SK(270,22),
     *SKB(270,22),DIS(270),DIST(270),DISO(270),DISE(6),NB(44),Y(224),
     *BJ(224),BM(224),CI(224),CJ(224),CM(224),SIGLM(224),SIS(4,224),
     *SIGT(4,224),SIGO(4,224),SIGD(4,224),IN(3),W(6,6),D(4,4),
     *B(4,6,224),DP(4,4,224),AREA(224),RBAR(224),SIGLMO(224), ND(224),
     *NFIX(44),NMIX(44),NIX(44),F(270),FO(270),Z(135),BI(224),EEP(224),
     *STY(2),NEL,NEQ,NBAND,NBR,NX,NY,NNP,MIT,STEP1,STEPO,ZETA1,ZETA2,
     *NFRIC,NSTIC,L,G,RATEF,SIGY,DIN,DOUT,ECY,IOUT,IMAX,LENGTH,E,NU
      IF(MIT-MIT/IOUT*IOUT)60,60,50
60    ST=-DISO(260) *10.
      PSIGM=0.
      I1=NEQ-2*NX
      DO 55 I=I1,NEQ,2
55    PSIGM=PSIGM-FO(I)*9.81/(10**6)
      WRITE(6,400)MIT,PSIGM
400   FORMAT(I5,E16.5)
      WRITE(1)MIT,ST,PSIGM
      WRITE(6,237)ST
237   FORMAT(1H ////// 26H THE PUNCH DISPLACEMENT IS,E13.5,4H MM. )
      WRITE (6, 152)
```

```
152   FORMAT (1H, //////
     1         49X, 33HTHE CALCULATED NODE DISPLACEMENTS /
     2         49X, 33H---------------------------------- /////
     3          3X, 47HNODE         U                 V                 ,
     4              47HNODE         U                 V                 ,
     5              30HNODE         U                 V /)
      DO 100 I=1,45
      M1=I$M2=2*I-1$M3=2*I
      N1=I+45$N2=2*(I+45)-1$N3=2*(I+45)
      J1=I+90$J2=2*(I+90)-1$J3=2*(I+90)
      WRITE(6,154)M1,DISO(M2),DISO(M3),N1,DISO(N2),DISO(N3),J1,DISO(J2),
     *DISO(J3)
154   FORMAT (1H , I5, 2E16.5, I15, 2E16.5, I15, 2E16.5)
100   CONTINUE
      WRITE(6,158)
158   FORMAT (1H, //////
     1         49X, 33HTHE CALCULATED NODE FORCES        /
     2         49X, 33H---------------------------------- /////
     3          3X, 47HNODE        FR               FZ                ,
     4              47HNODE        FR               FZ                ,  5
     5              30HNODE        FR               FZ /)
      DO 200 I=1,45
      M1=I$M2=2*I-1$M3=2*I
      N1=I+45$N2=2*(I+45)-1$N3=2*(I+45)
      J1=I+90$J2=2*(I+90)-1$J3=2*(I+90)
      WRITE(6,156)M1,FO(M2),FO(M3),N1,FO(N2),FO(N3);J1,FO(J2),FO(J3)
156   FORMAT (1H , I5, 2E16.5, I15, 2E16.5, I15, 2E16.5)
200   CONTINUE
      WRITE (6, 181)
181   FORMAT (1H  //////
     1          4X, 44HTHE CALCULATED ELEMENT STRESS COMPONENTS AND,
     2              43H MEAN STRESS IN THE SPACE AND THE PRINCIPAL,
     3              39H STRESSES IN THE PLANE SECTION REVOLVED /
     4          4X, 44H--------------------------------------------,
     5              43H-------------------------------------------,
     6              39H----------------------------------- /////
     7          1X, 45HELEMENT      SIGMMM              ELEMENT      ,
     8              35HSIGMMM           ELEMENT      SIGMM,
     9              35HELEMENT      SIGMM                 /)
      DO 300 I=1,56
      I1=I+56$I2=I+112$I3=I+168
      WRITE(6,310)I,SIGLM(I),I1,SIGLM(I1),I2,SIGLM(I2),I3,SIGLM(I3)
310   FORMAT(1H,I5,E16.5,I15,E16.5,I15,E16.5,I15,E16.5)
300   CONTINUE
50    RETURN
      END
      SUBROUTINE UPDATE2
      COMMON NPI(224),NPM(224),NPJ(224),R(135),ET(4,224),SK(270,22),
     *SKB(270,22),DIS(270),DIST(270),DISO(270),DISE(6),NB(44),Y(224),
     *BJ(224),BM(224),CI(224),CJ(224),CM(224),SIGLM(224),SIS(4,224),
     *SIGT(4,224),SIGO(4,224),SIGD(4,224),IN(3),W(6,6),D(4,4),
     *B(4,6,224),DP(4,4,224),AREA(224),RBAR(224),SIGLMO(224), ND(224),
     *NFIX(44),NMIX(44),NIX(44),F(270),FO(270),Z(135),BI(224),EEP(224),
     *STY(2),NEL,NEQ,NBAND,NBR,NX,NY,NNP,MIT,STEP1,STEPO,ZETA1,ZETA2,
     *NFRIC,NSTIC,L,G,RATEF,SIGY,DIN,DOUT,ECY,IOUT,IMAX,LENGTH,E,NU
      DO 100 L=1,NEL
      DO 50 I=1,4
50    SIGO(I,L)=SIGT(I,L)
```

```
      SIGLMO(L)=SIGLM(L)
      IF(ND(L).LT.0)GO TO 100
      Y(L)=SIGLMO(L)
100   CONTINUE
      DO 217 N=1,NNP
      I=2*N-1
      R(N)=R(N)+DIS(I)
      I=I+1
      Z(N)=Z(N)+DIS(I)
217   CONTINUE
      IF(MIT.NE.IMAX)GO TO 5
      WRITE(1)((N,R(N),Z(N),DIST(2*N-1),DIST(2*N)),N=1,NNP)
      WRITE(1)((L,SIGLM(L),EEP(L),(SIGT(I,L),I=1,4)),L=1,NEL)
5     IF(MIT.GT.IMAX)GO TO 216
      MA=MOD(MIT,5)
      IF(MA.NE.0)GO TO 200
      CALL FORMB
200   MIT=MIT+1
      CALL FORMK
      RETURN
216   STOP
      END
```

APPENDIX 'B'

LISTING OF THE COMPUTER

PROGRAM EPLAST2

USING QUADRILATERAL ELEMENTS

(COMPRISING OF FOUR TRIANGULAR ELEMENTS)

NOMENCLATURE

Variable	Definition
NNP	Number of nodal points
NEL	Number of elements
NEQ	Number of equations
NBAND	Number of bandwidth
NBR	Number of boundary nodal points with defined conditions
NPI, NPJ, NPM	Nodal connection of elements
R, Z	Coordinates of nodal points
BI, BJ, BM CI, CJ, CM	Local coordinates of elements
AREA	Area of elements
G	Shear modulus
NU	Poison's ratio
E	Modulus of elasticity
ET	Strain-increment of elements
SK	Overall stiffness matrix
K	Element stiffness matrix
SIGY	Yield stress of elements
B	Strain displacement matrix
D	Elastic material matrix
DP	Strain-stress matrix of elements
F	Nodal points forces
FO	Nodal points total forces
SIS	Stress-increment of elements
SIGT	Stress components

SIGD	Deviatoric stress components
SIGLM	Equivalent stress-increment of elements
SIGLMO	Equivalent stress of elements
DIS	Displacement-increments of nodal points
DIST	Total nodal points displacements
NB	Boundary nodal points that their status will be set in the program
NFIX	Status vector defining the status of nodal points as suppressed or free surfaces
ND	Pointer vector for indicating state of elements
NFRIC	Number of boundary nodal points with friction forces
NSTIC	Pointer vector for imposing friction forces
DIN	Internal diameter of the specimen
DOUT	Outer diameter of the specimen
LENGTH	Height of the specimen
IMAX	Number of load increments
RATEF	Rating factor
ZETA1, ZETA2	Tangent moduli of stress-strain curve at breaking points
HGT	Unsupported height of the specimen
HPRES	Hydrostatic pressure
SM	9th and 10th equations of eliminated element stiffness matrices for recovery of internal nodes
RM	Nodal load vectors for recovery of internal nodes
SE	Condensed stiffness matrices of quadrilateral elements
RE	Nodal load vectors of quadrilateral elements
RFLANG	Flange diameter

NELQ	Number of quadrilateral elements
RQ,ZQ	Coordinates of nodal points of quadrilateral elements
NSIZE	Number of degrees of freedom
NUM	Number of degrees of freedom to be eliminated by condensation
INT	Internal nodal points
LQ	Matrix for numbering triangular elements
INQ	Matrix for numbering nodal points of quadrilateral elements

```
C**********************************************************************
C**********************************************************************
C****** PROGRAM FOR ELASTIC-PLASTIC FINITE ELEMENT ANALYSIS OF THE ******
C****** AXI-SYMMETRIC TYPE, USING QUADRILATERAL ELEMENTS.         *******
C**********************************************************************
C**********************************************************************
      PROGRAM EPLAST2(OUTPUT,TAPE1,TAPE6=OUTPUT)
      COMMON NPI(360),NPJ(360),NPM(360),R(202),Z(202),ET(4,360) ,
     *SIGT(4,360),SIGO(4,360),SIGD(4,360),SIS(4,360),SIGLM(360),EEP(360)
     *,SK(224,18),SKB(224,18),DIS(404),DISO(224),DISQ(224),DISE(10),
     *NB(42),Y(360),NFIX(42),RT(224),RTF(224),FO(224),RE(10),SM(90,2,10)
     *,RM(90,2),LQ(4,90),INT(5,90),INQ(4,90),JN(6),BI(360),BJ(360),
     *BM(360),CI(360),CJ(360),CM(360),IN(3),W(6,6),D(4,4),B(4,6,360),
     *DP(4,4,360),AREA(360),RBAR(360),ND(360),NIX(42),D2(4,4),RQ(112),
     *ZQ(112),NFRIC(8),STY(2),NMIX(42),SEP(90),SGM(90),SGT(4,90),RXO(11)
     *,RYO(11),SIGLMO(360),NC,ECY,NSTIC,FFC,HPRES,IMAX,IOUT,IROUT,STEP1,
     *NSIZE,NUM,E,NU,SIGY,HGT,HCN,DIN,DOUT,NX,NY,NBR,NBAND,NNP,NEL,NELQ,
     *NEQ,ZETA1,ZETA2,IFRIC,MIT,G,L,RATEF,NNPT,STEPO,IF1,IF2,RFLANG
      INTEGER QA,O,P,ANP,Q
      IFRIC=0
100   MIT=0
C**********************************************************************
C****** INPUT OF DATA ************************************************
      CALL INPUT
C**********************************************************************
C****** GENERATE THE MESH DATA ***************************************
      CALL  MESH
C**********************************************************************
C****** FORM THE ELASTIC PROPERTY MATRIX *****************************
      CALL FORMD1
C**********************************************************************
C****** FORM THE ELEMENT DIMENSION MATRIX ****************************
      CALL FORMB
C**********************************************************************
C****** FORM THE ELEMENT STIFFNESS MATRIX AND THE OVERALL STIFFNESS *****
C****** MATRIX.                                                    *****
      CALL FORMK
C**********************************************************************
C****** APPLY THE HYDROSTATIC PRESSURE *******************************
200    CALL HYPRES
C**********************************************************************
C****** APPLY THE BOUNDARY CONDITIONS ********************************
      CALL BOUNDRY
C**********************************************************************
C****** SOLVE THE SYSTEM OF EQUATIONS ********************************
      CALL SOLVE
C**********************************************************************
C****** COMPUTE THE STRAIN COMPONENTS ********************************
      CALL STRAIN
C**********************************************************************
C****** COMPUTE THE STRESS COMPONENTS ********************************
      CALL STRESS
C**********************************************************************
C****** EVALUATION OF THE RATING FACTOR ******************************
      CALL RFACT
C**********************************************************************
C****** APPLY THE FRICTIONAL BOUNDARY CONDITIONS *********************
      CALL FRIC
```

```
      IF(IFRIC.EQ.1)GO TO 100
     C****** FORM THE ELASTOPLASTIC PROPERTY MATRIX **************************
      CALL FORMD2
     C*************************************************************************
     C****** OUTPUT THE REQUIRED RESULTS ***********************************
      CALL OUTPUT
     C*************************************************************************
     C****** UPDATE OF BOUNDARY CONDITIONS **********************************
      CALL UPDATE
      GO TO 200
      END
      SUBROUTINE INPUT
      COMMON NPI(360),NPJ(360),NPM(360),R(202),Z(202),ET(4,360) ,
     *SIGT(4,360),SIGO(4,360),SIGD(4,360),SIS(4,360),SIGLM(360),EEP(360)
     *,SK(224,18),SKB(224,18),DIS(404),DISO(224),DISQ(224),DISE(10),
     *NB(42),Y(360),NFIX(42),RT(224),RTF(224),FO(224),RE(10),SM(90,2,10)
     *,RM(90,2),LQ(4,90),INT(5,90),INQ(4,90),JN(6),BI(360),BJ(360),
     *BM(360),CI(360),CJ(360),CM(360),IN(3),W(6,6),D(4,4),B(4,6,360),
     *DP(4,4,360),AREA(360),RBAR(360),ND(360),NIX(42),D2(4,4),RQ(112),
     *ZQ(112),NFRIC(8),STY(2),NMIX(42),SEP(90),SGM(90),SGT(4,90),RXO(11)
     *,RYO(11),SIGLMO(360),NC,ECY,NSTIC,FFC,HPRES,IMAX,IOUT,IROUT,STEP1,
     *NSIZE,NUM,E,NU,SIGY,HGT,HCN,DIN,DOUT,NX,NY,NBR,NBAND,NNP,NEL,NELQ,
     *NEQ,ZETA1,ZETA2,IFRIC,MIT,G,L,RATEF,NNPT,STEPO,IF1,IF2,RFLANG
      REAL NU
      NC=2
      FFC=0.
      HPRES=0.
      IMAX=400$IOUT=20$IROUT=200
      E=100000.$NU=0.431$SIGY=61.15$SIGY2=147.8$ZETA1=1733.$ZETA2=271.7
      STEP1=-0.003$STEPO=-0.0005
      NSTIC=0
      HGT=3.4
      HCN=1.7
      DIN=2.5$DOUT=4.4
      RFLANG=100.
      NX=6$NY=15
      NNP=112$NELQ=90
      NEL=360
      NBR=42$NBAND=18
      NSIZE=10$NUM=2
      NFRIC(1)=42$NFRIC(2)=112
      DO 100 N=3,8
  100 NFRIC(N)=NFRIC(N-1)-1
      IF (NC.EQ.1)GO TO 150
      NFRIC(1)=35$NFRIC(2)=84
  150 STY(1)=SIGY$STY(2)=SIGY2
      STEP1=STEP1*(HGT/3.4)
      G=E/(2*(1+NU))
      NEQ=NNP*2
      DO 280 L=1,NEL
      EEP(L)=0.
      SIGLMO(L)=0.
      Y(L)=1.
      ND(L)=0
      DO 280 I=1,4
      SIGO(I,L)=0.
      ET(I,L)=0.
  280 CONTINUE
```

```
      DO 214 N=1,NEQ
      DISO(N)=0.
      FO(N)=0.
      DISQ(N)=0.
      IF(IFRIC.NE.0)GO TO 214
      RTF(N)=0.
214   RT(N)=0.
      DO 923 I=1,11
      RXO(I)=0.
923   RYO(I)=0.
      HPRES=HPRES*100./9.81
      RETURN
      END
      SUBROUTINE MESH
      COMMON NPI(360),NPJ(360),NPM(360),R(202),Z(202),ET(4,360) ,
     *SIGT(4,360),SIGO(4,360),SIGD(4,360),SIS(4,360),SIGLM(360),EEP(360)
     *,SK(224,18),SKB(224,18),DIS(404),DISO(224),DISQ(224),DISE(10),
     *NB(42),Y(360),NFIX(42),RT(224),RTF(224),FO(224),RE(10),SM(90,2,10)
     *,RM(90,2),LQ(4,90),INT(5,90),INQ(4,90),JN(6),BI(360),BJ(360),
     *BM(360),CI(360),CJ(360),CM(360),IN(3),W(6,6),D(4,4),B(4,6,360),
     *DP(4,4,360),AREA(360),RBAR(360),ND(360),NIX(42),D2(4,4),RQ(112),
     *ZQ(112),NFRIC(8),STY(2),NMIX(42),SEP(90),SGM(90),SGT(4,90),RXO(11)
     *,RYO(11),SIGLMO(360),NC,ECY,NSTIC,FFC,HPRES,IMAX,IOUT,IROUT,STEP1,
     *NSIZE,NUM,E,NU,SIGY,HGT,HCN,DIN,DOUT,NX,NY,NBR,NBAND,NNP,NEL,NELQ,
     *NEQ,ZETA1,ZETA2,IFRIC,MIT,G,L,RATEF,NNPT,STEPO,IF1,IF2,RFLANG
      REAL LAS
      INTEGER P,Q
      I=NFRIC(2)/(NX+1)
      IF(NC.EQ.2)I=I-1
      III=I
      DIVR=(DOUT-DIN)/(2.*FLOAT(NX))
      NHCN=NFRIC(1)/(NX+1)-1
      NNPT=(NX*2+1)*NY+NX+1
      IS=NX+1
      DRR=0.
      DO 206 I=1,IS
      RQ(I)=DIN/2.+DRR
      I3=I+NY*(NX+1)
      I1=I+IS
      DO 216 J=I1,I3,IS
216   RQ(J)=RQ(I)
      DRR=DRR+DIVR
206   CONTINUE
      RRT1=0.5$RRT2=0.6$RRT3=0.6
      RRT2=0.8
      BB=2.*HCN*(1-RRT1)/FLOAT(NHCN)
      DIV=BB/FLOAT(NHCN-1)
      LAS=HCN*(2.-RRT1)/FLOAT(NHCN)
      DO 208 I=1,IS
      ZQ(I)=0.
      I1=I+IS$I2=I+NHCN*IS
      DD=0.
      DO 208 J=I1,I2,IS
      ZQ(J)=ZQ(J-IS)+LAS-DD
208   DD=DD+DIV
      IF(NC.EQ.2)GO TO 2210
      NM=III-NHCN-1
      BB=2.*HGT*(1-RRT2)/FLOAT(NM)
```

```
      DIV=BB/FLOAT(NM-1)
      FIR=HGT*RRT2/FLOAT(NM)
      I1=NFRIC(1)-NX$I3=NFRIC(1)
      DO 209 J=I1,I3
      DD=0.
      ZQ(J)=HCN
      J1=J+IS$J2=NM*IS+J
      DO 209 I=J1,J2,IS
      ZQ(I)=ZQ(I-IS)+FIR+DD
209   DD=DD+DIV
      GO TO 600
2210  J1=NNP-NX
      DO 211 I=J1,NNP
      ZQ(I)=2.*HCN+HGT
      DD=0.
      DO 211 J=1,NHCN
      JJ=I-J*IS
      ZQ(JJ)=ZQ(JJ+IS)-(LAS-DD)
211   DD=DD+DIV
      HTT=HGT*6./15.
      BB=HTT*(1-RRT3)*2./3.
      DIV=BB/2.
      FIR=HTT*RRT3/3.
      J1=NFRIC(1)-NX$J2=NFRIC(1)
      DO 309 I=J1,J2
      ZQ(I)=HCN
      DD=0.
      DO 309 J=1,3
      JJ=I+J*IS
      ZQ(JJ)=ZQ(JJ-IS)+FIR+DD
309   DD=DD+DIV
      J1=NFRIC(2)-NX$J2=NFRIC(2)
      DO 409 I=J1,J2
      DD=0.
      ZQ(I)=HCN+HGT
      DO 409 J=1,3
      JJ=I-J*IS
      ZQ(JJ)=ZQ(JJ+IS)-(FIR+DD)
409   DD=DD+DIV
600   Q=-1
      DO 200 K=1,NX
      Q=Q+1
      KK=K+NX*(NY-1)
      P=K
      DO 200 LL=K,KK,NX
      L=((LL-1)/NX)*(NX*4)+K
      P1=P+1$P2=P+NX+1$P3=P+(2*NX+1)$P4=P+(NX+1)*2
      L1=L+Q+NX$L2=L1+1$L3=L+NX*3
      NPI(L)=P$NPJ(L)=P1$NPM(L)=P2
      NPI(L1)=P$NPJ(L1)=P2$NPM(L1)=P3
      NPI(L2)=P2$NPJ(L2)=P1$NPM(L2)=P4
      NPI(L3)=P2$NPJ(L3)=P4$NPM(L3)=P3
      LQ(1,LL)=L
      LQ(2,LL)=L1
      LQ(3,LL)=L2
      LQ(4,LL)=L3
      INT(1,LL)=P
      INT(2,LL)=P1
```

```
      INT(3,LL)=P4
      INT(4,LL)=P3
      INT(5,LL)=P2
      JJ=(LL-1)/NX
      INQ(1,LL)=LL+JJ
      INQ(2,LL)=LL+JJ+1
      INQ(3,LL)=LL+JJ+NX+2
      INQ(4,LL)=LL+JJ+NX+1
      P=P+NX*2+1
200   CONTINUE
      DO 274 LL=1,NELQ
      DO 264 I=1,4
      Z(INT(I,LL))=ZQ(INQ(I,LL))
      R(INT(I,LL))=RQ(INQ(I,LL))
264   CONTINUE
      Z(INT(5,LL))=(ZQ(INQ(1,LL))+ZQ(INQ(3,LL)))/2.
      R(INT(5,LL))=(RQ(INQ(1,LL))+RQ(INQ(2,LL)))/2.
274   CONTINUE
      I=0
      II=NY*(NX+1)+1
      IS=NX+1
      DO 210 N=1,II,IS
      I=I+1
      NB(I)=N
      NFIX(I)=10
210   IF(NSTIC.EQ.1.AND.N.LT.NFRIC(1))NFIX(I)=11
      DO 220 N=2,IS
      I=I+1
      NB(I)=N
      NFIX(I)=1
220   IF(NSTIC.EQ.1)NFIX(I)=11
      I1=II+1$I2=II+NX
      DO 230 N=I1,I2
      I=I+1
      NB(I)=N
      IF(N.EQ.I2)IF2=I
      NFIX(I)=1
230   IF(NSTIC.EQ.1)NFIX(I)=11
      I1=(NX+1)*2$I2=II-1
      IB=NFRIC(1)
      DO 250 N=I1,IB ,IS
      I=I+1
      IF(N.EQ.IB)IF1=I
      NB(I)=N
      NFIX(I)=10
250   IF(NSTIC.EQ.1)NFIX(I)=11
      IB=IB+7
      DO 240 N=IB,I2 ,IS
      I=I+1
      IF(N.EQ.NFRIC(2))IF2=I
      NB(I)=N
240   NFIX(I)=-1
      NFIX(1)=11$NFIX(NY+1)=11$NFIX(NX+NY+1)=11$NFIX(NY+NX*2+1)=11
      NFIX(IF1)=1$NFIX(IF2)=1
      IF(NSTIC.EQ.0)GO TO 801
      NFIX(IF1)=11$NFIX(IF2)=11
801   IF(NC.EQ.1)GO TO 100
      I1=IF2+1
```

```
      I2=2*NX+2*NY
      DO 805 I=I1,I2
805   NFIX(I)=10
100   DO 410 N=1,NBR
410   NMIX(N)=NFIX(N)
      RETURN
      END
      SUBROUTINE FORMD1
      COMMON NPI(360),NPJ(360),NPM(360),R(202),Z(202),ET(4,360) ,
     *SIGT(4,360),SIGO(4,360),SIGD(4,360),SIS(4,360),SIGLM(360),EEP(360)
     *,SK(224,18),SKB(224,18),DIS(404),DISO(224),DISQ(224),DISE(10),
     *NB(42),Y(360),NFIX(42),RT(224),RTF(224),FO(224),RE(10),SM(90,2,10)
     *,RM(90,2),LQ(4,90),INT(5,90),INQ(4,90),JN(6),BI(360),BJ(360),
     *BM(360),CI(360),CJ(360),CM(360),IN(3),W(6,6),D(4,4),B(4,6,360),
     *DP(4,4,360),AREA(360),RBAR(360),ND(360),NIX(42),D2(4,4),RQ(112),
     *ZQ(112),NFRIC(8),STY(2),NMIX(42),SEP(90),SGM(90),SGT(4,90),RXO(11)
     *,RYO(11),SIGLMO(360),NC,ECY,NSTIC,FFC,HPRES,IMAX,IOUT,IROUT,STEP1,
     *NSIZE,NUM,E,NU,SIGY,HGT,HCN,DIN,DOUT,NX,NY,NBR,NBAND,NNP,NEL,NELQ,
     *NEQ,ZETA1,ZETA2,IFRIC,MIT,G,L,RATEF,NNPT,STEPO,IF1,IF2,RFLANG
      REAL NU
      INTEGER P,Q
      DO 92 P=1,4
      DO 92 Q=1,4
 92   D(P,Q)=0.
      W1= NU
      W2 = 1. - W1
      W3 = 1. + W1
      W4 = 1. - 2. * W1
      W5=E/(W3*W4)
      D(1,1)=W5*W2
      D(1,2)=W5*W1
      D(1,3)=W5*W1
      D(2,1)=W5*W1
      D(2,2)=W5*W2
      D(2,3)=W5*W1
      D(3,1)=W5*W1
      D(3,2)=W5*W1
      D(3,3)=W5*W2
      D(4,4)=W5*W4/2.
      DO 150 L=1,NEL
      DO 150 M=1,4
      DO 150 N=1,4
150   DP(M,N,L)=D(M,N)
      RETURN
      END
      SUBROUTINE FORMB
      COMMON NPI(360),NPJ(360),NPM(360),R(202),Z(202),ET(4,360) ,
     *SIGT(4,360),SIGO(4,360),SIGD(4,360),SIS(4,360),SIGLM(360),EEP(360)
     *,SK(224,18),SKB(224,18),DIS(404),DISO(224),DISQ(224),DISE(10),
     *NB(42),Y(360),NFIX(42),RT(224),RTF(224),FO(224),RE(10),SM(90,2,10)
     *,RM(90,2),LQ(4,90),INT(5,90),INQ(4,90),JN(6),BI(360),BJ(360),
     *BM(360),CI(360),CJ(360),CM(360),IN(3),W(6,6),D(4,4),B(4,6,360),
     *DP(4,4,360),AREA(360),RBAR(360),ND(360),NIX(42),D2(4,4),RQ(112),
     *ZQ(112),NFRIC(8),STY(2),NMIX(42),SEP(90),SGM(90),SGT(4,90),RXO(11)
     *,RYO(11),SIGLMO(360),NC,ECY,NSTIC,FFC,HPRES,IMAX,IOUT,IROUT,STEP1,
     *NSIZE,NUM,E,NU,SIGY,HGT,HCN,DIN,DOUT,NX,NY,NBR,NBAND,NNP,NEL,NELQ,
     *NEQ,ZETA1,ZETA2,IFRIC,MIT,G,L,RATEF,NNPT,STEPO,IF1,IF2,RFLANG
      INTEGER P,Q
```

```
      DO 72  L = 1, NEL
      I = NPI (L)
      J = NPJ (L)
      M = NPM (L)
      BI (L) = Z (J) - Z (M)
      BJ (L) = Z (M) - Z (I)
      BM (L) = Z (I) - Z (J)
      CI (L) = - R (J) + R (M)
      CJ (L) = - R (M) + R (I)
      CM (L) = - R (I) + R (J)
      AREA(L)= (BJ (L) * CM (L) - BM (L) * CJ (L)) / 2.
      IF(AREA(L).LE.0.)GO TO  216
      RBAR(L) = (R (I) + R (J) + R (M)) / 3.
      W1=(2.*AREA(L))/(3.*RBAR(L))
      W2=1./(2.*AREA(L))
      DO 200 P=1,4
      DO 200 Q=1,6
200   B(P,Q,L)=0.
      B(1,1,L)=BI(L)*W2
      B(1,3,L)=BJ(L)*W2
      B(1,5,L)=BM(L)*W2
      B(2,2,L)=CI(L)*W2
      B(2,4,L)=CJ(L)*W2
      B(2,6,L)=CM(L)*W2
      B(3,1,L)=W1*W2
      B(3,3,L)=W1*W2
      B(3,5,L)=W1*W2
      B(4,1,L)=CI(L)   *W2
      B(4,2,L)=BI(L)   *W2
      B(4,3,L)=CJ(L)   *W2
      B(4,4,L)=BJ(L)    *W2
      B(4,5,L)=CM(L) *W2
      B(4,6,L)=BM(L)    *W2
72    CONTINUE
      RETURN
216   WRITE(6,100)L
100   FORMAT(33H1ZERO OR NEGATIVE AREA ELEMENT NO,I5)
      STOP
      END
      SUBROUTINE FORMK
      COMMON NPI(360),NPJ(360),NPM(360),R(202),Z(202),ET(4,360) ,
     *SIGT(4,360),SIGO(4,360),SIGD(4,360),SIS(4,360),SIGLM(360),EEP(360)
     *,SK(224,18),SKB(224,18),DIS(404),DISO(224),DISQ(224),DISE(10),
     *NB(42),Y(360),NFIX(42),RT(224),RTF(224),FO(224),RE(10),SM(90,2,10)
     *,RM(90,2),LQ(4,90),INT(5,90),INQ(4,90),JN(6),BI(360),BJ(360),
     *BM(360),CI(360),CJ(360),CM(360),IN(3),W(6,6),D(4,4),B(4,6,360),
     *DP(4,4,360),AREA(360),RBAR(360),ND(360),NIX(42),D2(4,4),RQ(112),
     *ZQ(112),NFRIC(8),STY(2),NMIX(42),SEP(90),SGM(90),SGT(4,90),RXO(11)
     *,RYO(11),SIGLMO(360),NC,ECY,NSTIC,FFC,HPRES,IMAX,IOUT,IROUT,STEP1,
     *NSIZE,NUM,E,NU,SIGY,HGT,HCN,DIN,DOUT,NX,NY,NBR,NBAND,NNP,NEL,NELQ,
     *NEQ,ZETA1,ZETA2,IFRIC,MIT,G,L,RATEF,NNPT,STEPO,IF1,IF2,RFLANG
      DIMENSION K(6,6),SE(10,10)
      REAL K
      INTEGER P,Q,O,PP,QQ
      DO 95 N=1,NEQ
      DO 95 M=1,NBAND
      SKB(N,M)=0.
95    SK(N,M)=0.
```

```
      DO 301 LL=1,NELQ
      DO 500 P=1,NSIZE
      RE(P)=0.
      DO 500 Q=1,NSIZE
500   SE(P,Q)=0.
      DO 200 II=1,4
      L=LQ(II,LL)
      IN(1)=NPI(L)
      IN(2)=NPJ(L)
      IN(3)=NPM(L)
      DO 93  P = 1, 4
      DO 93  Q = 1, 6
      W(P,Q)=0.
      DO 93  O = 1, 4
93    W(P,Q)=W(P,Q)+DP(P,O,L)*B(O,Q,L)
      DO 94  P = 1, 6
      DO 94  Q = 1, 6
      K (P, Q) = 0.
      DO 94  O = 1, 4
94    K(P,Q)=K(P,Q)+B(O,P,L)*W(O,Q)*2.*3.14159265*RBAR(L)*AREA(L)
      DO 240 P=1,3
      DO 240 Q=1,5
      IF(IN(P)-INT(Q,LL))240,250,240
250   DO 260 J=1,2
      QQ=2*Q+J-2$PP=2*P+J-2
260   JN(PP)=QQ
240   CONTINUE
      DO 270 I=1,6
      DO 270 P=1,6
270   SE(JN(I),JN(P))=K(I,P)+SE(JN(I),JN(P) )
200   CONTINUE
      DO 20 Q=1,NUM
      KL=NSIZE-Q
      KK=KL+1
      DO 20 L=1,KL
      DUM=SE(KK,L)/SE(KK,KK)
      DO 10 M=1,L
10    SE(L,M)=SE(L,M)-SE(KK,M)*DUM
20    RE(L)=RE(L)-RE(KK)*DUM
      P=NSIZE-1
      DO 300 I=1,P
      II=I+1
      DO 300 JJ=II,NSIZE
300   SE(I,JJ)=SE(JJ,I)
      DO 40 I=1,NUM
      Q=NSIZE-NUM+I
      DO 30 J=1,NSIZE
30    SM(LL,I,J)=SE(Q,J)
40    RM(LL,I)=RE(Q)
      DO 96 JJ=1,4
      NROW=(INQ(JJ,LL)-1)*2
      DO 96 J=1,2
      NROW=NROW+1
      I=(JJ-1)*2+J
      DO 98 KK=1,4
      NCOL=(INQ(KK,LL)-1)*2
      DO 99 KI=1,2
      KL=(KK-1)*2+KI
```

```
      NCL=NCOL+KI+1-NROW
      IF (NCL)99,99,100
  100 SK(NROW,NCL)=SK(NROW,NCL)+SE(I,KL)
   99 CONTINUE
   98 CONTINUE
   96 CONTINUE
      DO 305 I=1,4
      DO 305 J=1,2
      II=2*I+J-2
      KK=2*INQ(I,LL)+J-2
  305 RT(KK)=RE(II)+RT(KK)
  301 CONTINUE
      DO 170 N=1,NEQ
      DO 170 M=1,NBAND
  170 SKB(N,M)=SK(N,M)
      RETURN
      END
      SUBROUTINE HYPRES
      COMMON NPI(360),NPJ(360),NPM(360),R(202),Z(202),ET(4,360) ,
     *SIGT(4,360),SIGO(4,360),SIGD(4,360),SIS(4,360),SIGLM(360),EEP(360)
     *,SK(224,18),SKB(224,18),DIS(404),DISO(224),DISQ(224),DISE(10),
     *NB(42),Y(360),NFIX(42),RT(224),RTF(224),FO(224),RE(10),SM(90,2,10)
     *,RM(90,2),LQ(4,90),INT(5,90),INQ(4,90),JN(6),BI(360),BJ(360),
     *BM(360),CI(360),CJ(360),CM(360),IN(3),W(6,6),D(4,4),B(4,6,360),
     *DP(4,4,360),AREA(360),RBAR(360),ND(360),NIX(42),D2(4,4),RQ(112),
     *ZQ(112),NFRIC(8),STY(2),NMIX(42),SEP(90),SGM(90),SGT(4,90),RXO(11)
     *,RYO(11),SIGLMO(360),NC,ECY,NSTIC,FFC,HPRES,IMAX,IOUT,IROUT,STEP1,
     *NSIZE,NUM,E,NU,SIGY,HGT,HCN,DIN,DOUT,NX,NY,NBR,NBAND,NNP,NEL,NELQ,
     *NEQ,ZETA1,ZETA2,IFRIC,MIT,G,L,RATEF,NNPT,STEPO,IF1,IF2,RFLANG
      DO 50 N=1,NEQ
   50 RT(N)=0.
      IF(HPRES.EQ.0.)GO TO 200
      K=0
      HFIX=0.$HFIY=0.
      II=NX+1
      IIH=NFRIC(1)$KKH=NFRIC(2)
      DO 100 N=IIH,KKH,II
  100 RT(N)=RTF(N)
      DO 9327 N=IIH,KKH,II
      K=K+1
      IF(N.EQ.KKH)GO TO 1911
      I=N+NX+1
      DZ=ZQ(I)-ZQ(N)
      DR=RQ(I)-RQ(N)
      ALPHA=ATAN(ABS(DR/DZ))
      IF(ALPHA.EQ.0.)GO TO 2391
      AES=3.1416*ABS(RQ(I)**2-RQ(N)**2)/SIN(ALPHA)
      GO TO 2830
 2391 AES=3.1416*DZ*RQ(N)*2.
 2830 HF=AES*HPRES
      HFX=-HF*COS(ALPHA)
      HFY=HF*SIN(ALPHA)
      RTF(2*N-1)=HFX/2.+HFIX-RXO(K)
      IF(DR)1010,1010,3030
 1010 HFY=-HFY
 3030 RTF(2*N)=HFY/2.+HFIY -RYO(K)
      HFIX=HFX/2.$HFIY=HFY/2.
      GO TO 2543
```

```
1911  RTF(2*N-1)=HFIX-RXO(K)$RTF(2*N)=HFIY-RYO(K)
2543  RXO(K)=RTF(2*N-1)+RXO(K)$RYO(K)=RTF(2*N)  +RYO(K)
9327  CONTINUE
200   RETURN
      END
      SUBROUTINE BOUNDRY
      COMMON NPI(360),NPJ(360),NPM(360),R(202),Z(202),ET(4,360) ,
     *SIGT(4,360),SIGO(4,360),SIGD(4,360),SIS(4,360),SIGLM(360),EEP(360)
     *,SK(224,18),SKB(224,18),DIS(404),DISO(224),DISQ(224),DISE(10),
     *NB(42),Y(360),NFIX(42),RT(224),RTF(224),FO(224),RE(10),SM(90,2,10)
     *,RM(90,2),LQ(4,90),INT(5,90),INQ(4,90),JN(6),BI(360),BJ(360),
     *BM(360),CI(360),CJ(360),CM(360),IN(3),W(6,6),D(4,4),B(4,6,360),
     *DP(4,4,360),AREA(360),RBAR(360),ND(360),NIX(42),D2(4,4),RQ(112),
     *ZQ(112),NFRIC(8),STY(2),NMIX(42),SEP(90),SGM(90),SGT(4,90),RXO(11)
     *,RYO(11),SIGLMO(360),NC,ECY,NSTIC,FFC,HPRES,IMAX,IOUT,IROUT,STEP1,
     *NSIZE,NUM,E,NU,SIGY,HGT,HCN,DIN,DOUT,NX,NY,NBR,NBAND,NNP,NEL,NELQ,
     *NEQ,ZETA1,ZETA2,IFRIC,MIT,G,L,RATEF,NNPT,STEPO,IF1,IF2,RFLANG
      STEP=STEP1
      IF(MIT.EQ.0)STEP=STEPO
      DO 106 N=1,NEQ
      RT(N)=RT(N)+RTF(N)
106   DISQ(N)=0.
      DO 500 N=1,NBR
      NIX(N)=NFIX(N)
      MX=10
      I=NB(N)
      NR=2*(I-1)
      DO 490 M=1,2
      ALPHA=0.
      NR=NR+1
      IC=NIX(N)/MX
      IF(IC)450,450,430
430   NCP=NR-(NY*(NX+1)+1)*2
      IF(NC-1)100,100,200
200   IF(NR.EQ.(NFRIC(2)*2))GO TO 480
100   IF(NCP)420,460,460
460   IF(NCP-NCP/2*2)420,480,420
480   ALPHA=STEP
420   RT(NR)=SK(NR,1)*ALPHA*(10**8)
      SK(NR,1)=SK(NR,1)*(10**8)
      NIX(N)=NIX(N)-MX*IC
450   MX=MX/10
490   CONTINUE
500   CONTINUE
      RETURN
      END
      SUBROUTINE SOLVE
      COMMON NPI(360),NPJ(360),NPM(360),R(202),Z(202),ET(4,360) ,
     *SIGT(4,360),SIGO(4,360),SIGD(4,360),SIS(4,360),SIGLM(360),EEP(360)
     *,SK(224,18),SKB(224,18),DIS(404),DISO(224),DISQ(224),DISE(10),
     *NB(42),Y(360),NFIX(42),RT(224),RTF(224),FO(224),RE(10),SM(90,2,10)
     *,RM(90,2),LQ(4,90),INT(5,90),INQ(4,90),JN(6),BI(360),BJ(360),
     *BM(360),CI(360),CJ(360),CM(360),IN(3),W(6,6),D(4,4),B(4,6,360),
     *DP(4,4,360),AREA(360),RBAR(360),ND(360),NIX(42),D2(4,4),RQ(112),
     *ZQ(112),NFRIC(8),STY(2),NMIX(42),SEP(90),SGM(90),SGT(4,90),RXO(11)
     *,RYO(11),SIGLMO(360),NC,ECY,NSTIC,FFC,HPRES,IMAX,IOUT,IROUT,STEP1,
     *NSIZE,NUM,E,NU,SIGY,HGT,HCN,DIN,DOUT,NX,NY,NBR,NBAND,NNP,NEL,NELQ,
     *NEQ,ZETA1,ZETA2,IFRIC,MIT,G,L,RATEF,NNPT,STEPO,IF1,IF2,RFLANG
```

```
      DO 300 N=1,NEQ
      I=N
      DO 290 L=2,NBAND
      I=I+1
      IF(SK(N,L))240,290,240
240   C=SK(N,L)/SK(N,1)
      J=0
      DO 270 K=L,NBAND
      J=J+1
      IF(SK(N,K))260,270,260
260   SK(I,J)=SK(I,J)-C*SK(N,K)
270   CONTINUE
      SK(N,L)=C
      RT(I)=RT(I)-C*RT(N)
290   CONTINUE
300   RT(N)=RT(N)/SK(N,1)
      N=NEQ
      DISQ(N)=RT(N)
350   N=N-1
      IF(N)500,500,360
360   L=N
      DO 400 K=2,NBAND
      L=L+1
      IF(L.GT.NEQ)GO TO 600
      IF(SK(N,K))370,400,370
370   DISQ(N)=DISQ(N)+SK(N,K)*DISQ(L)
400   CONTINUE
600   DISQ(N)=RT(N)-DISQ(N)
      GO TO 350
500   DO 800 N=1,NEQ
800   RT(N)=0.
      DO 905 N=1,NBR
      NIX(N)=NFIX(N)
      J=NBAND-1
      MX=10
      I=NB(N)
      NR=2*(I-1)
      DO 950 ME=1,2
      FM=0.
      NR=NR+1
      IC=NIX(N)/MX
      IF(IC)955,955,960
960   IF(NR.EQ.(NFRIC(2)*2))GO TO 970
      II=((NX+1)*NY+1)*2
      IF(NR.LT.II.OR.NR.EQ.(II+2*NX-1))DISQ(NR)=0.
970   M=NR
      KK=1
      DO 910 K=1,J
      KK=1+KK
      MM=NR-K
      IF(MM)915,915,920
920   C=SKB(MM,KK)
      FM=FM+C*DISQ(MM)
910   CONTINUE
915   DO 925 L=2,NBAND
      M=M+1
      IF(M-NEQ)930,930,935
930   C=SKB(NR,L)
```

```
      FM=FM+C*DISQ(M)
925   CONTINUE
935   RT(NR)=FM+DISQ(NR)*SKB(NR,1)
955   NIX(N)=NIX(N)-MX*IC
      MX=MX/10
950   CONTINUE
905   CONTINUE
      DO 105 LL=1,NELQ
      DO 110 I=1,4
      DO 110 J=1,2
      II=2*I+J-2
      KK=2*INQ(I,LL)+J-2
110   DISE(II)=DISQ(KK)
      DO 60 J=1,NUM
      JJ=NSIZE-NUM+J
      DUM=0.
      K=JJ-1
      DO 50 I=1,K
50    DUM=DUM+SM(LL,J,I)*DISE(I)
60    DISE(JJ)=(RM(LL,J)-DUM)/SM(LL,J,JJ)
      DO 115 I=1,5
      DO 115 J=1,2
      II=2*I+J-2
      KK=2*INT(I,LL)+J-2
115   DIS(KK)=DISE(II)
105   CONTINUE
      RETURN
      END
      SUBROUTINE STRAIN
      COMMON NPI(360),NPJ(360),NPM(360),R(202),Z(202),ET(4,360) ,
     *SIGT(4,360),SIGO(4,360),SIGD(4,360),SIS(4,360),SIGLM(360),EEP(360)
     *,SK(224,18),SKB(224,18),DIS(404),DISO(224),DISQ(224),DISE(10),
     *NB(42),Y(360),NFIX(42),RT(224),RTF(224),FO(224),RE(10),SM(90,2,10)
     *,RM(90,2),LQ(4,90),INT(5,90),INQ(4,90),JN(6),BI(360),BJ(360),
     *BM(360),CI(360),CJ(360),CM(360),IN(3),W(6,6),D(4,4),B(4,6,360),
     *DP(4,4,360),AREA(360),RBAR(360),ND(360),NIX(42),D2(4,4),RQ(112),
     *ZQ(112),NFRIC(8),STY(2),NMIX(42),SEP(90),SGM(90),SGT(4,90),RXO(11)
     *,RYO(11),SIGLMO(360),NC,ECY,NSTIC,FFC,HPRES,IMAX,IOUT,IROUT,STEP1,
     *NSIZE,NUM,E,NU,SIGY,HGT,HCN,DIN,DOUT,NX,NY,NBR,NBAND,NNP,NEL,NELQ,
     *NEQ,ZETA1,ZETA2,IFRIC,MIT,G,L,RATEF,NNPT,STEPO,IF1,IF2,RFLANG
      DO 276 L=1,NEL
      IN(1)=NPI(L)
      IN(2)=NPJ(L)
      IN(3)=NPM(L)
      DO 316 I=1,3
      II=2*I-1
      KK=2*IN(I)-1
      DO 316 J=1,2
      II=II+J-1
      KK=KK+J-1
316   DISE(II)=DIS (KK)
      DO 315 I=1,4
      ET(I,L)=0.
      DO 315 J=1,6
315   ET(I,L)=ET(I,L)+B(I,J,L)*DISE(J)
      DO 314 I=1,4
      SIS(I,L)=0.
      DO 314 J=1,4
```

```
314   SIS(I,L)=SIS(I,L)+DP(I,J,L)*ET(J,L)
276   CONTINUE
      RETURN
      END
      SUBROUTINE STRESS
      COMMON NPI(360),NPJ(360),NPM(360),R(202),Z(202),ET(4,360) ,
     *SIGT(4,360),SIGO(4,360),SIGD(4,360),SIS(4,360),SIGLM(360),EEP(360)
     *,SK(224,18),SKB(224,18),DIS(404),DISO(224),DISQ(224),DISE(10),
     *NB(42),Y(360),NFIX(42),RT(224),RTF(224),FO(224),RE(10),SM(90,2,10)
     *,RM(90,2),LQ(4,90),INT(5,90),INQ(4,90),JN(6),BI(360),BJ(360),
     *BM(360),CI(360),CJ(360),CM(360),IN(3),W(6,6),D(4,4),B(4,6,360),
     *DP(4,4,360),AREA(360),RBAR(360),ND(360),NIX(42),D2(4,4),RQ(112),
     *ZQ(112),NFRIC(8),STY(2),NMIX(42),SEP(90),SGM(90),SGT(4,90),RXO(11)
     *,RYO(11),SIGLMO(360),NC,ECY,NSTIC,FFC,HPRES,IMAX,IOUT,IROUT,STEP1,
     *NSIZE,NUM,E,NU,SIGY,HGT,HCN,DIN,DOUT,NX,NY,NBR,NBAND,NNP,NEL,NELQ,
     *NEQ,ZETA1,ZETA2,IFRIC,MIT,G,L,RATEF,NNPT,STEPO,IF1,IF2,RFLANG
      DO 500 L=1,NEL
      DO 321 I=1,4
321   SIGT(I,L)=SIGO(I,L)+SIS(I,L)
      SIG=(SIGT(1,L)+SIGT(2,L)+SIGT(3,L))/3.
      DO 325 I=1,3
325   SIGD(I,L)=SIGT(I,L)-SIG
      SIGD(4,L)=SIGT(4,L)
      SIGM=0.
      DO 322 I=1,3
322   SIGM=3.*SIGD(I,L)*SIGD(I,L)/2.+SIGM
      SIGM=SIGM+3.*SIGD(4,L)*SIGD(4,L)
      SIGLM(L)=SQRT(SIGM)
500   CONTINUE
      RETURN
      END
      SUBROUTINE RFACT
      COMMON NPI(360),NPJ(360),NPM(360),R(202),Z(202),ET(4,360) ,
     *SIGT(4,360),SIGO(4,360),SIGD(4,360),SIS(4,360),SIGLM(360),EEP(360)
     *,SK(224,18),SKB(224,18),DIS(404),DISO(224),DISQ(224),DISE(10),
     *NB(42),Y(360),NFIX(42),RT(224),RTF(224),FO(224),RE(10),SM(90,2,10)
     *,RM(90,2),LQ(4,90),INT(5,90),INQ(4,90),JN(6),BI(360),BJ(360),
     *BM(360),CI(360),CJ(360),CM(360),IN(3),W(6,6),D(4,4),B(4,6,360),
     *DP(4,4,360),AREA(360),RBAR(360),ND(360),NIX(42),D2(4,4),RQ(112),
     *ZQ(112),NFRIC(8),STY(2),NMIX(42),SEP(90),SGM(90),SGT(4,90),RXO(11)
     *,RYO(11),SIGLMO(360),NC,ECY,NSTIC,FFC,HPRES,IMAX,IOUT,IROUT,STEP1,
     *NSIZE,NUM,E,NU,SIGY,HGT,HCN,DIN,DOUT,NX,NY,NBR,NBAND,NNP,NEL,NELQ,
     *NEQ,ZETA1,ZETA2,IFRIC,MIT,G,L,RATEF,NNPT,STEPO,IF1,IF2,RFLANG
      DIMENSION RF(360),SY(3)
      SY(1)=STY(1)$SY(2)=STY(2)
      IF(MIT.EQ.0)GO TO 305
      RFT=1.
      DO 500 L=1,NEL
      RF(L)=1.
      IF(ND(L))580,560,570
570   IF(ND(L).GT.1)GO TO 500
      I=2
      GO TO 150
560   I=1
      GO TO 150
580   I=3
      SY(3)=Y(L)
150   J=L
```

```
      DSIG=((SIS(1,J)-SIS(2,J))**2+(SIS(2,J)-SIS(3,J))**2+
     *(SIS(1,J)-SIS(3,J))**2+6.*(SIS(4,J)**2))/2.
      DSIGLM=SIGLM(J)-SIGLMO(L)
      BR=DSIG-DSIGLM**2-2*DSIGLM*SIGLMO(L)
      DELTA=BR**2+4*DSIG*(SY(I)**2-SIGLMO(L)**2)
      RF(L)=(BR+SQRT(DELTA))/(2*DSIG)
500   CONTINUE
      DO 601 I=1,NEL
      IF(RFT.LT.RF(I))GO TO 601
      RFT=RF(I)
601   CONTINUE
      IF(RFT.GT.1.)RFT=1.
      IF(RFT.LT.0.05)RFT=0.05
      STEP=STEP1*RFT
      RATEF=RFT
      WRITE(6,900)STEP,RATEF
900   FORMAT(2E16.5)
      DO 10 N=1,NEQ
      DISQ(N)=DISQ(N)*RATEF
10    RT(N)=RT(N)*RATEF
      DO 20 L=1,NEL
      DO 277 I=1,4
      ET(I,L)=ET(I,L)*RATEF
277   SIS(I,L)=SIS(I,L)*RATEF
20    CONTINUE
      CALL STRESS
305   DO 535 L=1,NEL
      IF(SIGLM(L)/Y(L)-0.99)555,565,565
555   ND(L)=-1
      GO TO 490
565   I=1
      IF(SIGLM(L)/STY(1)-0.9)480,545,545
545   IF(SIGLM(L)/STY(2).GT.0.9)I=I+1
      IF(ND(L).EQ.I)GO TO 600
      ND(L)=I
      RFF=STY(I)/SIGLM(L)
      SIGLM(L)=STY(I)
      DO 400 J=1,4
      SIGT(J,L)=SIGT(J,L)*RFF
400   SIGD(J,L)=SIGD(J,L)*RFF
600   GO TO 490
480   ND(L)=0
490   SIGLMO(L)=SIGLM(L)
      DO 160 I=1,4
160   SIGO(I,L)=SIGT(I,L)
      IF(ND(L).LT.0)GO TO 535
      Y(L)=SIGLMO(L)
535   CONTINUE
      RETURN
      END
      SUBROUTINE FRIC
      COMMON NPI(360),NPJ(360),NPM(360),R(202),Z(202),ET(4,360) ,
     *SIGT(4,360),SIGO(4,360),SIGD(4,360),SIS(4,360),SIGLM(360),EEP(360)
     *,SK(224,18),SKB(224,18),DIS(404),DISO(224),DISQ(224),DISE(10),
     *NB(42),Y(360),NFIX(42),RT(224),RTF(224),FO(224),RE(10),SM(90,2,10)
     *,RM(90,2),LQ(4,90),INT(5,90),INQ(4,90),JN(6),BI(360),BJ(360),
     *BM(360),CI(360),CJ(360),CM(360),IN(3),W(6,6),D(4,4),B(4,6,360),
     *DP(4,4,360),AREA(360),RBAR(360),ND(360),NIX(42),D2(4,4),RQ(112),
```

```
     *ZQ(112),NFRIC(8),STY(2),NMIX(42),SEP(90),SGM(90),SGT(4,90),RXO(11)
     *,RYO(11),SIGLMO(360),NC,ECY,NSTIC,FFC,HPRES,IMAX,IOUT,IROUT,STEP1,
     *NSIZE,NUM,E,NU,SIGY,HGT,HCN,DIN,DOUT,NX,NY,NBR,NBAND,NNP,NEL,NELQ,
     *NEQ,ZETA1,ZETA2,IFRIC,MIT,G,L,RATEF,NNPT,STEPO,IF1,IF2,RFLANG
      DO 381 N=1,NEQ
      FO(N)=FO(N)+RT(N)
      DISO(N)=DISO(N)+DISQ(N)
381   CONTINUE
      IF(HPRES.EQ.0.)GO TO 200
      IIH=NFRIC(1)$KKH=NFRIC(2)$II=NX+1
      DO 1447 N=IIH,KKH,II
      FO(2*N-1)=FO(2*N-1)+RTF(2*N-1)
1447  FO(2*N)=FO(2*N)+RTF(2*N)
200   DO 281 N=1,NEQ
281   RTF(N)=0.
      IF(FFC.LT.0.)GO TO 2325
      I=NFRIC(1)
      II=2*I-1
      RTF(II)=-RT(II+1)*FFC
      FO(II)=FO(II)+RTF(II)
      IIF=NY*(NX+1)+1
      I1=IIF
      I2=I1+NX
      IFF=2*IIF-1
      IF(NC.EQ.2)GO TO 1859
      DO 2814 N=I1,I2
      I=2*N-1
      RTF(I)=RT(I+1)*FFC
      FO(I)=FO(I)+RTF(I)
2814  CONTINUE
      GO TO 2325
1859  I=NFRIC(2)
      II=2*I-1
      RTF(II)=RT(II+1)*FFC
      FO(II)=FO(II)+RTF(II)
2325  INY=NY+1
      DO 339 N=1,INY
      I=NB(N)
      NR=2*I-1
      IF(FO(NR))750,229,229
750   NFIX(N)=-1
      IF(NR.EQ.1.OR.NR.EQ.IFF)NFIX(N)=1
      IF(NR.EQ.IFF)GO TO 339
      FO(NR)=0.
      GO TO 339
229   IF(NR.LT.((NFRIC(1)-2*(NX+1))*2)) GO TO 339
      IF(FFC.LT.0.)GO TO 339
      IF(RT(NR).LT.0.)GO TO 339
      RTF(NR+1)=RT(NR)*FFC
      IF(NR.EQ.IFF)GO TO 1555
      FO(NR+1)=FO(NR+1)+RTF(NR+1)
      GO TO 339
1555  FO(NR+1)=FO(NR+1)-RTF(NR+1)
339   CONTINUE
      IFRIC=IFRIC+1
      IF(FFC.LE.0.)IFRIC=5
      RETURN
      END
```

```
      SUBROUTINE FORMD2
      COMMON NPI(360),NPJ(360),NPM(360),R(202),Z(202),ET(4,360) ,
     *SIGT(4,360),SIGO(4,360),SIGD(4,360),SIS(4,360),SIGLM(360),EEP(360)
     *,SK(224,18),SKB(224,18),DIS(404),DISO(224),DISQ(224),DISE(10),
     *NB(42),Y(360),NFIX(42),RT(224),RTF(224),FO(224),RE(10),SM(90,2,10)
     *,RM(90,2),LQ(4,90),INT(5,90),INQ(4,90),JN(6),BI(360),BJ(360),
     *BM(360),CI(360),CJ(360),CM(360),IN(3),W(6,6),D(4,4),B(4,6,360),
     *DP(4,4,360),AREA(360),RBAR(360),ND(360),NIX(42),D2(4,4),RQ(112),
     *ZQ(112),NFRIC(8),STY(2),NMIX(42),SEP(90),SGM(90),SGT(4,90),RXO(11)
     *,RYO(11),SIGLMO(360),NC,ECY,NSTIC,FFC,HPRES,IMAX,IOUT,IROUT,STEP1,
     *NSIZE,NUM,E,NU,SIGY,HGT,HCN,DIN,DOUT,NX,NY,NBR,NBAND,NNP,NEL,NELQ,
     *NEQ,ZETA1,ZETA2,IFRIC,MIT,G,L,RATEF,NNPT,STEPO,IF1,IF2,RFLANG
      AA=0.$ECY=0.
      DO 310 L=1,NEL
      IF(ND(L)-1)320,315,315
315   ZETA=ZETA1
      IF(ND(L).EQ.2)ZETA=ZETA2
      SSC=SIGLM(L)*(1.+ZETA/(3.*G))
      C=(3.*G)/(SIGLM(L)*SSC)
      DEEP=0.
      DO 201 I=1,4
      DEEP=SIGD(I,L)*ET(I,L)/SSC+DEEP
      DO 201 J=1,4
201   DP(I,J,L)=D(I,J)-C*SIGD(I,L)*SIGD(J,L)
      IF(DEEP.LT.0.)DEEP=0.
      EEP(L)=EEP(L)+DEEP
      ECY=ECY+DEEP
      AA=AA+EEP(L)
      GO TO 310
320   DO 325 N=1,4
      DO 325 M=1,4
325   DP(M,N,L)=D(M,N)
310   CONTINUE
      RETURN
      END
      SUBROUTINE OUTPUT
      COMMON NPI(360),NPJ(360),NPM(360),R(202),Z(202),ET(4,360) ,
     *SIGT(4,360),SIGO(4,360),SIGD(4,360),SIS(4,360),SIGLM(360),EEP(360)
     *,SK(224,18),SKB(224,18),DIS(404),DISO(224),DISQ(224),DISE(10),
     *NB(42),Y(360),NFIX(42),RT(224),RTF(224),FO(224),RE(10),SM(90,2,10)
     *,RM(90,2),LQ(4,90),INT(5,90),INQ(4,90),JN(6),BI(360),BJ(360),
     *BM(360),CI(360),CJ(360),CM(360),IN(3),W(6,6),D(4,4),B(4,6,360),
     *DP(4,4,360),AREA(360),RBAR(360),ND(360),NIX(42),D2(4,4),RQ(112),
     *ZQ(112),NFRIC(8),STY(2),NMIX(42),SEP(90),SGM(90),SGT(4,90),RXO(11)
     *,RYO(11),SIGLMO(360),NC,ECY,NSTIC,FFC,HPRES,IMAX,IOUT,IROUT,STEP1,
     *NSIZE,NUM,E,NU,SIGY,HGT,HCN,DIN,DOUT,NX,NY,NBR,NBAND,NNP,NEL,NELQ,
     *NEQ,ZETA1,ZETA2,IFRIC,MIT,G,L,RATEF,NNPT,STEPO,IF1,IF2,RFLANG
      INY=NY+1
      DO 800 N=1,INY
      I=NB(N)
      NR=2*I-1
      IF(DISO(NR))700,800,800
700   NFIX(N)=NMIX(N)
      DISO(NR)=0.
800   CONTINUE
      IF(MIT-MIT/IOUT*IOUT)60,60,5050
60    ST=-DISO(NEQ)*10.
      PSIGM=0.
```

```
      IF(NC.EQ.2)PSIGM=-FO(NFRIC(2)*2)*9.81/(10.**6)
      I1=NEQ-2*NX
      DO 50 I=I1,NEQ,2
50    PSIGM=PSIGM-FO(I)  *9.81/(10.**6)
      WRITE(6,400)MIT,PSIGM
400   FORMAT(I5,E16.5)
      WRITE(1)MIT,ST,PSIGM
      WRITE(6,237)ST
237   FORMAT(1H ////// 26H THE PUNCH DISPLACEMENT IS,E13.5,4H MM. )
      WRITE (6, 152)
152   FORMAT (1H, //////
     1        49X, 33HTHE CALCULATED NODE DISPLACEMENTS /
     2        49X, 33H---------------------------------- /////
     3         3X, 47HNODE         U                V                ,
     4             47HNODE         U                V                ,
     5             30HNODE         U                V /)
      IK=112
      DO 100 I=1,37
      M1=I$M2=2*I-1$M3=2*I
      N1=I+37$N2=2*N1-1$N3=2*N1
      J1=I+74$J2=2*J1-1$J3=2*J1
      WRITE(6,154)M1,DISO(M2),DISO(M3),N1,DISO(N2),DISO(N3),J1,DISO(J2),
     *DISO(J3)
154   FORMAT (1H , I5, 2E16.5, I15, 2E16.5, I15, 2E16.5)
100   CONTINUE
      WRITE(6,500)IK,DISO(2*IK-1),DISO(2*IK)
500   FORMAT(85X,I15,2E16.5)
      WRITE(6,158)
158   FORMAT (1H, //////
     1        49X, 33HTHE CALCULATED NODE FORCES        /
     2        49X, 33H---------------------------------- /////
     3         3X, 47HNODE        FR               FZ               ,
     4             47HNODE        FR               FZ               ,
     5             30HNODE        FR               FZ /)
      DO 200 I=1,37
      M1=I$M2=2*I-1$M3=2*I
      N1=I+37$N2=2*N1-1$N3=2*N1
      J1=I+74$J2=2*J1-1$J3=2*J1
      WRITE(6,156)M1,FO(M2),FO(M3),N1,FO(N2),FO(N3),J1,FO(J2),FO(J3)
156   FORMAT (1H , I5, 2E16.5, I15, 2E16.5, I15, 2E16.5)
200   CONTINUE
      WRITE(6,600)IK,FO(2*IK-1),FO(2*IK)
600   FORMAT(85X,I15,2E16.5)
      WRITE (6, 181)
181   FORMAT (1H  //////
     1         4X, 44HTHE CALCULATED ELEMENT STRESS COMPONENTS AND,
     2             43H MEAN STRESS IN THE SPACE AND THE PRINCIPAL,
     3             39H STRESSES IN THE PLANE SECTION REVOLVED /
     4         4X, 44H-------------------------------------------,
     5             43H-------------------------------------------,
     6             39H----------------------------------- /////
     7         1X, 45HELEMENT      SIGMMM             ELEMENT      ,
     8             35HSIGMMM           ELEMENT      SIGMM,
     9             35HELEMENT      SIGMM                /)
      DO 300 I=1,90
      I1=I+90$I2=I+180$I3=I+270
      WRITE(6,310)I,SIGLM(I),I1,SIGLM(I1),I2,SIGLM(I2),I3,SIGLM(I3)
310   FORMAT(1H,I5,E16.5,I15,E16.5,I15,E16.5,I15,E16.5)
```

```
300    CONTINUE
5050   RETURN
       END
       SUBROUTINE UPDATE
       COMMON NPI(360),NPJ(360),NPM(360),R(202),Z(202),ET(4,360) ,
      *SIGT(4,360),SIGO(4,360),SIGD(4,360),SIS(4,360),SIGLM(360),EEP(360)
      *,SK(224,18),SKB(224,18),DIS(404),DISO(224),DISQ(224),DISE(10),
      *NB(42),Y(360),NFIX(42),RT(224),RTF(224),FO(224),RE(10),SM(90,2,10)
      *,RM(90,2),LQ(4,90),INT(5,90),INQ(4,90),JN(6),BI(360),BJ(360),
      *BM(360),CI(360),CJ(360),CM(360),IN(3),W(6,6),D(4,4),B(4,6,360),
      *DP(4,4,360),AREA(360),RBAR(360),ND(360),NIX(42),D2(4,4),RQ(112),
      *ZQ(112),NFRIC(8),STY(2),NMIX(42),SEP(90),SGM(90),SGT(4,90),RXO(11)
      *,RYO(11),SIGLMO(360),NC,ECY,NSTIC,FFC,HPRES,IMAX,IOUT,IROUT,STEP1,
      *NSIZE,NUM,E,NU,SIGY,HGT,HCN,DIN,DOUT,NX,NY,NBR,NBAND,NNP,NEL,NELQ,
      *NEQ,ZETA1,ZETA2,IFRIC,MIT,G,L,RATEF,NNPT,STEPO,IF1,IF2,RFLANG
       DO 100 N=1,NNP
       I=2*N-1
       RQ(N)=RQ(N)+DISQ(I)
       I=I+1
       ZQ(N)=ZQ(N)+DISQ(I)
100    CONTINUE
       DO 217 N=1,NNPT
       I=2*N-1
       R(N)=R(N)+DIS(I)
       I=I+1
       Z(N)=Z(N)+DIS(I)
217    CONTINUE
       IFF=(NX+NY)*2
       IF(NC.EQ.2)IFF=IF2
       DO 923 N=IF1,IFF
       I=NB(N)
       IF(RQ(I).LT.RFLANG)GO TO 923
       NFIX(N)=10
       IF(N.EQ.IF1.OR.N.EQ.IF2)NFIX(N)=11
923    CONTINUE
       IF(NC.EQ.2)GO TO 4455
       N=NY+2*NX+1
       I=NB(N)
       IF(RQ(I).GE.RFLANG)NFIX(N)=11
4455   IF(MIT-MIT/IROUT*IROUT)5,4,5
4      WRITE(1)((N,RQ(N),ZQ(N),DISQ(2*N-1),DISQ(2*N)),N=1,NNP)
       IF(MIT.EQ.0)GO TO 5
       DO 1282 LL=1,NELQ
       SGM(LL)=0.$SEP(LL)=0.
       DO 1292 I=1,4
1292   SGT(I,LL)=0.
       DO 1383 II=1,4
       J=LQ(II,LL)
       SGM(LL)=SGM(LL)+SIGLM(J)$SEP(LL)=SEP(LL)+EEP(J)
       DO 1383 I=1,4
1383   SGT(I,LL)=SGT(I,LL)+SIGT(I,J)
       SGM(LL)=SGM(LL)/4.$SEP(LL)=SEP(LL)/4.
       DO 1452 I=1,4
1452   SGT(I,LL)=SGT(I,LL)/4.
1282   CONTINUE
       WRITE(1)((L,SGM(L),SEP(L),(SGT(I,L),I=1,4)),L=1,NELQ)
5      IF(MIT.GT.IMAX)GO TO 216
       MA=MOD(MIT,5)
```

```
      IF(MA.NE.0)GO TO 1000
      CALL FORMB
1000  MIT=MIT+1
      CALL FORMK
      RETURN
216   STOP
      END
```

REFERENCES

1. Clapp, B.P., Economics of cold extrusion. NEL report No. 195, East Kilbride, Glasgow.
2. Husson, J., Four examples in which cold forging is more economical. Metal Treatment. PP.151-154, April 1966.
3. Watkins, M.T., Some costings of cold extrusion. NEL Report No. 345, East Kilbride, Glasgow.
4. Sachs, G., Some observations on the forging of strong aluminium alloys. J. Inst. of Metals, 64, 261-283, 1939.
5. Gartner, G., Experiments on the adoption of compression with conical anvils to the hot compression of metals, (In German), Frieburger Forschungshefte, B27, May 1958. PP. 28-51.
6. Hsu, T.C., A study of the compression test for ductile materials. ASME Paper No. 67 - WA/Met-11.
7. Hsu, T.C. and A.J. Young, Plastic deformation in the compression test of pure copper. J. Strain Analysis, 2, 159-170, 1967.
8. Hill, R., A general method of analysis for metal-working processes. J. Mech. Phys. Sol., 11, 305-326, 1963.
9. Kobayashi, S. and E.G. Thomsen, Upper and lower bound solutions to axisymmetric compression and extrusion problems, Int. J. Mech. Sci. P. 127, 1965.
10. Tarnovskii, I.Y., A.A. Prozdeyev and V.B. Lyashkov, Deformation of metals during rolling, Pergamon press, New York, 1965.
11. Stech, E. and K. Schmid, The application of the upperbound principle upon upsetting and forging operations, (in German), Industrie-Anzeiger, 87, P. 1751, Sept. 1965.
12. Avitzur, B., Metal forming: Process and analysis, Mc-Graw Hill, New York, 1965.

13. Shabaik, A., Prediction of the geometry changes of the free boundary during upsetting by the slip-line theory, ASME Paper No. 70 - WA/Pro-17.

14. Kulkarni, K.M. and S. Kalpakjian, A study of barrelling as an example of free deformation in plastic working. J. Eng. for Ind., 91, 3, 743-754, Aug. 1969.

15. Lee, C.H. and T. Altan, Influence of flow stress and friction upon metal flow in upset forging of rings and cylinders. J. Eng. for Ind., 94, 775-782, Aug. 1972.

16. Nagamatsu, A., T. Murota and T. Jimma, On the non-uniform deformation of material in axially symmetric compression caused by friction. Bull. JSME, 13, 66, P. 1389, 1970.

17. Nagamatsu, A., T. Murota and T. Jimma, On the non-uniform deformation of material in axially symmetric compression caused by friction. Bull. JSME, 14, 70, 331-338, 1971.

18. Kudo, H. and K Aoi, Effect of compression test condition upon fracturing of medium carbon steel - study on cold forgability test. Part II, J. Japan Soc. Tech. Plasticity, 8, 17-27, 1967.

19. Latham, D.J. and M.G. Cockcroft, The effect of stress system on the workability of metals. NEL Report No. 216, East Kilbride, Glasgow, Feb. 1966.

20. Thomason, P.F., The use of pure aluminium as an analogue for the history of plastic flow, in studies of ductile fracture criteria in steel compression specimens. Int. J. Mech. Sci., 10, 501-518, 1968.

21. Hill, R., The mathematical theory of plasticity. Oxford Univ. Press, London, 1950.

22. Hawkyard, J.B. and W. Johnson, An analysis of the changes in geometry

of a short hollow cylinder during axial compression. Int. J. Mech. Sci., 9, 163-182, 1967.

23. Kobayashi, S., Deformation characteristics and ductile fracture of 1040 steel in simple upsetting of solid cylinders and rings. J. Eng. Ind., 92, 2, 391-399, 1970.

24. Kunogi, M., On plastic deformation of hollow cylinders under axial compression. (In Japanese). J. Sci. Res. Inst., 30, P. 63, 1954.

25. Kudo, H., Some analytical and experimental studies of axisymmetric cold forming and extrusion. Part I, Int. J. Mech. Sci., 2, P. 102, 1960.

26. Male, A.T. and V DePierre, The validity of mathematical solutions for determining friction from the ring compression test. J. Lub. Tech., 92, 389-397, 1970.

27. Sawl, G., A.T. Male and V. DePierre, A new method for the determination of material flow stress values under metal-working conditions. AFML Technical Report, AFML-TR-70-19, 1970.

28. Avitzur, B., Bulge in hollow disk forging. AFML Technical Report, AFML-TR-69-261, 1969.

29. Liu, J.Y., An analysis of the forging of a flat ring. ASME, Paper No. 70 WA/Prod-28.

30. Liu, J.Y., An analysis of deformation characteristics and interfacial friction conditions in simple upsetting of rings. J. Eng. Ind., 1149-1156, Nov. 1972.

31. Travis, F.W., The inhomogeneous deformation of hollow cylinders subjected to static and dynamic axial compression. Int. J. Pro. Res., 8, 2, 133-148, 1970.

32. Biswas, S. and F.W. Travis, Deformation patterns of annular rings of

varying geometry subjected to static and dynamic axial compression. Int. J. Mach. Tool Des. Res., 2, 235-249, 1971.

33. Male, A.T. and M.G. Cockcroft, A method for the determination of the coefficient of friction of metals under conditions of bulk plastic deformation. J. Inst. Met., 93, P. 38, 1964-1965.

34. "The production of hollow flanged components from bar stock by upsetting and extrusion". NEL Report No. 628, Jan. 1977.

35. Dieterle, K., Determination of operational limits for the upsetting of tube blanks. (In German). Ind. Anz. 97(77), 1653-1656, 1975.

36. Shah, S.N. and S. Kobayashi, Rigid-plastic analysis of cold heading by the matrix method. Proc. 15th MTDR Conf. Birmingham, 603-610, 1974.

37. Lee, C.H. and S. Kobayashi, New solutions to rigid-plastic deformation problems using a matrix method. J. Eng. Ind., 95, 865-873, Aug. 1973.

38. Smith, T.B., Design for cold heading. Wire and wire products, 35, P. 1113, 1960.

39. Townend, G.H. and F.B. Wilson, Cold heading and upsetting processes. Proc. Conf. Tech. Eng. Manu., Inst. Mech. Eng., London, 135-140, 1958.

40. Johnson, W. and P.B. Mellor, Engineering Plasticity. Van Norstrand Reinhold Company, London, 1973.

41. Male, A.T., Variations in friction coefficients of metals during compressive deformation. J. Inst. Metals, 94, 121-125, 1966.

42. Jones, M.G., R. Davies and A. Singh, Some high-speed cold forging operations. Proc. 9th Int. Mach. Tool Des. Res. Conf., Pergamon Press, 1968.

43. Cogan, R.M., Hydrodynamic forming. Machinery, 1147-1151, Nov. 1964.

44. Cogan, R.M. and G.L. Campbell, Forging against back pressure. Amer. Mach., 107, 105-107, 1963.

45. Alexander, J.M. and B. Lengyel, On the cold extrusion of flanges against high hydrostatic pressure. J. Inst. Metals, 93, 137-145, 1965.

46. Fuchs, F.J., Production metal forming with hydrostatic pressures. Proc. Metals Eng. & Prod. Eng. Conf., Berkeley, California, Paper 65-PROD-17, June 1965.

47. "Some aspects of the cold extrusion of steel". NEL Report No. 196, East Kilbride, Glasgow, Oct. 1965.

48. "An investigation of the injection upsetting of six steels". NEL Report No. 494, East Kilbride, Glasgow, Dec. 1971.

49. Milner, P.R., The injection upsetting process. PhD Thesis, Univ. of Leeds, 1971.

50. Turner, J.L., R.W. Clough, H.C. Martin and L.J. Topp, Stiffness and deflection analysis of complex structures. J. Aero. Sci., 23, 9, 805-825, Sept. 1956.

51. Mendelson, A. and S.S. Manson, Practical solution of plastic deformation problems in the elastic-plastic range. NASA TR-28, 1959.

52. Gallagher, R.H., J. Padlog and P.P. Bijlaard, Stress analysis of heated complex shapes. ARS Journal, 32, 700-707, 1962.

53. Zienkiewicz, O.C., S. Valliappan and I.P. King, Elasto-plastic solutions of engineering problems. Initial stress, finite element approach. J. Inst. Num. Meth. Eng., 1, 75-100, 1969.

54. Nayak, G.C. and O.C. Zienkiewicz, Elastic-plastic stress analysis. Int. J. Num. Meth., 5, 113-135, 1972.

55. Pope, G.G., A discrete element method for the analysis of plane elasto-plastic stress problems. Royal Aircraft Est., TR-65028, 1965.

56. Marcal, P.V., The elastic-plastic straining of some shells of revolution with special reference to expansion belows. PhD Thesis, Univ. of London, 1965.

57. Marcal, P.V. and C.E. Turner, Numerical analysis of the elastic-plastic behaviour of axisymmetrically loaded shells of revolution. J. Mech. Eng. Sci., 5, 232-237, 1963.

58. Marcal, P.V., A stiffness method for elastic-plastic problems. Int. J. Mech. Sci., 7, 229-238, 1965.

59. Marcal, P.V. and I.P. King, Elastic-plastic analysis of two dimensional stress systems by the finite element method. Int. J. Mech. Sci., 9, 143-155, 1967.

60. Marcal, P.V., Elastic-plastic analysis of pressure vessel components. Proc. 1st Pressure Vessel and Piping Conf. ASME, Sept. 1968.

61. Yamada, Y., N. Yoshimura and T. Sakurai, Plastic stress-strain matrix and its application for the solution of elastic-plastic problems by the finite element method. Int. J. Mech. Sci., 10, 343-354, 1968.

62. Akyuz, F.A. and J.E. Merwin, Solution of non-linear problems of elasto-plasticity by the finite element method. AIAA Journal, 6, 1825-1831, 1968.

63. Lee, C.H. and S. Kobayashi, Elasto-plastic analysis of plane strain and axisymmetric flat punch indentation by the finite element method. Int. J. Mech. Sci., 12, 349-370, 1970.

64. Lee, C.H. and S. Kobayashi, Analysis of axisymmetric upsetting and plane strain side-pressing of solid cylinders by the finite element method. J. Eng. Ind., 93, 445-454, 1971.

65. Argyris, J.H. and D.W. Scharpf, Methods of elasto-plastic analysis. ZAMP, 23, 517-552, 1972.

66. Nagamatsu, A., T. Murota and T. Jimma, On the non-uniform deformation of block in plane strain caused by friction. Bulletin of the JSME, 13, 1385-1402, 1970.

67. Nagamatsu, A., T. Murota and T. Jimma, On the non-uniform deformation of material in axially symmetric compression caused by friction. Bulletin of the JSME, 14, 331-347, 1971.

68. Nagamatsu, A., T. Murota and T. Jimma, On the non-uniform deformation of material in axially symmetric compression caused by friction. Bulletin of the JSME, 89, 1339-1347, 1972.

69. Iwata, K., K. Osakada and S. Fujino, Analysis of hydrostatic extrusion by the finite element method. J. Eng. Ind., 64, 697-703, 1972.

70. Turner, M.J., E.H. Dill, H.C. Martin and R.J. Melosh, Large deflection analysis of complex structures subjected to heating and external loads. J. Aero. Space Sci., 27, 97-106, 1960.

71. Mallett, R.H. and P.V. Marcal, Finite element analysis of non-linear structures. J. Struct. Div. of ASCE, 94, 2081-2108, 1968.

72. Felippa, C.A., Refined finite element analysis of linear and non-linear two-dimensional structures. PhD Thesis, Univ. of California, 1966.

73. Kapur, K.K. and B.J. Hartz, Stability of plates using the finite element method. J. Eng. Mech. Div. ASCE, 92, 177-195, 1966.

74. Kawai, T., Finite element analysis of the geometrically non-linear

problems of elastic plates. USA - Japan Seminar on Matrix Methods of Structural Analysis and Design, Tokyo, 383-414, 1969.

75. Oden, J.T., A general theory of finite elements. Int. J. Num. Meth., 1, 205-221, 1969. (Part I).

76. Oden, J.T., A general theory of finite elements. Int. J. Num. Meth., 1, 247-259, 1969. (Part II).

77. Pian, P.H.H. and Pin Tong, Basis of finite element methods for solid continua. Int. J. Num. Meth., 1, 3-28, 1968.

78. Zienkiewicz, O.C. and P.N. Godbole, Flow of plastic and visco-plastic solids with special reference to extrusion and forming processes. Int. J. Num. Meth., 8, 3-16, 1974.

79. Gotoh, M., A finite element analysis of general deformation of sheet metals. Int. J. Num. Meth., 8, 731-741, 1974.

80. Hofmeister, L.D., G.A. Greenbaum and D.A. Evensen, Large strain elasto-plastic finite element analysis. J. AIAA, 9, 1248-1254, 1971.

81. Marcal, P.V., Finite element analysis of combined problems of non-linear material and geometric behaviour. Proc. ASME Joint Computer Conf. on Computational approach to Applied Mechanics, 133-149, 1969.

82. Stricklin, J.A. and W.E. Haisler, Evaluation of solution procedures for material and/or geometrically non-linear structural analysis. AIAA Journal, 292-299, 1972.

83. Hibitt, H.D., P.V. Marcal and J.R. Rice, A finite element formulation for problems of large strain and large displacement. Int. J. Sols. Structs., 6, 1068-1086, 1970.

84. Needleman, A., A numerical study of necking in circular cylindrical bars. J. Mech. Phys. Sols., 20, 111-127, 1972.

85. Hill, R., Some basic principles in the mechanics of solids without a natural time. J. Mech. Phys. Sols., 7, P. 209, 1959.

86. Felippa, C.A. and P. Sharifi, Computer implementation of non-linear structural problems. (Edited by R.E. Hartung), ASME, P. 31, 1973, New York.

87. McMeeking, R.M. and J.R. Rice, Finite element formulation for problems of large elastic-plastic deformation. Int. J. Sols. Structs., 11, 601-616, 1975.

88. Gunesekara, J.S., Matrix analysis of large deformation elastic-plastic problems. PhD Thesis, Univ. of London, 1972.

89. Blass, A., A finite element approach in metal working and its application to the radial upsetting process. PhD Thesis, Univ. of London, 1976.

90. Gordon, J.L. and A.S. Weinstein, A finite element analysis of the plane-strain drawing problem. Second NAMR Conf., Univ. of Wisconsin, Madison, 194-208, 1974.

91. Odell, E.J., A study of wall ironing by the finite element technique. J. Eng. Ind., 100, 31-36, 1978.

92. Price, J.W.H., A study of die-less drawing and isothermal forging. PhD Thesis, Univ. of London, 1977.

93. Matsumoto, H., S.I. Oh and S Kobayashi, A note on the matrix-method for rigid-plastic analysis of ring compression. Proc. 18th Int. MTDR Conf., Imperial College, London, 1977.

94. Hartley, P., Metal-flow and homogeneity in extrusion forging. PhD Thesis, Univ. of Birmingham, 1979.

95. Sharman, F.W., Electricity Council Report, RS81, 1975.

96. Zienkiewicz, O.C., P.C. Jain and E. Onate, Flow of solids during forging and extrusion: some aspects of numerical solutions. Int. J. Sols. Structs., 14, P. 15, 1978.

97. Hartley, P., C.E.N. Sturges and G.W. Rowe, Friction in finite element analysis of metal forming process. J. Inst. Mech. Sci., 21, 301-311, 1979.

98. Johnson, W., Overestimates of loads for some two dimensional forging operations. Third U.S. National Congress on Applied Mechanics, P. 571, 1958.

99. Johnson, W., Estimation of upper-bound loads for extrusion and coining operations. Proc. Int. Mech. Engrs., London, 173, P. 61, 1959.

100. Kudo, H., An upper-bound approach to plane-strain forging and extrusion. Int. J. Mech. Sci., 1, 57-83, 1960. (Part I).

101. Kudo, H., An upper-bound approach to plane-strain forging and extrusion. Int. J. Mech. Sci., 1, 229-252, 1960. (Part II).

102. Kudo, H., Some analytical and experimental studies of axi-symmetric cold forging and extrusion. Int. J. Mech. Sci., 2, 102-127, 1960. (Part I).

103. Kudo, H., Some analytical and experimental studies of axi-symmetric cold forging and extrusion. Int. J. Mech. Sci., 3, 91-117, 1961. (Part II).

104. Kobayashi, S., Upper-bound solutions of axi-symmetric forming problems. J. Eng. Ind., 122-126, 1964. (Part I).

105. Halling, J. and L.A. Mitchell, An upper-bound solution for axi-symmetric extrusion. Int. J. Mech. Sci., 7, 277-295, 1965.

106. Lambert, E.R., H.S. Mehta and S. Kobayashi, A new upper-bound method for analysis of some steady-state plastic deformation processes. J. Eng. Ind., 91, 731-742, 1969.

107. Shabaik, A., T. Altan and E.G. Thomsen, Investigation of the application of visioplasticity methods of analysis to metal deformation

processing. Final report prepared for the Navy, Bureau of Naval Weapons, 1965.

108. Lange, K. and E. Steck, Some recent results of investigations in rod, hooker and can extrusion and upsetting. Sheet Metal Ind., 43, P. 205, 1966.

109. Parsons, B., P.R. Milner and B.N. Cole, Study of injection upsetting of metals. J. Mech. Eng. Sci., 15, 410-421, 1973.

110. NAG Library Subroutine E01LCFF, Computer Centre, Imperial College of Science and Technology.

111. Pugh, H.Ll.D. and D.A. Gunn, Symposium on the Physics and Chemistry of High Pressures. Soc. Chem. Ind., London, 157-162, 1963.

112. Pugh, H.Ll.D. and D. Green, Progress report on the behaviour of materials under hydrostatic pressure. MERL Report No. 147, Nat. Eng. Lab., East Kilbride, Glasgow, 1958.

113. Butler, L.H., A method of continuous wire drawing aided by externally generated hydrostatic oil pressure. Metallurgical Engineering Note. J. Inst. Metals, 93, P. 123, 1964.

114. Bridgman, P.W., Studies in large plastic flow of fracture. McGraw-Hill, London and New York, 1952.

115. Crossland, B. and W.H. Dearden, The effect of fluid pressure on the shear properties of metals, Proc. Inst. Mech. Engs., 172, 805-820, 1958.